A Study of Mineralogical, Geochemical and Geochronological Characteristics and Ore Genesis in Phuoc Son Gold Deposit Area, Central Vietnam

by

Takayuki Manaka

B.Sc. (Hons.), MSc (Exploration Geoscience)

A thesis submitted in fulfilment of the requirements for the

degree of Doctor of Philosophy

CODES ARC Centre of Excellence in Ore Deposits

University of Tasmania (UTAS), Australia

January 2014

Declaration

I declare that this thesis does not contain material which has been accepted for the award of any other degree or diploma in any university; and to the best of my knowledge contains no material previously published or written by any other person, except where due reference is made in the text of the thesis.

Takayuki Manaka

_____

ABSTRACT

The Phuoc Son gold deposit area is located approximately 90 kilometres southwest of Danang, the capital city of central Vietnam. The deposit area occurs along the NW-SE trending Truong Son Fold Belt (TSFB), which extends from northern Laos to central Vietnam. The TSFB consists predominantly of Permian-Triassic igneous and metamorphic rocks. The Phuoc Son area comprises medium- to high-grade metamorphic rocks such as schist and gneiss with several intrusive phases. A large body of ultramafic units (i.e., metagabbro) are also exposed in the deposit area, as it occurs on the Phuoc Son-Tam Ky Suture Zone. The location is near the intersection of the regional N-S trending Po Ko and NW-SE trending Kham Duc-Tra Bong Faults which formed along the western and northern margins of the Kontum high-grade metamorphic core complex.

The Bai Dat and Bai Go deposits are the two major gold occurrences in Phuoc Son and gold resources at the two orebodies are currently delineated to be 3.1Mt @ 6.69 g/t Au for approximate 670,000 ounces of gold. The deposits are hosted predominantly by carbonaceous schist and phyllite with minor metagabbro units, and felsic intrusive units occur typically as dykes/sills. A LA-ICPMS zircon U-Pb geochronological study indicated that there were two magmatic-metamorphic events during the Ordovician-Silurian (490–430 Ma) and Permian-Triassic (270–220 Ma) periods at Phuoc Son and the surrounding area. Geochemical characteristics of the intrusive units indicate that the units are calc-alkaline with I-type affinity. All of the intrusive units of the Permo-Triassic period can be classified as ilmenite-series and one of the units (i.e., dacitic porphyry) shows a distinct adakitic signature.

Gold occurs in quartz-sulphide veins at the Bai Dat and Bai Go deposits. The veins generally trend N-S and dip moderately to the west (30–60°). Detailed mineralogical and paragenetic studies indicated that the main mineralisation events of the Bai Dat and Bai Go deposits are divided into the early sphalerite-rich and the late galena-rich stages. Of these, the major gold mineralisation stage is confined to the late galena-rich stage based on mineralogy and positive correlation of gold and lead in assay data. Pyritisation is a distinct alteration and is extensively formed in the host carbonaceous schist/phyllite units at the selvage of the quartz-sulphide veins. Gold occurs as electrums, associated with sulphide minerals including pyrite, pyrrhotite, sphalerite, galena and chalcopyrite. Gangue minerals such as biotite, muscovite,

carbonate, serpentinite and sericite are also commonly associated with the sulphide minerals in the mineralised veins.

The vein-located electrums at Bai Dat and Bai Go have fineness ranges of 500–800 and 350–1000, respectively. The pyrite trace element analysis revealed that the pyrite minerals in the mineralised veins and host rocks yielded less than 10 ppm Au, indicating that no refractory gold occurs in the structure of the pyrite minerals. FeS contents of the vein-located sphalerite in the early and late mineralisation stages ranged from 5.2 to 7.2 and 12.3 to 15.2 mole %. The estimated pressure from the sphalerite geobarometry of the late mineralisation stage at Bai Dat and Bai Go yielded a range of 6.4–7.5 and 5.3–5.8 kbar.

The sulphur isotope data of sulphide minerals in the mineralised veins show a well-constrained peak between -2 to 0 and 0 to +2 ‰ for Bai Dat and Bai Go. Although these ranges are considered to be a typical magmatic affinity, comparisons with data from other deposits in Phuoc Son indicate that sulphur isotopes systematically decreased towards the Bai Dat-Bai Go area from the Round Hill intrusion-hosted deposit and Khe Rin skarn deposit at the northwestern part of the Phuoc Son area. Hence, input of sulphur sourced from the host rocks (i.e., carbonaceous units) into the ore fluids is most likely to explain the sulphur isotope data. The carbon and oxygen isotope results of the vein-located carbonate minerals show wide ranges from -24 to +2 and +2 to +29 ‰ respectively, and plots of the data are linearly connected between the marble and organic carbon fields, suggesting that carbon and oxygen were mainly sourced from the country rocks. The lead isotopic data of galena imply that the metals were mainly derived from a crustal source and are comparable to the Bong Mieu deposit which occurs at 70 kilometres east of Phuoc Son and is associated with the late stage magmatism of the TSFB (255–230 Ma).

Various types of fluid inclusion were identified in the euhedral quartz crystals from the quartz-sulphide veins at Bai Dat and Bai Go, involving one-, two- and multi-phase inclusions. The carbonic two- and three-phase inclusions are the most common type. Minor daughter crystal-bearing inclusions are also recognised. Microthermometric analyses of the primary inclusions at Bai Dat and Bai Go yielded homogenisation temperatures ranging from 220 to >500 and 240 to >500 ºC, and salinity values from 0.5 to 45 and 0.5 to 16 NaCl wt.% equiv., respectively. Laser Raman Spectroscopic study detected that CO_2 gas is predominant with considerable N_2 and CH_4 gasses in the main ore zones at Bai Dat and Bai Go. Daughter crystals such as muscovite, calcite, dolomite and graphite were found. A depth range of 3.1–5.6 kbar was estimated using microthermometric data of the three-phase carbonic inclusions. The combined fluid inclusion data indicated the ore fluids at Bai Dat and Bai Go were

composed of mixed magmatic and metamorphic fluids, and the ore fluids had reduced and near neutral pH. Fluid inclusion data suggest that the gold was predominantly transported by bisulphide complexes and precipitated due to mixing of fluids and wall rock interaction at the Bai Dat and Bai Go deposits.

The current integrated field, geochronological, geochemical, mineralogy, paragenesis, isotopic and fluid inclusion data indicated that the gold mineralisation characteristics at the Bai Dat and Bai Go deposits share many similarities to those of the orogenic gold deposits in the Yilgarn Craton of Australia and intrusion-related gold deposits in Alaska. On the regional Phuoc Son area-scale, the deposits have characteristics similar to the Alaskan intrusion-related gold systems (e.g., tectonic setting, recognition of intrusion and metal zonation), whereas they are comparable to those of the orogenic gold deposits in Yilgarn Craton on a local-scale (e.g., alteration phase and mechanism of gold precipitation). The Bai Dat and Bai Go deposits may represent the distal part of a large (>several kilometres in lateral extent) intrusion-related gold system, in which the intrusion centre is present at the Khe Rin-Round Hill area in the northwestern part of the Phuoc Son area. The host rocks at Bai Dat and Bai Go (i.e., carbonaceous schist/phyllite and metagabbro) are considered to have played an important role, both physically (i.e., fragile nature) and chemically (i.e., wall rock reaction) on the deposit-scale, to promote gold precipitation at these deposits. The deposits are constrained to have formed during the Triassic (250–200 Ma) in a deep (c.a. 15 kilometres) environment. It is concluded that the genesis of the gold mineralisation at the Phuoc Son deposit area is linked to magmatism at the waning stage of the regional metamorphism of TSFB during the Indochina Orogeny, which occurred as a result of the collision between the Indochina and South China Terranes during the Permo-Triassic period.

ACKNOWLEDGEMENTS

Firstly, I would like to thank my supervisor, Professor Khin Zaw, for providing me with a great project and the opportunity to undertake research and fieldwork in Vietnam. Khin Zaw has given me motivation, advice, constructive criticism and full logistical support throughout my PhD program at CODES. I would also like to thank my co-supervisor, Dr Sebastien Meffre, for his helpful comments and for reviewing drafts of my thesis. This study was undertaken with financial support from Khin Zaw's Ore Deposits of SE Asia Project Grant and Olympus Pacific Minerals Inc. (now Besra Gold Inc.).

Secondly, I would like to thank Olympus Pacific Minerals Inc. for giving me access to my field areas and for providing support during my fieldwork in Vietnam. Olympus geologists including Rod Murfitt, Le Van Hai, Michael Banks, Ba Hung, Duc Hung, Tuong Buivan, Dinh and Khoa helped me to become familiar with the general geological setting in my study area. I also thank the local Vietnamese staff of Phuoc Son Gold Company for their help and assistance.

I wish to express my sincere thanks to Professor Ross Large, Professor Bruce Gemmell and Professor Jocelyn McPhie who have coordinated my PhD program since 2009.

Thank you to researchers who were willing to talk through all kinds of issues while I worked through this project - Hai Tran Thanh, Jacqueline Halpin, Somboon Khositanont, Clive Burrett, Kenzo Sanematsu, Andri Subandrio and Professor Tony Crawford - those discussions were extremely helpful.

Many thanks go to the staff at CODES, University of Tasmania, including Sarah Gilbert, Simon Stephens, Alexander Cuison, Katie McGoldrick, Phil Robinson, Ian Little, Jay Thompson, Peter Cornish, Isabella (Izzy) von Lichtan, Mazlinfalina Mohd Zin, Christian McKenzie, Keith Dobson, Karen Mollross, Helen Scott, Christine Higgins, Deborah Macklin, Nilar Hlaing and Rose Pongratz. Thanks to Christine Cook, Keith Harris, Karsten Goemann and Sandrin Feig at the Central Science Laboratory for helping with analyses.

My colleagues at CODES provided valuable support and encouragement during my study. I offer my sincere thanks to Abhisit Salam (Masoe), Chun Kit Lai, Mathew Ageneau, Lindsey

Clark, Andrea Agangi, Teera Kamvong, Bronto Sutopo, Jeff Steadman, Charles Makoundi, Yungu Lim, Basril Basori, Xuan Truong Le, Wojciech Zukowski, Nick Yansen, Victor Galvan, Liezl Cuison, Sang Dinh, Fiona Best, Gisela Cobanas, Pedro Fonseca, Nathan Fox, Dan Gregory, Jian Xiang Guan, Carlos Jimenez, Martin Jutzeler, Roisin Kyne, Alexey Lygan, Brendan McGee, Natalie Bonnici, Chris Large, Anite Parbhakar-Fox, Richelle Pascual, Daniele Redi, Marc Rinne, Ralf Schaa, Selina Wu, Lejun Zhang, Quiyue Huang, Ralf Schaa, David Hutchison, Kian Chee Goh and Joe Knight (Ko Sit Aung).

Finally, I would like to give special thanks to my family in Japan, who provided moral support for my studies in Hobart. I couldn't have finished my study at CODES without their kind contribution.

CONTENTS

Page

Chapter 1 Introduction

1.1. Preamble…… 1

1.2. Location and access…… 1

1.3. Exploration and mining history…… 5

1.4. Previous studies…… 6

1.5. Scope of research…… 6

1.6. Methodology…… 7

1.6.1. Field investigation…… 7

1.6.2. Laboratory work…… 7

1.7. Thesis structure…… 8

Chapter 2 Regional Geology and Metallogenic Setting

2.1. Introduction…… 10

2.2. Tectonic evolution of mainland SE Asia…… 10

2.2.1. Rifting…… 10

2.2.2. Drifting…… 12

2.2.3. Amalgamation…… 12

2.2.4. Post-amalgamation…… 14

2.3. Geological setting and ore deposits of Indochina Terrane…… 14

2.3.1. Early Palaeozoic tectonic history and ore deposits…… 14

2.3.2. Late Palaeozoic-Early Mesozoic tectonic history and ore deposits…… 16

2.3.3. Late Mesozoic tectonic history and ore deposits…… 20

2.4. Geology and copper-gold deposits of Truong Son Fold Belt…… 20

2.4.1. Introduction…… 20

2.4.2. Magmatism and metamorphism of the TSFB…… 20

2.4.3. Cu-Au Mineral Districts of the TSFB…… 21

2.4.3.1. Phu Bia Cu-Au District…… 21

2.4.3.2. Sepon Au-Cu District…… 26

2.4.3.3. Central Vietnam Au District……. 29
2.5. Summary…….…….. 34

Chapter 3 Deposit Geology, Geochronology and Geochemistry

3.1. Introduction……..…….……...…….. 35
3.2. Geology of the Phuoc Son area…..……. 35
3.2.1. Meta-volcano-sedimentary sequence..……... 37
3.2.1.1. Schist/phyllite…...……...……... 37
3.2.1.2. Metabasite…….…….……... 40
3.2.1.3. Amphibolite……...……..…….. 40
3.2.1.4. Marble…….……..……. 41
3.2.1.5. Hornfels…….…….. 41
3.2.2. Intrusive units.…….…….. 42
3.2.2.1. Metagabbro……. 44
3.2.2.2. Round Hill granite……... 44
3.2.2.3. Foliated dacitic porphyry..…….. 46
3.2.2.4. Syenite……....……..…….. 46
3.2.2.5. Granite dyke…….……... 47
3.2.2.6. Khe Rin granite…….. 48
3.2.2.7. Andesitic dyke……... 50
3.2.2.8. Diorite……. 50
3.2.2.9. Dacitic porphyry……. 50
3.2.3. Gneissic rocks of Kham Duc Formation……. 50
3.3. Structure……..……... 54
3.3.1. Introduction……. 54
3.3.2. Faults…….……. 54
3.3.3. Folds……..……. 56
3.3.4. Local structural setting at Bai Dat ……. 56
3.4. Geochronology..……...……... 60
3.4.1. Introduction……..……... 60
3.4.2. Analytical methods……...…….. 60
3.4.3. Zircon petrography…..……... 61

3.4.4. Results……...…… 61
3.5. Geochemistry……...……... 66
3.5.1. Introduction.……...……... 66
3.5.2. Analytical methods.…...…… 67
3.5.3. Geochemical results…..…….. 67
3.6. Magnetic susceptibility…..……...……... 73
3.6.1. Introduction…..……..……. 73
3.6.2. Analytical methods…..……... 75
3.6.3. Results……...…….. 75
3.7. Discussion……... 76
3.7.1. Ordovician-Silurian magmatism and metamorphism……. 77
3.7.2. Permian-Triassic magmatism and metamorphism…….……. 77
3.7.3. Adakitic magmatism……... 79
3.8. Summary……. 80

Chapter 4 Texture, Mineralogy and Paragenesis

4.1. Introduction……...……... 81
4.2. Mineralisation and paragenesis……..…….. 81
4.2.1. Methods of study……..……..……... 81
4.2.2. Mineralisation and paragenesis of the at Bai Dat and Bai Go deposit…….…….….. 83
4.2.2.1. Pre-mineralisation regional metamorphism stage……... 83
4.2.2.2. Early main mineralisation stage…….…… 83
4.2.2.3. Late main mineralisation stage……. 86
4.2.2.3. Post-mineralisation stage……... 88
4.2.3. Alteration……..... 88
4.3. Ore minerals……..…….. 92
4.3.1. Introduction……..……... 92
4.3.2. Pyrite……... 92
4.3.3. Pyrrhotite…… 94
4.3.4. Sphalerite……... 94
4.3.5. Galena……. 94
4.3.6. Chalcopyrite……... 94

4.3.7. Electrum…….. 96
4.4. Age of mineralisation…….. 96
4.4.1. Introduction……. 96
4.4.2. Sample preparation and methods……... 98
4.4.3. Age results…….. 99
4.5. Discussion……... 102
4.5.1. Indosinian Orogeny……..……... 102
4.5.2. Timing of mineralisation...…….. 102
4.6. Summary……..…..…….. 104

Chapter 5 Mineral Chemistry

5.1. Introduction……. 106
5.2. Fineness of electrum……... 106
5.2.1. Introduction……. 106
5.2.2. Analytical methods…… 107
5.2.3. Occurrence and petrology……... 107
5.2.4. Results……...…….. 107
5.3. Pyrite chemistry…….. 107
5.3.1. Introduction……...……... 107
5.3.2. Analytical methods..……... 109
5.3.3. Occurrence and texture of pyrites..…….. 111
5.3.4. Results……..……..... 111
5.4. Sphalerite chemistry……... 116
5.4.1. Introduction……. 116
5.4.2. Analytical methods……. 118
5.4.3. Sphalerite types……... 118
5.4.4. Results……. 118
5.5. Discussion……..…….. 123
5.5.1. Chemistry of ore fluids and gold fineness values……... 123
5.5.2. Pyrite trace element chemistry……... 125
5.5.3. Sphalerite FeS contents for geobarometer…….……. 126
5.6. Summary……. 126

Chapter 6 Stable and Radiogenic Isotopes

6.1. Introduction……. 128

6.2. Sulphur isotopes…….. 128

6.2.1. Introduction……. 128

6.2.2. Analytical methods…..…….. 129

6.2.3. Results……...…….. 130

6.3. Carbon and oxygen isotopes……..…… 130

6.3.1. Introduction……. 130

6.3.2. Analytical methods..……... 134

6.3.3. Results……...…….. 134

6.4. Lead isotopes…….…….……... 138

6.4.1. Introduction…..…….. 138

6.4.2. Analytical method……... 138

6.4.3. Results……..……... 140

6.5. Discussion……... 142

6.5.1. Sulphur isotopes…….. 142

6.5.2. Carbon and oxygen isotopes……... 147

6.5.3. Lead isotopes...……... 149

6.6. Summary……..……... 150

Chapter 7 Fluid Inclusions

7.1. Introduction……. 154

7.2. Analytical methods……..……... 154

7.2.1. Sample preparation……. 154

7.2.2. Microthermometry…….……. 156

7.2.3. Laser Raman Spectroscopy……..……... 156

7.2.4. Depth of fluid entrapment.…….. 158

7.3. Fluid inclusion petrography.…….…….. 158

7.4. Results……..……... 160

7.4.1. Microthermometric data….……. 160

7.4.2. Laser Raman Spectroscopy…...…….. 166

7.4.3. Depth of fluid entrapment……... 169

7.5. Discussion…….…….. 169
7.5.1. Depth of ore formation…….……... 170
7.5.2. Ore fluid characteristics and source(s)…….……... 170
7.5.3. Presence of N_2 and CH_4 gases and comparison with other gold deposits……. 170
7.5.4. Nature of ore fluids……..……... 173
7.5.5. Physico-chemical process of gold deposition…...…….. 174
7.6. Summary……..……... 176
Chapter 8 Summary, Conclusions, Genetic Model and Exploration Implications
8.1. Introduction……..……... 178
8.2. Summary…..…….……... 178
8.2.1. Geological and tectonic setting…….. 178
8.2.2. Nature of gold mineralisation..…….. 179
8.2.3. Structural control……... 180
8.2.4. Age of mineralisation…….. 180
8.2.5. Depth of ore formation……..……. 181
8.2.6. Physico-chemical conditions of ore fluids…….. 181
8.3. Discussion including comparison with orogenic and intrusion-related gold deposits……..... 182
8.3.1. Regional tectonic setting…...…….. 182
8.3.2. Mineralisation characteristics…...……... 185
8.3.3. Structural control……... 186
8.3.4. Source and transport of gold..……... 186
8.3.5. Deposition of gold..……..……. 187
8.3.6. Formation of depth…….…...…….. 189
8.4. Genetic model……..……...……... 189
8.4.1. A large intrusion-related model…….. 190
8.4.2. Wall rock reaction model at Bai Dat and Bai Go……... 190
8.5. Exploration implications……...…….. 193
8.6 Future research…….……... 194
References…….……... 196

APPENDICES

Appendix I: Rock catalogue

Appendix II: Structural measurement data at Bai Dat underground

Appendix III: Geochronological results (LA-ICPMS zircon U-Pb ages)

Appendix IV: XRF whole-rock geochemical results

Appendix V: Magnetic susceptibility data

Appendix VI: Re-Os molybdenite age result

Appendix VII: Ar-Ar geochronology

- **I: Analytical methods**
- **II: Ar-Ar age results**

Appendix VIII: Electrum fineness results

Appendix IX: LA-ICPMS pyrite trace element geochemical results

- **I: Spot analyses**
- **II: line analyses for mapping (CD-ROM)**

Appendix X: Sphalerite geochemical results

Appendix XI: Sulphur isotope results

Appendix XII: Carbon and oxygen isotope results

Appendix XIII: Fluid inclusion microthermometric results

Appendix XIV: Laser Ramam Spectroscopic results

- **I: Gaseous composition**
- **II: Daughter mineral identification**

FIGURES

Chapter 1

Page

Figure 1.1. Location of the Phuoc Son gold deposit area within the Indochina region ……..….. 2

Figure 1.2. Location of the Phuoc Son gold deposit area in central Vietnam……...……..….. 2

Figure 1.3. Geographical views of Danang and gold mining area in Phuoc Son……..…..…….. 3

Figure 1.4. Location of the Bai Dat and Bai Go deposits and prospects in Phuoc Son……. 4

Chapter 2

Figure 2.1. Tectonic divisions of mainland SE Asia and the surrounding region…..…..... 11

Figure 2.2. Reconstruction maps of the Gondwana-derived terranes……..... 13

Figure 2.3. Tectonic divisions of the Indochina Terrane…….…….…..... 15

Figure 2.4. Tectonic scenario for the Indochina Terrane during Cambrian-Silurian.....……..... 17

Figure 2.5. Reconstruction of formation of the mineralised belts of the Indochina Terrane……. 18

Figure 2.6. Distribution of volcanic-plutonic-metamorphic rocks of the Truong Son Fold Belt.. 22

Figure 2.7. Geochronolgical data of the Truong Son Fold Belt……..……... 22

Figure 2.8. Location of Cu-Au Mineral Districts of the Truong Son Fold Belt……..... 23

Figure 2.9. Simplified geology of the Phu Bia area with location of Cu-Au deposits…….. 24

Figure 2.10. Simplified geology of the Sepon area with location of Cu-Au orebodies……. 27

Figure 2.11. Geological setting of Central Vietnam…….. 30

Chapter 3

Figure 3.1. Simplified geological map of the Phuoc Son deposit area……..……..... 36

Figure 3.2. Simplified geological map of the the southern end of the Phuoc Son area…...…….. 37

Figure 3.3. NW-SE cross-section of the Bai Dat deposit area….……...….. 38

Figure 3.4. NW-SE cross-section of the Bai Go deposit area……..... 38

Figure 3.5. Schistose and phyllitic rock units of the Phuoc Son deposit area……... 39

Figure 3.6. Textural characteristics of metabasite unit…….. 41

Figure 3.7. Textural characteristics of amphibolite unit…..……... 42

Figure 3.8. Textural characteristics of marble unit……... 43
Figure 3.9. Textural characteristics of hornfels unit.....……. 43
Figure 3.10. Textural characteristics of metagabbro unit…….. 45
Figure 3.11. Textural characteristics of the Round Hill granite……..……. 46
Figure 3.12. Textural characteristics of foliated dacitic porphyry……. 47
Figure 3.13. Textural characteristics of syenite…..…….. 48
Figure 3.14. Textural characteristics of the granite dyke……... 49
Figure 3.15. Textural characteristics of the Khe Rin granite……. 49
Figure 3.16. Textural characteristics of the andesitic dyke……... 51
Figure 3.17. Textural characteristics of the diorite…….……... 51
Figure 3.18. Textural characteristics of dacitic porphyry…….. 52
Figure 3.19. Gneissic rocks of the Kham Duc Formation……. 53
Figure 3.20. Regional structural setting of the Phuoc Son deposit area, central Vietnam……. 55
Figure 3.21. Occurrence of Daksa and K7 faults zones in the southern end of Phuoc Son area... 57
Figure 3.22. Plots of measured foliation and faults in the Bai Dat underground mine site…….. 58
Figure 3.23. Orientation data of metamorphic foliation in the host rocks and faults…….…….. 58
Figure 3.24. Orientation data of metamorphic foliation of the host rocks of Bai Dat…….. 59
Figure 3.25. Zircon cathodoluminescence images of the igneous units from Phuoc Son…..….. 62
Figure 3.26. U-Pb zircon concordia diagrams of the igneous units from the Phuoc Son…….. 62
Figure 3.27. Location and distribution of the dated samples from the Phuoc Son area…….... 64
Figure 3.28. Summary of geochronological data from Phuoc Son and surrounding……. 65
Figure 3.29. Bivariate plots of SiO_2 versus selected major elements…….……... 68
Figure 3.30. Bivariate plots of SiO_2 versus minor elements……..….. 70
Figure 3.31. Chondrite-normalised REE patterns of lithological units from Phuoc Son……..... 71
Figure 3.32. N-MORB normalised multi-element patterns of rock units from Phuoc Son…….. 72
Figure 3.33. Geochemical discrimination diagrams of the igneous units in Phuoc Son…….. 74
Figure 3.34. Plots of magnetic susceptibility data of the major intrusive units at Phuoc Son….. 76
Figure 3.35. Geochronological framework of the Truong Son Fold Belt…….. 78
Figure 3.36. Tectonic reconstruction of the Indochina and South China Terranes……... 78

Chapter 4

Figure 4.1. Nature of foliation-parallel quartz-sulphide vein at Bai Dat underground…….. 82

Figure 4.2. Mineralisation stages and the paragenesis of the Bai Dat and Bai Go deposits…….. 84

Figure 4.3. Characteristics of the pre-mineralisation regional metamorphism……..... 85

Figure 4.4. Characteristics of quartz-sulphide vein of the early main mineralisation stage…….. 86

Figure 4.5. Characteristics of quartz-sulphide veins of the late main mineralisation stage…….... 87

Figure 4.6. Nature of the post-mineralisation faults observed at Bai Dat underground…….…... 89

Figure 4.7. Cross-sections showing the spatial distribution of pyritisation……..…. 90

Figure 4.8. Alteration characteristics of the Bai Dat and Bai Go deposits…….……... 91

Figure 4.9. Occurrence and textural characteristics of pyrites at Bai Dat and Bai G..…….. 93

Figure 4.10. Occurrence, texture and mineral association of sulphides at Bai Dat and Bai Go.... 95

Figure 4.11. Occurrence, texture and mineral association of electrums at Bai Dat and Bai Go... 97

Figure 4.12. Molybdenite-bearing sample from the Round Hill deposit……... 99

Figure 4.13. Occurrence of vein-located biotite at Bai Dat, Bai Go and Bai Chuou……. 100

Figure 4.14. Ar-Ar ages from the Phuoc deposit area, central Vietnam…….……... 101

Figure 4.15. Summary of cooling information obtained form age data of Phuoc Son…….. 104

Chapter 5

Figure 5.1. Histogram of gold fineness values in electrum from Bai Dat and Bai Go…….. 108

Figure 5.2. Time chart of the selected LA-ICPMS spot analysis of vein-located pyrite……... 110

Figure 5.3. Range and mean values of major selected trace elements in the studied pyrites…..... 113

Figure 5.4. Binary plots of selected trace elements in pyrites from Bai Dat and Bai Go…….. 114

Figure 5.5. LA-ICPMS pyrite maps of various elements…….. 115

Figure 5.6. Binary plots of selected trace elements in the host rock-located pyrite at Bai Go..... 117

Figure 5.7. Photomicrograph showing coexistence of sphalerite with pyrrhotite and pyrite..…... 119

Figure 5.8. Histogram of FeS mole % values of sphalerites from Bai Dat and Bai Go…….…... 120

Figure 5.9. Binary plots of calculated FeS. MnS and CdS mole % values of sphalerites……. 121

Figure 5.10. A ternary plot of Fes mole % - MnS mole % X 100 – CdS mole % X 10……..….. 122

Figure 5.11. Pressure determinations using FeS mole % values at Bai Dat and Bai Go……... 122

Figure 5.12. Comparison of the electrum fineness data with other gold-bearing deposits...…… 124

Chapter 6

Figure 6.1. Histograms of sulphur isotope data from the Bai Dat deposit……. 131

Figure 6.2. Histograms of sulphur isotope data from the Bai Go deposit…...…….. 132

Figure 6.3. Au assay data versus sulphur isotope values for sulphides of Bai Dat and Bai Go.... 133

Figure 6.4. Carbonate-bearing ore samples from the Bai Dat and Bai Go deposits…….. 134

Figure 6.5. Histograms of calculated $\delta\,^{13}C_{PDB}$ values of carbonates from Bai Dat and Bai Go... 135

Figure 6.6. Histograms of calculated $\delta\,^{18}O_{SMOW}$ values of carbonates from Bai Dat and Bai Go. 136

Figure 6.7. Plots of carbon and oxygen isotope data from Bai Dat and Bai Go…….……... 137

Figure 6.8. Galena-bearing samples from Bai Dat and Bai Go……. 139

Figure 6.9. Plot of $^{208}Pb/^{204}Pb$ versus $^{206}Pb/^{204}Pb$ from galena of Bai Dat and Bai Go…..……... 141

Figure 6.10. Plot of $^{207}Pb/^{204}Pb$ versus $^{206}Pb/^{204}Pb$ from galena of Bai Dat and Bai Go…..……... 141

Figure 6.11. Comparisons of sulphur isotope data with Au-bearing deposits and natures……..... 143

Figure 6.12. Comparisons of sulphur isotope data deposits with Cu-Au deposits of TSFB……. 145

Figure 6.13. Comparisons of sulphur isotope data with other gold prospects in Phuoc Son…..... 146

Figure 6.14. Plots of carbon and oxygen isotope raw data with other prospects in Phuoc Son.... 148

Figure 6.15. Comparison of $^{207}Pb/^{204}Pb$ versus $^{206}Pb/^{204}Pb$ with other deposits of TSFB……. 150

Figure 6.16. Comparison of $^{207}Pb/^{204}Pb$ versus $^{206}Pb/^{204}Pb$ with mineralised belts in Indochina. 151

Chapter 7

Figure 7.1. Fluid inclusion chips prepared from vein samples of Bai Dat and Bai Go……..….... 155

Figure 7.2. Cross-sections showing sampling points for fluid inclusion study……. 157

Figure 7.3. Examples of primary fluid inclusions identified in this study……. 159

Figure 7.4. Different types of fluid inclusions found in the samples from Bai Dat and Bai Go... 160

Figure 7.5. Histograms of homogenisation temperatures of fluid inclusions…….……... 163

Figure 7.6. Histograms of salinity data of fluid inclusions at Bai Dat and Bai Go……... 164

Figure 7.7. Histograms of solid CO_2 melting temperatures of fluid inclusions……..…. 165

Figure 7.8. An example of Lase Raman spectral profile of CO_2-CH_4-N_2 gas compositions..…. 167

Figure 7.9. Ternary plots of gas composition (CO_2-CH_4-N_2) in fluid inclusions……..…….. 168

Figure 7.10. Examples of daughter minerals identified by Lase Raman spectral profile…….. 169

Figure 7.11. Plots of salinities vs homogenisation temperatures of fluid inclusions……..……. 171

Figure 7.12. CO_2-CH_4-N_2 ternary plots of gas composition in comparison with other deposits.. 172

Figure 7.13. Log fO_2-pH diagram of Bai Dat and Bai Go ore fluids……...…….. 174

Chapter 8

Figure 8.1. Tectonic reconstruction of the Indochina Terrane during Triassic……...…… 184

Figure 8.2. Intrusion-related gold model at the Phuoc Son deposit area…….….. 191

Figure 8.3. Chemical model of the Bai Dat and Bai Go deposits…….. 192

TABLES

Page

Chapter 1

Table 1.1. Phuoc Son gold resources……...……..……...….. 6

Chapter 2

Table 2.1. Summary of gold and copper resources of the Truong Son Fold Belt ……..... 23

Table 2.2. Geological characteristics of Cu-Au deposits occurring in the Phu Bia area..... 25

Table 2.3. Geological characteristics of Cu-Au deposits occurring in the Sepon district……..... 28

Table 2.4. Geological characteristics of Cu-Au deposits occurring in the Central Vietnam..... 31

Chapter 3

Table 3.1. Summary of geochronological data of the Phuoc Son area and surroundings……. 63

Table 3.2. Summary of magnetic susceptibility values of intrusive units from Phuoc Son…….. 76

Table 3.3. Comparison of adakites with dacitic porphyry from Bai Dat and Bai Go ……..….. 79

Chapter 4

Table 4.1. Summary of geochronological results of the vein-located minerals at Phuoc Son….. 101

Chapter 5

Table 5.1. Summary of gold fineness values in electrum from Bai Dat and Bai Go……... 108

Table 5.2. Summary of trace element concentrations in the studied pyrites……...…… 112

Table 5.3. Summary of calculated chemical values of the sphlerite from Bai Dat and Bai Go.... 119

Chapter 6

Table 6.1. Summary of lead isotopic data from the Bai Dat and Bai Go deposits……...……. 140

Chapter 7

Table 7.1. Summary of microthermometry of fluid inclusions from Bai Dat and Bai Go…….... 161

Table 7.2. Summary of gas compositions in fluid inclusions from Bai Dat and Bai Go……. 167

Table 7.3. Identified solid phase crystals in fluid inclusions from Bai Dat and Bai Go……..... 169

Chapter 8

Table 8.1. Comparison of Bai dat and Bai Go with orogenic and intrusion-related deposits….. 183

CHAPTER 1 INTRODUCTION

1.1. PREAMBLE

This thesis provides an outcome of the author's PhD project on "A study on mineralogical, geochemical and geochronological characteristics and ore genesis in Phuoc Son gold deposit area, central Vietnam", which was conducted during 2009–2013. The project was logistically sponsored by the project property's owner, Olympus Pacific Minerals Inc. (recently changed to Besra Gold Inc.), and supervised through ARC Centre of Excellence in Ore Deposits (CODES) at University of Tasmania by Professor Khin Zaw and Dr. Sebastien Meffre. This PhD was partly included as a case study for the "Ore Deposits of SE Asia" Projects during 2008–2010 and 2011–2014, investigating genesis of major ore deposits (i.e., Cu, Au, Pb, Zn, W, Sn, REE) in SE Asia and characterising the metallogenic framework.

1.2. LOCATION AND ACCESS

The Phuoc Son gold deposit area is located approximately 90 km southwest of Danang and 6 km northwest of Kham Duc Town, Phuoc Son District, Quang Nam Province in central Vietnam (Figs. 1.1 and 1.2). Access to the Kham Duc Town can be made by car along 140 km sealed road from Danang, the third largest City of Vietnam (Fig. 1.3A). Olympus's exploration and mine camp is situated in the central part of the Kham Duc Town (Fig. 1.3B), and access to the Phuoc Son deposit area from the town is via sealed road and takes about 20 minutes by car or shuttle bus. The town has a current population of about 7000, and offers excellent infrastructure as a part of "bridge" towns along the 1000 km long Ho Chi Minh Highway that connects Hanoi and Ho Chi Minh City. Local people are mainly engaged in agriculture, typically working on rice farming at limited flat fields. Vietnam War history is also preserved at the edge of the Kham Duc Town as remain of old airport which was used during the war.

The Phuoc Son deposit area consists of two major economic orebodies (i.e., Bai Dat and Bai Go deposits; Fig. 1.4) and a number of gold prospects are also recognised in the area. The deposit area lies at an elevation of 500 m above sea level and is represented by undulating topography covered by thick rain forests (Fig. 1.3C, D and E). Climate in the area is divided into rainy (September-December) and dry (January-August) seasons, which is different from

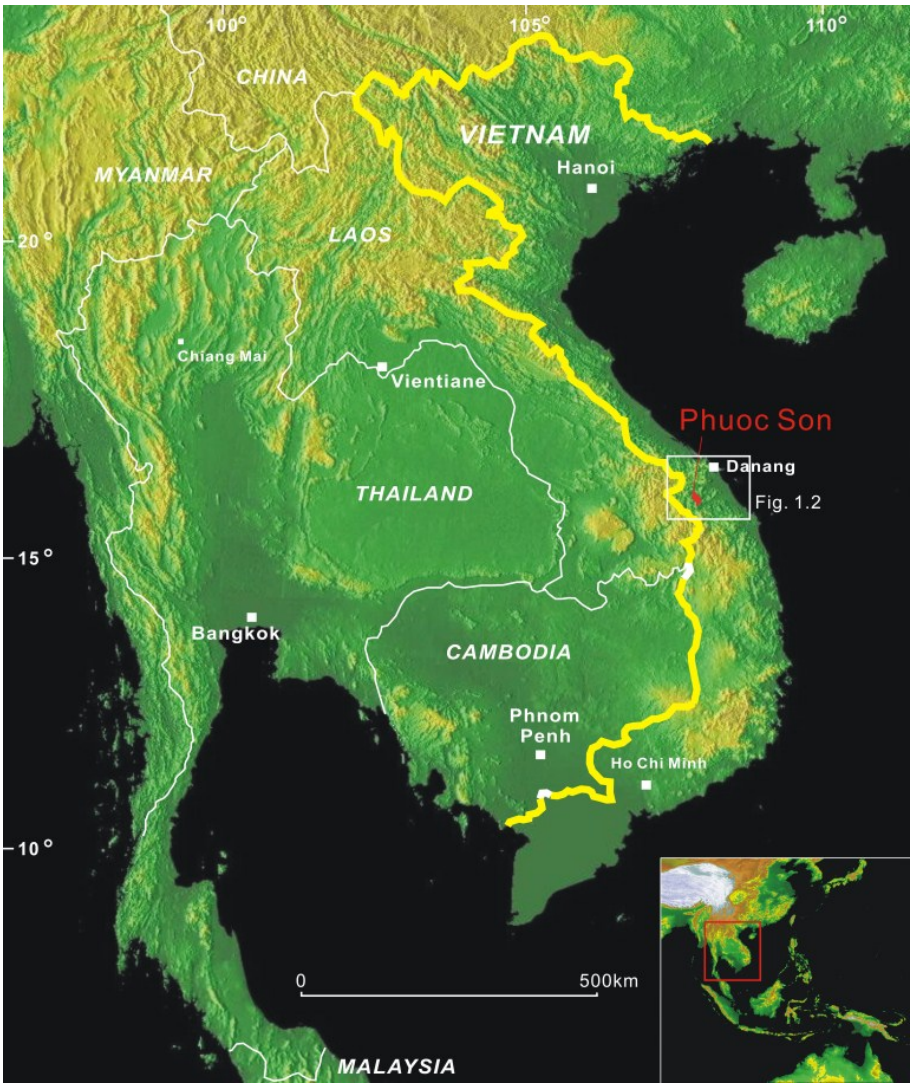

Fig. 1.1. Location of the Phuoc Son gold deposit area within the Indochina region.

Fig. 1.2. Location of the Phuoc Son gold deposit area in central Vietnam, together with the Bong Mieu (Au), Duc Bo (Cu-Pb-Zn) and Phuoc Thanh (Au) deposits.

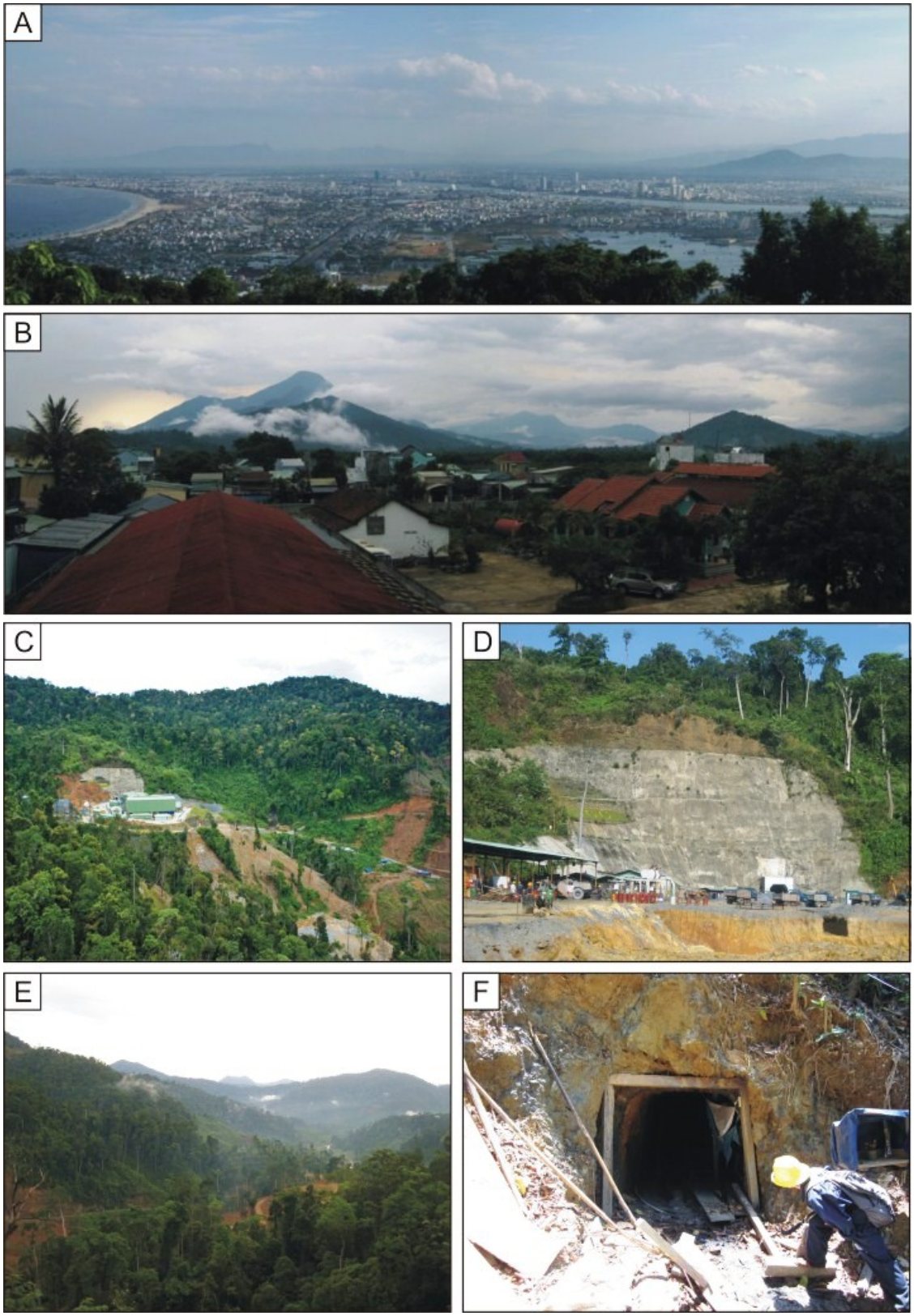

Fig. 1.3. Geographical views of Danang and gold mining area in Phuoc Son, central Vietnam. **A.** View of Danang City from nearby mountain. **B.** View from mine camp in Kham Duc Town of Phuoc Son District. **C.** View of processing plant at Bai Dat (from Olympus website). **D.** Entrance of underground mine site at Bai Dat. **E.** View of Bai Go deposit area from Bai Dat, covered by thick forests. **F.** Adit at the Tra Long deposit area, made by local miners for artisanal gold mining activities.

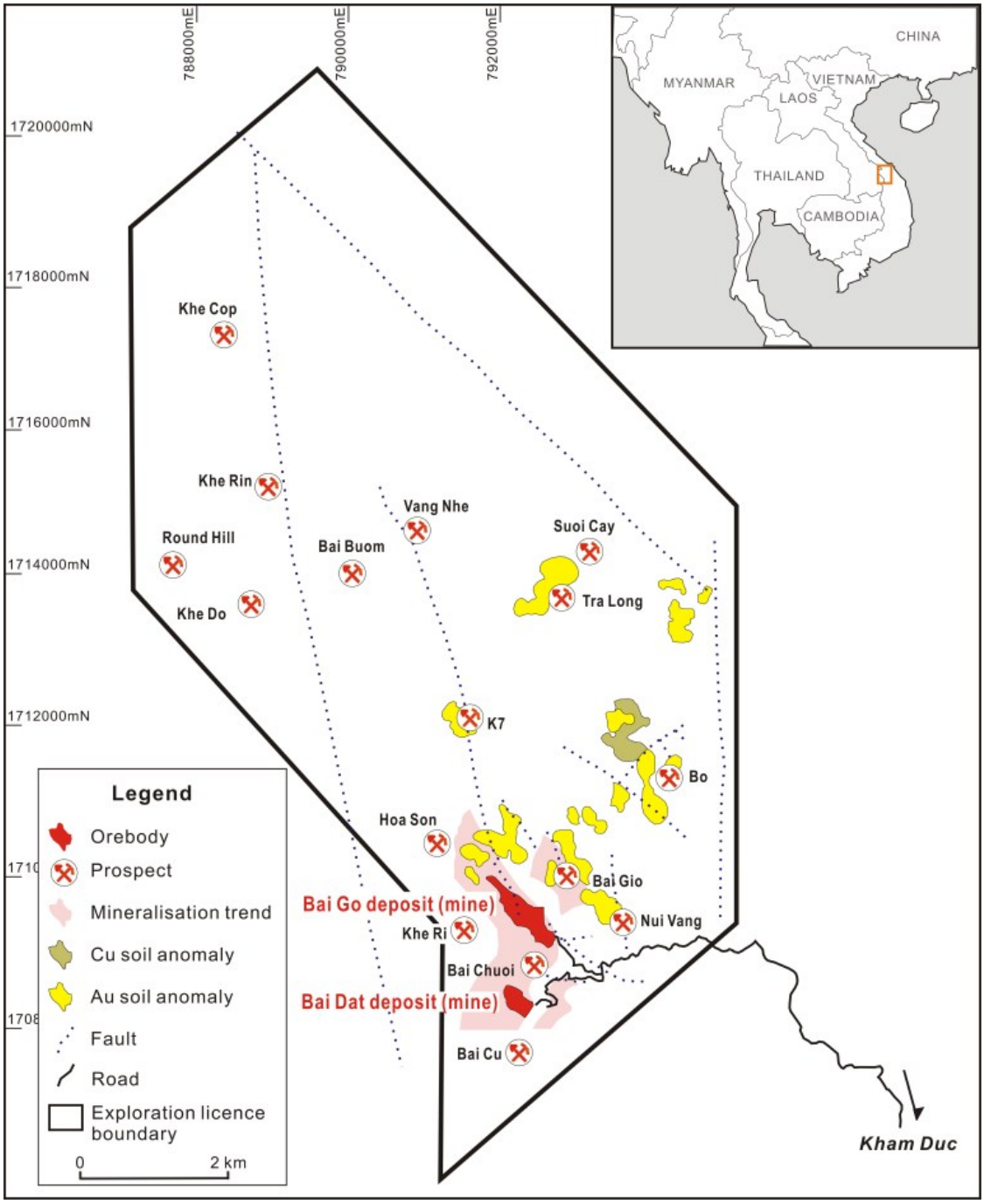

Fig. 1.4. Location of the Bai Dat and Bai Go deposits and other gold prospects in the Phuoc Son area, central Vietnam (modified after a map on the Olympus website).

typical Indochina region's monsoonal climate (rainy season of May-October and dry season of November-April), due to local affect by topographic nature of Truong Son mountains.

1.3. EXPLORATION AND MINING HISTORY

First mining activity at Phuoc Son is rumoured to have been undertaken sometime in 19th Century during French Colonial Period (Stevens and Fulton, 2008). Recorded initial exploration activity in the district was conducted during 1976–1985 by geologists from Vietnam Government Geological Survey (DGMV) and a regional 1:200,000 scale map was produced at that time (Banks et al., 2004). Recent artisanal mining in the area was started around early 1990's, and several thousand miners were engaged in alluvial and hard rock gold mining activities during the peak period of 1995–1997 at the deposit/prospect areas including Bai Dat, Bai Go, K7, Hoa Son, Tra Long, Vang Nhe and Khe Rin (Figs. 1.3F and 1.4; Stevens and Fulton, 2008).

Intensive regional gold exploration at Phuoc Son using modern technique was commenced in 1995 by Indochina Goldfields Company, in cooperation with DGMV, and a total of 507 BLEG (bulk leach extractable gold) stream sediment samples (average one sample per 5 km^2) were collected during the campaign. Of these, 61 samples had anomalous (>7 ppb) gold values including peak value of 592 ppb Au and more than 50 % anomalous samples were obtained from a single 240 km^2 area of Daksa (area encompassing Bai Dat to Bai Go) ridge catchment area (Banks et al., 2004; Stevens and Fulton, 2008). Accordingly, the Daksa area in Phuoc Son was quickly recognised as high potential for gold mineralisation.

However, Indochina Goldfields Company withdrew from Vietnam in 1997, and then Olympus Pacific Minerals Inc. took over and became an operator of the exploration and development programs at Phuoc Son. In 1998, Olympus was granted two 50 km^2 exploration licences and has continued exploration activity in the licenced area at Phuoc Son including more detailed geological, geochemical, geophysical and drilling programs (Banks et al., 2004).

First gold mineralisation was intersected in a drill hole at Bai Dat in 1999, and this indicated high potential of gold mineralisation in hard rock at Phuoc Son (Banks et al., 2004). By 2008, economic gold resources have been delineated at Bai Dat and underground mining was commenced, and until now two economic orebodies have been recognised at Bai Dat and Bai Go. Previous studies indicated that gold mineralisation at Phuoc Son is quartz-sulphide veins, particularly developed along shear zones (Banks et al., 2004). A total of measured, indicated and inferred resources at Phuoc Son are currently delineated to be 3.1 Mt @ 6.69 g/t Au (with 3 g/t Au cut-off grade) for approximate 670,000 ounces of gold from the Bai Dat and Bai Go orebodies (Table 1.1).

Table 1.1. Phuoc Son gold resources at 31/12/2010, using a 3 g/t Au cut-off grade (data from Olympus website).

Resource Category	Tonnes	Gold Grade (g/t)	Contained Gold (oz)
Measured	127,618	9.00	36,911
Indicated	493,321	9.52	150,937
Inferred	2,481,309	6.01	479,720
All total	**3,102,248**	**6.69**	**667,568**

1.4. PREVIOUS STUDIES

Several internal consultant reports (e.g., Corlett, 2001; Alexander, 2006; Encom Technology, 2008; Davies, 2010) and one published paper (Banks et al., 2004) were available to understand background geology of Phuoc Son, prior to this study. Main focuses of the consultant reports were descriptions of either structure or petrology, whereas the paper by Banks et al. (2004) reported comprehensive geological and mineralisation characteristics of the main gold prospect areas in Phuoc Son based on field observations and established ore deposit model. At least few different gold-bearing mineralisation styles are distinguished at the Phuoc Son deposit area and all of them are considered to be associated with magmatic fluids for the formation, indicating that the mineralisation environment at Phuoc Son is analogous to some known intrusion-related gold deposits such as Tanami and Pine Creek in Australia, Vasilkovskoye in Kazakhstan and Pogo in Alaska (Banks et al., 2004).

1.5. SCOPE OF RESEARCH

This PhD project is principally focused on investigating the two economic gold deposits in Phuoc Son (i.e., Bai Dat and Bai Go). Several gold prospect areas in Phuoc Son, where economic resources have not been delineated due to lack of exploration activities, were also partly studied (e.g., geochronology, stable isotopic characteristics) for aiming to understand district-scale geological and metallogenic setting and correlate with the data from the Bai Dat and Bai Go deposits.

The specific aims of the project are as follows:

1. To characterise the nature of the gold mineralisation systems in the Bai Dat and Bai Go areas, in terms of mineral paragenesis, mineral chemistry, fluid inclusions, stable isotopes (sulphur, carbon and oxygen) and radiogenic isotope (lead) signature of mineralising fluids and the environments.

2. To construct an improved genetic model linking magmatism and/or metamorphism that was responsible for ore formation and geologic-tectonic development of the region.

3. To apply implications based on this model towards the development of metallogenic evolution of the Phuoc Son gold deposit area.

1.6. METHODOLOGY

In this study, two principal methods were applied including field investigation and laboratory-based studies.

1.6.1. Field investigation

Field work in the Phuoc Son deposit area was conducted three times by the author during 2009–2011. As a scoping study, a several-days field work was initially made at the end of January 2009, aiming to collect key ore and host rock samples. Subsequently, a four-weeks field work was conducted twice in May of 2010 and July of 2011 and comprehensive field investigation was made during these periods involving diamond drill core logging, geological and structural mapping of the deposits/prospects in the Phuoc Son area. Approximately 150 rock and ore samples were collected (they are listed in Appendix I) during the field campaigns and they were used for laboratory-based studies.

1.6.2. Laboratory work

Petrographic investigation was conducted on ore minerals and host rocks using microscope by the author at CODES, University of Tasmania. Whole-rock geochemistry analysis (XRF) and solution ICP-MS for low-abundance trace and rare earth elements (REE) were also carried out at CODES. Laser ablation (LA) trace element analyses (ICPMS) of pyrite for study of pyrite chemistry and solution ICPMS analyses on galena were also conducted at CODES. In addition, comparative LA radiogenic lead isotope analyses by multi-collector ICPMS was performed at School of Earth Sciences, University of Melbourne. U-Pb zircon age dating of igneous units from Phuoc Son and the surrounding region was accomplished at CODES, whereas Ar/Ar age dating for biotite occurring within quartz-sulphide vein was conducted at School of Earth Sciences, University of Melbourne. Re-Os dating of one molybdenite sample was carried out at the Applied Isotope Research for Industry and Environment (AIRIE) laboratory, Department of Earth Resources at Colorado State University (CSU). Laser ablation and conventional sulphur isotopes of sulphide minerals, carbon and oxygen isotope analyses on carbonate minerals and mineral chemistry measurement of ore-associated minerals (electrum and sphalerite) using microprobe equipment were conducted at the Central

Science Laboratory (CSL), University of Tasmania. For fluid inclusion study, microthermometry was made at CODES, while Laser Raman Spectroscopy (LRS) was accomplished at Geoscience Australia in Canberra.

1.7. THESIS STRUCTURE

To fulfil the scope of this study, the thesis is structured by the following Chapters:

- Chapter 2 includes (a) overview on tectonic setting of mainland SE Asia (b) the geological and tectonic framework of Indochina Terrane, (c) the geology and metallogenic setting of Truong Son Fold Belt, and (d) regional geology and ore deposits of central Vietnam. The contents in this Chapter are based on previous studies, involving recent results from "Ore Deposits of SE Asia" Projects at CODES during 2008–2010 and 2011–14 (ongoing).

- Chapter 3 introduces district geology of Phuoc Son and local geology of the Bai Dat and Bai Go gold deposit areas. The contents involve (a) geological architecture of the host rocks, such as meta-volcano-sedimentary and intrusive units, (b) geochemistry and geochronology of the host rock units, and (c) description of deposit-scale structural geology and the link to controlling factors of the gold mineralisation.

- Chapter 4 describes the detailed mineralisation characteristics of the Bai Dat and Bai Go deposits principally including paragenetic relations of ore and gangue minerals. Based on the paragenesis, additional analyses focusing on ore associated minerals such as geochronology of vein-hosted biotite (Ar-Ar) and molybdenite (Re-Os) have been undertaken and the results are presented.

- Chapter 5 provides detailed analyses of mineral chemistry, including electrum, pyrite and sphalerite. The results are used to deduce the physico-chemical conditions of the ore fluids at the Bai Dat and Bai Go deposits.

- Chapter 6 demonstrates stable and radiogenic isotope chemistry which includes sulphur isotope of sulphide minerals from the mineralised veins, carbon and oxygen isotopes from vein-located carbonate minerals of the main ore mineralisation stage at Bai Dat and Bai Go. Radiogenic lead isotope data by solution ICP-MS and LA-MC-ICPMS on galena minerals are also involved.

- Chapter 7 studies fluid inclusions of ore-forming fluids at the Bai Dat and Bai Go mineralised systems using few different techniques (e.g., microthermometry, Laser Raman Spectroscopy), and efforts are made to understand gold transportation/ deposition mechanism responsible for the formation of economic gold orebodies at Bai Dat and Bai Go.

- Chapter 8 discusses and concludes a genetic model of the Bai Dat and Bai Go deposits based on the collected data in this study, and provides implications for gold exploration in the Phuoc Son deposit area and the surrounding region of the central Vietnam.

CHAPTER 2 REGIONAL GEOLOGY AND METALLOGENIC SETTING

2.1. INTRODUCTION

A number of recent studied have shown that a strong link exists between the tectonic events of the mainland SE Asia and major ore deposits in the region (e.g., Fan, 2000; Gatinsky, 2005; Khin Zaw et al., 2007a; 2009; 2010; Crow and Khin Zaw, 2011; Barber et al., 2011). Better and more widely available geochronological techniques (e.g., LA-ICPMS, Ar-Ar) as well as ease of access to the area have allowed these studies to provide a comprehensive regional and metallogenic framework for the area. In this Chapter, this both new and older geological data are synthesised and reviewed to provide background information of the regional geology and ore deposit setting, prior to focussing on the Phuoc Son gold deposit area in Vietnam.

2.2. TECTONIC EVOLUTION OF MAINLAND SE ASIA

The mainland SE Asia comprises several terranes (or microcontinents) including Indochina, South China, Sibumasu (Siam, Burma, Malaysia and Sumatra, and also known as Shan-Thai) and West Myanmar (West Burma) Terranes, all of which are allochthonous terranes that have been rifted from Gondwana in the Palaeozoic and Mesozoic (e.g., Metcalfe, 1999; Fig. 2.1). Their tectonic evolution is fundamentally explained by four main geological processes involving rifting, drifting, amalgamation and post-amalgamation events (e.g., Metcalfe, 1988). This tectonic framework was initially established based on palaeontological and sedimentological data (e.g., Ridd, 1971; Burrett, 1974) and it has been generally accepted since early 1970s, although there are still many uncertainties regarding the detailed geometry and timing of these events.

2.2.1. Rifting

The Indochina Terrane is generally interpreted to have rifted from the Gondwana in the Early to Middle Palaeozoic, along with the South China Terrane. The Sibumasu Terrane is thought to have rifted in the Middle to Late Palaeozoic. This is supported by palaeomagnetic and palaeo-faunal data (e.g., Sengor and Hsu, 1984; Metcalfe, 1988). However, the timing of the

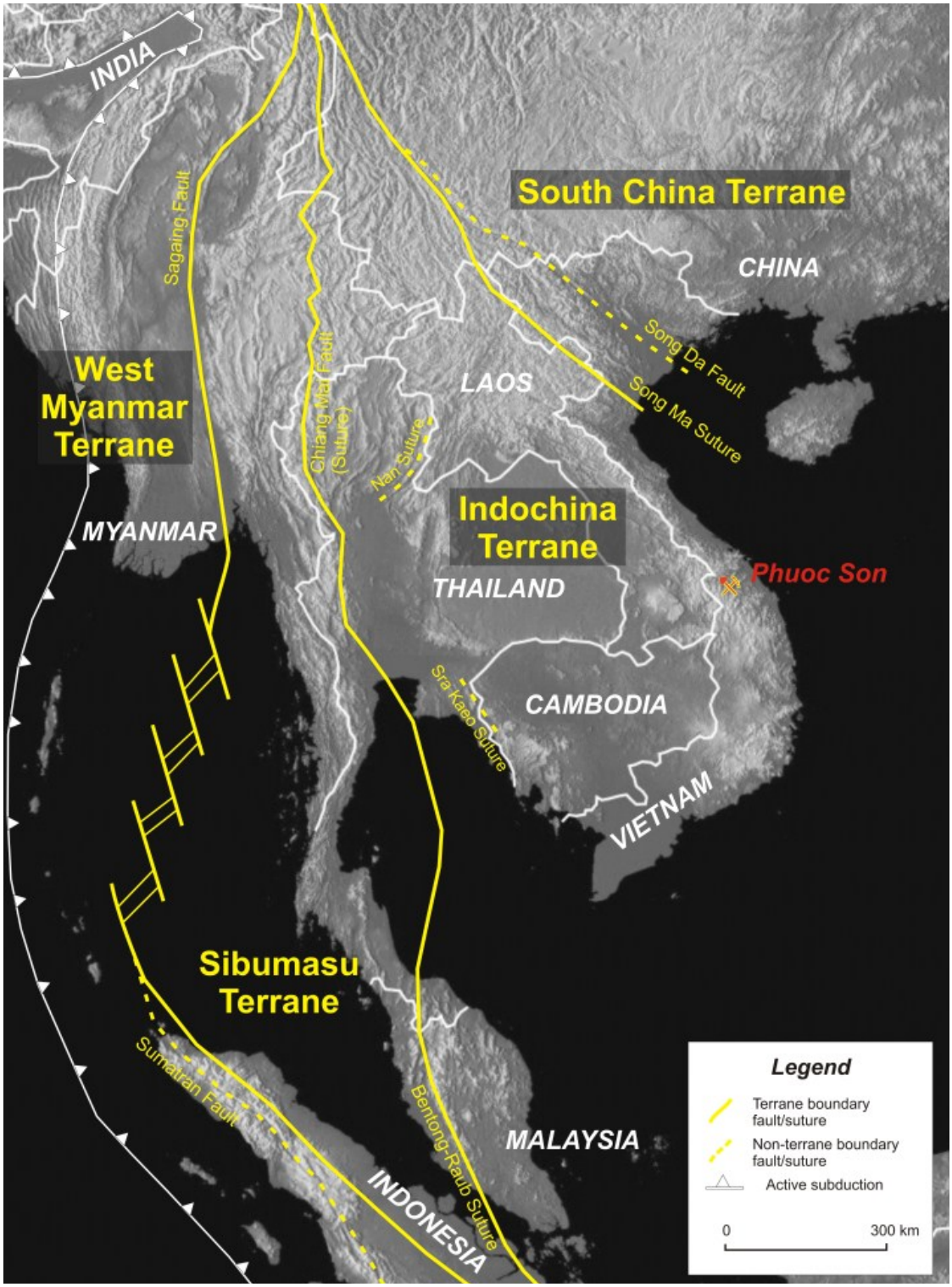

Fig. 2.1. Tectonic divisions of mainland SE Asia and the surrounding region, consisting of South China, Indochina, Sibumasu and West Myanmar Terranes as differentiated by sutures/faults (Modified after Sone and Metcalfe, 2008; Meffre et al., 2011).

rifting event from Gondwana is still widely debated. Metcalfe (1999) indicated that the rifting of the Indochina and South China Terranes from Gondwana occurred in the Devonian, and that the Sibumasu Terrane rifted in the Carboniferous-Early Permian (Fig. 2.2). A number of other scenarios have also been proposed, especially for the South China and Indochina Terranes, and some studies suggest that their rifting commenced as early as the Ordovician or Silurian (e.g., Hutchison, 1989; Charusiri et al., 2002).

2.2.2. Drifting

The Indochina and South China Terranes separated from the margin of Gondwana by the Late Devonian, before the Sibumasu Terrane, and subsequently drifted northwards, with the opening of the Palaeo-Tethys ocean (Metcalfe, 1999; Fig. 2.2). The drifting of these terranes is believed to have been underway by the Early Carboniferous, as there is no faunal or floral similarity or other connections with Gondwana by the Early Permian (Metcalfe, 1999). In contrast, the Sibumasu Terrane was part of Gondwana until Permian. By Late Permian, it was rifted from Gondwana and became a part of the Cimmerian continent drifting rapidly northwards (Metcalfe, 1999). This temporal evolution of the Sibumasu Terrane is demonstrated by the presence of cool water high latitude Carboniferous-Permian faunas, Lower Permian diamictites, and Upper Permian low latitude platform facies limestone within the Sibumasu Terrane (Hutchison, 1989). During this northwards drifting, the Meso-Tethys ocean was formed between the Cimmerian continent and Gondwana (Metcalfe, 1999).

2.2.3. Amalgamation

The amalgamation of the Indochina, South China and Sibumasu Terranes is considered to have occurred during the Late Palaeozoic to Early Mesozoic. It is believed that the Indochina Terrane initially collided with the South China Terrane and subsequently with the Sibumasu Terrane.

The amalgamation of the Indochina and South China Terranes is known to have commenced along the Song Ma Fault in North Vietnam (e.g., Hutchison, 1989; Metcalfe, 1999) where the occurrence of ophiolitic rocks indicates the presence of a closed ocean basin (e.g., Hutchison, 1989). The timing has been poorly constrained by previous studies with proposed amalgamation varying between the Carboniferous (Metcalfe, 1999) to the Triassic (Sengor and Hsu, 1984; Lepvrier et al., 1997). However, recent geochronological studies on magmatic and metamorphic rocks demonstrated that the timing of the amalgamation is confined to a Permian-Triassic time (270–240 Ma; e.g., Owada et al., 2006; Khin Zaw et al., 2010; Halpin et al., 2010).

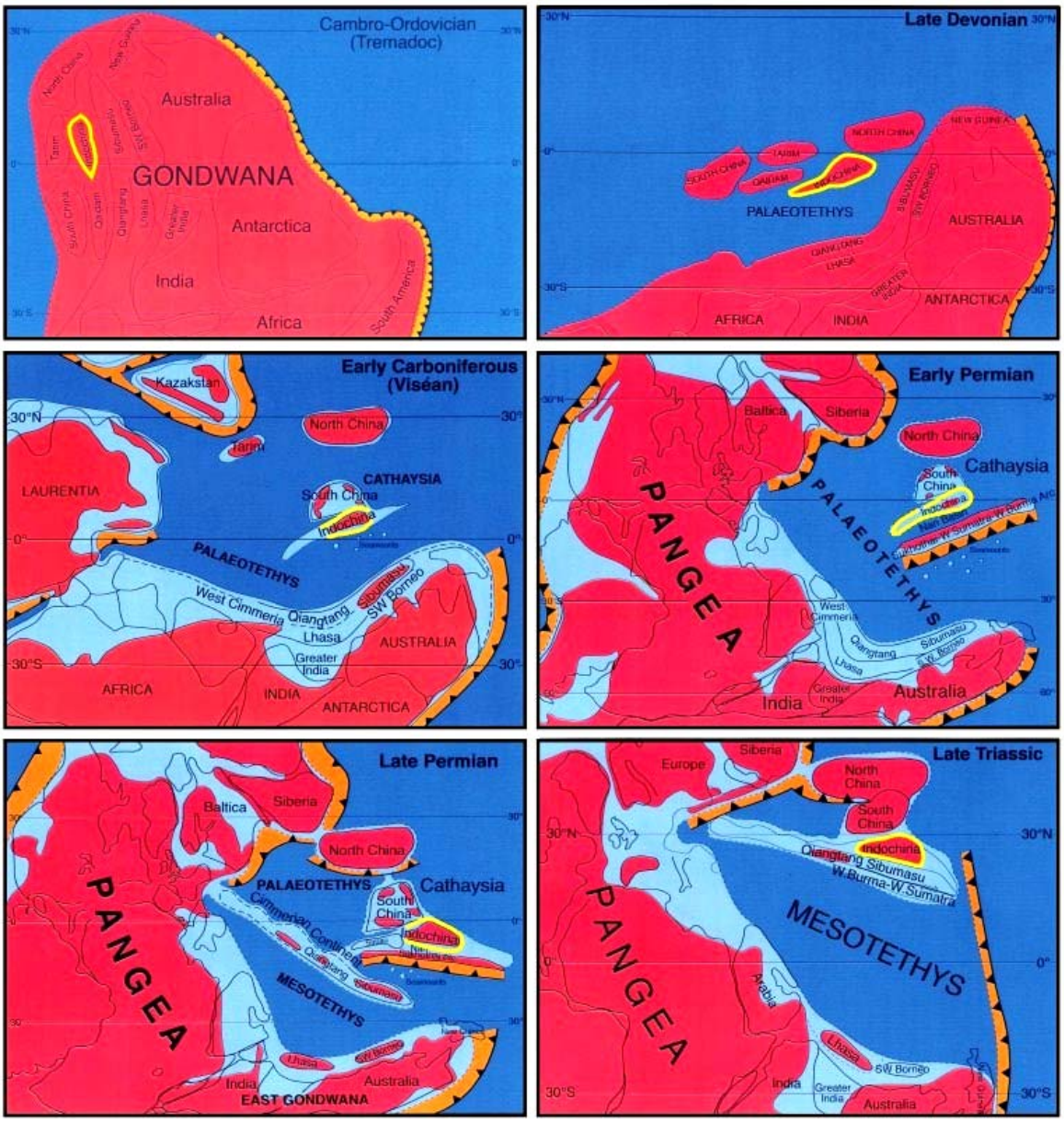

Fig. 2.2. Reconstruction maps of the Gondwana-derived terranes during Cambrian-Late Triassic period (modified after Barber et al., 2011). Note that the Indochina Terrane is marked by yellow rim.

The timing and location during the amalgamation of the Indochina and Sibumasu Terranes has also been widely debated. Various timings for this amalgamation have been suggested, from the Carboniferous-Permian (Hutchison, 1989), Triassic (Sengor et al., 1988; Metcalfe, 1988, 1996), and Triassic to Cretaceous (Aduley-Charles, 1983). The boundary between the Indochina and Sibumasu Terranes is generally thought to occur along the Bentong-Raub suture in Malaysia (e.g., Hutchison, 1989), but its continuation into Thailand has been more difficult to determine. Early researchers placed it along the Nan-Uttaradit/Sa Kaeo zones in central Thailand (Hada et al., 1999; Metcalfe, 1999). One study placed this boundary in westernmost Thailand along the Mae-Yuang (Mae Sariang-Mae Hong Son) Fault (Hisada et

al., 2004). Recent studies have favoured the Chiangmai Fault (similar to the Mae-Yuang Fault) as the main boundary of the two terranes (e.g., Sone and Metcalfe, 2008; Khin Zaw et al., 2010).

2.2.4. Post-amalgamation

During and after the major terrane assembly in the region, a number of important extensional episodes occurred, causing subsidence within the Indochina, South China and Sibumasu Terranes (e.g., Hall, 2002). Post-collisional tin-bearing granites were intruded in the Mesozoic throughout the area, and then most of the area subsided with sedimentation occurring in the mainland SE Asia as intracontinental red-bed basins. During the Cenozoic, part of the Indochina Terrane was extruded southeastwards from the remainder of continental Asia, as a result of the collision of the Indian Craton and Eurasia (Hutchison, 1989). The extruded area is bordered by the dextral Sagaing Fault in Myanmar and sinistral Red River Fault in South China and Vietnam (Hall, 2002).

2.3. GEOLOGICAL SETTING AND ORE DEPOSITS OF INDOCHINA TERRANE

The Indochina Terrane hosts several important mineralised belts consisting of significant precious and base metal deposits associated with plutonic, volcanic and metamorphic rocks. The currently-known important mineralised belts of the Indochina Terrane (in the territory of Vietnam, Laos, Cambodia, Thailand, Myanmar and Yunnan in South China) are shown in Figure 2.3 and listed below:

(1) Early Palaeozoic Basement in Vietnam, Laos and Thailand;
(2) Truong Son Fold Belt in Vietnam, Laos, Cambodia and Yunnan;
(3) Loei Fold Belt in Thailand, Laos, Cambodia, Malaysia and Yunnan;
(4) Sukhothai Belt in Thailand, Myanmar, Laos, Cambodia, Malaysia and Yunnan;
(5) Chiang Mai Belt in Thailand, Malaysia, Myanmar and Yunnan; and
(6) Dalat-Kratie Belt in Cambodia and Vietnam.

2.3.1. Early Palaeozoic tectonic history and ore deposits

Recent geochronological studies indicated that the oldest igneous units presenting in the Indochina Terrane are ranged from Cambrian to Devonian in age (490–400 Ma; Khin Zaw et al., 2007a, 2010). Their main occurrence is at (1) Central Vietnam-Southern Laos (Attapu Province) and (2) Northern Laos (Vientiane Province)-Northeastern Thailand (Loei

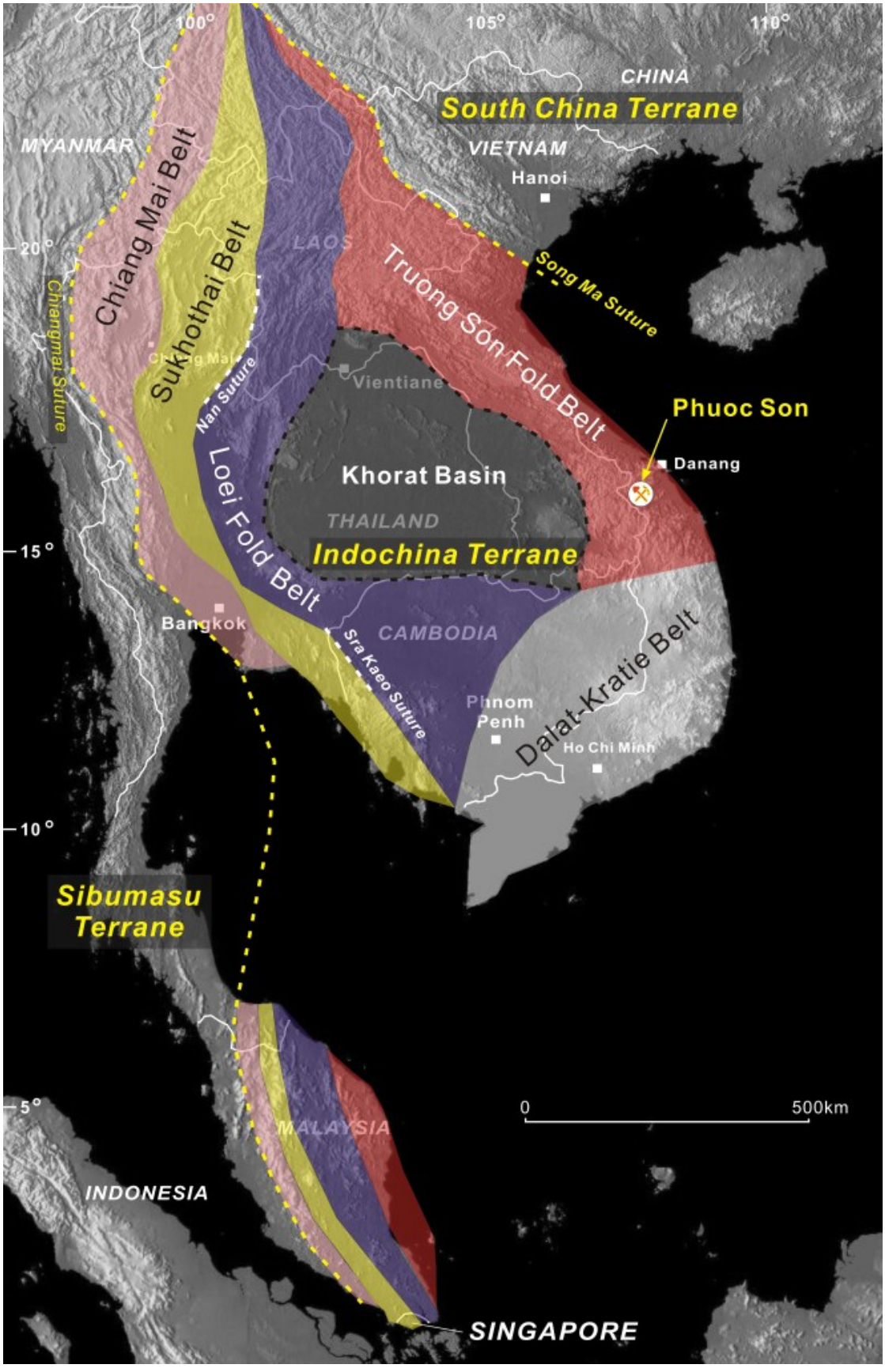

Fig. 2.3. Map showing tectonic divisions of the Indochina Terrane including, Truong Son Fold Belt, Loei Fold Belt, Sukhothai Belt, Chiang Mai Belt, and Dalat-Kratie Belt. Modified after Khin Zaw et al. (2010). Note the central part of the Indochina Terrane is covered by a thick Khorat Basin.

Province), which are located adjacent to the southeastern and northwestern margins of the Khorat Basin, respectively. Previous reports of a Precambrian basement to the area (e.g., Metcalfe, 1988) have not been substantiated.

In the Central Vietnam-Southern Laos area, the Early Palaeozoic rocks are composed of plutonic and volcanic rocks associated with high-grade metamorphic rocks. Geochemistry of the igneous units indicates subduction-collision-extension event with some of the rocks formed in an island-arc environment at the margin of Gondwana (Fig. 2.4). Early Palaeozoic rocks also occur throughout Northeastern Thailand to Northern Laos and include Silurian granites (comprising both I- and S-type) and minor volcanic rocks (Khin Zaw et al., 2010), but their tectonic setting is loosely constrained and link to those of the Central Vietnam-Southern Laos area is still poorly known.

Few ore deposits can be shown to have formed in the Early Palaeozoic, such as the Duc Bo volcanic-hosted deposit in central Vietnam and the Ang Noi intrusion-related deposit in northern Laos. The geological characteristics (e.g., deposit-scale geology, sulphur isotope and fluid inclusions) of the Duc Bo Cu-Zn-Pb deposit suggest that the system may be classified as a VHMS-style deposit (e.g., Anvil Mining, 2004; Khin Zaw et al., 2010) associated with Ordovician (460–410 Ma) volcanic rocks. Main orebodies at Duc Bo are deformed and distributed along the local shear zones, suggesting that the system formed prior to regional metamorphism during Middle Permian (Tran Thanh Hai, 2003). The gold-bearing system at Ang Noi occurs as stockwork veins predominantly hosted in Silurian granite (c.a. 430 Ma) and nature of the mineralisation is comparable to a typical intrusion-related gold system in Alaska (Maloney, 2008), although Pb isotope composition of the mineralisation suggests a younger age (around Late Carboniferous-Early Permian; Maloney, 2008).

2.3.2. Late Palaeozoic-Early Mesozoic tectonic history and ore deposits

The Gondwana-derived terranes were accreted, assembled, amalgamated and collided in the SE Asian region during Late Palaeozoic-Early Mesozoic, causing magmatism and metamorphism at the margins of the terranes (Fig. 2.5). Four magmatic belts can be recognised within the Indochina Terrane. The Truong Son, Loei, Sukhothai and Chiang Mai belts (Figs. 2.3 and 2.5; Khin Zaw et al., 2010; Meffre et al., 2011) were formed in the period between the Late Carboniferous (310 Ma) and the Early Jurassic (180 Ma), and the belts are different from each other based on geological, geochemical and geochronological characteristics and association of ore deposit types (e.g., Khin Zaw et al., 2007a, 2009, 2010).

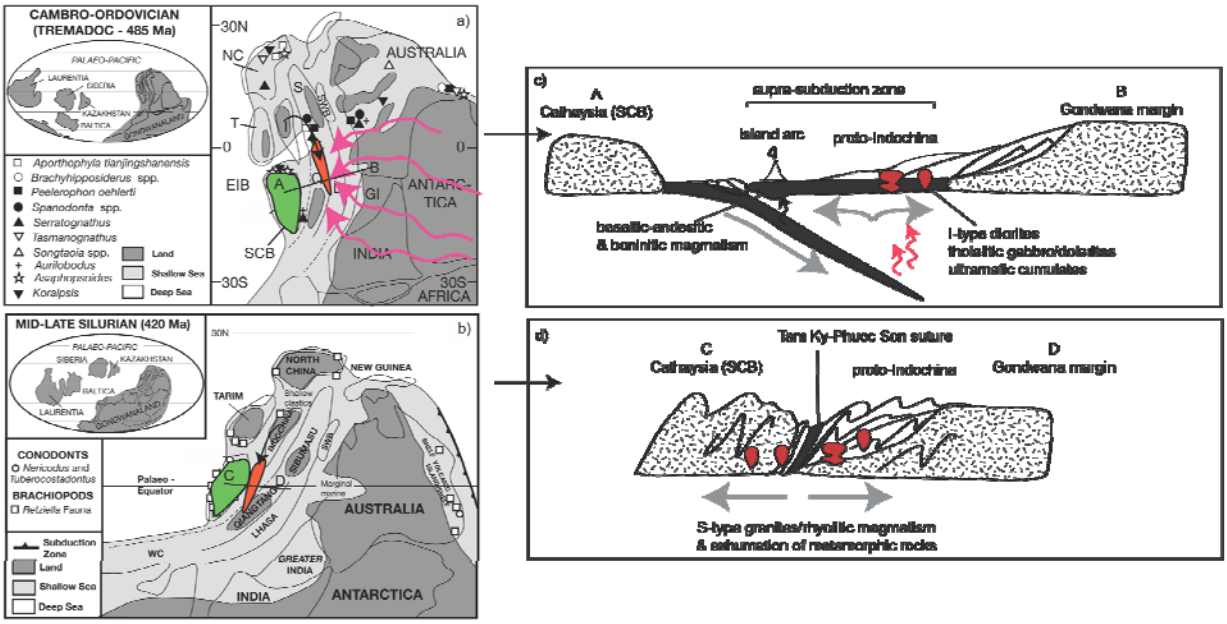

Fig. 2.4. Reconstructed tectonic scenario for the Indochina Terrane during Cambrian-Silurian (from Halpin et al., 2010). Red and green in (a) and (b) indicate Indochina and South China Terranes, respectively. Note that arrows in (a) show the inferred sedimentary transport from Gondwana.

Truong Son Fold Belt (TSFB)

The TSFB is distributed from northern Laos to central Vietnam via central Laos (Fig. 2.3) and is characterised by volcanic, plutonic and metamorphic rocks from Late Carboniferous to Late Triassic (310–230 Ma) ages, which were formed as a result of a long-lived (>80 Ma) subduction-collision-extension event between the Indochina and South China Terranes (e.g., Khin Zaw et al., 2010; Meffre, et al., 2011; Fig. 2.5). Formation of the belt is divided into two stages involving the early volcano-plutonic (I-type; 310–275 Ma) and the late plutono-metamorphic (I- to S-type; 265–230 Ma) stages and they are intercepted by a peak collisional event during 275–265 Ma. According to Khin Zaw et al. (2011), ore deposits of the TSFB are genetically associated with these two magmatic events:

1. Cu-Au mineralisation at Phu Bia in northern Laos and Sepon in central Laos. It is genetically linked to the early pluto-volcanic rocks, and
2. Polymetallic mineralisation (Au-Pb-Zn/Sn-W-REE) in central Vietnam (e.g., Phuoc Son and Bong Mieu) and central Laos. The deposits are associated with the late plutono-metamorphic event.

The ore deposits setting of the TSFB are described in detail later in this Chapter.

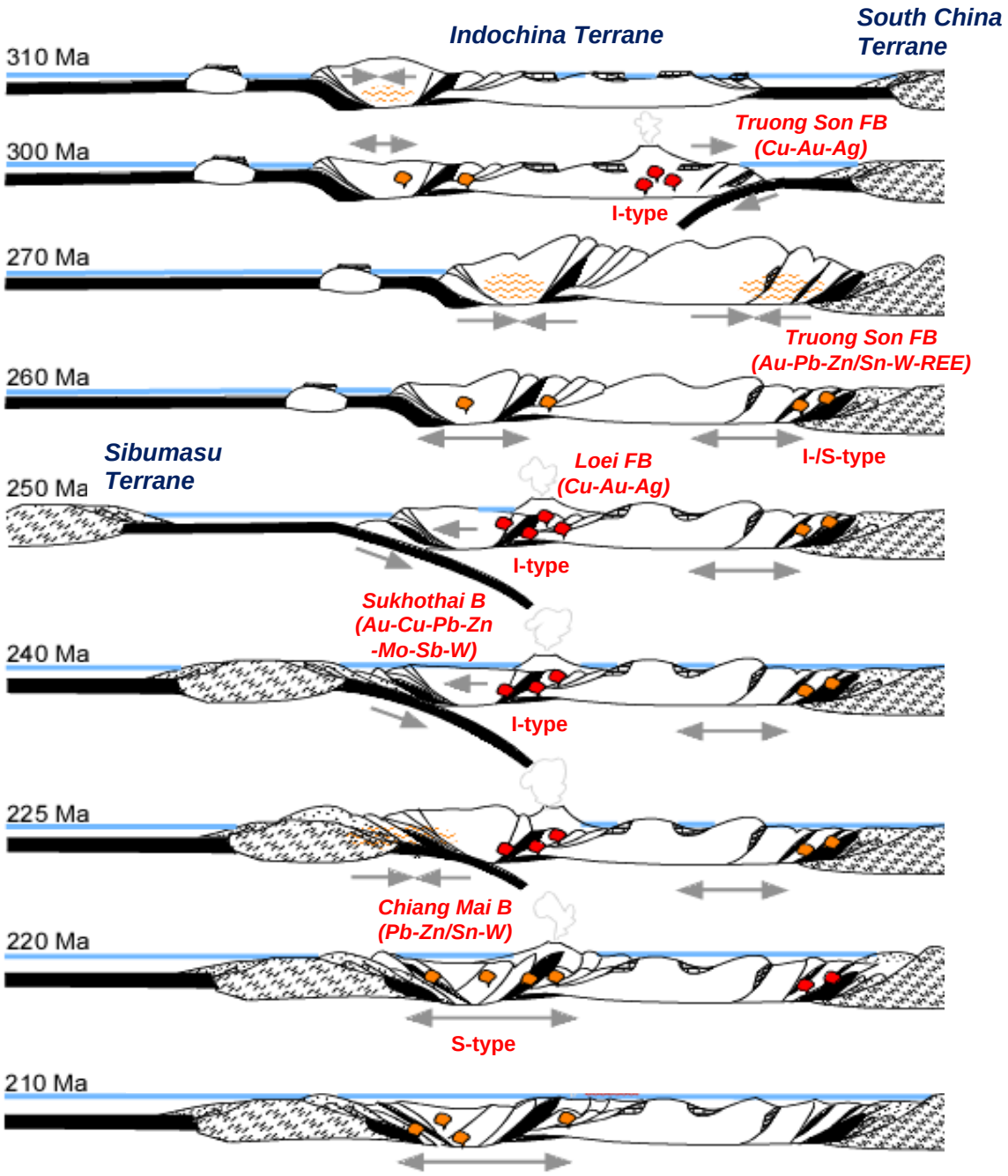

Fig. 2.5. Reconstruction of formation of the mineralised belts of the Indochina Terrane during Late Carboniferous (310 Ma)–Late Triassic (210 Ma) period. Modified after Meffre et al. (2011).

Loei Fold Belt (LFB)

Subduction has occurred along the western margin of the Indochina Terrane during Late Permian to the Late Triassic (260–220 Ma), producing arc volcanic and I-type plutonic rocks along the area from the northern Laos to western Cambodia, through northeastern Thailand (Figs. 2.3 and 2.5; Khin Zaw et al., 2007a, 2009, 2010). Significant economic Cu-Au-Ag resources have been discovered from several localities at the central and northern parts of the belt in Thailand, such as Chatree (Au-Ag), Wang Yai (Au-Ag), Puthep (Cu-Au), Phu Thap Fah (Au), Phu Lon (Cu-Au) and French Mine (Cu-Au). Geochronological studies indicated all of them are genetically linked to the local igneous activity, and the deposits are consisted either of skarn (including both oxidised and reduced skarns) or epithermal systems (e.g., Kamvong, 2004, 2006; De Little, 2005; Khin Zaw et al., 2007a, 2009, 2010; Salam, 2013).

Sukhothai Belt (SB)

The belt, in the eastern part of the northwestern Thailand, is mostly composed of Early Palaeozoic to Permian sedimentary rocks overlain and intruded by both Triassic island arc-type (250–220 Ma) and post-collisional (220–180 Ma) plutonic and volcanic rocks (e.g., Srichan et al., 2009; Khin Zaw et al., 2010). The belt continues northward into the eastern part of Shan State in Myanmar and the western part of northern Laos, and southwards into the eastern Thailand and western part of Cambodia (Fig. 2.3; Khin Zaw et al., 2010). Orogenic Au (e.g., Huai Kham On in Thailand; Khositanont et al., 2009), porphyry/skarn-like Cu-Ag-Mo (e.g., Luang Namtha in Laos; Amanta Resources website) and VHMS Cu-Pb-Zn (e.g., Mae Yom in Thailand; Thai Goldfields, 2012) deposits occur within the belt. Several mesothermal/epithermal Sb-W-Au deposits are also present along the belt (e.g., Dill et al., 2008). These ore deposit occurrences indicate that metallogenic setting of the SB is different from that of Loei Fold Belt. Although two belts have contemporaneous magmatism with similar geochemical signature (e.g., I-type; Fig. 2.5; Khin Zaw et al., 2009, 2010), the SB contains more post-collisional magmatic rocks (Srichan et al., 2009) and the LFB contains more arc-related rocks.

Chiang Mai Belt (CB)

The CB is composed of Late Triassic-Middle Jurassic (225–180 Ma) granites intruding into a Late Palaeozoic to Mesozoic accretionary complex along the westernmost part of the Indochina Terrane (Fig. 2.3; Khin Zaw et al., 2010). The granites are mostly S-type and intruded in a post-collisional tectonic setting following the collision between the Indochina and Sibumasu Terranes during the Late Triassic (Fig. 2.5; Meffre et al., 2011). The granites of the belt are commonly associated with skarn systems, such as Pb-Zn skarn (e.g., Muang Kut;

Yokart, 1977; Kiratisevee et al., 2000; Khin Zaw et al., 2010) and Sn-W skarn (e.g., Samoeng; Khositanont, 1990) deposits.

2.3.3. Late Mesozoic tectonic history and ore deposits

Extensive intra-continental red bed sedimentary sequences were deposited throughout mainland SE Asia during the Late Mesozoic. Magmatism was restricted to the southeastern margin of the Indochina Terrane (e.g., Khin Zaw et al., 2010).

Dalat-Kratie Belt (DKB)

The Dalat-Kratie belt consists of Triassic to Cretaceous sedimentary rocks intruded by Cretaceous (125–75 Ma) volcano-plutonic rocks, which are in turn overlain by Quaternary intraplate basalts. The belt extends across the region from Cambodia to Southern Vietnam and overlies the southern continuation of the TSFB and LFB (Khin Zaw et al., 2010; Fig. 2.3). The Cretaceous belt is chronologically comparable to the plutono-volcanic rocks of the late stage of the Yanshanian Orogeny in SE China (140–65 Ma; Manaka et al., 2012). Thus could have formed in a similar tectonic setting as a southern continuation of the Yanshanian belt, which was formed from the subduction of the Palaeo-Pacific Plate underneath the Eurasia Plate (including Indochina Terrane) (Thuy et al., 2004; Manaka et al., 2012). Ore deposits in the belt are mostly intrusion-related Au systems (e.g., Okvau, Snoul in Cambodia; Khin Zaw et al., 2010 and Tien Thuan in Southern Vietnam; Banks, 2008). Other deposit types such as porphyry-like Cu-Au, skarn Pb-Zn and sediment-hosted Au deposits may also be present in the area (e.g., North Kratie in Cambodia; Khin Zaw et al., 2010; Lim, 2012).

2.4. GEOLOGY AND COPPER-GOLD DEPOSITS OF TSFB

2.4.1. Introduction

A number of ore deposits have been recently discovered in the areas of Laos and central Vietnam where TSFB's igneous and metamorphic units are distributed, and intensive ore deposit studies have been conducted to understand the link between geological setting and genesis of the Cu-Au deposits within this area (Khin Zaw et al., 2007a, 2010).

2.4.2. Magmatism and Metamorphism of the TSFB

Recent studies have demonstrated that the TSFB is made up of the Carboniferous-Triassic magmatic and metamorphic rocks that overlies Early to Middle Palaeozoic sedimentary, igneous and metamorphic rocks and extends from Yunnan (e.g., Lai et al., 2013) to central Vietnam via central and northern Laos. The Late Carboniferous-Triassic igneous units within the TSFB were emplaced during two stages. The early (310–275 Ma) magmatic stage may

have occurred as a result of the subduction of oceanic crust attaching the South China Terrane to the underside of the Indochina Terrane (e.g., Khin Zaw et al., 2010), whereas the late magmatic and metamorphic event during the 265–230 Ma is interpreted to have been caused by collision-related metamorphism and post-collisional magmatism of the two terranes (Figs. 2.6A, B and 2.7; e.g., Khin Zaw et al., 2010). A 10 Ma gap (275–265 Ma) is identified between the two stages and the period is considered to be a peak of collision between the two terranes (Fig. 2.7; e.g., Khin Zaw et al., 2010)

2.4.3. Cu-Au Mineral Districts of the TSFB

Copper and gold resources have been discovered at main three districts along the TSFB (Fig. 2.8), including:

(1) Phu Bia area of northern Laos;
(2) Sepon area of central Laos; and
(3) Central Vietnam.

A total mineral resource of more than 11.1 Moz gold and 3.7 Mt copper has been delineated from the three districts including Phu Bia, Sepon and central Vietnam (Table 2.1.), suggesting that the TSFB contains the largest gold and copper resources of the Indochina Terrane. Geological setting of copper- and gold-bearing deposits in the three districts is reviewed and summarised below.

2.4.3.1. Phu Bia Cu-Au District

The Phu Bia area is the largest copper-gold mineral district in northern Laos and geology of the district is characterised by Late Carboniferous-Early Permian (310–275 Ma) magmatic rocks that intrude and overlie the older Silurian-Permian sedimentary rock sequences (Khin Zaw et al., 2007a, 2010; Fig. 2.9). A number of Cu-Au deposits have been discovered in the Phu Bia area and they are principally classified into two major systems involving porphyry-related skarn/skarn Cu-Au and epithermal Au-Ag deposits (Khin Zaw et al., 2010; Table 2.2).

Porphyry-related skarn Cu-Au; The porphyry-related skarn Cu-Au deposit is present in Phu Kham, at the southeastern end of the Phu Bia area and around Phonsavan at the northern part of the Phu Bia area (Fig. 2.9). The Cu-Au mineralisation at Phu Kham predominantly occurs in the host volcaniclastic rocks and is characterised by a typical oxidised exoskarn deposit (Tate, 2005; Kamvong, 2008). Genetic links of the systems to the Late Carboniferous

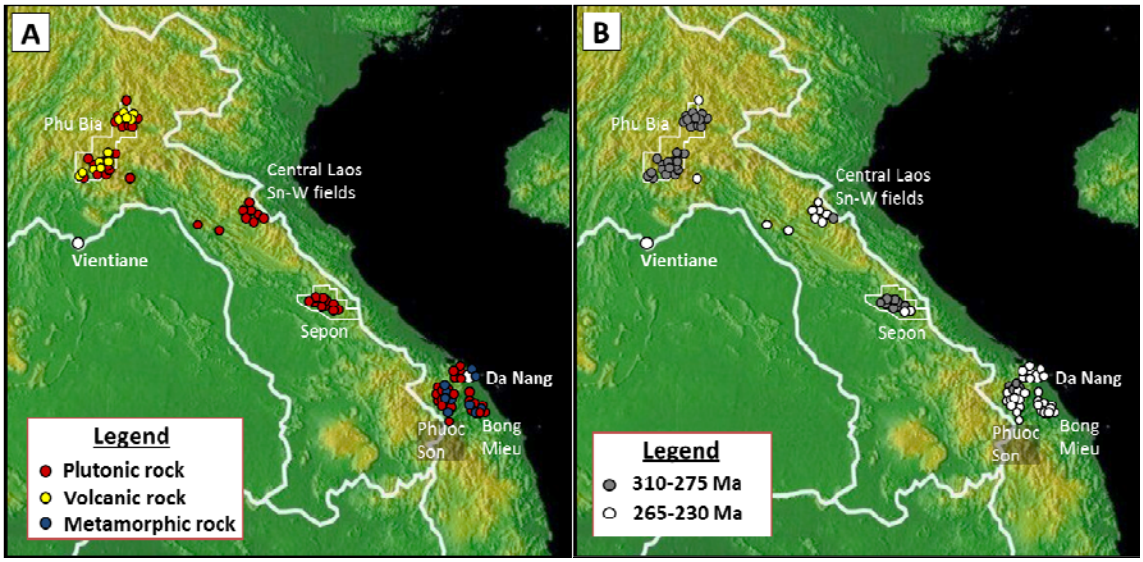

Fig. 2.6. Distribution of the studied volcanic-plutonic-metamorphic rocks of the Truong Son Fold belt, showing (A) rock types and (B) ages of early (310–275 Ma) and late (265–230 Ma) groups (data modified after Khin Zaw et al., 2010).

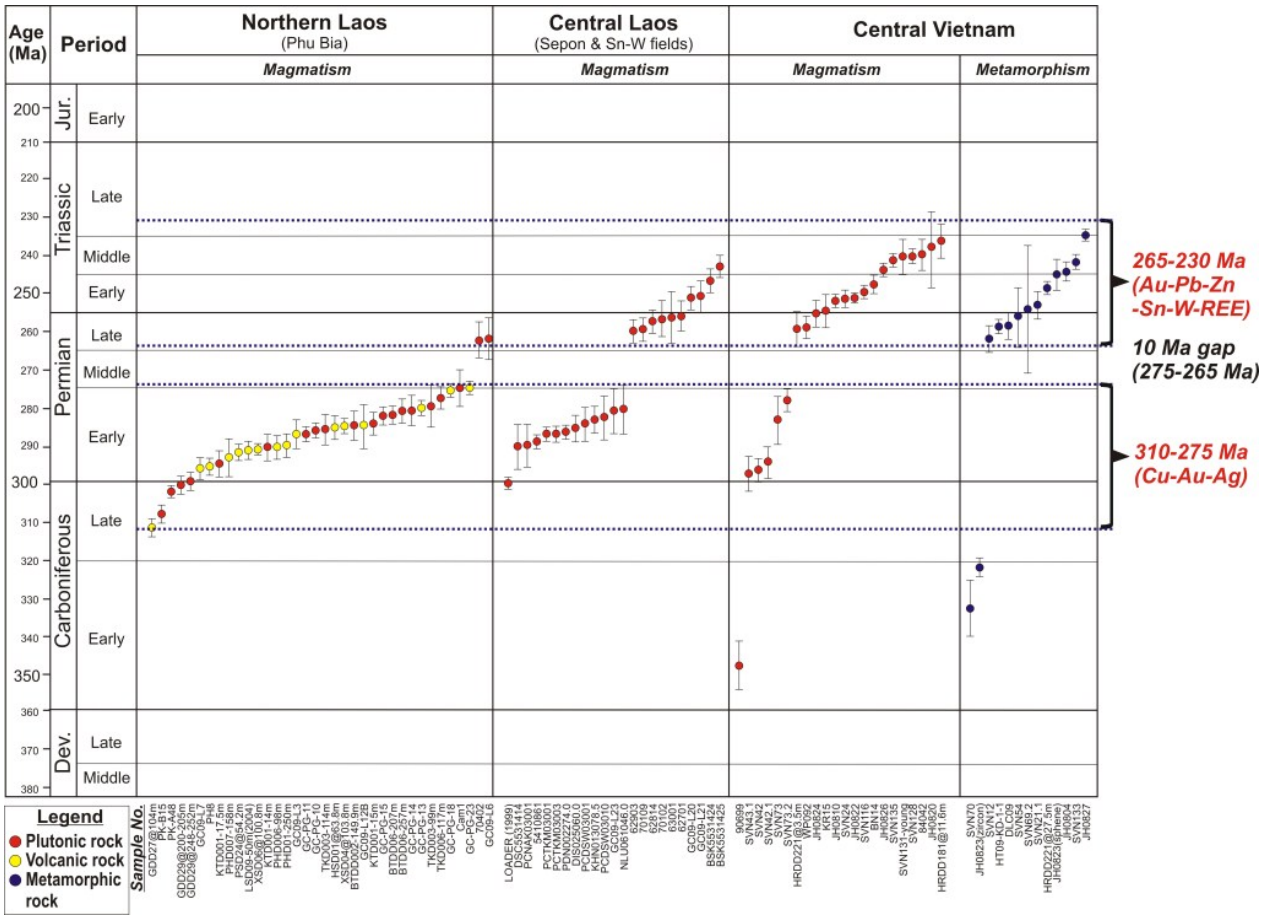

Fig. 2.7. Geochronolgical data of the magmatic and metamorphic rocks of the Truong Son Fold Belt in Laos and Vietnam, showing the ages are divided into the early magmatic stage (310–275 Ma) and the late magmatic-metamorphic stage (265–230 Ma), which are intercepted by 10 Ma gap (275–265 Ma). Cu-Au-Ag and polymetallic (Au-Pb-Zn-Sn-W-REE) mineralisation events are associated with the early and late tectonic events, respectively. Data mainly compiled from Khin Zaw et al. (2010) with some from Cromie (2010), Loader (1999) for Sepon.

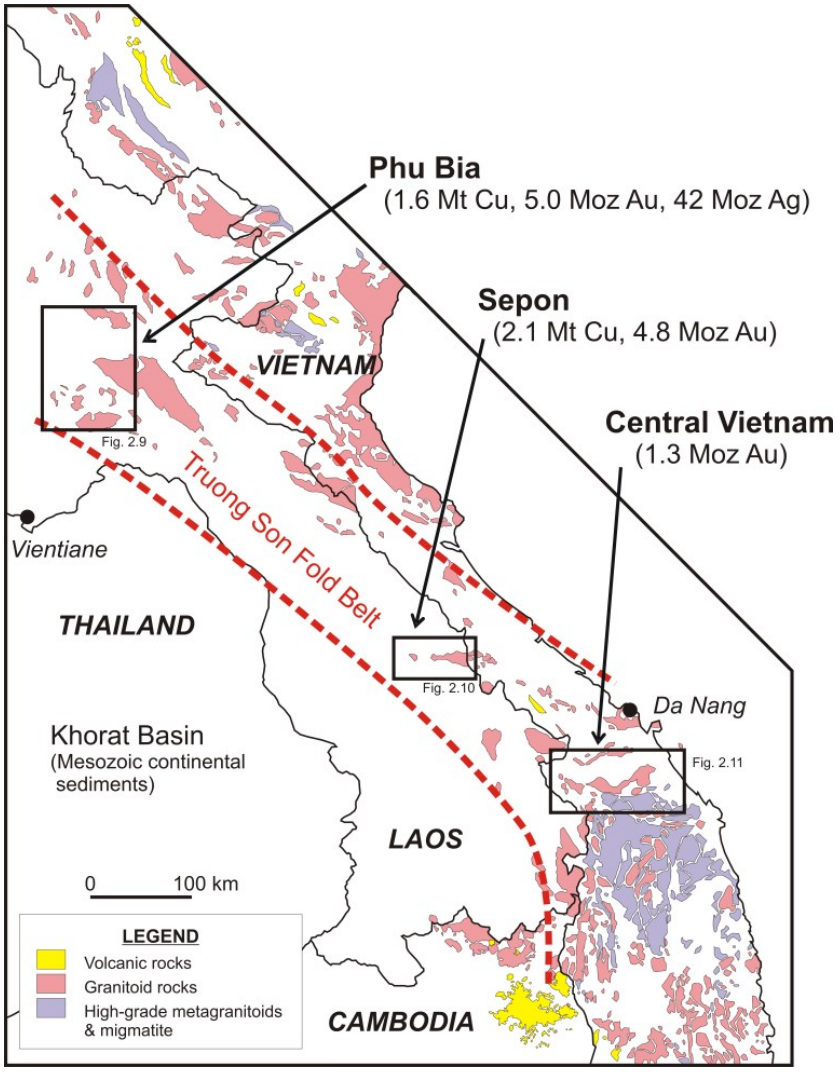

Fig. 2.8. Distribution of plutonic-volcanic-metamorphic rocks of Truong Son Fold Belt in Laos, Central Vietnam and Northeast Cambodia, together with main Cu-Au mineral districts. Distribution of igneous-metamorphic rocks is after United Nations (1990a) for Laos, Russian Geological Survey (1991) for Cambodia and United Nations (1990b) for Vietnam. Resource data are from PanAust website for Phu Bia, Smith et al. (2005) and Cannell and Smith (2008) for Sepon and Olympus website and Quynh et al. (2004) for Central Vietnam consisting of Phuoc Son and Bong Mieu.

Table 2.1. Summary of gold and copper resources of the Truong Son Fold Belt. See Fig. 2.8 for references of resource data.

Mineral district	Au-bearing ore deposit type	Contained Au resource (Moz)	Cu-bearing ore deposit type	Contained Cu resource (Mt)	Remarks
Phu Bia (N. Laos)	Porphyry-related skarn, epithermal	5.0	Porphyry-related skarn	1.6	Table 2.2 for details
Sepon (C. Laos)	Sedimentary rock-hosted (Carlin-like), skarn	4.8	Skarn (supergene & exotic)	2.1	Table 2.3 for details
Central Vietnam	Metasedimentary rock-hosted, skarn	1.3	N/A	N/A	Table 2.4 for details
	Total Au (Moz):	**11.1**	**Total Cu (Mt):**	**3.7**	

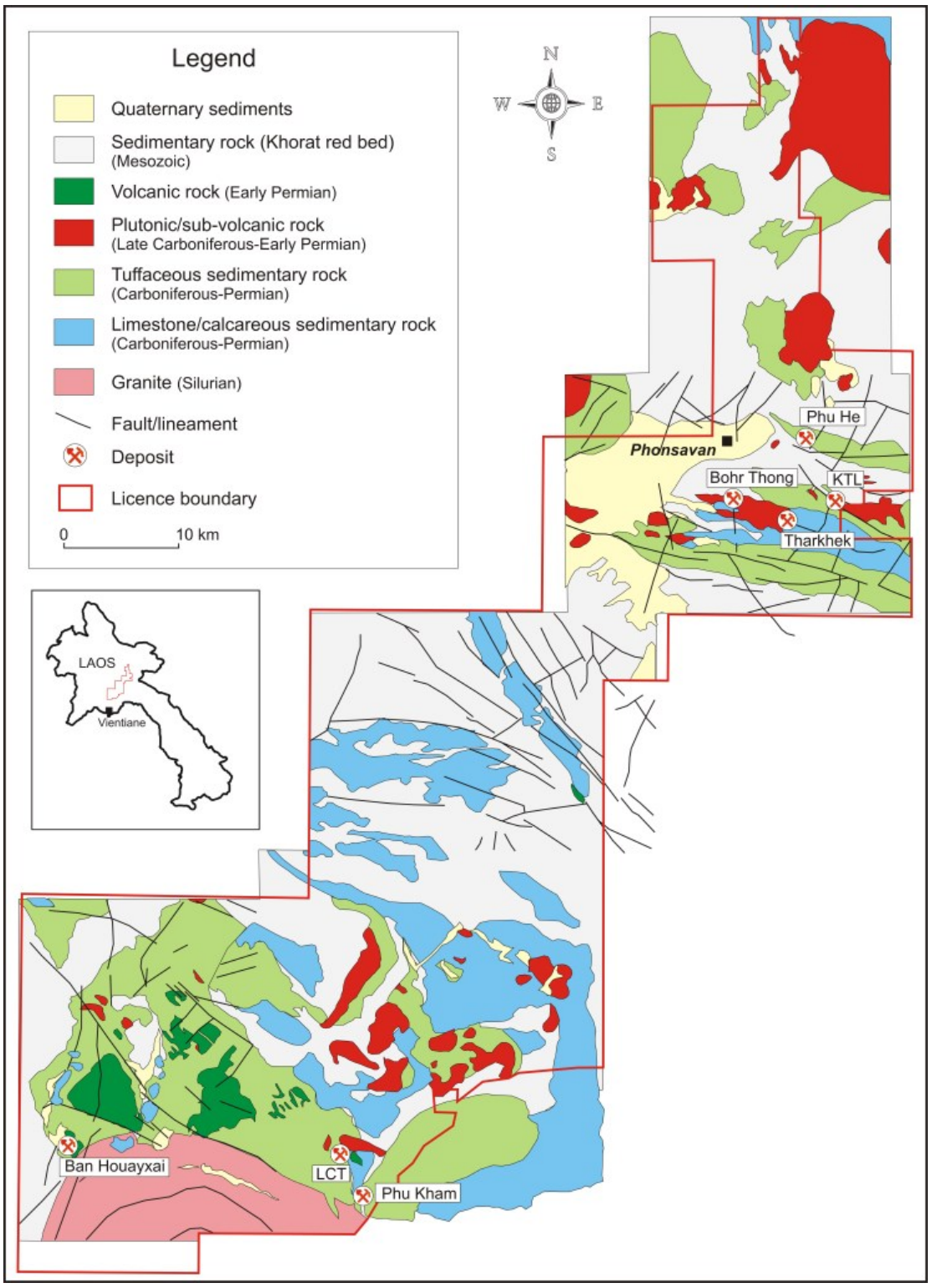

Fig. 2.9. Simplified geology of the Phu Bia area with location of Cu-Au deposits including Phu Kham, LCT, Ban Houayxai, Phu He, KTL, Tharkhek and Bohr Thong (Modified after Brost, 2011). Ages are adapted from Khin Zaw et al. (2007a, 2010).

Table 2.2. Geological characteristics of Cu-Au deposits occurring in the Phu Bia area of northern Laos, along the Truong Son Fold Belt.

Deposit name (& metal association)	Deposit type	Host rock (zircon U-Pb age)	Intrusion (zircon U-Pb age)	Age of mineralisation	Ore minerals	Alteration type	Resources	Reference
Phu Kham (Cu-Au)	Porphyry-related skarn	Volcaniclastics (306±2Ma), Diorite intrusion (306±2Ma & 305±4Ma)	Diorite intrusion (306±2Ma, 305±4Ma)	Late Carboniferous; 304.9±1.7Ma & 304.7±1.7Ma (Re-Os molybdenite)	Chalcopyrite, pyrite, magnetite, bornite, tetrahedrite, galena, enargite,sphalerite, gold	Porphyry: potassic (K-feldspar, biotite, magnetite), phyllic (sericite, pyrite), propylitic (epidote, pyrite); skarn prograde: garnet; retrograde: chlorite, epidote, carbonate, quartz, sericite, hematite; high-sulphidation with prophyllite at hanging wall zone	224Mt@0.54% Cu, 0.23g/t Au & 2.1g/t Ag	Backhouse (2004); Tate (2005); Kamvong (2006); Khin Zaw et al. (2009)
LCT (Au-Ag-Cu)	Epithermal	Tuffaceous rock, volcanic breccia, Carbonaceous shale (Early Carboniferous)	Dacitic porphyry (290.6±3.5Ma)	Early Permian	Pyrite, sphalerite, galena, chalcopyite, electrum	Silica, adularia, sericite, chlorite, pyrite, kaolinite, halloysite, alunite	32Mt@0.77g/t Au, 4.9g/t Ag & 0.12 % Cu	Mason (1997); Tate (2003); Manaka et al. (2007); Manaka (2008); PanAust website
Ban Houayxai (Au-Ag)	Epithermal	Andesite (286±4Ma) & volcanic breccia (283±4Ma)	No known intrusion	Early Permian	Pyrite, sphalerite, galena, chalcopyrite, electrum, stephanite, arsenopyrite	Silica, adularia, sericite, chlorite, pyrite,	76Mt@0.82g/t Au & 7.0g/t Ag	Tate (2004); Manaka (2008); Manaka et al. (2009); PanAust (2012)
Tharkhek (Cu-Au)	Skarn	Limestone & calcaresous sedimentary rock	Tonalite (279.6±4.4Ma, 277.4±2.7Ma)	Early Permian	Pyrite, chalcopyrite, molybdenite, bornite, sphalerite, galena, electrum	Silicification, propylitic (chlorite, epidote), phyllic (sericite, pyrite)	N/A	Tate (2006a); Webstbrook (2006); Kamvong (2008); Hotson (2009)
Bohr Thong (Cu-Au)	Skarn	Limestone & calcaresous sedimentary rock	Diorite (285.1±3.4Ma), tonalite (281.7±2.4Ma), granodiorite (282.4±2.8Ma)	Early Permian; 279.9±0.9Ma (Re-Os molybdenite)	Pyrite, magnetite, chalcopyrite, bornite, pyrrhotite, electrum	Skarn prograde: garnet; skarn retrograde: epidote, chlorite,	N/A	Tate (2006a); Webstbrook (2006); Kamvong (2008); Hotson (2009)
KTL (Cu-Au)	Skarn	Limestone, volcanic & volcaniclastic rock, calcaresous sedimentary rock	Diorite (290.0±2.9Ma, 286.9±4.3Ma, 284.8±2.4Ma)	Early Permian; 289.4±1.0Ma (Re-Os molybdenite)	Pyrite, chalcopyrite, pyrrhotite, galena, bornite, sphalerite, molybdenite, electrum	Silicification, propylitic (chlorite, epidote), phyllic (sericite, pyrite)	89Mt@0.44%Cu, 0.18g/tAu & 1.7 g/t Ag	Patterson (2005); Tate (2006a); Kamvong (2008); Hotson (2009); PanAust website
Phu He (Au-Ag)	Epithermal	Andesite (291.4±2.3Ma), dacite (289.8±3.2Ma), dacitic breccia (289.7±2.5Ma)	Rhyolite dyke (post-mineralisation)	Early Permian	Pyrite, galena, sphalerite, chalcopyrite, electrum	Propylitic (epidote, chlorite), phyllic (sericite, pyrite), argillic (clays)	N/A	Tate (2006b); Hotson (2009)

N/A = Not Available

diorite intrusions is geochronologically established applying LA-ICPMS zircon U-Pb and Re-Os molybdenite dating (e.g., Khin Zaw et al. 2007a, 2009). Cu-Au skarn systems around Phonsavan are present at KTL, Bohr Thong and Tharkhek, and they are mainly developed at contact to Early Permian intrusive units (Tate, 2006a; Kamvong, 2008; Hotson, 2009) with the Carboniferous to Early Permian limestone and calcareous sedimentary rocks.

Epithermal Au-Ag; A few epithermal systems have been recognised in the Phu Bia area, including LCT, Ban Houayxai and Phu He. They commonly are hosted in volcanic/subvolcanic and associated volcaniclastic rocks, and thus genetic link is indicated between the epithermal systems and Early Permian volcanism at Phu Bia. The LCT deposit consists of Au-bearing quartz-sulphide stockwork veins that are mainly hosted in Early Permian dacitic intrusion and the older tuffaceous sedimentary rocks. The geological data collected from LCT (i.e., geochronology, geochemistry, stable and radiogenic isotopes, fluid inclusions) suggest that the system can be classified to an epithermal style deposit (Manaka et al., 2007; Manaka, 2008). The Au-Ag mineralisation at Ban Houayxai occurs as quartz-sulphide stockwork veins hosted by a thick Early Permian andesite and the associated volcanic breccia unit, and the mineralisation characteristics (e.g., vein texture, mineralogy alteration, stable isotope, fluid inclusions) are compatible to a Ag-rich mesothermal system (Manaka, 2008; Manaka et al., 2009). At Phu He in the Phonsavan area, the Au-Ag mineralised veins are hosted in Early Permian dacitic volcanic and volcaniclastic rocks and the deposit is classified as an epithermal system, based on characteristics such as the metal association, vein texture and alteration (Tate, 2006b; Hotson, 2009).

2.4.3.2. Sepon Au-Cu District

Two styles of primary mineralisation have been identified at Sepon in central Laos, including sedimentary rock-hosted Carlin-like Au and porphyry-related skarn Cu-(Au) systems (e.g., Smith et al., 2005; Cannell and Smith, 2008; Cromie, 2010; Fig. 2.10; Table 2.3). Both systems are genetically linked to Early Permian rhyodacite porphyry intrusions that intruded into Early to Middle Palaeozoic sedimentary sequences (Cromie, 2010). Supergene enrichments are well-developed at the top of the hypogene systems and the significant copper and gold resources are currently being mined.

Porphyry-related skarn Cu; Porphyry-related skarn Cu mineralisation is developed at and around the two rhyodacite porphyry centres (i.e., Thengkham and Padan; Fig. 2.10; Cannell and Smith, 2008; Cromie, 2010). Weakly mineralised Cu-Mo system is also present within the core of the intrusive units at Padan and the system is characterised by porphyry style of

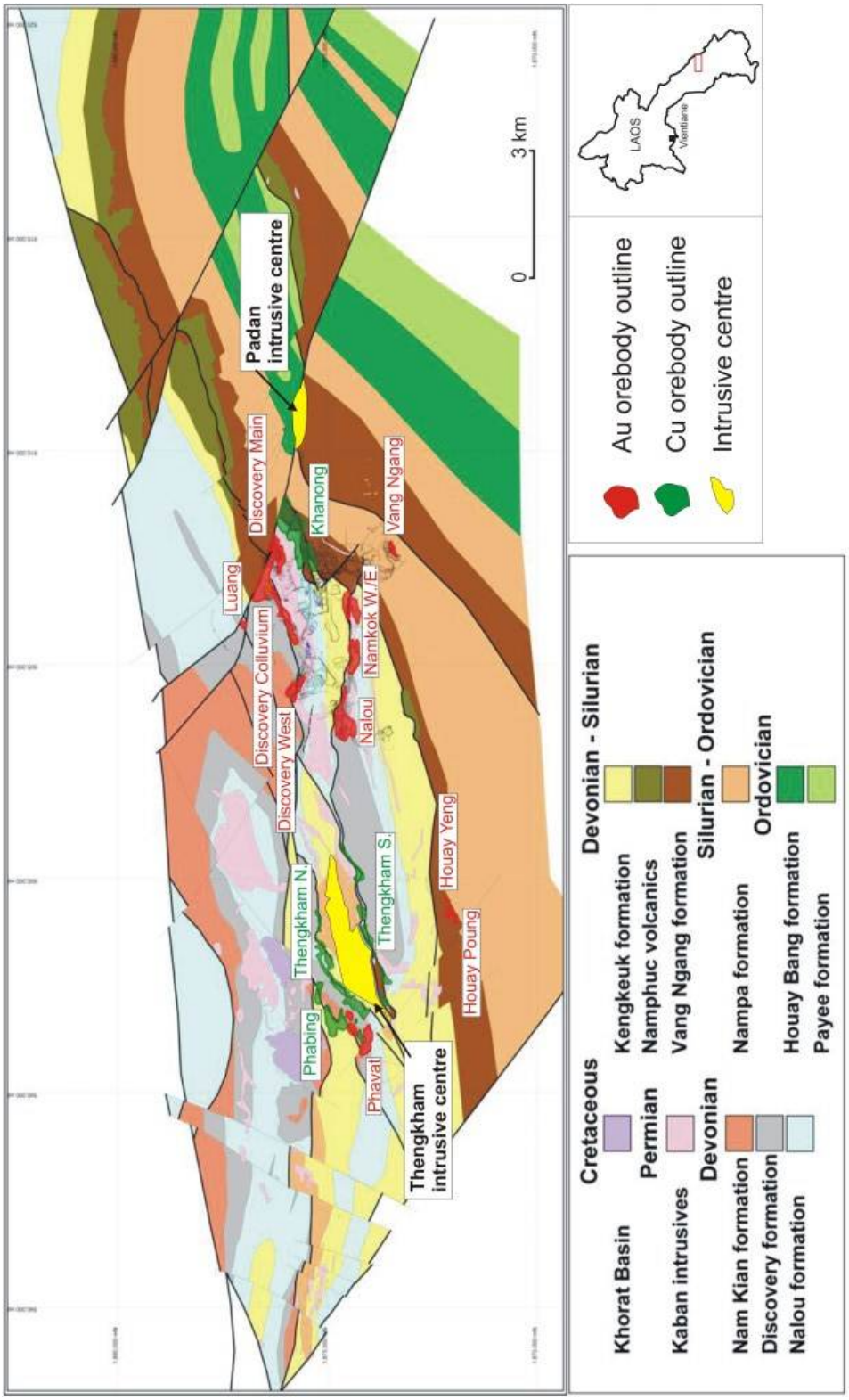

Fig. 2.10. Simplified geology of the Sepon area with location of Cu-Au orebodies, together with Padan and Thengkham intrusive centres (Modified after Cannell and Smith, 2008).

Table 2.3. Geological characteristics of Cu-Au deposits occurring in the Sepon district of central Laos, along the Truong Son Fold Belt.

Deposit name (& metal association)	Deposit type	Host rock (zircon U-Pb age)	Intrusion (zircon U-Pb age)	Age of mineralisation	Ore minerals	Alteration type	Resources	Reference
Padan (Cu-Mo)	Porphyry	Rhyodacite porphyry, mudstone	Rhyodacite porphyry (287.0±2.0Ma)	Early Permian: 282.4±1.6Ma, 280.2±1.0Ma (Re-Os molybdenite)	Pyrite, molybdenite, chalcopyrite, hematite	K-feldspar, chlorite, sericite, epidote, carbonate	N/A	Cannell and Smith (2008); Cromie (2010)
Khanong (Cu-Au)	Skarn/supergene/exotic copper-gold	Bioclastic sandstone, limestone, carbonaceous and calcareous mudstone, siltstone and sandstone	Rhyodacite porphyry (283.0±3.0Ma)	Early Permian	Hypogene: pyrite, galena, chalcopyrite, sphalerite, molybdenite; Supergene: chalcocite, malachite, azurite, cuprite, native copper; Exotic: Cu-Mu-wad	Skarn prograde: garnet, pyroxene; skarn retrograde: chlorite epidote, calcite, hematite	25.5Mt@3.5% Cu & 18.2Mt@0.76g/t Au (Au cap.)	Cannell and Smith (2008); Cromie (2010)
Thengkham South & North (Cu)	Porphyry/skarn/supergene/exotic copper	Bioclastic sandstone, limestone, carbonaceous and calcareous mudstone, siltstone and sandstone	Rhyodacite porphyry (287.8±2.5Ma)	Early Permian: 287.2±1.0Ma, 286.1±1.0Ma (Re-Os molybdenite)	Hypogene: pyrite, chalcopyrite, molybdenite; Supergene: malachite, chalcocite, azurite, cuprite, native copper	Skarn prograde: garnet, pyroxene, biotite; skarn retrograde: chlorite, epidote, quartz, hematite, carbonate	10.7Mt@1.8% Cu (South) & 10.4Mt@2.2% Cu (North)	Cannell and Smith (2008); Cromie (2010)
Phabing (Cu)	Exotic copper	Bioclastic sandstone, limestone, carbonaceous mudstone, chert	No known intrusion	N/A	Malachite, native copper	No known alteration	2.0Mt@3.4% Cu	Cannell and Smith (2008)
Discovery Main (Au)	Sedimentary rock-hosted Carlin-like	Dolomite, calcareous shale, shale, chert	Rhyodacite porphyry (286.0±3.0Ma)	Early Permian	Pyrite, sphalerite, galena, chalcopyrite	Silicification (jasperoid), pyritisation; skarn prograde: garnet; skarn retrograde: chlorite, calcite	8.8Mt@2.87g/t Au	Loader (1999); Smith et al. (2005); Cromie (2010)
Discovery Colluvial (Au)	Sedimentary rock-hosted Carlin-like	Calcareous shale	Rhyodacite porphyry (290.0±6.0Ma), dolerite dyke (post-mineralisation)	Early Permian	Pyrite, galena, sphalerite, chalcopyrite, tetrahedrite, malachite, azurite	Silicification (jasperoid), sericitisation	2.9Mt@2.87g/t Au	Smith et al. (2005); Cromie (2010)
Discovery West (Au)	Sedimentary rock-hosted Carlin-like	Dolomite, carbonaceous mudstone, calcareous mudstone, chert	Rhyodacite porphyry (284.4±4.5Ma, 282.7±5.6Ma)	Early Permian	Pyrite, sphalerite, galena, gold,	Silicification (jasperoid), decarbonatisation, dolomitisation, pyritisation, sericitisation	13.4Mt@2.2g/t Au	Smith et al. (2005); Cromie (2010)
Nalou (Au)	Sedimentary rock-hosted Carlin-like	Calcareous shale, limestone	Rhyodacite porphyry (280.0±6.0Ma)	Early Permian	Pyrite, sphalerite, galena, stibnite	Silicification (jasperoid), pyritisation, dolomitisation	30.2Mt@1.69g/t Au	Smith et al. (2005); Cromie (2010)
Namkok East & West (Au)	Supergene	Calcareous shale, dolomite	Rhyodacite porphyry	Early Permian	Ferruginous and manganiferous clay	No known alteration	3.2Mt@1.19g/t Au (East) & 4.2Mt@2.48g/t Au (West)	Smith et al. (2005); Cromie (2010)
Vang Ngang (Au)	Sedimentary rock-hosted Carlin-like	Sandstone, siltstone, mudstone, limestone	Rhyodacite porphyry	Early Permian	Pyrite, sphalerite, galena,	Silicification (jasperoid)	1.0Mt@2.86g/t Au	Smith et al. (2005); Cromie (2010)

N/A = Not Available

mineralisation (Cromie, 2010). The primary skarn mineralisation is hosted in the calcareous units at Khanong and Thengkham, where the units are in contact with the intrusive centres. Economic Cu orebodies at Sepon predominantly consist of supergene enrichment zones (mainly chalcocite and malachite) developed over the primary skarn systems (Cannell and Smith, 2008; Cromie, 2010).

Sedimentary rock-hosted Carlin-like Au; Gold resources at Sepon are made up of several orebodies such as Discovery Main, Discovery Colluvial, Discovery West, Luang, Nalou, Namkok West, Namkok East, Vang Ngang and Khanong (Fig. 2.10; Smith et al., 2005). All of them, except Khanong where gold is present in skarn, are associated with disseminated pyrite in decalcified calcareous sedimentary units that occur together with jasperoid (silica replacement) zone at the contact with the rhyodacitic porphyry stocks (Smith et al., 2005; Cromie, 2010). Previous studies have demonstrated that a number of geological characteristics of the primary gold mineralisation at Sepon are comparable to those of Carlin-type gold deposits in Nevada (Smith et al., 2005; Cromie, 2010).

2.4.3.3. Central Vietnam Au District

The Phuoc Son deposit area of this study lies on the central Vietnam Au District. Geological setting of TSFB in central Vietnam is slightly different from that of the Phu Bia and Sepon Districts in Laos, as it is predominantly composed by the late stage (265–230 Ma), plutono-metamorphic rocks (Fig. 2.11). In addition, the Phuoc Son-Tam Ky Suture Zone comprising Ordovician-Silurian mafic-ultramafic rocks is exposed in the region (e.g., Tran Thanh Hai et al., 2009) and overlaps with the plutono-matamorphic rocks belonging to the TSFB, suggesting that the geological setting of the central Vietnam is more complex than that at Phu Bia and Sepon.

Three gold deposits are present in Central Vietnam including Phuoc Son, Bong Mieu and Phuoc Thanh (Fig. 2.11; Table 2.4). Mineralisation style of the systems includes skarn and metasedimentary rock-hosted systems, but the styles are not well-established due to the complex geological setting (i.e., the systems are commonly deformed due to overprinting by later orogenic and metamorphic events).

Phuoc Son Au deposit: The Phuoc Son gold deposit area is consisted predominantly of meta-volcano-sedimentary rocks of Nui Vu Formation, which are contacted to high-grade metamorphic rocks (mainly gneissic rocks) of Kham Duc Formation by high-angle fault to the east and south sides of the deposit area (Banks et al., 2004). A series of younger intrusive

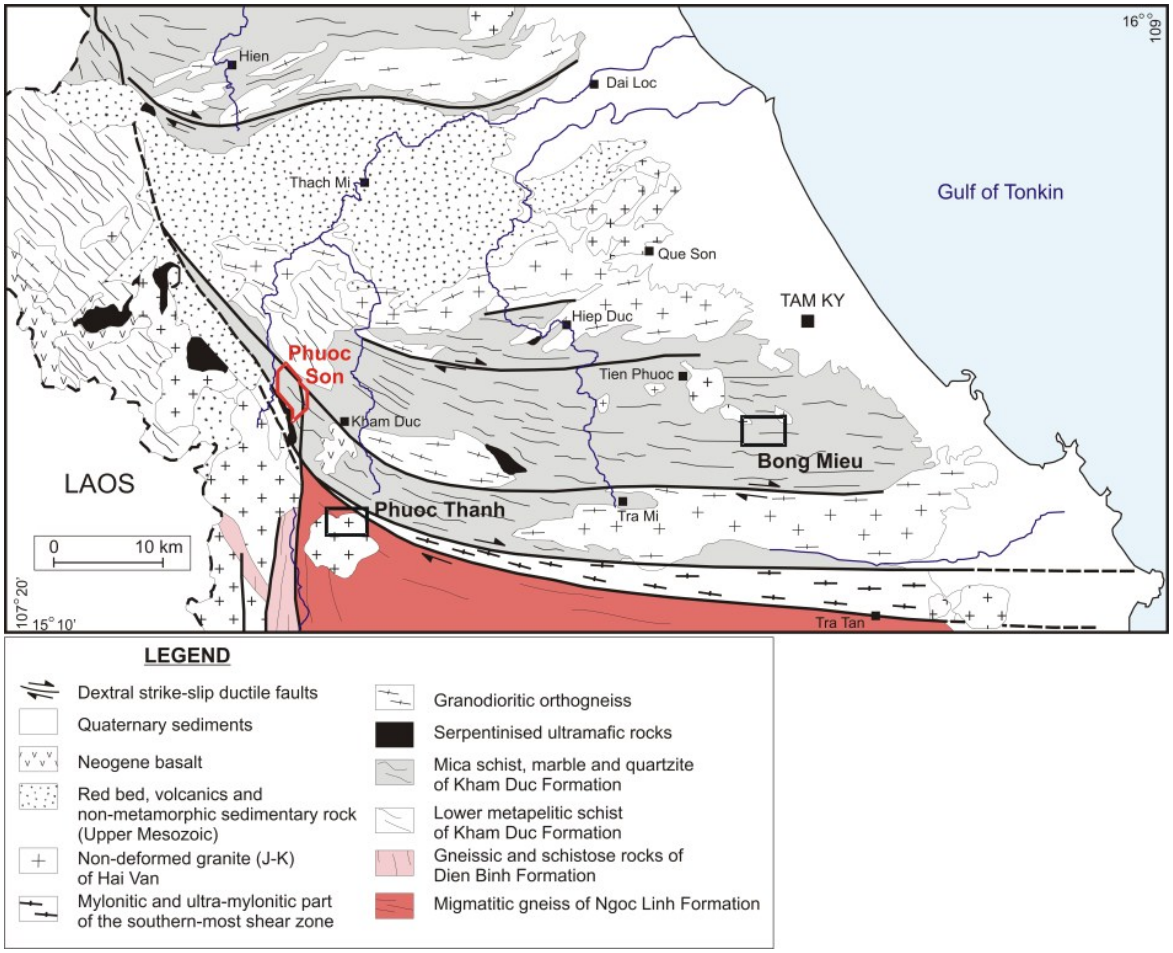

Fig. 2.11. Geological setting of Central Vietnam, together with location of the Phuoc Son deposit area and other major deposits including Duc Bo, Bong Mieu and Phuoc Thanh. Modified after Vu Van Tich et al. (2007).

units ranging from ultramafic to felsic in composition intrude into the meta-volcano-sedimentary units (Banks et al., 2004). A large mafic to ultramafic body at the southern end of the deposit area may be Ordovician in age (from zircon dating of gabbro unit; c.a. 483 Ma; Sang Quang Dinh et al., 2010). The area is interpreted to be a part of the Tam Ky-Phuoc Son Suture Zone, which may represent an Early Palaeozoic suture (Ordovician-Silurian; Tran Thanh Hai et al., 2009). U-Pb zircon geochronology has demonstrated that major intermediate-felsic intrusive units in the area are Triassic (e.g., Halpin et al., 2010; Sang Quang Dinh et al., 2010).

The Phuoc Son deposit area hosts two economic gold orebodies at Bai Dat and Bai Go and a number of prospects are also identified in the area (Banks et al., 2004). Several styles of gold-bearing mineralised systems are reported, including intrusion-hosted (e.g., Round Hill), skarn

Table 2.4. Geological characteristics of Au deposits occurring in the Central Vietnam, along the Truong Son Fold Belt.

Deposit name (& metal association)	Deposit type	Host rock (zircon U-Pb age)	Intrusion (zircon U-Pb age)	Age of mineralisation	Ore minerals	Alteration type	Resources	Reference
Phuoc Son								
Bai Dat (Au-Zn-Pb)	Metasedimentary rock-hosted	Graphitic & micaceous schist, marble, metabasite	Dacitic porphyry, andesitic porphyry, granite dyke	Not known	Pyrite, pyrrhotite, galena, sphalerite, chalcopyrite, electrum	Silicification, pyritisation	3.1Mt@6.69g/t Au (combined Bai Dat & Bai Go)	Banks et al. (2004); Stevens and Fulton (2008)
Bai Go (Au-Zn-Pb)	Metasedimentary rock-hosted	Micaceous schist, gabbro, metabasite	Dacitic porphyry, andesitic porphyry, granite dyke	Not known	Pyrite, pyrrhotite, galena, sphalerite, chalcopyrite, electrum	Silicification, pyritisation	See Bai Dat	Banks et al. (2004); Stevens and Fulton (2008)
Bai Chuoi (Au)	Metasedimentary rock-hosted	Graphitic & micaceous schist	Granite dyke	Not known	Pyrite, pyrrhotite, galena, sphalerite	Silicification, pyritisation	N/A	Banks et al. (2004); Stevens and Fulton (2008)
Nui Vang (Au)	Serpentinite-hosted	Serpentinite	Gabbro, diorite	Not known	Pyrhotite, pentlandite, chromite, gold	Serpentinite, talc, carbonate	N/A	Banks et al. (2004); Stevens and Fulton (2008)
Bai Gio (Au)	Metasedimentary rock-hosted	Graphitic & micaceous schist	No known intrusion	Triassic: 248.8±3.1Ma (Ar-Ar age of fuchsite), 236.4±2.5Ma (Ar-Ar age of sericite)	Pyrite, pyrrhotite	No known alteration	N/A	Banks et al. (2004); Borisenko et al. (2006); Stevens and Fulton (2008)
Bo (Au)	Metasedimentary rock-hosted	Amphibole schist	Granite dyke	Not known	Pyrite, pyrrhotite	No known alteration	N/A	Banks et al. (2004); Stevens and Fulton (2008)
K7 (Au)	Metasedimentary rock-hosted	Micaceous schist	Granite dyke	Not known	Pyrrhotite, pyrite, bismuthinite	No known alteration	N/A	Banks et al. (2004); Stevens and Fulton (2008)
Khe Do (Au-Cu)	Marble-hosted	Marble, metabasite	No known intrusion	Not known	Pyrite, hematite, chalcopyrite	Amphibole, vesuvianite	N/A	Banks et al. (2004); Stevens and Fulton (2008)
Khe Rin (Cu-Au-W-Mo)	Skarn	Metabasite, marble	Granite, syenite, granodiorite	Not known	Pyrite, pyrrhotite, chalcopyrite, sphalerite, molybdenite, scheelite	Skarn prograde: garnet, actinolite, tremolite; skarn retrograde: quartz, chlorite, sericite, sphene	N/A	Corlett (2001); Banks et al. (2004); Stevens and Fulton (2008)
Round Hill (Au-Cu-W-Mo)	Intrusion-hosted	Granite	Granite	Not known	Pyrite, pyrrhotite, chalcopyrite, scheelite, molybdenite	Epidote, albite, pyrite, sericite	N/A	Banks et al. (2004); Stevens and Fulton (2008)

N/A = Not Available

Table 2.4 (cont.). Geological characteristics of Au deposits occurring in the Central Vietnam, along the Truong Son Fold Belt (cont.).

Deposit name (& metal association)	Deposit type	Host rock (zircon U-Pb age)	Intrusion (zircon U-Pb age)	Age of mineralisation	Ore minerals	Alteration type	Resources	Reference
Bong Mieu								
Nui Kem (Au-Zn-Pb)	Metasedimentary rock-hosted	Gneiss, schist	No known intrusion	Mesozoic; c.a. 200 Ma (Pb-Pb galena age)	Pyrite, sphalerite, galena, pyrrhotite, chalcopyrite, electrum	Biotite, chlorite, carbonate	1.4Mt@7.9g/t Au	Baxter et al. (1992); Wallis and Ward (1997); Quynh et al. (2004); Lee (2010)
Ho Gan (Au)	Mesothermal	Schist, Orthogneiss, granite, pegmatite	Granite, pegmatite	Not known	Pyrite, galena, arsenopyrite, pyrrhotite	Muscovite (greisen)	2.0Mt@1.9g/t Au	Quynh et al. (2004)
Ho Ray-Thac Trang (Au-W)	Skarn	Schist, gneiss, granite, pegmatite, quartzite, amphibolite, Leucocratic dyke (237±5 Ma)	Leucocratic dyke (237±5 Ma)	239.6±0.8Ma (Re-Os molybdenite)	Pyrite, pyrrhotite, chalcopyrite, galena, bismuthinite, scheelite, cassiterite, arsenopyrite, molybdenite, magnetite, scheelite, electrum	Pyroxene, garnet, epidote, chlorite, biotite, carbonate	2.3Mt@1.8g/t Au	Wallis and Ward (1997); Quynh et al. (2004); Lee (2010)
Phuoc Thanh								
Phuoc Thanh (Au-Ag)	Epithermal(?)	Gneiss, schist, granite	Granite, aplite	Not known	Pyrite, galena, sphalerite, pyrrhotite, arsenopyrite, chalcopyrite, electrum	Silica, epidote, chlorite, sericite,	N/A	KORES (1999); Lee and Shin (2003)

N/A = Not Available

(e.g., Khe Rin), marble footwall-hosted (e.g., Khe Do) and low-angle shear-hosted (e.g., Bai Dat and Bai Go) systems (Banks et al., 2004; Stevens and Fulton, 2008; Table 2.4). Systematic geological, geochemical and geophysical data of the orebodies show that there are spatial relationships from the intrusion-hosted system at centre to the low-angle shear-hosted systems at the distal part. It is therefore possible that the deposits are grouped as an intrusion-related gold deposit (Banks et al., 2004).

Bong Mieu Au deposit: The Bong Mieu deposit area is located 90 km south of Danang and the area consists predominantly of high-grade metamorphic rocks (i.e, gneissic and schistose rocks) of Kham Duc Formation (e.g., Quynh et al., 2004). Gold resources at Bong Mieu are distributed in three orebodies (i.e., Nui Kem, Ho Gan and Ho Ray-Thac Trang). The deposits are located around a local anticlinal structure (e.g., Quynh et al., 2004; Tran Thanh Hai et al., 2009). The Ho Ray-Thac Trang Au-W deposit occurs at the notheastern part of the Bong Mieu area and has a skarn style of mineralisation, typically associated with leucocratic dykes (Lee, 2010). Gold mineralisation at the Nui Kem deposit occurs as a quartz-sulphide vein system commonly associated with lead and zinc, and is hosted in gneissic rocks with ore veins paralleling the metamorphic foliations (Quynh et al., 2004; Lee, 2010). The Ho Gan deposit is located on the axis of the anticlinal structure and is characterised by quartz-sulphide veins similar to that of the Nui Kem deposit, but with less lead and zinc (Quynh et al., 2004). Zircon, sphene and monazite U-Pb geochronological studies have indicated that the host metamorphic rocks were formed during Early-Middle Triassic, though the dated minerals commonly preserve Ordovician-Silurian inherited ages in the core of the grains (e.g., Halpin et al., 2010). Geochronological study of ore minerals (i.e., Re-Os molybdenite dating) has demonstrated that precipitation or recrystallisation of the ore occurred in the Triassic (c.a. 240 Ma; Lee, 2010).

Phuoc Thanh Au deposit: The Phuoc Thanh gold deposit is present in the Phuoc Son District of the Quang Nam Province, about 100 km southwest of Danang and 10 km southeast of Phuoc Son gold deposit area (Fig. 2.11). The deposit was initially assessed by KORES (Korean Resources Corporation) during the late 1990s. In the Phuoc Thanh area, the geology is chiefly composed of alternating layers of schist and gneiss of Kham Duc Formation intruded by the Ta Vi and Ba Na igneous complex (KORES, 1999). At least twenty-four individual quartz-sulphide veins have been identified, and most of them have similar characteristics, such as several tens centimetres in width, several hundred metres in length (maximum 500 m in length) and NE-SW trend with dip towards southeast (KORES, 1999; Lee and Shin, 2003). Gold occurs in two stages with early electrum inclusions in pyrite, pyrrhotite, chalcopyrite and galena and late electrum infills along fractures in the quartz-

sulphide veins (Lee and Shin, 2003). Fluid inclusion data indicated that the boiling of CO_2-bearing fluids is the main effect to have caused the gold deposition at Phuoc Thanh (Lee and Shin, 2003).

2.5. SUMMARY

Several major points of regional geological and ore deposit setting of the mainland SE Asia are summarised in the following:

- The mainland SE Asia comprises several Gondwana-derived terranes including Indochina, South China, Sibumasu and West Myanmar Terranes, which were assembled and amalgamated by subduction-collision processes during Late Palaeozoic-Mesozoic time.

- The Indochina Terrane is made up of several tectonic units, which are dominantly characterised by magmatic and metamorphic rocks and associated with specific metals. They include: Early Palaeozoic rock basement (Cu-Pb-Zn-Au), Truong Son Fold Belt (Cu-Au-Ag-Pb-Zn-Sn-W-REE), Loei Fold Belt (Cu-Au-Ag), Sukhothai Belt (Au-Cu-Pb-Zn-Mo-Sb-W), Chiang Mai Belt (Pb-Zn-Sn-W) and Dalat-Kratie Belt (Au-Cu-Pb-Zn).

- The Late Carboniferous-Late Triassic (310–230 Ma) magmatic-metamorphic rocks of the Truong Son Fold Belt extend from northern Laos to central Vietnam. The development is divided into the early volcanic and plutonic rock emplacement (310–275 Ma) and the late plutonic intrusion and metamorphism (265–230 Ma).

- Gold and copper resources of the Truong Son Fold Belt consist mainly of three mineral districts involving Phu Bia, Sepon and Central Vietnam. Porphyry-related skarn, epithermal and sedimentary rock-hosted systems are the main economic deposit types.

- In the Central Vietnam, several deposits occur including Phuoc Son, Bong Mieu and Phuoc Thanh, and they are commonly hosted in medium- to high-grade metamorphic rocks. They are probably associated with the late plutonic and metamorphic stage of the Truong Son Fold Belt. The mineralisation style and age of the deposits is different from those at Phu Bia and Sepon of Truong Son Fold Belt.

- At Phuoc Son deposit area, several styles of Au-bearing mineralised systems are present including intrusion-hosted, skarn, marble footwall and low angle shear-hosted types, and they are suggested to be an analogous to an intrusion-related gold deposit.

CHAPTER 3 DEPOSIT GEOLOGY, GEOCHRONOLOGY AND GEOCHEMISTRY

3.1. INTRODUCTION

The Phuoc Son deposit area is situated at about 6 km northwest of Kham Duc Town in central Vietnam, on a block approximately 12 km N-S by 5 km E-W, within a 60 km^2 area (Fig. 3.1). The Olympus Company has conducted exploration activities in the Phuoc Son area since the late 1990's, and the two gold orebodies that were delineated at Bai Dat and Bai Go are currently being mined. In addition, a number of gold prospects were recognised at Round Hill, Khe Rin, Khe Do, K7, Tra Long, Hoa Son, Bai Chuoi, Bai Cu, Bai Gio, Nui Vang and Bo (Fig. 3.1). Current exploration activities in the Phuoc Son area involve evaluating the economic potential of these prospects, as well as understanding detailed geological setting of the Bai Dat and Bai Go deposits.

In this Chapter, the geological setting of the Phuoc Son area including geology, geochronology and geochemistry of the host rocks at the Bai Dat and Bai Go deposits will be described and discussed to assist in developing a genetic model of gold mineralisation at Phuoc Son. Geological data presented in this Chapter are mainly based on field investigations and diamond drill core logging by the author, incorporating data from a published paper by Banks et al. (2004) and unpublished internal company reports provided to the author. This Chapter also provides new geochronological and geochemical results from the major igneous units, which will help to constrain the tectonic environment and timing of gold mineralisation of the Phuoc Son deposit area.

3.2. GEOLOGY OF THE PHUOC SON AREA

The Phuc Son deposit area is composed predominantly of a meta-volcano-sedimentary rock sequence which is strongly deformed and folded. The rock sequence is intruded by a series of intrusive units ranging from ultramafic to felsic in composition. Some of the intrusive units have large batholith-like bodies and are exposed, but most of the units occur as dykes/sills and/or stocks that are only recognised in diamond drill holes. All the lithological units observed in the Phuoc Son deposit area are herein described, in particular those recognised at the Bai Dat and Bai Go (Figs. 3.2, 3 and 4).

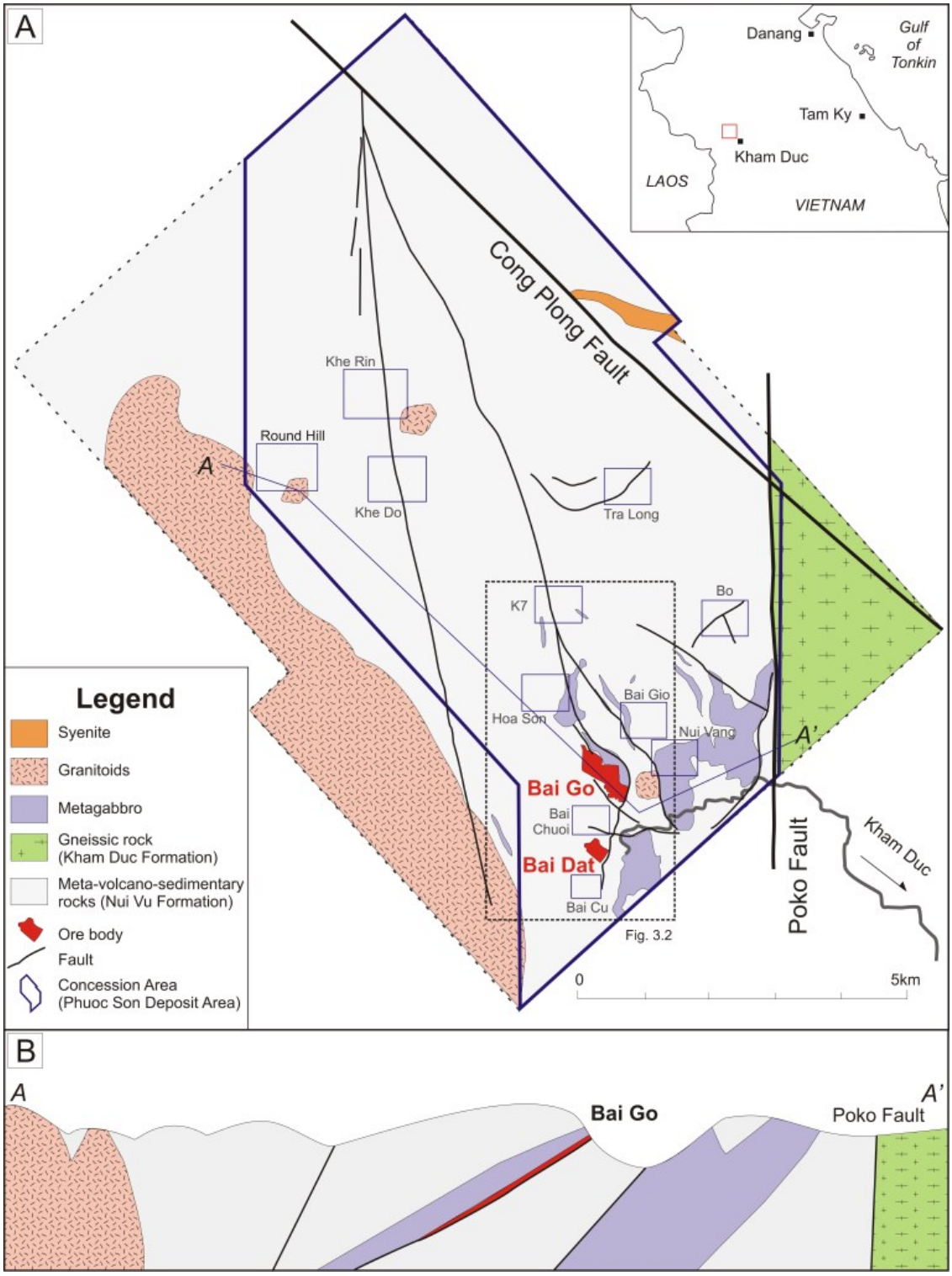

Fig. 3.1. Simplified geological map of the Phuoc Son deposit area (A) and the generalised NW-SE cross-section (B). Modified after Banks et al. (2004) and Olympus Company data. Note location of major prospects including Round Hill, Khe Rin, Khe Do, Tra Long, K7, Hoa Son, Bai Chuoi, Bai Cu, Bai Gio, Nui Vang and Bo are shown, along with the Bai Dat and Bai Go deposits.

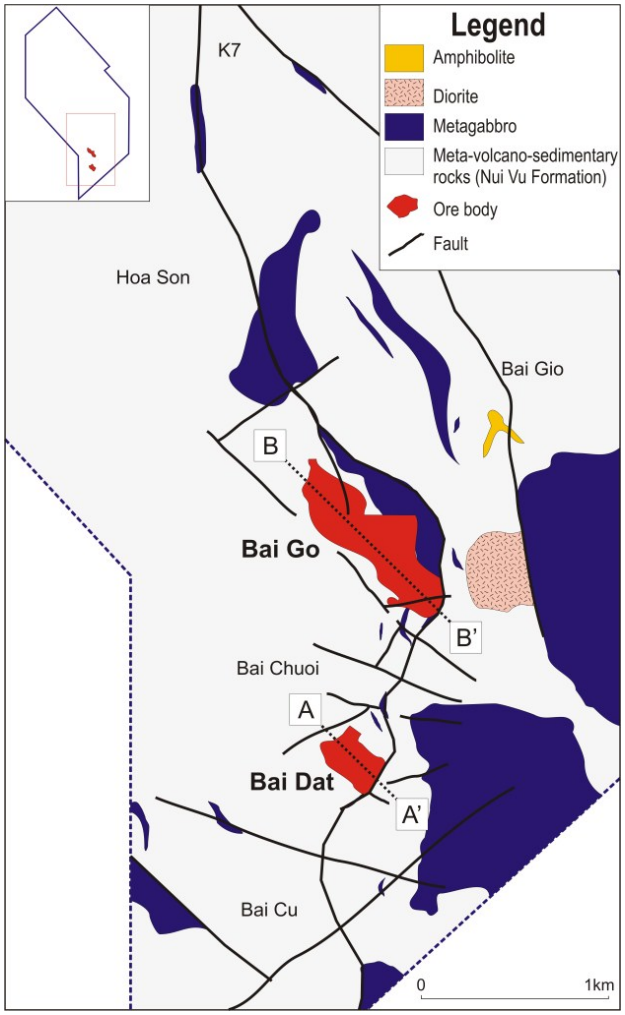

Fig. 3.2. Simplified geological map of the the southern end of the Phuoc Son area including the Bai Dat and Bai Go deposits, Phuoc Son, Central Vietnam. Modified after Olympus Company data and Banks et al. (2004).

3.2.1. Meta-volcano-sedimentary Sequence

The sequence is composed of several units including schist, phyllite, metabasite, amphibolite, marble and hornfels. The schist and phyllite units occur as large outcrops throughout the deposit area, whereas the rest of the units are present locally as observed in drill holes. The schist, phyllite and marble units are considered to be metamorphosed from sedimentary protolith, while the mafic volcanic unit is interpreted to be the protolith of the metabasite, amphibolite and hornfels units. Banks et al. (2004) interpreted that the sequence belongs to the Nui Vu Formation, which is regionally extended in central Vietnam and is overlain by the Kham Duc Formation.

3.2.1.1. Schist/phyllite

This unit has a distinct schistose texture and is well exposed in the Bai Dat deposit area (Fig. 3.5A and B). A few different types of schistose rocks can be distinguished including

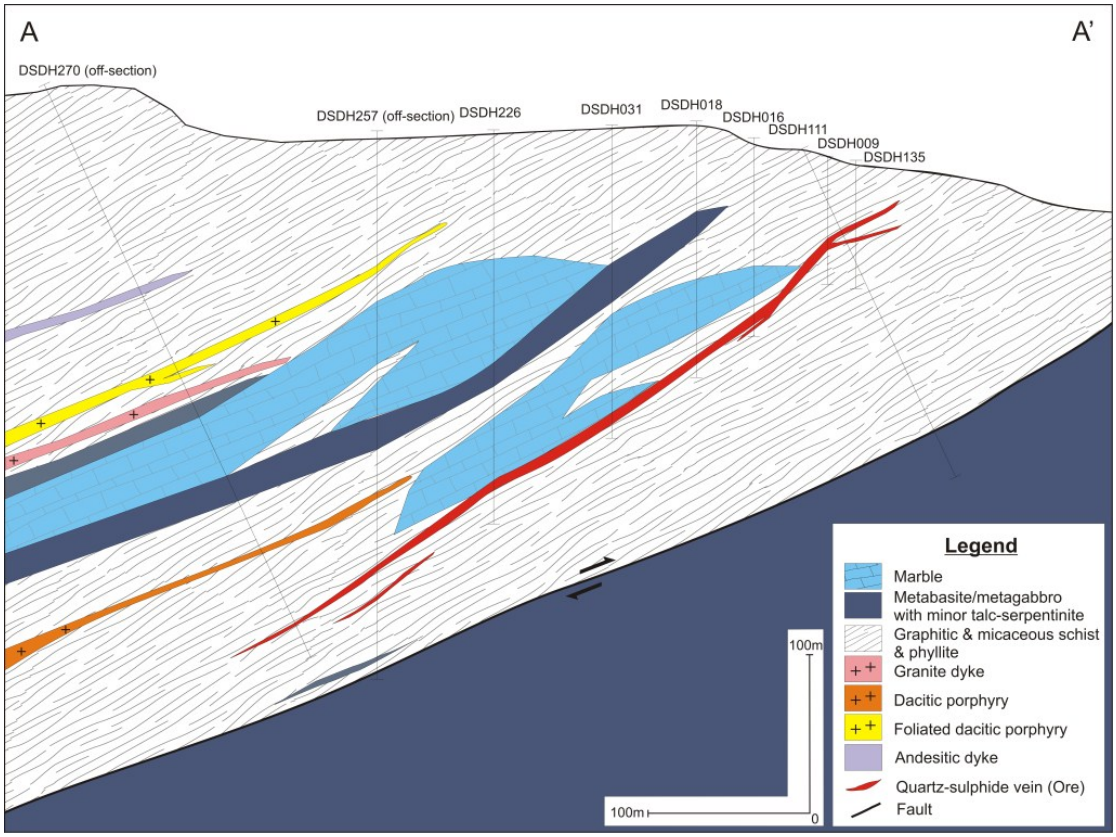

Fig. 3.3. NW-SE cross-section (A-A' in Fig. 3.2) of the Bai Dat deposit area in Phuoc Son, central Vietnam.

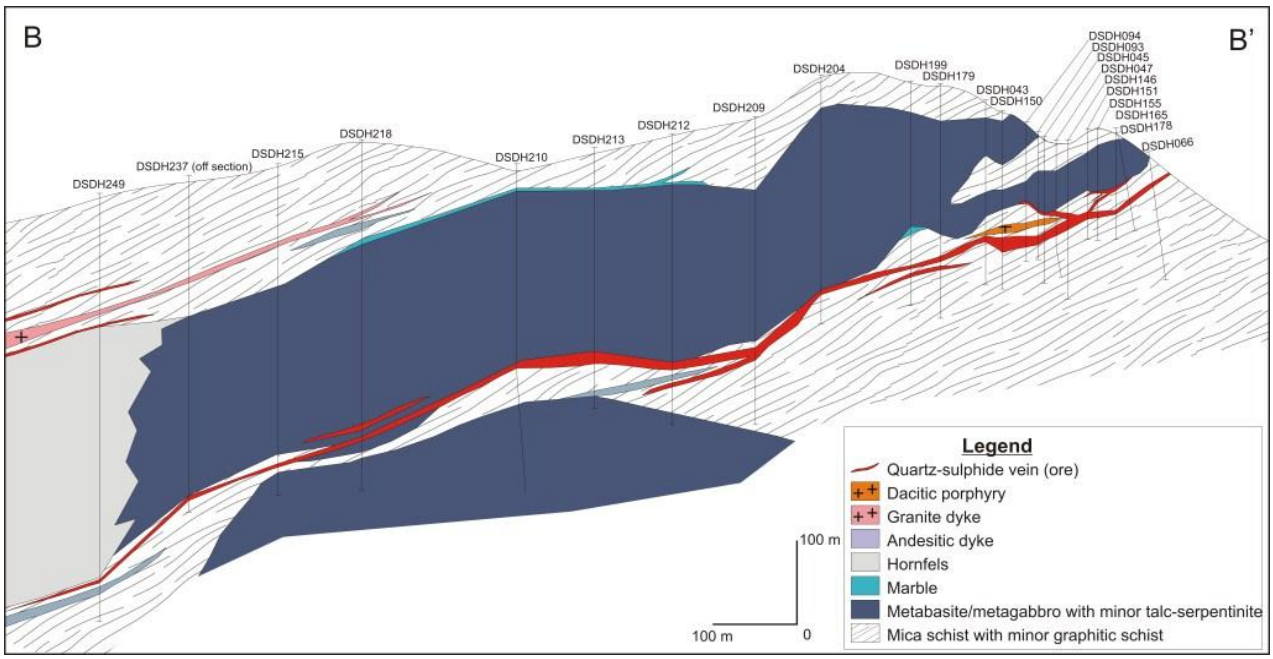

Fig. 3.4. NW-SE cross-section (B-B' in Fig. 3.2) of the Bai Go deposit area in Phuoc Son, central Vietnam.

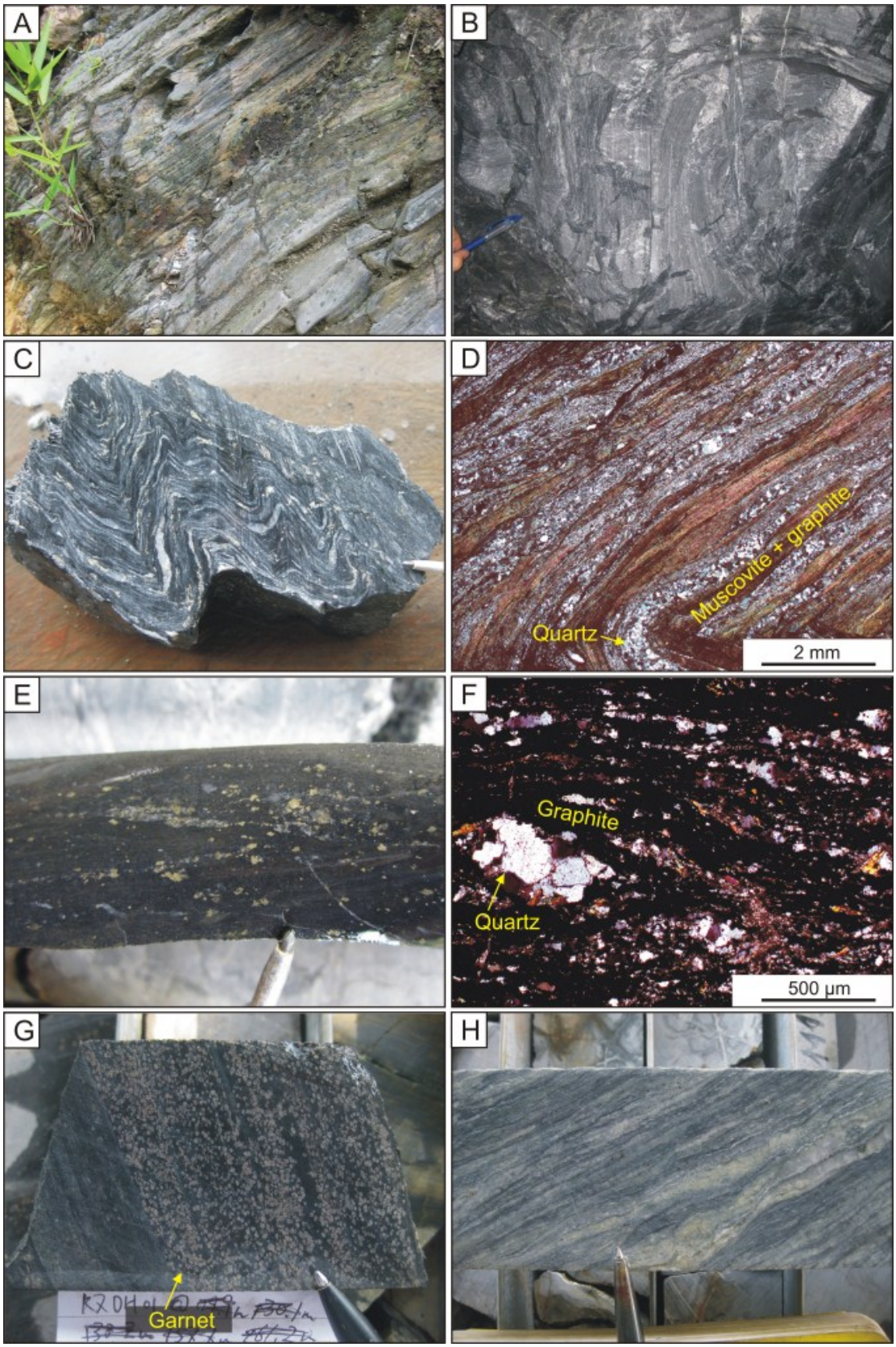

Fig. 3.5. Schistose and phyllitic rock units of the meta-volcano-sedimentary sequence in the Phuoc Son deposit area, central Vietnam. **A.** Outcrop of schist at Bai Cu Creek, south of Bai Dat. **B**. Folded schist observed in the Bai Dat underground mine. **C**. Hand specimen of folded schist from Bai Dat. Sample No. 101763. **D**. Photomicrograph of schist showing quartz-muscovite-graphite assemblage. Sample No. 101763. **E**. Drill core sample of phyllite with disseminated pyrite. Sample No. DSDH270@400.5m (Bai Dat). **F**. Photomicrograph of phyllite showing graphite-quartz assemblage. Sample No. DSDH270@400.5m (Bai Dat). **G**. Drill core sample of garnet-rich schist. Sample No. K7DH01@52.9m (K7). **H**. Drill core sample of tremolite-rich schist. Sample No. BODH02@74.6m (Bo).

micaceous, carbonaceous (graphitic), garnet and tremolite schists. Of these, the micaceous schist is the most common type in the Phuoc Son area and is composed of finely layered (typically 0.5 mm) alternating quartz-muscovite-graphite folded bands with strongly transposed primary bedding (Fig. 3.5C and D). Occurrence of the carbonaceous schist is spatially limited to the Bai Dat and Bai Go deposit areas, and the unit is frequently interlayered with carbonaceous phyllite consisting mainly of dark foliated graphite-quartz-pyrite minerals (Figs. 3.5E and F). Trace amount of opaques such as magnetite and ilmenite are also present in the carbonaceous schist/phyllite. The carbonaceous schist/phyllite units are the main host rock of the mineralised quartz-sulphide veins at Bai Dat. The garnet schist contains patchy pink garnet grains of mm size together with a quartz-muscovite-biotite assemblage (Fig. 3.5G) and commonly is intersected in drill holes at the K7 deposit, 2 km north of Bai Go. The tremolite schist is developed locally at the Bo deposit area, a few km northeast of the area encompassing Bai Dat and Bai Go. It is texturally characterised by banded creamy tremolite and dark graphite components (Fig. 3.5H).

3.2.1.2. Metabasite

The metabasite unit forms a part of the meta-volcano-sedimentary sequence at Phuoc Son and occurs typically as sills- or lens-like shaped body varying in thickness from a few tens of centimetres (e.g., at Round Hill and Bai Dat) to a few hundred metres (e.g., at Bai Go). In drill core, rocks are generally characterised by green, homogeneous aphyric fine-grained texture (Fig. 3.6A). Under microscope, the samples show interlocking minerals of pyroxene, amphibole, quartz, feldspar and epidote (20□200 μm; Fig. 3.6B). The metabasite unit is locally deformed and schistose (Fig. 3.6C) and partially altered to talc and serpentinite (Fig. 3.6D). Detailed drill core logging at Bai Dat and Bai Go reveals that the metabasite unit is emplaced parallel to the schistosity and following the orientation of the other meta-sedimentary units (e.g., schist, phyllite), suggesting that the initial protolith unit occurred as basaltic sills in the sedimentary sequence.

3.2.1.3. Amphibolite

Amphibolite is locally exposed in the Phuoc Son deposit area and boulders of amphibolite are commonly found along creeks at the northeastern part of Bai Go (Fig. 3.7A). Hand specimen shows that the unit is composed mainly of amphibole with minor feldspar and quartz (Fig. 3.7B and C). In drill holes at Bai Dat and Bai Go, the amphibolite unit generally occurs as thin layers/lenses within the metabasite unit (Fig. 3.7D), indicating that the protolith of amphibolite may be similar to that of metabasite (i.e., basaltic sill), but with a higher degree of metamorphism.

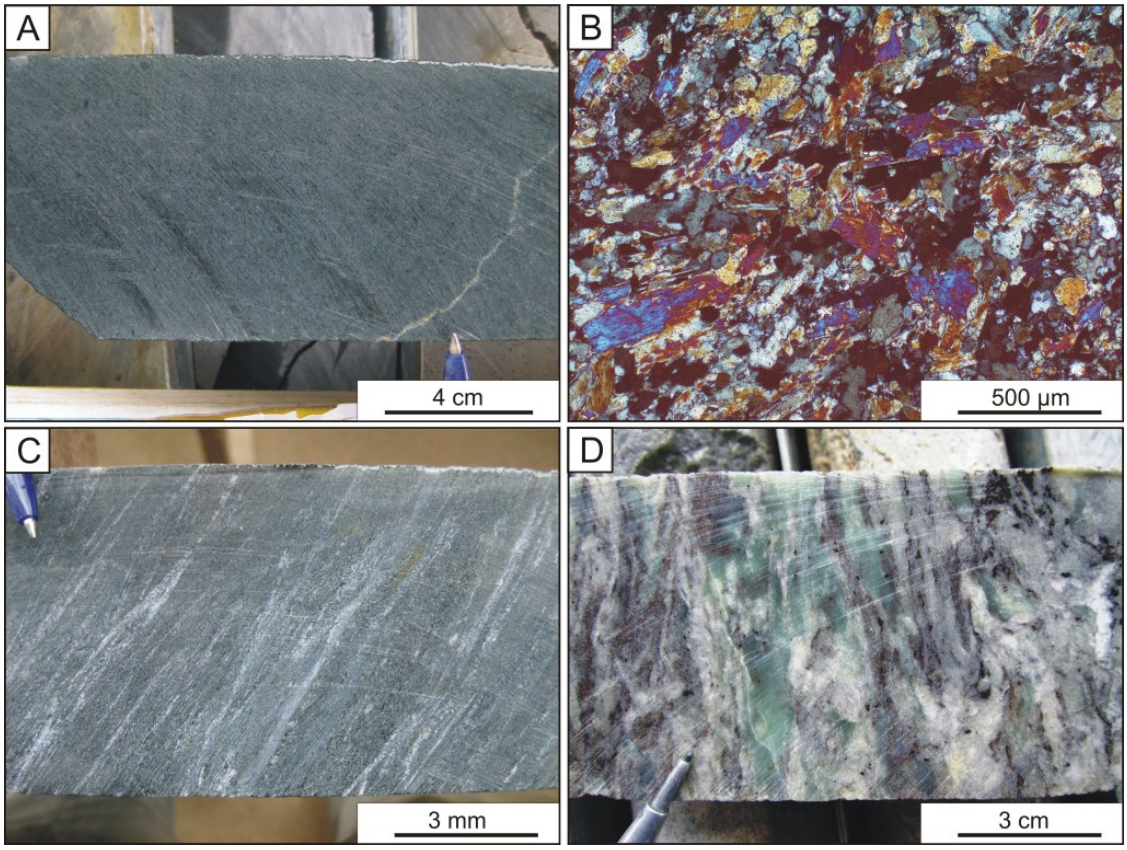

Fig. 3.6. Textural characteristics of metabasite unit of the meta-volcano-sedimentary sequence in the Phuoc Son deposit area, central Vietnam. **A**. Hand specimen of the least altered metabasite showing aphyric texture. Sample No. RHDH03@61.9m (Round Hill). **B**. Photomicrograph showing interlocking pyroxene, amphibole, quartz and feldspar assemblage. Sample No. RHDH03@34.9m (Round Hill). **C**. Drill core sample showing metabasite with schistose texture. Sample No. DSDH31@104.9m (Bai Dat). **D**. Drill core sample showing altered metabasite by talc-serpentinite assemblage. Sample No. DSDH40@77.8m (Bai Go).

3.2.1.4. Marble

In the Phuoc Son deposit area, marble occurs as thin lenses (normally a few to few tens of metres in thickness) within the meta-volcano-sedimentary sequence (e.g., Bai Dat, Bai Go, Bo, Khe Rin and Khe Do). Hand specimens commonly either have a pale uniform texture (e.g., at Tra Long, Bo, Khe Do; Figs. 3.8A and B), or have a distinct folded schistose texture (e.g., at the Bai Dat and Bai Go deposits; Fig. 3.8C and D).

3.2.1.5. Hornfels

The hornfels unit does not outcrop in the Phuoc Son deposit area, but is intersected in drill holes at Bai Go and Tra Long. A thick (at least a few hundreds of metres) hornfels unit is locally developed at the northwestern part of the Bai Go deposit area, where the unit is dark green in colour and appears to replace the metabasite/metagabbro unit (Fig. 3.4). Hand

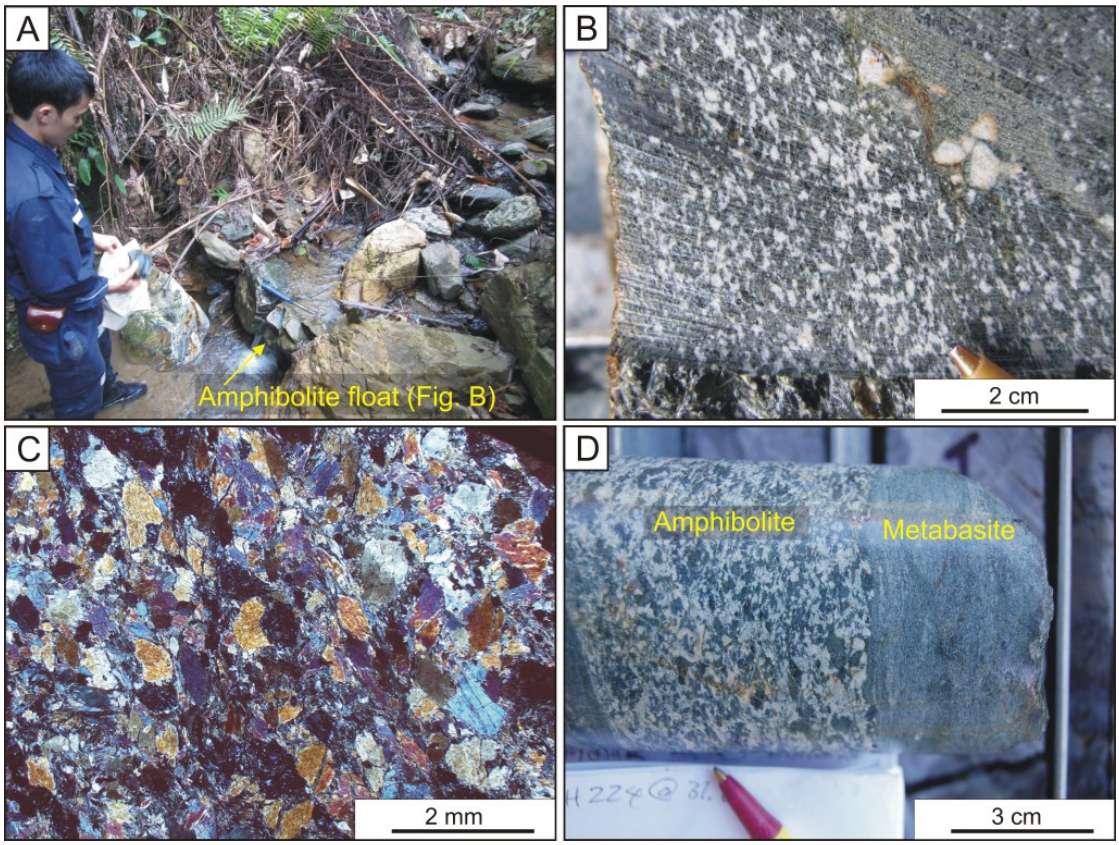

Fig. 3.7. Textural characteristics of amphibolite unit in the meta-volcano-sedimentary sequence in the Phuoc Son deposit area, central Vietnam. **A**. Amphibolite floats are commonly found in creeks at the northeastern part of the Bai Go deposit area. **B**. Hand specimen sample showing a typical texture of amphibolite. Sample No. TMVN11-07 (Bai Go). **C**. Photomicrograph showing interlocking crowded amphibole with minor feldspar and quartz. Sample No. TMVN11-07 (Bai Go). **D**. In drill holes, amphibolite typically occurs as thin lenses/layers within metabasite unit. Sample No. DSDH224@31.6m (Bai Go).

specimen of the unit is commonly homogenous in texture and colour due to intense silicification, with patches of pink garnets (Fig. 3.9A). Under microscope, they consist dominantly an interlocking fine-grained (<100 μm) quartz and biotite (Fig. 3.9B).

3.2.2. Intrusive units

In addition to the metabasite, which occurs as strongly metamorphosed sill-like bodies described above, several additional igneous rock types have intruded into the meta-volcano-sedimentary sequence. Their compositions vary from ultramafic to felsic and some have been dated using LA-ICPMS zircon U-Pb geochronology, so that their relationship to both the foliation and the meta-sedimentary rocks are helpful to constrain timing of magmatic and regional metamorphic events at Phuoc Son. All the intrusive units identified at the Phuoc Son deposit area are described below.

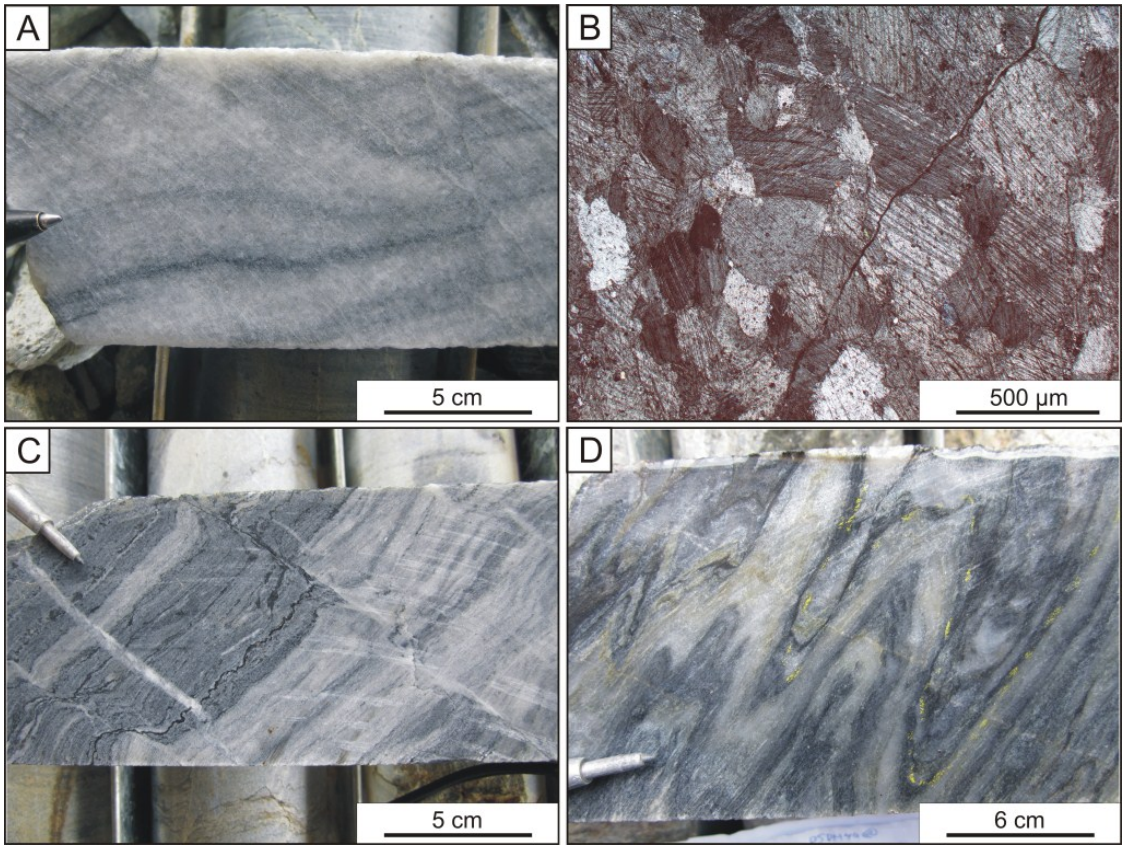

Fig. 3.8. Textural characteristics of marble unit within the meta-volcano-sedimentary sequence in the Phuoc Son deposit area, central Vietnam. **A**. Hand specimen showing typical marble unit at Phuoc Son. Sample No. TLDH01@139.9m (Tra Long). **B**. Photomicrograph showing interlocking calcite grains of the marble unit. Sample No. TLDH01@139.9m (Tra Long). **C**. Hand specimen of the marble unit at Bai Dat showing distinct schistose texture. Sample No. DSDH241@259.8m (Bai Dat). **D**. Hand specimen of the marble unit at Bai Go, showing foliated schistose texture. Sample No. DSDH40@116.2m (Bai Go).

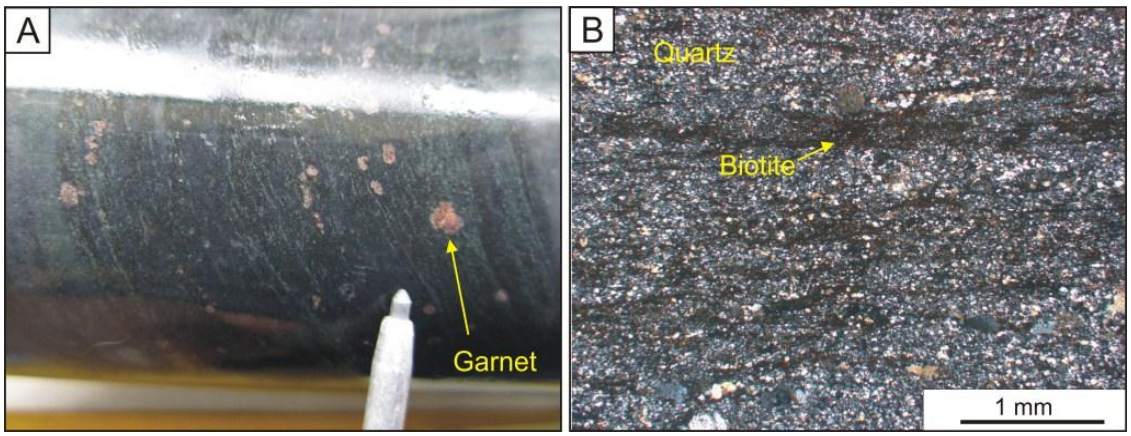

Fig. 3.9. Textural characteristics of hornfels in the meta-volcano-sedimentary sequence in the Phuoc Son deposit area, central Vietnam. **A**. Drill core sample showing aphyric texture with patchy pink garnets. Sample No. DSDH249@372.8m (Bai Go). **B**. Photomicrograph showing fine-grained quartz and biotite assemblage. Sample No. DSDH249@372.8m (Bai Go).

3.2.2.1. Metagabbro

The metagabbro occurs at the southern end of the Phuoc Son deposit area and is well-exposed along the road-cut on the access road to the Bai Dat mine site from Kham Duc Town (Fig. 3.10A). The unit is commonly intersected in the drill holes at the Nui Vang deposit. In drill cores, the least-altered sample is characterised by a dark grey colour and an aphyric texture (Fig. 3.10B). The unit is typically altered by serpentinite with minor talc and carbonate minerals (Fig. 3.10C). Visible chromite grains (up to several cm in size) are locally present (Fig. 3.10D). The alteration mineral assemblage of serpentinite, talc, carbonate and chromite is also confirmed under microscope (Figs. 3.10E and F). Sulphide minerals of pyrite, pyrrhotite and pentlandite are locally disseminated in the unit.

In the Bai Dat and Bai Go deposit area, the metagabbro occurs at the eastern part of Bai Dat and southeastern part of Bai Go. At Bai Dat, the unit underlies the meta-volcano-sedimentary rocks and is bounded by a reverse fault (Fig. 3.3), whereas the unit overlies the mineralised quartz-sulphide veins at Bai Go and is commonly associated with the metabasite and amphibolite of the meta-volcano-sedimentary sequence (Fig. 3.4). In some drill holes at Bai Dat, the metagabbro units cannot be distinguished from metabasite by texture, cross-cutting/overprinting relationships, suggesting that they are possibly the same magmatic unit in origin.

3.2.2.2. Round Hill granite

The granite is exposed at the Round Hill deposit, which is located at the northwestern part of the Phuoc Son deposit area (Fig. 3.1). Fresh samples of the unit are commonly intersected in diamond drill holes. In hand specimen sample, the unit is characterised by an equigranular texture consisting mainly of quartz and feldspar together with minor ferromagnesian and opaque minerals, which are sparsely distributed in the sample (Fig. 3.11A). In thin section, the granite is composed of euhedral to subhedral K-feldspars (<2mm: 50 vol. %) with interstitial (40 vol. %) aggregated quartz crystals (<few hundreds μm; Fig. 3.11B). Biotite (<5 vol. %) and opaques (5–10 vol. % as major magnetite with a trace of pyrite) are sparse. As well observed in drill holes, the granite is locally strongly fractured (Fig. 3.11C) and is cross-cut/overprinted by the younger basaltic dykes (Fig. 3.11D). It is also noted that the Round Hill granite is characterised by unique chemical compositions (e.g., tholeiite and A-/M-type affinities; see geochemistry section in this Chapter for details), and is distinct from the other granites in Phuoc Son and the surrounding area.

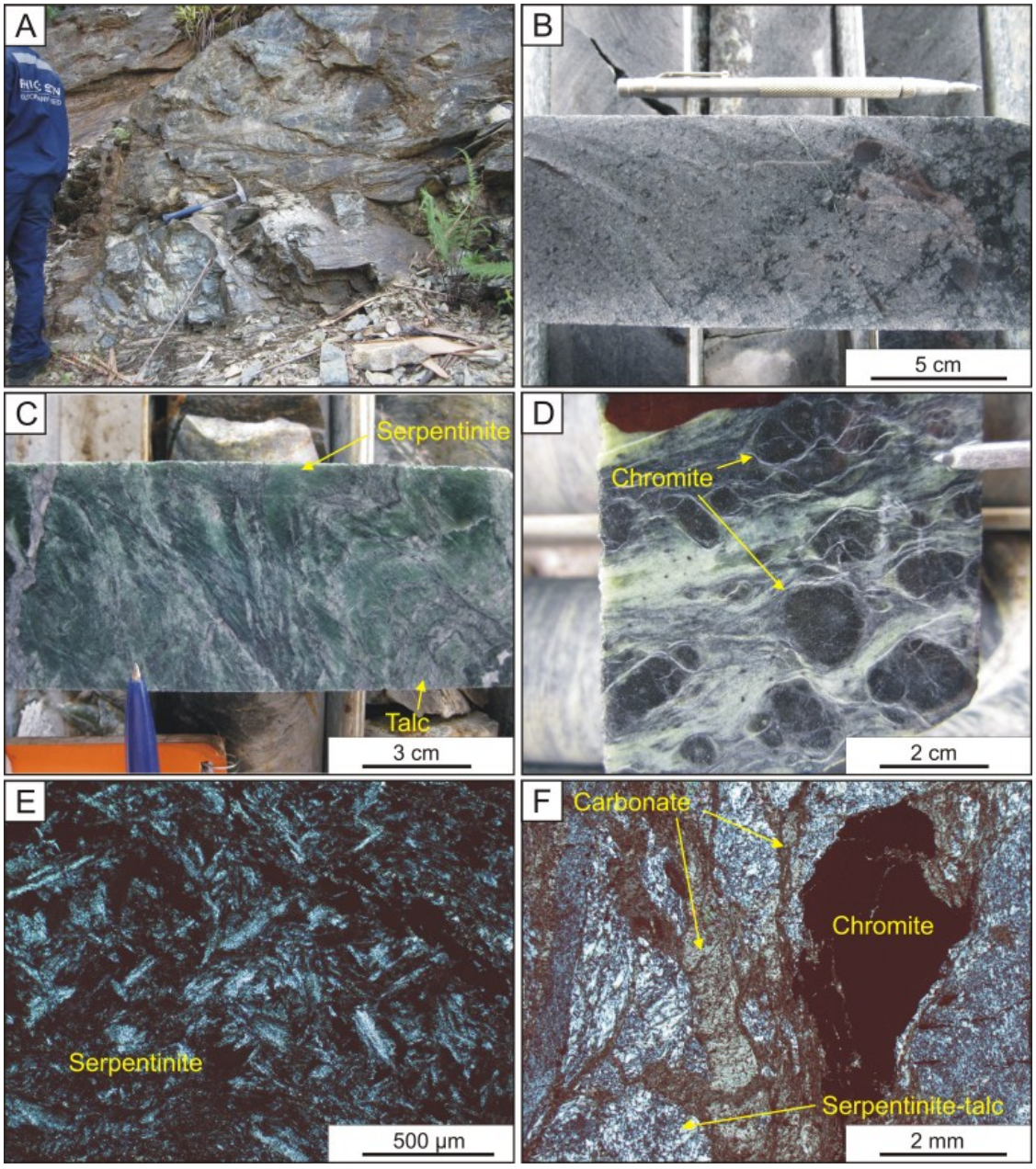

Fig. 3.10. Textural characteristics of metagabbro unit in the Phuoc Son deposit area, central Vietnam. **A**. Outcrop showing typical deformed/foliated texture of metagabbro (Nui Vang). **B**. The least-altered drill core sample showing typical texture of metagabbro, consisting of grey to dark fine-grained components. Sample No. DSDH112@31.7m (Bai Dat). **C**. Drill core sample showing alteration of metagabbro by serpentinite-talc assemblage. Sample No. NVDH03@42.3m (Nui Vang). **D**. Drill core sample showing occurrence of chromite together with serpentinite-talc assemblage. Sample No. DSDH112@268.3m (Bai Dat). **E**. Photomicrograph showing interlocking flaky serpentinite minerals. Sample No. NVDH01@55.1m (Nui Vang). **F**. Photomicrograph showing the chromite-serpentinite-talc-carbonate alteration assemblage of the metagabbro unit. Sample No. DSDH199@64.4m (Bai Go).

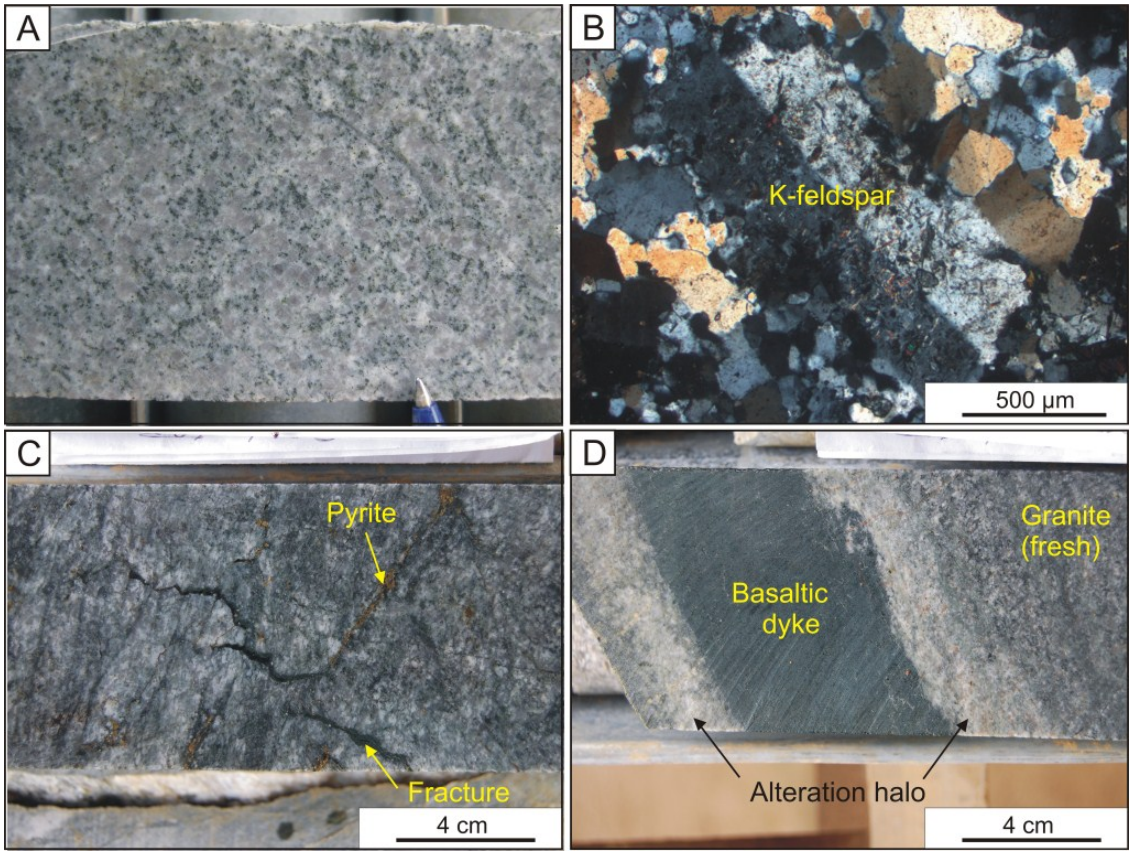

Fig. 3.11. Textural characteristics of the Round Hill granite in the Phuoc Son deposit area, central Vietnam. **A**. Fresh drill core sample of the Round Hill granite unit. Sample No. RHDH04@79.8m (Round Hill). **B**. Photomicrograph showing equigranular texture consisting of large K-feldspar phenocrysts with interlocking quartz-feldspar matrix. Sample No. RHDH04@80.6m (Round Hill). **C**. Drill core sample showing the unit is deformed and altered by disseminated pyrite. Sample No. RHDH03@79.1m (Round Hill). **D**. Drill core sample showing basaltic dyke cross-cuts the granite unit. Note alteration halo at selvage of the dyke is distinct. Sample No. RHDH03@83.7m (Round Hill).

3.2.2.3. Foliated dacitic porphyry

The foliated dacitic porphyry at Bai Dat has clear intrusive contact with the meta-volcano-sedimentary rocks in one of the drill holes. The dacitic porphyry is several metres in width and is characterised by crowded, sheared/foliated phenocrysts of feldspar and quartz (<cm across; Fig. 3.12A and B). Schistose foliation is well developed at the margin of the unit (Fig. 3.12C), where the foliation is similar in orientation to that in the dacitic porphyry and the host schist (Fig. 3.12D). This may indicate the foliated dacitic porphyry was intruded into the host volcano-sedimentary sequence, before the final episode of deformation in the region.

3.2.2.4. Syenite

The occurrence of syenite was recognised and mapped at the northeastern end of the Phuoc Son deposit area (Fig. 3.1), but it rarely outcrops on surface. At the Tra Long Prospect which

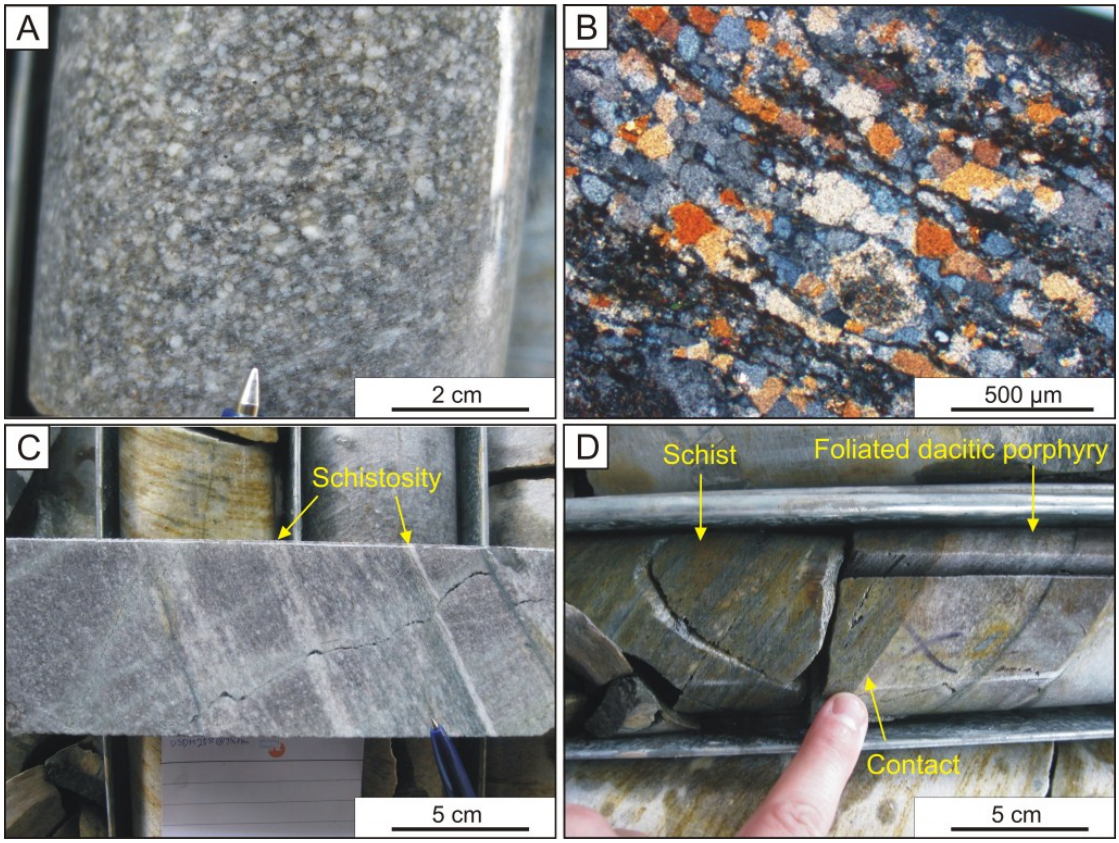

Fig. 3.12. Textural characteristics of foliated dacitic porphyry in the Phuoc Son deposit area, central Vietnam. **A**. Drill core sample showing porphyritic texture consisting of crowded feldspar and quartz phenocrysts. Sample No. DSDH257@98.3m (Bai Dat). **B**. Photomicrograph showing texture of sheared quartz and feldspar phenocrysts. Sample No. DSDH257@98.3m (Bai Dat). **C**. Photograph showing visible foliated texture in a drill core sample. Sample No. DSDH257@95.1m (Bai Dat). **D**. Photograph showing sharp contact relationships between schist and foliated dacitic porphyry with schistose foliations in the both units. Sample No. DSDH257@98.5m (Bai Dat).

is located about 3–4 km north of Bai Go (Fig. 3.1), the syenite dykes intersected in drill holes are characterised by abundant amphibole phenocrysts in a fine-grained light green/grey coloured groundmass (Fig. 3.13A). The unit appears to have undergone strong alteration as the phenocrysts and the groundmass are partly to completely replaced by chlorite. A sheared texture is also commonly noted in the unit (Fig. 3.13B), and this may indicate that the unit was emplaced prior to the other un-deformed/un-metamorphosed intrusive units (e.g., Khe Rin granite, dacitic porphyry and andesitic dyke) in Phuoc Son.

3.2.2.5. Granite dyke

Granite dykes are frequently intersected in drill holes at Bai Dat, Bai Go, Bai Chuoi, Bo and K7. The dykes are several tens of centimetres to few metres in width. In hand specimen the

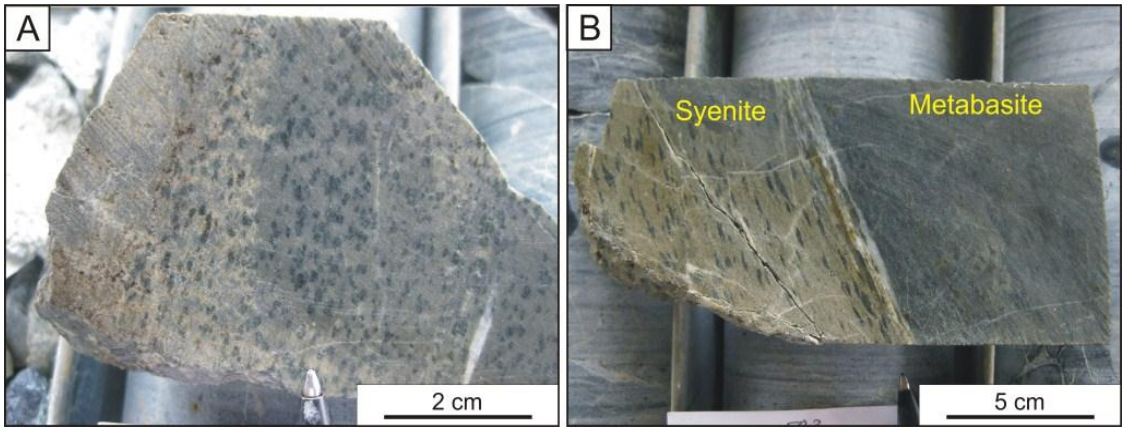

Fig. 3.13. Textural characteristics of syenite unit in the Phuoc Son deposit area, central Vietnam. **A**. Drill core sample showing porphyritic texture consisting of chloritised amphibole phenocrysts in the fine-grained groundmass. Sample No. TLDH02@74.9m (Tra Long). **B**. Drill core sample showing sheared texture of amphibole phenocrysts and a sharp contact relationship against the host metabasite unit. Sample No. TLDH02@73.3m (Tra Laong).

dykes are generally pale white in colour and are composed of quartz, feldspar and muscovite (Fig. 3.14A and B). Under microscope, the granite contains coarse-grained plagioclase and muscovite (up to a few mm in size) in a fine-grained quartz-rich groundmass (Fig. 3.14C). Deformation was recognised in some plagioclase phenocrysts under microscope (Fig. 3.14C), whereas in the drill core samples the dyke seems to cross-cut the metamorphic foliations in the meta-volcano-sedimentary sequence (Fig. 3.14D). These paragenetic relationships suggest that the dyke was intruded into the host units during the syn- to post-deformation phases, probably during the waning stage of regional deformation at Phuoc Son.

3.2.2.6. Khe Rin granite

The granite is found at the Khe Rin deposit and the surrounding area in the northwestern part of the Phuoc Son deposit area. Hand specimen of the least-altered sample shows no evidence of deformation, and the rock is strongly altered (Fig. 3.15A). Under microscope, the sample is composed of interlocking plagioclase (>50 vol. %) and quartz (40 vol. %) mineral assemblage. The minerals are typically euhedral to subhedral in shape and several hundreds μm in size (Fig. 3.15B). The sample has undergone strong alteration to a quartz-sericite-muscovite-carbonate-pyrite assemblage associated with narrow veinlets. Trace of chlorites are also present (<5 vol. %), replacing mafic minerals (probably biotites).

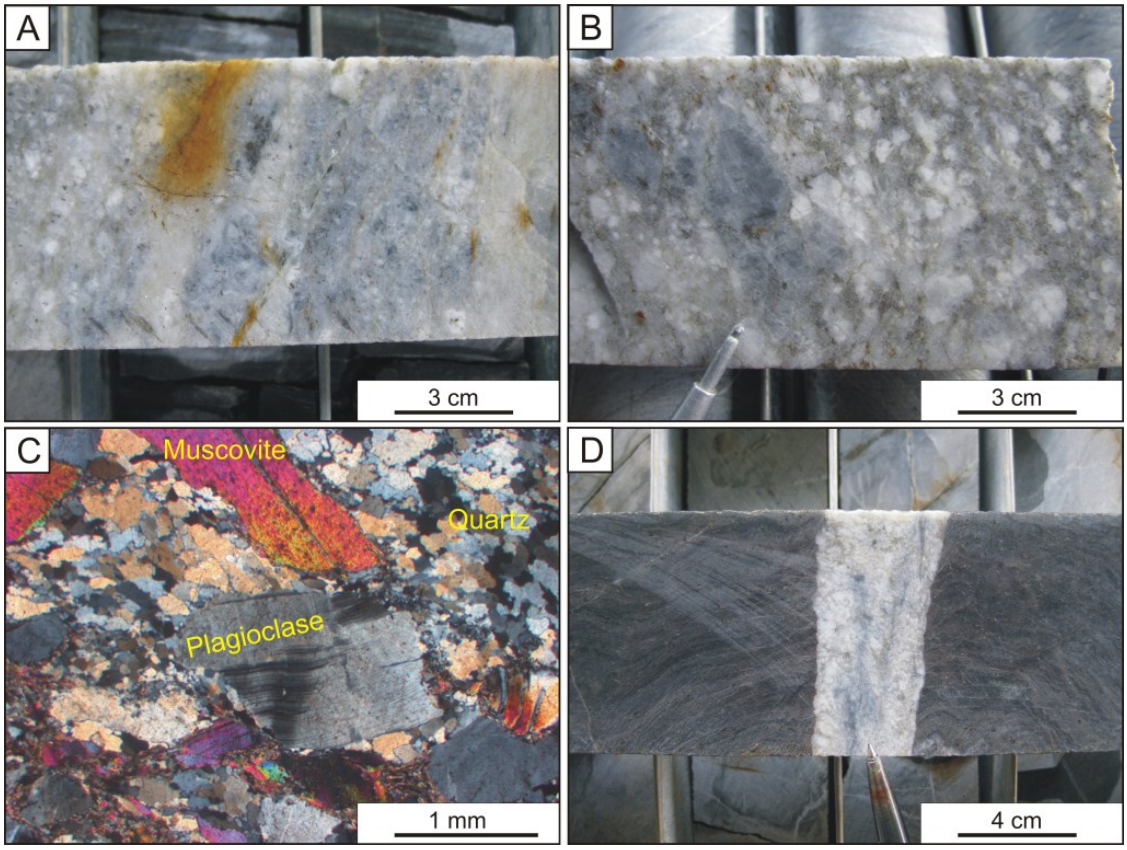

Fig. 3.14. Textural characteristics of the granite dyke in the Phuoc Son deposit area, central Vietnam. **A**. Drill core sample showing textural feature of granite dyke. Sample No. K7DH01@108.7m (K7). **B**. Granite dyke having visible, coarse-grained muscovite and plagioclase phenocrysts. Sample No. DSDH257@45.0m (Bai Chuoi). **C**. Photomicrograph showing plagioclase and muscovite phenocrysts in the fine-grained quartz-rich groundmass. Sample No. K7DH01@108.7m (K7). **D**. Granite dyke cross-cutting phyllite unit, at perpendicular against the metamorphic foliation. Sample No. BODH02@108.5m (Bo).

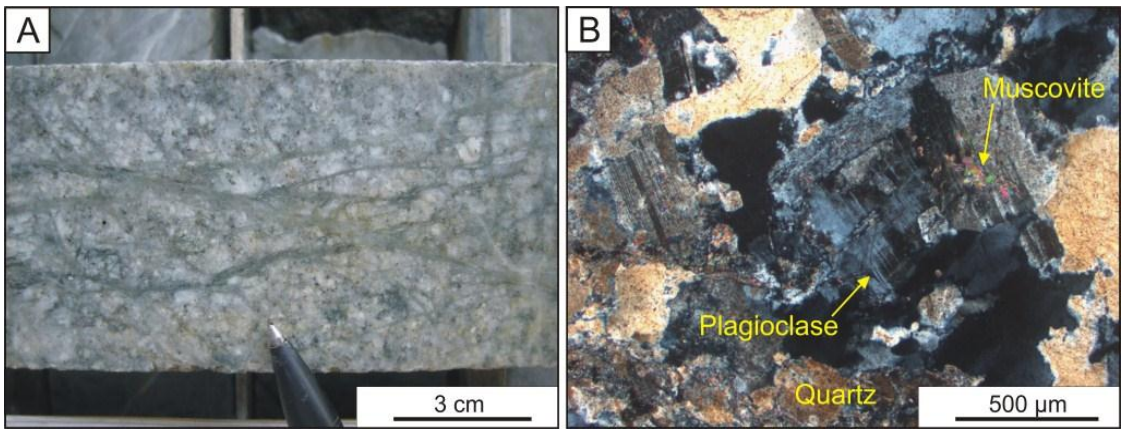

Fig. 3.15. Textural characteristics of the Khe Rin granite in the Phuoc Son deposit area, central Vietnam. **A**. Drill core sample of the least-altered unit showing presence of intense veinlets. KRDH31@259.8m (Khe Rin). **B**. Photomicrograph showing interlocking plagioclase (twinned) and quartz, partly replaced by muscovite. Sample No. KRDH31@259.8m (Khe Rin).

3.2.2.7. Andesitic dyke

Andesitic dykes are not exposed at surface in the Phuoc Son deposit area, but are intersected in drill holes at Bai Dat, Bai Go and Khe Do. The dykes are few metres in width, and are characterised by a porphyritic texture and the presence of hornblende phenocrysts in a strongly altered fine-grained groundmass (Fig. 3.16A, B and C). The alteration minerals are a sericite-silica-carbonate assemblage, replacing both the hornblende phenocrysts and the groundmass. The unit is not deformed and has a sharp contact with the country rocks of the meta-volcano-sedimentary sequence (Fig. 3.16D). At Bai Dat and Bai Go, the dykes are emplaced parallel to the mineralised quartz-sulphide veins (Figs. 3.3 and 4).

3.2.2.8. Diorite

The occurrence of diorite is recorded at the western part of the Nui Vang deposit area (also equivalent to the eastern part of the Bai Go deposit area), in the southern part of the Phuoc Son area (Stevens and Fulton, 2008). However, the unit does not outcrop and is only recognised from boulders along small creeks. Hand specimen sample shows porphyritic texture in the rock, which has undergone intense alteration to a tremolite-chlorite-garnet assemblage (Fig. 3.17A and B).

3.2.2.9. Dacitic porphyry

The dacitic porphyry was identified in drill holes from the Bai Dat, Bai Go and Bai Chuoi deposit areas, where the unit occurs as dykes and/or stocks ranging from a few tens of centimetres to several metres in width. The porphyry is characterised by large feldspar phenocrysts (30 vol. %, 0.5–3mm across; Fig. 3.18A) in a fine-grained groundmass of quartz and feldspar (70 vol. %, <100μm; Fig. 3.18B). A trace of hornblende, biotite and pyrite are also sparsely distributed in the sample. Sericitisation is pervasively developed, replacing feldspars (Fig. 3.18C). Mafic minerals (biotite and hornblende) are partly to completely altered to chlorite.

In drill cores, xenoliths of metamorphosed sedimentary units (i.e., schist) are locally involved in the dacitic porphyry (Fig. 3.18D). The unit has a sharp contact relationship with the host meta-volcano-sedimentary sequence, indicating that it was emplaced after deformation. This is also evidenced by lack of deformation/foliation textures in this unit.

3.2.3. Gneissic rocks of Kham Duc Formation

The gneissic rocks of the Kham Duc Formation are exposed along the N-S trending Po Ko Fault Zone in the eastern part of the Phuoc Son deposit area (Fig. 3.1). A few different types of gneisses have been identified by Khin Zaw et al. (2010) along the Hoh Chi Minh Highway

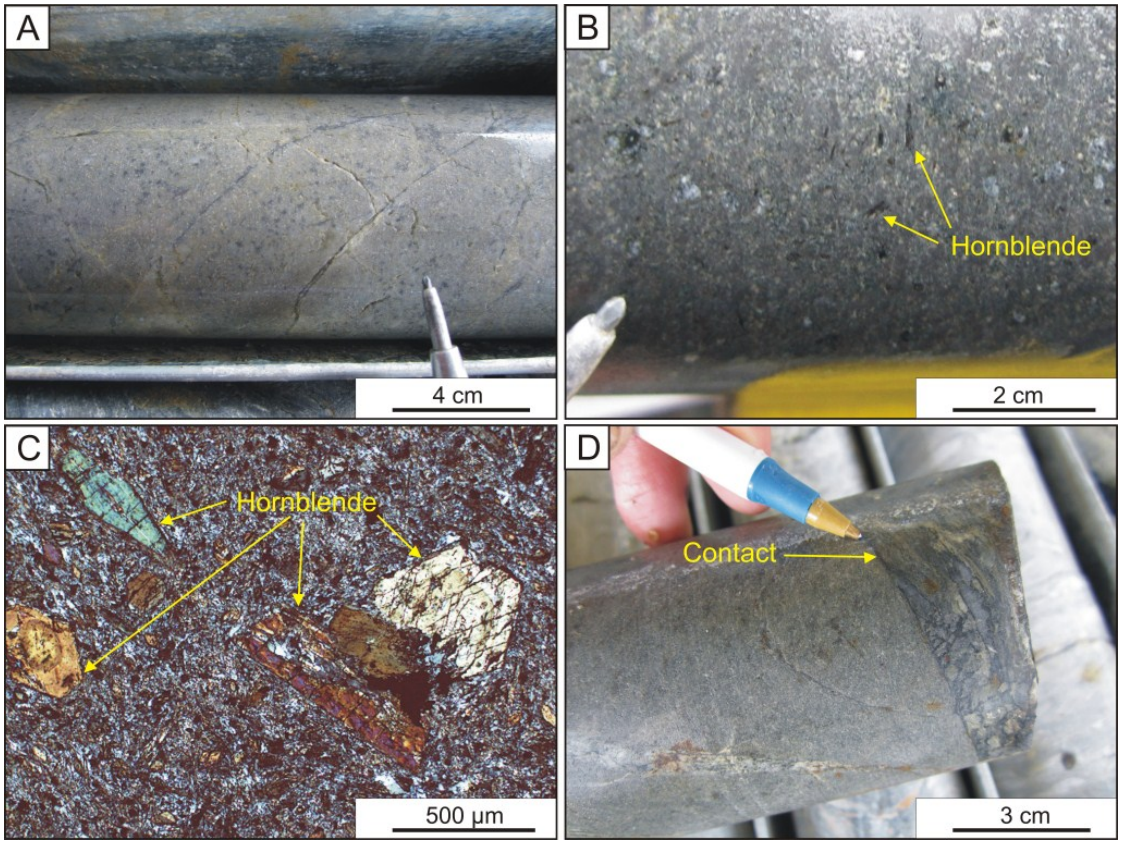

Fig. 3.16. Textural characteristics of the andesitic dyke in the Phuoc Son deposit area, central Vietnam. **A**. Drill core sample showing a typical appearance of andesitic dyke, which has undergone strong alteration. Sample No. DSDH270@95.0m (Bai Dat). **B**. Drill core sample of andesitic dyke consisting of hornblende phenocrysts in the grey, fine-grained groundmass. Sample No. DSDH249@515.2m (Bai Go). **C**. Photomicrograph showing hornblende phenocrysts in the fine-grained groundmass. Sample No. DSDH249@515.2m (Bai Go). **D**. Photograph showing sharp contact of the andesitic dyke to the host schist unit. Sample No. DSDH218@86.6m (Bai Go).

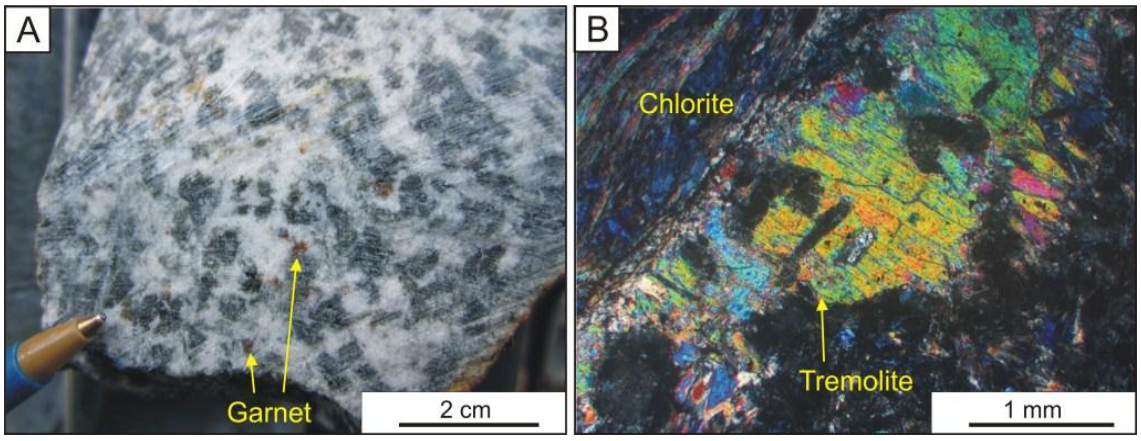

Fig. 3.17. Textural characteristics of the diorite in the Phuoc Son deposit area, central Vietnam. **A**. Hand specimen sample of the least-altered diorite showing phenocrysts and the groundmass are totally replaced by alteration minerals of tremolite (creamy colour), chlorite (green) and patchy garnet. TMVN11-06 (near Nui Vang). **B**. Photomicrograph showing alteration mineral assemblage of tremolite and chlorite. Sample No. TMVN11-06 (near Nui Vang).

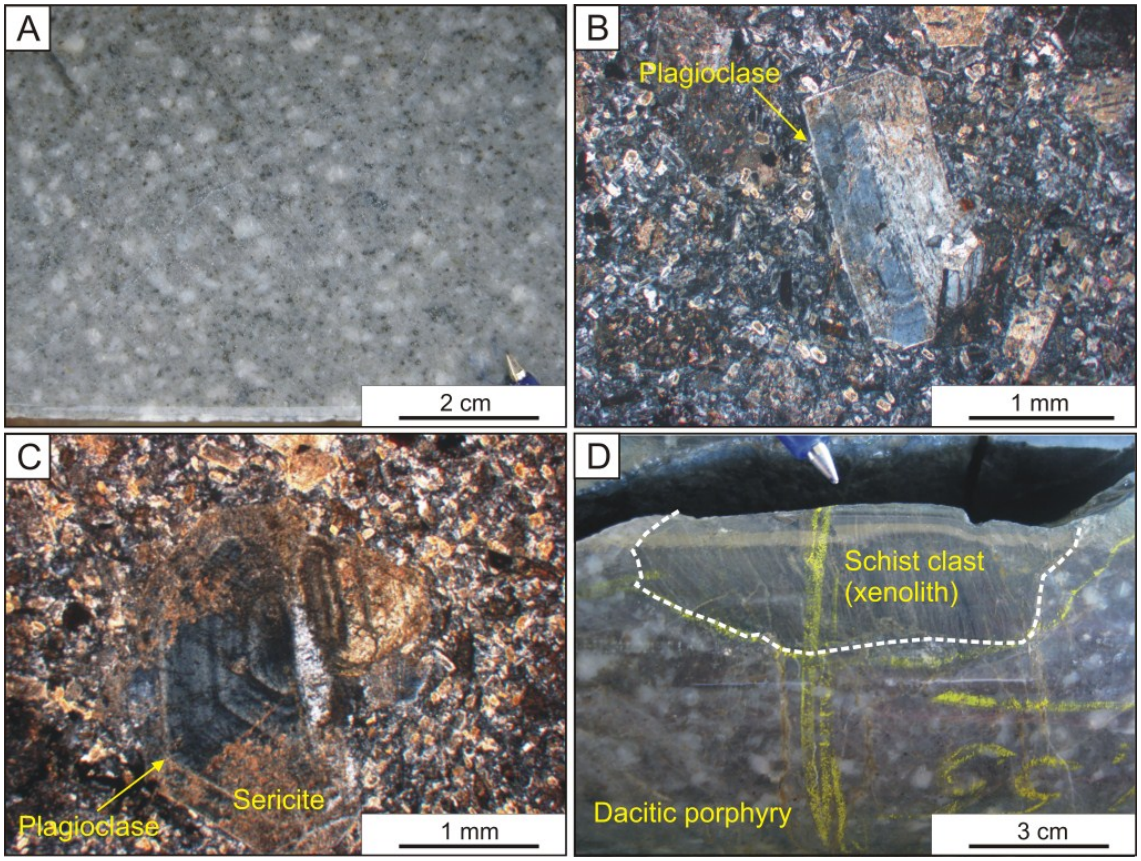

Fig. 3.18. Textural characteristics of dacitic porphyry in the Phuoc Son deposit area, central Vietnam. **A**. Hand specimen sample showing porphyritic texture. Sample No. DSDH89@187.7m (Bai Go). **B**. Photomicrograph showing porphyritic texture with plagioclase phenocrysts in the fine-grained feldspar-quartz groundmass. Sample No. DSDH40@148.8m (Bai Go). **C**. Photomicrograph showing pervasive sericitisation over plagioclase phenocrysts and groundmass. Sample No. DSDH40@148.8m (Bai Go). **D**. Drill core showing dacitic porphyry involves wall rock clast/xenolith of the schist of the meta-volcano-sedimentary sequence. Sample No. DSDH89@191.6m (Bai Go).

outcrops near Kham Duc Town. The rock types include granitic gneiss (Fig. 3.19A and B), garnet-hornblende-biotite gneiss (Fig. 3.19C and D) and felsic gneiss (Fig. 3.19E and F), and they are considered to have formed through two orogenic events, one occurring in the Ordovician to Silurian period and the other in the Middle Permian to Early Triassic (see geochronological section for details).

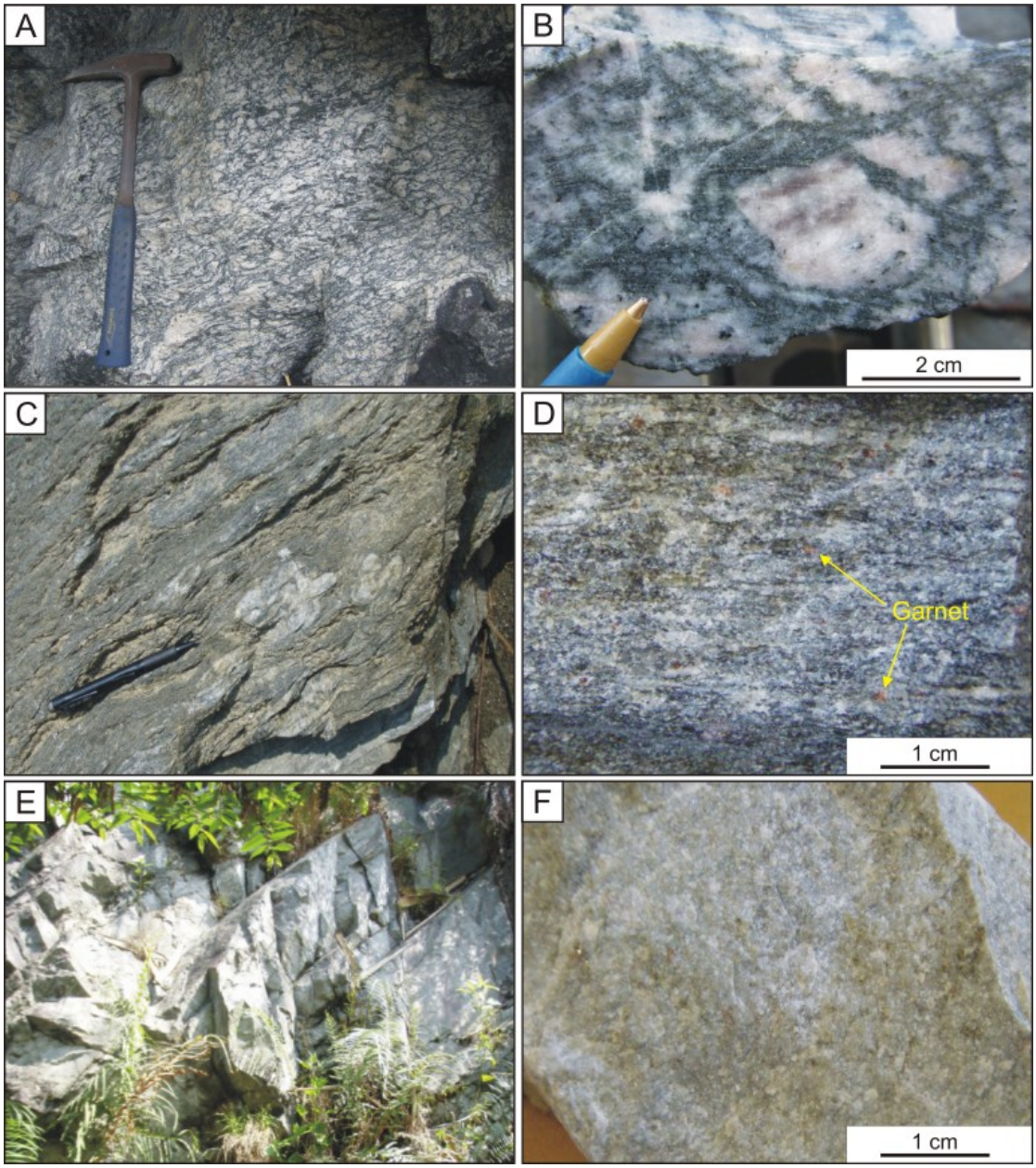

Fig. 3.19. Gneissic rocks of the Kham Duc Formation exposed around the Kham Duc Town in central Vietnam. **A.** Outcrop of granitic gneiss. **B**. Hand specimen sample of granitic gneiss in Fig. A, composing predominantly of quartz and biotite. Sample No. TMVN11-01. **C**. Outcrop of garnet-hornblende-biotite gneiss. **D**. Hand specimen sample of garnet-hornblende-biotite gneiss in Fig. C. Sample No. JH0813 (from Khin Zaw et al., 2010). **E**. Outcrop of felsic gneiss. **F**. Hand specimen sample of felsic gneiss in Fig. E. Sample No. JH0814 (from Khin Zaw et al., 2010).

3.3. STRUCTURE

3.3.1. Introduction

A complex structural setting at the Phuoc Son deposit area has previously been reported (Banks et al., 2004; Encom Technology, 2008; Davies, 2010). Structural deformation of major lithological units in the Phuoc Son area is documented in previous reports based on observation of outcrops and in drill cores, but relationship of the structural architecture with the gold mineralisation at Phuoc Son has been poorly understood. Recent mining operation at the Bai Dat underground allowed the author to investigate detailed structural setting of the gold mineralisation. In this section, the structural architecture of the Phuoc Son deposit area is described at both regional- and deposit-scales, with an emphasis on the Bai Dat deposit.

3.3.2. Faults

Major regional structures, such as faults and folds, were recognised in Phuoc Son and surrounding areas based on satellite image interpretation and local field observations. The Phuoc Son deposit area is situated near the confluence of two regional fault zones (i.e., Poko and Cong Plong Fault Zones; Fig. 3.20). The close spatial and temporal relationships of the gold mineralising event with the two fault systems suggest that these structures have had an important role in ore genesis (e.g., Banks et al., 2004). Two smaller N-S trending faults (i.e., Khe Rin and K7 Faults) in the Phuoc Son deposit area also show close relationships with gold deposits and may also have played a role.

Poko Fault Zone

The Poko Fault Zone trending N-S is a regional fault system and is recognised from satellite images. The fault is also observed along a zone attached to the eastern boundary of the Phuoc Son deposit area, where displacement of lithological units occurs (i.e., gneissic rocks to the east and schistose and phyllitic rocks to the west; Fig. 3.20A, B, C and D). The fault is interpreted to have formed by reverse-dextral movement of >30 km lateral and length of more than 100 km in N-S displacement (Pham Khoan et al., 1995; Banks et al., 2004). As the fault zone is juxtaposed to the western margin of the high-grade Kontum metamorphic block in the central Vietnam, it is inferred that the fault was formed by up-lift at the end of the regional metamorphic event during Late Palaeozoic and Early Mesozoic Indosinian Orogeny (Banks et al., 2004).

Cong Plong Fault Zone

The Cong Plong Fault Zone is a 2 km wide regional-scale fault system trending NW-SE and

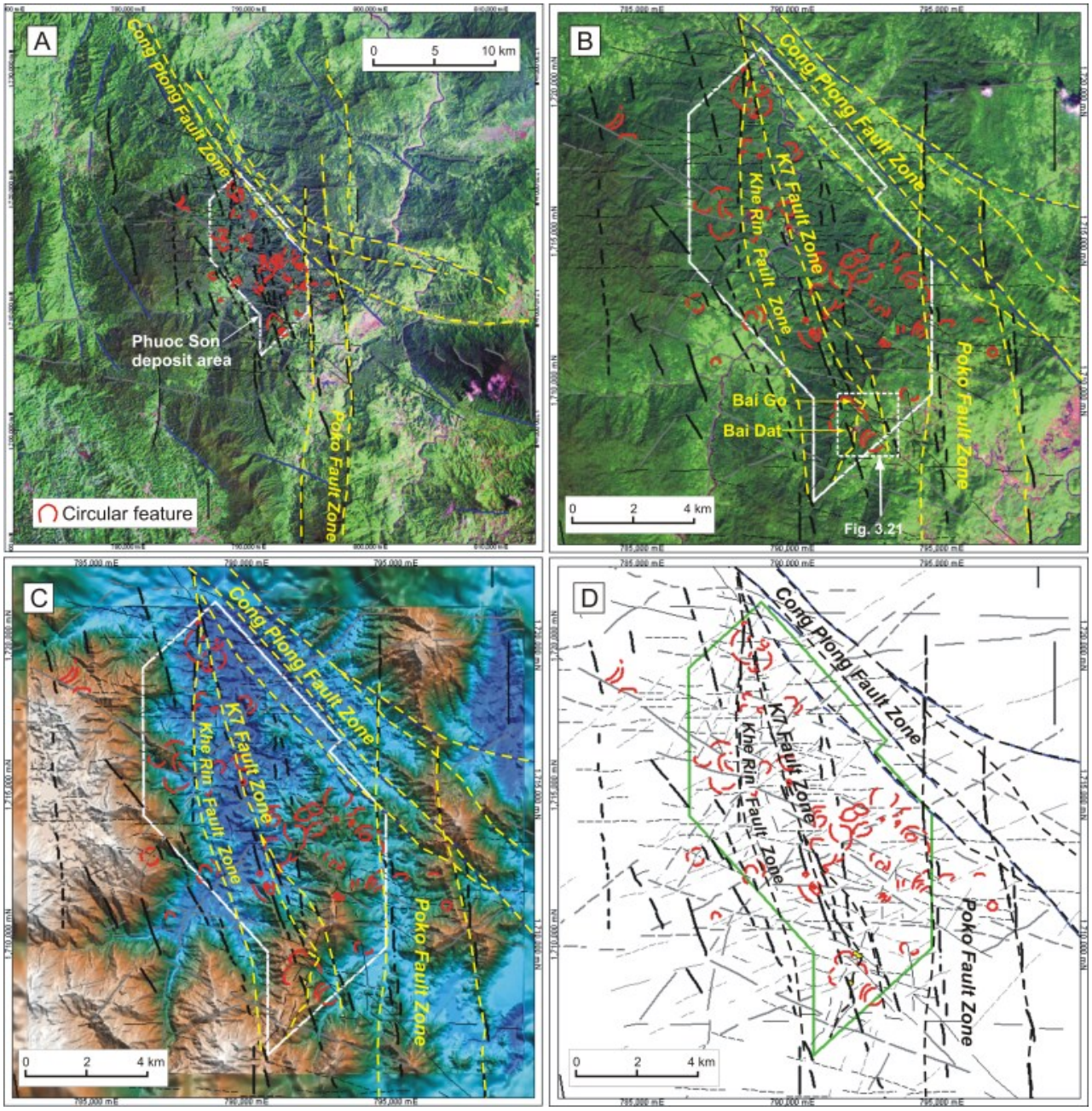

Fig. 3.20. Regional structural setting of the Phuoc Son deposit area, central Vietnam. Modified from Encom Technology (2008). Note red circles represent identified circular features. **A**. Structural interpretation of the Phuoc Son deposit area and surroundings using Landsat image. Note that the Phuoc Son deposit area is located near the intersection of the regional Poko and Cong Plong Fault Zones. **B**. Structural interpretation of the Phuoc Son deposit area using ASTER image shows that the Khe Rin and K7 Faults trend from the northern end to southern end of the deposit area. **C**. Structural interpretation of the Phuoc Son deposit area using elevation data image also shows that the Khe Rin and K7 Faults trend from the northern end to southern end of the deposit area. **D**. Structural setting of the Phuoc Son deposit area showing main fault zones and identified local lineaments.

dipping southwesterly (Cao Dinh Trieu, 1991; Banks et al., 2004). The fault zone forms the northeastern margin of the Phuoc Son deposit area, and Cenozoic olivine basalt flows are emplaced at Kham Duc along the fault (Banks et al., 2004). A dextral strike-slip movement during Indosinian Orogeny and sinistral reactivated movement during the Cenozoic Himalayan Orogeny are inferred to have occurred along fault system (Banks et al., 2004).

Khe Rin and K7 Fault Zones

The Khe Rin and K7 Fault Zones are the two main fault systems occurring in the Phuoc Son deposit area and they trend NNW-SSE in the centre of the deposit area with a westerly to sub-vertical dip (Fig. 3.20; Encom Technology, 2008). Close link of the fault zones and gold mineralisation in Phuoc Son are recognised at a number of mineralised systems (e.g., Bai Dat, Bao Go, Khe Rin, Khe Do, K7, Bai Gio and Nui Vang). They are considered to be splays of the regional Cong Plong Fault Zone (Banks et al., 2004).

3.3.3. Folds

The Phuoc Son deposit area is dominated by a large anticlinal fold system, plunging to NNE (Banks et al., 2004). Deformation associated with the folding is marked in major rock units in Phuoc Son, but it is also observed that different lithologic units at Phuoc Son have different degrees of deformation, with competent units often slightly folded while ductile units are tightly folded (Banks et al., 2004).

3.3.4. Local structural setting at Bai Dat

A small amount of structural information was gathered in this study to measure foliation of the host rocks at the Bai Dat the underground mine. All the measurement data are listed in Appendix II. Structural data from previous studies (e.g., Davies, 2010) are also incorporated in this study.

Daksa Fault Zone

The mineralised quartz-sulphide veins at Bai Dat and Bai Go are associated with local fault zone called Daksa Fault Zone. The fault zone is characterised by a low-angle, northwesterly dipping, 4 km long, thrust fault system (Banks et al., 2004; Fig. 3.21). The fault zone is interpreted to be a splay of the K7 Fault Zone and also hosts a few other deposits, such as Bai Chuoi and Bai Cu at the southern end of the Phuoc Son deposit area.

The metamorphic foliation of the host schist and phyllite was measured at exposure of the Bai Dat underground mine by the author and the results are shown in Figure 3.22. The foliation

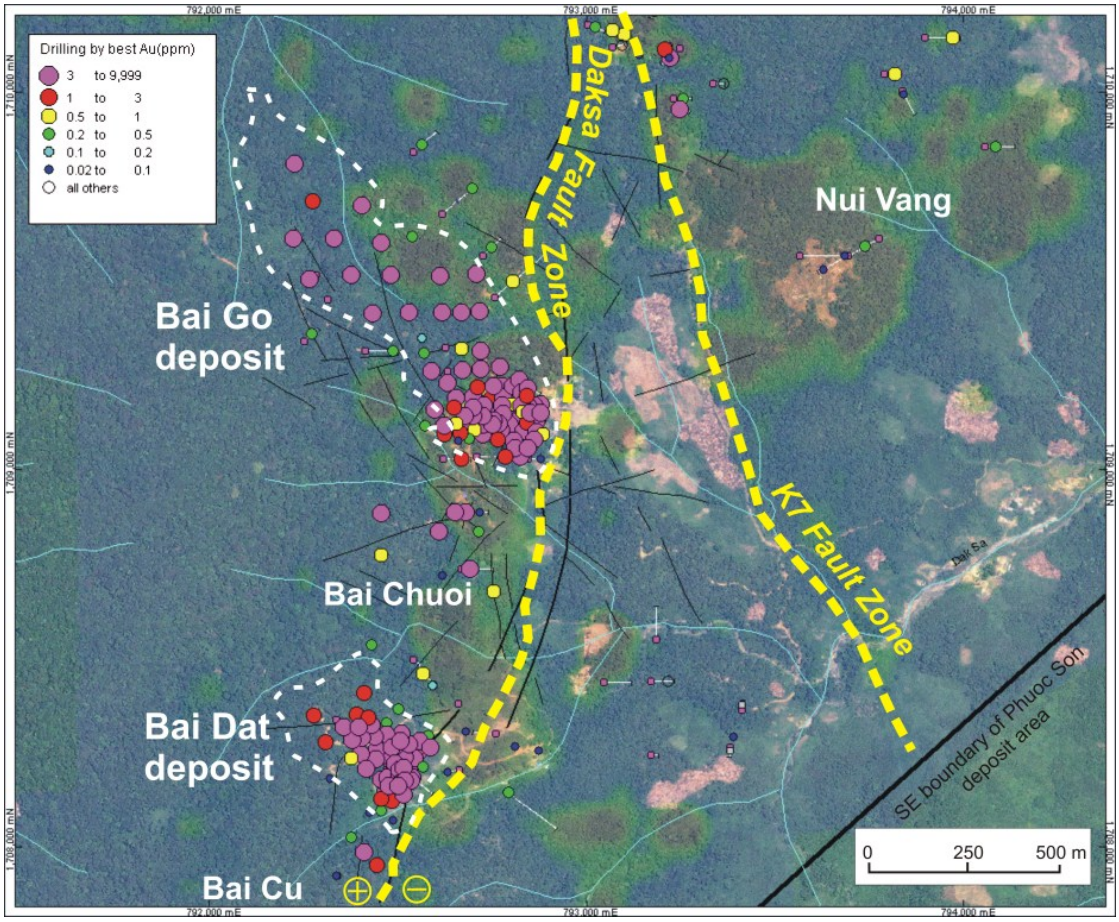

Fig. 3.21. Occurrence of Daksa and K7 faults zones in the southern end of the Phuoc Son deposit area. Modified after Encom Technology (2008). Note that the Bai Dat and Bai Go deposits are hosted in the Daksa fault zone.

uniformly dips to northwest (30–60°; Fig. 3.23), and the data are consistent with the orientation reported by Davies (2010; Fig. 3.34). The faults that perpendicularly cross-cut the metamorphic foliation in host rocks and the mineralised quartz-sulphide veins (see Chapter 4 for more details) were also measured and the data indicate that the post-peak metamorphic faults trend to N-S with vertical to sub-vertical dips (Fig. 3.23).

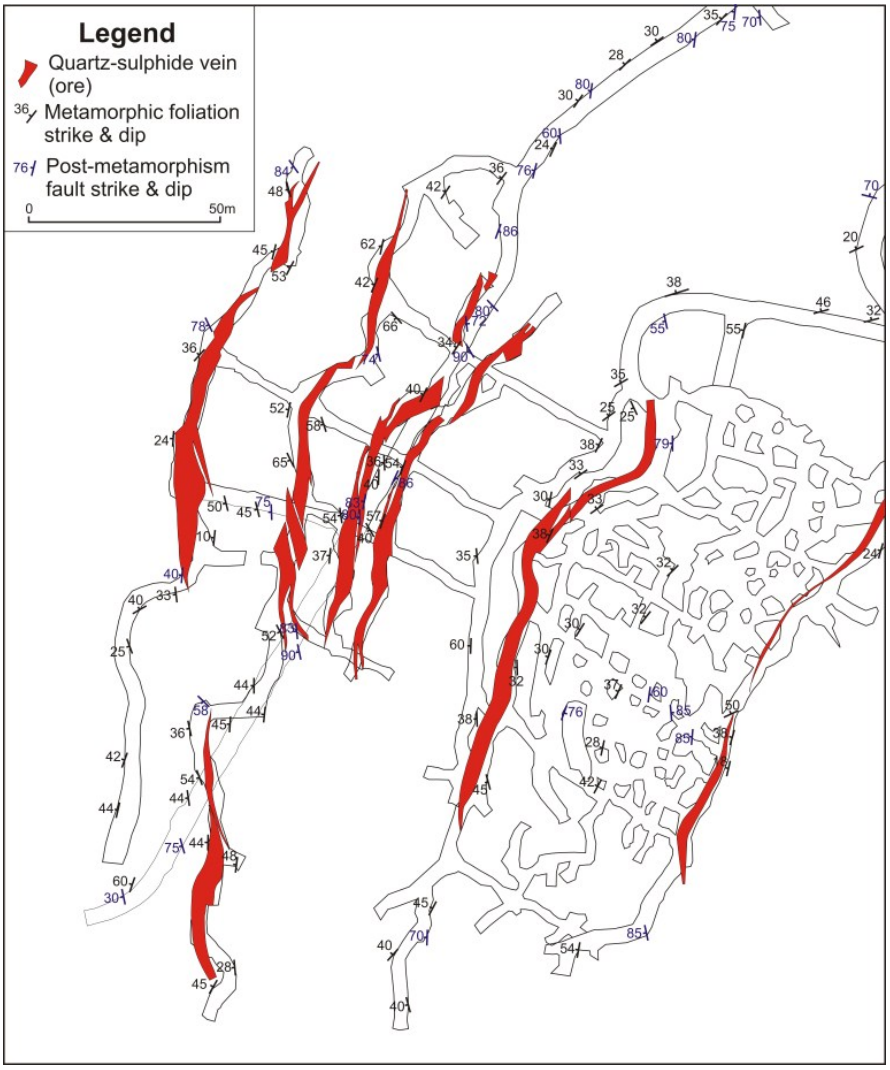

Fig. 3.22. Plots of measured foliation and faults in the Bai Dat underground mine site. Note the ore body (quartz-sulphide veins) are projected to surface.

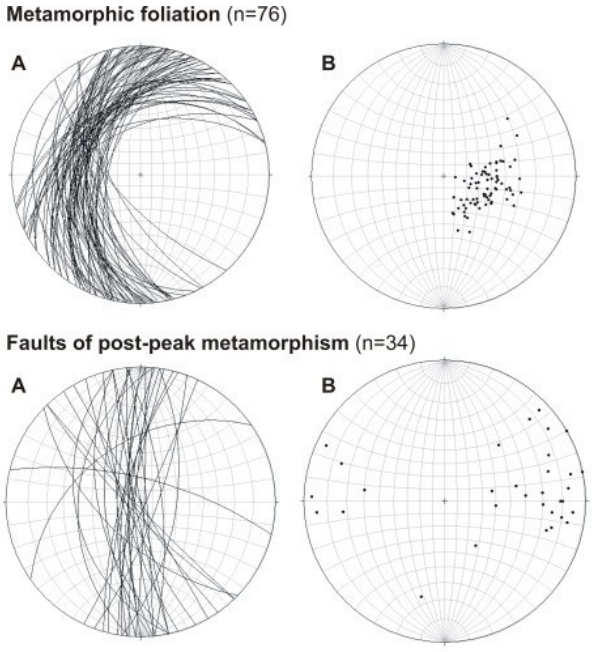

Fig. 3.23. Orientation data of metamorphic foliation in the host rocks (top) and faults of post-peak metamorphism (bottom). **A**. Great circles representing stereo plot of poles to foliation. **B.** Stereo plot of poles to foliation.

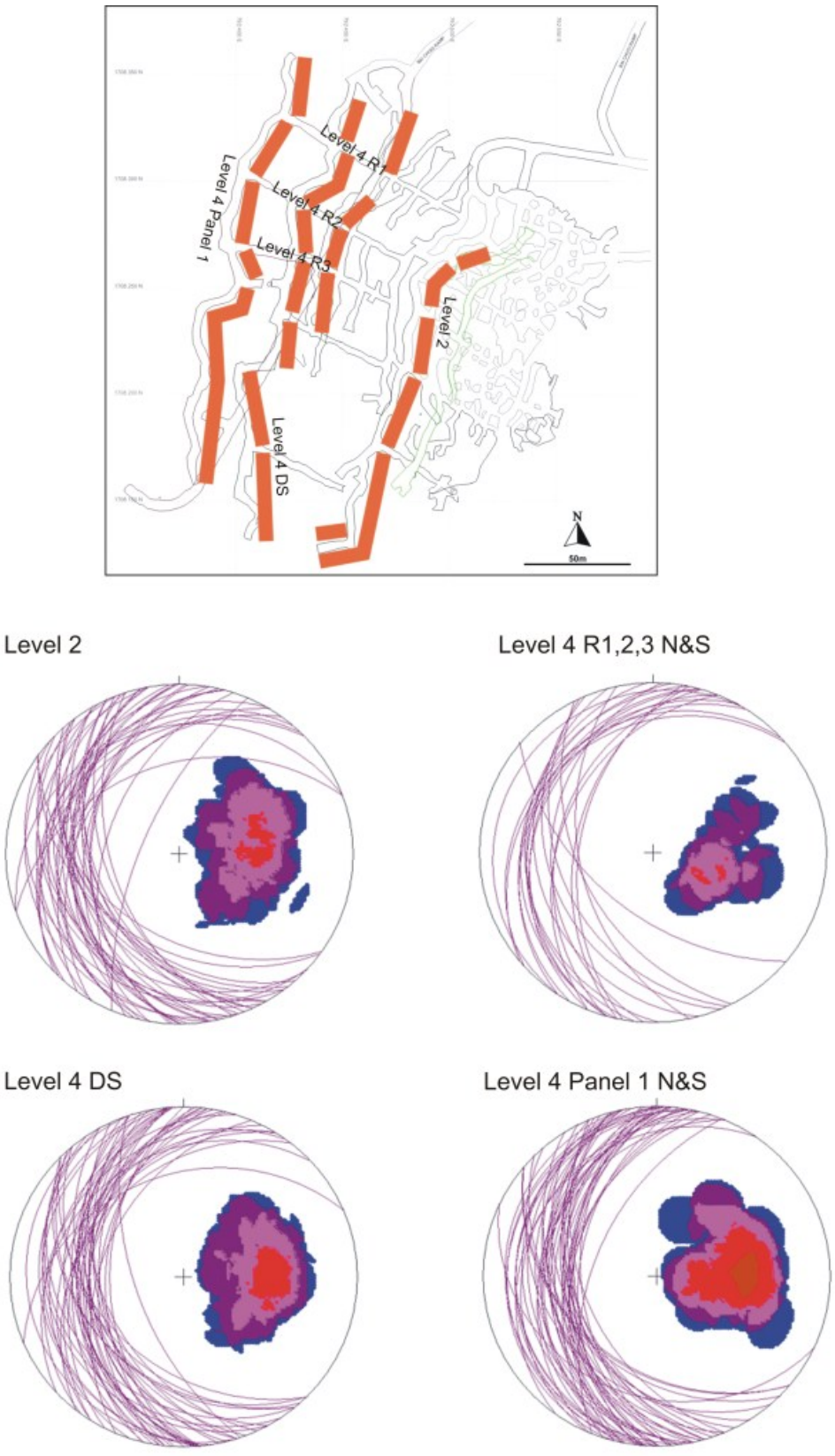

Fig. 3.24. Orientation data of metamorphic foliation of the host rocks measured at the Level 2 and Level 4 of the Bai Dat underground mine site. Modified from Davies (2010). Note that the data show the metamorphic foliation has westerly dipping with varying of degree (10–65˚).

3.4. GEOCHRONOLOGY

3.4.1. Introduction

Geochronological study has been widely applied in mineral deposit research as one of the most important methods to constrain the timing of the mineralisation and ages of host rock units and associated geological events (e.g., sedimentation, magmatism and metamorphism). In modern mineral exploration, geochronology is commonly used in particular to screen and prioritise the targets by comparing ages of nearby economic deposits. In this study, the Laser Ablation-Inductively Coupled Plasma Mass Spectrometry (LA-ICPMS) technique was applied at CODES, University of Tasmania, to determine ages of the main intrusive units and link to gold mineralising event in the Phuoc Son deposit area.

3.4.2. Analytical methods

Zircon crystals were separated from the key intrusive units in Phuoc Son including the foliated dacitic porphyry and dacitic porphyry at Bai Dat and Bai Go and granite in Khe Rin. No zircons were recovered from the other intrusive units, such as the metagabbro, Round Hill granite, diorite, andesitic dyke and granite dyke.

Approximately 100 g of the rocks was crushed in a Cr-steel ring mill to a grain size <400 μm. Non-magnetic heavy minerals were then separated using a gold pan and a Fe-B-Nd hand magnet. The zircons were hand-picked from the heavy mineral concentrate under microscope in cross-polarised transmitted light. The selected crystals were placed on double sided sticky tape and epoxy glue was then poured into a 2.5 cm diameter mould on top of the zircons. The mount was dried for 12 hours and polished using clean sandpaper and a clean polishing lap. The samples were then washed in distilled water in an ultrasonic bath.

The analysis in this study was performed on an Agilent 7500cs quadrupole ICPMS with a 193 nm Coherent Ar-F gas laser and the Resonetics M50 ablation cell at the University of Tasmania. The downhole fractionation, instrument drift and mass bias correction factors for Pb/U ratios on zircons were calculated using two analyses on the primary (91500 standard of Wiendenbeck et al., 1995) and one analysis on each of the secondary standard zircons (Temora standard of Black et al., 2003 and JG1 of Jackson et al., 2004) analysed at the beginning of the session and every twelve unknown zircons (roughly every half an hour) using the same spot size and conditions as used on the samples. Additional secondary standards (The Mud Tank Zircon of Black and Gulson, 1978) were also analysed. The correction factor for the $^{207}Pb/^{206}Pb$ ratio was calculated using three large spot of NIST610

analysed at the beginning and end of the day and corrected using the values recommended by Baker et al. (2004).

Each analysis on the zircons began with a 30 second blank gas measurement followed by a further 30 seconds of analysis time when the laser was switched on. Zircons were sampled on 32 micron spots using the laser at 5 Hz and a density of approximately 2 J/cm^2. A flow of He carrier gas at a rate of 0.6 litres/minute carried particles ablated by the laser out of the chamber to be mixed with Ar gas and carried to the plasma torch. Elements measured include ^{49}Ti, ^{96}Zr, ^{146}Nd, ^{178}Hf, ^{202}Hg, ^{204}Pb, ^{206}Pb, ^{207}Pb, ^{208}Pb, ^{232}Th and ^{238}U with each element being measured sequentially every 0.16 s with a longer counting time on the Pb isotopes compared to the other elements. Data reduction used was based on the method outlined in detail in Meffre et al. (2008) similar to that outlined in Black et al. (2004) and Paton et al. (2010).

Element abundances of zircons were calculated using the method outlined by Kosler (2001) using Zr as the internal standard element, assuming stoichiometric proportions and using the secondary standard 91500 to correct for mass bias (Meffre et al., 2008).

3.4.3. Zircon petrography

Prior to LA-ICPMS analysis, the mounted zircon crystals were examined using a petrographic microscope and a cathodoluminescence (CL) image detector on a scanning electron microprobe (SEM). The images of the growth zones within the crystals were used to help with the interpretation of the geochronological data (Corfu et al., 2003). The images show that all of the zircon crystals separated in this study are of igneous origin as shown by well-developed internal crystal-growth zones (Fig. 3.25A and B). Inherited core was also recognised in some crystals (Fig. 3.25C and D).

3.4.4. Results

All the processed data from the LA-ICPMS zircon U-Pb analyses undertaken as part of this study are listed in Appendix III, and examples of concordia diagrams of the dated intrusive units are shown in Figures 3.26A and B. The results of the LA-ICPMS zircon U-Pb ages are summarised in Table 3.1, together with ages from previous studies on some intrusive and metamorphic units in and around the Phuoc Son deposit area. The age data are also shown on a map (Fig. 3.27) and in a time-space diagram (Fig. 3.28). The data indicate that there are two main magmatic age groups in the Phuoc Son area. A Carboniferous age (c.a.350 Ma) is also recorded in one granite sample from Phuoc Son.

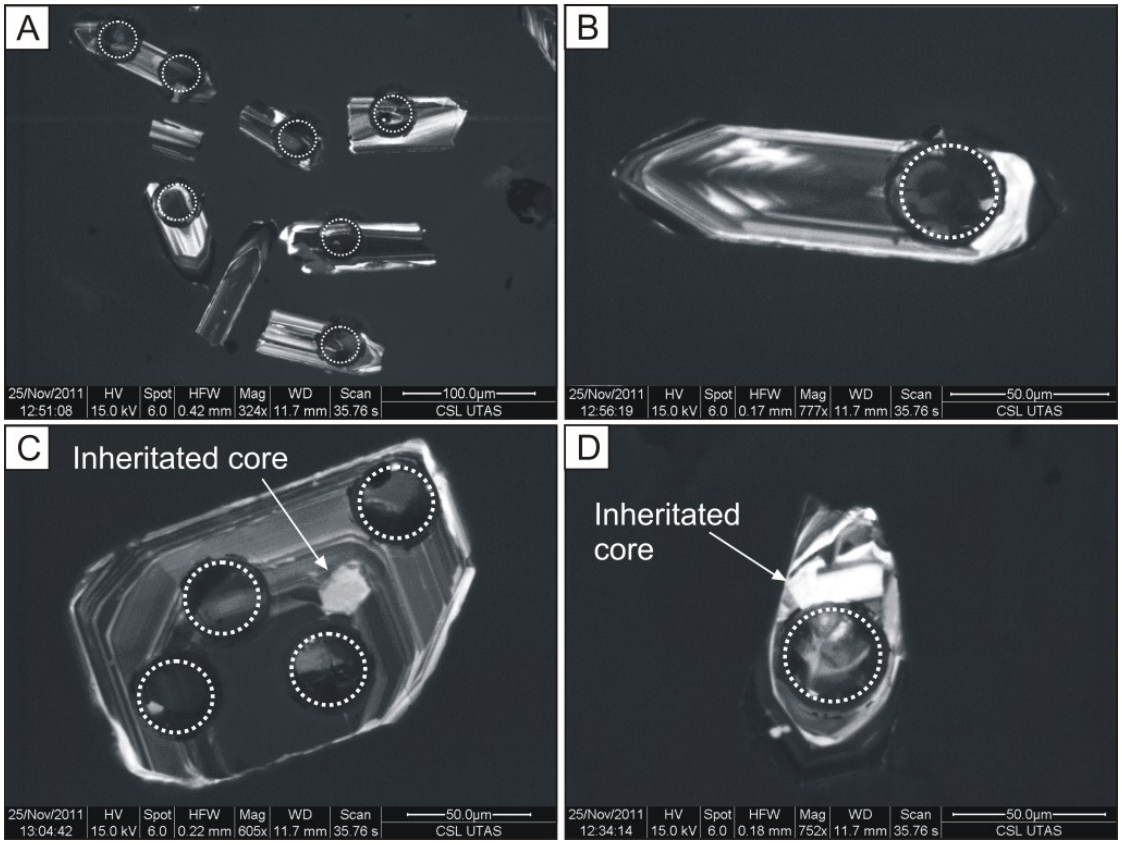

Fig. 3.25. Representative zircon cathodoluminescence (CL) images of the igneous units in the Phuoc Son deposit area, central Vietnam. Note white dashed circles showing holes ablated by laser. **A.** Zircons from foliated dacitic porphyry at Bai Dat. Sample No. DSDH257@94.5m. **B.** Zoomed CL image showing a zircon from foliated dacitic porphyry at Bai Dat. Sample No. DSDH257@94.5m. **C.** CL image showing a zircon of dacitic porphyry at Bai Go. Sample No. DSDH89@187.7m. Note inherited core is present. **D.** CL image showing a zircon of granite at the Khe Rin Prospect. Note inherited core is present. Sample No. KRDH31@259.8m.

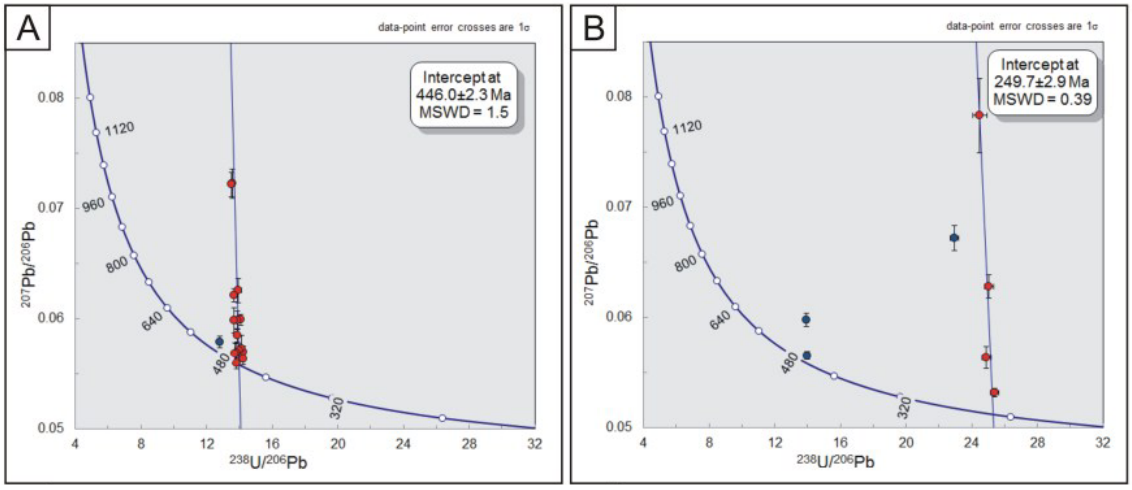

Fig. 3.26. Representative U-Pb zircon concordia diagrams of the igneous units from the Phuoc Son deposit area, central Vietnam. **A.** Foliated dacitic porphyry at Bai Dat. Sample No. DSDH257@94.5m. **B.** Dacitic porphyry at Bai Dat. Sample No. DSDH257@336.4m.

Table 3.1. Summary of LA-ICPMS zircon/sphene U-Pb and Ar-Ar geochronological data of main rock units from the Phuoc Son deposit area and the surrounding, central Vietnam.

Deposit Area	Sample ID	Rock unit	Mineral	Age (Ma)	Remarks
Phuoc Son deposit area					
Bai Dat	DSDH257@94.5m	Foliated dacitic porphyry	Zircon (LA-ICPMS)	446.0±2.3	In this study (1st analysis)
	DSDH257@94.5m	Foliated dacitic porphyry	Zircon (LA-ICPMS)	443±11	In this study (2nd analysis)
	DSDH257@336.4m	Dacitic porphyry	Zircon (LA-ICPMS)	249.7±2.9	In this study (1st analysis)
	DSDH257@336.4m	Dacitic porphyry	Zircon (LA-ICPMS)	249±11	In this study (2nd analysis)
Bai Go	DSDH89@187.7m	Dacitic porphyry	Zircon (LA-ICPMS)	250.5±2.3	In this study (1st analysis)
	DSDH89@187.7m	Dacitic porphyry	Zircon (LA-ICPMS)	250.9±9.7	In this study (2nd analysis)
Round Hill	84015	Granite	Zircon (LA-ICPMS)	472±6	Sang Quang Dinh et al. (2010)
Khe Rin	KR15	Granite	Zircon (LA-ICPMS)	255±4	Sang Quang Dinh et al. (2010)
	KRDH31@259.8m	Granite	Zircon (LA-ICPMS)	251.1±4.4	In this study
Surrounding area					
Nui Vu Fm.	SVN.72.2	Basaltic dyke	Zircon (LA-ICPMS)	484±8	Sang Quang Dinh et al. (2010)
	SVN16.1	Metagabbro	Zircon (LA-ICPMS)	483±7	Sang Quang Dinh et al. (2010)
Kham Duc Fm.	JH0815	Felsic gneiss	Zircon (LA-ICPMS)	462.1±4.6	Khin Zaw et al. (2010)
	SVN27.2	Granite	Zircon (LA-ICPMS)	456±3	Sang Quang Dinh et al. (2010)
	SVN27.2	Granite	Sphene (LA-ICPMS)	268±8	Sang Quang Dinh et al. (2010)
	JH0813	Gneiss	Zircon (LA-ICPMS)	432.7±3.7	Khin Zaw et al. (2010)
	HT09-KD-1-1	Granite gneiss	Zircon (LA-ICPMS)	258.9±2.2	Khin Zaw et al. (2010)
	VN580	Orthogneiss	Amphibole (Ar-Ar)	239.5±1.5	Vu Van Tich et al. (2007)
	VN866	Mica schist	Biotite (Ar-Ar)	229.1±2.6	Vu Van Tich et al. (2007)
	VN577	Mica schist	Biotite (Ar-Ar)	229.8±3.0	Vu Van Tich et al. (2007)
	VN576	Mica schist	Biotite (Ar-Ar)	237±3	Vu Van Tich et al. (2007)
SW of Phuoc Son	90699	Granite	Zircon (LA-ICPMS)	348±7	Sang Quang Dinh et al. (2010)
	84042	Granite	Zircon (LA-ICPMS)	240±4	Sang Quang Dinh et al. (2010)

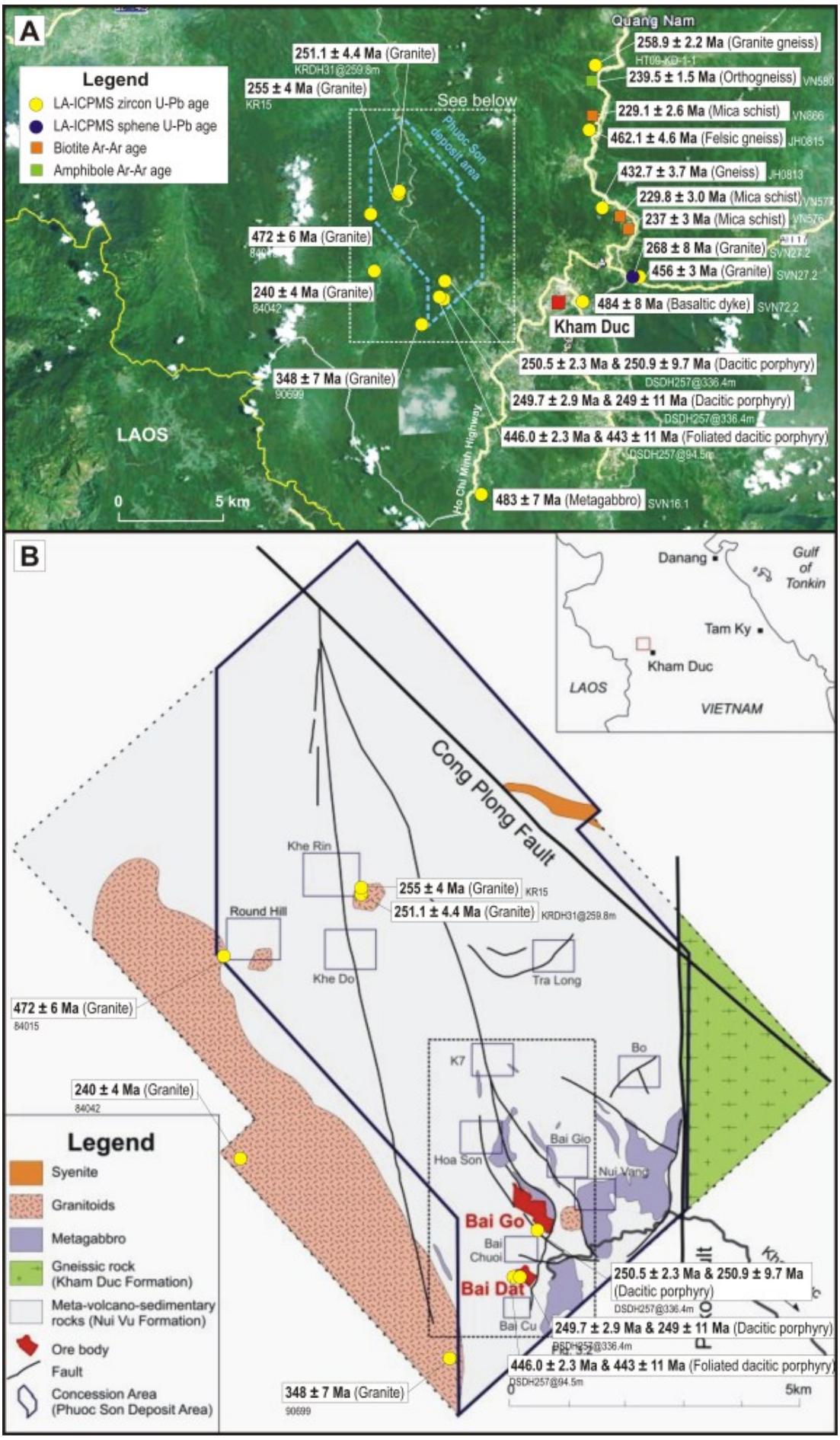

Fig. 3.27. Location and distribution of the dated samples from the Phuoc Son deposit and the surrounding area. **A**. The results from the Phuoc Son deposit and the surrounding area. **B**. The results from the Phuoc Son deposit area. See Table 3.1 for details of the samples.

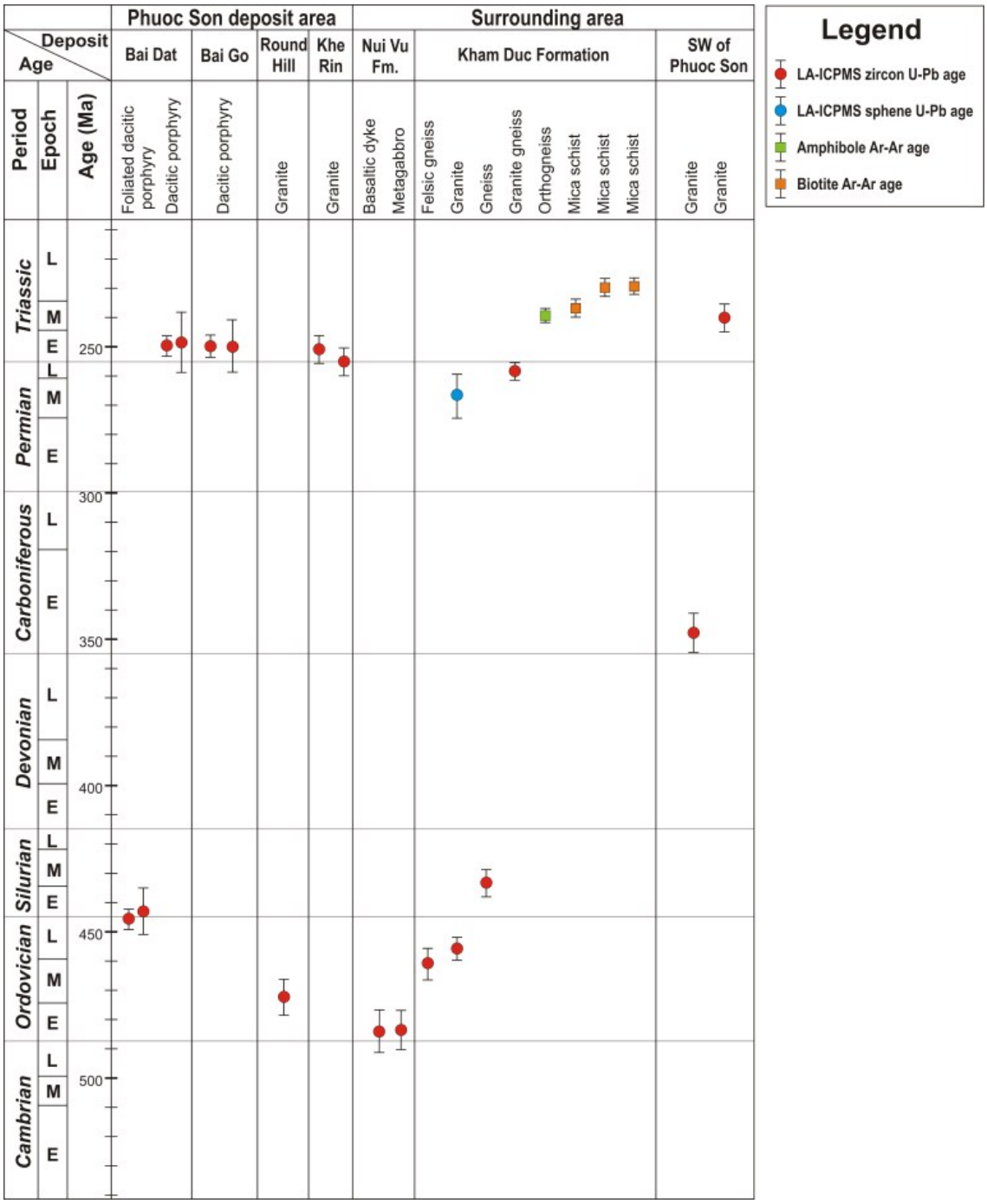

Fig. 3.28. Summary and comparison of geochronological data in time-space relation of the Phuoc Son deposit area and the surrounding, central Vietnam. See Table 3.1 for data sources.

490-420 Ma (Ordovician-Silurian)

The older age group (490–430 Ma) was recorded at the Phuoc Son deposit and the surrounding area. The oldest ages are recorded in the basaltic dyke and metagabbro (484±8 and 483±7 Ma, respectively; Sang Quang Ding et al., 2010), both of which are considered to belong to the Nui Vu Formation. Granite and gneiss samples from the Kham Duc Formation along the Ho Chi Minh Highway yielded age ranges of 465–430 Ma (462.1±4.6 Ma, 456±3 Ma and 432.7±3.7 Ma; Sang Quang Dinh, 2010; Khin Zaw et al., 2010). In the Phuoc Son deposit area, the Ordovician-Silurian ages are noted from two intrusive units; the Round Hill granite (472±6 Ma; Sang Quang Dinh et al., 2010) and foliated dacitic porphyry at Bai Dat (446.0±2.3 Ma and 443±11 Ma). The granite from the southwest of the Phuoc Son area yielded a Carboniferous age (348±7 Ma), which is distinguished from the Ordovician-Silurian and Permian-Triassic age groups.

270-220 Ma (Permian-Triassic)

The younger age group (270–220 Ma) was recorded from various locations in the Phuoc Son deposit area and the surroundings. In the Phuoc Son deposit area, the following ages were found: dacitic porphyry at Bai Dat (249.7±2.9 Ma and 249±11 Ma) and Bai Go (250.5±2.3 Ma and 250.9±2.7 Ma), Khe Rin granite (251.1±4.4 Ma and 255±4 Ma) and granite to the southwest of the Phuoc Son deposit area (240±4 Ma; Sang Quang Dinh et al., 2010). Similar ages are also recognised from the granite gneiss of the Kham Duc Formation (258.9±2.2 Ma; Khin Zaw et al., 2010). Vu Van Tich et al. (2007) also reported similar ages from Ar-Ar dating of amphibole in orthogneiss (239.5±1.5 Ma) and biotite in mica schists (229.8±3.0 Ma, 229.1±2.6 Ma and 237±3 Ma), both of which belong to the Kham Duc Formation.

The oldest age of the group was from LA-ICPMS sphene U-Pb dating of a granite sample (268±8 Ma; Sang Quang Dinh et al., 2010) of the Kham Duc Formation. The age is considered to be a metamorphic age as the sample also yielded older LA-ICPMS zircons with a U-Pb age of 456±3 Ma, which is likely to be protolith age (Sang Quang Dinh et al., 2010).

3.5. GEOCHEMISTRY

3.5.1. Introduction

Igneous geochemistry is commonly used to understand the nature of the lithological and tectonic settings of igneous and sedimentary rocks. A number of types of ore deposits are genetically linked to magmatism, and thus an understanding nature of magmas is an important step in establishing a deposit model. In this study, geochemical analyses were conducted on major igneous units of the Phuoc Son deposit area, aiming to (1) classify igneous units using

chemical compositions and (2) reconstruct tectonic environment based on discrimination diagrams. However, a comprehensive petrogenetic study was not attempted as the main scope of the thesis was the ore characterisation and ore genesis rather than igneous geochemistry, petrology and tectonics. To date, no detailed geochemical study has been carried out on the lithological units of the Phuoc Son deposit area, but a number of geochemical studies have been conducted on igneous-metamorphic rocks occurring in the region of central Vietnam (e.g., Owada et al., 2007).

3.5.2. Analytical methods

A total of forty-one samples, including one foliated dacitic porphyry, five dacitic porphyry, three andesitic dyke, six granite dyke, three metagabbro, four Khe Rin granite and five Round Hill granite, twelve metabasite and two schist samples, were analysed for major (Si, Ti, Al, Fe, Mn, Mg, Ca, Na, K, P and S) and trace (Rb, Sr, Cr, Cu, Ba, Bi, Sn, Zr, Mo, Nb, V, Zn, Ni, Pb, Th, Sc, U and Y) elements using X-Ray Fluorescence (XRF) at CODES, the University of Tasmania, with the help of Phil Robinson, Katie McGoldrick, Ian Little and Jay Thompson. The detailed analytical technique is outlined by Norrish and Chappell (1977) and Norman et al. (2003). Of the forty-one samples, nineteen samples were additionally analysed for rare earth elements (REE: La, Ce, Pr, Nd, Sm, Eu, Gd, Tb, Dy, Ho, Er, Tm, Yb and Lu) using the solution ICP-MS technique at the University of Tasmania. The detailed analytical method for the solution ICP-MS technique is described by Yu et al. (2000). To obtain reliable results, samples for the analyses were carefully selected from the least-altered samples (mainly drill core samples). They were initially crushed using a jaw crusher to make rock fragments several centimetres in size and were subsequently ground using a tungsten carbide rig mill to produce rock powder.

3.5.3. Geochemical results

Full results of the whole-rock geochemical data of lithological units at Phuoc Son are listed in Appendix IV.

Major and trace elements

The igneous and meta-sedimentary rocks from the Phuoc Son area have a wide range of SiO_2 contents from 35–80 wt.% (Fig. 3.29). In bivariate plots between major elements versus SiO_2, most of the major elements such as Fe_2O_3, MnO, MgO, P_2O_5, TiO_2 and CaO show decreasing trends with increasing SiO_2 content (Fig. 3.29A, B, C, D, E and G). In contrast, Na_2O has a

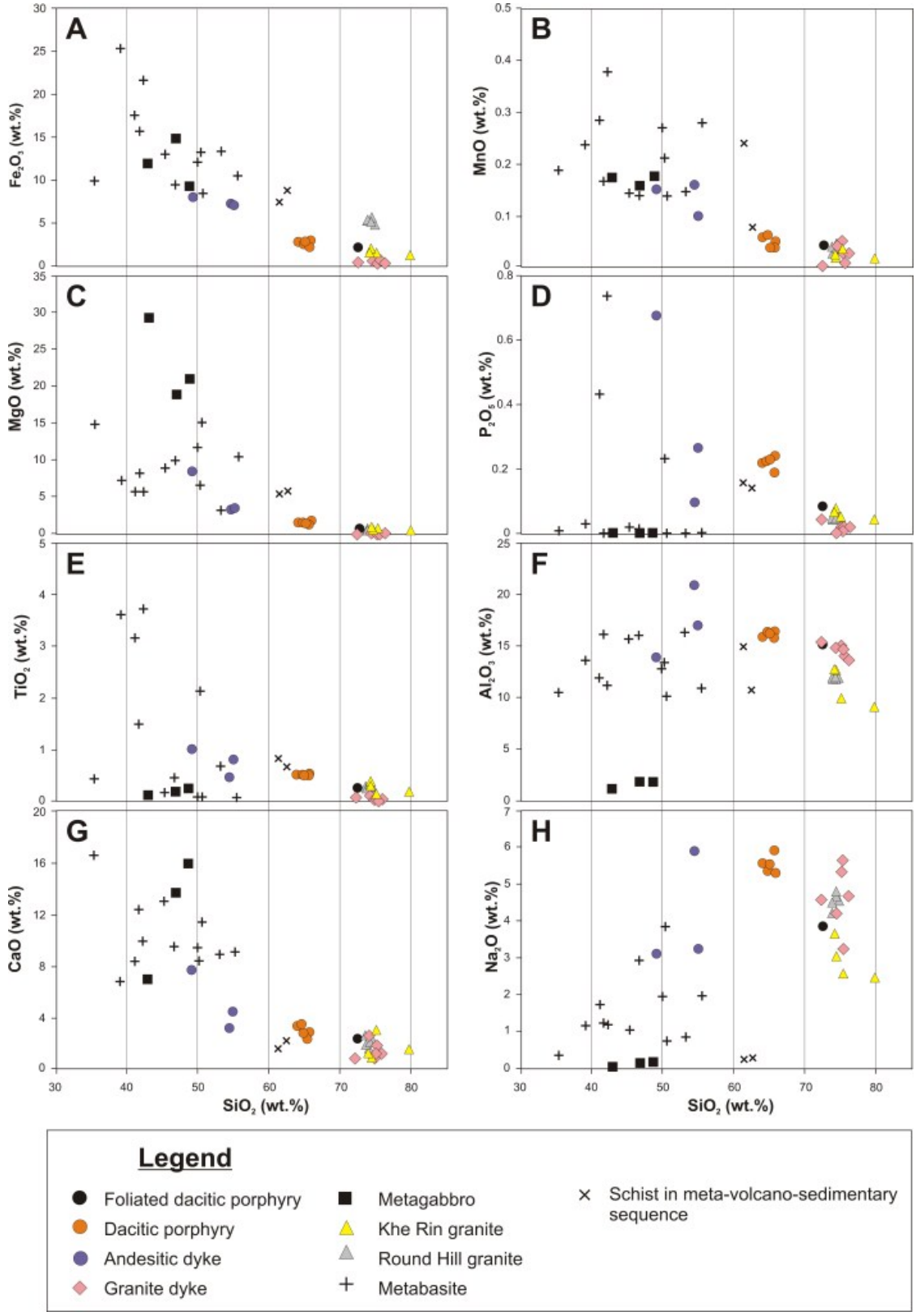

Fig. 3.29. Bivariate plots of SiO_2 versus selected major elements. **A**. SiO_2 vs Fe_2O_3, **B**. SiO_2 vs MnO, **C**. SiO_2 vs MgO, **D**. SiO_2 vs P_2O_5, **E**. SiO_2 vs TiO_2, **F**. SiO_2 vs Al_2O_3, **G**. SiO_2 vs CaO and **H**. SiO_2 vs Na_2O of the different lithological units from the Phuoc Son deposit area.

positive correlation with SiO_2 (Fig. 3.29H). Regardless of SiO_2 concentration, all of the studied units have consistent Al_2O_3 values ranging of 10–20 wt.%, except the metagabbro unit which has a very low (<5 wt.%) Al_2O_3 content (Fig. 3.29F).

Trace elements such as Sc, V and Zn show decreasing trends against SiO_2 (Fig. 3.30A, C and J), whereas increasing trends are recognised in Th, U, Y, Mo and Pb versus SiO_2 values (Fig. 3.30D, E, F, H and I). Cu concentrations are generally lower than 200 pm in all of the studied rocks except one metabasite sample which has nearly 1000 ppm (Fig. 3.30G). A wide range of Zr concentrations from 20 to 200 ppm are found in the felsic units (>70 wt.% SiO_2; foliated dacitic porphyry, Khe Rin granite, Round Hill granite and granite dyke units), whereas the schist, andesitic dyke and dacitic porphyry units and few matabasite samples have a range of 100–200 ppm in Zr (Fig. 3.30B). Zr values in the metagabbro and major metabasite units are less than 50 ppm (Fig. 3.30B).

Rare earth elements and multi-elements

Chondrite-normalised rare earth element (REE) patterns of the different lithological units from Phuoc Son are shown in Figure 3.31. The dacitic porphyry, foliated dacitic porphyry, Khe Rin granite and schist units are characterised by similar patterns of enriched light rare earth elements (LREE) and depletion of heavy rare earth elements (HREE) with weak negative Eu anomalies. One of the two andesitic dyke samples also has a similar pattern. The other andesitic dyke, together with granite dyke and metabasite units exhibit flat REE patterns with various Eu anomalies including weak positive anomalies in the metabasite and strong negative anomalies in the granite dyke. The REE profiles of the Round Hill granite and metagabbro units are characterised by depletion of LREE, with weak negative Eu anomalies.

The N-MORB normalised multi-element diagrams of the units from the Phuoc Son area are presented in Figure 3.32. Of these, the REE patterns of the intrusive units including the foliated dacitic porphyry, dacitic porphyry, Round Hill granite, Khe Rin granite and granite dyke are characterised by enrichment in large-ion lithophile elements (LILE; Cs, Rb, K, Ba Sr and Eu) and depletion in the high field strength elements (HFSE; Y, Hf, Zr, Ti, Nb and Ta). Similar trace element characteristics are also recognised in the schists. The granite dykes are enriched in both LILE and HFSE, in particular Th, U and Pb, and depleted in certain elements such as P, Zr and Eu. Almost all of the measured incompatible elements are enriched in the andesitic dyke unit, whereas they are depleted in the metagabbro.

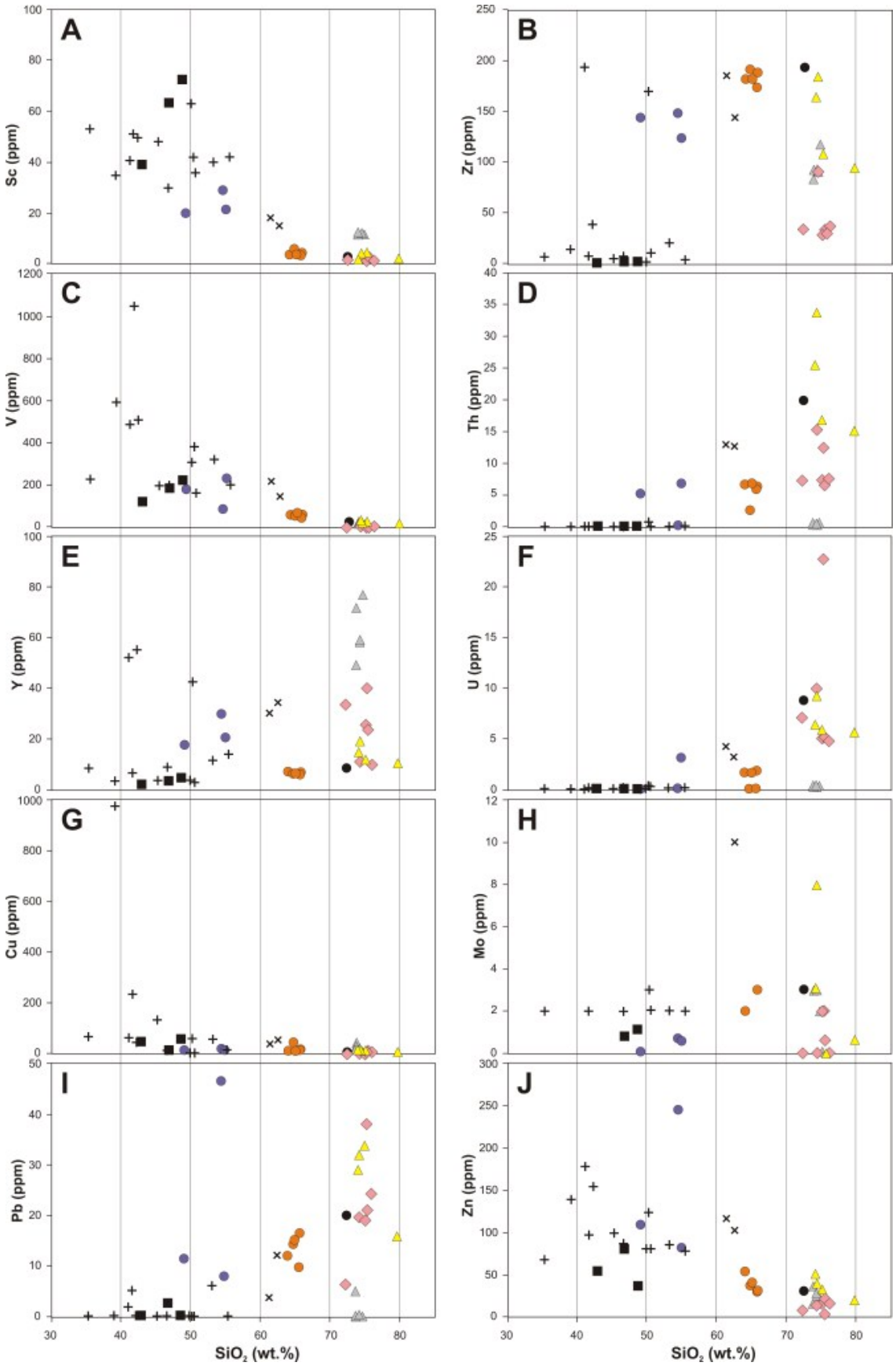

Fig. 3.30. Bivariate plots of SiO_2 versus minor elements. **A**. SiO_2 vs Sc, **B**. SiO_2 vs Zr, **C**. SiO_2 vs V, **D**. SiO_2 vs Th, **E**. SiO_2 vs Y, **F**. SiO_2 vs U, **G**. SiO_2 vs Cu, **H**. SiO_2 vs Mo, **I**. SiO_2 vs Pb and **J**. SiO_2 vs Zn of the different lithological units from the Phuoc Son deposit area. See Figure 3.24 for legend.

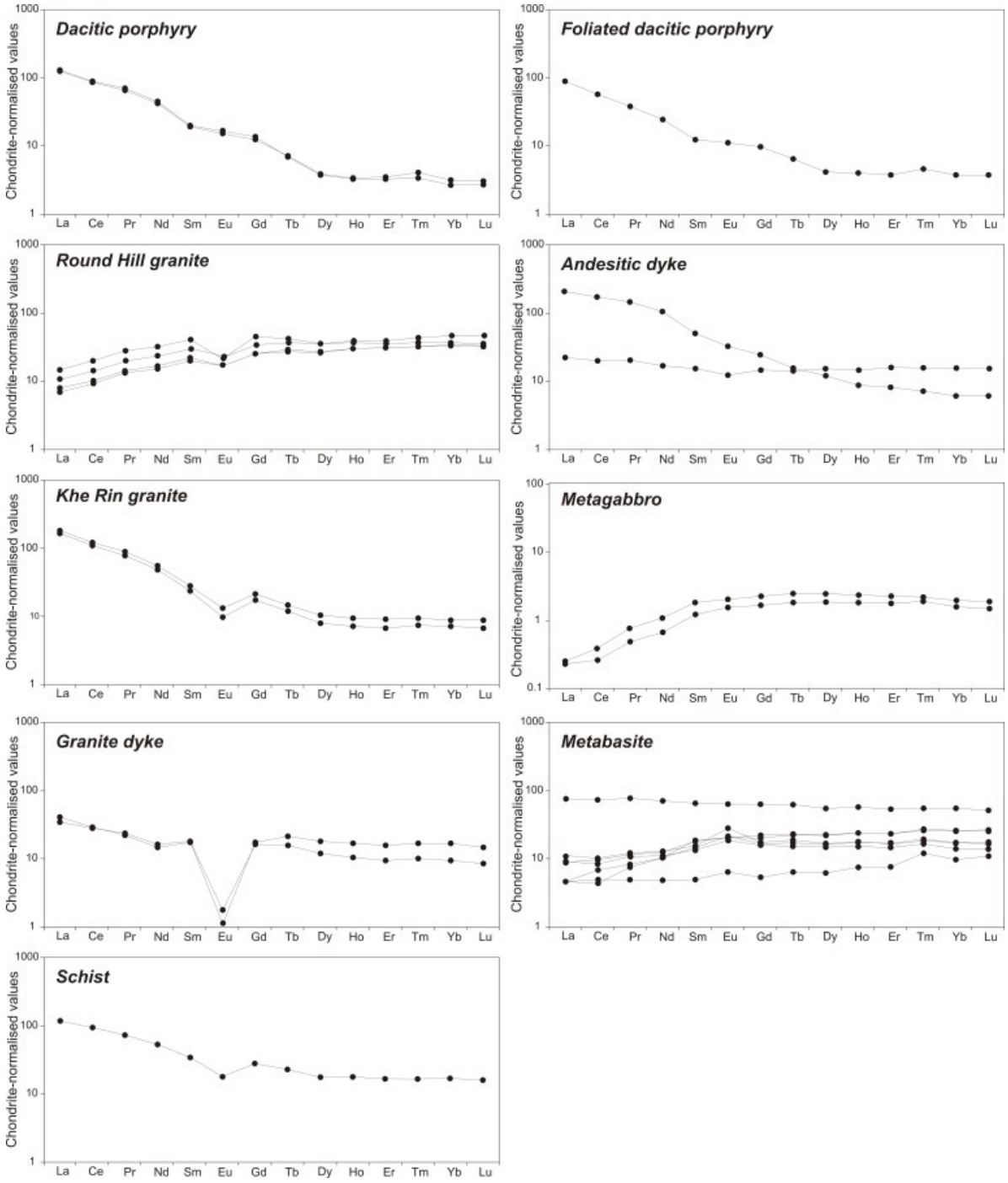

Fig. 3.31. Chondrite-normalised REE patterns of the different lithological units from the Phuoc Son deposit area, central Vietnam. Normalising values of Sun and McDonough (1989) were applied. Note that the metagabbro data are expressed in different scale compared to other units.

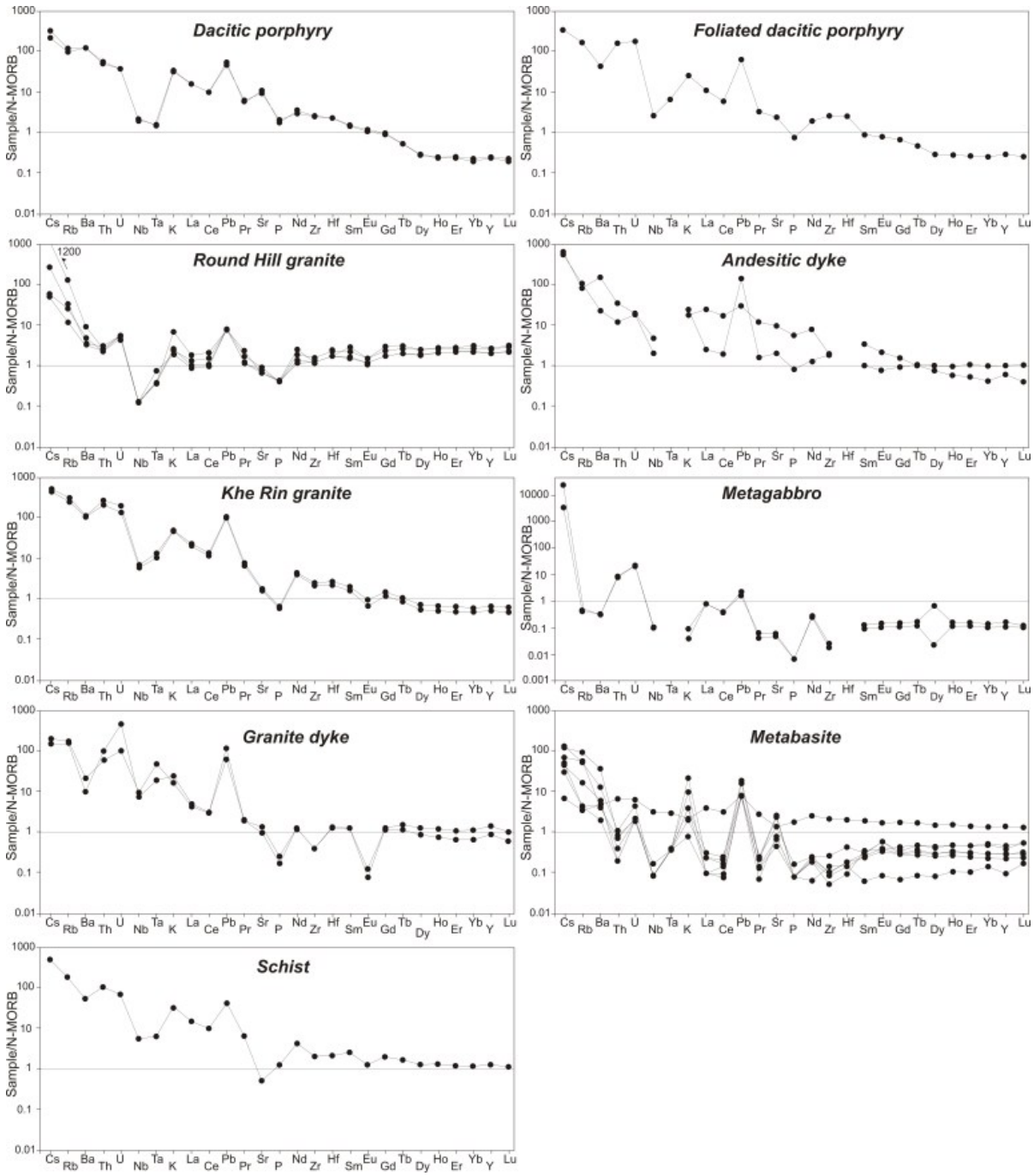

Fig. 3.32. N-MORB normalised multi-element patterns of the different lithological units from the Phuoc Son gold deposit area, central Vietnam. N-MORB normalising values are from Sun and McDonough (1989). Note that the metagabbro data are expressed in different scale compared to other units.

Geochemistry and tectonic setting

Compositional variations of the igneous units at the Phuoc Son deposit area were applied to understand the tectonic setting (Fig. 3.33). All of the units fall on a sub-alkaline field except some metabasite and andesitic dyke units (Fig. 3.33A). The three alkaline metabasites have very high TiO_2 (3–4 %; Fig. 3.29E) strongly indicating an intraplate hotspot related eruption and/or juvenile rifting environments. The lithological units show sub-alkaline affinity ranging from low-K calc-alkaline (tholeiite) to high-K calc-alkline fields (Fig. 3.33B). However, this diagram is strongly affected by K mobility and enrichment during alteration and many of the units may be misclassified. The metagabbro and Round Hill granite units appear to be of low-K calc-alkaline affinity which is corroborated by the relatively low LREE contents, low contents of the less mobile LILE (e.g., Rb) and low P relative to the other lithological units. These compositions contrast with the dacitic porphyry, foliated dacitic porphyry and andesitic dyke, which plot in the medium- and high-K calc-alkaline fields of the diagram and have higher LREE and LILE, as well as the immobile HFSE.

The dacitic porphyry and foliated dacitic porphyry units are discriminated to be trachy andesite, the andesitic dyke is to be andesite and the metabasite is to be basalt to basalt/andesite in compositions (Fig. 3.33C). Some of the dacitic porphyries have adakitic composition (Fig. 3.33D), contrasting with the rest of the units in the Phuoc Son area. Major igneous units of the Phuoc Son area are classified as I-type affinity (Fig. 3.33E and F), except the Round Hill granite data which tend to plot in A- or M-type field in Figure 3.33E and F. The andesitic dyke falls on the both within-plate and plate margin fields in Figure 3.33G, and shows a within-plate affinity in Figure 3.33H.

3.6. MAGNETIC SUSCEPTIBILITY

3.6.1. Introduction

The magnetite- and ilmenite-series granite classification has been widely applied based on magnetite contents of granitic rocks, to investigate redox states of the granitic magma (Ishihara, 1977). Measuring magnetic values of the granites is a reliable tool to classify the granite series and thus magnetic susceptibility values of granitoids are commonly accepted as a practical tool to discriminate the granite series using a boundary of 3.0×10^{-3} SI unit (Kanaya and Ishihara, 1973; Ishihara, 1979, 1981). As the granite series reflect redox states of granitic magma (i.e., magnetite- and ilmenite-series correspond to oxidised- and reduced-type, respectively), the scheme is often applied to study parental magma of magmatic deposits such as porphyry, skarn and intrusion-related systems because metal association of the systems are

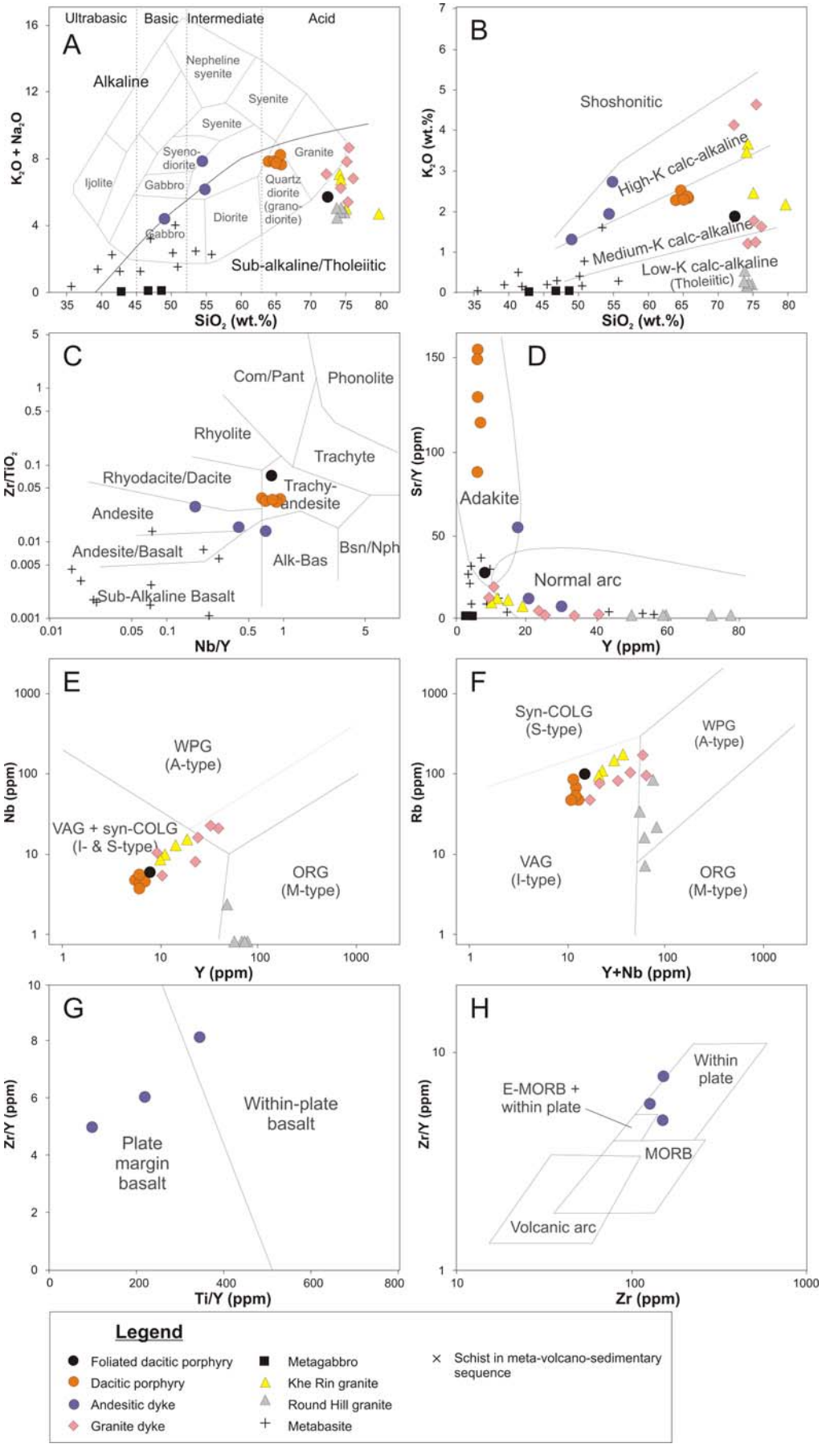
A
Ultrabasic
Basic
Intermediate
Acid
Alkaline
Nepheline syenite
Syenite
Syenite
Syeno-diorite
Granite
Ijolite
Gabbro
Quartz diorite (grano-diorite)
Diorite
Gabbro
Sub-alkaline/Tholeiitic
K2O + Na2O
SiO2 (wt.%)
B
Shoshonitic
High-K calc-alkaline
Medium-K calc-alkaline
Low-K calc-alkaline (Tholeiitic)
K2O (wt.%)
SiO2 (wt.%)
C
Com/Pant
Phonolite
Rhyolite
Trachyte
Rhyodacite/Dacite
Trachy-andesite
Andesite
Andesite/Basalt
Alk-Bas
Bsn/Nph
Sub-Alkaline Basalt
Zr/TiO2
Nb/Y
D
Adakite
Normal arc
Sr/Y (ppm)
Y (ppm)
E
WPG (A-type)
VAG + syn-COLG (I- & S-type)
ORG (M-type)
Nb (ppm)
Y (ppm)
F
Syn-COLG (S-type)
WPG (A-type)
VAG (I-type)
ORG (M-type)
Rb (ppm)
Y+Nb (ppm)
G
Within-plate basalt
Plate margin basalt
Zr/Y (ppm)
Ti/Y (ppm)
H
Within plate
E-MORB + within plate
MORB
Volcanic arc
Zr/Y (ppm)
Zr (ppm)
Legend
Foliated dacitic porphyry
Dacitic porphyry
Andesitic dyke
Granite dyke
Metagabbro
Khe Rin granite
Round Hill granite
Metabasite
Schist in meta-volcano-sedimentary sequence

Fig. 3.33 (previous page). Geochemical discrimination diagrams for the major igneous units in the Phuoc Son gold deposit area, central Vietnam. **A.** Subdivision of igneous rocks into alkaline and sub-alkaline/tholeiitic compositions using SiO_2 versus K_2O+Na_2O. Fields of granitoids are after Cox et al. (1979). **B.** Subdivision of sub-alkaline/tholeiitic rocks using SiO_2 versus K_2O. **C.** Volcanic rock discrimination diagram using immobile elements of Nb/Y versus Zr/TiO_2, after Winchester and Floyd (1977). **D.** Sr/Y versus Y adakite discrimination diagram after Defant and Drummond (1990). **E.** Nb versus Y tectonic discrimination diagram for felsic units after Pearce et al. (1984). **F.** Rb versus Y+Nb tectonic discrimination diagram for felsic units after Pearce et al. (1984). **G.** Zr/Y versus Ti/Y tectonic discrimination diagram for basaltic rocks after Pearce and Gale (1977). **H.** Zr/Y versus Zr tectonic discrimination diagram for basaltic rocks after Pearce and Norry (1979).

linked to redox states of the magma and the associated hydrothermal fluids (Cu, Pb, Zn and Mo for oxidised and Sn and W for reduced fluids; e.g., Ishihara, 1998). However, it is known that gold is associated with the both oxidised fluids of the magnetite-series granite (e.g., Cu-Au porphyry deposit) and reduced fluids of ilmenite-series granite (e.g., intrusion-related Au deposit).

In this study, magnetic susceptibility values of major igneous units in the Phuoc Son area were measured to classify the granite series and assess their redox states for linking to the gold mineralisation at Phuoc Son.

3.6.2. Analytical methods

A KT-10 magnetic susceptibility meter was used to measure magnetic susceptibility values of the intrusive units from the Phuoc Son deposit area. Unaltered or the least-altered samples were selected for the analysis and three or four measurements were made for each sample to obtain reliable mean values.

3.6.3. Results

All the measured data are listed in Appendix V, and the data are summarised in Table 3.2 and Figure 3.34. Both the magnetite- and ilmenite-series were recognised in the intrusive units of the Phuoc Son deposit area. The metagabbro and Round Hill granite yielded high values of 33.2–86.0 ($\times 10^{-3}$ SI) and 17.0–44.6 ($\times 10^{-3}$ SI), respectively (Table 3.2), and therefore they are classified to be magnetite-series (Fig. 3.34). In contrast, the other intrusive units including the granite dyke, Khe Rin granite, andesitic dyke, diorite and dacitic porphyry have lower values of 0.077–0.233, 0.081–0.102, 0.344–0.414, 0.159–0.239 and 0.22–0.562, respectively (Table 3.2), suggesting that they are of the ilmenite-series (Fig. 3.34).

Comparisons of the magnetic susceptibility data of different units with the relevant LA-ICPMS zircon U-Pb ages indicate that there the units of the Ordovician age group correspond

Table 3.2. Summary of magnetic susceptibility values of intrusive units from the Phuoc Son deposit area, central Vietnam.

Rock type (No. of measurements)	**Magnetic susceptibility value** (X 10^{-3} SI)		
	Mean	Minimum	Maximum
Dacitic porphyry (7)	0.407	0.220	0.562
Diorite (3)	0.200	0.159	0.239
Andesitic dyke (7)	0.369	0.303	0.414
Khe Rin granite (4)	0.098	0.081	0.120
Granite dyke (12)	0.161	0.077	0.233
Round Hill granite (14)	30.5	14.0	44.6
Metagabbro (8)	43.2	33.2	50.0

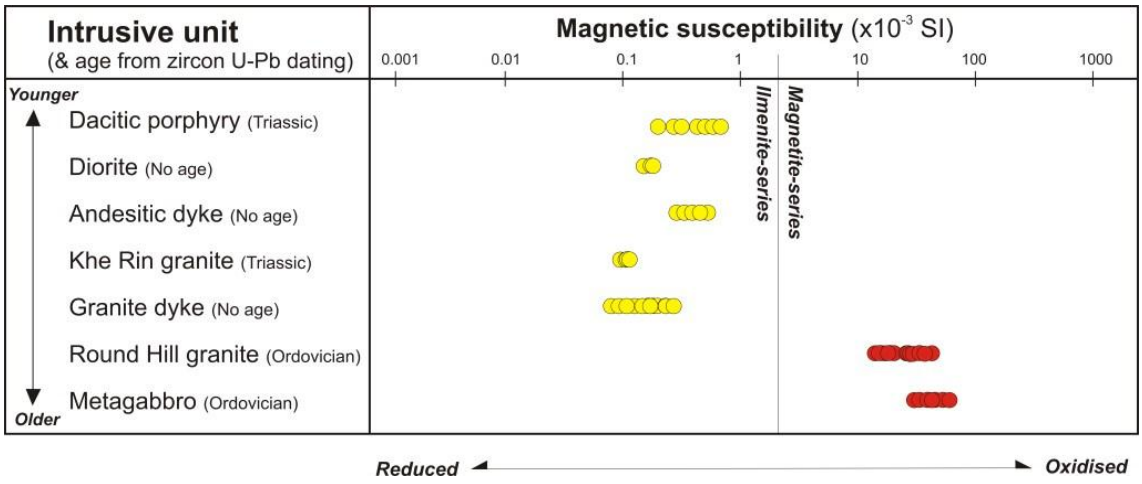

Fig. 3.34. Plots showing magnetic susceptibility data of the major intrusive units at the Phuoc Son deposit area, central Vietnam. Note Gabbro and Round Hill granite units are classified to be magnetite-series, whereas the other units are discriminated to be ilmenite-series.

to the magnetite-series, whereas the other units, all of which are considered to be of Triassic age, are classified into ilmenite-series (Fig. 3.34). This may suggest that the magmas formed during the Ordovician was oxidised, whereas the magma produced during the Triassic at Phuoc Son was formed under reduced conditions.

3.7. DISCUSSION

The geological, geochronological and geochemical data of the Phuoc Son deposit area demonstrate that there were two distinct magmatic-metamorphic events in the region; (1) Early Palaeozoic (490–430 Ma; Ordovician-Silurian) and (2) Late Palaeozoic to Early Mesozoic (270–220 Ma; Permian-Triassic). The tectonic processes related to these two events

are discussed below. In addition, adakitic magmatism was recognised in the dacitic porphyry unit at the Bai Dat and Bai Go deposits, and thus the nature of the magmatism is also discussed in terms of the source of the magma and metals at Phuco Son. Many examples of a link between adakitic magma and Cu-Au mineralisation were recently reported from modern subduction-related arcs, such as Philippines (Sajona and Maury, 1998) and South America (Richards and Kerrich, 2007) and collisional and post-collisional settings such as that in Tibet following the Indian-Eurasian collision (e.g., Gao et al., 2007).

3.7.1. Ordovician-Silurian magmatism and metamorphism

The region encompassing the Phuoc Son deposit area has undergone a subduction-collision event during Late Ordovician-Silurian period as supported by a number of geological data. Geochronological data of granites from the central Vietnam and Attapu district in southern Laos indicate that the subduction was initiated around 490 Ma (Early Silurian) and it was continued until 410 Ma (Late Silurian). The subduction was probably initiated as an island arc-type, as indicated by the low HFSE and LILE contents of the tholeiitic metagabbros/granites and I-type/magnetite-series affinity of the igneous units at Phuoc Son. This is also supported by boninitic affinity of some of the amphibolite at Phuoc Son (Sang Quang Dinh et al., 2010). The Late Ordovician to Silurian metamorphic event is evidenced by late S-type granites and rhyolites which may have formed under a post-collisional setting similar to that observed elsewhere in the eastern part of central Vietnam (e.g., Duc Bo; Khin Zaw et al., 2010). These tectonic events are considered to have occurred along the Tam Ky-Phuoc Son Suture Zone, which may represent the suturing event of the Proto-Indochina and Proto-South China Terranes Ordovician-Silurian (Tran Thanh Hai et al., 2009).

3.7.2. Permian-Triassic magmatism and metamorphism

The intrusive units with the Late Permian-Early Triassic ages in Phuoc Son (i.e., Khe Rin granite, dacitic porphyry, andesitic dyke and granite dyke; 260–240 Ma) are classified as I-type/ilmenite-series, and the ages are comparable to the late stage magmatic-metamorphic event of the TSFB (Fig. 3.35). This indicates that the Permian-Triassic magmatic event at Phuoc Son was associated with a post-collisional process which followed collision of the Indochina and South China Terranes at around 275–265 Ma (Figs. 3.35 and 36). A previous study in Laos has shown that the Sn-W(-Au) mineralisation of TSFB is typically associated with I-type/ilmenite-series, Late Permian and Early Triassic granites (Sanematsu et al., 2009, 2011). These are similar in chemistry and age to the intrusive units of Phuoc Son to that of the Sn-W granites in Laos. At the Bong Mieu gold deposit, similar ages are also recorded from

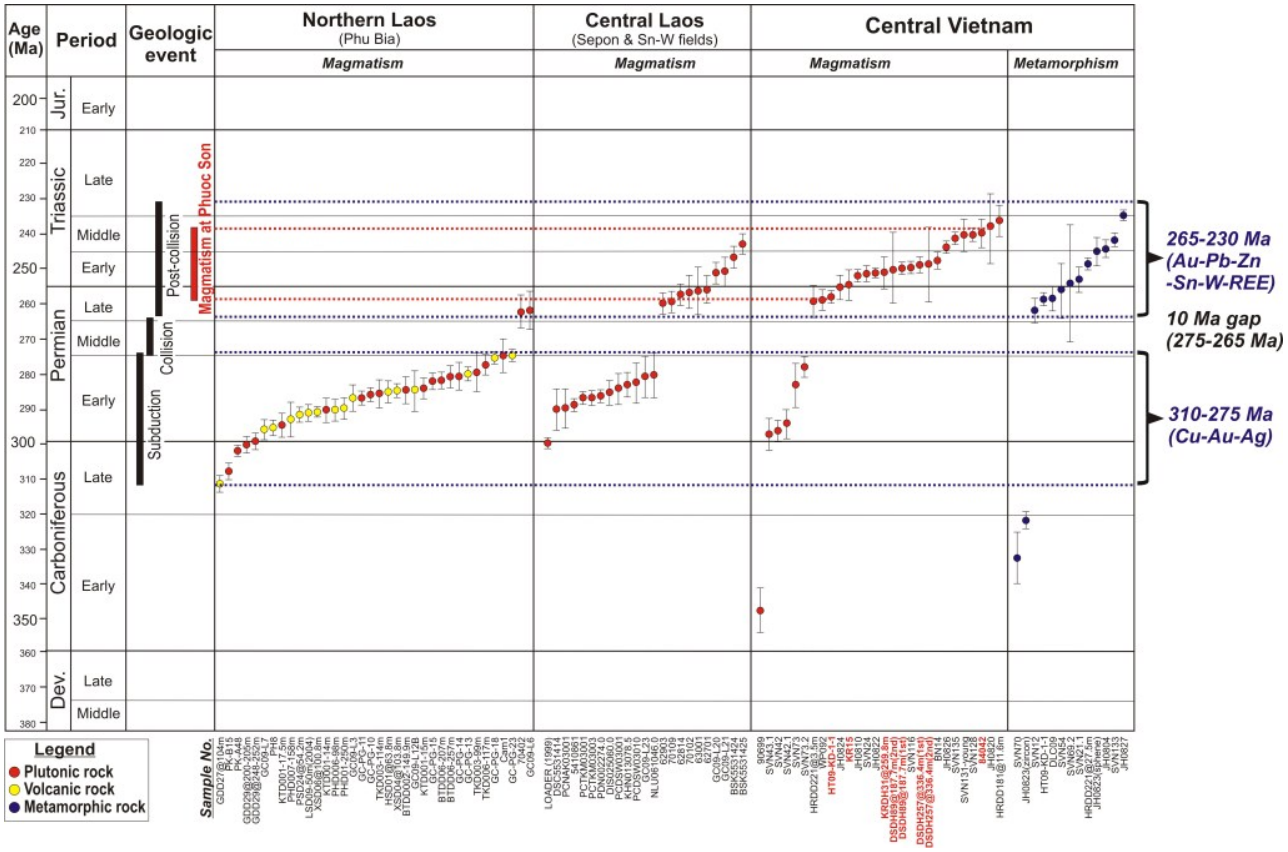

Fig. 3.35. Geochronological framework of the Truong Son Fold Belt showing the belt is made up of early volcano-plutonism (310–275 Ma) and late plutonic-metamorphism (265–230 Ma). Data modified after Khin Zaw et al. (2010). Note the age range of Phuoc Son and the surrounding area is coloured in red, corresponding to the post-collision setting.

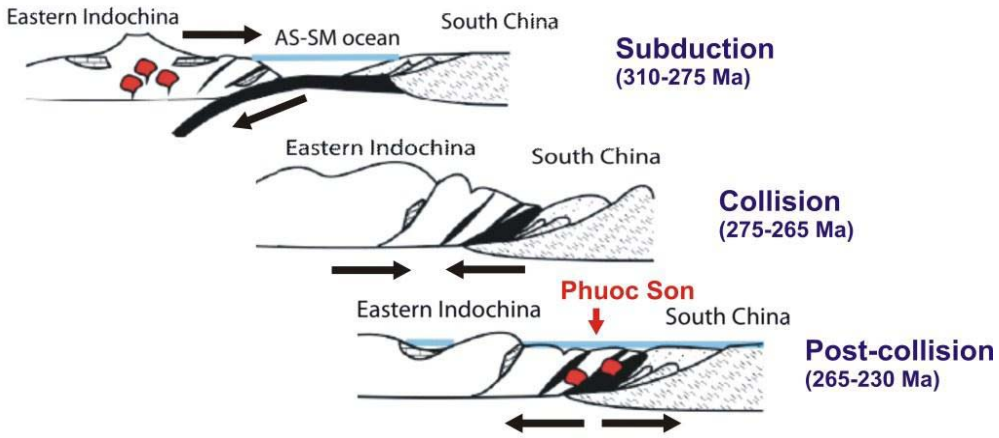

Fig. 3.36. Tectonic reconstruction of the Indochina and South China Terranes during 310–230 Ma (Late Carboniferous-Triassic), responsible for formation of the Truong Son Fold Belt. Modified after Halpin et al. (2010).

the intrusions associated with gold mineralisation (i.e., leucocratic dyke at the Ho Ray-Thac Trang Au-W deposit; Lee, 2010), indicating that the gold mineralisation of the late stage magmatic-metamorphism of the TSFB is commonly associated with these reduced magmas.

3.7.3. Adakitic magmatism

An adakitic magmatic signature was recognised in the dacitic porphyry units at Bai Dat and Bai Go (Fig. 3.33D), and the recognition of adakite is also supported by the definition and criteria of Defant and Drummond (1990) (Table 3.3). Metallogenically, a close link between Cu-Au mineralisation and adakitic rocks has been recently documented by many researchers (e.g., Thieblemont et al., 1997; Sajona and Maury, 1998; Oyarzun et al., 2001; Richards and Kerrich, 2007). These studies show that adakitic magmas can form in two different ways, (1) partial melting of hydrated oceanic crust in a subduction zone (e.g., Kay, 1978; Defant and Drummond, 1990; Dummond et al., 1996) and (2) deep fractionation processes of normal tholeiite and calc-alkaline arc magma (e.g., Richards and Kerrich, 2007; Richards, 2011). In mainland SE Asia, the occurrence of adakitic porphyries associated with Cu-Au mineralisation have been reported by Kamvong et al. (2007) at the Phu Kham and Puthep deposits in Laos and Thailand. Thus, it is possible that adakites may have played a significant role in Cu-Au ore formation during Permian-Triassic magmatism along the TSFB and LFB, including Bai Dat and Bai Go in the Phuoc Son deposit area. However, both adakitic and non-adakitic magamas were present at that time in the area and further evidence is required to determine if a genetic link exists between adakitic magma and gold mineralisation in the Phuoc Son area.

Table 3.3. Comparison of adakites with dacitic porphyry from the Bai Dat and Bai Go deposit areas in Phuoc Son, central Vienam.

Characteristics	**Adakites***	**Dacitic porphyry** (Bai Dat & Bai Go)
high SiO_2 (wt%)	≥56	64.0-65.7
high Al_2O_3	≥15	15.8-16.4
low MgO (wt%)	<3	1.3-1.6
high Sr (ppm)	>300	508-976
low Y (ppm)	<15	6.1-7.0
low Yb (ppm)	<1.9	0.6-0.7
high Sr/Y	>20	84-153
high La/Yb	>20	58-74
Eu anomaly	absent	absent
low HFSE (ppm)	Nb, Ta	Nb, Ta

* From Defant and Drummond (1990).

3.8. SUMMARY

Several conclusions can be made based on the geological, geochemical and geochronological data from the Phuoc Son deposit area:

- The Phuoc Son deposit area is dominated by a meta-volcano-sedimentary sequence, which is intruded by a number of intrusive units ranging from mafic to felsic composition (metagabbro, granite, andesitic dyke, foliated dacitic porphyry, dacitic porphyry, granite dyke, diorite and syenite).

- Geochronological and geochemical data indicate that the major igneous and metamorphic units of the Phuoc Son deposit area were formed by two episodes of subduction-collision events, one during the Ordovician-Silurian (490–430 Ma) and the other in the Permian-Triassic (270–220 Ma) periods. The Ordovician-Silurian igneous units in Phuoc Son are related to subduction process, whereas the Permo-Triassic episode at Phuoc Son was associated with a post-collisional event between the South China and Indochina Terranes. The Permo-Triassic magma at Phuoc Son is characterised by I-type and ilmenite-series, suggesting the magma was formed in reduced conditions. Sn-W(-Au) mineralisation is commonly associated with a similar type of magma of TSFB in Laos.

- The Phuoc Son deposit area is bounded by two main regional fault zones including N-S Poko and NW-SE Plong Cong Fault Zones at the eastern and northern boundaries, respectively. These faults are considered to have formed during a collisional event during the Permian-Triassic period. Two main local faults including Khe Rin and K7 Fault Zones trending in N-S are present in the Phuoc Son deposit area. The Bai Dat and Bai Go deposits are hosted in the Daksa Fault Zone, which is a spray of the K7 Fault Zone at the southern end of the deposit area. Structural data of the Bai Dat underground mine indicate the metamorphic foliation in the host rocks strikes N-S to NE-SW with westerly dips and is parallel to the Daksa Fault Zone.

- The dacitic porphyry unit in the Bai Dat and Bai Go deposit areas exhibits an adakitic signature as evidenced by a Sr/Y-Y plot and geochemical criteria of Defant and Drummond (1990). This suggests that gold mineralisation in the Phuoc Son deposit area could be linked to the adakitic magma.

CHAPTER 4 TEXTURE, MINERALOGY AND PARAGENESIS

4.1. INTRODUCTION

This Chapter documents the mineralisation characteristics of the Bai Dat and Bai Go deposits, emphasising the nature of the gold-bearing mineralisation styles including vein textures, ore and alteration mineralogy and the paragenetic relationships of pre-, syn- and post-mineralisation events. Observations come mainly from drill core logging, underground mapping and petrographic studies. Results of a geochronological study are also incorporated in this Chapter to integrate field and age data to constrain the timing of gold mineralisation at Phuoc Son.

4.2. MINERALISATION AND PARAGENESIS

At the Bai Dat and Bai Go deposits, gold occurs as quartz-sulphide veins which are hosted parallel to metamorphic foliation of host rocks (Fig. 4.1A, B and C). Emplacement of the foliation-parallel quartz-sulphide veins is also controlled by lithological units (i.e., carboniferous schist/phyllite at Bai Dat, and the boundary of metagabbro and carboniferous schist/phyllite at Bai Go; see Figs. 3.2 and 3.3 in Chapter 3). Paragenetic textures are commonly recognised in the quartz-sulphide veins of drill core samples from the Bai Dat and Bai Go deposits and underground outcrops at Bai Dat. The textures were carefully observed to establish paragenesis of the veins and to identify the main gold-bearing stage. In this section, the paragenesis of quartz-sulphide veins of the main mineralisation stage(s) with pre- and post-mineralisation events are described in detail, including ore and gangue mineral assemblages of each stage.

4.2.1. Methods of study

The paragenetic relations of the gold-bearing mineralisation stages at Bai Dat and Bai Go were principally investigated on the basis of textural relationships (e.g., cross-cutting, overprinting). Textures in hand specimen samples and on outcrop underground at Bai Dat were carefully recorded and interpreted. Microscopic examination of some samples was also conducted including Scanning Electronic Microprobe (SEM) examination to help in identifying unknown ore and alteration minerals.

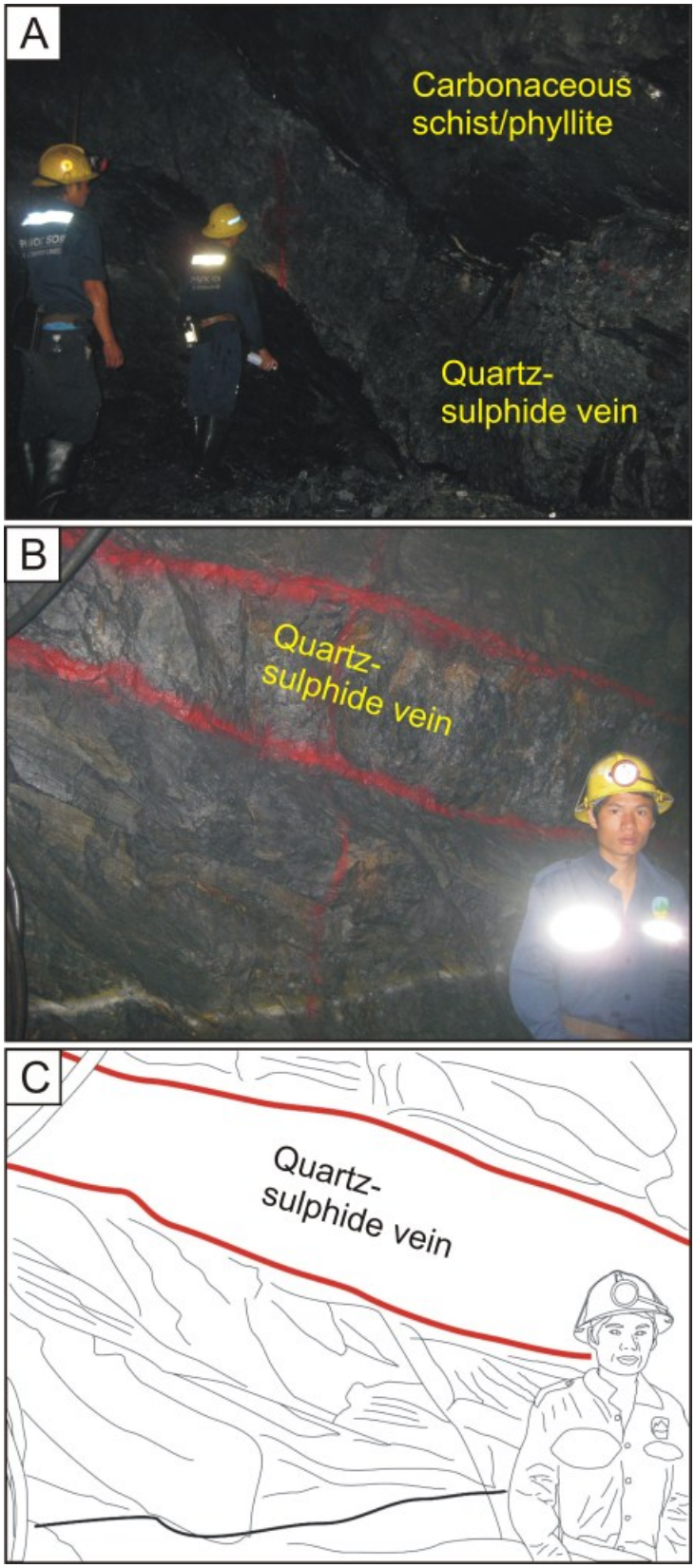

Fig. 4.1. Nature of foliation-parallel quartz-sulphide vein, underground, Bai Dat, Phuoc Son. **A.** Quartz-sulphide vein is one metre thick, hosted by carbonaceous schist/phyllite unit. **B** and **C.** Quartz-sulphide vein is hosted parallel to metamorphic foliation of the host rock unit.

4.2.2. Mineralisation and paragenesis of the Bai Dat and Bai Go deposits

At least two gold mineralisation stages are identified at the Bai Dat and Bai Go deposits. The two mineralisation stages are divided into early sphalerite-rich and late galena-rich stages: both of which commonly occur as quartz-sulphide veins and are characterised by more or less similar mineral assemblages. Textural relationships indicate that the regional metamorphic event predates the gold-bearing stages, whereas extensive faulting occurred during the post-mineralisation stage. These are summarised in Figure 4.2 and are described below in terms of mineral assemblages:

Early main mineralisation stage; Quartz + carbonate minerals + sulphide minerals + sericite + muscovite ± chlorite ± electrum, and

Late main mineralisation stage; Sulphide minerals + quartz + carbonate minerals ± micas ± sericite ± serpentinite ± electrum

4.2.2.1. Pre-mineralisation regional metamorphism stage

Textural relationships suggest that metamorphic foliation in the host rocks was developed prior to the gold mineralising stages at Bai Dat and Bai Go, as evidenced by (1) presence of metamorphosed clasts in the quartz-sulphide veins (Fig. 4.3A and B), (2) splays of the quartz-sulphide veins cross-cutting/overprinting metamorphic foliation in the host rocks (Fig. 4.3C), and (3) marble formation associated with the quartz-sulphide vein stage overprinting the schistose texture (Fig. 4.3D). The mineral assemblage of quartz, biotite, muscovite and sericite is widely present along schistose bands in the schists. Opaque minerals such as major pyrite and trace magnetite, ilmenite and pyrrhotite are also present. Serpentinite, talc, carbonate, chromite, pyrrhotite, chalcopyrite and pentlandite are commonly disseminated in the metagabbro unit (Fig. 4.2; see Chapter 3 for details).

4.2.2.2. Early main mineralisation stage

The early gold mineralisation stage at Bai Dat and Bai Go is characterised by quartz-sulphide veins which range from a few tens of centimetres to several metres in width and occur parallel to metamorphic foliation of the host rocks (mainly carbonaceous schist/phyllite). The veins are composed predominantly of quartz with trace sulphide minerals, but they are locally

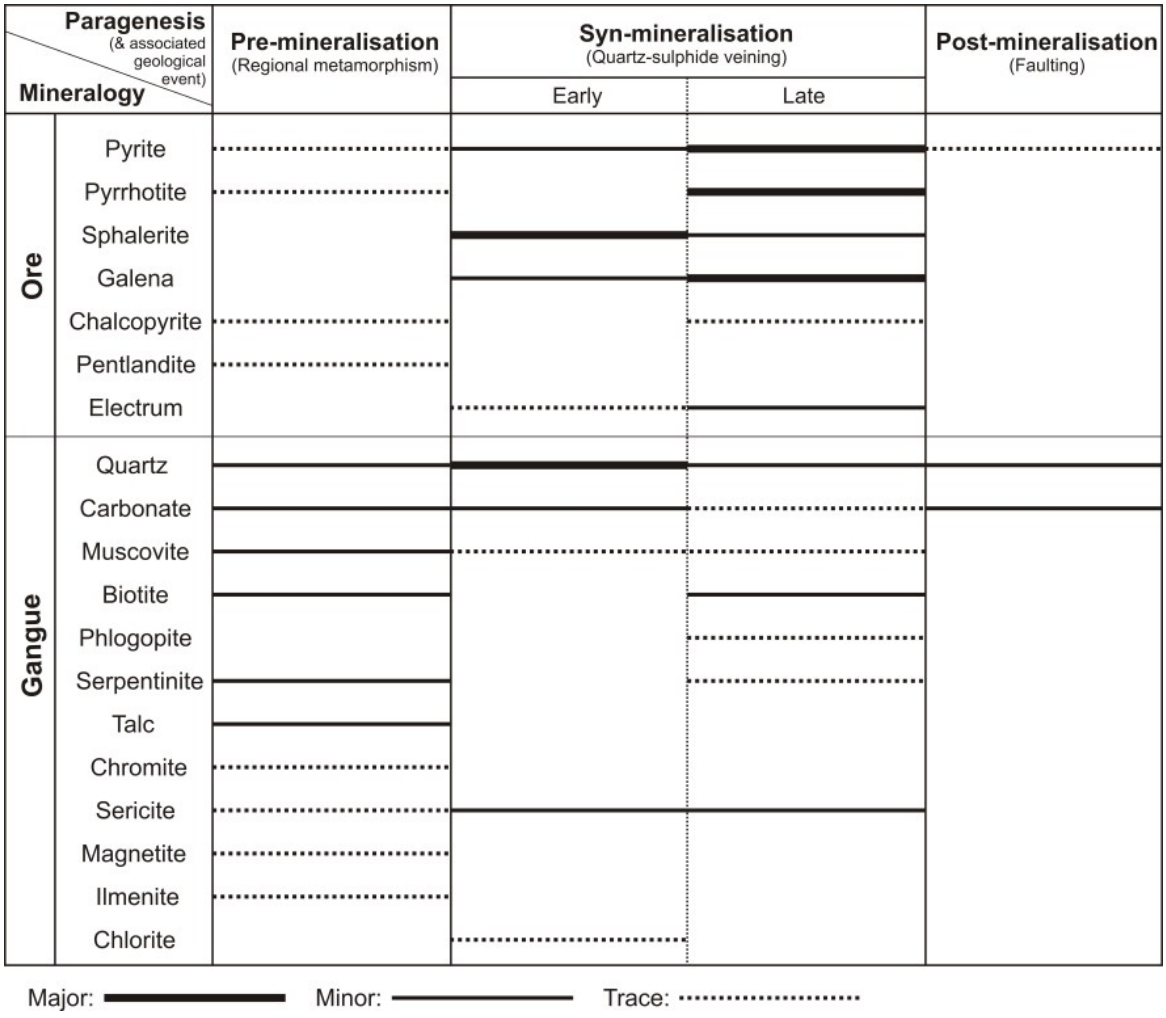

Fig. 4.2. Mineralisation stages and the paragenesis of the Bai Dat and Bai Go deposits in Phuoc Son, central Vietnam.

enriched in sphalerite and form massive sphalerite in the veins (Fig. 4.4A and B). The massive sphalerite (up to several tens of centimetres in thickness) is developed locally within a thicker part (>few metres) of the ore zone. Minor galena is commonly associated with the massive sphalerite (Fig. 4.4A and B). Under the microscope, the presence of trace pyrite is identified in the massive sphalerite sample. Gangue minerals such as carbonate minerals, muscovite, sericite and chlorite are commonly involved in the barren zone of the veins of this stage (Fig. 4.4C).

Textures recognised in the massive sphalerite samples show a paragenetic relationship between the pre-mineralisation regional metamorphism and the early main mineralisation

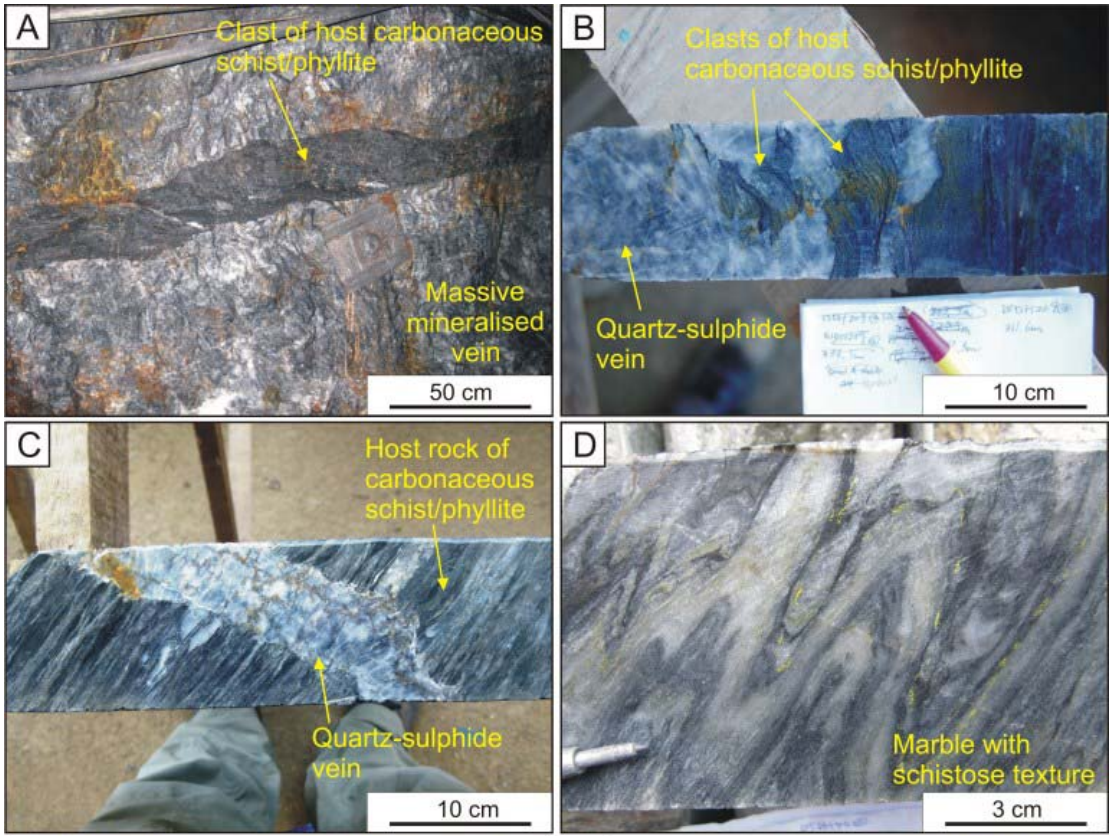

Fig. 4.3. Textural and paragenetic characteristics of the pre-mineralisation regional metamorphism at Phuoc Son. **A.** A large carbonaceous schist/phyllite clast involved in the massive quartz-sulphide vein at the Bai Dat Underground. **B.** Drill core sample showing presence of carbonaceous schist/phyllite clasts in the quartz-sulphide vein. Sample No. DSDH209@311.6m (Bai Go). **C.** Quartz-sulphide vein perpendicularly cross-cutting metamorphic foliation in the host carbonaceous schist/phyllite. Sample No. DSDH31@199.8m (Bai Dat). **D.** Marble developing and overprinting schistose texture of the host rock. Sample No. DSDH40@116.2m (Bai Go).

stage at Bai Dat and Bai Go. Presence of the host rock clasts with foliated textures was observed in the quartz-sulphide veins (Fig. 4.3A and B), suggesting that the quartz-sulphide veins were emplaced after the peak regional metamorphism. In contrast, some textures imply that formation of the vein emplacement occurred during the pre-mineralisation regional metamorphism, as evidenced by (1) the veins, which are hosted parallel to metamorphic foliation of the host rocks and (2) sheared/foliated textures that are recognised in massive sphalerite samples (Fig. 4.4D). These pieces of evidence may indicate that the regional metamorphism was still active during the formation of the early main mineralisation stage.

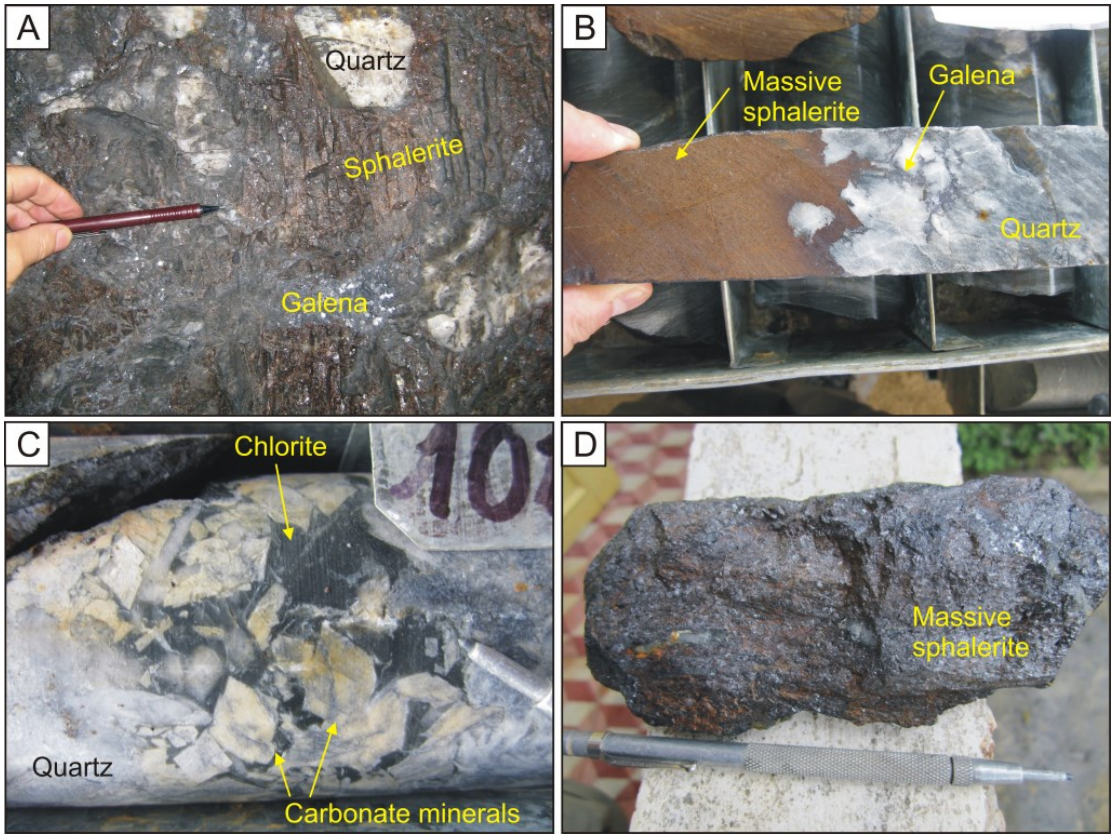

Fig. 4.4. Textural and paragenetic characteristics of quartz-sulphide vein of the early main mineralisation stage at the Bai Dat and Bai Go deposits, in the Phuoc Son deposit area. **A.** Massive sphalerite and galena in the quartz-sulphide vein at Bai Dat underground. **B.** Drill core sample consisting of massive sphalerite with minor galena in quartz vein. Sample No. DSDH111@78.2m (Bai Dat). **C.** Drill core sample of a barren vein composed of a quartz-carbonate minerals-chlorite assemblage. Sample No. DSDH249@101.4m (Bai Go). **D.** Foliated massive sphalerite sample from the Bai Dat underground. Note the sample is flattened probably due to metamorphic processes. Sample No. TMBD11-12 (Bai Dat).

4.2.2.3. Late main mineralisation stage

The mineralised quartz-sulphide veins of the late mineralisation stage consist of abundant sulphide minerals including pyrite, pyrrhotite, galena, sphalerite and chalcopyrite, and they generally occur as crack infills of the quartz-sulphide/barren quartz veins of the earlier stage (i.e., early main mineralisation stage; Fig. 4.5A and B). Pyrite and pyrrhotite are commonly enriched in veins of this stage, and galena is also locally enriched, forming a massive galena zone at the thicker part of the quartz-sulphide vein (Fig. 4.5C and D). Some gangue minerals including carbonate minerals, biotite, phlogopite, serpentinite, muscovite and sericite are intimately associated with sulphide minerals in the veins (Fig. 4.5E and F).

Paragenetic textures that differentiate between the early and late main mineralisation stages

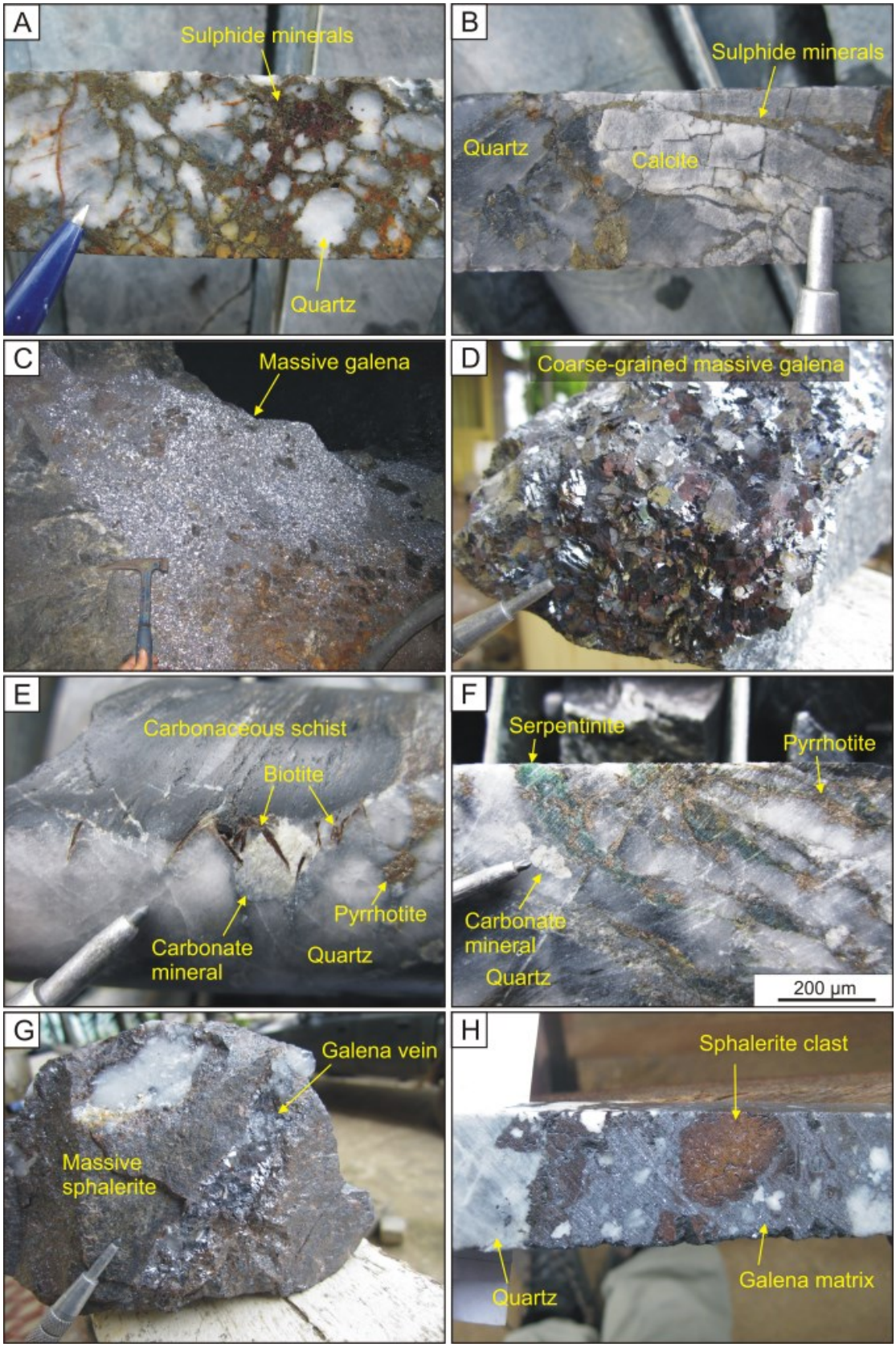
A
Sulphide minerals
Quartz
B
Sulphide minerals
Quartz
Calcite
C
Massive galena
D
Coarse-grained massive galena
E
Carbonaceous schist
Biotite
Pyrrhotite
Carbonate mineral
Quartz
F
Serpentinite
Pyrrhotite
Carbonate mineral
Quartz
200 µm
G
Galena vein
Massive sphalerite
H
Sphalerite clast
Quartz
Galena matrix

Fig. 4.5 (previous page). Textural and paragenetic characteristics of quartz-sulphide veins of the late main mineralisation stage at the Bai Dat and Bai Go deposits, Phuoc Son deposit. **A.** Drill core sample of quartz-sulphide vein. Note sulphide veinlets infill cracks of quartz. Sample No. DSDH09@80.9m. (Bai Dat). **B.** Quartz-sulphide vein showing sulphide veinlets occurring along a crack in calcite. Sample No. DSDH146@88.4m (Bai Go). **C.** Massive galena in quartz-sulphide vein underground at Bai Dat. **D.** Massive galena sample consisting of coarse-grained materials. Sample No. TMBD11-07 (Bai Dat). **E**. Presence of biotite and carbonate mineral in the quartz-sulphide vein. Sample No. DSDH267@387.1m (Bai Chuoi). **F**. Presence of serpentinite and carbonate mineral in quartz-sulphide vein. Sample No. DSDH267@424.1m (Bai Chuoi). **G.** Galena-rich vein cross-cutting massive sphalerite. Sample No. TMBD11-09 (Bai Dat). **H.** Sphalerite of early mineralisation stage is brecciated and involved in galena of late mineralisation stage. Sample No. DSDH135@59.4m (Bai Dat).

are observed in drill core samples from ore zones of Bai Dat and Bai Go. These textures include; (1) the galena-rich veins cross-cutting the foliated massive sphalerite (Fig. 4.5G), and (2) brecciated sphalerite clasts hosted in the galena-rich matrix (Fig. 4.5H). These lines of evidence suggest that the galena-rich mineralising event postdated the sphalerite-rich early mineralisation stage at Bai Dat and Bai Go. As high gold grade is typically associated with high levels of lead values in drill hole assay (Stevens and Fulton, 2008), the late stage is likely to be the main gold-bearing mineralisation stage at Bai Dat and Bai Go.

4.2.2.4. Post-mineralisation stage

The post-mineralisation stage at Bai Dat and Bai Go is dominantly characterised by faulting, and these faults can be clearly observed underground at Bai Dat. The faults perpendicularly cross-cut the metamorphic foliation of the host rock and mineralised quartz-sulphide veins (Fig. 4.6A). The faults are infilled with quartz, carbonate minerals and fault gauge (i.e., carbonaceous components) with traces of pyrite, and range from several centimetres to a few tens of centimetres in width (Fig. 4.6B and C). The faults generally trend N-S and dip vertically to sub-vertically (see structure section in Chapter 3). At the Bai Dat underground mine, the faults commonly displace the ore body (quartz-sulphide vein) up to several metres, hence structural feature of these post-mineralisation faults is important for mining activity to ensure the displaced ore bodies are followed up adequately.

4.2.3. Alteration

At the Bai Dat and Bai Go deposits, two types of alteration are recognised including pyritisation and silicification. These alteration phases, in particular pyritisation, are spatially associated with the mineralised quartz-sulphide veins, which may suggest that formation of the alteration is genetically important for the main mineralisation stages.

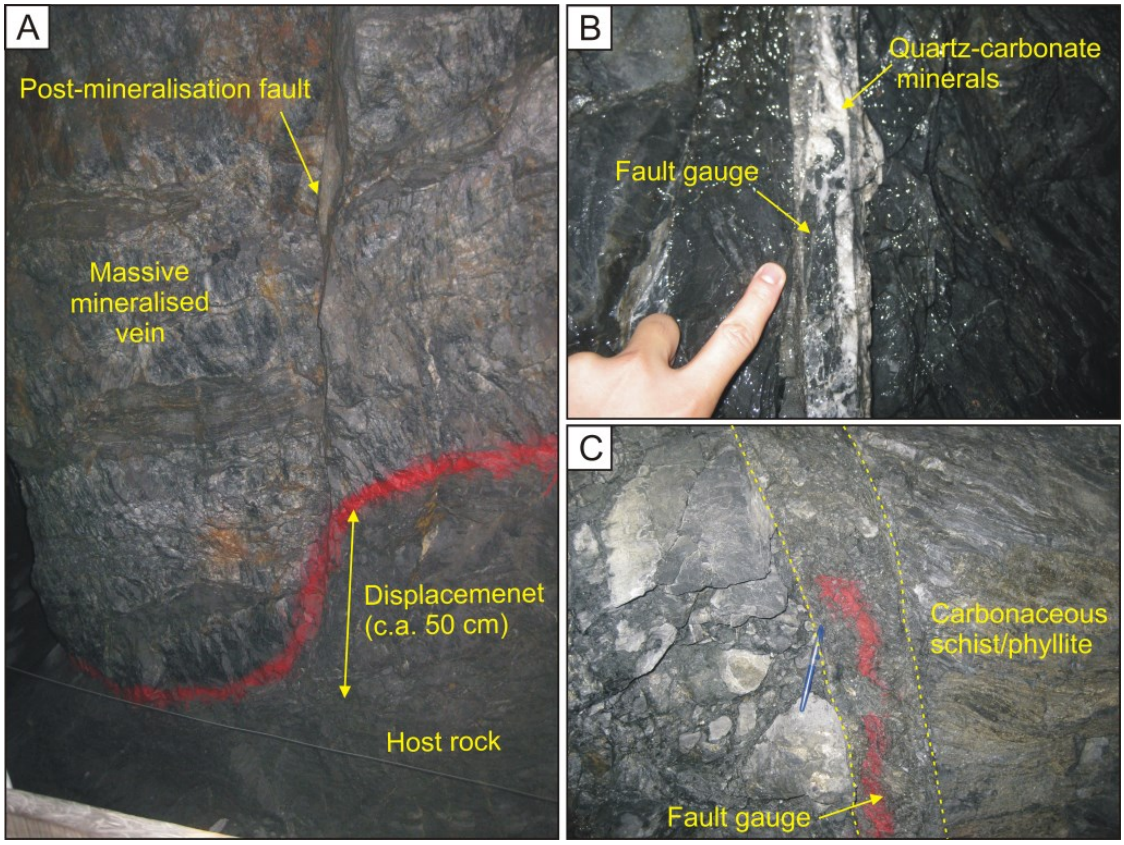

Fig. 4.6. Nature of the post-mineralisation faults observed at Bai Dat underground mine site, Phuoc Son. **A.** Post-mineralisation fault perpendicularly cross-cutting the massive quartz-sulphide vein and displacing the ore. **B.** Post-mineralisation fault infilled by quartz-carbonate minerals component. **C.** Post-mineralisation fault consisting of fault gauges cross-cutting the foliation of the host carbonaceous schist/phyllite.

Pyritisation

The pyrite alteration is the most distinctive alteration in the host rocks at Bai Dat and Bai Go, forming as haloes around the quartz-sulphide veins; it is developed at selvages of the gold-bearing quartz-sulphide veins (<several metres in general; Fig. 4.7A and B). The alteration is commonly characterised by patchy, visible euherdral pyrite crystals in carbonaceous schist/phyllite (Fig. 4.8A). Pyrrhotite is also abundantly but locally involved (Fig. 4.8B). In particular, the pyritisation is distinctly formed at the transitional zone of the host carbonaceous schist/phyllite and veins (Fig. 4.8C), and is also commonly present in the strongly deformed parts of the schist/phyllite and serpentinised mafic units (Figs. 4.8D and E).

Silicification

The silica alteration is locally developed in the schist/phyllite unit at the selvage of the quartz-sulphide veins at the Bai Dat and Bai Go deposits, but the spatial development is much less

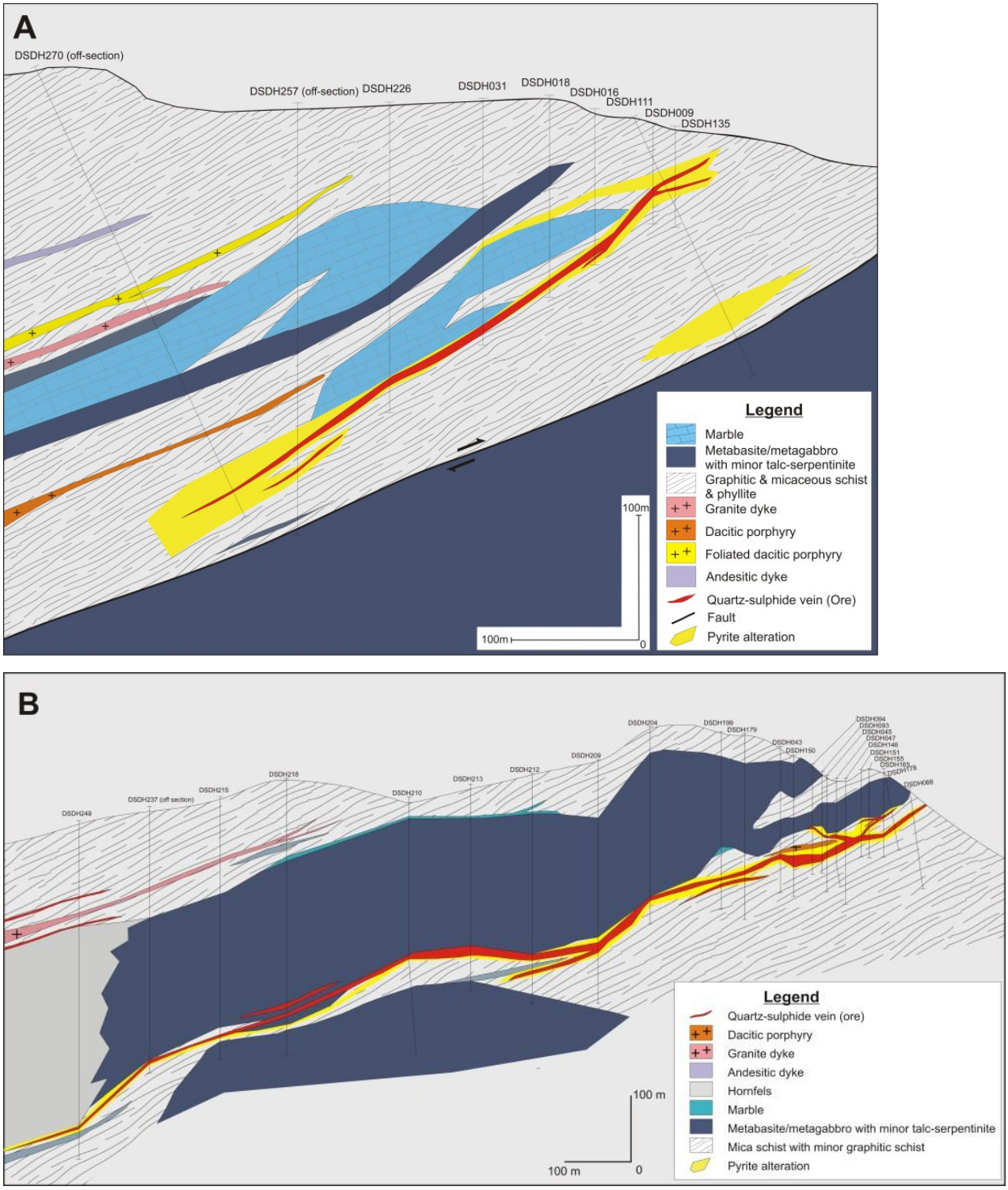

Fig. 4.7. The main NW-SE cross-section of the Bai Dat (**A**) and Bai Go (**B**) deposits, showing spatial association between the quartz-sulphide vein and pyrite alteration.

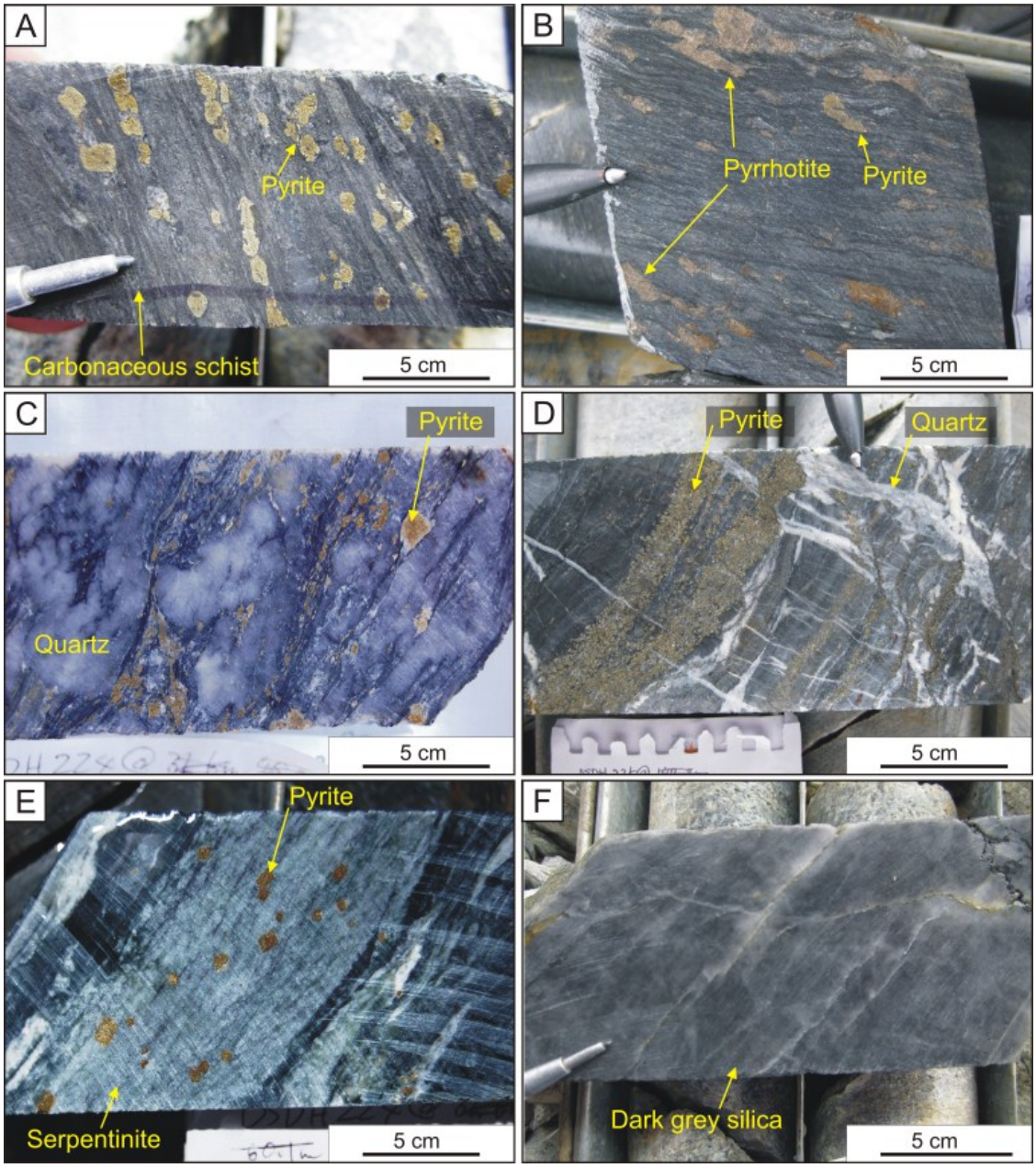

Fig. 4.8. Alteration characteristics of the Bai Dat and Bai Go deposits, the Phuoc Son deposit. **A.** Pyritisation in the carbonaceous schist, comprising patchy coarse-grained euhedral pyrites. Sample No. DSDH155@101.2m (Bai Go). **B.** Pyrite alteration consisting of a pyrrhotite-rich assemblage in the carbonaceous schist/phylite unit. Sample No. DSDH74@164.2m (Bai Go). **C.** Well-developed pyritisation at transitional zone between the carbonaceous schist and quartz-sulphide vein. Sample No. DSDH224@439.5m (Bai Go). **D.** Intense pyritisation at strongly deformed part of the carbonaceous schist. Sample No. DSDH235@124.5m (Bai Go). **E**. Pyritisation in the serpentinised mafic unit. Sample No. DSDH224@249.2m (Bai Go). **F**. Silicification consisting of dark-grey silica replacement of the carbonaceous schist unit. Sample No. DSDH155@80.2m (Bai Go).

than pyritisation (<few tens centimetres). This alteration phase is normally difficult to identify due to an uncertain boundary between the silicified host rock and quartz-rich part of the quartz-sulphide vein, and thus it is only recognised in the altered rocks with relicts of schistose textures. The rock that undergone intense silicification mainly comprises a dark-grey fine-grained silica assemblage and shows a quartz vein-like phase (Fig. 4.8F).

4.3. ORE MINERALS

4.3.1. Introduction

This section describes in detail the gold-bearing minerals and the associated sulphides of the Bai Dat and Bai Go deposits, which are characterised by abundant pyrite and pyrrhotite assemblage. They are commonly present in quartz-sulphide veins of the early and late main mineralisation stages.

4.3.2. Pyrite

Pyrite is the most abundant sulphide mineral at Bai Dat and Bai Go. The occurrence is principally divided into two main phases including pyrite in quartz-sulphide veins (Fig. 4.9A) and in the host rock (Fig. 4.9B). The vein-located pyrite commonly occurs along cracks of quartz veins and is associated with other sulphide minerals such as pyrrhotite, sphalerite, galena and chalcopyrite. The pyrite metablasts in the host rock selectively and predominantly occur in the carbonaceous schist/phyllite unit. They are predominated along metamorphic foliation of the host rock, associated with pyrrhotite and traces of chalcopyrite.

Several different textures are recognised in pyrite of the Bai Dat and Bai Go deposits under microscope. The vein-located pyrite is characterised by a homogeneous texture with abundant galena inclusions (Fig. 4.9C). The pyrite is intimately associated with pyrrhotite and galena. In contrast, at least a few distinct textures are identified in pyrite of the host carbonaceous schist/phyllite unit. The main pyrite type in the host rocks includes a homogeneous texture (Fig. 4.9D), and sometimes aggregated, fine-grained pyrite inclusions are present in the homogeneous pyrite (Fig. 4.9E). Mixed homogeneous and spongy textures are also identified in the pyrite of carbonaceous schist/phyllite unit, which is uniformly composed of a homogeneous core and rim with spongy interstitials (Fig. 4.9F). The grain size of the pyrites ranges from a few tens of μm to a few cm (few hundreds of μm in general); large crystals (>1 cm) are visible in some hand specimen samples (see Fig. 4.8A, B, C, D and E).

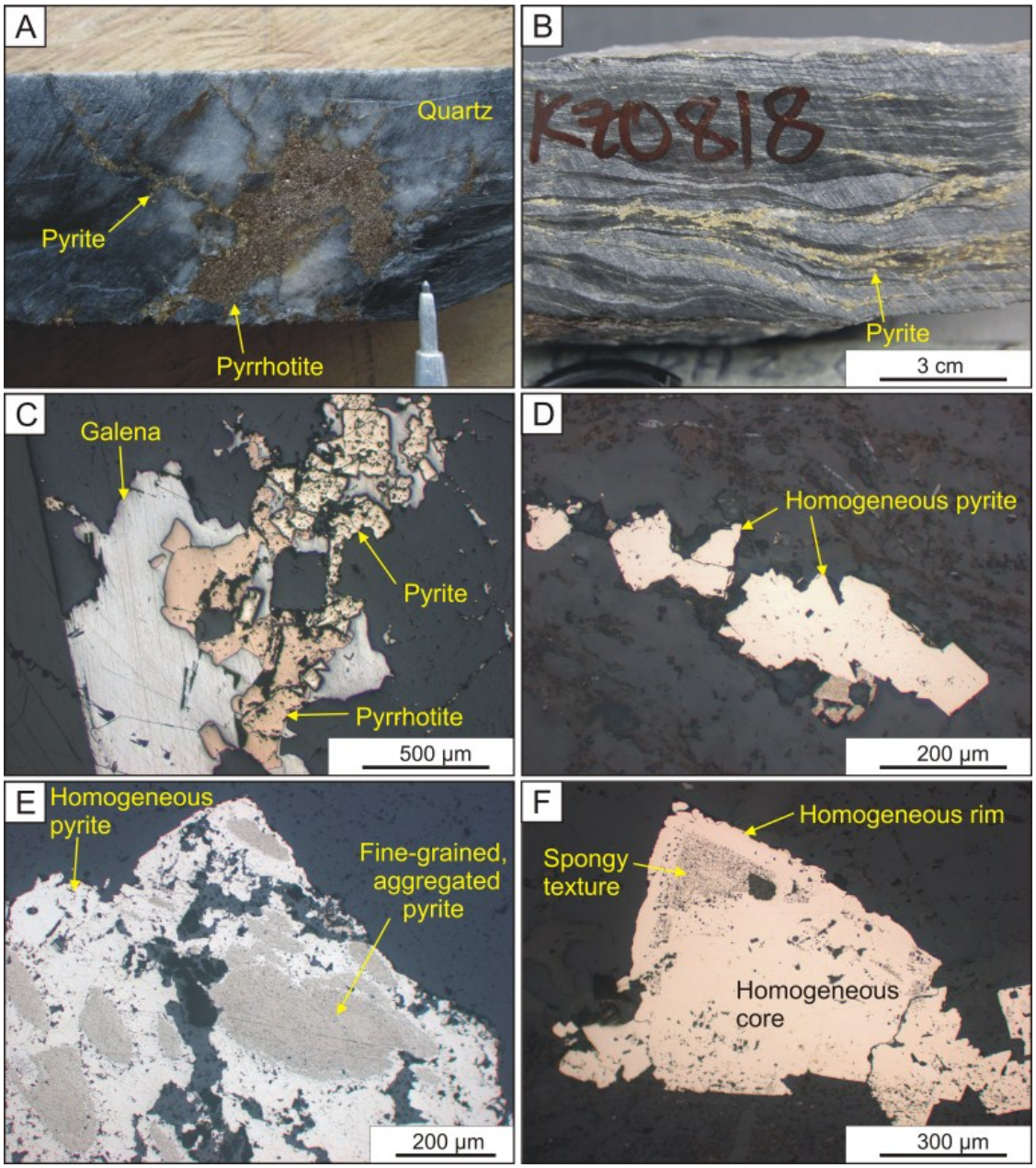

Fig. 4.9. Occurrence and textural characteristics of pyrite at the Bai Dat and Bai Go deposits, Phuoc Son. **A.** Pyrite in pyrrhotite-rich quartz-sulphide vein. Sample No. DSDH257@463.5m (Bai Dat). **B.** Pyrite presenting along schistose texture of carbonaceous schist. Sample No. KZVN0818 (Bai Dat). **C.** Vein-located pyrite with homogeneous texture associated with pyrrhotite and galena. Note the pyrite has abundant galena inclusions. Sample No. DSDH209@325.0m (Bai Go). **D.** Homogeneous pyrite in the host carbonaceous schist. Sample No. KZVN0818 (Bai Dat). **E.** Pyrite in host carbonaceous schist showing an aggregated, fine-grained core with homogeneous rim. Sample No. KZVN0818 (Bai Dat). **F.** Pyrite in host carbonaceous schist showing combination of spongy and homogeneous textures. Sample No. DSDH224@298.9m (Bai Go).

4.3.3. Pyrrhotite

Pyrrhotite is a common sulphide mineral at Bai Dat and Bai Go, although its volume is subordinate to pyrite. It commonly occurs with pyrite in the mineralised veins (Fig. 4.9A and 4.10A), and is locally associated with other sulphide minerals, such as sphalerite, galena and chalcopyrite. Trace pyrrhotite is also observed in the host carbonaceous schist/phyllite (Fig. 4.8B), together with pyrite and chalcopyrite (Fig. 4.10B). Grain size of the pyrrhotite typically ranges from a few tens of μm to a few cm (commonly a few hundreds of μm).

4.3.4. Sphalerite

Two types of sphalerite are identified in hand specimen samples from the Bai Dat and Bai Go deposits in terms of colour, texture and mineral associations. The massive sphalerite of the early main mineralisation stage is orange and coarse-grained (Fig. 4.10C), and commonly associated with minor galena and trace pyrite. In contrast, sphalerite in quartz-sulphide veins of the late main mineralisation stage is dark and fine-grained (Fig. 4.10D). Sulphide minerals such as pyrite, pyrrhotite, galena and chalcopyrite are commonly associated with the dark sphalerite. As evidenced in paraganetic textures of some hand specimen samples, the orange sphalerite predates the dark sphalerite (Fig. 4.10E and F).

4.3.5. Galena

Galena is one of the abundant sulphides in the quartz-sulphide veins of the late main mineralisation stage at Bai Dat and Bai Go. It is normally coarse-grained (mm to few cm in size) and locally forms as massive galena in the thick part of the ore zones (Fig. 4.5C and D). The galena is associated with other sulphide minerals involving pyrite, pyrrhotite, sphalerite and chalcopyrite (Fig. 4.10G and H), and intimately occurs with electrum in the mineralised samples. Trace galena is also recognised in the early main mineralisation stage; it occurs together with massive sphalerite.

4.3.6. Chalcopyrite

Chalcopyrite rarely occurs at the Bai Dat and Bai Go deposits. It is not visible in hand specimen samples, and is only found using a microscope. The occurrence is identified in the both quartz-sulphide veins and wall rocks. The chalcopyrite grains are normally less than a few hundreds μm in size (Fig. 4.10H). The vein-located chalcopyrite is commonly associated with pyrrhotite, sphalerite and galena (Fig. 4.10H and G), whereas in wall rocks it occurs with pyrite and pyrrhotite (Fig. 4.10B).

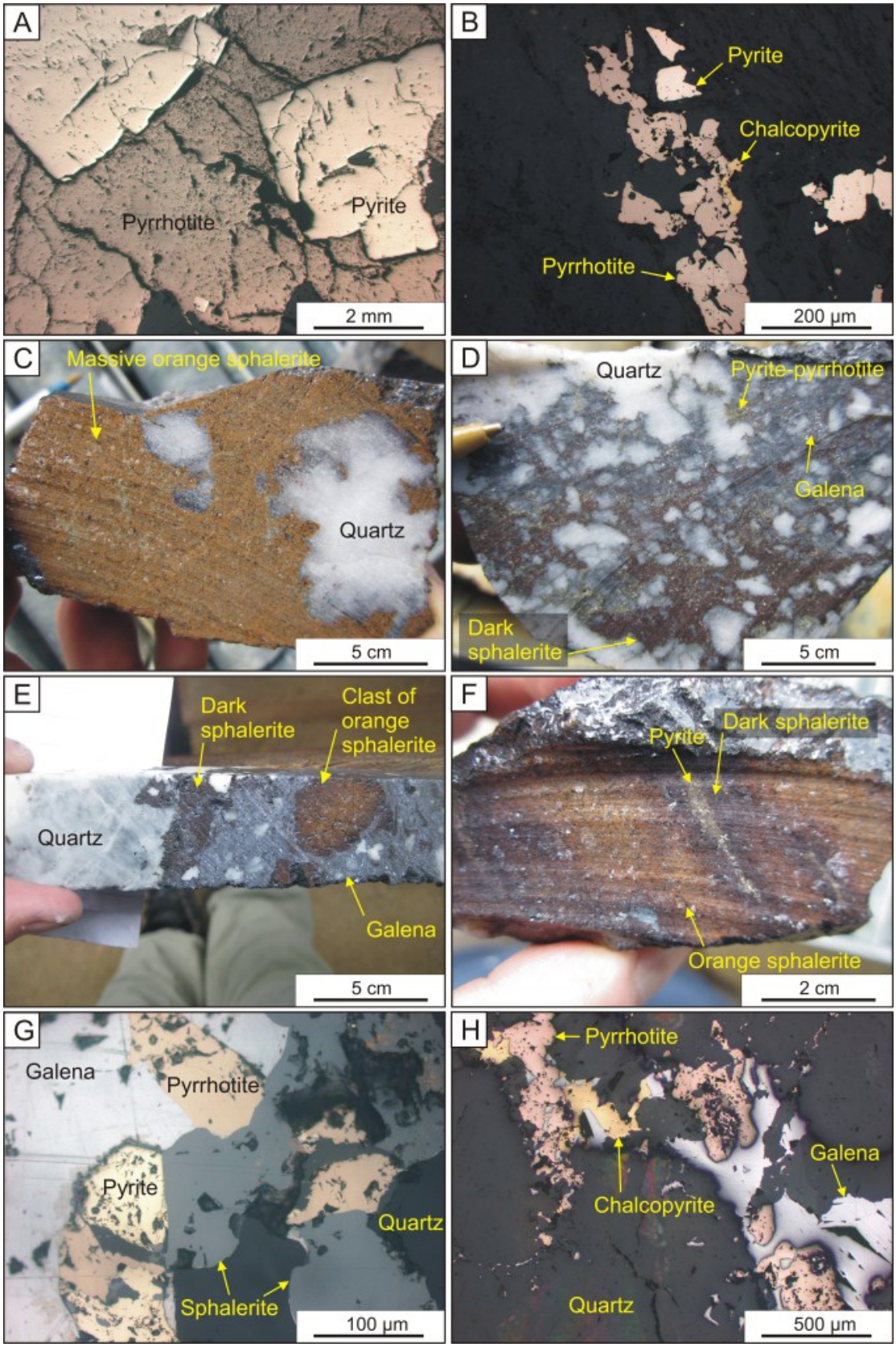
A
Pyrrhotite
Pyrite
2 mm
B
Pyrite
Chalcopyrite
Pyrrhotite
200 µm
C
Massive orange sphalerite
Quartz
5 cm
D
Quartz
Pyrite-pyrrhotite
Galena
Dark sphalerite
5 cm
E
Dark sphalerite
Clast of orange sphalerite
Quartz
Galena
5 cm
F
Pyrite
Dark sphalerite
Orange sphalerite
2 cm
G
Galena
Pyrrhotite
Pyrite
Quartz
Sphalerite
100 µm
H
Pyrrhotite
Galena
Chalcopyrite
Quartz
500 µm

Fig. 4.10 (previous page). Occurrence, texture and mineral association of sulphides (except pyrite) at the Bai Dat and Bai Go deposits, Phuoc Son. **A.** Pyrrhotite-pyrite associated with mineralised vein. Sample No. DSDH257@463.5m (Bai Dat). **B.** Pyrrhotite associated with pyrite and chalcopyrite in the wall rock. Sample No. DSDH224@453.2m (Bai Go). **C.** Massive orange sphalerite with quartz inclusions. Sample No. TMBD11-09 (Bai Dat). **D.** Sulphides of dark sphalerite-galena-pyrite-pyrrhotite assemblage in mineralised quartz vein. Sample No. TMBD11-15 (Bai Dat). **E.** Brecciated orange sphalerite clasts in the mixed galena-dark sphalerite matrix. Sample No. DSDH135@59.4m (Bai Dat). **F.** Dark sphalerite associated with pyrite along sheared parts of massive orange sphalerite sample. Sample No. TMBD11-12 (Bai Dat). **G.** Photomicrograph showing coexistence of sphalerite with pyrite, pyrrhotite and galena. Sample No. TMBD11-15 (Bai Dat). **H.** Photomicrograph showing sulphide assemblages in mineralised vein, including pyrrhotite, galena and chalcopyrite. Sample No. DSDH40@145.2m (Bai Go).

4.3.7. Electrum

Electrum is recognised as the main gold-bearing ore mineral at the Bai Dat and Bai Go deposits, and its major occurrence is confined to quartz-sulphide veins. A trace of electrum is also identified in the pyritised carbonaceous schist/phyllite unit, which occurs at the selvage of the mineralised quartz-sulphide veins and commonly contains sub-economic gold grades (<1 g/t Au). Electrum has a wide range of grain size from less than a few tens of μm to more than a few mm. Large electrum crystals (>1 mm) are commonly identified in quartz-sulphide vein samples (Fig. 4.11A), and they are visible in some hand specimen samples. Under microscope, the vein-located electrum occurs generally as free and/or inclusions in sulphides of pyrrhotite, pyrite, galena and sphalerite (Fig. 4.11B, C and D). The electrum grains in the pyritised carbonaceous schist/phyllite samples are small (<10 μm). They occur normally as free grains (Fig. 4.11E), and rarely occur along cracks of pyrite grains, together with pyrrhotite (Fig. 4.11F).

4.4. AGE OF MINERALISATION

4.4.1. Introduction

To constrain the timing of gold mineralisation at the Phuoc Son deposit area, minerals associated with the gold-mineralising event (i.e., vein-hosted minerals) were dated using radiogenic isotope methods. In this study, two dating methods were applied including; (1) Re-Os dating of molybdenite from the sulphide vein at the Round Hill deposit, and (2) Ar-Ar dating of biotite in the quartz-sulphide veins at the Bai Dat and Bai Chuoi deposits. In addition, previous Ar-Ar ages of vein-located fuchsite and sericite from the Bai Gio deposit, near Bai Dat and Bai Go (Borisenko et al., 2006) were also incorporated in this study to better constrain the timing of the gold mineralisation at Phuoc Son.

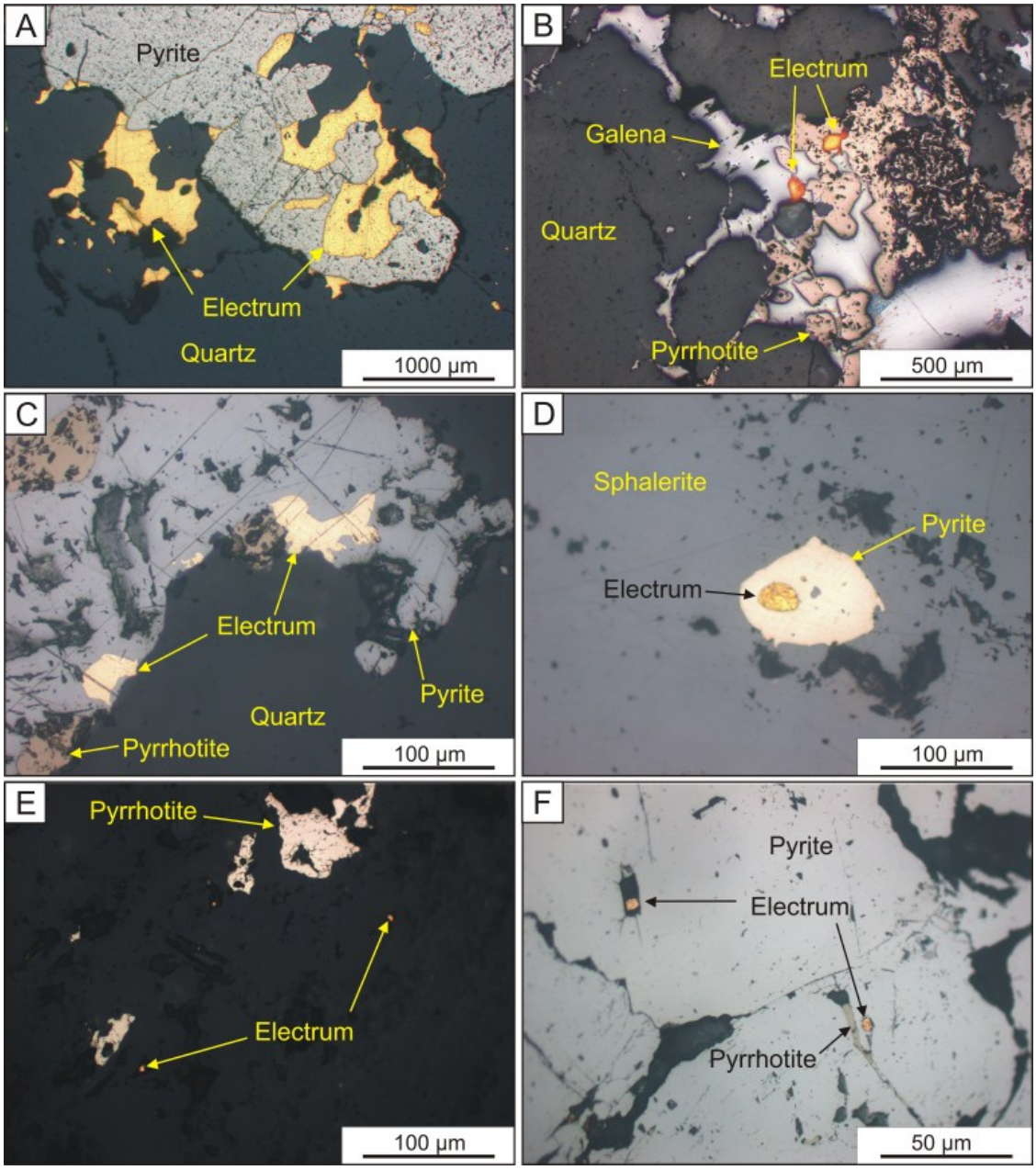

Fig. 4.11. Occurrence, texture and mineral association of electrum grains at the Bai Dat and Bai Go deposits, Phuoc Son. **A.** Large electrum grains (>1000 µm) associated with pyrite in vein-located samples. Sample No. KZVN09S (Bai Dat). **B.** Electrum grains associated with galena and pyrrhotite. Sample No. DSDH40@145.4m (Bai Go). **C.** Electrum grains associated with pyrite and pyrrhotite. Sample No. TMBD11-15 (Bai Dat). **D.** Electrum hosted in pyrite inclusion of sphalerite. Sample No. TMBD11-09 (Bai Dat). **E.** Disseminated electrum grains in carbonaceous schist/phyllite. Sample No. KZ0818 (Bai Dat). **F.** Electrum grains associated with pyrrhotite in cracks of pyrite. Sample No. KZ0818 (Bai Dat).

4.4.2. Sample preparation and methods

Molybdenite for Re-Os dating

During preliminary petrographic study of ore minerals, molybdenite was found in a sulphide-rich vein hosted in granite at the Round Hill Au-W-Cu-Mo deposit, approximately 5 km northwest of Bai Go (Fig. 4.12A and B). A polished mount was made from the sample and the presence of molybdenite was tested and confirmed using a scanning electron microscope (SEM) and backscattered secondary electron (BSE) imaging (Fig. 4.12C and D).

The molybdenite-bearing sample from Round Hill was submitted to Dr. Holly Stein, at the AIRIE facility at the Department of Earth Resources at Colorado State University (CSU), for determination of Re-Os age. The AIRIE molybdenite laboratory at CSU determined the total Re (^{187}Re and ^{185}Re) and ^{187}Os concentrations of the sample from the Au-W-Cu-Mo Round Hill deposit (RHDH03@89.1m). A Carius-tube digestion method was used for this study, whereby samples containing between 10 to 31 mg molybdenite were dissolved and equilibrated with double ^{190}Os spikes in HNO_3-HCl (inverse aqua regia) by sealing in a thick-walled glass ampoule and heating for 12 hours at 230°C. The Os was recovered by direct distillation from the Carius tube into HBr, then micro-distillation was used to purify. Anion exchange was used to recover Re.

The extracted Re and Os was loaded onto Pt filaments and the isotopic compositions were determined using ID-NTIM mass spectrometry at CSU. Two in-house molybdenite standards, calibrated at AIRIE, were run routinely as an internal check (Stein et al., 1997; Markey et al., 1998). The assumed initial $^{187}Os/^{188}Os = 0.2 + 0.1$. The age was calculated by applying the equation $^{187}Os = {}^{187}Re\ (e\lambda t - 1)$, where λ is the decay constant for ^{187}Re and t is the calculated age. The ^{187}Re decay constant used is 1.666 10-11 yr-1 with an uncertainty of 0.31% (Smoliar et al., 1996). All errors were reported two-sigma and absolute for the last decimal place indicated. The uncertainties that may be involved in the age calculations include those associated with: (1) magnification with spiking, (2) ^{185}Re and ^{190}Os spike calibrations, 0.05% and 0.15%, respectively, (3) mass spectrometric measurement of isotopic ratios, and (4) the ^{187}Re decay constant (0.31%). The AIRIE molybdenite laboratory blanks used for this study were (a) 24.2 + 0.2 pg for Re, (b) 2.00 + 0.02 pg for Os and (c) $^{187}Os/^{188}Os = 0.231 + 0.001$ (H. Stein pers. comm., 2011).

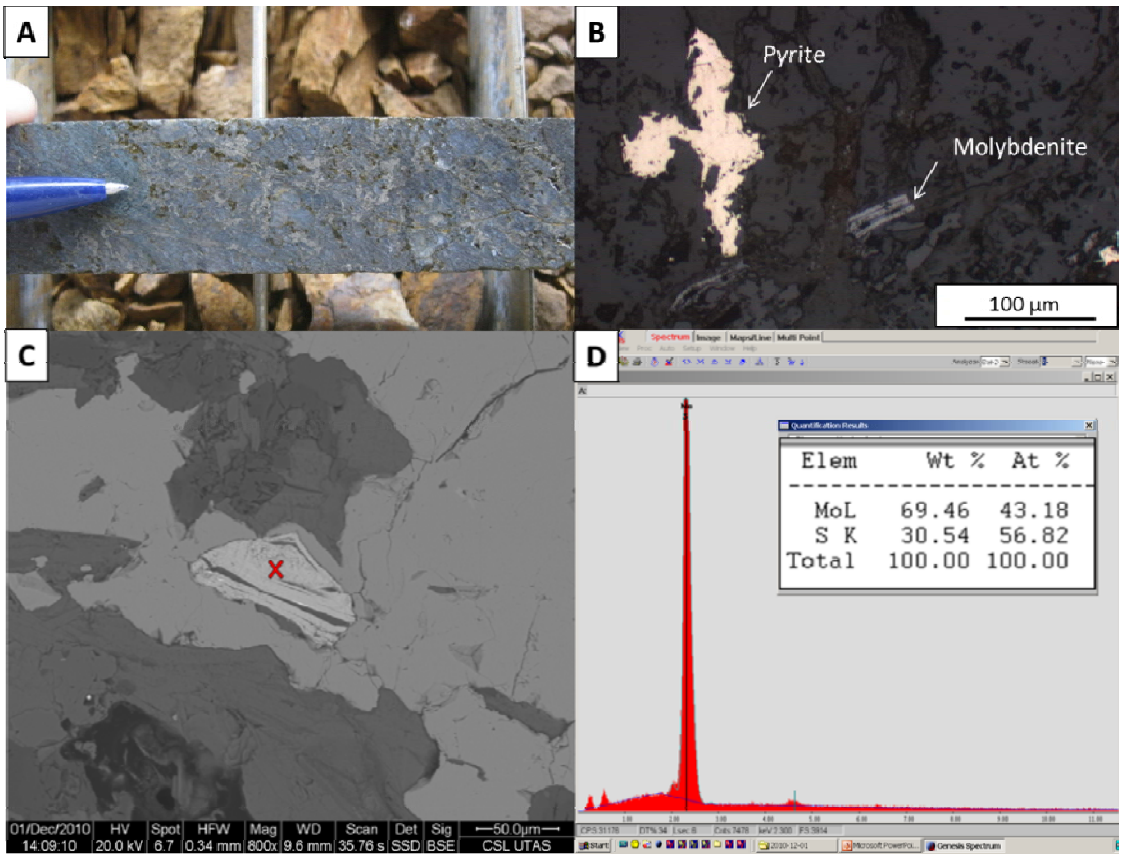

Fig. 4.12. Molybdenite-bearing sample from the Round Hill deposit analysed for Re-Os molybdenite geochronology. Sample No. RHDH03@89.1m. **A.** Photograph showing a sulphide vein drill core sample from the Round Hill deposit. **B.** Photomicrograph showing occurrence of molybdenite associated with pyrite. **C.** Scanning electron microscope (SEM) backscattered secondary electron (BSE) image of molybdenite. **D.** Graph showing the SEM energy dispersive spectral profile and measured chemical composition of the molybdenite in Fig. C.

Biotite for Ar-Ar dating

Biotite is closely associated with sulphide minerals in quartz-sulphide veins at Phuoc Son (Fig. 4.13A and B). Thus, visible biotite crystals hosted in the quartz-sulphide veins were sampled from drill cores of the Bai Dat and Bai Chuoi deposits (Fig. 4.13C and D), and polished mounts were prepared from the samples. The samples were submitted to Dr. David Phillips and the analysis was conducted at the University of Melbourne. The detailed methods of the Ar-Ar dating are described in Appendix VII-I.

4.4.3. Age results

The Re-Os molybdenite age from the Round Hill deposit and Ar-Ar ages of vein-hosted biotite from the Bai Dat and Bai Chuoi deposits, together with the reported Ar-Ar fuchsite

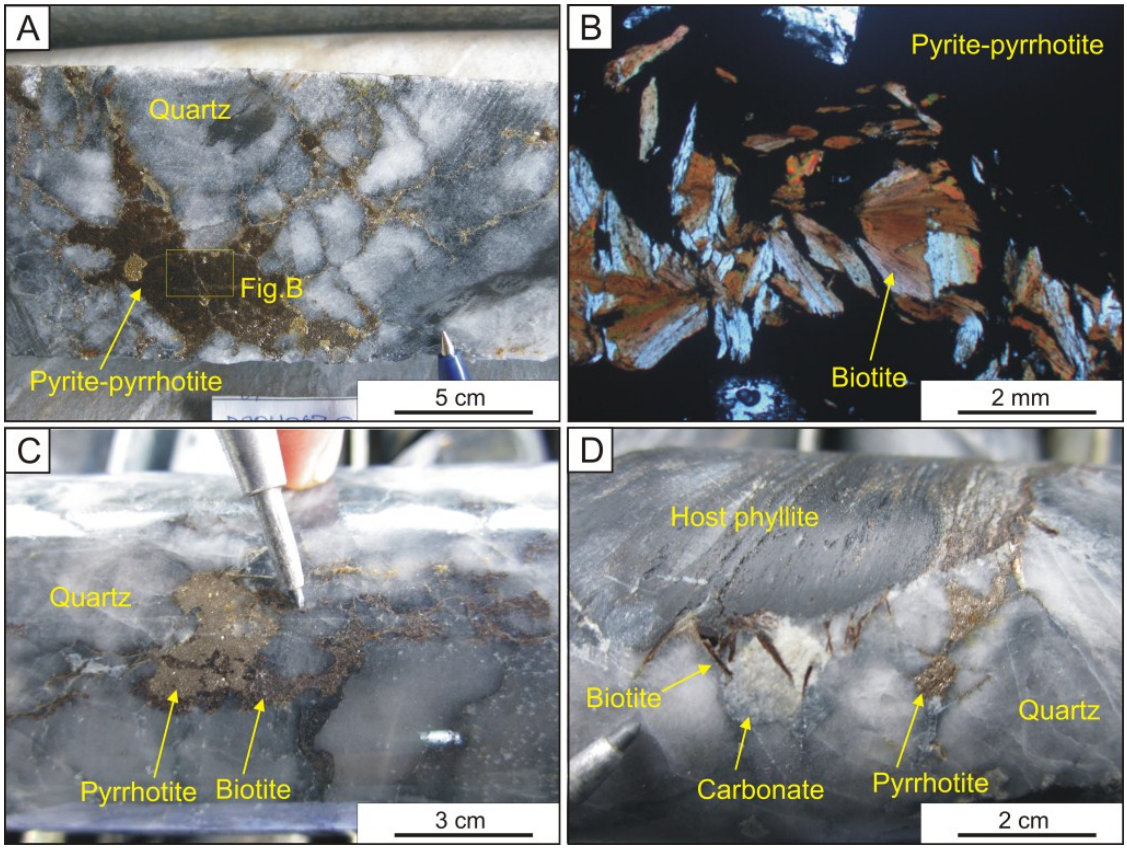

Fig. 4.13. Occurrence of vein-located biotite at the Bai Dat, Bai Go and Bai Chuoi deposits in the Phuoc Son deposit area, central Vietnam. **A** and **B.** A quartz-sulphide vein drill core sample showing interlocking biotites in the sulphide minerals. Sample No. DSDH257@463.5m (Bai Dat). **C**. Flaky biotite closely associated with pyrrhotite in the quartz-sulphide vein sample. Sample No. DSDH270@187.6m (Bai Dat). **D**. Biotite associated with carbonate in the quartz-sulphide vein sample. Sample No. DSDH267@387.1m (Bai Chuoi).

and sericite ages of the Bai Gio deposit by Borisenko et al. (2006) are summarised in Table 4.1. The Re-Os age of molybdenite yielded 526 ± 6 Ma (Early Cambrian; see Appendix VI for details). Late Triassic ages were obtained from the Ar-Ar ages of the biotite, including 211.6 ± 0.1 Ma (Late Triassic) from Bai Dat (Fig. 4.14A) and 203.9 ± 0.1 Ma (Late Triassic) from Bai Chuoi (Fig. 4.14B) (see Appendix VII-II for the detailed results). As discordant age spectra were produced in both samples (Fig. 4.14A and B), the ages were interpreted based on total gas ages. In contrast, Borisenko et al. (2006) performed Ar-Ar dating of the vein-hosted fuchsite and sericite samples from the Bai Gio deposit, and interpreted ages from the oldest plateau steps, yielded 248.8 ± 3.1 Ma (Fig. 4.14C; Early Triassic) and 236.4 ± 2.5 Ma (Fig. 4.14D; Middle-Late Triassic).

Table 4.1. Summary of geochronological results of the vein-located minerals from the Phuoc Son deposit area, central Vietnam.

Deposit	Sample No.	Technique (& mineral)	Age (Ma)	Remarks
Round Hill	RHDH03@89.1m	Re-Os (molybdenite)	**525±6**	Early Cambrian; in this study
Bai Dat	DSDH270@187.6m	Ar-Ar (biotite)	**211.6±0.1** (total age)	Late Triassic; in this study
Bai Chuoi	DSDH267@387.1m	Ar-Ar (biotite)	**203.9±0.1** (total age)	Late Triassic; in this study
Bai Gio	DL1620/3	Ar-Ar (fuchsite)	**248.8±3.1** (plateau age)	Early Triassic; from Borisenko et al. (2006)
Bai Gio	DL2538	Ar-Ar (sericite)	**236.4±2.5** (plateau age)	Middle-Late Triassic; from Borisenko et al. (2006)

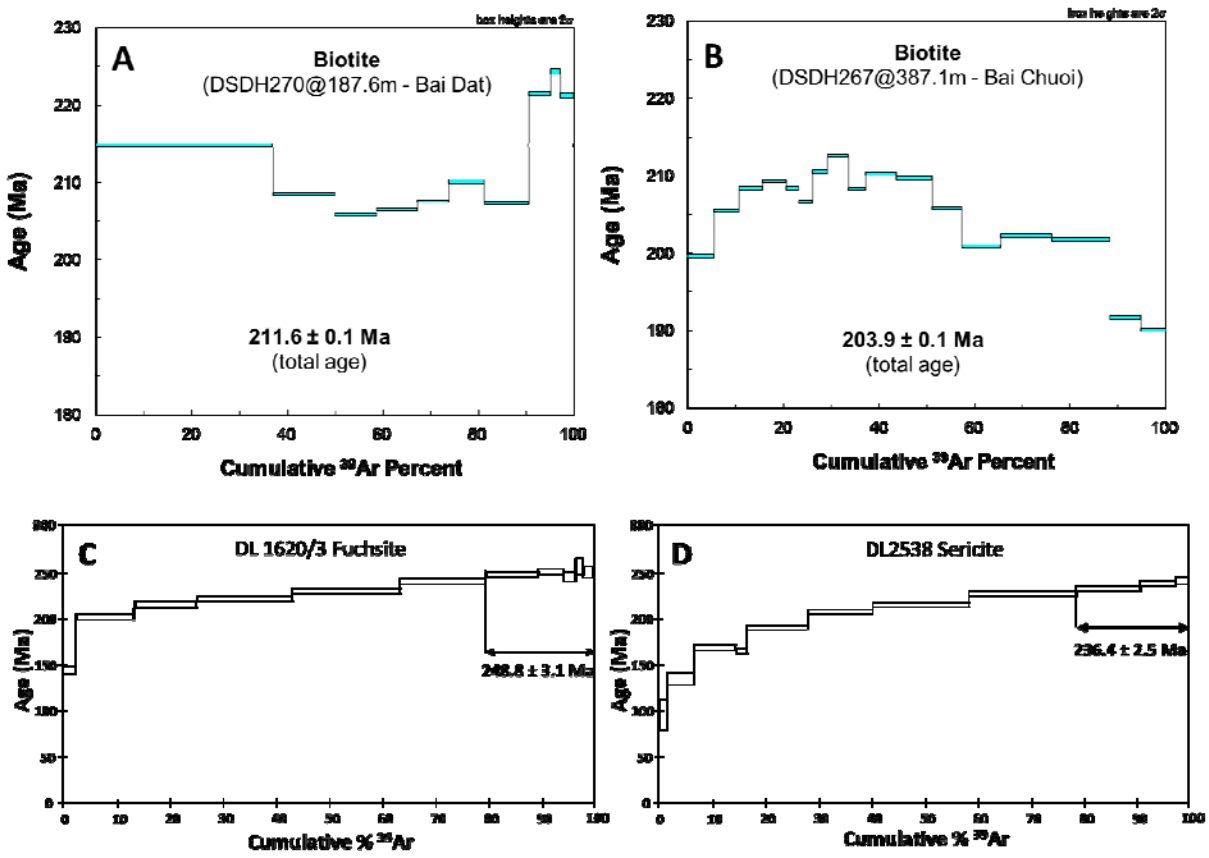

Fig. 4.14. Ar-Ar ages from the Phuoc deposit area, central Vietnam. **A**. Total Ar-Ar age of vein-hosted biotite from the Bai Dat deposit. **B**. Total Ar-Ar age of vein-hosted biotite from the Bai Chuoi deposit. **C**. Ar-Ar age of the interpreted step heating spectra for vein-located fuchsite from the Bai Gio deposit. **D**. Ar-Ar age of the interpreted step heating spectra for vein-located sericite from the Bai Gio deposit. Note Fig. C and D are from Borisenko et al. (2006).

4.5. DISCUSSION

Based on the data presented in this Chapter, relationships of the gold mineralising event at Bai Dat and Bai Go with the regional metamorphism are discussed. In addition, the age data are combined and discussed herein to constrain the timing of the gold mineralisation at the Phuoc Son area.

4.5.1. Indosinian orogeny

The gold-bearing quartz-sulphide veins at Bai Dat and Bai Go, including both the early sphalerite-rich and late galena-rich stages, are hosted parallel to the metamorphic foliation in the host rocks. This suggests that emplacement of the veins was temporally associated with the regional metamorphic event which formed the host metamorphic units at Phuoc Son. However, the paragenetic textures recorded in the quartz-sulphide veins (e.g., metamorphosed clasts involved in the veins and veins perpendicularly cross-cutting the metamorphic foliation) show that they formed later than the peak of the regional metamorphic event. Thus, these pieces of textural evidence may indicate that the gold-bearing veins at Bai Dat and Bai Go were emplaced during the waning/cooling stage of the regional metamorphism.

It is widely accepted that central Vietnam, including the Phuoc Son area, has undergone high-grade regional metamorphism during the Late Permian-Triassic Indosinian Orogeny as a consequence of the collision between the Indochina and South China Terranes (e.g., Carter et al., 2001; Osanai et al., 2001; Lepvrier et al., 2004; see Chapter 2 for details). Therefore, the regional geological setting of central Vietnam may suggest that the gold mineralising event at Bai Dat and Bai Go is genetically associated with the Indosinian Orogeny.

4.5.2. Timing of mineralisation

Timing of the gold mineralising event at the Phuoc Son deposit area can be constrained based on the new geochronological data from this study. In particular, the Ar-Ar ages of vein-hosted biotite and LA-ICPMS zircon U-Pb ages of post-mineralisation dacitic porphyry provide key information to constrain the timing of the event.

The Ar-Ar age results of the vein-located biotite from the Bai Dat and Bai Chuoi deposits (211-204 Ma) show younger ages than those of vein-located fuchsite and sericite at Bai Gio reported by Borisenko et al. (2006) which yielded 248.8 ± 3.1Ma (Early Triassic) and 236.4 ± 2.5 Ma (Middle-Late Triassic). The differences in the Ar-Ar ages are probably due to interpretation of the data. The Ar-Ar biotite ages in this study were obtained from total gas ages as no plateau was recognised in the step spectra of the Bai Dat and Bai Chuoi data,

whereas Borisenko et al. (2006) interpreted the Ar-Ar ages from the oldest plateau ages in the step profiles of the Bai Gio samples. These different interpretations of the Ar-Ar age results indicate that ages of the vein-located mica minerals are broadly confined to the Triassic (250–200 Ma), although the minerals contain different closing temperatures and this should be taken into account to interpret the ages (see below).

The Triassic Ar-Ar ages of the vein-located mica minerals at Bai Dat, Bai Chuoi and Bai Gio are younger than LA-ICPMS zircon U-Pb ages of dacitic porphyry (c.a., 250 Ma; see Chapter 3 for details), and this is inconsistent with field evidence. In the field, the dacitic porphyry unit cross-cuts the quartz-sulphide vein, based on an interpretation from the compiled cross-section data at Bai Go, thus it is recognised as a post-mineralisation unit (Sullivan and Kociumbas, 2004; M. Banks pers. comm., 2012). However, the discrepancy of the ages can be explained by considering closing temperatures of the different dating techniques of different minerals. For instance, Khin Zaw et al. (2010) obtained LA-ICPMS zircon U-Pb ages from the Sn-bearing granite samples from Truong Son Fold Belt in Laos, from which Sanematsu et al. (2009, 2011) have previously collected Ar-Ar biotite/muscovite ages. The results yielded a range of 10□60 Ma difference between the two techniques on the same granite samples, and the age differences demonstrated the cooling history of the granite emplacement, indicating that granites in the eastern part of the belt (Nape granites near Vietnam) cooled slowly (5–25 °C/Ma) compared with that of the western part (Boneng granites; 30–50 °C/Ma) (Fig. 4.15). Field data indicate that the formation of the quartz-sulphide veins at Phuoc Son is associated with the regional metamorphism. This may indicate that the large inconsistency in the Ar-Ar ages of the mineralised vein-hosted micas and LA-ICPMS zircon U-Pb ages of post-mineralisation dacitic porphyry was caused due to (1) different closing temperatures of the minerals and (2) the slow cooling history of the intrusive and metamorphic units in the area, which were interpreted from the age data of the Nape Sn-bearing granites in Laos (Fig. 4.15).

Two interpretations can be made regarding the Re-Os age of molybdenite (525 ± 6 Ma) from the granite-hosted sulphide vein at Round Hill. One possibility is that the age represents the timing of the earlier, un-/weakly-mineralised gold stage (i.e., emplacement of the sulphide veins) at Round Hill, but the age is discordant with the age of the host granite (474 ± 6 Ma; see Chapter 3 for details) as the molybdenite appears about 50 Ma older than the host granite. The other possibility is that the molybdenite was sourced from the meta-sedimentary rocks in Phuoc Son and the age represents the formation of the protolith rocks, as the Re-Os

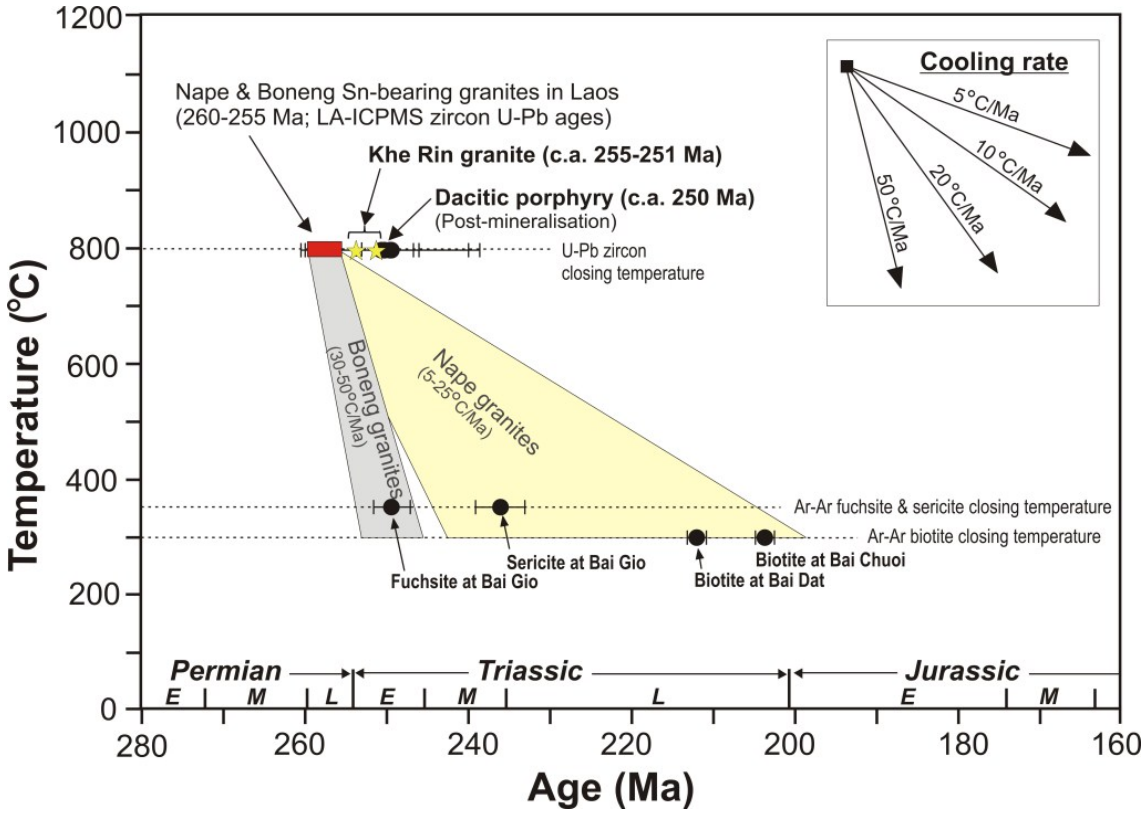

Fig. 4.15. Summary of cooling information obtained from age data of the Phuoc Son deposit area, compared with Sn-bearing granites of Truong Son Fold Belt in Laos. Age data of the Lao granites were compiled from Sanematsu et al. (2009, 2011) and Khin Zaw et al. (2010). Sources of the closure temperatures include fuchsite from Purdy and Jager (1976) and zircon, biotite and sericite (as muscovite) from Spear (1993).

molybdenite age predates the age of the oldest intrusive unit in Phuoc Son (i.e., metagabbro at Nui Vang; 483 ± 7 Ma; see Chapter 3 for details). In addition, whole rock geochemical data suggest that the schist contains the highest molybdenum content among all the studied units from Phuoc Son (see Chapter 3 for details). Thus, the latter possibility could be more plausible to interpret the Re-Os age in terms of the geological and geochronological context at Phuoc Son.

4.6. SUMMARY

The following conclusions can be summarised based on the results and discussion in this Chapter:

- Gold occurs as foliation-parallel quartz-sulphide veins at Bai Dat and Bai Go. At least two gold-bearing mineralisation stages (early and late) are recognised. The early main mineralisation stage is characterised by sphalerite-rich sulphide minerals and

associated with less gold, whereas the late mineralisation stage is enriched in galena and the main gold-bearing stage.

- Two types of sphalerite are identified in the quartz-sulphide veins at Bai Dat and Bai Go. Orange sphalerite occurs as massive sphalerite in the early main mineralisation stage, while dark sphalerite is associated with the quartz-sulphide vein of the late main mineralisation stage.

- Paragenetic textures recorded in the ore zones at Bai Dat and Bai Go suggest that regional metamorphism predated the main gold mineralisation stages, but some textures indicate that regional metamorphism was still active during the early main mineralisation stage (i.e., foliation in massive sphalerite). Post-mineralisation faults are commonly developed, and these displace the ore bodies (i.e., quartz-sulphide veins).

- Gold at Bai Dat and Bai Go occurs predominantly as electrum grains associated with sulphide minerals, such as pyrite, pyrrhotite, galena, sphalerite and chalcopyrite in the quartz-sulphide veins of the late main mineralisation stage. Traces of electrum are also disseminated in the host pyritised carbonaceous schist/phyllite unit.

- The timing of gold mineralisation at Bai Dat and Bai Go is broadly constrained to the Triassic (250–200 Ma) as indicated by Ar-Ar ages of vein-located biotite from Bai Dat and Bai Chuoi (Late Triassic) and fuchsite (Early Triassic) and sericite (Middle-Late Triassic) from Bai Gio. This is inconsistent with the LA-ICPMS zircon U-Pb ages of the post-mineralisation dacitic porphyry (c.a. 250Ma), and the discrepancy of the Ar-Ar and U-Pb zircon ages is considered to be caused by different closing temperatures of different minerals. The Cambrian age (525 ± 6 Ma) recorded from Re-Os dating of molybdenite at Round Hill may represent the age of the protolith of the meta-sedimentary unit at Phuoc Son.

- Based on the combined field and geochronological data, it is likely that the gold mineralisation events (i.e., formation of quartz-sulphide veins) at Bai Dat and Bai Go were formed in the Triassic (250–200 Ma), at the waning stage of the regional metamorphism associated with the Indosinian Orogeny.

CHAPTER 5 MINERAL CHEMISTRY

5.1. INTRODUCTION

In hydrothermal ore deposits, some ore minerals show varieties of trace element compositions (e.g., pyrite, sphalerite) as such minerals can be formed under a wide range of physico-chemical environments. For this reason, the field of mineral chemistry is increasingly investigated in current research of mineral deposits to understand the depositional environment of ores. Mineral chemistry also plays a significant role in modern mineral exploration for vectoring and targeting main ore zones.

This Chapter documents the trace element chemical compositions of ore minerals at the Bai Dat and Bai Go deposits, including electrum, pyrite and sphalerite. Previous geochemical studies involved only a few consultant and internal reports reviewing soil geochemistry of the Phuoc Son deposit area to identify anomalies of gold and associated elements (e.g., Pb, Cu, Ni; Encom Technology, 2008). Prior to this study, no studies have been conducted on trace element chemistry of hypogene ore minerals at Phuoc Son. Thus, the results of this Chapter provide new insights into the physico-chemical environment of the ore-forming fluids at the Bai Dat and Bai Go deposits.

5.2. FINENESS OF ELECTRUM

5.2.1. Introduction

The gold fineness of electrum in a hydrothermal deposits has been studied to understand the geochemical behaviour of gold and silver transport in gold-bearing ore fluids (e.g., Shikazono and Shimizu, 1987; Huston et al., 1992). High gold fineness values with a narrow range are commonly reported in some deposit types such as orogenic (>900; Groves et al., 2003) and porphyry (>900; Sillitoe, 2000) deposits. In contrast, a wide range of gold fineness values is often recognised in epithermal (e.g., Shikazono and Shimizu, 1987) and VHMS (e.g., Huston et al., 1992) deposits. It is generally considered that the gold fineness variation in hydrothermal systems is controlled by depositional conditions such as depth, acidity and temperature (Spycher and Reed, 1989; Huston et al., 1992). In this study, the gold fineness of electrum in the Bai Dat and Bai Go deposits was analysed to understand the geochemical conditions of the gold and silver depositional environment.

5.2.2. Analytical methods

The CAMECA SX-100 microprobe equipment at CSL, University of Tasmania, was used for the mineral chemistry measurements in this study. A total of thirty grains (spots) of five samples from Bai Dat and twenty grains (spots) of three samples from Bai Go were analysed to determine the gold and silver concentrations of electrum. The fineness values were calculated using a formula of (Au/(Au + Ag) x 1000).

5.2.3. Occurrence and petrology

Prior to analysis, petrography of electrum samples from the Bai Dat and Bai Go deposits was undertaken using a microscope to examine size, shape and mineral associations (see Fig. 4.11 in Chapter 4 for details). The occurrence of electrum at the Bai Dat and Bai Go deposits is predominantly confined within quartz-sulphide vein samples of the late main mineralisation stage. A trace volume of electrum is also identified in the massive sphalerite samples of the early mineralisation stage and in the pyritised carbonaceous schist/phyllite samples. Accordingly, electrum samples in the both vein- and host rock-located samples were analysed in this study.

5.2.4. Results

The gold fineness values of the electrum from Bai Dat and Bai Go were calculated and summarised in Table 5.1, and full results are listed in Appendix VIII. The variation of the gold fineness values is graphically shown in Figure 5.1. The Bai Dat electrum grains in the quartz-sulphide veins have a fineness range of 527 to 775, whereas the electrum in massive sphalerite and the host pyritic carbonaceous schist units yielded high fineness values ranging from 916 to 1000 (Fig. 5.1). The electrums in the quartz-sulphide veins from Bai Go show a wider range variation of fineness values from 387 to 971 (Fig. 5.1).

5.3. PYRITE CHEMISTRY

5.3.1. Introduction

Pyrite is one of the most common sulphide minerals in metallic ore deposits and can be found under a wide range of physico-chemical conditions. Varieties of textures and trace element compositions are commonly observed in pyrite from hydrothermal systems and such pyrite contains important information for chemical conditions of the ore-forming environments. Trace element chemistry of pyrite has been studied in various styles of gold-bearing deposits such as Carlin-type (e.g., Hofstra and Cline, 2000; Cromie, 2010), sediment-hosted orogenic (e.g., Wood and Large, 2007; Large et al., 2007; Thomas et al., 2011), epithermal

Table. 5.1. Summary of gold fineness values in electrum from the Bai Dat and Bai Go deposits, Phuoc Son, central Vietnam.

Sample No.	Sample type	Fineness	No. of analysis	Au/Ag ratio in assay	Remarks
Bai Dat					
TMBD11-15	Quartz-sulphide vein	**527-698**	8	N/A	
TMBD11-09A	Quartz-sulphide vein	**732-775**	6	N/A	
TMBD11-09B	Quartz-sulphide vein	**916-935**	4	N/A	Inclusions of massive sphalerite
DSDH257-454.2m	Quartz-sulphide vein	**656-758**	8	N/A	
KZ0818b	Pyritised carbonaceous schist/phyllite (wall rock)	**1000**	4	N/A	
Bai Go					
DSDH26-87.1m	Quartz-sulphide vein	**387-404**	4	0.3	
DSDH209-295m	Quartz-sulphide vein	**913-971**	8	8.2	
DSDH210-246.8m	Quartz-sulphide vein	**633-844**	8	2.3	

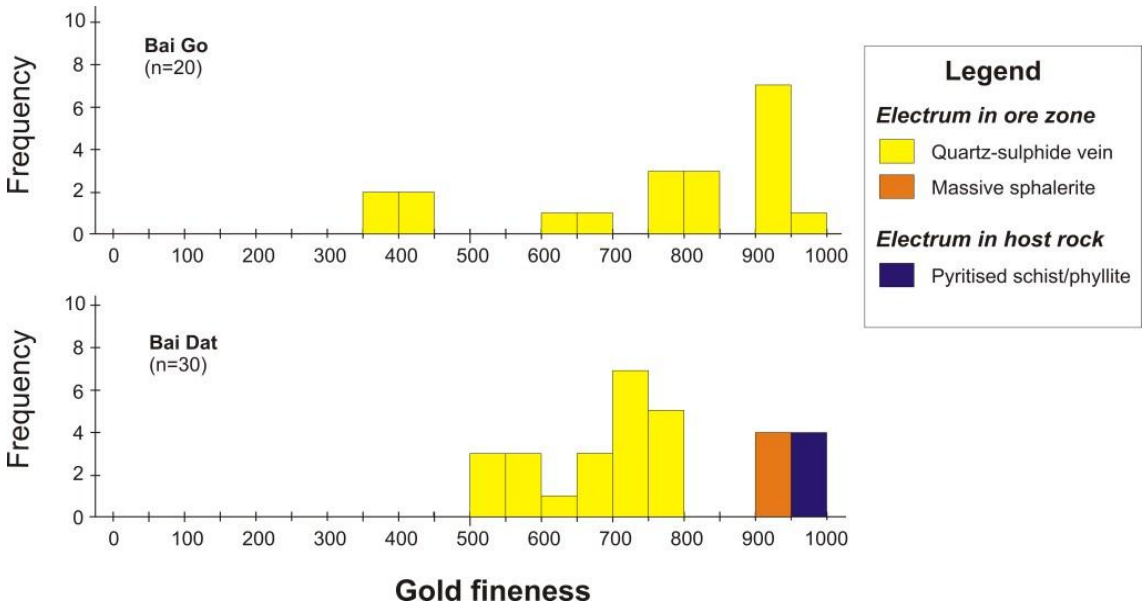

Fig. 5.1. Histogram of gold fineness values in electrum from the Bai Dat and Bai Go deposits in Phuoc Son, central Vietnam.

(e.g., Baker et al., 2006; Salam, 2013) and VHMS systems (e.g., Huston et al., 1995a). A number of experimental analyses on pyrite chemistry have also been conducted in recent years (e.g., Reich et al., 2005). These recent studies revealed that some specific elements (including Au and As) can substitute iron in pyrite structures in specific hydrothermal conditions and they can be concentrated in various magnitudes. Thus, the trace element concentration in pyrite can be used as a tool to interpret physico-chemical conditions of ore-forming fluids and also as exploration guides, such as assessing nature of ore fluids, vectoring to ores and discriminating deposit styles (e.g., Huston et al., 1995a; Reich et al., 2005; Baker et al., 2006; Large et al., 2007).

In this study, the trace element geochemistry of pyrite in the Bai Dat and Bai Go deposits was investigated using the LA-ICPMS technique to examine the chemical compositions and the environment of ore-forming fluids. The primary objectives of this study are: (1) to document the trace element geochemical signature of pyrite from vein and host rock, and (2) to determine the residence of gold and the associated elements in the pyrites of the hydrothermal systems.

5.3.2. Analytical methods

The pyrite study using the LA-ICPMS instrument requires few steps involving preparation, ablation and data reduction processes, as described below:

Sample preparation

A total of twenty polished mount samples, including six samples from vein and fourteen samples from host rock at Bai Dat and Bai Go, were prepared to study the pyrite trace element geochemistry using the LA-ICPMS technique developed at CODES, University of Tasmania. Prior to the analysis, all the samples were etched with nitric acid to clarify the internal texture of pyrite. This etching was conducted by placing a few drops of nitric acid (70% HNO_3) on the surface of the polished mounts and by subsequent rinsing with water after 20–30 seconds. In most cases, the studied pyrite crystals from Bai Dat and Bai Go did not show any internal texture.

LA-ICPMS analysis

Spot and line analyses were applied for this study. The spot analysis was chiefly conducted on the homogeneous pyrite, and line analysis was performed focussing particularly on mapping pyrite with distinct internal textures. For spot analysis, the targeted pyrite samples were pre-ablated with the laser to remove surface contamination (1 Hz pulse for 5 s), followed by analysis of the gas background (30 s) and analysis of the pyrite (70 s) (Fig. 5.2). The samples

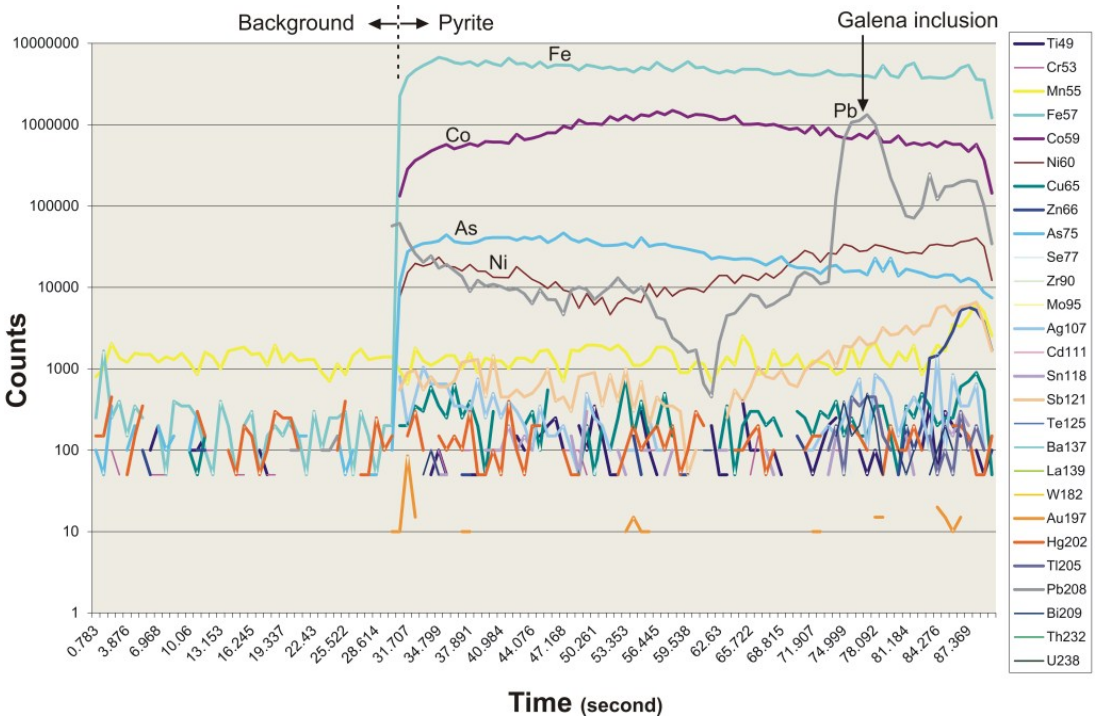

Fig. 5.2. Time chart of the selected LA-ICPMS spot analysis of vein-located pyrite, showing enrichment of Fe, Co, As, Ni and Pb with local high Pb concentration due to galena inclusion in the studied pyrite. Sample No. DSDH209-325.0m (Bai Go).

were normally ablated with a laser beam size of either 15 or 30 µm in diameter with 10 Hz pulse rate. For lines across the surface of the samples, the laser was set to 8 µm in diameter with 10 Hz pulse rate without pre-ablation. Instrumental mass bias and machine drift were monitored by analysing 4 spots of an in-house Fe, Li, B glass standard every hour. As a result, a total of twenty-six elements including Ti, Cr, Mn, Fe, Co, Ni, Cu, Zn, As, Se, Zr, Mo, Ag, Cd, Sn, Sb, Te, Ba, La, W, Au, Tl, Pb, Bi, Th and U were measured for the pyrite grains from Bai Dat and Bai Go.

Data reduction and interpretation

The analysed data were compiled and the concentrations were calculated using Microsoft Excel. The data were initially plotted as a line graph of contents versus time, and the integration times for the background and signal were selected for each analysis. This was straightforward for the analysis of standards which give a flat signal after an initial setting period of about 10 seconds. To calculate the signal intensity, the counts were averaged over the selected interval and the average background counts subtracted. Analyses of pyrite grains selected from Bai Dat and Bai Go were generally more complex than standards and require careful interpretation of time charts and the selection of integration intervals, as they commonly include inclusions of some other minerals (e.g., galena). Interpretations tend to be

element dependent, based on the chemistry of the sulphide and knowledge of associated minerals in the sample.

Once integration intervals were selected for each analysis, the data were compiled in an Excel spread sheet, where the counts were corrected for instrument drift and converted to concentration (ppm). In order to quantify the concentration of one element, the initial standard needed to be known. For most sulphide minerals, stoichiometric concentrations for Fe and Cu were assumed. The drift was calculated by comparing the average counts-per-second, normalised to the intensity of the internal standard, of the two standards run at the beginning and end of a set of analyses. The unknowns were then corrected using a linear regression. The average counts-per-seconds of the standard analyses were used to calculate ppm. The detection limit (DL) is herein defined as the lowest concentration that can be confidently measured above the background. The DL varies with spot size, being larger for small spots since there are fewer counts-per-ppm.

5.3.3. Occurrence and texture of pyrites

Petrological characteristics of the pyrite from the Bai Dat and Bai Go deposits were studied prior to the LA-ICPMS analysis. These are described in Chapter 4 for more details (also in Fig. 4.9). The pyrite at the Bai Dat and Bai Go deposits can be classified into three different types in terms of occurrence and texture. Pyrite with a homogeneous texture is identified in quartz-sulphide veins, and only this type of pyrite is recognised in the veins. In contrast, few types of pyrite are found in the host rocks, involving (1) pyrite with a homogeneous texture, (2) aggregated, fine-grained pyrite and (3) pyrite with mixed homogeneous and spongy textures.

5.3.4. Results

All the measured data are listed in Appendix IX for spot and line analyses, and the results of the selected elements are herein summarised.

Spot analysis

A total of thirty-eight spot analyses were conducted to cover all the identified types of pyrite at Bai Dat and Bai Go. Elements including Ti, Mn, Co, Ni, Cu, Zn, As, Zr, Ag, Sb, Ba, Au, Tl, Pb and Bi yielded concentrations above detection limit. The elements show a wide range of values and are summarised in Table 5.2 and Figure 5.3. Of the elements, Co and Pb appear to be distinct in vein-located pyrite grains as they are concentrated at more than 1000 ppm,

Table 5.2. Range (and mean) of trace element concentrations (ppm) in the studied pyrite types from the Bai Dat and Bai Go deposits, Phuoc Son, central Vietnam.

Sample type	**Vein-located**	**Host rock-located**	
Pyrite type	**Homogeneous**	**Fine-grained, aggregated inclusion**	**Homogeneous**
No. of analysis	7	10	19
Ti	1.9 - 15.0 (4.3)	1.57 - 2.97 (2.11)	1.4 - 534 (41)
Cr	0 - 0.6 (0.16)	0 - 0.55 (0.11)	0 - 26.8 (3.4)
Co	2091 - 22151 (6037)	89 - 601 (280)	0.2 - 801 (173)
Ni	45 - 312 (176)	59 - 948 (332)	7.6 - 1605 (342)
Cu	0.08 - 9.7 (2.3)	0 - 31.7 (3.4)	0 - 10.3 (2.5)
Zn	0.56 - 7.3 (2.8)	1.3 - 59.8 (13.1)	0.3 - 96 (19)
As	70 - 530 (273)	0.04 - 0.7 (0.20)	0.1 - 931 (138)
Se	0.52 -210 (41)	1.0 - 29.8 (7.1)	0 - 35.6 (12.0)
Mo	0 - 1.86 (0.41)	0.04 - 5.5 (1.8)	0 - 5.0 (0.3)
Ag	0.84 - 1088 (253)	0.07 - 1.4 (0.50)	0 - 5.8 (0.8)
Sb	1.85 - 614 (198)	0.05 - 2.3 (0.53)	0.01 - 120 (15.4)
W	0 - 0.17 (0.02)	1.2 - 236 (107)	0 - 112 (13.3)
Au	0.002 - 4.1 (0.6)	0.0008 - 0.009 (0.004)	0.0003 - 0.3 (0.05)
Pb	188 - 661569 (142281)	0.7 - 85 (26)	0.2 - 189 (39)
Bi	0.04 -104 (19)	0.001 - 6.4 (0.1)	0 - 12.7 (2.1)

although Pb is mainly derived from galena inclusions as detected in time-chart profile, whereas all the measured elements in pyrite crystals from the host rocks are less than 1000 pm (Fig. 5.3). Comparisons of Au with other elements are displayed in Figure 5.4, and show that there are weak positive correlation with some elements such as As, Ag, Sb, Co and Pb (Fig. 5.4A, B, C, D and E). These correlation data suggest that the vein-located homogeneous pyrite grains are particularly enriched in Co and Pb compared with those in the host rock (Fig. 5.4F). Thus, the two elements can discriminate the fields between pyrite from the vein and that from the host rock, although galena inclusions should be taken into account for the high Pb concentration in the vein-located pyrite.

Line analysis (mapping)

Mapping of pyrite with distinct internal texture from the host carbonaceous schist/phyllite was conducted using line analysis to visualise trace element distribution in the grain and correlate with the internal texture. The results of a pyrite with mixed homogeneous and spongy textures are shown in Figure 5.5. Zonation of Co, Ni and Sb elements are pronounced

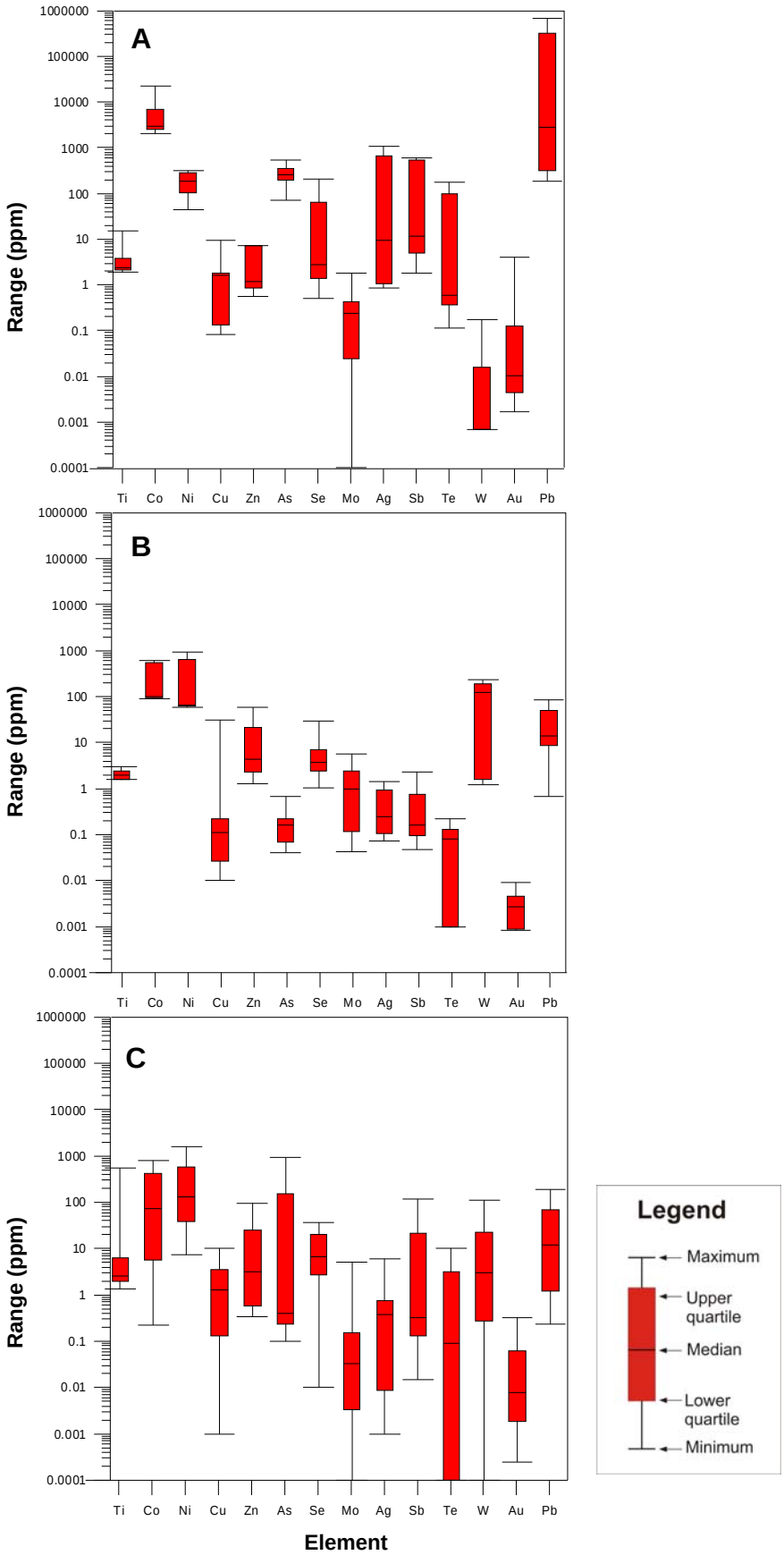

Fig. 5.3. Range and mean values of selected trace elements measured in the studied pyrite from the Bai Dat and Bai Go deposits in the Phuoc Son deposit area. **A.** Homogeneous pyrite from the mineralised veins. **B.** Fine-grained, aggregated pyrite in host rock. **C.** Homogeneous pyrite in host rock.

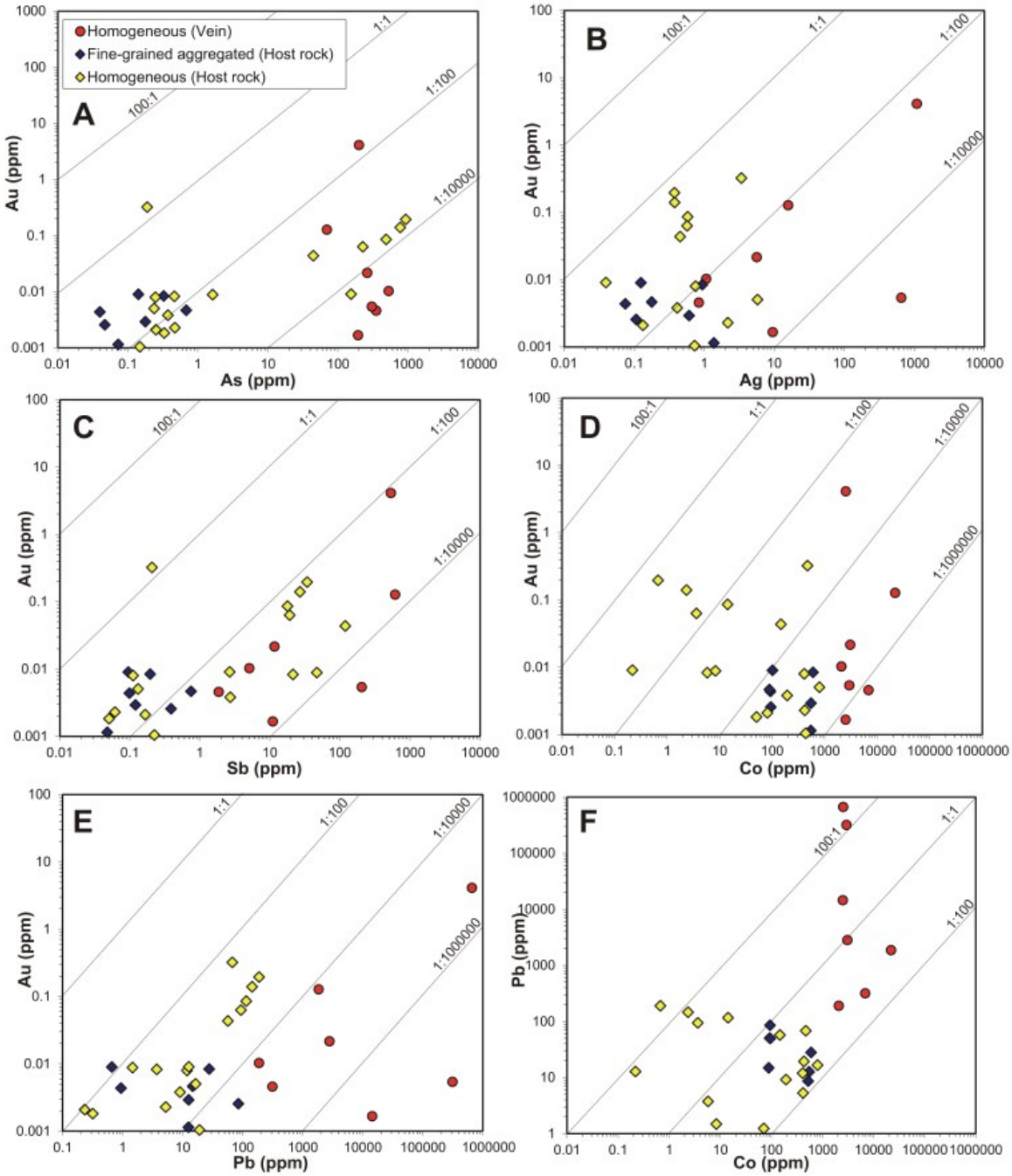

Fig. 5.4. Binary plots of selected trace elements in pyrite from the Bai Dat and Bai Go deposits in the Phuoc Son deposit area. **A.** Au-As. **B.** Au-Ag. **C.** Au-Sb. **D.** Au-Co. **E.** Au-Pb. **F.** Pb-Co.

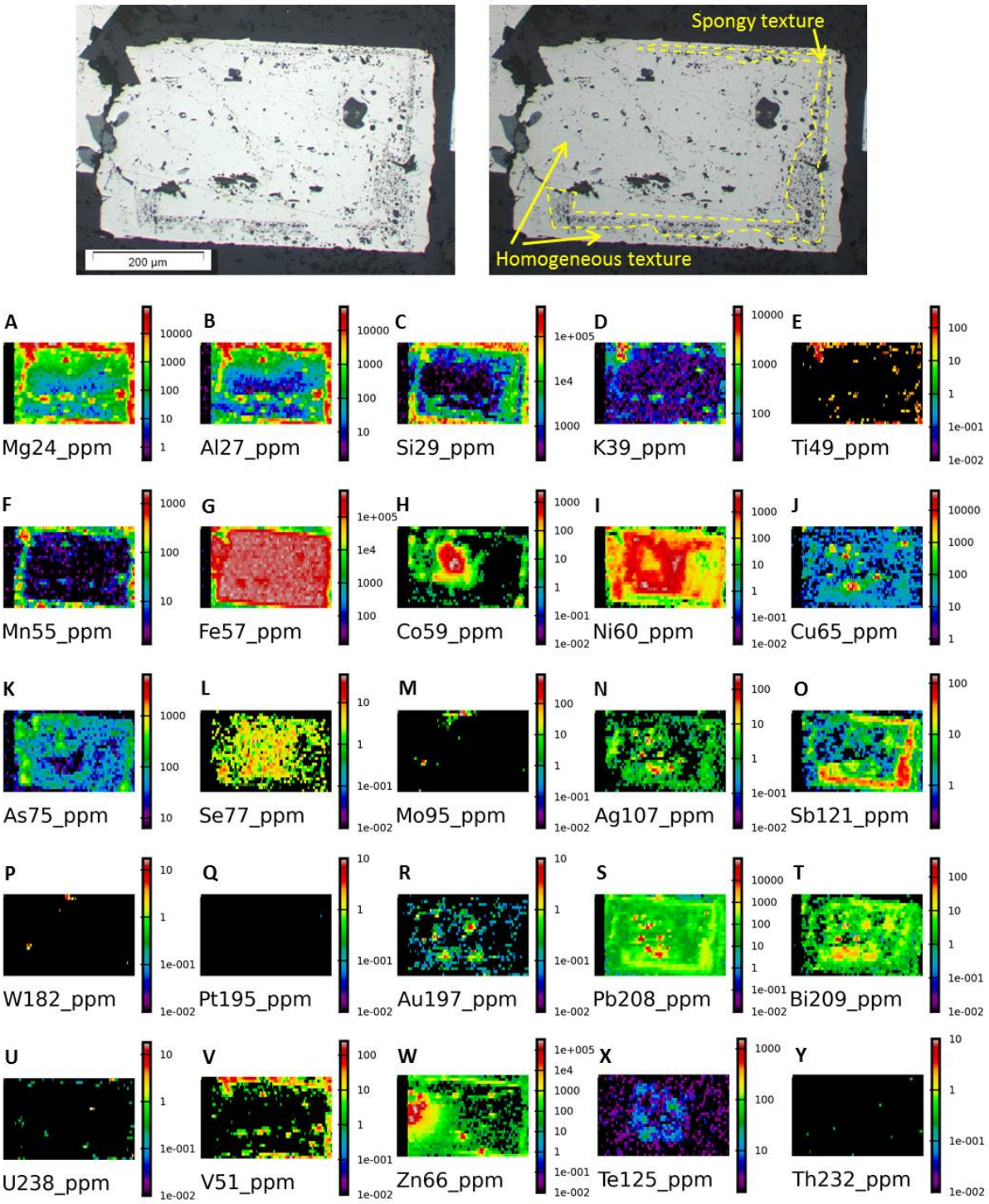

Fig. 5.5. LA-ICPMS pyrite maps of various elements including **A**. Mg, **B**. Al, **C**. Si, **D**. K, **E**, Ti, **F**. Mn, **G**. Fe, **H**. Co, **I**. Ni, **J**. Cu, **K**. As, **L**. Se, **M**. Mo, **N**. Ag, **O**. Sb, **P**. W, **Q**. Pt, **R**. Au, **S**. Pb, **T**. Bi, **U**. U, **V**. V, **W**. Zn, **X**. Te, and **Y**. Th. The pyrite with homogeneous texture at the core and rim with interstitials of spongy texture was selected from the host carbonaceous schist/phyllite unit at Bai Go. Sample No. DSDH224@298.9m.

in the pyrite. It is also recognised that some other elements such as Cu, Ag, Pb, Zn and Au are also locally concentrated and probably occur as mineral inclusions (Fig. 5.5).

Binary plots of selected elements in the mapped pyrite are displayed in Figure 5.6. Negative correlation was observed between Au and As (Fig. 5.6A), and some data are plotted above the saturation line of Reich et al. (2005), indicating that Au probably occurred as inclusions in the pyrite rather than nano particles in the structure of the pyrite. There is no positive correlation between Au and Ag (Fig. 5.6B), whereas Au is weakly correlated with Ni (Fig. 5.6C). Distinct Co and Ni zonation is recognised in Figure 5.5, and the elements show a clear trend from the core to rim of the pyrite which is characterised by a high Co/Ni ratio in the core and low Co/Ni ratio in the rim via the lowest Co/Ni ratios (Fig. 5.6D). Zn and Pb in the pyrite have a wide range of values (Fig. 5.6E). High concentrations of the two elements may suggest they occur mainly as inclusions of sphalerite and galena, as indicated by uneven distribution of the elements in Figure 5.5. Various concentrations of Cu in the pyrite are also recognised (Fig. 5.6F), and small chalcopyrite inclusions are also involved in the pyrite as identified in the Cu distribution in the mapped pyrite.

5.4. SPHALERITE CHEMISTRY

5.4.1. Introduction

The chemical composition of sphalerite can be used as an indicator of the physico-chemical conditions of ore-forming hydrothermal fluids (e.g., Cook et al., 2009; Murakami and Ishihara, 2013). A number of studies have been undertaken on sphalerite-bearing deposits such as VHMS (e.g., Hannington and Scott, 1989; Khin Zaw and Large, 1996), epithermal and mesothermal (e.g., Shikazono and Shimizu, 1987; Khin Zaw and Henderson, 1993), MVT (e.g., Diehl and Kern, 1981) and skarn (Murakami and Ishihara, 2013) systems. In particular, FeS contents in sphalerite are commonly investigated to assess the contribution of magmatic fluids to the mineralised systems, as they show a wide range of concentrations in different types of deposits and also have different zoning in a deposit (e.g., skarn and epithermal deposits; Gemmell et al., 1988; Cromie, 2010).

The FeS contents of sphalerite are also analysed using geobarometry to estimate metamorphic conditions of the ore formation or ore overprinted by later metamorphic process (e.g., Scott, 1976; Lynch and Mengel, 1995; Khin Zaw and Large, 1996), as FeS contents of sphalerite are dominantly controlled by pressure in metamorphic environment. For this application, sphalerite has to be in equilibrium with pyrite and hexagonal pyrrhotite (Scott and Barnes, 1971; Scott, 1973, 1976; Bryndzia et al., 1988, 1990).

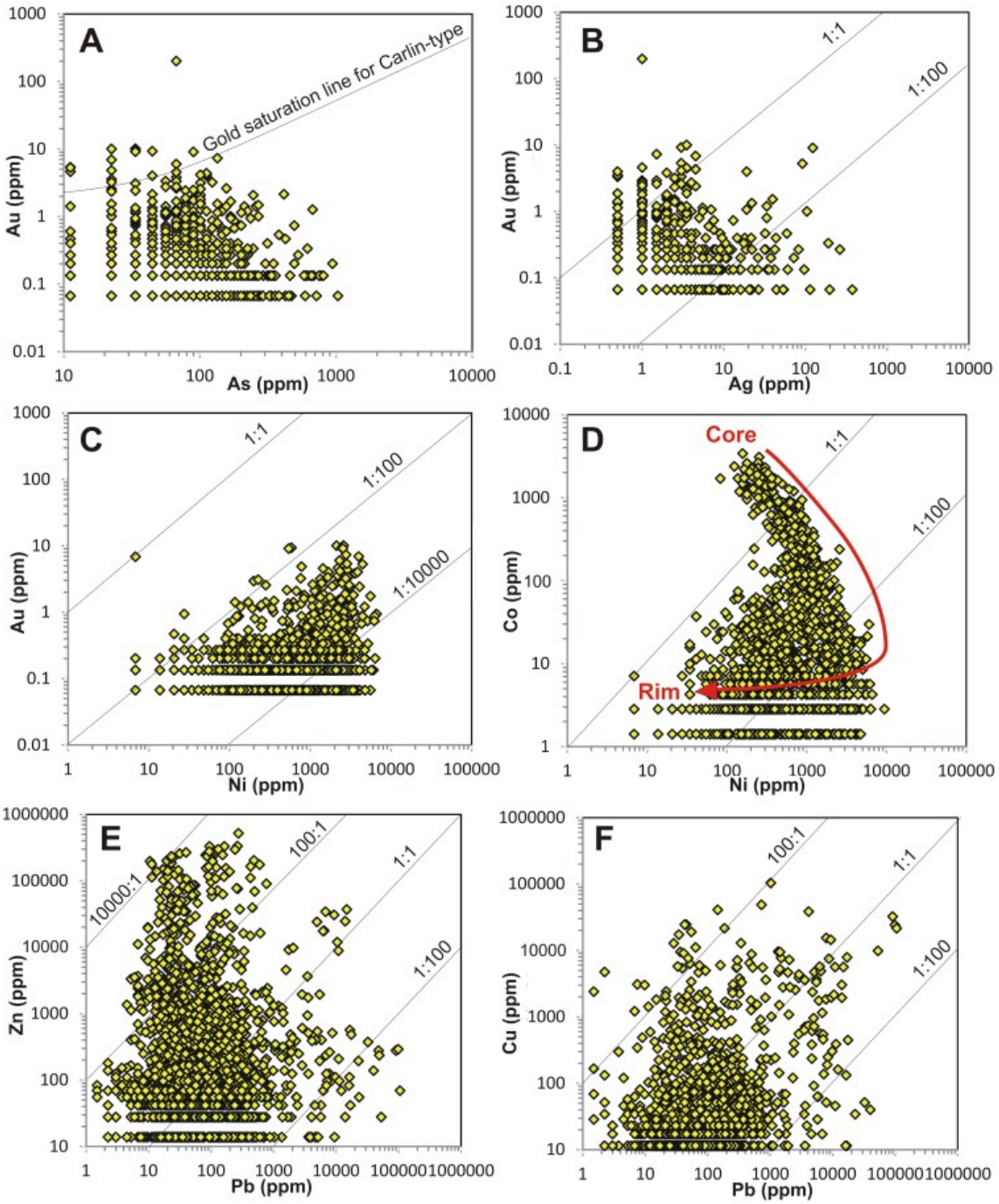

Fig. 5.6. Binary plots of selected trace elements in the host rock-located pyrite from the Bai Go deposit in the Phuoc Son deposit area. **A.** Au-As. **B.** Au-Ag. **C.** Au-Ni. **D.** Co-Ni. **E.** Zn-Pb. **F.** Cu-Pb. Gold saturation line in Fig. A is after Reich et al. (2005).

In this study, trace element chemistry of sphalerite was analysed to determine the chemical environment of ore fluids at Bai Dat and Bai Go. In addition, the sphalerite was used as geobarometer to estimate the depths of ore formation at Bai Dat and Bai Go.

5.4.2. Analytical method

For this study, the CAMECA SX-100 microprobe equipment at CSL, University of Tasmania, was used for the measurement. A total of thirty and nineteen (spots) of four samples from the Bai Dat and three samples from Bai Go deposits were analysed to determine the Zn, S, Fe Mn and Cd elements in the sphalerite samples.

5.4.3. Sphalerite types

Two types of sphalerite were identified at the Bai Dat and Bai Go deposits, including orange sphalerite in the early main mineralisation stage and dark sphalerite in the late main mineralisation stage. Detailed petrography of the sphalerite is described in Chapter 4. The orange sphalerite is associated with pyrite, and occurs as massive sphalerite or breccia as sphalerite clasts in the galena matrix. The dark sphalerite commonly coexists with pyrite, pyrrhotite and galena in quartz-sulphide veins. Although detailed chemical compositions of pyrrhotite (i.e., XRD data) were not obtained, the pyrrhotite at Bai Dat and Bai Go appears to be hexagonal type based on fluid inclusion microthermometric data in the associated quartz (a mode of 250–400°C) as hexagonal pyrrhotite is formed at high temperatures (>254°C; Vaughan and Craig, 1997). Thus, the FeS contents of sphalerite coexisting with pyrite and pyrrhotite (Fig. 5.7A and B) were applied for geobarometry in this study.

5.4.4. Results

The measured chemical compositions of sphalerite from the Bai Dat and Bai Go deposits are listed in the Appendix X. The calculated FeS mole % values are summarised in Table 5.3 together with CdS mole % and MnS mole % and calculated pressures. A distinct range of FeS mole % values of sphalerite was recorded between the orange sphalerite in massive sphalerite and dark sphalerite in quartz-sulphide veins. The orange sphalerite from Bai Dat has a range of 5.2–7.2 FeS mole %, whereas the dark sphalerite of Bai Dat is ranged from 12.3 to 14.2 FeS mole % and those of Bai Go ranged from 13.9 to 15.2 FeS mole % (Fig. 5.8).

Distinctive ranges of MnS and CdS mole % values were also recognised in the sphalerite from Bai Dat and Bai Go. The CdS mole % values of the orange and dark sphalerites from Bai Dat are ranged from 1.0–2.4 and these values are lower than those of dark sphalerite from

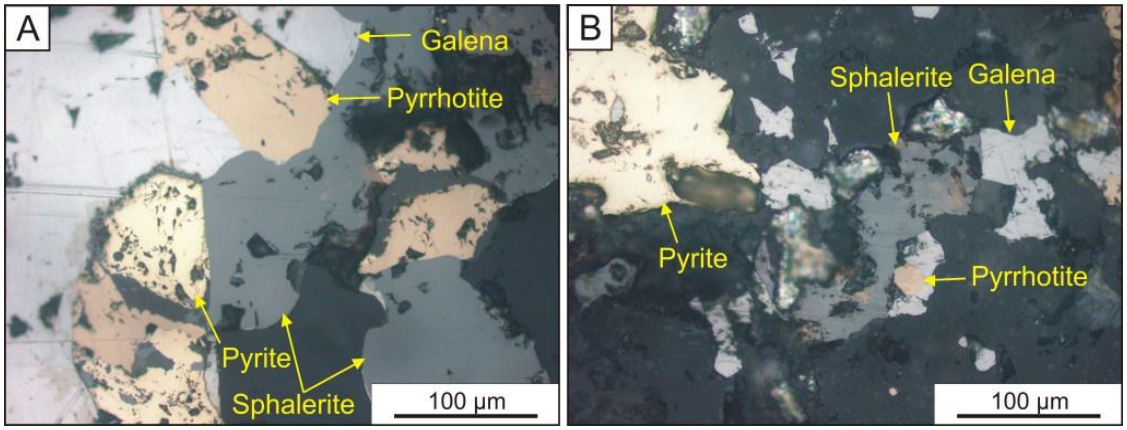

Fig. 5.7. Photomicrograph showing association of sphalerite with other sulphide minerals in the quartz-sulphide veins at the Bai Dat and Bai Go deposits, Phuoc Son. **A.** TMBD11-05 (Bai Dat). B. DSDH199@230.2m (Bai Go).

Table 5.3. Summary of calculated chemical values of the studied sphalerite from the Bai Dat and Bai Go deposits, Phuoc Son.

Sample No (No. of analysis)	Sample type	FeS mole %	CdS mole %	MnS mole %	Associated sulphides[1]	Pressure (kbar)[2]
Bai Dat						
TMBD11-15 (8)	Quartz-sulphide vein	12.3 - 13.3	1.45 - 1.50	0.06 - 0.09	py-sph-ga-po	6.4 - 7.5
TMBD11-12 (8)	Massive sphalerite	7.1 - 7.2	1.00 -1.05	0.01 - 0.04	sph-py	N/A
TMBD11-09 (6)	Massive sphalerite	5.2 - 5.4	1.30 -1.55	0.01 - 0.04	sph-py	N/A
DSDH257@454.2m (8)	Quartz-sulphide vein	13.9 - 14.2	2.25 - 2.35	0.22 - 0.26	po-sph-ga-py	N/A
Bai Go						
DSDH26@87.1m (2)	Quartz-sulphide vein	14.1 - 14.2	4.25 - 4.50	0.03 - 0.05	po-py-sph	5.4 - 5.6
DSDH199@230.2m (8)	Quartz-sulphide vein	13.9 - 14.2	3.50 - 3.65	0.05 - 0.09	ga-sph-py-po	5.3 - 5.8
DSDH249@499.1m (9)	Quartz-sulphide vein	14.5 - 15.2	4.40 - 4.65	0.04 - 0.12	py-sph	N/A

1. Abbreviations; py = pyrite, po = pyrrhotite, sph = sphalerite, ga = galena.

2. Geobarometer after Hutchison and Scott (1981). N/A = Not Available.

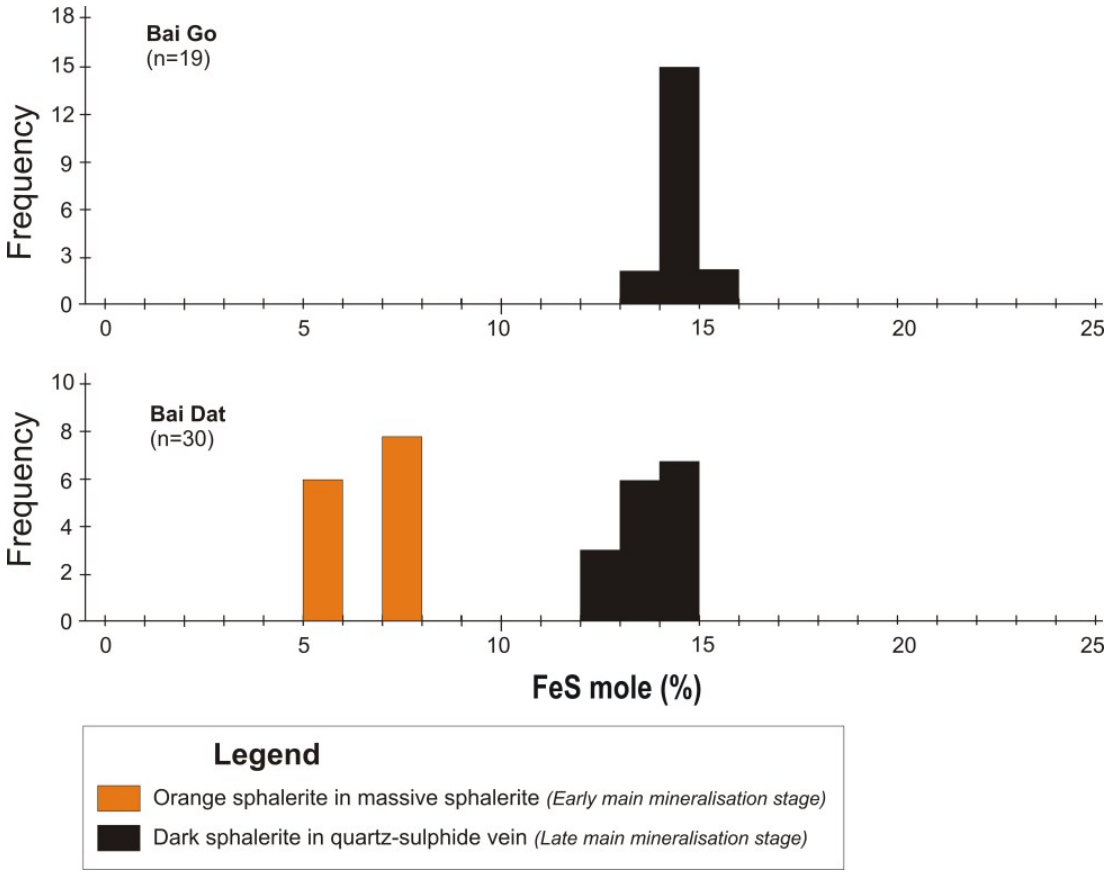

Fig. 5.8. Histogram of FeS mole % values of sphalerite from the Bai Dat and Bai Go deposits in Phuoc Son, central Vietnam.

Bai Go which has a range of 3.5–4.7 CdS mole % (Fig. 5.9A). MnS contents are mostly less than 0.12 MnS mole % in the sphalerite from all of the studied samples, except one sphalerite sample from the shallower part of the ore zone at Bai Dat having a range of 0.22–0.26 MnS mole % (Fig. 5.9B). A plot of CdS mole %-MnS mole % shows that there are three distinctive fields in the Bai Dat and Bai Go samples (Fig. 5.9C). Sphalerite of all the Bai Go samples has low MnS mole % and high CdS mole % values. The dark sphalerite in the quartz-sulphide veins from the shallower ore zone at Bai Dat have high MnS mole % and low CdS mole % values, while orange and dark sphalerites in the rest Bai Dat samples have low values in both the MnS mole % and CdS mole %. On the ternary diagram relating FeS, MnS and CdS contents of sphalerites from Bai Dat and Bai Go, the data display different compositional fields (Fig. 5.10). The dark sphalerite between the Bai Dat and Bai Go deposits appears to be differentiated as the Bai Go sphalerite is more enriched in CdS contents. The compositional field of the orange sphalerite of Bai Dat is partly overlapped with the field of the dark sphalerite of Bai Go.

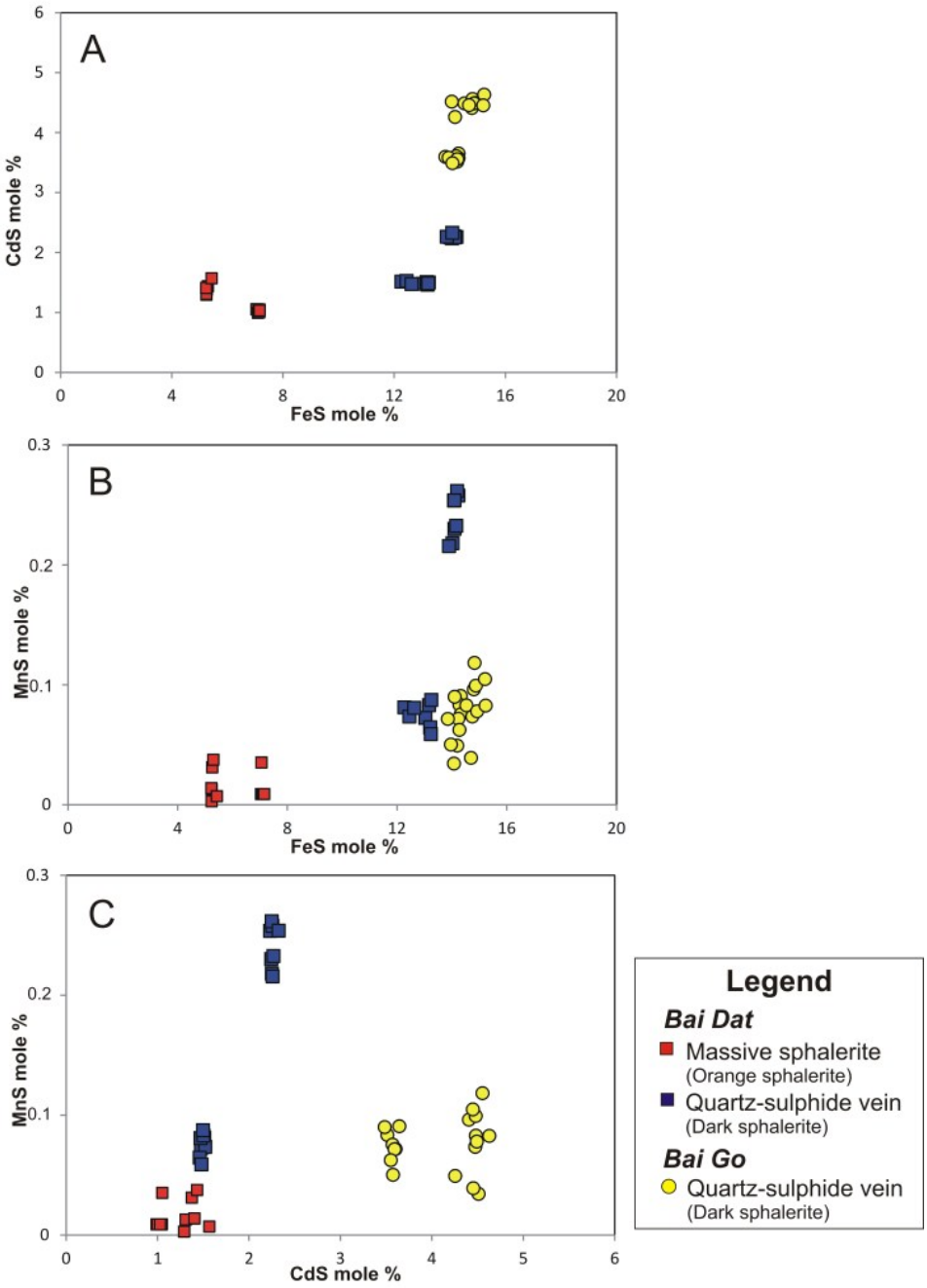

Fig. 5.9. Binary plots of calculated FeS, MnS and CdS mole % values of sphalerite at the Bai Dat and Bai Go deposits in the Phuoc Son deposit area. **A.** FeS mole %-CdS mole %. **B.** FeS mole %-MnS mole %. **C**. CdS mole %-MnS mole %.

The calculated pressures for the vein-located dark sphalerite at Bai Dat range from 6.4–7.5 kbar, whereas those of Bai Go have a range of 5.3–5.8 kbar (Fig. 5.11). The Bai Dat and Bai Go data correspond to depths of 19.2–22.5 km and 15.9–17.4 km respectively, based on assumed rock density of 3 g/cm^3.

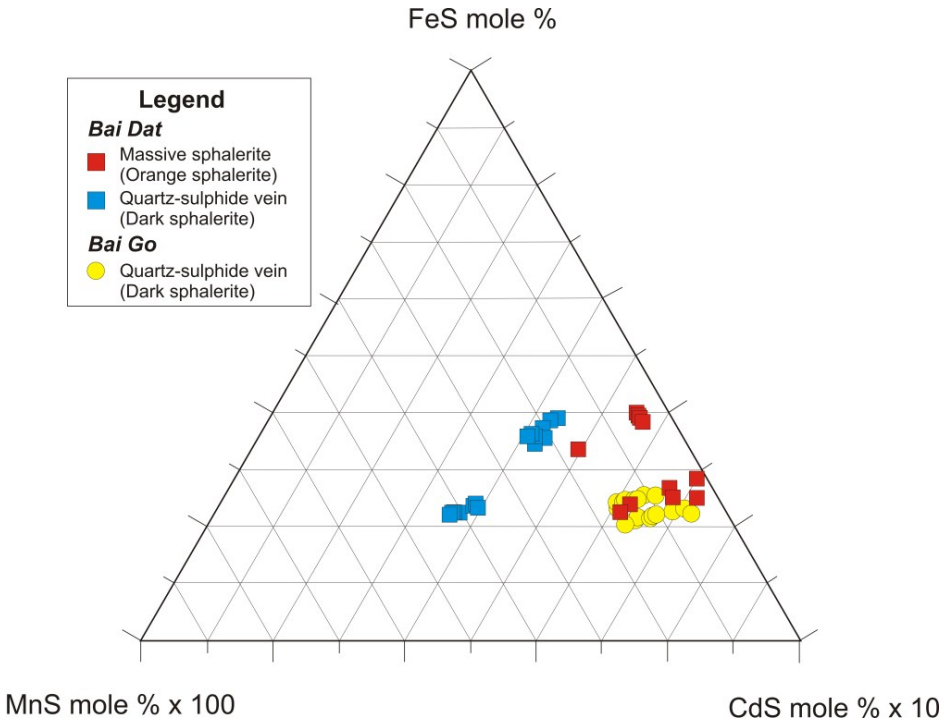

Fig. 5.10. A ternary plot of Fes mole % - MnS mole % X 100 – CdS mole % X 10 in sphalerite from the Bai Dat and Bai Go deposits, Phuoc Son, central Vietnam.

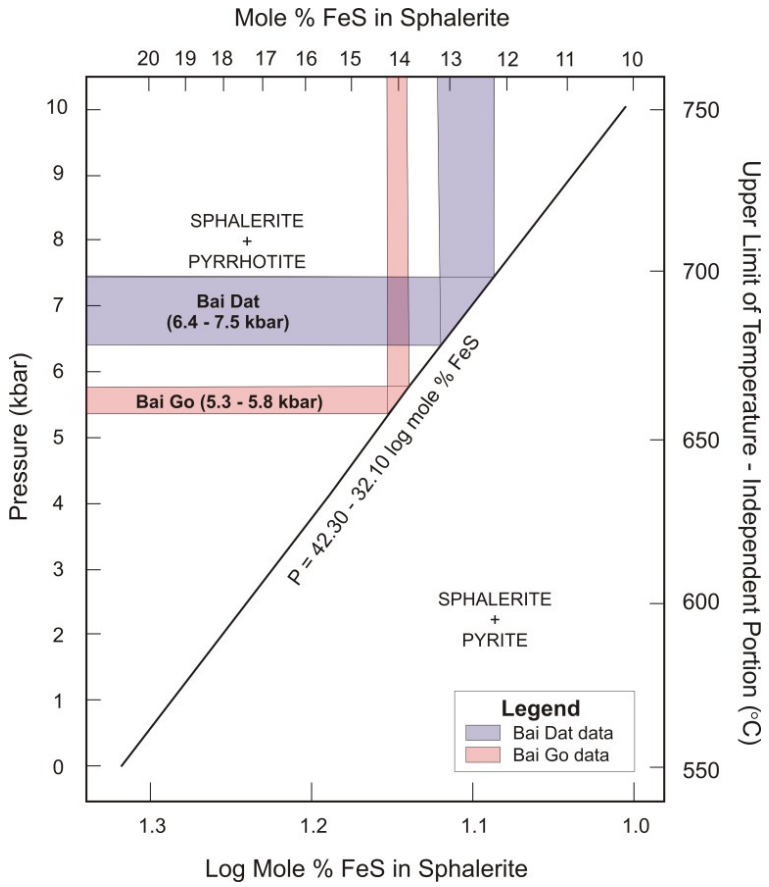

Fig. 5.11. Pressure determinations after the method of Hutchison and Scott (1981) using FeS mole % values of dark sphalerite at the Bai Dat and Bai Go deposits in the Phuoc Son deposit area.

5.5. DISCUSSION

The mineral chemistry data presented in this Chapter are discussed below to constrain the physico-chemical environment of ore fluids at the Bai Dat and Bai Go deposits.

5.5.1. Chemistry of ore fluids and gold fineness values

The gold fineness values of electrum from the Bai Dat and Bai Go deposits are compared with those from other gold-bearing deposits (Fig. 5.12). High and narrow ranges are commonly recorded in the porphyry (>900; Sillitoe, 2000) and intrusion-related (>750; e.g., Rombach et al., 2002) deposits. The ranges are generally considered to be caused because gold was transported by chloride complexes in high temperature fluids (>350°C), which contain high Au/Ag ratio (Morrison et al., 1991). The sediment-hosted orogenic systems also yield electrums with high gold fineness (>900; Groves et al., 2003), and it is explained that gold was carried by bisulphide complex in which silver is rarely involved in high temperature fluids (>350°C; Morrison et al., 1991). However, lower fineness values (750–800) are recorded in the sediment-hosted system at Tersang in Malaysia, which underwent a later deformation event and contains remobilised electrums (Makoundi, 2012). Wide ranges of fineness values are recognised in the skarn and VHMS systems (500–1000 in skarn and 200–1000 in VHMS). Precipitation of electrum in skarn systems is commonly associated with lower temperature fluids of the retrograde stage (e.g., 250–400°C at Big Gossan in Indonesia; Meinert, 1997), and gold is considered to be transported by mixed chloride and bisulphide complexes in such fluid conditions (e.g., Shikazono and Shimizu, 1987).

The distinct variations of gold fineness values are identified between Cu-Au (700–1000) and Zn-Au (200–1000) zones of VHMS systems in Australia (Huston et al., 1992). The researchers interpreted that the gold was transported as a bisulphide complex in the lower temperature (200–300°C) fluids and deposited in the Zn-Au zone, whereas gold transported by a chloride complex in the higher temperature range (300–350°C) was precipitated in the Cu-Au zone. A wide range of fineness values (0–900) is noted in epithermal low- and intermediate-sulphidation Au-Ag deposits (e.g., Ban Houayxai; Manaka, 2008, and Chatree; Dedenczuk, 1998; Greener, 1999; Kromkhun, 2005; Salam, 2013). The wide range in Au-Ag epithermal systems is generally interpreted by the fact that gold is predominantly transported by bisulphide complexes in low temperature (<300°C) fluids (Shikazono and Shimizu, 1987).

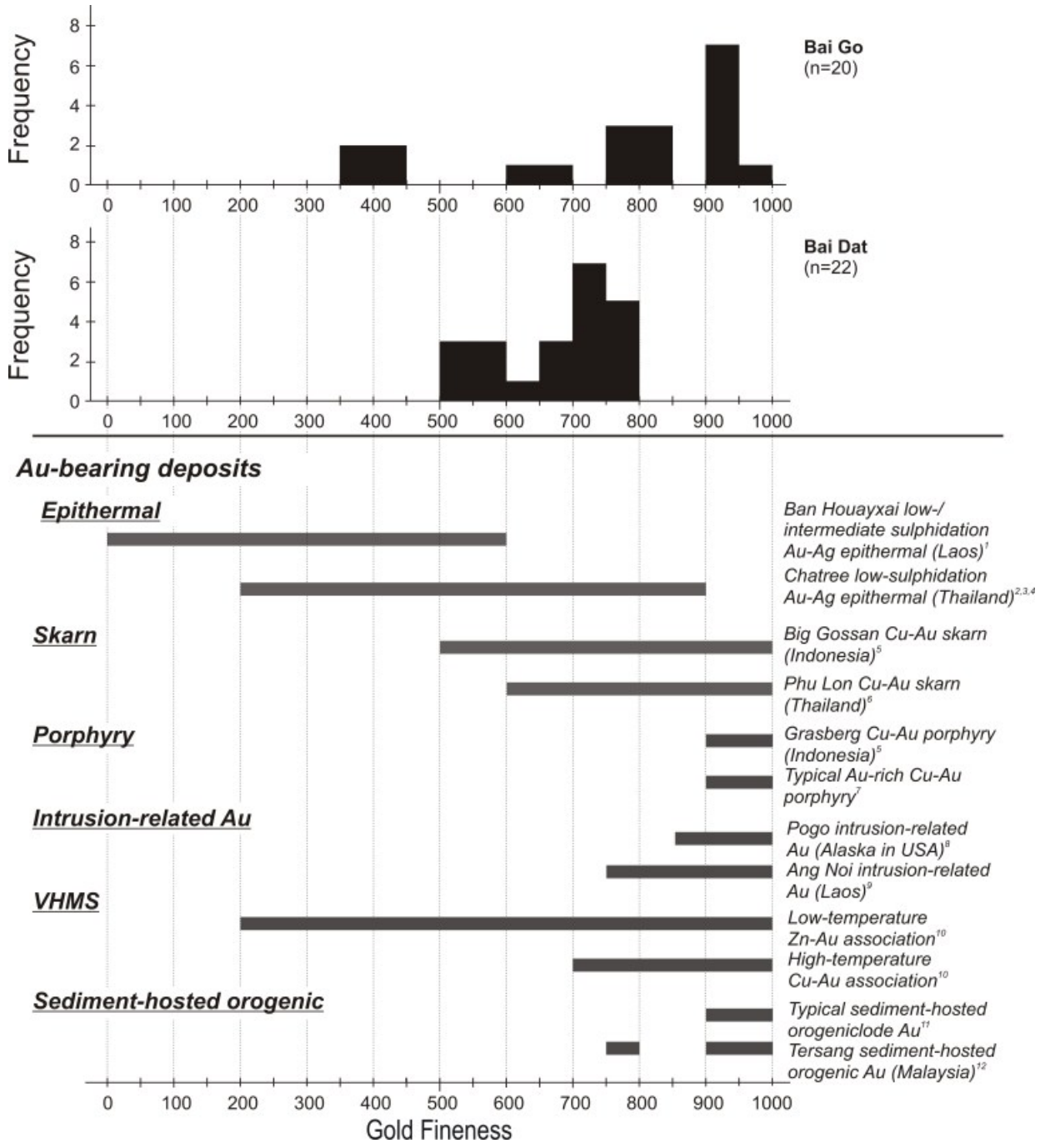

Fig. 5.12. Comparison of electrum fineness data from the Bai Dat and Bai Go deposits in Phuoc Son with typical gold-bearing deposits. References; 1=Manaka (2008), 2=Kromkhun (2005), 3=Dedenczuk (1998), 4=Greener (1999), 5=Burin and Kyle (1997), 6=Sitthithaworn (1989), 7=Sillitoe (2000), 8=Rombach et al. (2002), 9=Maloney (2008), 10=Huston et al. (1992), 11=Groves et al. (2003), and 12=Makoundi (2012).

These comparisons show the gold fineness data of the Bai Dat and Bai Go deposits are comparable to those of skarn, epithermal and Zn-Au zone of VHMS systems in which gold is dominantly transported by a bisulphide complex in relatively low temperature (<300°C) fluids. This suggests that gold of the Bai Dat and Bai Go deposits was also mainly transported by bisulphide complex. This is consistent with the fluid inclusion data which also constrain that gold was predominantly carried by a bisulphide complex at the Bai Dat and Bai Go deposits (see Chapter 7 for details). However, it cannot be ruled out that gold was transported by a chloride complex. Presence of massive galena and sphalerite at Bai Dat and Bai Go may indicate that ore fluids involved certain amounts of chloride complex as lead and zinc are carried predominantly by chloride complex in hydrothermal deposits (e.g., Seward and Barnes, 1997).

5.5.2. Pyrite trace element chemistry

Gold in pyrite

Complex textural variation was recognised in the vein and host rock pyrite at the Bai Dat and Bai Go deposits. Such textural complexity is also reported in gold-bearing pyrite from other sediment-hosted gold deposits such as Bendigo in Australia (e.g., Thomas et al., 2011). In this study, no significant concentration of gold (<10 ppm in general) was found in the vein-hosted pyrite at Bai Dat and Bai Go (Fig. 5.4A). >100 ppm gold concentrations were recorded in some data of pyrite from the host rock, but are likely due to gold inclusions in pyrite as suggested by the gold saturation line of Reich et al. (2005; Fig. 5.6A). Reich et al. (2005) noted that the gold occurs together with As in the pyrite structure as refractory Au at Carlin type deposits, and experimentally established the maximum Au concentration in arsenic pyrite (i.e., gold saturation line) which is positively correlated with As concentration (Fig. 5.6A). The presence of gold inclusions in the pyrite at Bai Dat and Bai Go is also visually demonstrated in the mapping result in Figure 5.5, as a high concentration of gold is unevenly distributed in the map. These results are consistent with the petrological observation that small gold grains are commonly found in the pyritised carbonaceous schist/phyllite unit (see Chapter 4 for details). On this basis, it is found that gold at the Bai Dat and Bai Go deposits predominantly occurs as electrum grains in the both quartz-sulphide vein and pyritised carbonaceous schist/phyllite samples.

High Ni and Co concentration in metamorphic pyrite

In addition to Cu, Zn and Pb, which are considered to occur as chalcopyrite, sphalerite and galena inclusions of pyrite, high concentrations of Ni and Co were noted in the host rock pyrite (Figs. 5.5 and 5.6D). From a pyrite study of the sediment-hosted gold deposit at

Bendigo, Ni and Co are two of the few elements which are accumulated in pyrite/pyrrhotite during metamorphism (Thomas et al., 2011). This process may be consistent with the pyrite at Bai Dat and Bai Go which were probably formed during regional metamorphism. Thomas et al. (2011) reported that the pyrite at Bendigo is hosted by a thick turbidite sequence. In comparison, the pyrite at the Bai Dat and Bai Go is hosted in the carbonaceous schist/phyllite and mafic units (e.g., metabasite and metagabbro). As the mafic units contain high background concentrations of Ni and Co, the high Ni and Co concentration in the pyrite at Bai Dat and Bai Go may indicate that they were sourced from the host rocks. Hence, the mafic units also played an important role as the source of the Ni and Co into ore-forming fluids at Bai Dat and Bai Go. The presence of fuchsite in the mineralised veins at Bai Gio (Borisenko et al., 2006) and occurrence of serpentinite in the gold-bearing veins at Bai Dat and Bai Go (see Chapter 4) also support the interpretation above that input of metamorphic fluids was sourced from the mafic units.

5.5.3. Sphalerite FeS contents for geobarometer

The FeS contents of sphalerite indicate that the Bai Dat and Bai Go deposits were formed at ranges of 6.4–7.5 kbar and 5.3–5.8 kbar, which correspond to the depth ranges of 19.2–22.5 km and 15.9–17.4 km, respectively. The estimated depths are broadly comparable to the range of orgenic lode gold deposits in the Yilgarn Craton of Western Australia (i.e., 5–20 km; Goldfarb et al., 2005). However, the estimated depths for Bai Dat and Bai Go are deeper than those estimated from carbonic fluid inclusion data hosted in euhedral quartz of the massive galena vein (3.3–4.3 kbar; see Chapter 7 for details). The estimated depths of ore formation are discussed further in Chapter 8 to establish a genetic model for the Bai Dat and Bai Go deposits.

5.6. SUMMARY

Based on the results and discussions made in this Chapter, the following conclusions are made:

- Gold at Bai Dat and Bai Go occurs predominantly as electrum associated with sulphide minerals such as pyrite, pyrrhotite, galena, sphalerite and chalcopyrite in the quartz-sulphide veins. Trace amounts of electrum are also disseminated in the pyritised carbonaceous schist/phyllite unit.

- The vein-located pyrite has a homogeneous in texture, whereas pyrite in the wall rocks is characterised by complex textures. The trace element composition using LA-

ICPMS demonstrated that gold concentrations in the pyrite are very minor (<10 ppm) at Bai Dat and Bai Go, and Co and Pb are distinctly concentrated in the vein-located pyrite. High concentrations of Ni and Co with clear zoning are found in the host rock pyrite, and the elements are considered to have sourced from the host mafic units (e.g., metabasite and metagabbro).

- The fineness values of the vein-located electrums at Bai Dat and Bai Go ranged between 500–800 and 350–1000, respectively. Very high fineness values (>900) are also recorded in the electrum grains from the pyritised carbonaceous schist/phyllite and massive sphalerite samples of Bai Dat.

- Comparisons of the gold fineness ranges with those in other gold-bearing systems suggest that the gold was predominantly carried by bisulphide complex in ore fluids at Bai Dat and Bai Go. However, gold could have been transported partly by chloride complex as evidenced by the presence of massive galena and sphalerite at Bai Dat and Bai Go.

- Sphalerite chemistry indicates that there are bimodal FeS mole % contents in the sphalerite at Bai Dat and Bai Go. The lower values ranging between 5–8 FeS mole % were recorded from the massive orange sphalerite, whereas higher values of 12–16 FeS mole % are obtained from dark sphalerite in the quartz-sulphide veins of the main gold-bearing stage.

- The depths calculated from the FeS mole % contents of the vein-located dark sphalerite coexisting with pyrite and pyrrhotite yielded the ranges of 6.4–7.5 kbar and 5.3–5.8 kbar for Bai Dat and Bai Go respectively. They are corresponded to the depth ranges of 19.2–22.5 km and 15.9–17.4 km.

CHAPTER 6 STABLE AND RADIOGENIC ISOTOPES

6.1. INTRODUCTION

Stable and radiogenic isotope studies have routinely been used in mineral deposit research to understand the physico-chemical conditions of ore formation, and as tracers to the source(s) of metals and fluids (e.g., Ohmoto and Rye, 1979; Sheppard, 1986; Rollinson, 1993; Huston et al., 1995b).

Stable isotopes are powerful tools to investigate the nature of ore-forming fluids, as light stable isotopes of H, C, N, O and S are often the main constituents of ore fluids in mineralised systems (e.g., Rollinson, 1993). Two types of data are mainly used in stable isotopes for ore deposit research. One is the isotopic relationships (i.e., fractionation factors) among co-existing minerals, and the other is the isotopic value of a mineral phase. The isotopic relationships among a variety of minerals in ore deposits help to provide several key factors; such as (1) the temperature of mineralising environment, (2) source(s) of metals and the associated minerals, (3) chemistry of ore-forming fluids, and (4) mechanism of ore-forming processes (Ohmoto and Rye, 1979).

Radiogenic isotope chemistry is also used in two principal ways: (1) to determine the age of rocks and minerals and (2) to identify geological processes and sources (e.g., Rollinson, 1993). Results of the study can lead to important geochemical constraints on the nature of ore-forming fluids and provide evidence to deduce physico-chemical conditions of ore deposits (e.g., Rollinson, 1993). In this study, stable (S, C, O) and radiogenic (Pb) isotopes were applied to characterise the nature of the gold-bearing mineralising fluids at the Bai Dat and Bai Go deposits in Phuoc Son.

6.2. SULPHUR ISOTOPES

6.2.1. Introduction

Heavy metals are commonly bound as sulphide minerals in metallic ore deposits. Even in deposits where the ores are non-sulphides (e.g., gold), sulphide minerals are commonly associated with the ores (Ohmoto and Rye, 1979). Thus, geochemistry of sulphur in ore deposits through the application of sulphur isotopes has become an essential part of ore

deposit research by addressing such issues as the source, transport and precipitation mechanisms of sulphur (Ohmoto and Rye, 1979).

Sulphur has four stable isotopes (^{32}S, ^{33}S, ^{34}S and ^{36}S) whose percentage abundances are approximately 95.02, 0.75, 4.21 and 0.02, respectively (MacNamara and Thode, 1950). The ratio between the two most abundant isotopes ($^{34}S/^{32}S$) is often used in geochemistry (e.g., Rollinson, 1993). Deposits containing sulphides exhibit an apparent ability to retain the original sulphur isotope compositions throughout most post-mineralisation processes involving metamorphism and/or deformation (Sangster, 1979). For this reason, sulphur isotopes are commonly used in mineral deposit studies to provide information such as; (1) sources of sulphur in ore-forming fluids, (2) mechanism of ore deposition and (3) temperature of mineralisation environment, by measuring fractionation factors of coexisting sulphides and the isotopic values (Ohmoto and Rye, 1979).

6.2.2. Analytical methods

In this study, a total of fifty-four samples from Bai Dat and fifty-one from Bai Go deposits were collected and analysed. The sulphide samples included pyrite, pyrrhotite, sphalerite, galena and chalcopyrite, and they were collected from both vein and wall rock units. The analysis was conducted using two methods involving conventional and laser ablation techniques:

Conventional technique: Visible sulphide minerals in the hand specimen samples were manually drilled out using a dentist's drill to obtain powdered (>5 mg) sulphide samples at CODES, University of Tasmania. The powdered samples were submitted to Central Science Laboratory (CSL), University of Tasmania, and the isotopic compositions were measured using the $^{34}S/^{32}S$ sulphide combustion method, operated by Mrs. Christine Cook. The detailed analytical method of this combustion technique is explained by Robinson and Kusakabe (1975).

Laser ablation technique: For the samples containing disseminated sulphides, polished thin sections with 150 μm thickness were prepared, and they were analysed using VG Micromass SIRA Series II mass spectrometer at CSL, University of Tasmania. The samples were ablated in an oxygenated environment, and SO_2 gas was generated and separated from other gases using freezing and heating taps. Subsequently, the $\delta^{34}S$ value in the obtained SO_2 gas was analysed using the known standards of galena from Broken Hill and Rosebery. The detailed analytical technique is given by Huston et al. (1995b).

6.2.3. Results

Sulphur isotope values

The sulphur isotope data of Bai Dat and Bai Go are graphically presented in Figures 6.1 and 6.2, respectively, and the complete detailed results are listed in Appendix XI. The results show very consistent sulphur isotope data for almost all of the base metal-bearing (i.e., galena, sphalerite and chalcopyrite) samples, all of which were collected from quartz-sulphide veins. They are narrowly confined within a range of -4 to +4 ‰, whereas values of pyrite and pyrrhotite taken from both the vein and wall rock units range widely between -18 and +26 ‰ (Figs. 6.1A and 6.2A). All of the data obtained from the vein-located samples have a constrained range of -4 to +4 ‰, with a few exceptions in the Bai Dat pyrite and pyrrhotite samples, which yielded values of -18 to -14 ‰ and +6 to +14 ‰ (Figs. 6.1B and 6.2B).

Comparison of S isotope values versus gold grade

As major quartz-sulphide vein samples for the sulphur isotope analyses were taken from drill cores, it was possible to compare the sulphur isotope values with gold assay data (provided by Olympus Company). Their relationships are expressed in Figure 6.3, together with additional ore samples collected from outcrops of underground at the Bai Dat which are tentatively assigned to 10 g/t Au (average ore grade at Phuoc Son). The plots show that all of the ore samples (>3 g/t Au cut-off grade) are confined to a range of -4 to +4 ‰, whereas samples below cut-off grade (3 g/t Au) have a broad sulphur isotope range from -15 to +26 ‰ (Fig. 6.3).

6.3. CARBON AND OXYGEN ISOTOPES

6.3.1. Introduction

Fewer carbon and oxygen isotope studies of ore deposits have been undertaken compared with the sulphur isotope studies. This is primarily due to the limited occurrence of carbonate minerals compared with sulphide minerals in ore deposits (Ohmoto and Rye, 1979). A carbon and oxygen isotope signature is often closely collaborated with sulphur isotope data as precipitation of sulphide minerals from solutions is typically caused by a reaction with carbonate minerals (e.g., skarn systems; Ohmoto and Rye, 1979). For these reasons, carbon and oxygen isotopic co-variations in carbonate minerals associated with hydrothermal fluids have been widely studied to use the data as an indicator of their origin, the nature of dissolved carbonate species and hydrothermal processes (e.g., cooling, fluid mixing, fluid/rock interaction and secondary alteration; Rollinson, 1993).

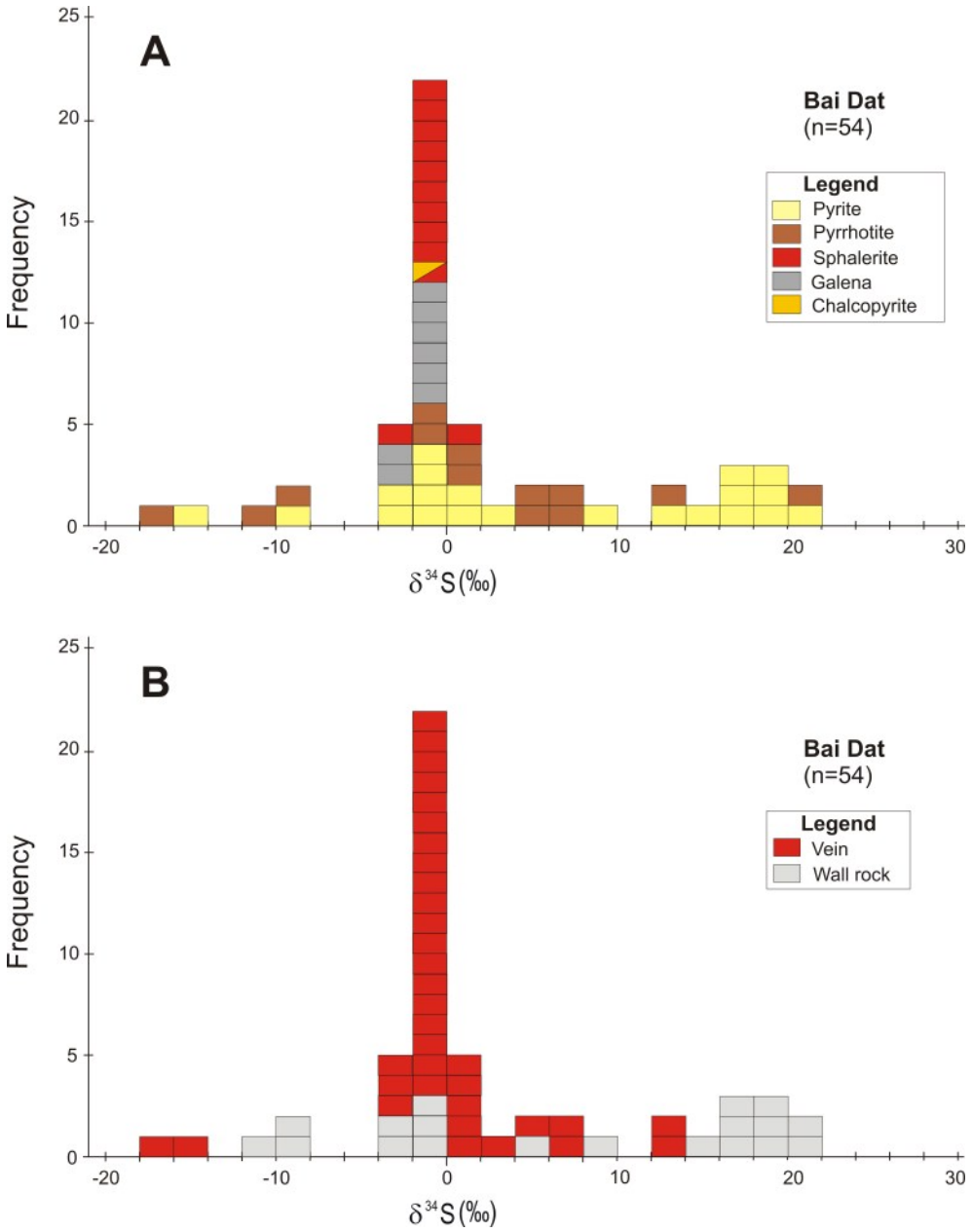

Fig. 6.1. Histograms of sulphur isotope data from the Bai Dat deposit in Phuoc Son. The results are illustrated in terms of **A.** sulphide mineralogy, and **B.** sample type.

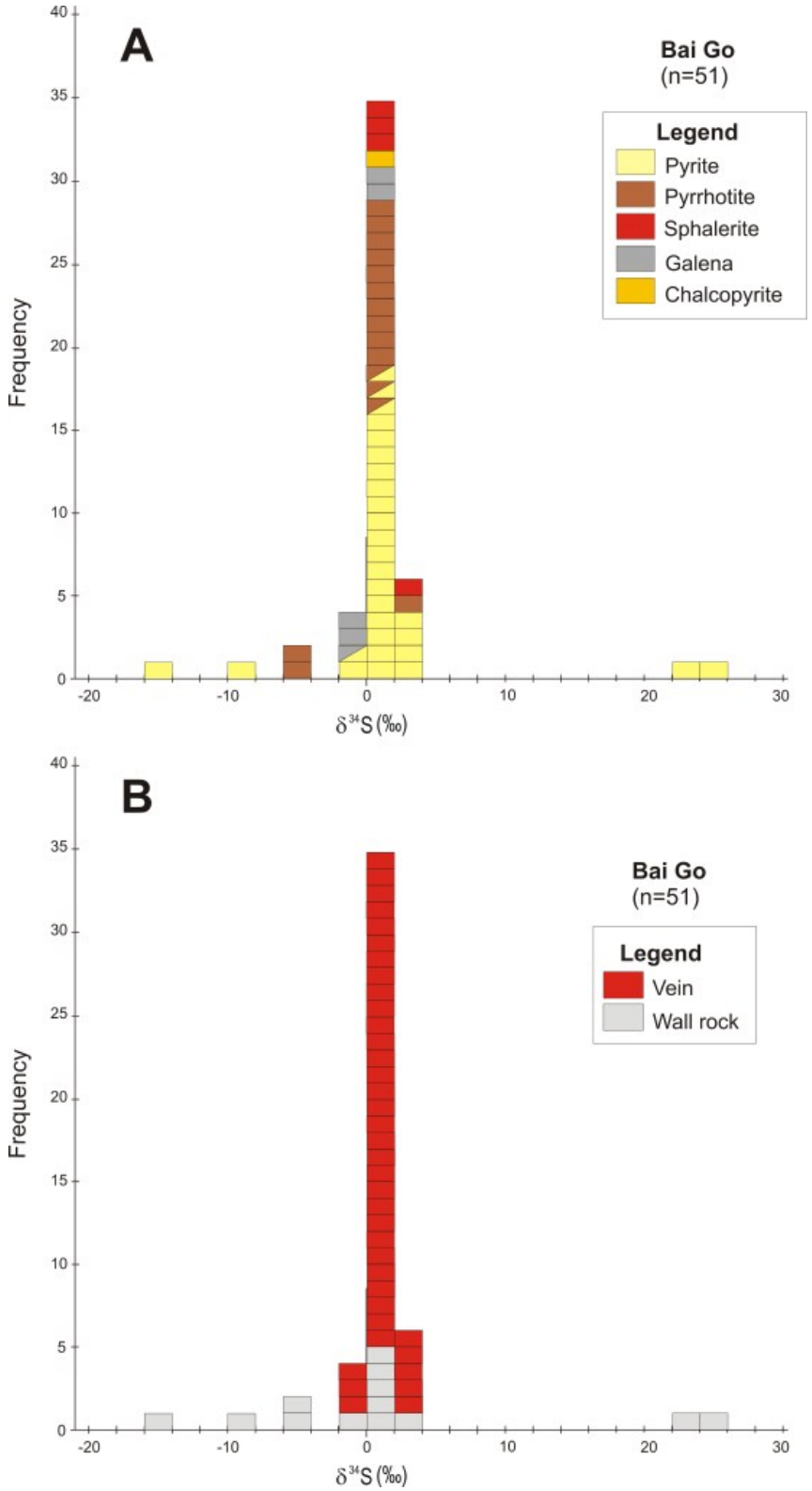

Fig. 6.2. Histograms of sulphur isotope data from the Bai Go deposit in Phuoc Son. The results are illustrated in terms of **A.** sulphide mineralogy, and **B.** sample type.

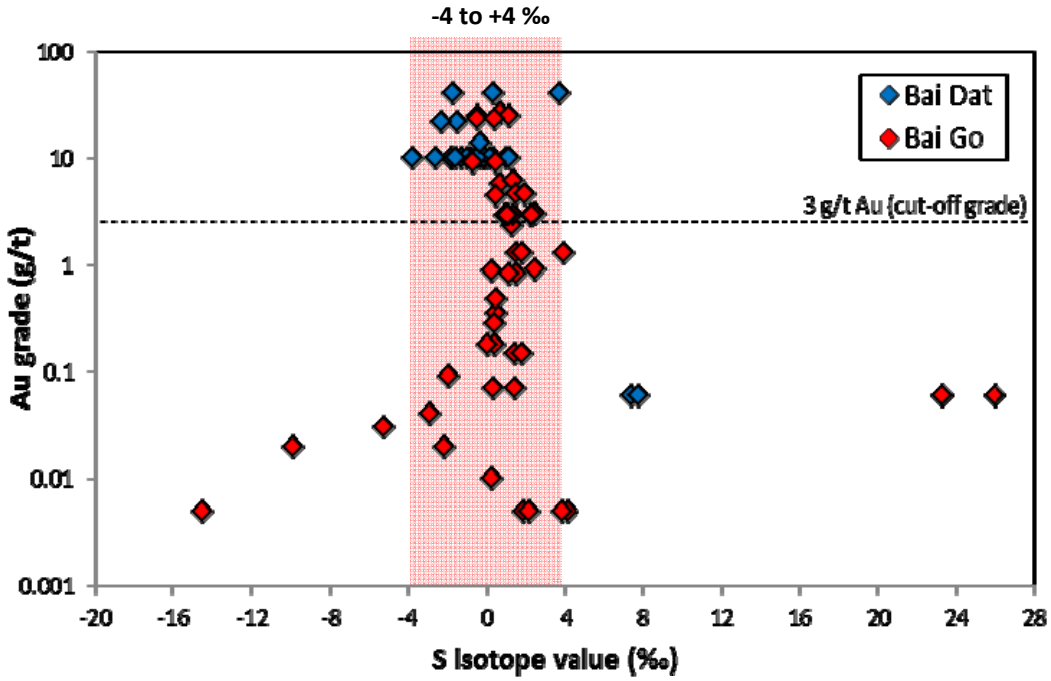

Fig. 6.3. Plot of gold assay grade versus sulphur isotope values for sulphides from the Bai Dat and Bai Go deposits, Phuoc Son deposit area. Note all of the high grade samples (in pink) range from -4 to +4 ‰.

Carbon has two stable isotopes, ^{12}C and ^{13}C, with an approximate natural abundance of 98.89% and 1.11%, respectively (Craig, 1957). The carbon isotopic composition of a compound is expressed as $\delta^{13}C$ relative to $^{13}C/^{12}C$ of the Chicago PDB (Belemnite from the Peedee Formation) standard, which is defined to have $^{13}C/^{12}C$ = 0.0112372 (Craig, 1957). Oxygen has three stable isotopes including ^{16}O, ^{17}O and ^{18}O with an abundance of 99.763%, 0.0375% and 0.1995%, and the isotope ratio $^{18}O/^{16}O$ is normally determined in oxygen isotope study (Rollinson, 1993). There are two isotopic standards used for oxygen isotope measurements involving PDB (a belemnite from the Cretaceous Peedee Formation of South Carolina) and SMOW (Standard Mean Ocean Water), and they are used for low and high temperature geothermometry measurements. The latter is commonly applied to ore deposit research (Rollinson, 1993).

Carbonate minerals were found to be intimately associated with the sulphide minerals in the mineralised veins at Bai Dat and Bai Go (Fig. 6.4A and B). Hence, carbon and oxygen isotopes of the vein-hosted carbonate minerals were analysed in this study to constrain the source of ore fluids and ore-forming conditions.

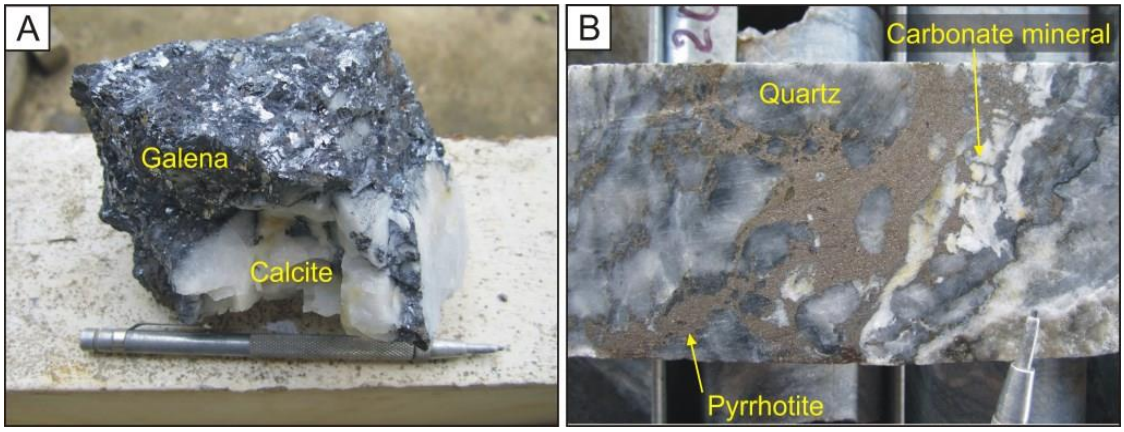

Fig. 6.4. Carbonate mineral-bearing ore samples from the Bai Dat and Bai Go deposits. **A.** Calcite associated with massive galena sample from Bai Dat underground mine. Sample No. TMBD11-13. **B.** Carbonate mineral associated with quartz-sulphide (mainly pyrrhotite) vein in drill core from Bai Dat. Sample No. DSDH270@122.7m.

6.3.2. Analytical method

In this study, a total of forty-three samples were selected for carbon and oxygen isotope analysis including thirteen samples each from Bai Dat and Bai Go and seventeen samples from other prospects in the Phuoc Son area. Carbonate minerals of the samples were measured at the CSL, University of Tasmania, following the method of McCrea (1950). The studied carbonate minerals were initially separated from hand specimen samples using a dentist's drill to obtain approximately 100 mg of powder. The separated samples were reacted with phosphoric acid at 25˚C for approximately 12 hours. The carbon dioxide gas liberated by this process was analysed using a Finnigan Isogas 2000 mass spectrometer. Carbon results are expressed in standard $\delta^{13}C$ per mil (‰) notation relative to the Pee Dee Belemnite (PBD), whereas oxygen data are expressed in standard $\delta^{18}O$ per mil (‰) relative to standard mean ocean water (SMOW).

6.3.3. Results

The raw and calculated carbon and oxygen isotope values of Bai Dat and Bai Go are illustrated in Figures 6.5 and 6.6, respectively, together with known values of major carbon- and oxygen-bearing materials in nature. The full carbon and oxygen isotope results including raw and calculated values are listed in Appendix XII. In this study, the isotopic compositions of the original fluids were determined using fractionation factors of the carbon and oxygen isotope values of Ohmoto and Rye (1979) and O'Neil et al. (1969). Temperature conditions of 300°C and 400°C were applied for the calculation based on the homogenisation temperatures (i.e., mode of 250–400°C) recorded from fluid inclusion microthermometry (see Chapter 7 for details).

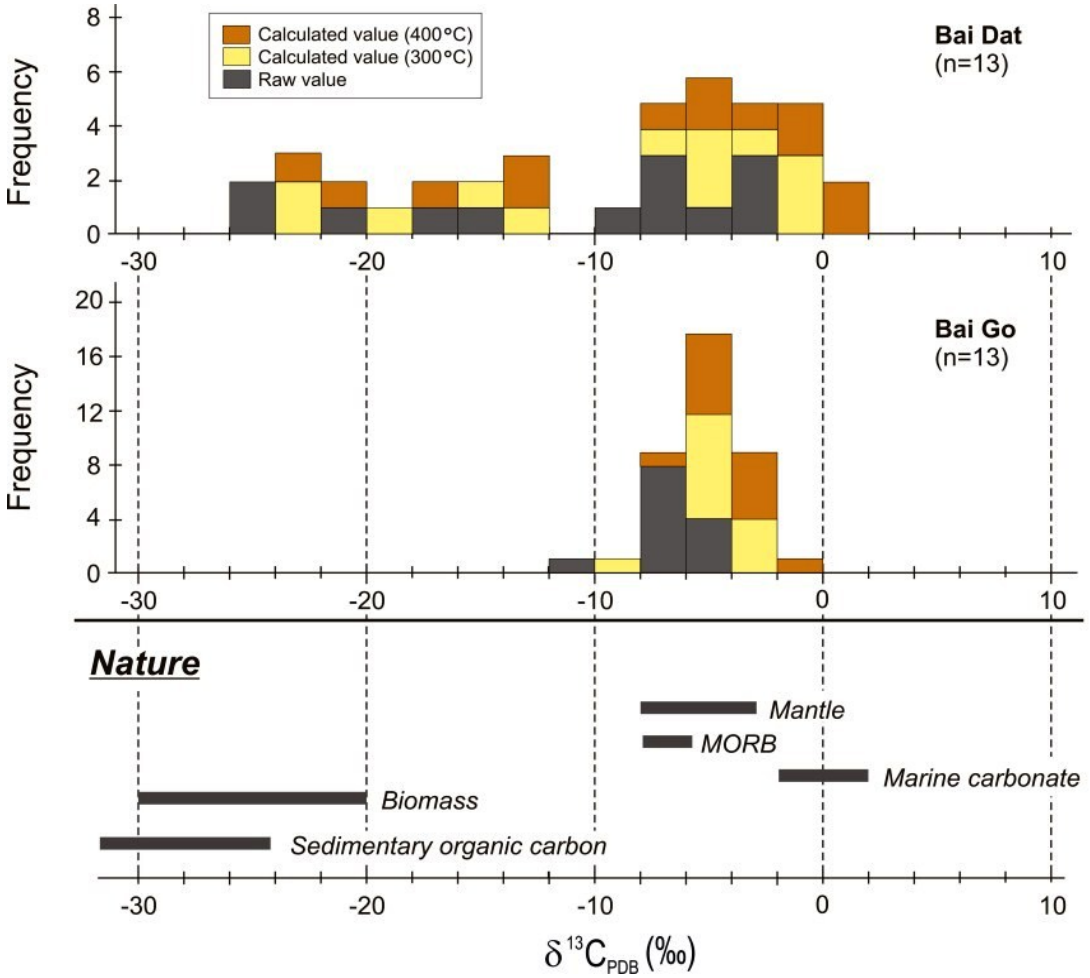

Fig. 6.5. Histograms of calculated $\delta^{13}C_{PDB}$ values of carbonates from Bai Dat and Bai Go. The isotopic compositions were calculated using temperatures of 300˚C and 400˚C and fractionation factors in Ohmoto and Rye (1979). Sedimentary organic carbon/bacteriogenic, magmatic and marine carbonate compositions are after Hoefs (1997).

The calculated carbon isotope results of the Bai Dat data show a wide range from -24 to +2 ‰, including two distinct values of -24 to -12 ‰ and -8 to +2 ‰, whereas the values of Bai Go are limited within a range of -10 to 0 ‰ (Fig. 6.5). The lighter populated data of Bai Dat are comparable to biomass/organic carbon values, while the heavier values of Bai Dat and all the measured values of Bai Go are within the isotopic range of mantle, MORB or marine values. The calculated oxygen isotope data of Bai Dat also have a wide range from -2 to +26 ‰ consisting of two distinctive ranges of -2 to +12 ‰ and +16 to +26 ‰ (Fig. 6.6). In contrast, the calculated oxygen isotope values of Bai Go are relatively confined to a range between +8 and +22 ‰ (Fig. 6.6). The range of the lighter values at Bai Dat is consistent with many reservoirs in nature such as mantle, igneous rocks (e.g., MORB and granitoids), metamorphic rocks and waters sourced from magmatic, metamorphic and meteoric reservoirs (Fig. 6.6).

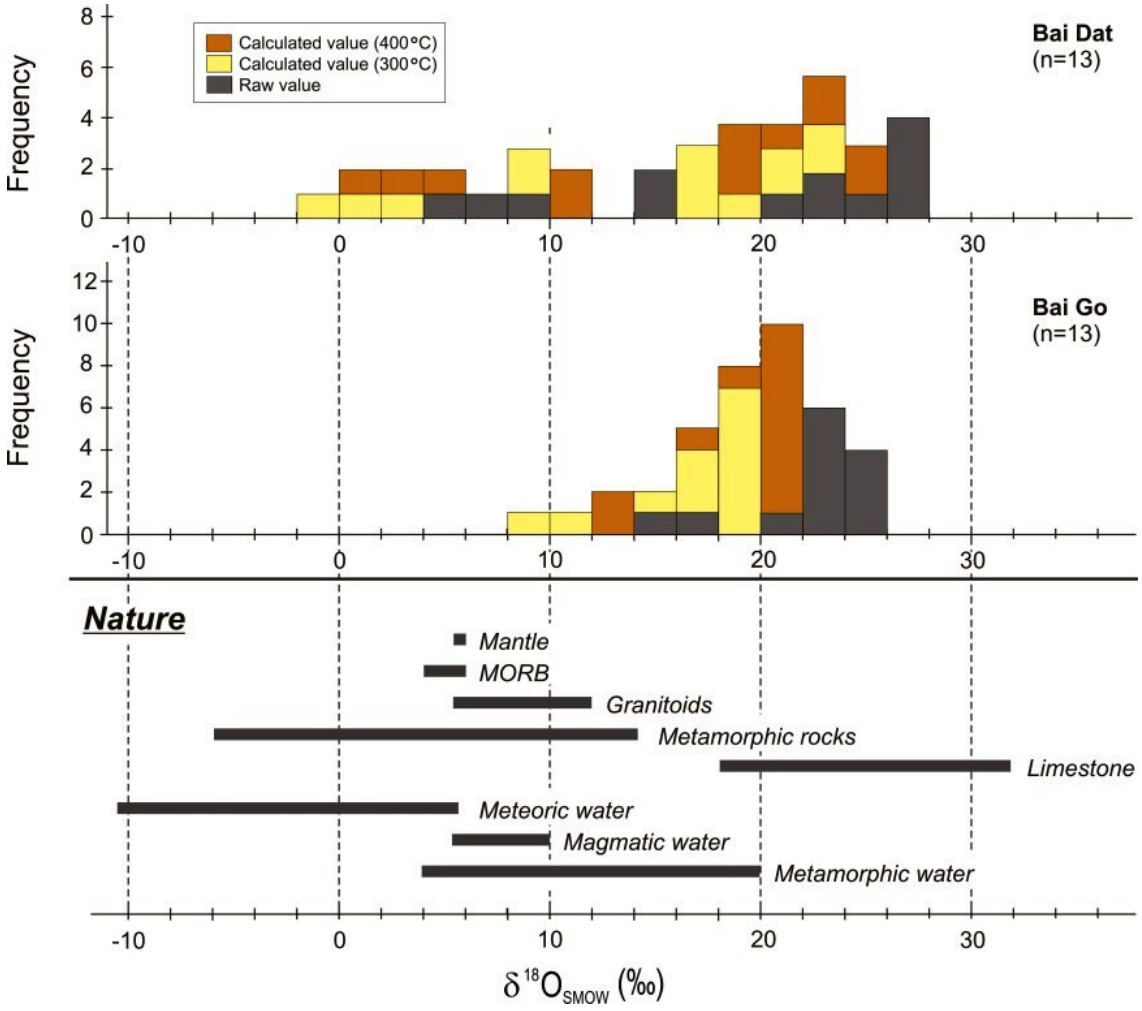

Fig. 6.6. Histograms of calculated $\delta^{18}O_{SMOW}$ values of carbonates from Bai Dat and Bai Go. The isotopic compositions were calculated using temperatures of 300˚C and 400˚C and fractionation factors in O'Neil et al. (1969). Magmatic, meteoric, metamorphic and marine carbonate compositions are after Hoefs (1997) and Best (2003).

Meanwhile, the heavier populated values obtained at Bai Dat and values of Bai Go are mainly comparable to ranges of limestone and/or metamorphic water (Fig. 6.6).

Plots of raw and calculated carbon and oxygen isotopic data of Bai Dat and Bai Go, together with marbles from other prospects in Phuoc Son, are shown in Figure 6.7A and B. It is interesting to note that the C-O plots of both raw and calculated data display a linear trend which connects limestone/marble and organic carbon fields, except two instances of data from wall rock at Bai Go (Fig. 6.7A and B). In addition, some of the Bai Dat data show distinctive light isotopic compositions and they plot on the organic carbon field. To assume the source(s) of carbon and oxygen, the data incorporated with those of other prospects in Phuoc Son are discussed in the later section of this Chapter.

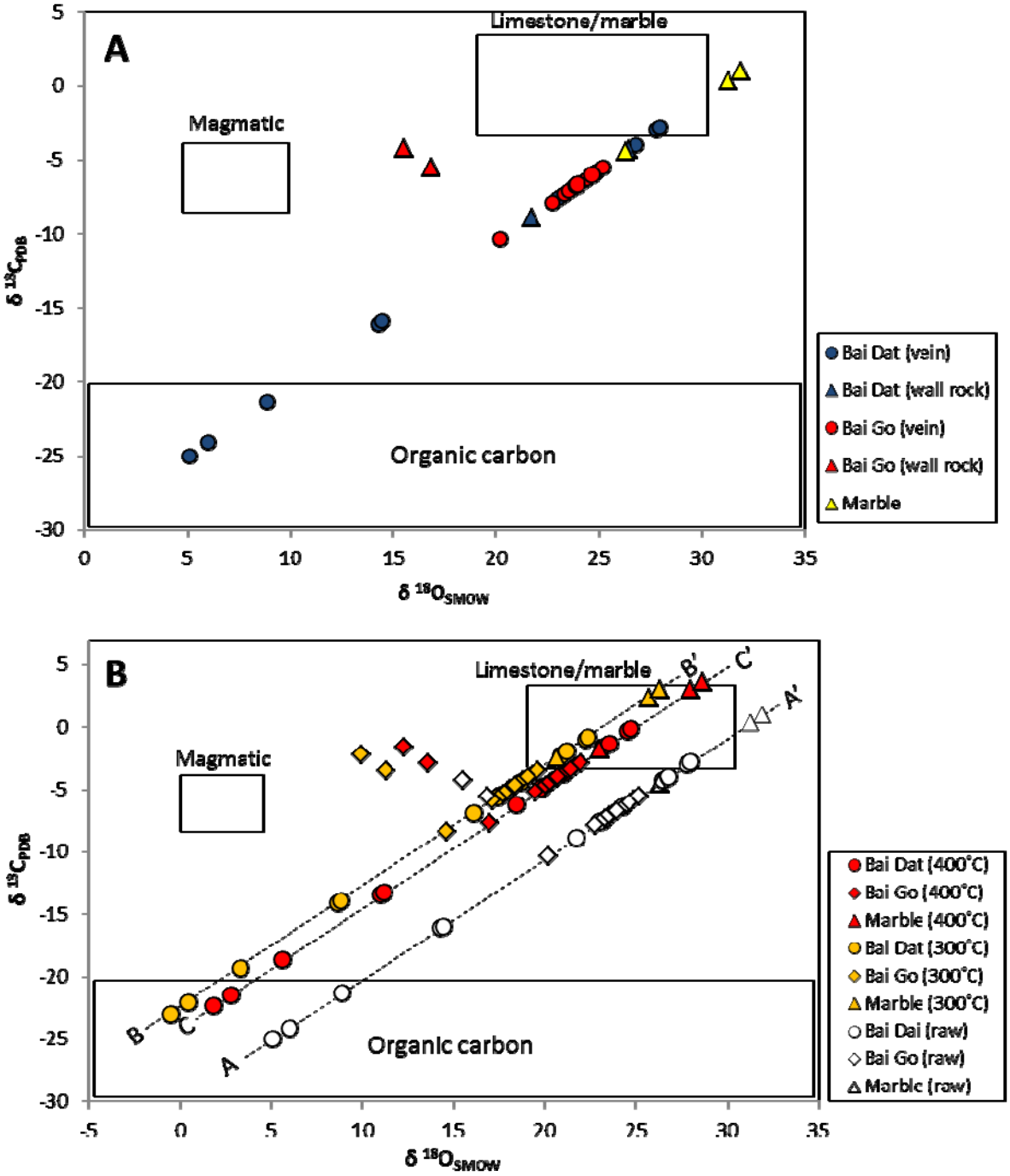

Fig. 6.7. Plots of carbon and oxygen isotope data from the Bai Dat and Bai Go deposits in Phuoc Son. **A**. Raw isotopic compositions and **B**. The isotopic compositions calculated using a temperature of 300°C and 400°C using fractionation factors of O'Neil et al. (1969) and Ohmoto and Rye (1979). Linear trends of raw data (A-A') and calculated data at 300°C (B-B') and 400°C (C-C') are noted. Calculated isotopic compositions are listed in See Appendix XII. Fields of typical magmatic fluids and limestone/marble are after Rollinson (1993) and organic carbon field is after Hofstra and Cline (2000).

6.4. LEAD ISOTOPES

6.4.1. Introduction

The ratios of ^{204}Pb, ^{206}Pb, ^{207}Pb and ^{208}Pb in Pb-rich minerals (e.g., galena, pyrite, K-feldspar) can provide information about the age and source of lead in ore deposits (Gulson, 1986). The lead isotopic composition in minerals and rocks is a mixture of primordial lead, which has existed on earth since it was formed (i.e., 4.57 Ga ago), and lead derived from the radioactive decay of U and Th (Gulson, 1986). Uranium and thorium are at the upper end of the decay chain, which proceeds through many intermediate steps before eventually ending at three different isotopes of Pb (^{206}Pb, ^{207}Pb and ^{208}Pb). One isotope of Pb (^{204}Pb) is not derived from the decay Th and U so that the $^{206}Pb/^{204}Pb$, $^{207}Pb/^{204}Pb$ and $^{208}Pb/^{204}Pb$ are continually changing through time. As a result of this, the age of Pb-rich minerals can be estimated as they preserve lead isotopic ratios present in the rocks when they were formed. Different Pb reservoirs in the earth have different U/Pb ratio (μ) so that Pb evolution does not proceed at the same rates in different parts of the crust and the mantle. The evolution of Pb in a reservoir is generally represented by a growth curve. One of the growth curves widely used for describing the evolution of the crust as a whole is the two stage model of Stacey and Kramers (1975). A more complicated set of growth curves for different reservoirs within the earth is outlined in Zartman and Doe (1981) in their plumbo-tectonic model.

The lead isotopic values are unique from region to region and have been used extensively in mineral exploration, in particular prioritising targets (prospects) by comparing data with nearby economic ore bodies. As galena commonly occurs in the mineralised veins at Bai Dat and Bai Go (Fig. 6.8A and B), the lead isotopic compositions were investigated to determine the model age and source of lead and the associated metals of the deposits.

6.4.2. Analytical method

In order to obtain lead isotopic compositions of sulphides in the main mineralisation stage at Bai Dat and Bai Go, eight samples including five from Bai Dat and three from Bai Go were selected for this study. All of the samples were collected from the galena-bearing mineralised veins. Two techniques including aqua regia acid digestion and LA-MC-ICPMS methods were used in this study to investigate the lead isotopic composition of the galena samples from the Bai Dat and Bai Go deposits. The two techniques are described below.

Aqua regia acid digestion (Galena solution): This technique was used for samples with large galena crystals which can be easily drilled out using a dentist's drill. 4 ml aqua regia (3 ml

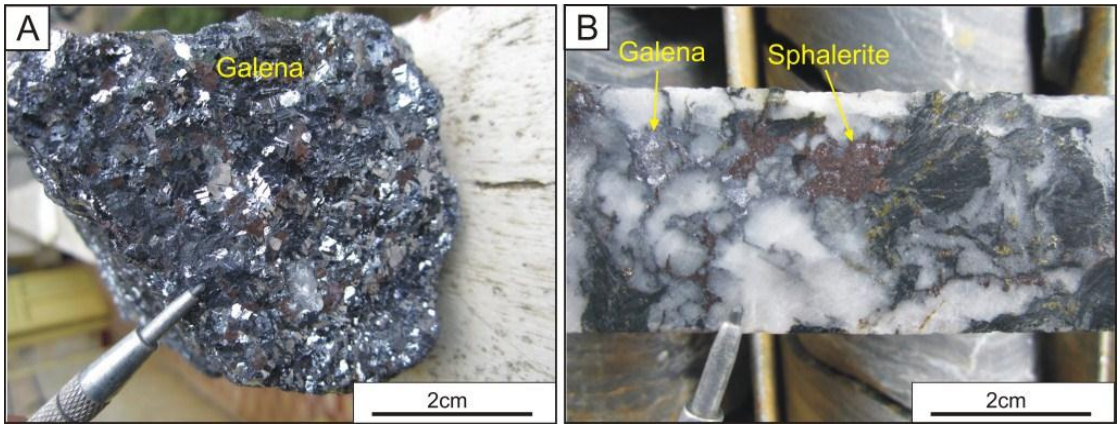

Fig. 6.8. Galena-bearing samples from Bai Dat and Bai Go. **A.** Massive galena collected from Bai Dat underground mine. Sample No. TMBD11-10. **B.** Galena-bearing quartz-sulphide vein from drill core of Bai Go. Sample No. DSDH199@230.2m.

HCl, 1ml HNO_3) was added to 50 mg of powdered galena sample in 7 ml screw top Teflon Savillex vessels, and heated on a hotplate at 120^{o}C overnight (~16 hours). They were then evaporated and placed on a hotplate to incipient dryness. To remove all HCl, 1ml of HNO_3 was added and evaporated to incipient dryness, and this step was repeated. The final residue was dissolved in 4 ml 50 % HNO_3 and heated at ~100^{o}C overnight. Samples were then diluted to 100 ml (1000 times dilution) with the final solutions in an acid matrix of 2% HNO_3. The samples were further diluted to 100,000 times, to measure the concentration of Pb, and then a final dilution was made to give ~150 ppb Pb in solution for isotope analysis. The samples were analysed on an Agilent 4500 ICP-MS within 24 hours of dilution. For more details of the technique see Townsend et al. (1988).

LA-MC-ICPMS: The LA-MC-ICPMS (laser ablation multi-collector inductively coupled plasma mass spectrometry) technique was applied in this study to lead isotopic composition of three galena samples from Bai Dat and Bai Go. All LA-MC-ICPMS analyses conducted at the University of Melbourne were performed on a Nu Plasma MC-ICPMS instrument, coupled to a HelEx laser ablation system, constructed around a Lambda Physik™ Compex 110 excimer laser operated with ArF providing an output wavelength of 193 nm. The system has been described by Eggins et al. (1998, 2005) and Woodhead et al. (2004, 2005, 2009). The laser output was adjusted to provide a fluence in the region of ~1 Jcm^{-2} and the laser was typically operated at a repetition rate of around 5 Hz, with spot sizes ranging from 150 to 200 μm. All data deconvolution was undertaken using the Iolite software package (Hellstrom et al., 2008), which allows for detailed visualisation of ion beam intensities versus time and integration of specific portions of the ablated signal. In this way it was possible to avoid any complications due to surface Pb contamination from sample polishing (surficial

contamination at some level is almost unavoidable during polishing of sulphides). Hg interferences on the ^{204}Pb isotope were corrected using an initial 'on peak' baseline followed by subtraction of any sample-derived Hg signal by monitoring the ^{202}Hg isotope and peak stripping. External mass bias corrections were applied, based upon analyses of sulphide standard 700380 (Jaguar deposit, W.A.), previously characterised by solution ICPMS while another sulphide (110028 Cobar, NSW), was used as secondary standard for monitoring data quality. The precision of this LA-MC-ICPMS system is 0.2 (2 s.e.) for the ^{206}Pb/^{204}Pb ratio and 0.005 (2 s.e.) for the ^{207}Pb/^{206}Pb ratio. A detailed description of the analytical methodology is provided in Woodhead et al. (2009).

6.4.3. Results

The lead isotopic composition data of the galena samples from Bai Dat and Bai Go are summarised in Table 6.1 for the values of ^{206}Pb/^{204}Pb, ^{207}Pb/^{204}Pb and ^{208}Pb/^{204}Pb, and the isotopic compositions are plotted in Figures 6.9 and 10. The Bai Dat samples have Pb isotopic values of 18.57–18.65 (^{206}Pb/^{204}Pb), 15.67–15.72 (^{207}Pb/^{204}Pb) and 38.54–38.71 (^{208}Pb/^{204}Pb). The lead isotopic compositions of Bai Go samples show ranges of 18.41–18.58 (^{206}Pb/^{204}Pb), 15.64–15.69 (^{207}Pb/^{204}Pb) and 38.40–38.58 (^{208}Pb/^{204}Pb). It is also noted in both the Bai Dat and Bai Go data that the lead isotopic values analysed by LA-MC-ICPMS are radiogenic and have heavier values than those analysed by solution technique (Figs. 6.9 and 10), particularly in the Bai Go data.

Table 6.1. Summary of lead isotopic data from the Bai Dat and Bai Go deposits, Phuoc Son.

Sample No.	Mineral	^{206}Pb/^{204}Pb	±1S	^{207}Pb/^{204}Pb	±1S	^{208}Pb/^{204}Pb	±1S	Method
Bai Dat								
TMBD11-07	Galena	18.61	0.06	15.72	0.04	38.63	0.05	1
TMBD11-10	Galena	18.61	0.09	15.69	0.08	38.54	0.09	1
TMBD11-13	Galena	18.57	0.06	15.68	0.06	38.58	0.07	1
PHUOC SON SOUTH	Galena	18.65	0.01	15.67	0.00	38.64	0.02	2
KZ0821	Galena	18.65	0.02	15.69	0.02	38.71	0.04	2
Bai Go								
DSDH40-145.4m	Galena	18.46	0.09	15.68	0.09	38.43	0.08	1
DSDH199-230.2m	Galena	18.41	0.09	15.64	0.06	38.40	0.07	1
DSDH209-325m	Galena	18.58	0.01	15.69	0.00	38.58	0.02	2

Methods; 1 = Aqua regia acid digestion, 2 = LA-MC-ICPMS

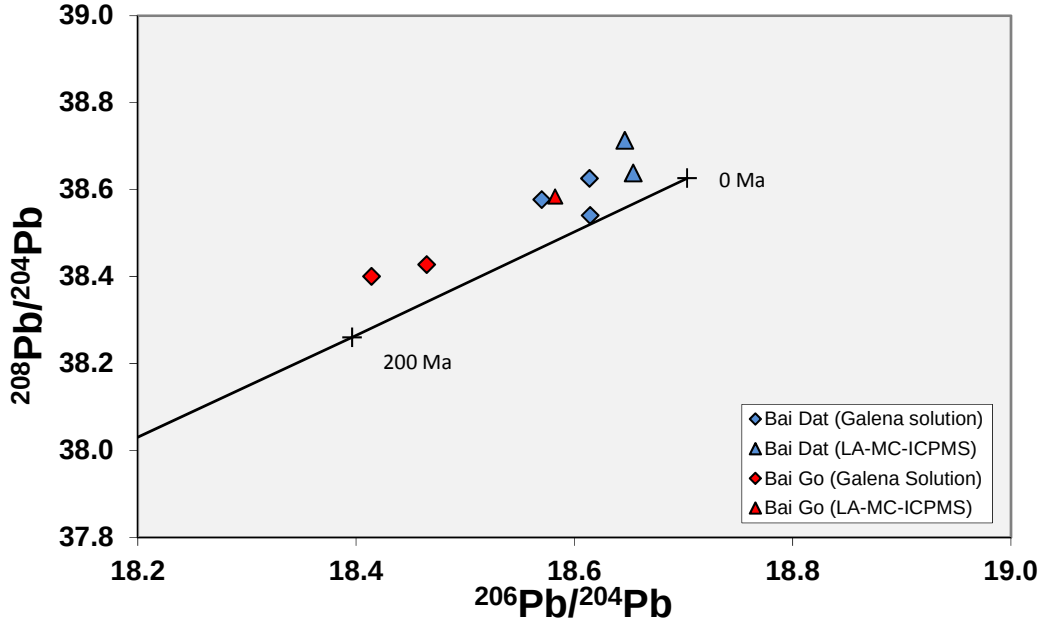

Fig. 6.9. Plot of lead isotopic compositions for $^{208}Pb/^{204}Pb$ versus $^{206}Pb/^{204}Pb$ from galena of the Bai Dat and Bai Go deposits, Phuoc Son. The growth curve is after Stacey and Kramer (1975).

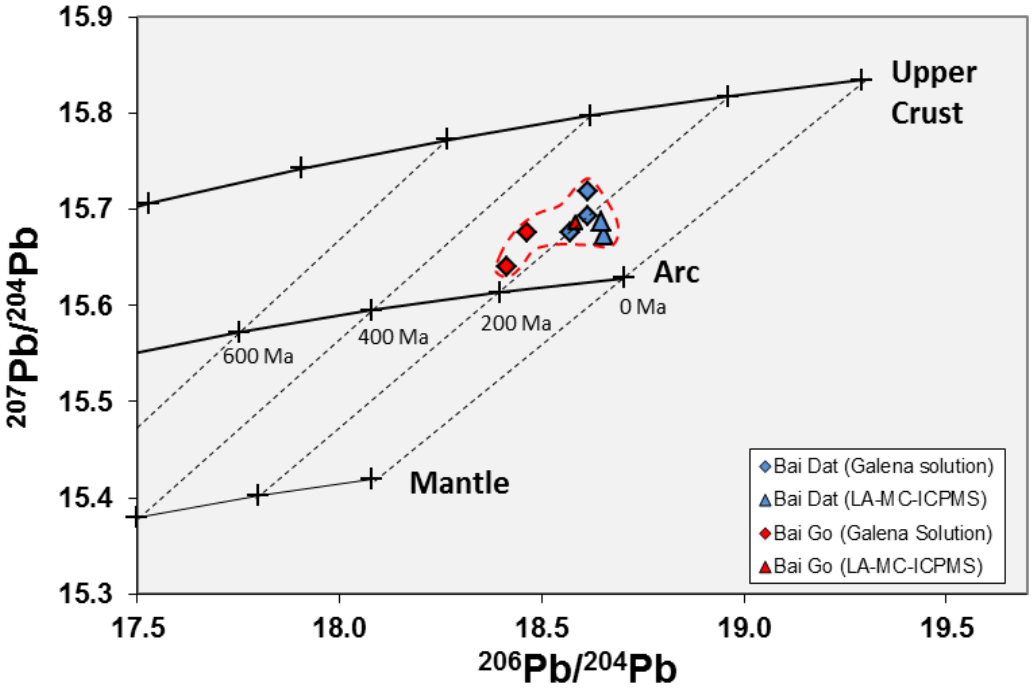

Fig. 6.10. Plot of lead isotopic compositions for $^{207}Pb/^{204}Pb$ versus $^{206}Pb/^{204}Pb$ from galena of the Bai Dat and Bai Go deposits, Phuoc Son. The growth curves are after Zartman and Doe (1981).

The lead isotope data of the Bai Dat and Bai Go deposits are plotted in a field between the upper crustal and arc growth curves of Zartman and Doe (1981; Fig. 6.10), suggesting that the lead source is a well-mixed source. To constrain timing of lead concentration (mineralisation), the lead isotope values of the Bai Dat and Bai Go deposits are correlated with the 200 Ma isochron of the growth curves of Zartman and Doe (1981), but the plotted data have large errors approximately ±100 Ma (Fig. 6.10). This suggests that the timing of lead concentration at Phuoc Son cannot be well constrained by the Pb-Pb model ages. However, the region covering central Vietnam has experienced two magmatic-metamorphic events during the Ordovician-Silurian and Permian-Triassic periods, which can be discriminated on the lead isotope plots, and thus the lead isotope data support the Permian-Triassic for the timing of mineralisation at Bai Dat and Bai Go.

6.5. DISCUSSION

6.5.1. Sulphur isotopes

The sulphur isotope data of the Bai Dat and Bai Go deposits constrained the sulphur isotopic compositions of sulphides from the mineralised quartz-sulphide veins (-4 to +4 ‰) and the wall rocks (-18 to +26 ‰). The source of the sulphur is discussed below.

Comparison with natural reservoirs and other Au-bearing deposits

The comparison of sulphur isotope values of Bai Dat and Bai Go with those of natural reservoirs and data from major gold-bearing deposits are shown in Figure 6.11. The comparison shows that the Bai Dat and Bai Go data are inferred to be a magmatic-derived source, which is broadly constrained to a range from -10 to +10 ‰, as represented by ranges of mantle, MORB and granites (Fig. 6.11). Although the Triassic granitic rocks in the Phuoc Son area are classified to be I-type, ilmenite-series (see Chapter 3 for details), the sulphur isotope values of Bai Dat and Bai Go are not clearly comparable to the ranges of I-type (-4 to +5 ‰) or S-type (-10 to +7 ‰), and magnetite- (+1 to +9 ‰) or ilmenite-series (-11 to +1 ‰) which are reported in literatures (Fig. 6.11; Coleman, 1977; Sasaki and Ishihara, 1979). In contrast, a wide range of sulphur isotope values in the wall rock samples (i.e., -18 to +26 ‰) may suggest that the sulphur was sourced from the meta-sedimentary units (i.e., schist and phyllite), as the wide range is only correlated with that of the sedimentary unit in nature (Fig. 6.11).

The comparison of the Bai Dat and Bai Go sulphur isotope data with other gold-bearing systems indicates that the sulphur isotope data of the vein-located sulphur (-4 to +4 ‰)

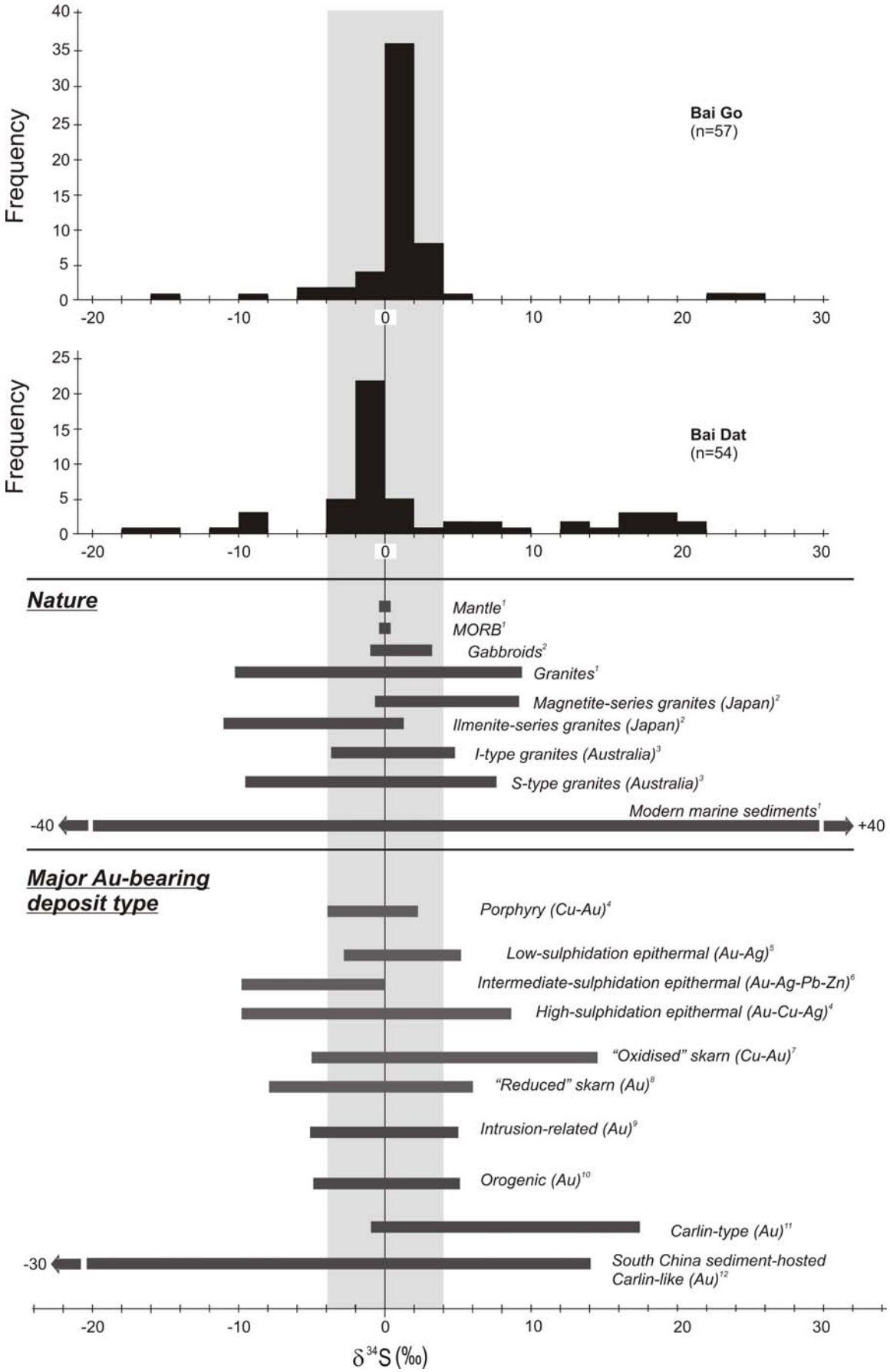

Fig. 6.11. Comparisons of sulphur isotope data of Bai Dat and Bai Go with major Au-bearing mineralised systems (sulphides) and reservoirs in nature. References are; 1= Rollinson (1993), 2= Sasaki and Ishihara (1979), 3=Coleman (1977), 4= Cooke and Simmons (2000), 5=Christie et al. (2007), 6=Camprubi and Albinson (2007), 7=Bowman (1998), 8=Khin Zaw et al. (2007b), 9=Thompson and Newberry (2000), 10=Hodkiewicz et al. (2009), 11=Hofstra and Cline (2000), 12=Zhang et al. (2005).

almost totally overlapped with the ranges of all of the magmatic deposits such as porphyry, epithermal (including low-, intermediate- and high-sulphidation), skarn (both oxidised and reduced) and intrusion-related systems (Fig. 6.11). These data indicate that the sulphur in the Bai Dat and Bai Go deposits is magmatic in origin.

Comparison with other systems of Truong Son Fold Belt (TSFB)

The main Bai Dat and Bai Go data (i.e., -4 to +4 ‰) are comparable to the values from the known skarn, epithermal and metamorphic-hosted Au-bearing deposits of TSFB (Fig. 6.12). Almost all of the TSFB's deposits exhibit sulphur isotope values ranging between -10 and +6 ‰. A genetic link to local magmatic activities was recognised at all of the deposits (see Chapter 2 for details), and thus the range is consistent with a typical magmatic sulphur range (-10 to +10 ‰; e.g., Rollinson, 1993). In contrast, the Carlin-like gold and Cu-Mo porphyry systems at Sepon contain light isotopic values (down to -14 ‰ and -30 ‰), suggesting involvement of other sulphur sources, such as biogenic or sedimentary origins (Cromie, 2010).

Comparisons with other deposits in the Phuoc Son deposit area

As well as Bai Dat and Bai Go, additional sulphur isotope data were analysed from other deposits (all of them are prospects) in the Phuoc Son deposit area (see Appendix VI for the values from the other prospects). Figure 6.13 shows that the sulphur isotope values in the Phuoc Son area appear to have consistently shifted from heavier to lighter values from the northernmost part (i.e., Khe Rin; +4 to +12 ‰) to Bai Dat (-4 to +2 ‰) in the southern part, via Round Hill, Khe Do, K7, Bai Go and Bai Chuoi deposits. Two deposits including Nui Vang and Bo are situated outside of the geographic trend and show heavier isotopic values than that of Bai Dat. The consistent change in sulphur isotopic values in the systems from the north to the south suggests possibilities, such as (1) temperature and/or redox changes of hydrothermal process, and/or (2) incorporation of external sulphur.

Wilson et al. (2007) studied the sulphur isotope behaviour of a few alkalic porphyry deposits in the Cadia District of Australia and identified a systematic sulphur isotope shift from negative to positive values from the core to the rim in the porphyry systems. They interpreted the shift in isotopic values to be due to cooling of ore-fluids, which occurred under oxidised conditions as heavy isotopes preferentially fractionate into oxidised sulphur species. However, the range of sulphur isotope values produced under reduced conditions is small according to Rye (1993). Wilson et al. (2007) demonstrated that the variation is limited to a few ‰ even from 600 to 250°C in the case of reduced ore-fluids, and thus cooling of reduced magmatic

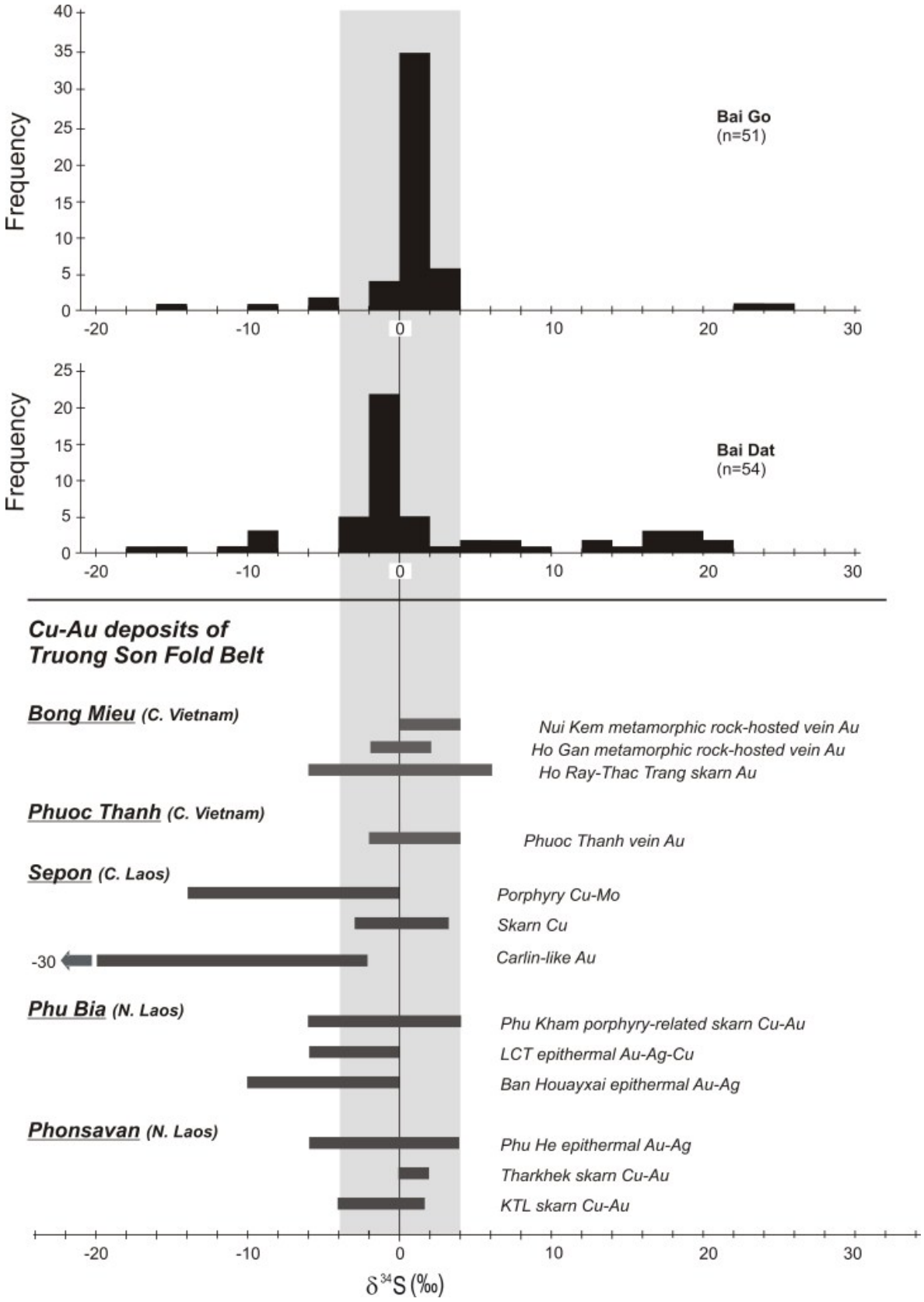

Fig. 6.12. Comparisons of sulphur isotope data of the Bai Dat and Bai Go deposits with major Cu-Au deposits of Truong Son Fold Belt in Laos and Central Vietnam. A range highlighted in grey (-4 to +4 ‰) is constrained from high gold grade values at Bai Dat and Bai Go (see Figs. 6.1 and 2). Bong Mieu data from Lee (2010) and Khin Zaw (unpub), Phuoc Thanh data from KORES (1999), Sepon data from Cromie (2010), Phu Bia data involving Phu Kham from Backhouse (2004) and Ban Houayxai and LCT from Manaka (2008), and Phonsavan data including Tharkhek, KTL and Phu He from Hotson (2009).

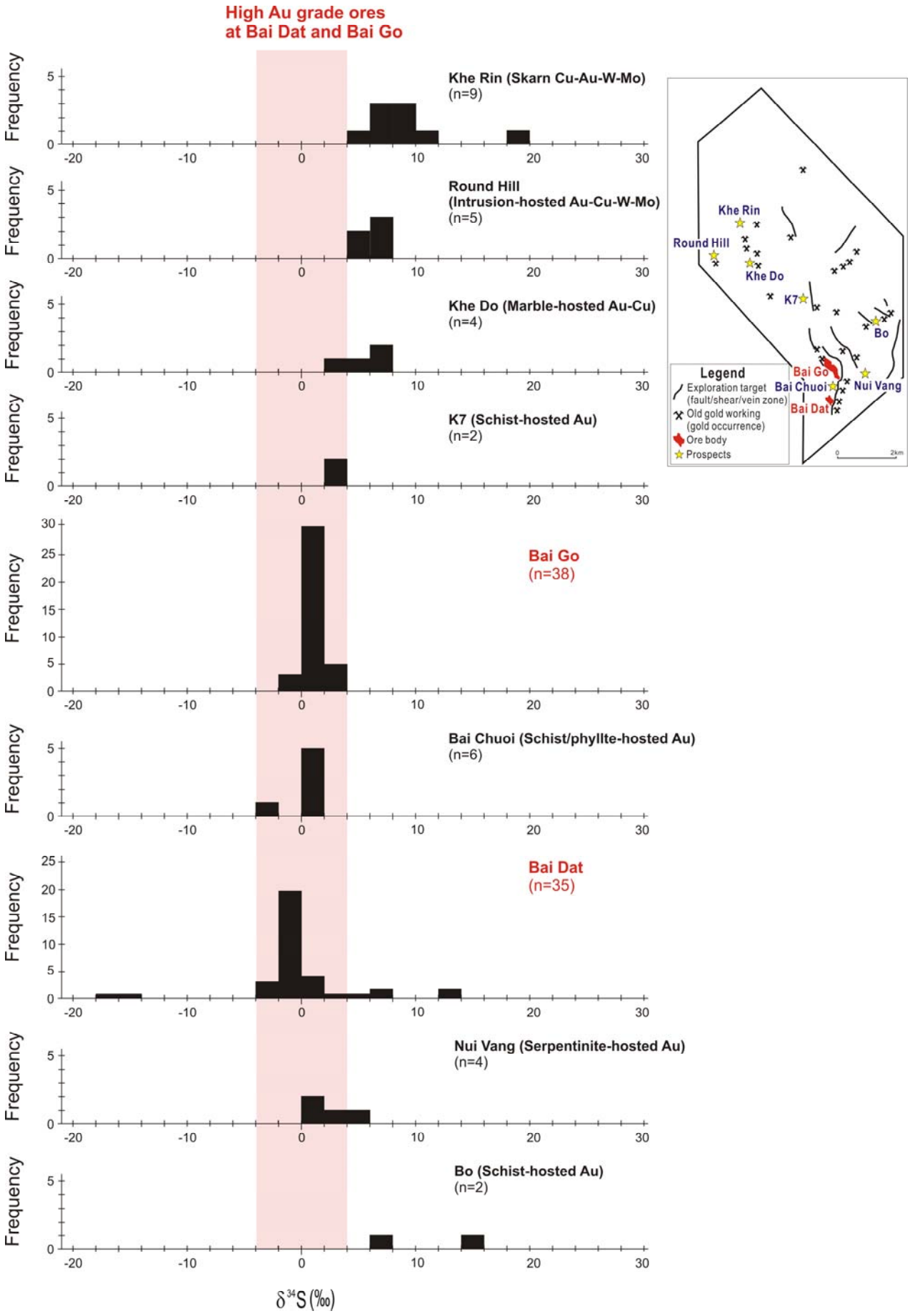

Fig. 6.13. Comparisons of sulphur isotope data of vein-located samples of Bai Dat and Bai Go with those of other prospects in the Phuoc Son deposit area. Note that all the data collected from ore samples from Bai Dat and Bai Go are confined to a range of -4 to +4 ‰ (coloured in pink).

fluids cannot fully explain the wide range in variation of the sulphur isotope values (>10 ‰) at the Phuoc Son deposit area.

Instead, a better explanation for the wide range of sulphur isotopes at Phuoc Son is possibly due to presence of two mixed sulphur sources. The heaviest values (up to +20 ‰) are recorded from Khe Rin, and in turn the lightest values (-16 to -14 ‰) are measured from un-mineralised veins at Bai Dat, which are geographically located at the northern and southern ends of the mineralised trend of Phuoc Son (Fig. 6.13). Based on the styles of mineralisation at Phuoc Son, skarn and intrusion-hosted deposits are located at the north (i.e, Khe Rin and Round Hill), whereas the deposits in the south (i.e., Bai Dat and Bai Go) are hosted by a carbonaceous schist/phyllite unit. This indicates that magmatic sulphur was sourced in the north whereas biogenic/sedimentary sulphur was sourced in the south and they were well mixed in the area between them during the mineralising event. A similar scenario is also reported by Yang and Lentz (2010), who investigated intrusion-related gold deposits at New Brunswick associated with reduced, ilmenite-series granitoids and explained the wide range sulphur isotopic values (i.e., -7 to +13 ‰) in the systems. They demonstrated that sulphur of external source (mainly sulphur from sedimentary unit in country rocks) is required to produce such a wide range of isotopic values.

6.5.2. Carbon and oxygen isotopes

A possible source of the carbon and oxygen in the Bai Dat and Bai Go deposits is discussed based on the carbon and oxygen isotopic compositions together with data from other mineralised systems in the Phuoc Son area.

Comparisons with other systems in Phuoc Son

Comparisons of the raw carbon and oxygen isotopic compositions of Bai Dat and Bai Go with those from other mineralised systems in Phuoc Son are shown in Figure 6.14, aiming to interpret the carbon and oxygen isotopic behaviour in terms of the Phuoc Son deposit area-scale. Although the data were obtained from different styles of mineralisation, such as intrusion-hosted (Round Hill), skarn (Khe Rin), marble-hosted (Khe Do), serpentinite-hosted (Nui Vang) and metasedimentary rock-hosted systems (K7, Bai Chuoi and Bo), all the data are linearly plotted along a 1:1 depletion line, which connects two points in the limestone/marble and organic carbon fields. The trend appears to be similar to that of Bai Dat and Bai Go, and thus carbon and oxygen behaviour in ore-fluids can be discussed based on the Phuoc Son deposit area-scale.

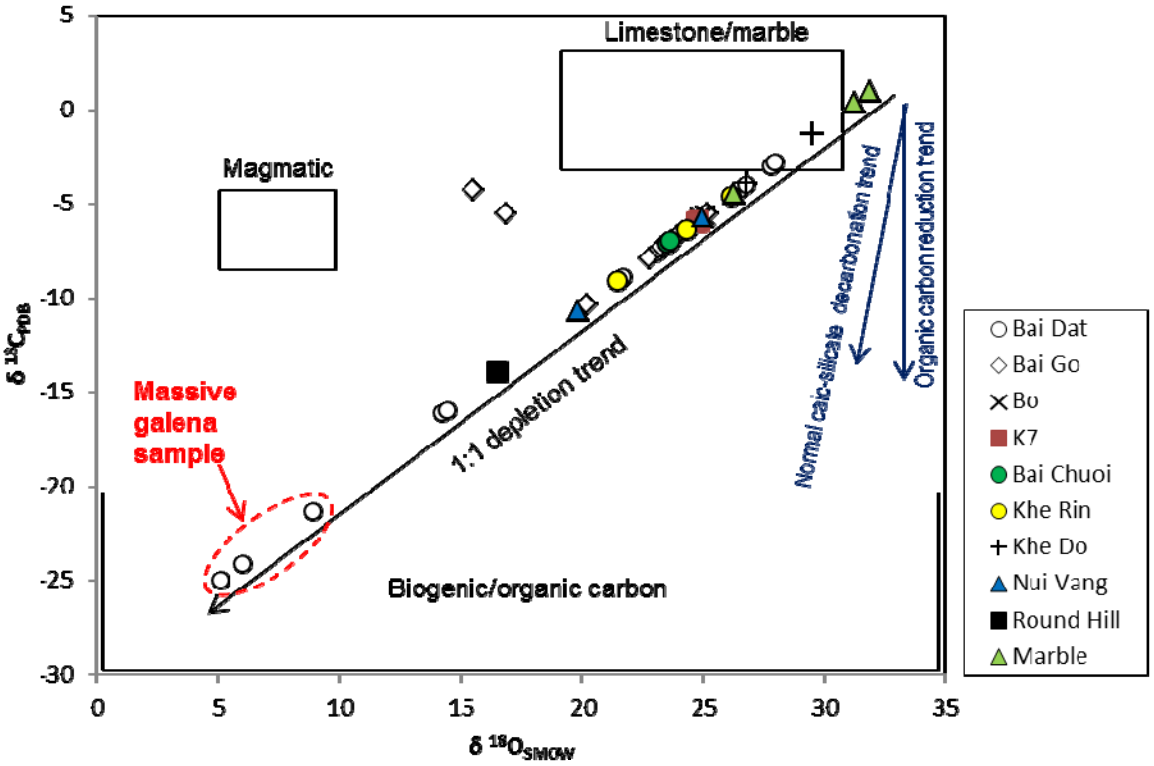

Fig. 6.14. Plots of carbon and oxygen isotope raw data from the Bai Dat and Bai Go deposits and other prospects in Phuoc Son. See Appendix XII for details. Fields of typical magma and limestone/marble are after Rollinson (1993) and organic carbon field is after Hofstra and Cline (2000). The trends of normal calc-silicate decarbonation and organic carbon reduction are after Bowman (1998).

Significant C-O depletion trend and source of carbon and oxygen

The 1:1 depletion trend provides a significant meaning to interpret the data. In general, a linear depleted trend in C-O isotopic plots is interpreted to be due to decarbonation and/or graphite exchange reactions (see Fig. 6.14 for typical trends). Both reactions can account for a large depletion in carbon isotopic values, but depletion of oxygen is commonly minor (or none for graphite exchange trend, in theory). Thus, the simple decarbonation and/or graphite exchange reactions cannot explain the significant C-O depletion trend of the Phuoc Son data. The most likely process to explain the linear C-O isotope trend in Phuoc Son data is exchange of fluids sourced from limestone/marble and organic carbon-rich units. This is consistent with the field geology of the Phuoc Son area as both the marble and organic carbon-rich (i.e., carbonaceous schist/phyllite) units are commonly present in the deposit area. It is remarkable that the most depleted carbon and oxygen data in the C-O isotope trend are from massive galena samples of the Bai Dat deposit in which the carbonaceous schist/phyllite unit is dominant. In addition, the geological setting during the mineralising event at Phuoc Son supports the interpretation, as the regional metamorphism could have let the exchange process

proceed slowly and homogenise the values to form a linear depletion trend (i.e., 1:1 depletion trend).

Near-linear carbon-oxygen isotopic plots are known in a few skarn deposits as reported by Bowman (1998), and the interpretations made therein will assist to interpret the Phuoc Son data. For example, the Osgood Mountains W-Cu-Au deposit in USA has a near-linear trend in C-O isotopic plots of calcite and it is interpreted that the trend indicates a process of exchange between calcite and graphite in the wall rocks. As graphite is commonly present in the marbles of the Osgood Mountains, this process could produce additional C isotope depletion in calcite (Taylor and O'Neil, 1977; Bowman, 1998).

6.5.3. Lead isotopes

The lead isotopic compositions of the Bai Dat and Bai Go deposits in Phuoc Son are compared with other deposits of TSFB and those of other mineralised belts in the Indochina Terrane, to provide a concrete interpretation of the Bai Dat and Bai Go data.

Comparisons with other systems of TSFB

The Bai Dat and Bai Go data are compared with major copper and gold deposits of the TSFB which are genetically linked to the local magmatism (Fig. 6.15). As well as Phuoc Son and Bong Mieu in central Vietnam, almost all of the deposits of the TSFB including Phu Bia (Phu Kham Cu-Au skarn, Ban Houayxai Au-Ag epithermal and LCT Au-Ag-Cu epithermal deposits), Phonsavan (KTL Cu-Au skarn, Phu He Au-Ag epithermal and NNN Au epithermal deposits) and Sepon (Carlin-like Au and skarn Cu-Au deposits) fall in a field between the upper crust and arc growth curves of Zartman and Doe (1981). This indicates that lead in the deposits of the TSFB was homogeneously derived from a well-mixed crustal source (Fig. 6.15). The lead isotope data from Phuoc Son and Bong Mieu in central Vietnam are slightly more radiogenic compared to those of Phu Bia, Phonsavan and Sepon areas. This may have resulted from the timing of lead concentration as the magmatic-metamorphic event in central Vietnam is slightly younger (265–230 Ma) than the magmatism at Phu Bia, Phonsavan and Sepon districts (310–275 Ma). Lead isotope data in the granites of TSFB are more radiogenic, probably because the lead isotopic compositions in K-feldspars are affected by decay of U and Th and additional radiogenic lead is involved.

Comparisons with other mineralised belts in the Indochina Terrane

A comparison of lead isotopic signatures of TSFB including the Bai Dat and Bai Go deposits with those of other mineralised belts in the Indochina Terrane including Loei, Sukhothai,

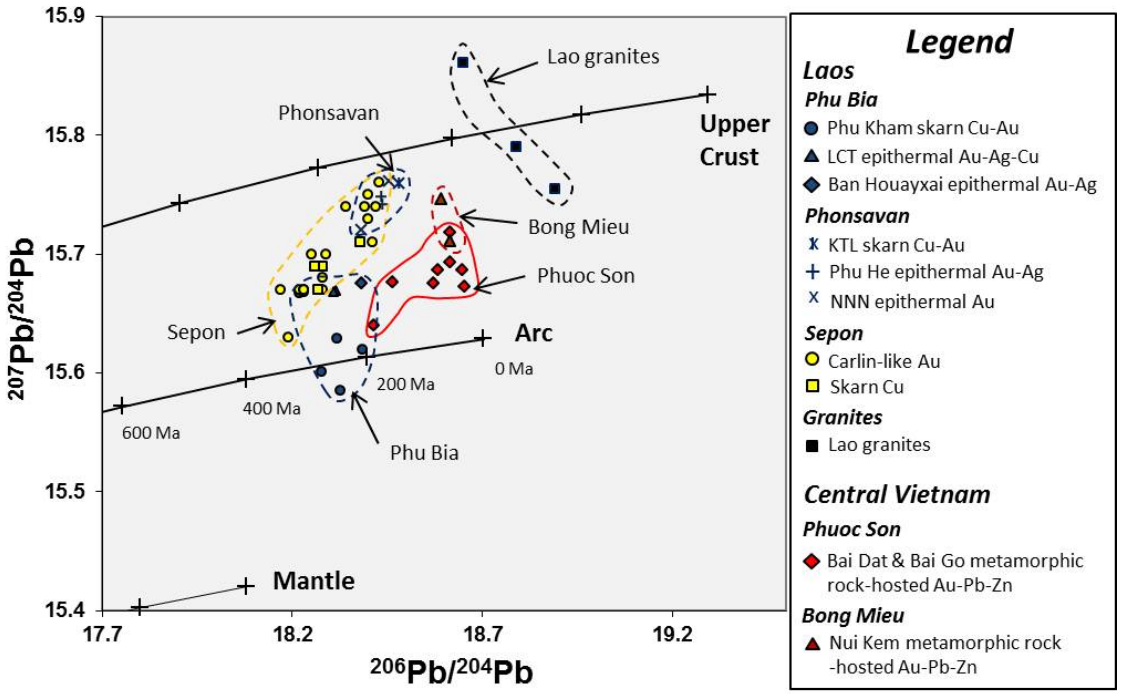

Fig. 6.15. Comparison of lead isotopic compositions for $^{207}Pb/^{204}Pb$ versus $^{206}Pb/^{204}Pb$ from Phuoc Son with data from other deposits and granites of Truong Son Fold Belt. The data sources are: Sepon from Cromie (2010), LCT and Ban Houayxai from Manaka (2008), Phu Kham, KTL, Phu He, NNN, Lao granites and Bong Mieu are from Khin Zaw et al. (2010) and Phuoc Son from this study.

Chiang Mai and Dalat-Kratie Belts is shown in Figure 6.16. The comparison indicates that data of all of the mineralised belts are plotted on a field between the arc and crust growth curves. The lead isotopic model ages of the fields are more or less consistent with ages of the local magmatic(-metamorphic) events (e.g., Khin Zaw et al., 2010), suggesting that the lead was sourced from the localised magma. The mineralised systems in the Chatree area contain exceptionally older lead isotopic ages (c.a., 400 Ma), although the deposits are hosted by the Permian-Triassic igneous units, and this lead isotopic composition suggests that the lead may have been sourced from the local source rocks (i.e., older basement rocks underlying the Chatree District; Salam, 2013). Thus, these comparisons support the interpretation that the gold mineralisation at Bai Dat and Bai Go occurred during the Permo-Triassic magmatic and metamorphic event.

6.6. SUMMARY

Major conclusions drawn from the sulphur, carbon, oxygen and lead isotope data include:

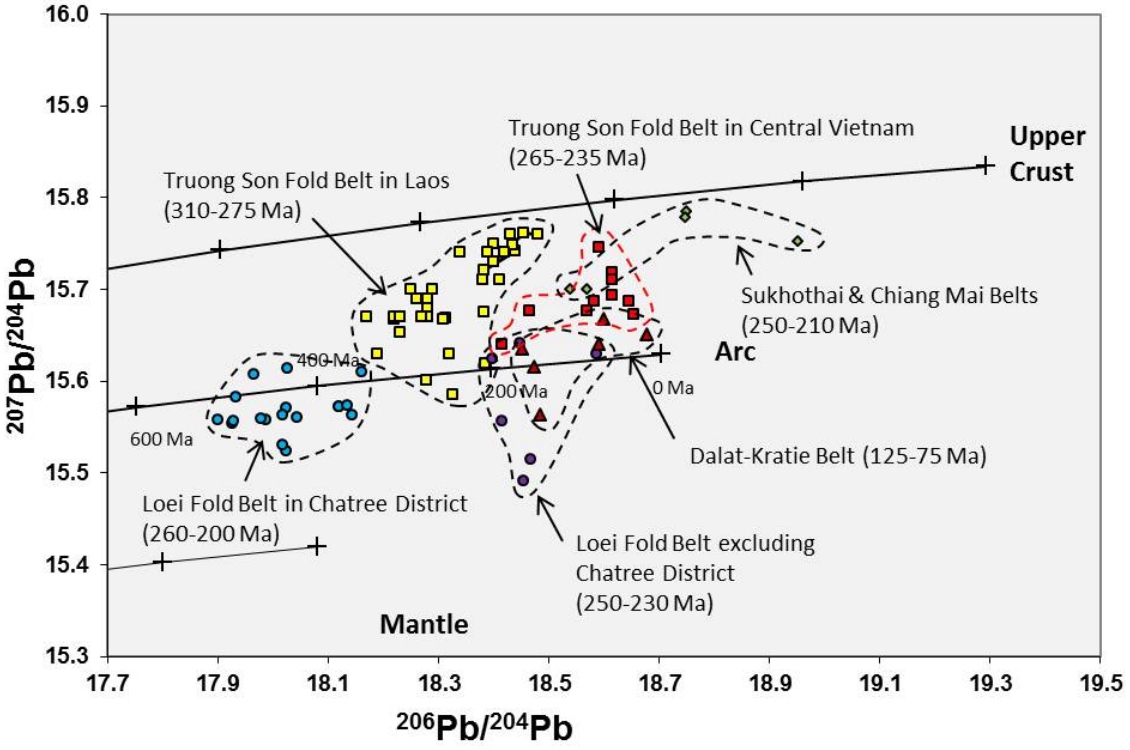

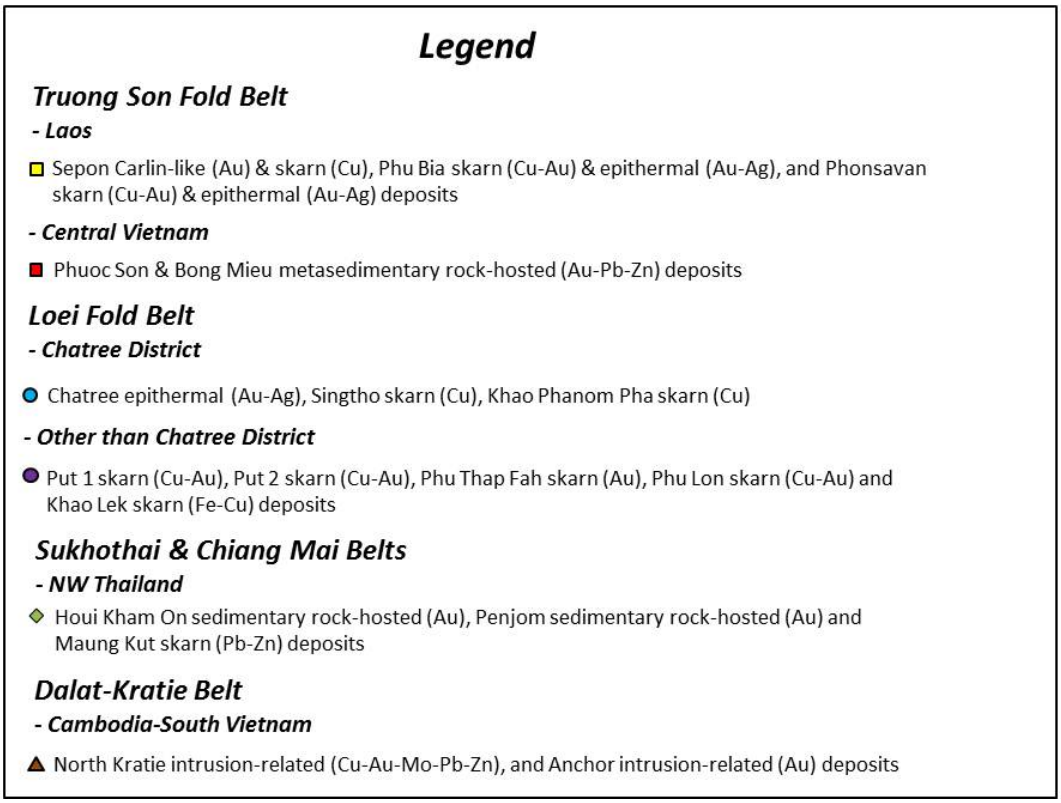

Fig. 6.16. Comparison of lead isotopic compositions for $^{207}Pb/^{204}Pb$ versus $^{206}Pb/^{204}Pb$ of ore deposits of the Truong Son Fold Belt with other mineralised belts of Indochina Terrane including Loei, Sukhothai-Chiang Mai and Dalat-Kratie Belts. The growth curves are after Zartman and Doe (1981). Sources of lead isotope data include Sepon from Cromie (2010), Chatree from Salam (2013), LCT and Ban Houayxai from Manaka (2008), Penjom from Makoundi (2012), Phuoc Son from this study, and the rests from Khin Zaw et al. (2010).

Sulphur isotopes

- The sulphur isotope values from the Bai Dat and Bai Go deposits have two groups of sulphur isotope compositions including narrowly ranging values (mainly -4 to +4 ‰) in vein-located sulphides and widely ranging values (-18 to +26 ‰) in wall rock sulphides.

- The range of the vein-located sulphides is consistent with a magmatic source compared with magmatic sulphur isotope range in nature and other magmatic deposits (e.g., porphyry, skarn and epithermal systems).

- The comparison of the Bai Dat and Bai Go data with other deposits in the Phuoc Son area shows that the values consistently shift from heavier to lighter values from the northern to the southern parts of the Phuoc Son area. The heaviest values in the Khe Rin skarn and Round Hill intrusion-related deposits at the northernmost part are characterised by magmatic sulphide. The Bai Dat deposit located at the southernmost part of the systems contains the lightest sulphur isotope values and thus they are interpreted to have been additionally sourced from the host carbonaceous schist/phyllite.

Carbon and oxygen isotopes

- Plots of C-O isotope data of Bai Dat and Bai Go, together with those from other prospects in Phuoc Son, show that almost all of the data are plotted on a linear trend connecting the limestone/marble and organic carbon fields.

- The trend may indicate that carbon and oxygen in ore fluids were mainly supplied from two sources involving marble and carbonaceous schist/phyllite. This interpretation is also supported by the field data of the Phuoc Son area as the lightest C and O isotope values are recognised in the samples from Bai Dat where a carbonaceous schist/phyllite unit is dominant. In addition, it is marked that the data are well homogenised and this may indicate that the exchange reaction occurred very slowly.

Lead isotopes

- Lead isotope data of the Bai Dat and Bai Go deposits indicate that the lead was sourced from a mixed crustal and mantle source, which commonly occurs at subduction-related arc environments. Timing of the lead concentration is suggested to be approximately 200 Ma (with large errors; ±100 Ma).

- This interpretation is supported by a comparison with data of other deposits and mineralised belts in the Indochina Terrane, suggesting that the gold mineralisation at Phuco Son is related to the local Triassic magmatic-metamorphic event at the Phuoc Son area.

CHAPTER 7 FLUID INCLUSIONS

7.1. INTRODUCTION

Fluid inclusions provide important information about the nature and origin of ore-forming fluids and the physico-chemical conditions of ore formation such as temperature, salinity, pressure and redox changes. In particular, fluid inclusion data indicate ore depositional mechanism such as mixing, boiling and conductive cooling (e.g., Roedder, 1984; Shepherd et al., 1985; Bodnar, 2007), and thus their study often plays a key role in ore deposit research. Information about fluid inclusions is also commonly applied in exploration activities to characterise the nature of hydrothermal fluids and constrain deposit types (e.g., Roedder and Bodnar, 1997).

In this study, fluid inclusions were investigated to characterise the ore-forming fluids of the Bai Dat and Bai Go deposits, based on detailed petrography, microthermometry and Laser Raman Spectroscopy (LRS). Microthermometry provides two significant aspects of fluid conditions involving fluid temperatures and salinities by heating/freezing experiments, and also allows an estimate of pressure and depth of ore formation to be made. The LRS studies can detect the gaseous composition of inclusions and identify daughter minerals as an in-situ non-destructive method.

7.2. ANALYTICAL METHODS

7.2.1. Sample preparation

For this study, samples were carefully and systematically collected from the deeper to shallower parts of mineralised veins at Bai Dat and Bai Go, aiming to detect temporal chemical gradients, which will explain the mechanism of metal deposition.

Careful attention was also paid to the preparation of fluid inclusion chips to select and measure primary fluid inclusions associated with the mineralising event. Samples were mainly chosen from quartz-sulphide veins in drill cores of Bai Dat and Bai Go (Fig. 7.1A and B), and massive sulphide samples from the Bai Dat underground mine were also used. In particular, galena-rich massive sulphide samples were preferentially selected for this study as

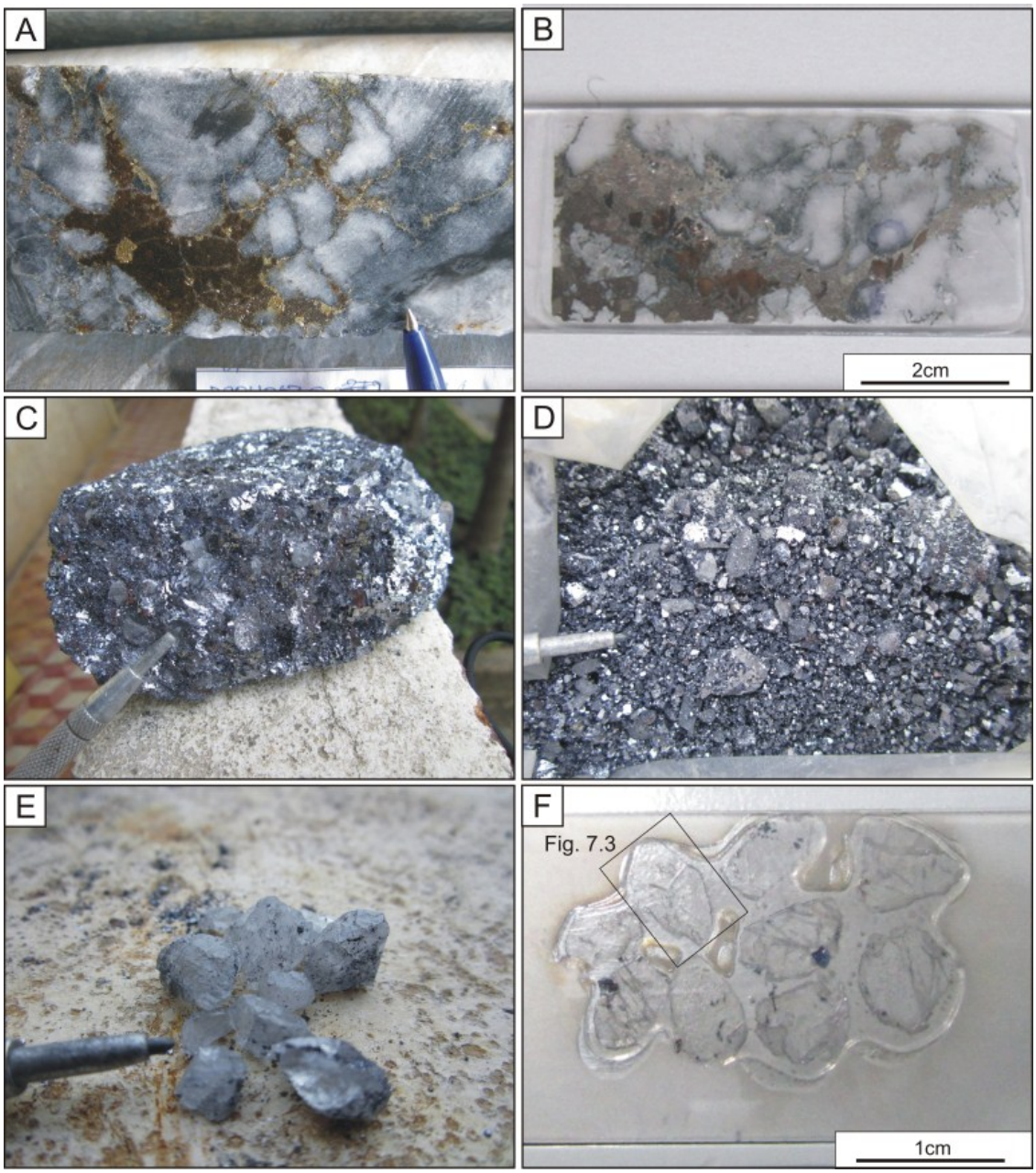

Fig. 7.1. Photographs showing fluid inclusion chips prepared from quartz-sulphide vein and massive sulphide samples of the Bai Dat and Bai Go deposits. **A.** Drill core sample of quartz-sulphide vein selected for fluid inclusion study. Sample No. DSDH257@463.4m (Bai Dat). **B**. Fluid inclusion chip prepared from the drill core sample in Fig. A. **C.** Massive galena sample collected from underground mine site at Bai Dat. Sample No. TMBD11-07 (Bai Dat). **D.** Massive galena sample in Fig. C was crushed in order to separate quartz grains from galena crystals. **E.** Euhedral quartz crystals picked up from the crushed massive galena sample of Fig. D. **F.** Fluid inclusion chip prepared from the quartz crystals in Fig. E.

they are associated with the main gold mineralisation stage at Bai Dat and Ba Go and commonly involve visible, euhedral quartz crystals and can be easily separated by hand picking (Fig. 7.1C, D, E and F).

7.2.2. Microthermometry

A total of six quartz-sulphide vein and massive galena samples were used for microthermometric analysis, including three each from Bai Dat and Bai Go. The samples were spatially collected from the shallower to the deeper parts at the both Bai Dat and Bai Go deposits (Fig. 7.2A and B). The microthermometric measurements were conducted using Linkham TH600 heating/freezing stage at CODES, University of Tasmania, to determine the homogenisation temperature and salinity of fluid inclusions at Bai Dat and Bai Go. The general method and procedure for heating/freezing experiments are reported elsewhere (e.g., Roedder, 1984). The precision of the temperature measurements is better than ± 1°C for heating and ± 0.3°C for freezing. Accuracy of the measurements was insured by calibration against the triple point of CO_2 (-56.6°C), the freezing point of water (0.0°C), the critical point of water (374.1°C) and synthetic fluid inclusions. Either clathrate melting or final ice melting temperatures were measured to estimate salinity values using the equations of Chen (1972) and Bodnar (1993), respectively. The equation of Bodnar (2003) was also applied to calculate salinity values using halite dissolution temperature for halite-bearing inclusions.

7.2.3. Laser Raman Spectroscopy

The LRS study was attempted to estimate the volatile composition of fluid inclusions such as CO, CO_2, CH_4, H_2, H_2S, N_2, NH_3 and SO_2, and also to identify some unknown daughter minerals in inclusions of the Bai Dat and Bai Go samples. The LRS analysis was conducted by Terry Mernagh at Geoscience Australia in Canberra using a Dilor® SuperLabram spectrometer equipped with a hologenic notch filter, 600 and 1800 g/mm gratings, and a liquid-N_2-cooled, 2000 × 450 pixel CCD detector. The inclusions were illuminated with 514.5 nm laser excitation from a Spectra Physics Model 2017 argon ion laser, using 5 nW powers on the samples, and a single 30 second accumulation. The focused laser spot on the samples was ~1 μm in diameter. Wavenumbers are accurate to ±1 cm^{-1} as determined by plasma and neon emission lines. For the analysis of CO, CO_2, O_2, N_2, H_2S and CH_4 in the vapour phase, spectra were recorded from 1000 to 3800 cm^{-1} using a single 20 seconds integration time per spectrum. Raman detection limits are estimated to be ~0.1 mol. % for CO_2, O_2 and N_2, and 0.03 mol. % for H_2S and CH_4, and errors in the calculated gas ratios are generally <1 mol. %.

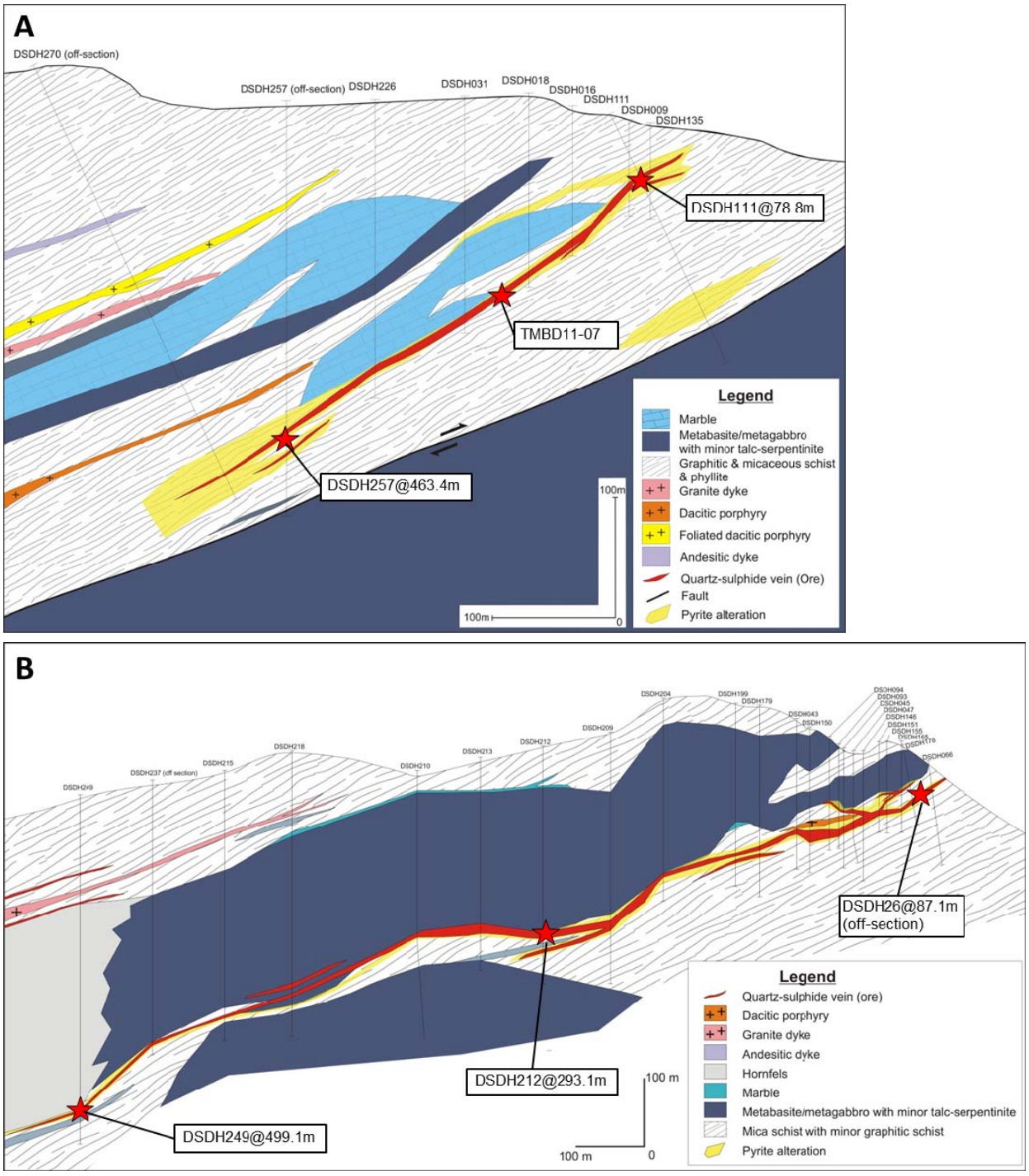

Fig. 7.2. Cross-sections showing sample points at **A.** Bai Dat and **B.** Bai Go, for microthermometric analysis .

7.2.4. Depth of fluid entrapment

The equation of Brown and Lamb (1986) in FLINCOR software was applied to calculate the depth of fluid entrapment using carbonic inclusions (i.e., Type IIIa inclusions in this study). Prior to the calculation, volume of CO_2 content in the inclusions was estimated by petrography and microthermometric data of the inclusions were acquired including clathrate melting temperature, CO_2 liquid and vapour homogenisation temperatures.

7.3. FLUID INCLUSION PETROGRAPHY

Prior to this study, some of quartz crystals from the fluid inclusion chips were studied by cathodoluminescence (CL) imaging to record internal crystal growth zones containing primary fluid inclusions. Although the quartz crystals of the Bai Dat and Bai Go samples are typically characterised by the absence of clear zoning, growth zones are locally found in the core of the crystals. The primary fluid inclusions located along the growth zones were selected for further analyses (Fig. 7.3). Detailed fluid inclusion petrography was also conducted on the Bai Dat and Bai Go samples to distinguish fluid inclusion types: primary, pseudo-secondary and secondary, as defined by Roedder (1984). Primary fluid inclusions provide information about syn-mineralisation fluid characteristics, whereas secondary fluid inclusions do not include significant information about ore deposition, although they may indicate post-mineralisation fluid conditions. In this study, workable primary fluid inclusions were identified in quartz grains of the mineralised vein samples from the Bai Dat and Bai deposits. Various types of fluid inclusions were recognised including one-, two- and multi-phase inclusions.

Four main types of fluid inclusions can be classified in the samples from the Bai Dat and Bai Go deposits on the basis of microscopic identification, and some of them (i.e., Types II and III) are divided into sub-types. They include:

Type I: One-phase vapour inclusions (V), where the vapour of the inclusions is typically dark (Fig. 7.4A). The inclusions range from <5 to 30 μm in size.

Type II: Two-phase inclusions - the most abundant type of inclusions at Bai Dat and Bai Go. These range from 5 to 100 μm in size and are divided into two sub-types:

Type IIa: Liquid and vapour inclusions (L-V). These inclusions have high liquid/vapour ratios and are homogenised into a liquid phase (Fig. 7.4B).

Type IIb: Vapour and liquid inclusions (V-L). These inclusions have low liquid/vapour ratios and are homogenised into a vapour phase (Fig. 7.4C).

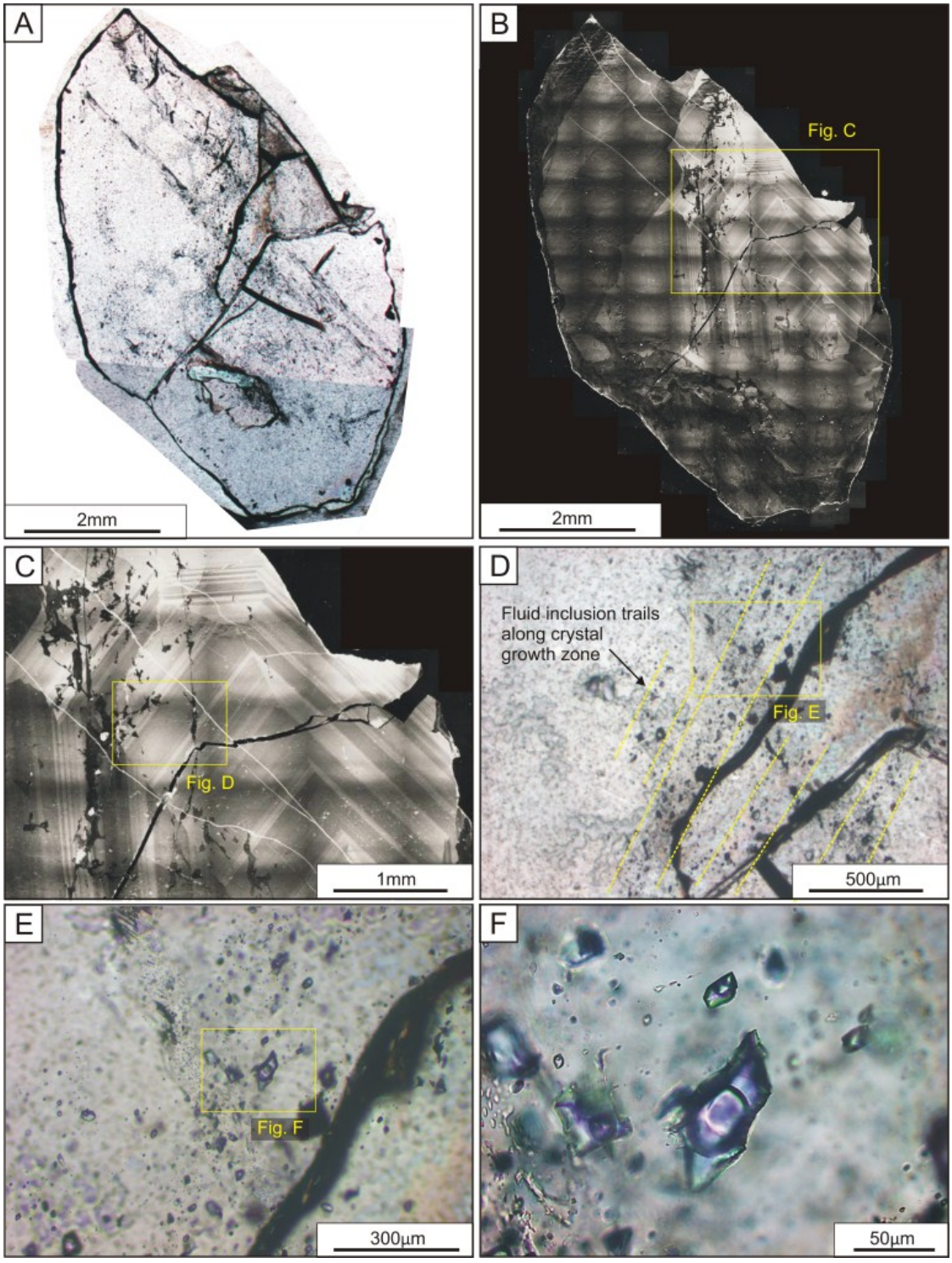

Fig. 7.3. Photomicrographs and images showing examples of primary fluid inclusions identified in this study. Sample No. TMBD11-07 (Bai Dat). **A.** Photomicrograph of a quartz grain from massive galena ore sample in Fig. 7.1F. **B.** CL image of the quartz grain in Fig. A. **C.** CL image of a quartz grain, zooming from Fig. B. **D.** Fluid inclusion trails locating parallel to crystal growth zones. **E** and **F**. Primary fluid inclusions located along crystal growth zones.

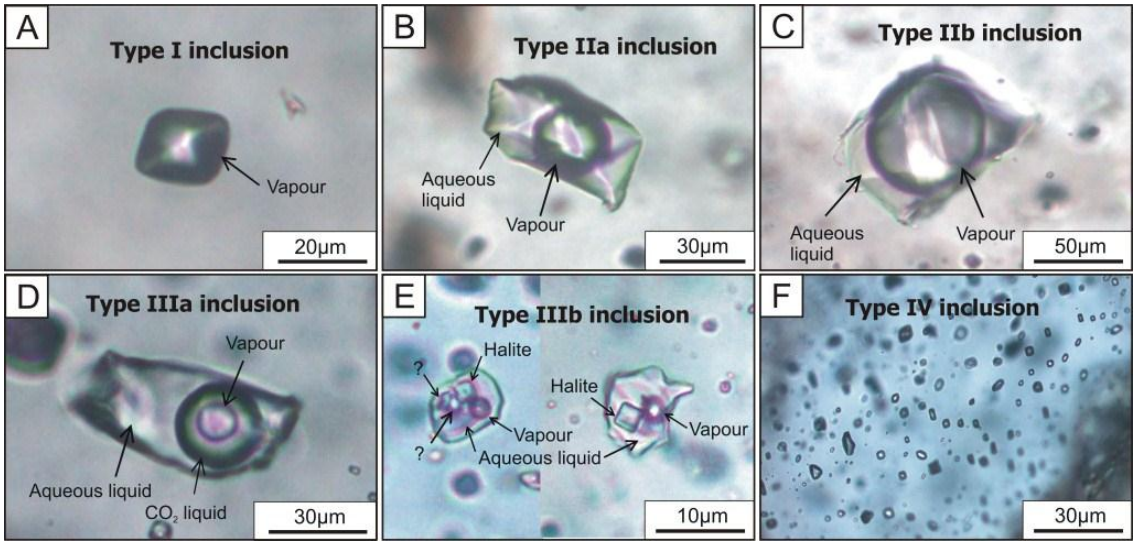

Fig. 7.4. Different types of fluid inclusions found in the samples from the Bai Dat and Bai Go deposits. **A.** Type I inclusion. Sample No. TMBD11-10 (Bai Dat). **B.** Type IIa inclusion. Sample No. TMBD11-07 (Bai Dat). **C.** Type IIb inclusion. Sample No. TMBD11-07 (Bai Dat). **D.** Type IIIa inclusion. Sample No. TMBD11-10 (Bai Dat). **E.** Type IIIb inclusions. Sample No. DSDH270@453.4m (Bai Dat). **F.** Type IV inclusions. Sample No. DSDH270@453.4m (Bai Dat).

Type III: Multi-phase inclusions. These are further divided into two types:

Type IIIa: CO_2-liquid bearing inclusions which contain CO_2-liquid, vapour bubbles and H_2O liquid (L-L-V; Fig. 7.4D). Inclusions of this type are commonly found in the studied samples and typically range 10–30 μm in size.

Type IIIb: Multi-phase inclusions which contain liquid, vapour and daughter minerals (L-V-daughter minerals; Fig. 7.4E). One of the daughter minerals is identified as halite by optical characteristics. These inclusions are small (normally <10 μm in size) and are rarely present in most of the studied samples.

Type IV: Two-phase liquid and vapour inclusions - typically small in size (<10 μm). These are mainly found on secondary trails and will not be used for further analyses (Fig. 7.4F).

In this study, only the primary Type I to III inclusions of measurable size (>5 μm) were analysed.

7.4. RESULTS

7.4.1. Microthermometric data

The microthermometric data are summarised in Table 7.1 and full results are listed in Appendix XIII. The measurements were largely made for Type IIa, IIb and IIIa inclusions, which are commonly present in all the samples.

Table 7.1. Summary of microthermometric results for fluid inclusions from the Bai Dat and Bai Go deposits, Phuoc Son, central Vietnam.

Deposit/ Sample No.	Sample type	Host mineral	Inclusion type	Homogenisation temperature (°C)	Salinity (NaCl wt% equiv.)[1]	CO_2 solid melting temperature (°C)	Calculated depth (kbar)[2]
Bai Dat							
DSDH111-78.8m	Quartz-sulphide vein	Quartz, sphalerite	I, IIa, IIb, IIIa, IIIb	235–>500 (n=36)	4.2–44.8 (n=15)	-57.5 to -57.1 (n=2)	4.4–5.6 (n=3)
TMBD11-07	Massive galena	Quartz	IIa, IIIa	245–355 (n=31)	3.4–9.2 (n=24)	-58.7 to -56.8 (n=24)	3.1–4.3 (n=17)
DSDH257-463.4m	Quartz-sulphide vein	Quartz	I, IIa, IIb, IIIa	270–415 (n=42)	0.4–14.5 (n=33)	-58.7 to -56.6 (n=28)	
Bai Go							
DSDH26-87.1m	Quartz-sulphide vein	Quartz	I, IIa, IIb, IIIa	285–450 (n=30)	1.0–11.1 (n=33)	-58.4 to -56.5 (n=18)	
DSDH212-293.1m	Quartz-sulphide vein	Quartz	I, IIa, IIb, IIIb	265–>500 (n=41)	2.6–13.1 (n=17)	-59.0 to -57.7 (n=3)	
DSDH249-499.1m	Quartz-sulphide vein	Quartz	IIa, IIb, IIIa	240–465 (n=34)	0.5–15.5 (n=32)	-60.8 to -56.8 (n=9)	

1 = calculated based on equation of Bodnar (1993) for Type IIa and IIb, Chen (1972) for Type IIIa, and Bodnar (2003) for Type IIIb inclusions.

2 = calculated using equation of Brown and Lamb (1986) in FLINCOR software.

Homogenisation temperatures

The homogenisation temperature results of the Bai Dat and Bai Go samples are shown based on the depth of the samples from the shallower to the deeper levels in Figure 7.5A, B, C, D, E and F. The homogenisation temperatures of the samples from the shallower level at Bai Dat (DSDH111@78.8m) range widely from 220 to >500°C with a general mode of 300–400°C (Fig. 7.5A). In contrast, homogenisation temperatures of the samples from the middle and deeper levels are restricted to 240–360°C with a mode of 300–340°C (TMBD11-07) and 260 to 420°C with a mode of 340–400°C (DSDH257@463.4m) (Fig. 7.5B and C). The Bai Go samples from the shallower to the deeper levels yielded consistent homogenisation temperatures ranging mainly from 240 to 440°C with a mode of 280–400°C (Fig. 7.5C, D and E).

Salinities

The salinity values of the Bai Dat and Bai Go samples show a wide range from 0.5 to >20 NaCl wt.% equiv. (Fig. 7.6A, B, C, D, E and F). In some samples, presence of halite-bearing inclusions was also noted and salinities yielded up to 44.8 NaCl wt.% equiv.

The samples from the shallower part of the ore body at Bai Dat (DSDH111@78.8m) yielded a wide range of salinities from as low as 4–5 to 44.8 NaCl wt.% equiv., with a mode of 8–15 NaCl wt.% equiv. (Fig. 7.6A). Massive galena (TMBD11-07) samples from the main ore zone at Bai Dat yielded a narrow range of 3–10 NaCl wt.% equiv. (Fig. 7.6B). The salinity values at the deeper part of the ore body (DSDH257@463.4m) recorded a range from 0.5 to 15 NaCl wt.% equiv. (Fig. 7.6C).

The salinity range of 1–12 NaCl wt.% equiv. was recorded in the Bai Go sample from the shallower part of the quartz-sulphide vein (DSDH26@87.1m), with a mode of 3–8 NaCl wt.% equiv. (Fig. 7.6D) A salinity range of the 2–6 NaCl wt.% equiv. with two high values (11–14 NaCl wt.% equiv.) were yielded at the middle zone (DSDH212@293.1m; Fig. 7.6E). A dominant salinity range of 0.5–6 NaCl wt.% equiv. was found at the deeper zone (DSDH249@499.1m), and minor values of 9–16 NaCl wt.% equiv. were also recorded in the zone (Fig. 7.6F).

Volatile compositions

Melting temperatures of solid CO_2 gas in Type I, IIa, IIb and IIIa inclusions of the Bai Dat and Bai Go samples yielded temperature ranges of -56.5 to -58.7°C (Fig. 7.7A, B and C) and

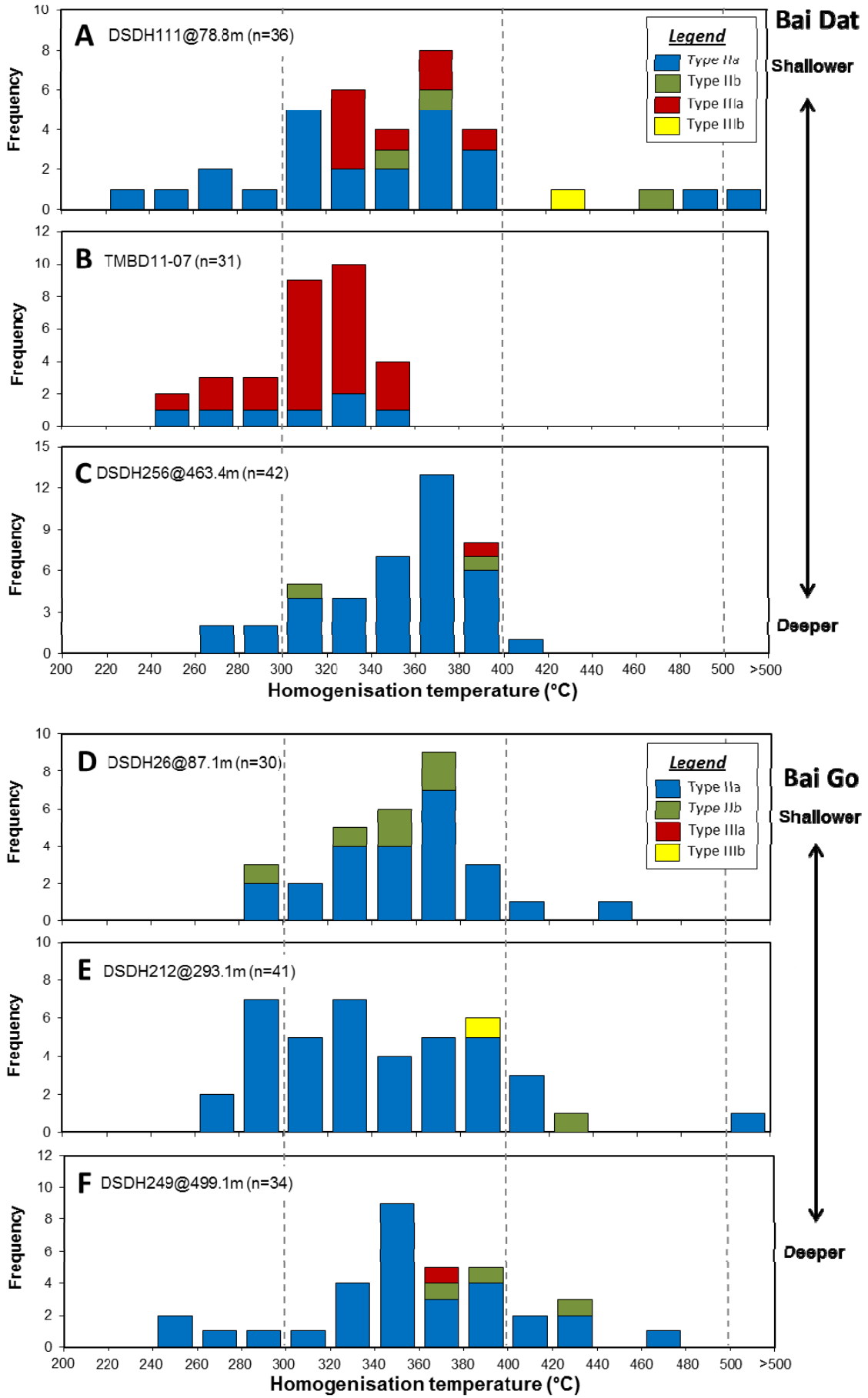

Fig. 7.5. Histograms of homogenisation temperatures of fluid inclusions. The data are shown in terms of **A**. shallower, **B**. middle and **C**. deeper zones for Bai Dat, and **D**. shallower, **E**. middle and **F**. deeper zones for Bai Go.

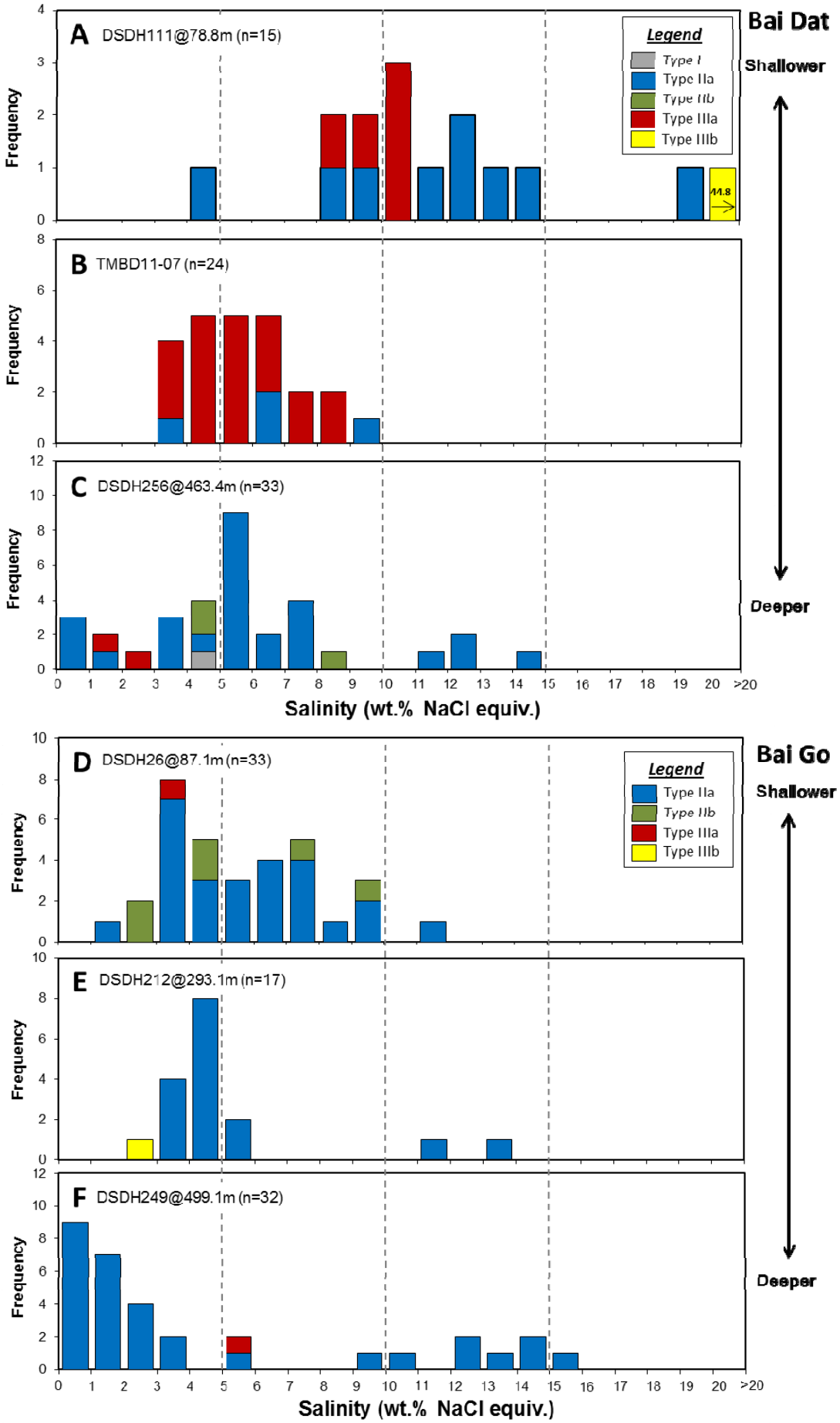

Fig. 7.6. Histograms of salinity data of fluid inclusions at the Bai Dat and Bai Go deposits. The data are displayed in terms of **A**. shallower, **B**. middle and **C**. deeper zones for Bai Dat, and **D**. shallower, **E**. middle and **F**. deeper zones for Bai Go.

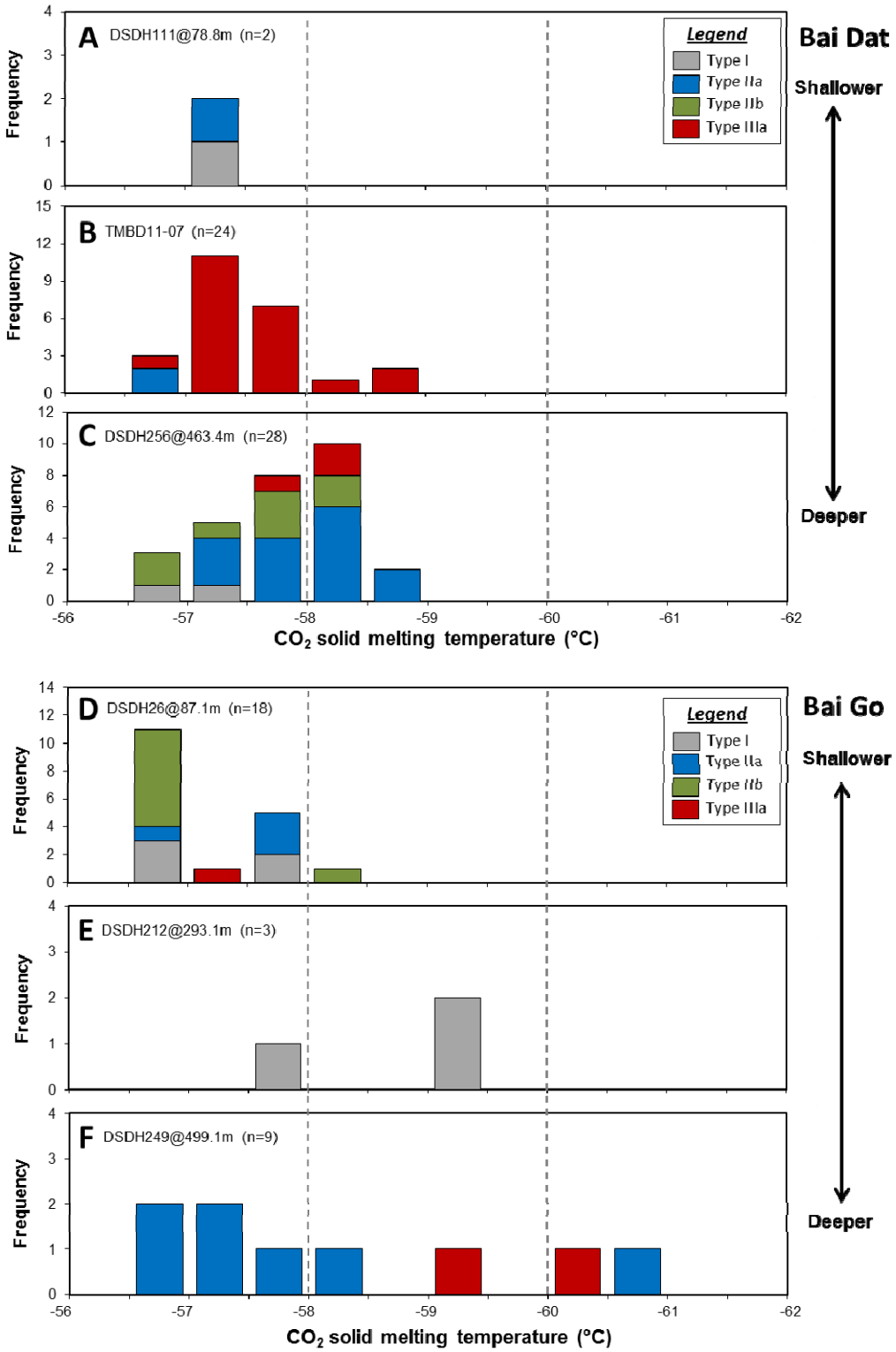

Fig. 7.7. Histograms of solid CO_2 melting temperatures of fluid inclusions from the Bai Dat and Bai Go deposits. The data are presented in terms of **A**. shallower, **B**. middle and **C**. deeper zones for Bai Dat, and **D**. shallower, **E**. middle and **F**. deeper zones for Bai Go.

-56.5 to -60.8°C (Fig. 7.7D, E and F), respectively. In both deposits, the lowest temperature was recorded in the samples from the deeper zone (Fig. 7.7C and F). The solid CO_2 gas melting temperatures below -56.6°C indicate the presence of other dissolved gases such as N_2 and CH_4 (e.g., Huff and Nebelek, 2007), and this is supported by LRS data as N_2 and CH_4 gases are commonly detected in the middle and/or deeper zones of Bai Dat and Bai Go samples (see later section in this Chapter).

7.4.2. Laser Raman Spectroscopy

A total of thirteen samples, including eight and five for Bai Dat and Bai Go, respectively, were analysed by LRS study. The analyses were conducted on 3–10 inclusions for each of the selected samples and an example of the Raman spectra is shown in Figure. 7.8. Detailed results including gas compositions and daughter mineral identification are listed in Appendices XIV-I and -II.

Gas compositions

The results of the LRS analysis of the Bai Dat and Bai Go samples are summarised in Table 7.2. Gases at both Bai Dat and Bai Go are dominantly composed of CO_2, commonly with minor amounts of CH_4 and N_2. The CH_4 gas is enriched in the Bai Go samples (up to 55.3 mole %), whereas the N_2 gas is mainly present at the the Bai Dat deposit (up to 43.6 mole %). Trace amounts of H_2S gas (<1.5 mole %) are also recorded in a few samples from Bai Dat (e.g., TMBD11-09, DSDH257@463.5m). The variation of major gas compositions is found on CO_2-CH_4-N_2 ternary plots (Fig. 7.9A and B), indicating that CO_2 gas is the major component in the Bai Dat and Bai Go inclusions. This also shows that N_2 gas is present at the deeper part of the Bai Dat deposit with few data which totally composed of CH_4-N_2 gases (Fig. 7.9A), whereas CH_4 gas is generally more enriched in the shallower and middle zones of the Bai Go deposit (Fig. 7.9B).

Daughter minerals

LRS was used to identify some unknown solid-phase crystals in Type IIIb inclusions. As a result, several minerals were found including muscovite, calcite, dolomite and graphite (Table 7.3 and Fig. 7.10). Some crystals did not produce Raman spectrum, and thus they are assumed to be salt crystals (e.g., NaCl, KCl, $CaCl_2$) as mono-atomic ions such as Na^+, K^+, Ca^{2+}, Mg^{2+} and Cl^- do not cause Raman response (Burruss, 2003; T. Mernagh pers.com., 2011). This is consistent with the microscopic results in which the presence of halite in inclusions of the Bai Dat samples was recognised.

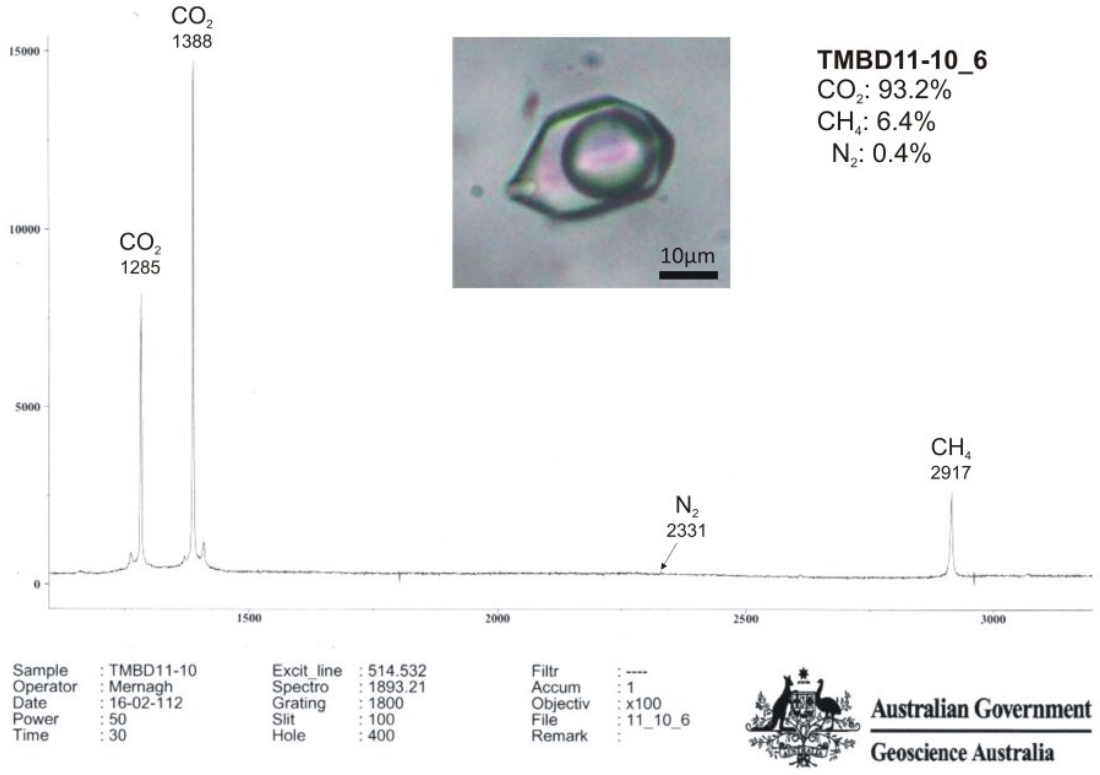

Fig. 7.8. An example of Laser Raman spectral profile of CO_2-CH_4-N_2 gas compositions in Type IIa fluid inclusion from the Bai Dat deposit, Phuoc Son. Sample No. TMBD11-10_6 (Bai Dat).

Table 7.2. Summary of Laser Raman Spectroscopic data of gas compositions in primary fluid inclusions from the Bai Dat and Bai Go deposits, Phuoc Son.

Deposit & depth	Sample No. (No. of analysis)	CO_2 mole %	N_2 mole %	H_2S mole %	CH_4 mole %	Compositions
Bai Dat						
Shallower	DSDH111@78.8m (5)	98.1–94.0	0	0	6.0–1.9	CO_2-CH_4
	TMBD11-13 (7)	100–96.6	0.4–0	0	3.0–0	CO_2-CH_4-N_2
	TMBD11-10 (6)	95.1–90.5	6.6–0	0	6.9–2.3	CO_2-CH_4-N_2
	TMBD11-09 (6)	100–91.2	5.4–0	1.5–0	3.8–0	CO_2-CH_4-N_2-H_2S
	TMBD11-07 (6)	98.0–62.9	35.4–0	0	7.9–0	CO_2-N_2-CH_4
	DSDH257@463.4m (10)	100–94.8	4.8–0	0	0.5–0	CO_2-N_2-CH_4
	DSDH257@463.5m (6)	98.5–0.7	22.5–0	0.9–0	82.9–1.5	CO_2-CH_4-N_2-H_2S
Deeper	DSDH270@453.4m (3)	80.6–54.6	43.6–14.0	0	5.4–1.8	CO_2-N_2-CH_4
Bai Go						
Shallower	DSDH146@88.8m (5)	100–98.6	0	0	0–1.4	CO_2-CH_4
	DSDH40@195.8m (5)	93.7–59.6	0	0	40.4–6.3	CO_2-CH_4
	DSDH199@230.2m (6)	100–47.7	0	0	55.3–0	CO_2-CH_4
	DSDH212@293.1m (5)	95.1–60.0	7.4–0	0	40.0–3.0	CO_2-CH_4-N_2
	DSDH224@443.3m (10)	99.0–97.9	0	0	3.3–1.0	CO_2-CH_4
	DSDH218@366.2m (5)	91.8–88.4	0	0	11.6–8.2	CO_2-CH_4
Deeper	DSDH249@499.1m (4)	96.9–90.1	0	0	9.9–3.1	CO_2-CH_4

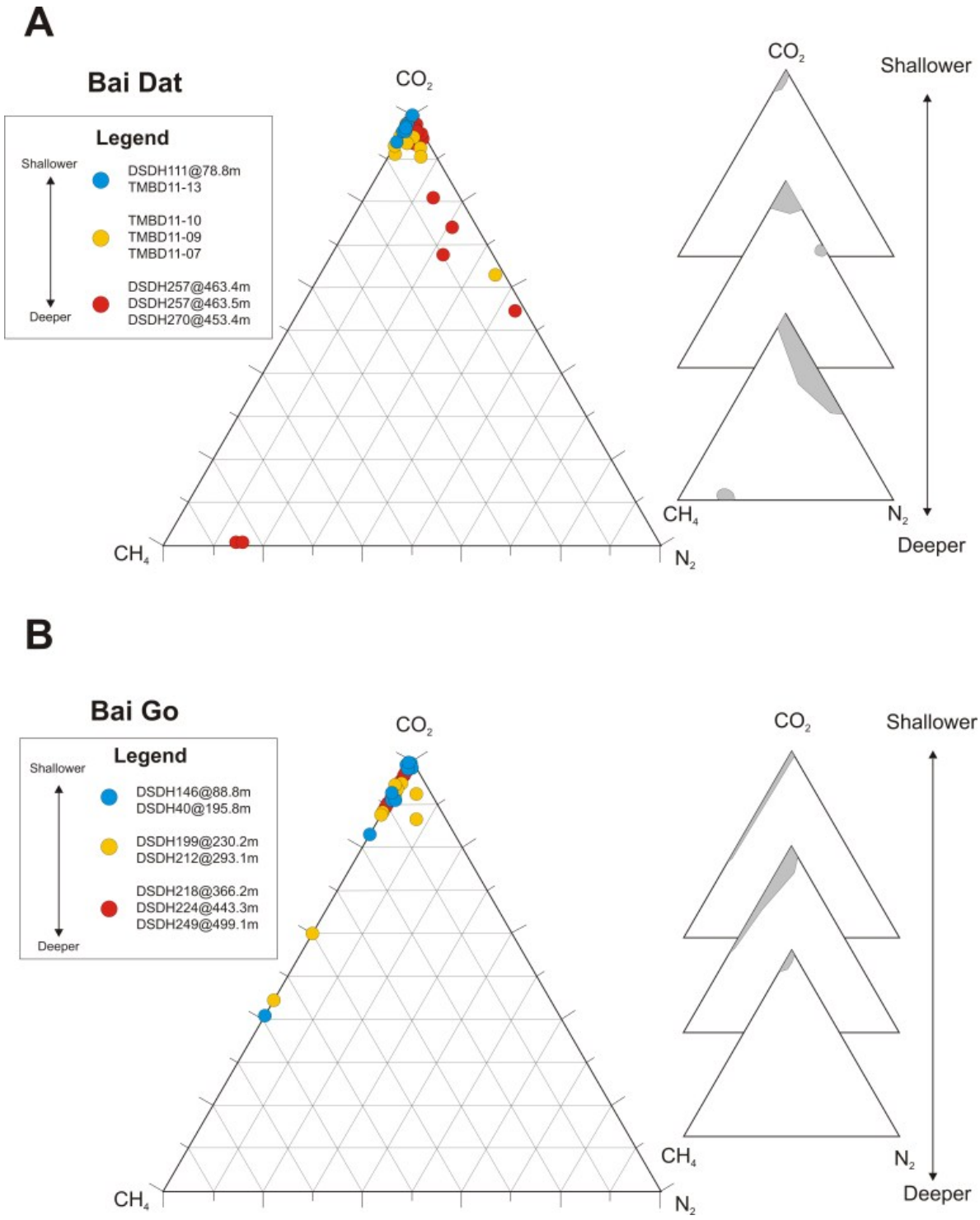

Fig. 7.9. Ternary plots of gas composition (CO_2-CH_4-N_2) in fluid inclusions from the Bai Dat (**A**) and Bai Go (**B**) deposits, Phuoc Son.

Table 7.3. Summary of Laser Raman Spectroscopy showing identified solid phase crystals in fluid inclusions from the Bai Dat and Bai Go deposits, Phuoc Son.

Sample No.	Identified mineral	Remarks
Bai Dat		
TMBD11-13	Muscovite	Several other solid phases produced no Raman response
TMBD11-10	Dolomite	Several other solid phases produced no Raman response
TMBD11-07	Calcite	Several other solid phases produced no Raman response
DSDH257@463.5m	Calcite	Several other solid phases produced no Raman response
DSDH270@453.4m	Muscovite	Several other solid phases produced no Raman response
Bai Go		
DSDH212@293.1m	Graphite	

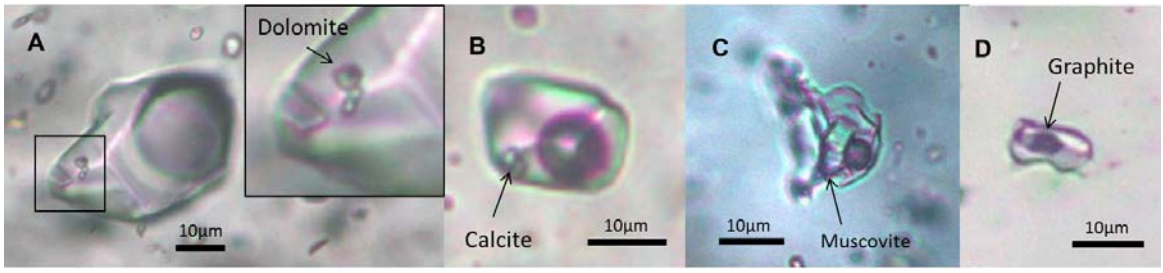

Fig. 7.10. Examples of daughter minerals identified by Laser Raman spectral profile. **A.** Dolomite with other daughter crystals in Type IIIb inclusion. Sample No. TMBD11-10 (Bai Dat). **B.** Presence of calcite in Type IIIb inclusion. Sample No. TMBD11-07 (Bai Dat). **C.** Type IIIb inclusion hosting a muscovite crystal. Sample No. DSDH270@453.4m (Bai Dat). **D.** Presence of graphite in inclusion. Sample No. DSDH212@293.1m (Bai Go). Note full results are listed in Appendix XII-II.

7.4.3. Depth of fluid entrapment

The calculated depths of fluid entrapment based on the Type IIIa fluid inclusion data from the middle and shallower parts of Bai Dat yielded a range of 3.1–4.3 kbar (TMBD11-07) and 4.4–5.6 kbar (DSDH111@78.8m) (Table 7.1). This may indicate that the depth of ore formation at Bai Dat is estimated to be around 3.1–5.6 kbar.

7.5. DISCUSSION

In this section, physico-chemical conditions of the ore fluids at the Bai Dat and Bai Go deposits will be discussed to constrain their sources and to indicate the possible mechanism of gold deposition based on the fluid inclusion characteristics, microthermometry and volatile composition.

7.5.1. Depth of ore formation

The calculated data of Type IIIa inclusions in euhedral quartz of massive galena and quartz-sulphide vein samples from Bai Dat yielded a range of 3.1–5.6 kbar for the estimated depths of fluid entrapment. This range corresponds to a depth of 8.3–15.1 km (using average lithostatic pressure gradient of 1kbar=3km), suggesting that the depth of the ore formation at Bai Dat and Bai Go is similar to the deposits forming in deep environments, such as orogenic lode gold deposits in the Yilgarn Craton of Western Australia (i.e., 5–20 km; Goldfarb et al., 2005) and intrusion-related gold deposits of Alaska (<1–10 km; Baker, 2002).

7.5.2. Ore fluid characteristics and source(s)

The bivariate plots of homogenisation temperature versus salinity for fluid inclusions from the Bai Dat and Bai Go deposits are shown in terms of fluid inclusion types and depth levels of the collected samples in Figure 7.11. Based on comparisons with typical trends of fluid evolution process by Wilkinson (2001), a fluid dilution/isothermal mixing trend is recognised in the Bai Dat fluid data (Fig. 7.11A and B), whereas isothermal mixing trends are identified in the Bai Go fluid inclusions (Fig. 7.11C and D). The fluid dilution/isothermal mixing trend of the Bai Dat data may indicate that brine/highly saline fluids mixed with lower salinity fluids in the main ore zone at Bai Dat. For the isothermal mixing trends in the Bai Go data, it can be inferred that two types of fluids including low (<5 NaCl wt.% equiv.) and high (12–15 NaCl wt.% equiv.) saline fluids, mixed in the middle zone at the Bai Go deposit. The samples from the main ore zone at Bai Dat and Bai Go (i.e., TMBD11-07 of Bai Dat and DSDH26@87.1m and DSDH212@293.1m of Bai Go) have a well homogenised and restricted data for the homogenisation temperatures (250–350 °C at Bai Dat and 300–400 °C at Bai Go) and salinities (3–10 NaCl wt.% equiv. at the both Bai Dat and Bai Go). This supports the interpretation that mixing in the middle mineralised zone was a major process during ore fluid evolution at the Bai Dat and Bai Go deposits. Based on the geological setting during the ore formation at Phuoc Son (i.e., regional magmatic-metamorphic event; see Chapter 3 for details), it is likely that the high saline fluids were magmatic origin, whereas the low salinity fluids were sourced from metamorphic fluids.

7.5.3. Presence of N_2 and CH_4 gases and comparison with other gold deposits

The high concentration of N_2 and CH_4 gases was found in inclusions from the Bai Dat and Bai Go deposits and the characteristics were compared with other gold deposits (Fig. 7.12A, B, C, D and E). CH_4 gas-rich inclusions are reported in the main ore zone of the Nui Kem gold deposit in Bong Mieu, central Vietnam (Fig. 7.12B; Lee, 2010). The deposit is hosted by

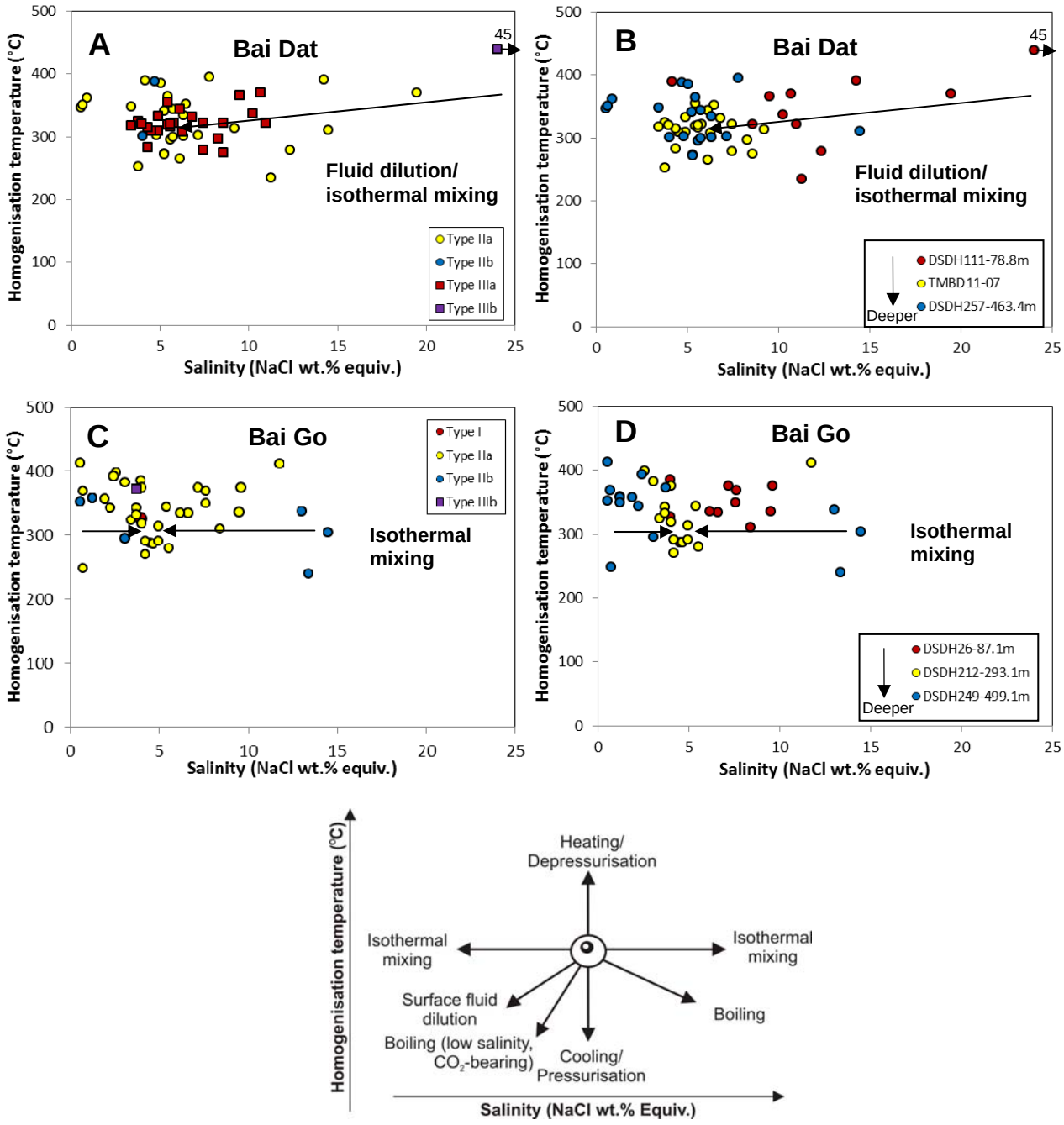

Fig. 7.11. Plots of salinities vs homogenisation temperatures of fluid inclusions from the Bai Dat and Bai Go deposits, Phuoc Son. The data are shown in terms of **A**. inclusion types and **B**. depth level of samples for Bai Dat and **C**. inclusion type and **D**. depth level of samples for Bai Go. Typical fluid process trends are after Wilkinson (2001). Note that a fluid dilution trend is recognised in the Bai Dat data, whereas isothermal mixing trends are found in the Bai Go data.

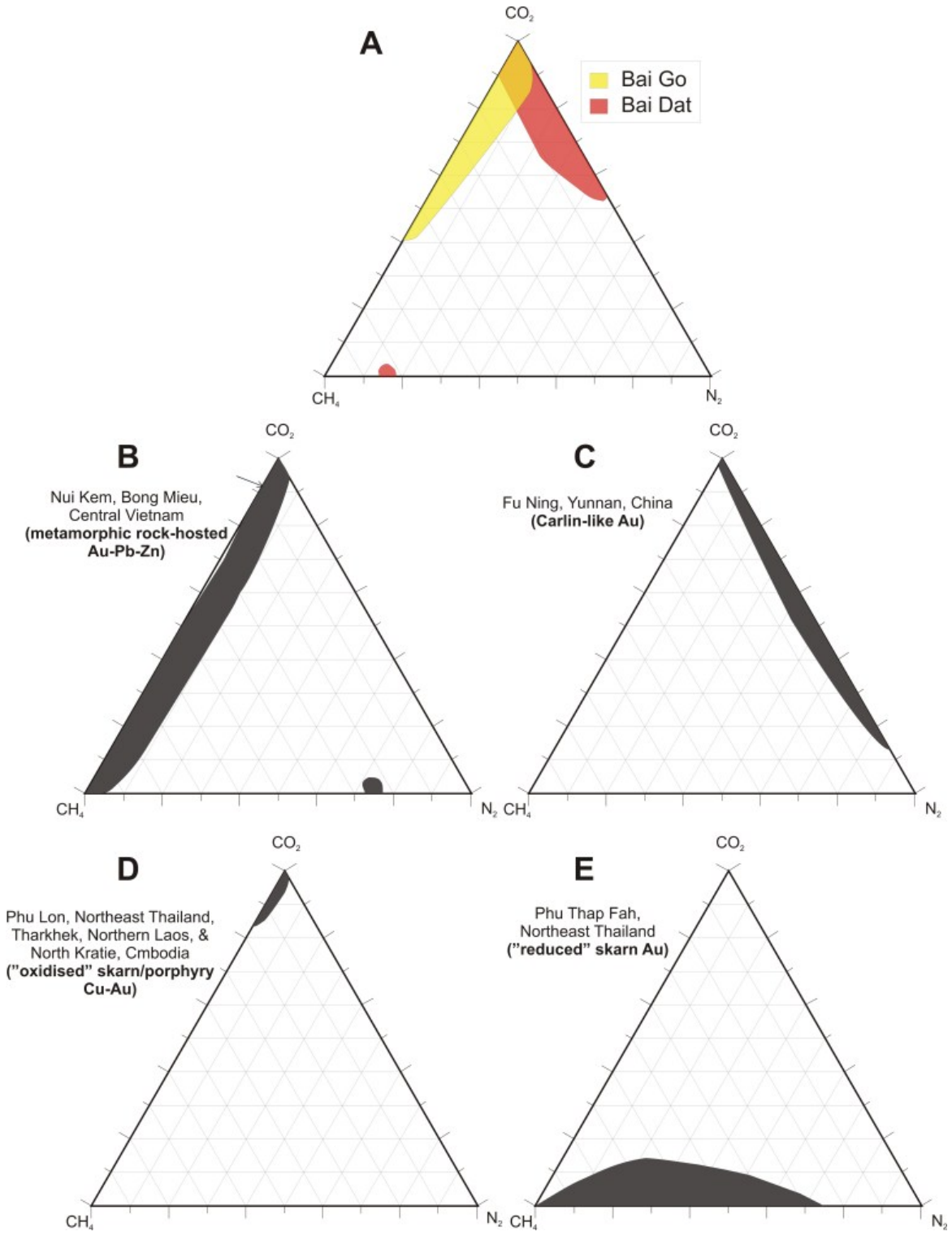

Fig. 7.12. CO_2-CH_4-N_2 ternary plots of gas composition of primary fluid inclusions in comparison with different styles of gold deposits in mainland SE Asia and Yunnan. **A.** Bai Dat and Bai Go deposits, **B.** Nui Kem metamorphic rock-hosted Au-Zn-Pb deposit of Bong Mieu (Lee, 2010; Khin Zaw, unpub data), **C.** Fu Ning Carlin-like Au deposits of South China (Cromie and Khin Zaw, 2003), **D.** "Oxidised" Cu-Au skarn deposits including Phu Lon of northeastern Thailand (Kamvong, 2004), Tharkhek of northern Laos (Khin Zaw, unpub data) and North Kratie in Cambodia (Lim, 2012), and **E.** Phu Thap Fah "reduced" Au skarn deposit of northeastern Thailand (Khin Zaw et al., 2007b).

schistose and gneissic rocks intercalated with carbonaceous units, and Lee (2010) postulated that the carbonaceous materials in the host rocks are considered to be source of the CH_4 gases. N_2 is also commonly found in ore fluids of Carlin-type deposits in Carlin trend in USA (Hofstra and Cline, 2000). The presence of N_2 gases is also recorded in quartz from the main mineralised zone of the Carlin-like Fu Ning gold deposits in South China (Cromie and Khin Zaw, 2003; Fig. 7.12C). In the Carlin-type gold deposits, the ore is dominantly hosted in carbonaceous sedimentary rocks (e.g., black shale) and the N_2 source is considered to be from such host units (e.g., Hofstra and Cline, 2000).

Contribution of carbonaceous units for producing reduced fluids is also considered from the presence of N_2 and CH_4 gases in skarn/porphyry systems (e.g., Khin Zaw et al., 2007b, 2008). In the "oxidised" Cu-Au skarn deposits of mainland SE Asia, CO_2 gas is dominant in the ore-forming fluids (Fig. 7.12D; Kamvong, 2004; Khin Zaw, unpub data; Lim, 2012). In contrast, enrichment of CH_4 and N_2 gases in the ore fluids are reported from the "reduced" Au skarn deposit at Phu Thap Fah, northeast Thailand (Khin Zaw et al., 2007b, 2008). As the Phu Thap Fah deposit is predominantly hosted by carbonaceous shale/limestone, it is interpreted that the reduced ore fluids were derived from the interaction of ore fluids with the host carbonaceous units (Fig. 7.12E; Khin Zaw et al., 2007b, 2008). Khin Zaw et al. (1994) detected N_2-bearing fluids in the Tennant Creek Au-Cu deposit in which the gold-copper-bismuth mineralised veins are hosted by ironstones. They suggested that the N_2 was probably released from the country rock and incorporated in the ascending hydrothermal fluids during wall rock reaction. In a similar deduction, the N_2 and CH_4 gases at the Bai Dat and Bai Go deposits are also considered to have been mainly sourced from the host carbonaceous units.

7.5.4. Nature of ore fluids

The ore fluids of the Bai Dat and Bai Go deposits are found to be reduced and of neutral pH. The reduced condition in ore fluids at Bai Dat and Bai Go is supported by; (1) pyrite-pyrrhotite assemblage in the mineralised quartz-sulphide veins, and (2) enriched CH_4 and N_2 gases and presence of a graphite daughter mineral in the ore fluids. The reduced condition is also demonstrated by the pyrite-pyrrhotite assemblage on the log fO_2-pH diagram using fluid condition of 350°C, 3.5 kbar and 0.01 mole/kg in $\sum S$, which is similar to the Bai Dat and Bai Go fluid environment (Fig. 7.13). The pH of the ore fluids at Bai Dat and Bai Go can be broadly estimated to be a neutral condition, based mainly on the presence of daughter mineral assemblages of muscovite, calcite and dolomite in the inclusions as detected by LRS analyses (Table 7.3 and Fig. 7.10). The constrained ore fluid condition at Bai Dat and Bai Go indicates that the gold was predominantly transported by bisulphide complexes (i.e., $Au(HS)_2^-$) (Fig. 7.13).

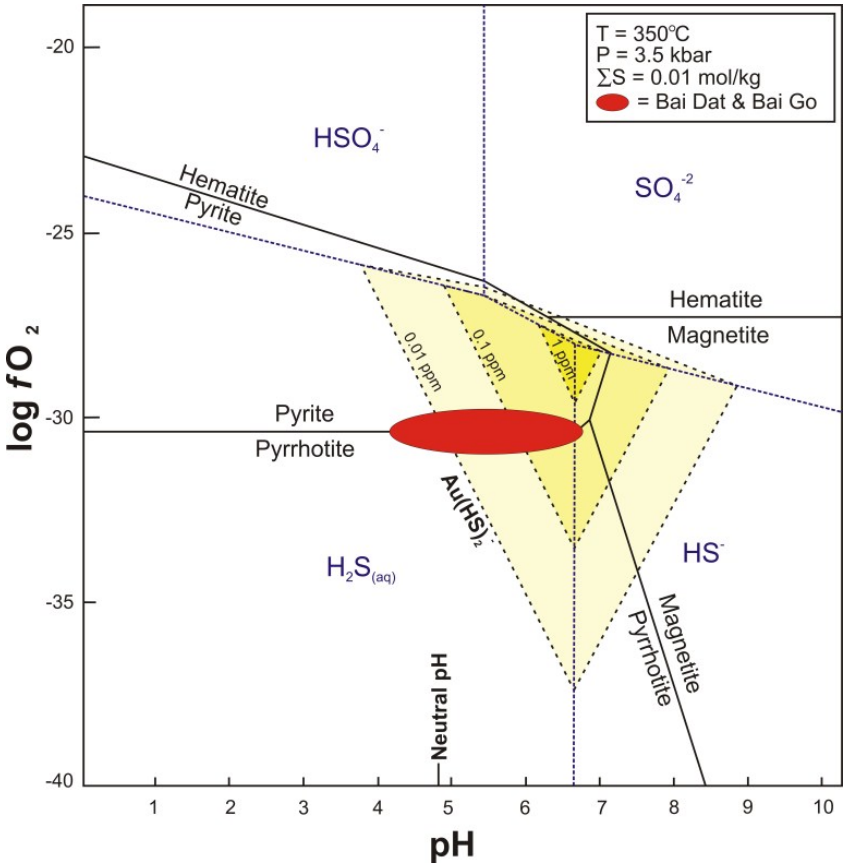

Fig. 7.13. LogfO_2-pH diagram showing the predominant fields of sulphur species and stability fields of sulphides at 350°C, 3.5 kbar and ∑S=0.01 mol/kg. Note: red field displays a conditioned field for the Bai Dat and Bai Go ore fluids, indicating gold was predominantly transported by bisulphide complexes. Thermodynamic data are modified after Pandalai et al. (2003) and references therein.

7.5.5. Physico-chemical process of gold deposition

Several important physico-chemical mechanisms are commonly recognised to promote gold deposition in hydrothermal systems (e.g., boiling, sulphidation, oxidation, cooling; Williams-Jones et al., 2009). The potential gold depositional mechanism at Bai Dat and Bai Go can be constrained based on the nature of the ore fluids (i.e., reduced and near neutral pH conditions) together with the geological setting and mineralisation characteristics of the deposits.

Wall rock interaction

The wall rock interaction or "sulphidation" (e.g., Phillips et al., 1986) is likely to be a main process of gold precipitation at Bai Dat and Bai Go as supported by fluid inclusion and geological data, such as (1) pyrite (with minor pyrrhotite) alteration in the host carbonaceous schist/phyllite which is spatially associated with the quartz-sulphide veins, (2) enrichment of the CH_4 and N_2 gases in the main ore zones, and (3) presence of mafic units which are

enriched in iron (see XRF results in Chapter 4). All of these factors can promote the gold precipitation associated with wall rock interaction, which is expressed as:

$Fe^{2+} + 2Au(HS)_2^- \leftrightarrow 2Au + FeS_2 + 2H_2S$ …….. (1)

Presence of the CH_4 and N_2 gases may not be directly involved in the above reaction. However, it is possible that they originated from the local host rock units and were in the main ore fluids at Bai Dat and Bai Go, suggesting that the reaction of ore fluids with the host rocks occurred during the ore formation. Minor amounts of H_2S gas was also detected at Bai Dat by LRS analysis (Table 7.2) and this appears to support the reaction above.

Fluid dissolution and cooling

Dissolution of gold-bearing ore fluids is also proposed for promoting gold deposition at Bai Dat and Bai Go, as fluid inclusion microthermometric data indicate the mixing of magmatic fluids with metamorphic fluids in the main ore zones (Fig. 7.11). In the following reaction, gold precipitation is caused via:

$Au(HS)_2^- + 1/2H_2O_{(aq)} \leftrightarrow Au + 2HS^- + H^+ + 1/4O_2$ ……. (2)

The mixing of fluids can also potentially cause other physical processes such as cooling. As the ore fluids at Bai Dat and Bai Go have a wide homogenisation temperature range from >500 to as low as 240°C, the cooling process could also promote the gold precipitation at Bai Dat and Bai Go. This is consistent with empirical data indicating that gold solubility in bisulphide complexes can be abruptly dropped below 350°C (e.g., Williams-Jones et al., 2009),

Other effects

Few other possible depositional mechanisms such as boiling, fluid immiscibility and oxidation are also recognised to promote gold deposition in hydrothermal gold deposits (e.g., Williams-Jones et al., 2009). However, there is very little evidence supporting these processes at Bai Dat and Bai Go. Boiling in hydrothermal system is typically recognised from the presence of adularia and/or bladed calcite (e.g., Henley and Brown, 1985), but a lack of these minerals in the mineralised veins at Bai Dat and Bai Go indicates that boiling was not a dominant process. There was no fluid inclusion evidence of boiling (e.g., vapour-rich and liquid-rich inclusions in the same growth zones) at Bai Dat and Bai Go. Fluid immiscibility, which is considered to be a major process causing gold deposition in orogenic gold deposits

(e.g., McCuaig and Kerrich, 1998; Hagemann and Cassidy, 2000; Bodnar, 2007), is not considered to be a major effect at Bai Dat and Bai Go as only mixing trends are identified in the microthermometric data (Fig. 7.11). As pyrite-pyrrhotite association is ubiquitously present in the quartz-sulphide veins and the associated alteration assemblage without magnetite, oxidation may not have played a key role for gold precipitation at Bai Dat and Bai Go.

7.6. SUMMARY

Fluid inclusion studies of the gold-bearing quartz-sulphide veins from the Bai Dat and Bai Go deposits revealed:

- Four types of fluid inclusions are found in mineralised vein-located quartz and sphalerite. They are one-, two- and multiple-phase (e.g., daughter crystal-bearing and carbonic) inclusions. The three-phase carbonic and two-phase inclusions are the most common types at the Bai Dat and Bai Go deposits.

- Homogenisation temperatures of fluid inclusions from the Bai Dat deposit range from 220 to >500°C (with a mode of 300–400°C), whereas the Bai Go deposit yielded homogenisation temperatures from 240 to >500 °C (with a mode of 280–400°C). The salinity value ranges from 0.5 to 44.8 NaCl wt.% equiv. at Bai Dat and 0.5 to 16 NaCl wt.% equiv. at Bai Go. The homogenisation temperatures and salinity data suggest that a mixing of magmatic and metamorphic fluids occurred in the main ore zones of the Bai Dat and Bai Go deposits.

- LRS detected gaseous compositions of CO_2-N_2-CH_4(-H_2S) and CO_2-CH_4(-N_2) for Bai Dat and Bai Go. It is considered that the N_2 and CH_4 gases were sourced from the host carbonaceous schist/phyllite unit. Presence of daughter minerals of muscovite, calcite, dolomite and graphite in the fluid inclusions were also identified by LRS and the assemblages imply that the ore fluids at Bai Dat and Bai Go appear to be reduced and near neutral in pH.

- The physico-chemical conditions deduced from the fluid inclusion data indicated that wall rock interaction (sulphidation) is the most effective mechanism to facilitate gold deposition at Bai Dat and Bai Go. Other processes such as dissolution and cooling are also considered to have promoted gold precipitation at Bai Dat and Bai Go.

- The entrapment depth of 8.3–15.1 km is estimated for ore fluids at the Bai Dat deposit. This depth range is broadly comparable to depths of orogenic lode gold deposits in the Yilgarn Craton of Western Australia (5–20 km; Goldfarb et al., 2005) and intrusion-related gold deposits of Alaska (<1–10 km; Baker, 2002).

CHAPTER 8 SUMMARY, CONCLUSIONS, GENETIC MODEL AND EXPLORATION IMPLICATIONS

8.1. INTRODUCTION

All the geological and geochemical data and interpretations made in previous Chapters are summarised and integrated in this Chapter to develop a genetic model of the Bai Dat and Bai Go gold deposits in the Phuoc Son area. Prior to establishing the model, the main aspects of the geology and mineralisation characteristics of the Bai Dat and Bai Go deposits are summarised and discussed to constrain the nature of the origin of gold mineralised systems and style of the mineralisation at Bai Dat and Bai Go.

8.2. SUMMARY

The major conclusions drawn in the previous Chapters of this study are:

8.2.1. Geological and tectonic setting

- The Phuoc Son deposit area is located in the Indochina Terrane and has undergone two orogenic events. This is evidenced by the magmatic and metamorphic rocks in the Phuoc Son area, which predominantly yielded either Ordovician-Silurian (490–430 Ma) or Permian-Triassic (270–220 Ma) ages.

- The Late Permian-Triassic regional metamorphism and magmatism at the Phuoc Son deposit area belong to the late magmatic-metamorphic stage of the TSFB, which formed under the post-collision extensional tectonic setting following the collision between the Indochina and South China Terranes during the Indosinian Orogeny.

- Various metamorphic rocks are observed at Phuoc Son and the surrounding area, ranging from low-grade phyllitic (the Nui Vu Formation at Bai Dat) to high-grade gneissic rocks (the Kham Duc Formation at Kham Duc). This is consistent with the regional geological setting as the area is situated at the northwestern margin of the Kontum high-grade metamorphic complex, where regional fault zones (i.e., Poko Fault Zone) occur along the margins and the degree of regional metamorphic grade changes abruptly across the zones.

- The granitic units intruded in the Phuoc Son deposit area during the Late Permian-Triassic regional metamorphism are characterised by I-type/ilmenite-series affinity. An adakitic signature is also recognised in the dacitic porphyries, which cross-cut the mineralised veins and are interpreted as a post-mineralisation unit at Bai Dat and Bai Go.

8.2.2. Nature of gold mineralisation

- The gold-bearing quartz-sulphide veins are predominantly hosted by carbonaceous schist/phyllite and metagabbro units at Bai Dat and Bai Go. They are emplaced parallel to metamorphic foliation of the host rocks, which strikes N-S to NE-SW with westerly dips (30–60°).

- The gold mineralisation event at Bai Dat and Bai Go is divided into the early sphalerite-rich and late galena-rich stages, based on cross-cutting/overprinting relationships. The early main mineralisation stage is characterised by massive sphalerite and associated with minor gold, whereas the late mineralisation stage is enriched in galena and recognised as the main gold-bearing stage. The sphalerite is orange in the early stage, whereas the quartz-sulphide veins of the late stage hosts dark sphalerite.

- Gold at the Bai Dat and Bai Go deposits occurs predominantly as electrum associated with sulphide minerals including pyrite, pyrrhotite, galena, sphalerite and chalcopyrite in the quartz-sulphide veins. Gangue minerals such as carbonate minerals, biotite, muscovite, sericite and serpentinite are also present in the veins and associated with the sulphide minerals. Traces of electrum are also disseminated in the host pyritised carbonaceous schist/phyllite unit.

- Pyritisation and silicification are present in the host rocks of the Bai Dat and Bai Go deposits. The pyritisation occurs as a distinct alteration halo and shows spatial association with the quartz-sulphide veins at Bai Dat and Bai Go.

- The fineness values of the vein-hosted electrum from the Bai Dat and Bai Go deposits yielded ranges of 500–800 and 350–1000, respectively. Such wide ranges suggest that gold was predominantly transported by bisulphide complex in ore fluids. However, as gold is closely associated with massive galena and sphalerite at Bai Dat and Bai Go, gold may have been carried partly by chloride complex which is considered as the main transport agent for the lead and zinc.

- LA-ICPMS analysis of pyrite shows that low grade gold (<10 ppm) is concentrated in the structure of vein-located pyrite and gold normally occurs as inclusions. Trace amounts of gold are also present with pyrite in the host rock as free grains and/or inclusions of pyrite.

- The FeS contents of sphalerite vary significantly between the orange and dark sphalerite. Lower values of 5–8 mole % are recorded from the massive orange sphalerite, whereas higher values of 12–16 mole % are obtained from the dark sphalerite in the quartz-sulphide veins of the main gold-bearing stage.

8.2.3. Structural control

The Daksa Fault Zone hosts the Bai Dat and Bai Go deposits, and several other deposits also occur along the fault zone. The fault is a splay of the regional NW-SE trending Cong Plong Fault and may have played an important role in allowing the gold-bearing fluids to travel for a long distance (>several km). The close relationships of the occurrences of gold deposits and the faults may indicate that formation of the gold mineralisation at Phuoc Son was strongly controlled by structure.

8.2.4. Age of mineralisation

- Ar-Ar ages of the vein-hosted mica minerals (i.e., biotite, fuchsite and sericite) at Bai Dat, Bai Chuoi and Bai Gio yielded a broad Triassic range of 250–200 Ma. This is inconsistent with the LA-ICPMS zircon U-Pb ages of the post-mineralisation dacitic porphyries (c.a. 250 Ma). It is interpreted that the discrepancy is resulted from different closing temperatures of the minerals which formed in a slow cooling environment. This interpretation is consistent with the age data of Triassic Sn-bearing granites in Laos and is also supported by the geological setting at that time, indicating the area was in the waning stage of the regional metamorphic event during the Indosinian Orogeny.

- The lead isotope data of the vein-hosted galena from the Bai Dat and Bai Go overlap with the data from the Bong Mieu gold deposit, central Vietnam. As the timing of mineralisation at Bong Mieu is well constrained to the Triassic (c.a. 240 Ma) using the Re-Os molybdenite and LA-ICPMS zircon U-Pb ages (Lee, 2010), the lead isotope data suggest that the gold mineralisation at the Bai Dat and Bai Go also occurred during Triassic.

8.2.5. Depth of ore formation

- A depth range of 5.3–7.5 kbar was calculated using the FeS mole % contents of the dark sphalerite coexisting with pyrite and pyrrhotite in the quartz-sulphide vein at Bai Dat and Bai Go. In contrast, the carbonic three-phase inclusion data at Bai Dat yielded a calculated depth range of 3.1–5.6 kbar. These depth data can be corresponded to a broad range of 9.3–22.2 km (with a mean depth of c.a. 15 km) based on the lithostatic pressure gradient of 1 kbar = 3 km.

8.2.6. Physico-chemical conditions of ore fluids

- Ore fluids at Bai Dat have a range of 220–>500°C in homogenisation temperature (with a mode of 300–400°C) and of 0.5–44.8 NaCl wt.% equiv. in salinity. The ore fluids at Bai Go yielded a range from 240 to >500°C (with a mode of 280–400°C) in homogenisation temperature and salinities of 0.5–16 NaCl wt.% equiv. The ore fluids at both Bai Dat and Ba Go deposits indicate a mixing array of magmatic and metamorphic fluids in the main ore zones. The mixing may have caused an abrupt change in physical (e.g., temperature) and chemical (e.g., salinity, pH and redox) conditions of the ore fluids.

- Although presence of CO_2 gases is common, N_2 and CH_4 gases are locally enriched in fluid inclusions in the main ore zones at Bai Dat and Bai Go. They are considered to have been sourced from the host rocks (i.e., carbonaceous schist/phyllite and metagabbro). Presence of these gases in the mineralised quartz-sulphide veins may indicate that the reaction of ore fluids with the host rocks played an important role in gold precipitation.

- The ore fluids at Bai Dat and Bai Go are indicated to be reduced and near neutral in pH. Based on these conditions, it is possible that the gold was predominantly transported by bisulphide complex in the ore fluids. Meanwhile, it is inferred that the lead and zinc were mainly transported by chloride complex.

- The combined data of fluid inclusions and the distinct pyrite alteration halo of the quartz-sulphide veins at Bai Dat and Bai Go suggest that wall rock interaction (i.e., pyrite precipitation) is the main effect to promote the gold precipitation at the deposits. This is also supported by the stable isotope data (i.e., S, C and O), which also indicate that there was a strong input of fluids/elements from carbonaceous unit into the magmatic fluids at the Bai Dat and Bai Go deposits.

8.3. DISCUSSION INCLUDING COMPARISONS WTH OROGENIC AND INTRUSION-RELATED GOLD DEPOSITS

On the basis of geological, geochronological, geochemical and isotopic data of the Bai Dat and Bai Go deposits, their gold depositional environments are discussed including tectonic setting, the source, transport and deposition of the gold, depth of ore formation and structural control. The discussion also involves comparisons of the geological and mineralisation characteristics of the Bai Dat and Bai Go deposits with those of the orogenic gold deposits in the Yilgarn Craton of Australia and intrusion-related gold deposits in Alaska, as the Bai Dat and Bai Go deposits share many similarities with them (Table 8.1).

8.3.1. Regional tectonic setting

The host rock sequence at the Phuoc Son area is dominated by metamorphic units that have formed during the peak stage of regional metamorphism (c.a. 275–265 Ma), and this was followed by intrusions of granites, which are characterised by I-type, ilmenite-series affinity and emplaced during the waning stage of regional metamorphism (<260 Ma). Field and geochronological data indicate that the emplacement of the gold-bearing quartz-sulphide veins at Bai Dat and Bai Go occurred during the Triassic (250–200 Ma), and this period corresponds to a post-collision extensional setting in the context of the regional geology of central Vietnam. In addition, the gold-bearing veins at Bai Dat and Bai Go are hosted by the Daksa Fault Zone, which is a splay of the regional NW-SE trending Cong Plong Fault. These geological data appear to indicate that the gold mineralising event at Bai Dat and Bai Go is genetically linked to the regional orogenic event during the Indosinian Orogeny, which occurred as a consequence of the collision between the Indochina and South China Terranes in the Permian-Triassic (Fig. 8.1).

The close relationships of the gold mineralising event with the regional orogeny are well established in the orogenic gold deposits of the Yilgarn Craton and intrusion-related gold deposits in Alaska as they commonly occurred during the accretion-collision process of orogenic events (Table 8.1). At Yilgarn Craton in Western Australia, formation of the Archean orogenic gold deposits is contemporaneous with peak regional metamorphism at 2.64–2.63 Ga, during accretion and assembly of multiple blocks (Hagemann and Cassidy, 2000). Formation of the intrusion-related gold deposits in Alaska is genetically linked to the reduced, I-type granites, which were emplaced just after the peak accretionary orogenic event at the continental margin behind the accreted terrane (Hart, 2007).

Table 8.1. Comparison of geological setting and mineralisation characteristics of the Bai Dat and Bai Go gold deposits in Phuoc Son with orogenic gold deposits of Yilgarn Craton in Australia and intrusion-related gold deposits in Alaska.

Deposit types	Phuoc Son Au (Vietnam)	Orogenic Au (Western Australia)	Intrusion-related Au (Alaska)
Examples	Bai Dat, Bai Go	Golden Mile, Kalgoorlie, Mt Charlotte	Fort Knox, Pogo, Donlin Creek
Deposit size (Contained Au in Moz)	0.67	0.1–>67	1–>28
Gold grade (g/t)	6.69	4–12	0.8–4
Geological setting			
Tectonic setting	Post-collisional, extensional terrane	Accretionary and collisional terrane	Post-collisional, extensional terrane
Host rock types	Carbonaceous schist/phyllite, metagabbro	Mafic volcanic rocks, banded-iron formation, granitoids	Granites and the surrounding country rocks
Igneous association	Major (I-type, ilmenite-series)	Minor	Major (I-type, ilmenite-series)
Regional metamorphic association	Major (up to amphibolite facies)	Major (greenschist -amphibolite facies)	Minor (post-peak metamorphism)
Structural controls of ore formation	Local fault (Daksa Fault) & intersection of two regional faults (Poko & Cong Plong Faults)	Regional-scale deformation zone & local brittle-ductile shear zone	Regional strike-slip fault (Tintina Fault) & local brittle structures
Mineralisation characteristics			
Ore textures	Foliation-parallel veins	Breccia, laminated and sheared veins, dissemination	Sheeted, stockwork & fault veins, breccia, dissemination, replacement, skarn
Ore minerals	Pyrite, pyrrhotite, galena, sphalerite, chalcopyrite, electrum, native gold	Pyrite, pyrrhotite, ilmenite, loellengite, rutile, magnetite, hematite, native gold	Pyrrhotite, pyrite, arsenopyrite, molybdenite, scheelite, galena, sphalerite, chalcopyrite, bismuthinite, loellengite, stibnite, cinnabar, native gold
Metal suite	Au-Ag-Pb-Zn	Au-Ag(-As-Sb-W-Te-Se-Mo-Bi)	Au-Bi-Te-W-Mo-As (-Sb-Sn-Pb-Cu)
Alteration minerals	Pyrite, pyrrhotite, quartz	Carbonate, muscovite, biotite, amphibole, diopside,	Quartz, sericite, albite, carbonate, clay, biotite,
Electrum fineness	350–1000	900–1000	850–1000
Stable isotopes			
S source (data range; ‰)	Mixed magmatic & Carbonaceous schist/phyllite (-4 to +4)	Magmatic/crustal (-1 to +8)	Magmatic (-5 to +5)
C source (raw data range; ‰)	Marble & carbonaceous schist/phyllite (-25 to -3)	Magmatic (-6 to -5)	Magmatic/metamorphic (-9.5 to -3)
O source (raw data range; ‰)	Marble & carbonaceous schist/phyllite (+5 to +28)	Metamorphic/magmatic (+5 to +15)	Magmatic (+5 to +10)

Table 8.1 (cont.). Comparison of geological setting and mineralisation characteristics of the Bai Dat and Bai Go gold deposits in Phuoc Son with orogenic gold deposits of Yilgarn Craton in Australia and intrusion-related gold deposits in Alaska. N/A = Not Avilable.

Deposit types	Phuoc Son Au (Vietnam)	Orogenic Au (Western Australia)	Intrusion-related Au (Alaska)
Fluid inclusions			
Inclusion types	Major three-phase carbonic & two-phase carbonic aqueous inclusions, & trace halite-bearing inclusions	Mixed aqueous and carbonic inclusions	Carbonic inclusions (in deep system), carbonic & brine inclusions (in shallow system)
Gaseous compositions	$CO_2 \pm CH_4 \pm N_2 (\pm H_2S)$	$CO_2 \pm CH_4 \pm N_2$	$CO_2 \pm CH_4 \pm N_2$
Fluid temperature (°C)	250–400	250–400	250–380
Fluid salinity (wt.% NaCl equiv.)	0.5–45 (Majority of 0.5–15)	<6	<5–>30
Depth environment (km)	9–22 (mean of 15)	5–20	<1–10
pH	Near neutral	Near neutral	N/A (should be near neutral)
Fluid sources	Magmatic & metamorphic	Metamorphic ± magmatic	Magmatic
Redox	Reduced	Reduced	Reduced
Source of gold	Magma(?)	Magma(?)	Magma
Gold transport	Bisulphide complexes	Bisulphide complexes	Bisulphide ± chloride complexes
Effect of gold deposition	Fluid mixing, wall rock interaction, cooling, dissolution	Boiling, wall rock interactions (pyrite precipitation), fluid immescibility & fluid mixing	Cooling & wall rock interaction
References	Banks et al. (2004); Stevens and Fulton (2008); Olympus Company website; This study	McCuaig and Kerrich (1998); Hagemann and Cassidy (2000); Goldfarb et al. (2005); Bodnar (2007)	Newberry et al. (1995); Thompson et al. (1999); Thompson and Newberry (2000); Baker (2002); Hart (2007)

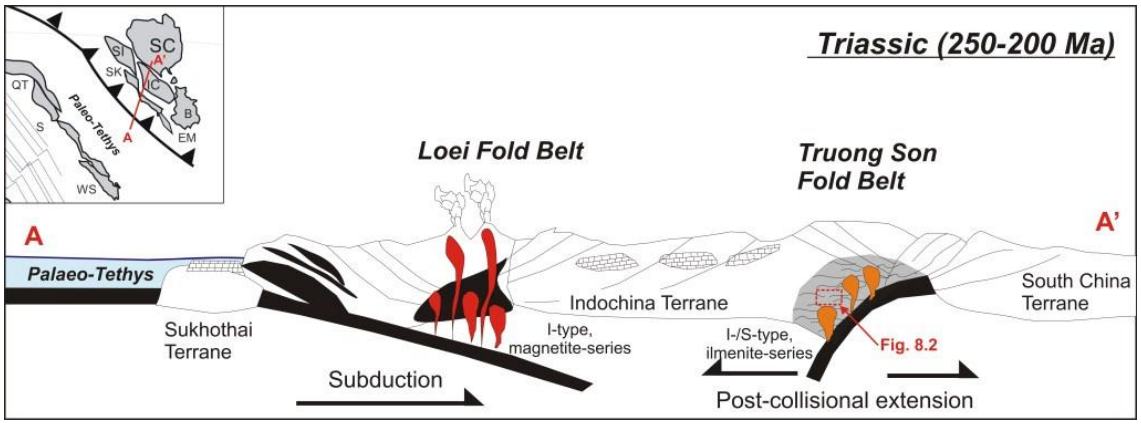

Fig. 8.1. Reconstructed tectonic setting of the Indochina Terrane during Triassic (250–200 Ma), showing that the post-collisional extension was associated with magmatism and metamorphism along the northeastern margin of the terrane, whereas the subduction-related magmatism (volcano-plutonism) occurred along the western margin of the terrane. Modified after Meffre et al. (2011).

8.3.2. Mineralisation characteristics

The foliation-parallel quartz-sulphide veins at the Bai Dat and Bai Go deposits provide distinct textural evidence suggesting that the formation of the veins is linked to the regional metamorphism of Indosinian Orogeny (see Chapter 4). The strong structural control on emplacement of the gold-bearing veins is also commonly observed in the orogenic and intrusion-related deposits, such as the laminated and sheared veins in the orogenic deposits of the Yilgarn Craton (McCuaig and Kerrich, 1998) and sheeted veins in intrusion-related deposits of Alaska (Hart, 2007).

The ore mineral assemblage at Bai Dat and Bai Go includes abundant pyrrhotite and pyrite, with minor galena, sphalerite and chalcopyrite. The lead and zinc are locally enriched and form massive sulphides within the quartz-sulphide veins. The pyrite-pyrrhotite assemblage is recognised as a diagnostic feature of a reduced condition of ore fluids (e.g., Williams-Jones et al., 2009), and is very similar to that of intrusion-related deposits in which ore fluids are predominantly derived from reduced magma (i.e., ilmenite-series granites; Baker, 2002) and thus pyrrhotite is stable (with no magnetite or hematite; Thompson et al., 1999). Meanwhile, various Fe-bearing minerals are commonly present in the orogenic deposits including pyrite, pyrrhotite, arsenopyrite, hematite, magnetite, rutile and ilmenite (Hagemann and Cassidy, 2000), indicating that the ore fluids involve a wide range of redox and sulphur fugacity conditions. The ore mineral assemblage and the associated ore fluids of the Bai Dat and Bai Go deposits are comparable to those of the Alaskan intrusion-related deposits rather than those in the orogenic deposits in Western Australia.

The Au-Pb-Zn metal association at the Bai Dat and Bai Go deposits is confined from the intimate occurrence of gold with galena and sphalerite in the quartz-sulphide veins. Such metal association is not commonly recognised in the orogenic deposits, but is reported from the intrusion-related systems of Alaska. The Alaskan intrusion-related gold deposits typically show a spatial zonation of metal assemblages (e.g., Au-Bi-Te-W-Mo-Se at core, Au-As-W-Sb at proximal and Au-As-Sb-Ag-Pb-Zn at distal parts of intrusions; Hart, 2002). On this basis, the metal association of Au-Pb-Zn at Bai Dat and Bai Go may be compatible to the distal part of the intrusion-related gold deposit model of Hart (2002).

The pyritisation consisting of abundant pyrite with minor pyrrhotite in the host rocks is a distinct alteration halo of the quartz-sulphide veins at the Bai Dat and Bai Go deposits. It is similar to the orogenic deposits as an alteration assemblage of pyrite-arsenopyrite-pyrrhotite is commonly present in the systems at the Yilgarn Craton (Hagemann and Cassidy, 2000). The alteration is considered to be a consequence of a wall rock interaction of ore fluids with

Fe-rich host rocks (Bodnar, 2007). In contrast, pyritisation is rarely observed in the intrusion-related deposits and sericitisation is recognised as a typical alteration halo of the Ag-Pb-Zn veins at the distal part of the intrusion-related gold deposits (Hart, 2007).

8.3.3. Structural Control

Structural control of the gold mineralisation at Bai Dat and Bai Go is indicated as the orebodies are hosted in the Daksa Fault Zone, which is one of major N-S trending faults in the Phuoc Son deposit area and is juxtaposed to the regional Po Ko Fault. It also appears that the development of the Daksa Fault Zone is controlled by lithological units, due to the fragile nature of the carbonaceous schist/phyllite at Bai Dat and at the boundary of the metagabbro and carbonaceous units at Bai Go. As a result, a large deformation (>several km in length) caused the Daksa Fault Zone which allowed a large volume of ore fluids (in particular magmatic fluid) to migrate from the northwestern part of the Phuoc Son area to the Bai Dat and Bai Go deposits, where the magmatic fluids mixed with the local fluids. From the detailed geochronology in this study, the timing of the deformation and the associated gold mineralisation is considered to be Triassic (250–200 Ma), under a post-collision extensional setting.

Similar structural control of gold mineralisation is often recognised at regional and local scales in the orogenic gold deposits in the Yilgarn Craton in Australia and intrusion-related gold deposits in Alaska, although the timing relationships with the regional orogeny are slightly different between the two systems. In the orogenic gold deposits at the Yilgarn Craton, the deposits which formed in an amphibolite facies metamorphic environment are contemporaneous with peak metamorphism, while those in a subgreenschist- to greenschist-facies metamorphic environment commonly post-date the peak regional metamorphism (Hagemann and Cassidy, 2000). Almost all of the granites associated with the intrusion-related gold deposits in Alaska occur along the strike-slip Tintina Fault, which formed at the back-arc setting during the mid-Cretaceous after the peak regional metamorphism of the Cordilleran Orogeny (Hart, 2007).

8.3.4. Source and transport of gold

Fluid inclusion data of the Bai Dat and Bai Go deposits share many similarities to those in the orogenic gold deposits of the Yilgarn Craton and intrusion-related gold deposits of Alaska (Table 8.1). The distinct three-phase carbonic inclusions at Bai Dat and Bai Go are also normally present in the orogenic deposits in Yilgarn Craton (Bodnar, 2007) and the deeper systems of the intrusion-related deposits in Alaska (Baker, 2002). The homogenisation

temperature range of 250–400°C of the Bai Dat and Bai Go fluid inclusions overlaps with that of the Yilgarn Craton's orogenic (250–400°C; Bodnar, 2007) and Alaskan intrusion-related gold systems (250–380°C; Baker, 2002). The main salinity range of the Bai Dat and Bai Go inclusions (0.5–15 NaCl wt.% equiv.) is comparable to that of the intrusion-related systems (<5–>30 NaCl wt.% equiv.; Baker, 2002) rather than that of the orogenic deposits (<6 NaCl wt.% equiv.; Bodnar, 2007). The higher salinity is consistent with the fact that the gold at Bai Dat and Bai Go is associated with massive galena and sphalerite, which were predominantly transported by chloride complexes in saline magmatic fluids. Hence this suggested that magmatic fluids were largely involved in the ore fluids at Bai Dat and Bai Go. Based on the daughter mineral assemblage in the fluid inclusions, the ore fluids at Bai Dat and Bai Go were reduced, near neutral pH and the gold was predominantly transported by bisulphide complexes. These fluid characteristics are consistent with those of the orogenic gold systems at Yilgarn Craton and intrusion-related gold systems in Alaska (Table 8.1).

8.3.5. Deposition of gold

Fluid inclusion data indicated that there are two main physico-chemical mechanisms for promoting gold precipitation at Bai Dat and Bai Go, including (1) fluid mixing and (2) wall rock interaction. The two effects may have operated closely to precipitate gold at Bai Dat and Bai Go.

(1) Mixing of magmatic and metamorphic fluids

Fluid inclusion microthermometric data indicated that the magmatic and metamorphic fluids were involved and mixed at the main ore zones of the Bai Dat and Bai Go deposits (Chapter 7). Given that the metals were transported by magmatic fluids, the mixing has caused abrupt changes in both the physical (e.g., temperature) and chemical (e.g., salinity, redox and pH) conditions of ore fluids. This may have resulted in precipitation of gold and associated metals (Pb and Zn). The metamorphic fluids sourced from the country rocks at Bai Dat and Bai Go (carbonaceous schist/phyllite and mategabbro units) are considered as the other fluids which mixed with the magmatic fluids at the deposits. Vein-located and wall rock pyrites at Bai Dat and Bai Go are enriched in Ni and Co. These elements are considered to have been sourced from the host rock (i.e., metagabbro), suggesting that the local metamorphic fluids were considerably involved in the main ore zones at the Bai Dat and Bai Go deposits. The mixture of metamorphic and magmatic fluids is a typical feature of the orogenic gold systems at Yilgarn Craton (Bodnar, 2007), rather than that of the intrusion-related gold systems at Alaska in which magmatic fluids are predominant (Baker, 2002).

(2) Wall rock interaction

A number of geological data suggested that the wall rock interaction was one of the main effects to promote gold precipitation at the Bai Dat and Bai Go deposits. It was evidenced by (1) pyritisation halo of the quartz-sulphide veins, (2) stable isotope characteristics, and (3) fluid inclusion data. The spatial association of the pyritisation with the mineralised quartz-sulphide veins is interpreted to have been caused by the reaction between S-rich ore fluids and Fe-rich host rocks (i.e., metagabbro; see Chapter 7). This reaction is also often recognised in the orogenic gold deposits at Yilgarn Craton and is considered to be one of the main mechanisms to precipitate gold (e.g., McCuaig and Kerrich, 1998). Cooling, the main process for gold precipitation in the intrusion-related gold deposits in Alaska (e.g., Baker, 2002), was not identified as the main gold precipitation process at the Bai Dat and Bai Go deposits.

The sulphur isotope data of Bai Dat and Bai Go with the other deposits in Phuoc Son show that the heaviest values are observed in the deposits which are closely associated with intrusive units at the northwestern part of the Phuoc Son area (i.e., Khe Rin skarn and Round Hill intrusion-hosted systems), whereas the lightest values are recorded from Bai Dat at the southern end of the Phuoc Son area. Based on the consistent variation of the sulphur isotopic values from the northwestern part of the Phuoc Son area to the Bai Dat area with few deposits existing between the two areas (i.e., Khe Do, K7, Bai Go and Bai Chuoi), it is suggested that the light sulphurs at Bai Dat and Bai Go were dominantly derived from the host carbonaceous unit. Sulphur isotope values at the orogenic gold deposits of Yilgarn Craton are broadly confined to a range from -1 to +8 ‰ and the range is interpreted to be related to magmatic and/or crustal sources (McCuaig and Kerrich, 1998). Sulphur isotopes in the intrusion-related gold systems in Alaska typically show a range from -5 to +5 ‰, which appears to indicate magmatic source (Thompson and Newberry, 2000).

The carbon and oxygen isotope data of the vein-located carbonate minerals at Bai Dat and Bai Go, together with those from other deposits in Phuoc Son, also revealed that the carbon and oxygen were predominantly sourced from the two main country rocks including the marble and carbonaceous units. In particular, predominance values of the carbonaceous schist/phyllite units are found in the main ore zone at Bai Dat. These data strongly suggest that metamorphic fluids derived from the local country rocks were involved in ore fluids at Phuoc Son. Carbon and oxygen isotope data in the orogenic gold deposits in Yilgarn Craton and intrusion-related gold deposits in Alaska are commonly interpreted as mixed magmatic and metamorphic sources (Table 8.1).

Volatile components of the Bai Dat and Bai Go fluid inclusions are commonly enriched in CO_2 gas with a considerable amount of N_2 and CH_4 gases in the main ore zones at Bai Dat and Bai Go. This evidence may indicate that the N_2 and CH_4 gases were locally sourced from the host rocks (carbonaceous schist/phyllite and mategabbro units; see Chapter 7). Such gaseous compositions (i.e., CO_2-CH_4-N_2) are commonly identified in both the orogenic gold deposits of Yilgarn Craton and intrusion-related gold deposits of Alaska (Table 8.1).

8.3.6. Formation of Depth

Depths of ore formation at the Bai Dat and Bai Go deposits were estimated using (1) FeS contents of the vein-located dark sphalerites which coexist with pyrite and pyrrhotite, and (2) microthermometric data of the three-phase carbonic inclusions in the quartz-sulphide veins. The calculated depths yielded ranges of 5.3–7.5 kbar (Chapter 5) and 3.1–5.6 kbar (Chapter 7), respectively. These pressure ranges can be translated to the depth ranges of 13.2–22.2 km and 9.3–16.8 km (based on typical lithostatic pressure gradient of 1kbar=3 km) with mean depths of 17.7 km and 13.1 km respectively. These estimated depths are broadly consistent with the wide range of metamorphic grades observed at Phuoc Son and the surrounding area, ranging from low (phyllite) to high grade (gneiss). The depth of ore formation at Bai Dat and Bai Go is estimated at approximately 15 km, which is comparable to the depths estimated for the orogenic gold systems in Yilgarn Craton (5–20 km; Goldfarb et al., 2005), rather than the Alaskan intrusion-related gold systems (<1–10 km; Baker, 2002).

8.4. GENETIC MODEL

The detailed discussions above reveal that the nature of the gold mineralisation at the Bai Dat and Bai Go deposits shares many similarities to the orogenic gold deposits in the Yilgarn Craton of Australia and intrusion-related gold deposits in Alaska. However, it can be concluded that on the regional Phuoc Son area-scale (>several km scale), the deposits show many similarities to the Alaskan intrusion-related gold systems (e.g., tectonic setting, recognition of intrusion and metal zonation), whereas they are comparable to those of the orogenic gold deposits in Yilgarn Craton on a local-scale (e.g., alteration phase and mechanism of gold precipitation). Based on these conclusions, the genetic model of the gold mineralisation at the Bai Dat and Bai Go deposits is developed in terms of district- and local deposit-scales.

8.4.1. An intrusion-related model on regional scale

In terms of the regional Phuoc Son deposit area-scale, the Bai Dat and Bai Go deposits can be classified as the distal part of the intrusion-related gold system, in which the intrusion centre is present at the Round Hill-Khe Rin area (Fig. 8.2). The intrusion-related deposit model is indicated by a few lines of evidence, such as (1) metal zonation in the gold deposits in the Phuoc Son area, and (2) a large involvement of magmatic fluids in the ore fluids.

Copper, tungsten and molybdenum are associated with gold in the intrusion-hosted and skarn systems at the Round Hill-Khe Rin area, at the northwestern part of the Phuoc Son area. In contrast, gold occurs with lead and zinc in quartz-sulphide veins hosted by metamorphic rocks (i.e., carbonaceous schist/phyllite and metagabbro) at the Bai Dat and Bai Go deposits in the southern part of the Phuoc Son area. An involvement of magmatic fluids in ore fluids at the Bai Dat and Bai Go deposits is demonstrated by fluid inclusion microthermometric data. Mernagh et al. (2007) reported that these two signatures (i.e., spatial metal zonation and presence of saline fluids) are the critical criteria to distinguish an intrusion-related gold system from an orogenic gold system in Australia as they share many similar mineralisation characteristics. These data indicate the Bai Dat and Bai Go deposits appear to be distal part of the large intrusion-related gold system, which is likely to be centred at the Round Hill-Khe Rin area and has lateral extent at least several kilometres. Banks et al. (2004) also initially proposed a similar model based on the spatial relationships of deposit types and the associated metals.

A similar intrusion-related gold deposit model is also reported from Bong Mieu (Quynh et al., 2004; Lee, 2010). A close association of gold with lead and zinc is found at the Nui Kem deposit, in which the gold-bearing quartz-sulphide veins are hosted parallel to the metamorphic foliation of the carbonaceous schists and gneisses (e.g., Quynh et al., 2004; Lee, 2010). As the intrusion-related Au-W skarn system of the Ho Ray-Trac Thang deposit is hosted in the same structure (“Bong Mieu Anticline”) of the Nui Kem Au-Pb-Zn system, an intrusion-related gold deposit model is established at Bong Mieu, in which the Nui Kem deposit represents the distal part of the system (Quynh et al., 2004; Lee, 2010).

8.4.2. Wall rock interaction model on local scale

As described before, the gold precipitation at the Bai Dat and Bai Go deposits may have caused by two main effects, including (1) mixing of magmatic and metamorphic fluids, and (2) wall rock interaction (Fig. 8.3).

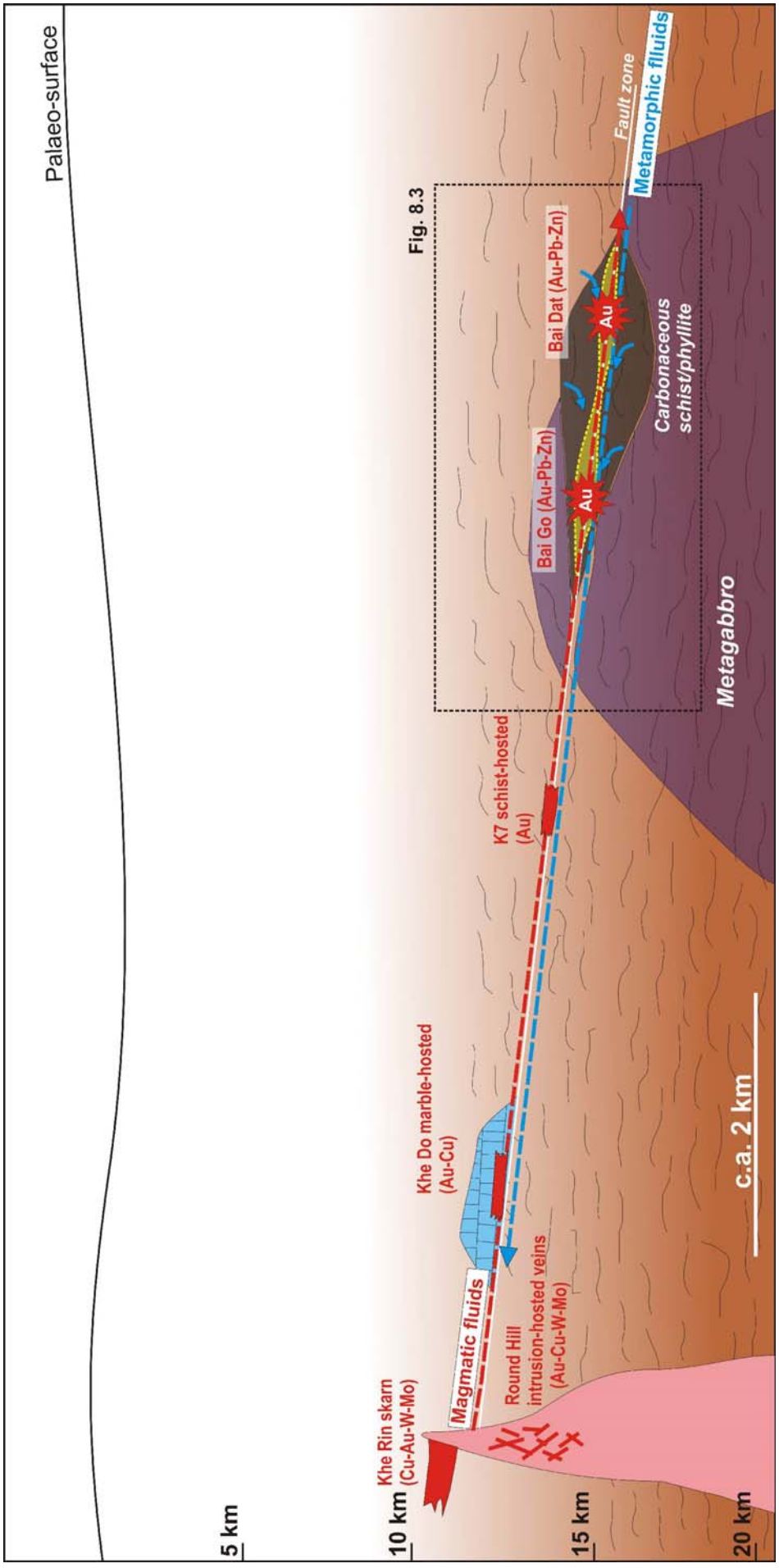

Fig. 8.2. Ore deposit model of the Phuoc Son deposit area, showing the Bai Dat and Bai Go deposits represent the distal part of a large (>several km) intrusion-related system, which has intrusion centre at the Round Hill-Khe Rin area, at the northwestern part of the Phuoc Son area. See Fig. 8.3 for detailed chemical model for the Bai Dat and Bai Go deposits.

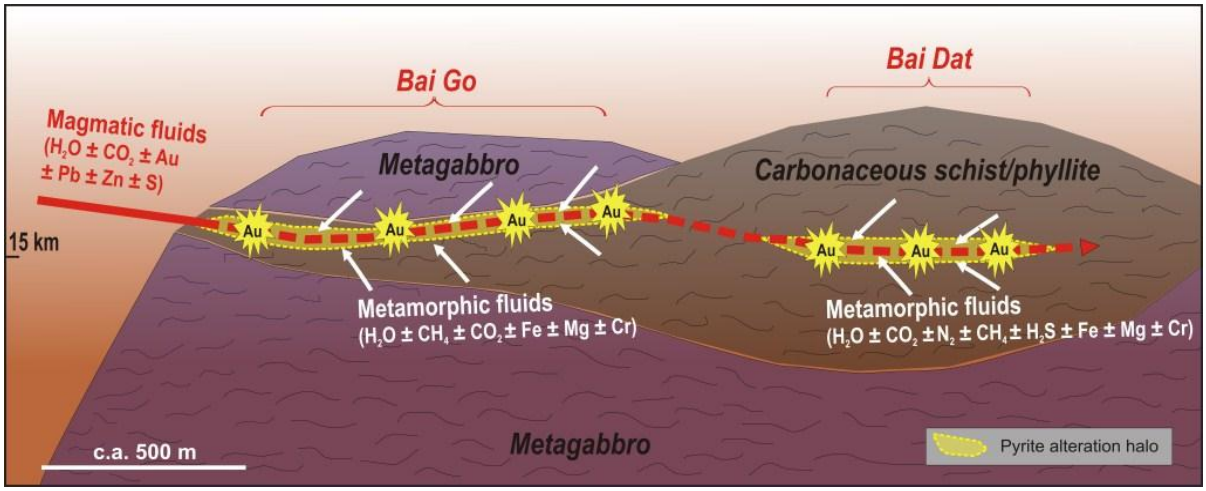

Fig. 8.3. Chemical model of the Bai Dat and Bai Go deposits of the Phuoc Son deposit area, indicating the gold precipitation occurred predominantly due to mixing of magmatic fluids with metamorphic fluids from the host rocks and wall rock interaction at Bai Dat and Bai Go.

The reduced, S-rich magmatic fluids including gold and the associated metals (i.e., Pb, Zn) travelled from the Khe Rin-Round Hill intrusion centre where the reduced granites were emplaced during the Early Triassic. The fluids later reacted with the fluids from the host rocks at Bai Dat and Bai Go (i.e., carbonaceous schist/phyllite and metagabbro) enriched particularly in Fe. The reaction may have caused precipitation of the abundant pyrite-pyrrhotite. During the interaction, destabilisation of gold-bearing fluids occurred by extraction of sulphur from the bisulphide complex and caused precipitation of the gold (see Chapter 7 for the detailed reaction). Strong evidence for this process is found in the distinct pyrite alteration halo of the quartz-sulphide veins at Bai Dat and Bai Go.

The wall rock intereaction and alteration may have occurred slowly as evidenced by; (1) large age gaps (up to 50 Ma) between the minerals having different blocking temperatures, (2) the well homogenised linear trend of the carbon-oxygen isotope data of the major deposits in Phuoc Son, and (3) a systematic sulphur isotope variation in the deposits from the northwestern to the southern parts of the Phuoc Son deposit area. This process is consistent with the geological environment at that time as the area was very deep (c.a. 15 km depth) with cooling rates as slow as 5°C/Ma during the waning stage of the regional metamorphism of Indochina Orogeny.

8.5. EXPLORATION IMPLICATIONS

Based on the established genetic model of the gold mineralisation at Bai Dat and Bai Go, several implications can be made for exploration of similar mineralised systems in the Phuoc Son deposit and the surrounding area. They are described from regional- to local-scale as below:

Margin of high grade metamorphic core complex

The origin and emplacement of gold mineralisation at Bai Dat and Bai Go are closely associated with regional metamorphic event of the Indosinian Orogeny during the Late Permian-Triassic period. This orogenic event caused the formation of a large metamorphic core complex in central Vietnam (i.e., Kontum Massif). Almost all of the known gold deposits in central Vietnam, including Phuoc Son, Phuoc Thanh and Bong Mieu, occur along the margin of the Kontum Massif, where regional faults such as Poko and Tam Ky-Phoc Son (extension of the local Cong Plong Fault at Phuoc Son) Faults are present. Hence, a strong structural influence on gold mineralising events is considered in central Vietnam and this indicates that the areas lying on or nearby the regional faults are worth being prioritised for exploration area selection.

Carbonaceous schist/phyllite and ultramafic units

The carbonaceous schist/phyllite and metagabbro units are the main host rocks of the gold-bearing quartz-sulphide veins at Bai Dat and Bai Go. These units played an important role in gold precipitation through the source of metamorphic fluid and wall rock interaction. In particular, pyritisation is a distinct alteration product in the host units at the selvage of the mineralised veins, and was most likely to have been caused due to the high iron contents of the host units (e.g., metagabbro). These results suggest that the carbonaceous schist/phyllite and metagabbro units are important for both regional- and deposit-scale exploration.

Gold associated with lead and zinc

Lead and zinc are key indicators for vectoring towards orebodies in the Phuoc Son area. Galena and sphalerite are commonly present in the gold-bearing quartz-sulphide veins, and in particular massive galena and sphalerite occur in the thicker part of ore zones at Bai Dat and Bai Go. The Au-Pb-Zn mineralisation occurs at the distal part of the large intrusion-related gold system in Phuoc Son, where the highest gold grade is found. A similar metal association (i.e., Au-Pb-Zn) is also reported from the Nui Kem deposit at Bong Mieu (Quyenh et al., 2004; Lee, 2010) and Phuoc Thanh deposit (KORES, 1999; Lee and Shin, 2003). These facts

may indicate that enrichment of lead and zinc is one of the criteria to assess the economic significance of gold prospects in regional exploration in central Vietnam.

Fluid inclusions enriched in N_2 and CH_4 gases

Fluid inclusion data can be used to identify the types of hydrothermal fluids to prioritise exploration targets in the Phuoc Son area, in which many gold prospects occur as quartz-sulphide veins. For example, if quartz-sulphide samples contain considerable amounts of N_2 and CH_4 gases in fluid inclusions, the prospect should be prioritised for exploration as these gases were found in the main mineralised zone at the Bai Dat and Bai Go deposits and they are considered to have been produced during the gold deposition (i.e., wall rock interaction of hydrothermal fluids). It is reported at the Dolgellau gold belt, North Wales, UK, that black shale-hosted auriferous quartz veins have higher levels of CH_4 and N_2 gases in fluid inclusions compared to quartz from barren veins and thus it is used as the first screening step in a regional exploration programme to prioritise targets (Shepherd et al., 1991).

8.6. FUTURE RESEARCH

A genetic model of the gold mineralisation at Bai Dat and Bai Go was established in this study, and future research that would help to constrain some of the additional questions for the formation of the Bai Dat and Bai Go deposits involves:

- *Further work to investigate the linkage between adakitic magma and gold mineralisation at Bai Dat and Bai Go:* Although the adakitic unit at Phuoc Son (i.e., dacitic porphyry) is post-mineralisation, the ages of the unit are close to the timing of gold formation at Bai Dat and Bai Go. Recent other studies also indicate that there is a close link between adakitic magma and gold and copper in magmatic deposits of the Loei and Truong Son Fold Belts in Thailand and Laos (e.g., Kamvong et al., 2007).

- *Fluid inclusion study using LA-ICPMS technique:* Although it was interpreted that gold was sourced from magma and carried by bisulphide complex in magmatic fluids, there was no absolute evidence to prove this theory. The ore fluids at Bai Dat and Bai Go were made up of two types of fluids (i.e., metamorphic and magmatic fluids), and LA-ICPMS analysis of trace elements and ore metals (e.g., Au, Ag, Pb, Zn, Cu, W) will directly constrain the source of metals and type of ore fluids carrying ore metals.

- *Detailed comparison of the Phuoc Son and Bong Mieu deposit areas:* The Phuoc Son and Bong Mieu deposits have similar geological characteristics and ore deposit types.

However, the Bong Mieu area contains an economic gold skarn deposits (i.e., the Ho Ray-Thac Trang Au-W deposit), whereas no economic skarn gold deposits were recognised at the intrusion centre (i.e., the Round Hill-Khe Rin area) in the Phuoc Son area. Comparative studies of the Phuoc Son and Bong Mieu areas will demonstrate potential for the presence of economic skarn deposit at Phuoc Son.

- *Further study of the Tra Long deposit (Prospect) and the surrounding area at the northeastern part of the Phuoc Son area:* A high gold grade has been intersected in drill holes at Tra Long, but the economic potential of the deposit is under-estimated, probably because the system is hosted in a different structure from the Daksa Fault Zone in which the Bai Dat and Bai Go and several other deposits (prospects) are present. However, detailed research of the Tra Long area could delineate the other mineralised structure and will improve understanding of the ore deposit setting in the Phuoc Son area.

REFERENCES

Alexander, B.R., 2006, 2005 Geological compilation Phuoc Son gold project and Bai Go deposit area diamond drill report. Unpublished consultant report to Olympus Pacific Minerals Inc.

Amanta Resources website. Amanta Resources Ltd. website (amantaresources.com)

Anvil Mining, 2004, Anvil Mining Annual Report 2003, 64p.

Audley-Charles, M.G., 1983, Reconstruction of eastern Gondwanaland, Nature (London), v.306, p.48-50.

Backhouse, D.J., 2004, Geological setting, alteration and nature of mineralisation at the Phu Kham copper-gold deposit, Laos PDR, Unpublished Honours thesis, CODES University of Tasmania, Hobart, Australia, 75p.

Baker, J., Peate, D., Waight, T. and Meyzen, C., 2004, Pb isotopic analysis of standards and samples using a Pb-207-Pb-204 double spike and thallium to correct for mass bias with a double-focusing MC-ICP-MS. Chemical Geology, v.211, p.275-303.

Baker, T., 2002, Emplacement depth and CO_2-rich fluid inclusions in intrusion-related gold deposits. Economic Geology, v.97, p.1111-1117.

Baker, T., Mustard, R., Brown, V., Pearson, N., Stanley, C.R., Radford, N.W. and Butler, I., 2006, Textural and chemical zonation of pyrite at Pajingo: a potential vector to epithermal gold veins. Geochemistry: Exploration, Environment, Analysis. v.6, n.4, p.283-293.

Banks, M.J., Murfitt, R.H., Quynh, N.N., Hai, L.V., 2004, Gold exploration of the Phuoc Son-Tam Ky Suture, central Vietnam - A case study, Proceedings of PacRim Congress 2004, Adelaide, p.95-104.

Banks, M., 2008, Stage one exploration results, Tien Thuan Project, Binh Dinh Province, Vietnam. Unpublished consultant report by Zedex Minerals, 65p.

Barber, A.J., Ridd, M.F. and Crow, M.J., 2011, Chapter 19; The origin, movement and assembly of the pre-Tertiary tectonic units of Thailand; in Ridd, M.F., Barber, A.J. and Crow, M.J. (eds.). The Geology of Thailand, The Geological Society London, p.507-538.

Baxter, J.L., Chisholm, J.M. and Morrison, A.D., 1992, Resource assessment at 10 June 1992, Nui Kem project, Socialist Republic of Vietnam. Unpublished consultant report by Continental Resource Management Pty Ltd.

Best, M.G., 2003, Igneous and Metamorphic Petrology, 2nd edition. Blackwll Publ. 729p.

Black L.P. and Gulson B.L., 1978, The age of the Mud tank Carbonatite, Strangways Range, Northern Territory. BMR Journal of Australian Geology and Geophysics v.3, p.227-232.

Black, L. P., Kamos, L., Allen, C.M., Aleinikoff, J.N., Davis, D.W., Korsch, R.J. and Foudoulis, C., 2003, TEMORA 1: a new zircon standard for Phanerozoic U–Pb geochronology. Chemical Geology, v.200, p.155–170.

Black, L.P., Kamo, S.L., Allen, C.M., Davis, D.W., Aleninikoff, J.N., Valley, J.W., Mundil, R., Campbell, I.H., Korsch, R.J., Williams, I.S. and Foudoulis, C., 2004, Improved $^{206}Pb/^{238}U$ microprobe geochronology by the monitoring of a trace-element related matrix effect; SHRIMP, ID-TIMS, ELA-ICP-MS, and oxygen isotope documentation for a series of zircon standards. Chemical Geology, v.205, p.115-140.

Bodnar, R.J., 1993, Revised equation and table for determining the freezing point depression of H_2O-NaCl solutions. Geochimica et Cosmochimica Acta, v.57, p.683-684.

Bodnar, R.J., 2003, Introduction to aqueous fluid systems. In: Simon, I., Anderson, A. and Marshall, D. (eds.), Fluid Inclusions: Analysis and Interpretation. Mineralogical Association of Canada, Short Course 32. p.81-99.

Bodnar, R.J., 2007, Fluid inclusions in magmatic and hydrothermal ore deposits, with applicants to exploration, in Ores and Orogenesis 2007 short course manual, 25, September, 2007, Tucson, Arizona.

Borisenko, A.S., Tran Trong Hoa, Izokh, A.E., Ngo Thi Phuong, Tran Tuan Anh, Bui An Nien and Travin, A.V., 2006, Stages of formation of gold mineralisation in the Central Vietnam., Journal of Geology, Series B., n.28, p.1-11.

Bowman, J.R., 1998, Stable-isotope systematics of skarns. In Lentz, D.R. (eds.), Mineralized intrusion-related skarn systems, Mineralogical Association of Canada Short Course Series, v.26, p.99-145.

Brost, D., 2011, Exploring and developing mineral deposits in northern Laos – the Ban Houayxai gold-silver deposit. PDF presentation file of SMEDG meeting in August 2011, 40p.

Brown, P.E. and Lamb, W.M., 1986, Mixing of H_2O-CO_2 in fluid inclusions; Geobarometry and Archean gold deposits. Geochimica et Cosmochimica Acta, v.50, p.847-852.

Bryndzia, L.T., Scott, S.D. and Spry, P.G., 1988, Sphalerite and hexagonal pyrrhotite geobarometer: experimental calibration and application to the metamorphosed sulphide ores at Broken Hill, Australia, Economic Geology, v.83, p.1193-1204.

Bryndzia, L.T., Scot, S.D. and Spry, P.G., 1990, The sphalerite and hexagonal pyrrhotite geobarometer: correction and application. Economic Geology, v.85, p.408-411.

Burin, J.N. and Kyle, J.R., 1997, Precious metal mineralogy in porphyry-, skarn- and replacement-type ore deposits of the Ertsberg (Gunung Bijih) District, Irian Jaya, Indonesia. Economic Geology, v.92, p.535-550.

Burrett, C.F., 1974, Plate tectonics and the fusion of Asia. Earth and Planetary Science Letters, v.21, p.181-189.

Burruss, R.T., 2003, Chapter 11. Raman Spectroscopy of fluid inclusions. In: Simon, I., Anderson, A. and Marshall, D. (eds.), Fluid Inclusions: Analysis and Interpretation. Mineralogical Association of Canada, Short Course 32. p.279-289.

Camprubi, A. and Albinson, T., 2007, Epithermal deposits in Mexico – Update of current knowledge, and an empirical reclassification, The Geological Society of America Special Paper 442, p.377-415.

Cannell, J. and Smith S., 2008, High-grade supergene enriched and exotic copper deposits in the Sepon Mineral District, Lao PDR, Proceedings of PacRim Congress 2008, November 2008, Gold Coast, p.355-361.

Cao Dinh Trieu, 1991, Deep structures and characteristics of seismic activity on the territory of Vietnam, 140p.

Carter, A., Roques, D., Bristow, C. and Kinny, P., 2001, Understanding Mesozoic accretion in Southeast Asia: Significance of Triassic thermotectonism (Indosinian orogeny) in Vietnam. Geology, vol.29, p.211-214.

Charusiri, P., Daorek, V., Archibald, D., Hisada, K. and Ampaiwan, T., 2002, Geotectonic Evolution of Thailand; A new synthesis, Journal of the Geological Society of Thailand, n.1, p.1-20.

Chen, H., 1972, The thermodynamics and composition of carbon dioxide hydrate, Unpublished MSc thesis, Syracuae University, New York, 67p.

Christie, A.B., Simpson, M.P., Brathwaite, R.L., Mauk, J.L. and Simmons, S.F., 2007, Epithermal Au-Ag and related deposits of the Hauraki Goldfield, Coromandel volcanic zone, New Zealand. Economic Geology, v.102, p.785-816.

Coleman, M.L.,1977, Sulphur isotopes in geology, Journal of Geological Society of London, v.133, p.593-608.

Cook, N.J., Ciobanu, C. L., Pring, A., Skinner, W., Shimizu, M., Danyuahevaky, L., Saini-Eidukat, B. and Melcher, F., 2009, Trace and minor elements in sphalerite: A LA-ICPMS study. Geochimica et Casmochimica Acta, v.73, p.4761-4791.

Cooke, D.R. and Simmons, S.F., 2000, Characteristics and genesis of epithermal gold deposits, Reviews in Economic Geology, v.13, p.221-244.

Corfu, F., Hanchar, J.M., Hoskin, P.W.O. and Kinny, P.D., 2003, Atlas of zircon textures, Reviews in Mineralogy and Geochemistry, v.53, p.469-500.

Corlett, G., 2001, Petrogaphic analysis of two grab samples from Khe Rin, the Phuoc Son gold project, central Vietnam. Unpublished consultant report for Olympus Pacific Minerals Inc., 25p.

Cox, K.G., Bell, J.D. and Pankhurst, R.J., 1979, The interpretation of igneous rocks. George, Allen and Unwin, London, 450p.

Craig, H., 1957, Isotope standards for carbon and oxygen and correction factors for mass spectrometric analysis of carbon dioxide. Geochimica et Cosmochimica Acta., v.12, p.133-149.

Cromie, P.W., 2010, Geological setting, geochemistry and genesis of the Sepon gold and copper deposits, Laos, Unpublished PhD thesis, CODES University of Tasmania, 395 p.

Cromie, P.W. and Khin Zaw, 2003, Geological setting, nature of ore fluids and sulphur isotope geochemistry of the Fu Ning Carlin-type gold deposits, Yunnan Province, China. Geofluids, v.3, p.133-143.

Crow, M.J. and Khin Zaw, 2011, Chapter 17; Metalliferous Minerals; in Ridd, M.F., Barber, A.J. and Crow, M.J. (eds.). The Geology of Thailand, The Geological Society London, p.459-492.

Davies, B., 2010, Structural geology, veining and mineralisation at Dak Sa. Unpublished consultant report to Olympus Pacific Minerals Inc.53p.

Dedenczuk, D., 1998, Epithermal gold mineralisation at Khao Sai, Central Thailand. Unpublished Honours thesis at CODES University of Tasmania, Hobart, Australia, 104p.

Defant, M.J. and Drummond, M.S., 1990, Deviation of some modern arc magmas by melting of young subducted lithosphere. Nature, v.347, p.662-665.

De Little, J.V., 2005, Geological setting, nature of mineralisation, and fluid characteristics of the Wang Yai prospects, central Thailand. Unpublished Honours thesis, CODES University of Tasmania, Hobart, Australia, 113p.

Diehl P. and Kern H., 1981, Geology, mineralogy, and geochemistry of some carbonate-hosted Lead-Zinc deposits in Kanchanaburi Province, Western Thailand. Economic Geology, v.76, p.2128-2146.

Dill, H.G., Melcher, F. and Botz, R., 2008, Meso- to epithermal W-bearing Sb vein-type deposits in calcareous rocks in western Thailand; with special reference to their metallogenic position in SE Asia. Ore Geology Reviews, v.34, p.242-262.

Drummond, M.S., Defant, M.J. and Kepezhinskas, P.K., 1996, Petrogenesis of slab-derived trondhjemite-tonlite-dacite/adakite magmas. Geological Society of America, Special Paper 315, p.205-215.

Eggins, S.M., Grun, R., McMulloch, M.T., Pike, A.W.G., Chappell, J., Kinsley, L., Mortimer, G., Shelley, M., Murray-Wallace, C.V., Spotl, C. and Taylor, L., 2005, In situ U-series dating by laser ablation multi-collector ICPMS: new prospects for Quaternary geochronology: Quaternary Science Review, v.24, p.2523-2538.

Eggins, S.M., Kinsley, L.P.J. and Shelley, J.M.G., 1998, Deposition and element fractionation processes during atmospheric pressure laser sampling for analysis by ICP-MS: Applied Surface Science, p.278-286.

Encom Technology, 2008, Phuoc Son project data interpretation. Unpublished consultant report to Olympus Pacific Minerals Inc., 19p.

Fan, P-F., 2000, Accreted terranes and mineral deposits of Indochina, Journal of Asian Earth Sciences, v.18, n.3, p.343-350.

Gao, Y., Hou, Z., Kamber, B.S., Wei, R., Meng, X. and Zhao, R., 2007, Adakite-like porphyries from the southern Tibetan continental collision zones: evidence for slab melt metasomatism. Contributions to Mineralogy and Petrology, v.153, p.105-120.

Gatinsky, G.Y., 2005, Tectonics and geodynamic prerequisites of mineral resource distribution in the Indochina region, Geology of Ore Deposits, v.47, n.4, p.309-325.

Gemmell, J.B., Simmons, S.F. and Zantop, H., 1988, The Santo Nino silver-lead-zinc vein, Fresnillo district, Zacatecas, Mexico: Part I. structure, vein stratigraphy, and mineralogy. Economic geology, v.83, p.1597-1618.

Goldfarb, R.J., Baker, T., Dube, B., Groves, D.I., Hart, C.J.R. and Gosselin, P., 2005, Distribution character, and genesis of gold deposits in metamorphic terranes. In: Hedenquist, J.W., Thompson, R.J., Goldfarb, R.J. and Richards, J.P. (eds.), Economic Geology 100th Anniversary Volume, p.407-450.

Greener, S., 1999, Wall rock alteration and vein mineralogy of C-zone of low sulphidation Au-Ag epithermal deposit in the Chatree Prospect, Thailand. Unpublished Honours thesis at CODES University of Tasmania, Hobart, Australia, 113p.

Groves, D.I., Goldfarb, R.J., Robert, F. and Hart, C.J.R., 2003, Gold deposits in metamorphic belts: Overview of current understanding, outstanding problems, future research and exploration significance. Economic Geology, v.98, p.1-29.

Gulson, B.L., 1986, Lead isotopes in mineral exploration. Developments in Economic Geology, v.23, p.1-245.

Hada, S., Bunopas, S., Ishii, K. and Yoshikura, S., 1999, Rift-drift history and the amalgamation of Shan-Thai and Indochina/East Malaya blocks; in Metcalfe, I., Ren, J., Charvet, J. and Hada, S. (eds.), Gondwana dispersion and Asian accretion. IGCP 321 final results volume, p.67-87.

Hall, R., 2002, Cenozoic geological and plate tectonic evolution of SE Asia and the SW Pacific; computer-based reconstructions, model and animations, Journal of Asian Earth Sciences, v.20, n.4, p.353-431.

Halpin, J., Khin Zaw, Hai Thanh Tran, Meffre, S., Lai, C.K., Sang Quang Dinh, Manaka, T., Cumming, G. and Crawford, T., 2010, The Early Palaeozoic to Early Mesozoic tectonic history of eastern Indochina and the southern South China margin. Final report on "Ore Deposits of SE Asia" Project. 29p.

Hagemann, S.G. and Cassidy, K.F., 2000, Archean Orogenic Gold Deposits. SEG Reviews, v.13, p.9-68.

Hannington, M.D. and Scott, S.D., 1989, Gold mineralisation in volcanogenic massive sulphide deposits: implications of data from active hydrothermal vents in the modern seafloor. In: Keays, R.R., Ramsay, W.R.H., Groves, D.I. (eds). The geology and gold deposits: perspective in 1988. Economic Geology Monograph 6, p.491-507.

Hart, C.J.R., 2007, Reduced intrusion-related gold systems. In Goodfellow,W.D. (ed.), Mineral deposits of Canada: A synthesis of major deposit types, district metallogeny, the evolution of geological provinces, and exploration methods. Geological Association of Canada, Minerals Deposits Division, Special Publication No.5, p.95-112.

Hart, C.J.R., McCoy, D., Goldfarb, R.J., Smith, M., Roberts, P., Hulstein, R., Bakke, A.A. and Bundtzen, T.K., 2002, Geology, exploration and discovery in the Tintina gold province, Alaska and Yukon. Society of Economic Geologists Special Publication, vol. 9, p.241-274.

Hellstorm, J., Paton, C., Woodhead, J. and Hergt, J., 2008, Lolite: software for spatially resolved LA-(quadrupole and MC) ICPMS analysis. Mineralogical Association of Canada short course series 40.

Henley, R.W. and Brown, K.L., 1985, A practical guide to the thermodynamics of geothermal fluids and hydrothermal ore deposits: In Berger, B.R. and Bethke, P.M. (eds.). Geology and geochemistry of epithermal systems: Review in Economic Geology, v.2, p.25-44.

Hisada, K., Sugiyama, M. Ueno, K., Charusiri, P. and Arai, S., 2004, Missing ophiolite rocks along the Mae Yuam Fault as the Gondwana-Tethys divide in north-west Thailand, Island Arc, v.13, p.119-127.

Hodkiewicz, P.F., Groves, D.I., Davidson, G.J., Weinberg, R.F. and Hagemann, S.G., 2009, Influence of structural setting on sulphur isotopes in Archean orogenic gold deposits, Eastern Goldfields Province, Yilgarn, Western Australia, Mineralium Deposita, v.44, p.129-150.

Hoefs, J., 1997, Stable Isotope Geochemistry. Springer-Verlag, New York. 201p.

Hofstra, A.H. and Cline J.S., 2000, Characteristics and models for Carlin-type gold deposits. Reviews in Economic Geology, v.13, p.163-220.

Hotson, M.D., 2009, The geology and tectonic framework of Cu-Au prospects in the Phonsavan District, northern Laos, Unpublished Honours thesis, CODES University of Tasmania, Hobart, Australia, 115p.

Huff, T.A. and nebelek, P.I., 2007, Production of carbonic inclusions during metamorphism of graphitic pelites in a collisional orogeny-An assessment from fluid inclusions. Geochimica et Cosmochimica Acta, v.71, p.4997-5015.

Huston, D.L., Bottrill, R.S., Creelman, R.A., Khin Zaw, Ramsden, T.R., Rand, S.W., Gemmell, J.B., Jablonski, W., Sie, S.H. and Large, R.R., 1992, Geologic and geochemical controls on the mineralogy and grain size of gold-bearing phases, Eastern Australian Volcanic-Hosted Massive Sulfide deposits. Economic Geology, v.87, p.542-563.

Huston, D.L., Sie, S.H., Suter, G.F., Cooke, D.R. and Both, R.A., 1995a, Trace elements in sulfide minerals from eastern Australian volcanic-hosted massive sulfide deposits: Part 1. Proton microprobe analyses of pyrite, chalcopyrite and sphalerite, and Part 2. Selenium levels in pyrite: Comparison with ^{34}S source of sulfur in volcanogenic hydrothermal systems. Economic Geology, v.90, p.1167-1196.

Huston, D.L., Power, M., Gemmell, J., B. and Large, R., R., 1995b, Design, calibration and geological application of the first operational Australian laser ablation sulphur isotope microprobe. Australian Journal of Earth Sciences, v.42, p.549-555.

Hutchison, C.S., 1989, Geological evolution of South-east Asia, Oxford Monographs on Geology and Geophysics, v.13, 368p, Oxford University Press.

Hutchison, M.N. and Scott, S.D., 1981, Sphalerite geobarometry in the Cu-Fe-Zn-S systems. Economic Geology, v.76, p.143-153.

Ishihara, S., 1977, The magnetite-series and ilmenite-series granitic rocks: Mining Geology, v.27, p.293-305.

Ishihara, S., 1979, Lateral variation of magnetic susceptibility of the Japanese granitoids. The Journal Geological Society of Japan, v.85, p.509-523.

Ishihara, S., 1981, The granitoid series and mineralisation. Economic Geology, 75th Anniversary Volume, p.458-484.

Ishihara, S., 1998, Granitoid series and mineralisation in the circum Pacific Phanerozoic granitic belts. Resource Geology, v.48, p.219-224.

Jackson, S.E., Pearson, N.J., Griffin, W.L. and Belousova, E.A., 2004, The application of laser ablation-inductively coupled plasma-mass spectrometry to in situ U–Pb zircon geochronology. Chemical Geology, v.211, p.47-69.

Kamvong, T., 2004, Geochemistry and genesis of Phu Lon Cu-Au skarn deposit, Northeast Thailand, Unpublished Honours thesis, CODES University of Tasmania, Hobart, Australia, 96p.

Kamvong, T., 2006, Geology and genesis of porphyry-skarn Cu-Au deposits at the northern Loei Fold Belt, Northeastern Thailand and Laos, In geochronology, metallogenesis and deposit styles of the Loei Fold Belt in Thailand and Laos PDR: Progress report for ARC Linkage Project, November, 2006.

Kamvong, T., 2008, Technical report review of the copper prospects, Xiengkhouang Region, Laos. Unpublished report for Phu Bia Mining Limited, 41p.

Kamvong, T., Khin Zaw and Meffre, S., 2007, Possible adakitic porphyries and their tectonomagmatic and metllogenic implications: Evidence from the northern Loei Fold Belt, Thailand and Laos; in Andrew, C.D. (ed.). Proceedings of the 9th Bbiennial SGA meeting, Dublin, 2007, p.399-402.

Kanaya, H. and Ishihara, S., 1973, Regional variation of magnetic susceptibility of the granitic rocks in Japan: The Journal of the Japanese Association of Mineralogists, Petrologists and Economic Geologists, v.68, p.219-224.

Kay, R.W., 1978, Aleutian magnesian andesites: Melts from subducted Pacific ocean crust. Journal of Volcanology and Geothermal Research, v.4, p.117-132.

Khin Zaw, Huston, D.L., Large, R.R., Mernagh, T. and Hoffmann, C.F., 1994, Microthermometry and geochemistry of fluids inclusions from the Tennant Creek gold-copper deposits: implications for ore deposition and exploration. Mineralium Deposita, v.29, p.288-300.

Khin Zaw and Large, R.R., 1996, Petrology and geochemistry of sphalerite from the Cambrian VHMS deposits in the Rosebery-Hercules district, western Tasmania: implications for gold mineralisation and Devonian metamorphic-metasomatic processes. Mineralogy and Petrology, v. 57, p.97-118.

Khin Zaw, Meffre, S. and higher degree students, 2007a, Metallogenic relations and deposit-scale studies, Final Report, Geochronology, metallogenesis and deposit styles of Loei Fold Belt in Thailand and Laos PDR, ARC Linkage Project.

Khin Zaw, Rodmanee, T., Khositanont, S., Thanasuthipitak, T. and Ruamkid, S., 2007b, Geology and genesis of Phu Thap Fah gold skarn deposit, northeastern Thailand: Implications for reduced gold skarn formation and mineral exploration; in Tantiwanit, W. (ed.). Proceedings of GEOTHAI'07 International Conference on Geology of Thailand, 21-22 November 2007, Bangkok, Thailand, p.93-95.

Khin Zaw, Rodmanee, T., Khositanont, S. and Ruamkid, S., 2008, Geology and genesis of reduced gold skarn formation at Phu Thap Fah deposit, northeast Thailand. Proceedings of the 33rd International Geological Congress (IGC). Oslo, Norway, 6-14 August 2008. CD-ROM.

Khin Zaw, Meffre, S. and the team, 2010, Final report on "Ore Deposits of SE Asia" Project.

Khin Zaw, Meffre, S. and the team, 2011, Implementation report on "Ore Deposits of SE Asia" Project.

Khin Zaw, Meffre, S., Kamvong, T., Stein, H., Vasconcelos, P. and Golding, S., 2009, Geochronological and metallogenic framework of Cu-Au skarn deposits long Loei Fold Belt, Thailand and Lao PDR. Proceedings of the 10th biennial SGA meeting: 17-20 August 2009, Townsville, Australia, p. 309-311.

Khositanont, S., 1990, The genesis of the Sn-W deposits at Samoeng Mine, Thailand: Evidence from fluid inclusions. Unpublished MSc thesis at McGill University, Montreal, Quebec, Canada, 124p.

Khositanont, S., Khin Zaw and Ounchanum, P., 2009, Mineralisation characteristics and ore fluid of Huai Kham On gold deposit, northern Thailand. Advances in Geoscience (AOGS), v.13, p.1-12.

Kiratisevee, S., Prewett, W. and Asnachinda, P., 2000, Synthetic manganese dioxide as a collector for trace elements in stream water surveys. Journal of Geochemical exploration, v.68, p.47-55.

KORES (Korea Resources Corporation), 1999, Report on the joint geological and mineral exploration in Phuoc Son District, Quang Nam Province, the Socialist Republic of Vietnam. KORES and the Department of Geology and Minerals of Vietnam, Seoul, 289p.

Kosler, J., 2001, Laser-ablation ICPMS study of metamorphic minerals and processes; in Sylvester P. J. (ed.). Laser-ablation-ICPMS in the earth sciences; principles and applications Mineralogical Association of Canada Short Course Handbook 29, p.185-202.

Kromkhun, K., 2005, Geological setting, mineralogy, alteration and nature of ore fluid of the H zone, the Chatree deposit, Thailand. Unpublished MSc thesis at CODES University of Tasmania, Hobart, Australia, 157p.

Lai, C.K., Meffre, S., Crawford, A.J., Khin Zaw, Halpin, J.A., Xue, C.D. and Salam, A., 2013 (in press), The Central Ailaoshan ophiolite and modern analogs. Gondwana Research.

Large, R.R., Maslennikov, V.V., Robert, F., Danyushevsky, L.V. and Chang, Z., 2007, Multistage sedimentary and metamorphic origin of pyrite and gold in the giant Sukhoi Log deposit, Lena Gold Province, Russia. Economic Geology, v.102, p.1233-1267.

Lee, I. and Shin, D., 2003, Trimodal distribution of CO_2-bearing fluid inclusions in the gold-silver-bearing quartz veins of the Phuoc Thanh area, central Vietnam: Its implication to the Au-Ag precipitation. Geosciences Journals, v.7, n.1, p.21-26.

Lee, Y., 2010, Geological setting and mineralisation characteristics of the Bong Mieu gold mine, central Vietnam, Unpublished Master of Economic Geology thesis, CODES University of Tasmania, Hobart, Australia, 97p.

Lepvrier, C., Maluski, H., Nguyen, V.V., Roung, D., Axente, V. and Rangin, C., 1997, Indosinian NW-trending shear zones within the Truong Son Belt (Vietnam); ^{40}Ar-^{39}Ar Triassic ages and Cretaceous to Cenozoic overprints, Tectonophysics, v.283, n.1-4, p.105-127.

Lepvrier, C., Maluski, H., Vu Van Tich, Leyreloup, A., Phan Truong Thi and Nguyen Van Vuong, 2004, The Early Triassic Indosinian orogeny in Vietnam (Truong Son Belt and Kontum Massif); implications for the geodynamic evolution of Indochina. Techtonophysics, v.393, p.87-118.

Lim, Y., 2012, Geological setting and mineralisation characteristics of the Steung Nambrai-Elephant Au-base metal system, eastern Cambodia. Unpublished Master of Economic Geology thesis, CODES University of Tasmania, Hobart, Australia.

Loader, S.E., 1999, Supergene enrichment of the Khanong copper resources, Sepon Project, Lao PDR. Proceedings of the PACRIM'99 Conference, Bali, Indonesia, 1999, p.263-270.

Lynch, G. and Mengel, F., 1995, Metamorphism of arsenopyrite-pyrite-sphalerite-pyrrhotite lenses, Western Cape Breton Island, Nova Scotia. The Canadian Mineralogist, v.33, p.105-114.

MacNamara, J. and Thode, H.G., 1950, Comparison of the isotopic constitution of terrestrial and meteoric sulphur. The Physical Review, v.78, p.307-308.

Makoundi, C., 2012, Geology, geochemistry and metallogenesis of selected sediment-hosted gold deposits in the Central Gold Belt, Peninsular Malaysia, Unpublished MSc thesis at CODES University of Tasmania, Hobart, Australia, 212p.

Maloney, S., 2008, Mineralisation characteristics of Ang Noi Prospect, Century tenement, Lao PDR. Unpublished Honours thesis, CODES University of Tasmania, Hobart, Australia, 90p.

Manaka, T., Khin Zaw and Meffre, S., 2007, Mineralisation characteristics of the Long Chieng Track (LCT) deposit, Lao PDR, in Tantiwanit, W. (ed.). Proceedings of GEOTHAI'07 International Conference on Geology of Thailand, 21-22 November 2007, Bangkok, Thailand, p.199-201.

Manaka, T., 2008, Geological setting and mineralisation characteristics of the Long Chieng Track and Ban Houayxai deposits, Lao PDR, Unpublished MSc thesis at CODES University of Tasmania, Hobart, Australia, 159p.

Manaka, T., Khin Zaw and Meffre, S., 2009, Geology and mineralisation characteristics of the Ban Houayxai epithermal Au-Ag deposit, Lao PDR. Proceedings of the 10th biennial SGA meeting: 17-20 August 2009, Townsville, Australia, p.530-532.

Manaka, T., Khin Zaw, Lim, Y. and Meffre, S., 2012, Update geology and tectonic framework of Cambodia and South Vietnam. 1st quarterly report for "Ore Deposits of SE Asia" project, 9p.

Markey, R.J., Stein, H.J. and Morgan, J.W., 1998, Highly precise Re-Os dating of molybdenite using alkaline fusion and NTIMS. Talanta, v.45, p.935-946.

Mason, D., 1997, Petrographic descriptions and interpretation for eleven drill core rock samples, Long Chieng Track prospect (Lao PDR). Consultants Report for Phu Bia Mining Ltd.

McCrea, J.M., 1950, On the isotopic chemistry of carbonates and a paleo-temperature scale. J. Chem. Phys., v.18, p.849-857.

McCuaig, T.C. and Kerrich, R., 1998, P-T-t-deformation-fluids characteristics of lode gold deposits: evidence from alteration systemtics. Ore Geology Review, v.12, p.381-453.

Meffre, S., Khin Zaw and team, 2011, Tectonic models and ore genesis. Report for the implementation meeting of Ore Deposits of SE Asia Project, 17th October, 2011, Hobart, Tasmania.

Meffre, S., Large, R. R., Scott, R., Woodhead, J., Chang, Z., Gilbert, S. E., Danyushevsky, L. V., Maslennikov, V., and Hergt, J. M., 2008, Age and pyrite Pb-isotopic composition of the giant Sukhoi Log sediment-hosted gold deposit, Russia: Geochimica et Cosmochimica Acta, v.72, p.2377-2391.

Meinert, L.D., 1997, Geology, zonation, and fluid evolution of the Big Gossan Cu-Au skarn deposit, Ertsberg District, Iriyan Jaya. Economic Geology, v.92, p.509-534.

Mernagh, T.P., Bastrakov, E.N., Khin Zaw, Wygralak, A.S., Wyborn, A.I., 2007, Comparison of fluid inclusion data and mineralization process for Australian orogenic gold and intrusion-related gold systems. Acta Petrologica Sinica, v.22(1), p.21-32.

Metcalfe, I., 1988, Origin and assembly of south-east Asian continental terranes; In Audley-Charles, M.G. and Hallam, A. (eds.), Gondwana and Tethys, Geological Society Special Publications, v.37, p.101-118.

Metcalfe, I., 1996, Gondwanaland dispersion, Asian accretion and evolution of eastern Tethys, Australian Journal of Earth Sciences, v.43, n.6, p.605-623.

Metcalfe, I., 1999, Gondwana dispersion, Asian accretion: an overview; in Metcalfe, I. (ed.), Gondwana dispersion and Asian accretion. IGCP 321 final results volume, p.9-28.

Morrison, G.W., Rose, W.J. and Jaireth, S., 1991, Geological and geochemical controls on the silver content (fineness) of gold in gold-silver deposits. Ore Geology Reviews, v.6, p.333-364.

Murakami, H. and Ishihara, S., 2013 (in press), Trace elements of Indium-bearing sphalerite from tin-polymetallic deposits in Bolivia, China and Japan: A femto-second AL-ICPMS study. Ore Geology Reviews.

Newberry, R.J., McCoy, D.T. and Brew, D.N., 1995, Plutonic-hosted gold ores in Alaska: Igneous vs. metamorphic origins. Resource Geology Japan, Special Issue No.18, p.57-100.

Norman, M., Robinson, P. and Clark, D., 2003, Major- and trace-element analysis of sulphide ores by laser-ablation ICP-MS, solution ICP-MS, and XRF; new data on international reference materials. The Canadian Mineralogist, v.41, Part 2, p.293-305.

Norrish, K. and Chappell, B.W., 1977, X-ray fluorescence spectrometry, in Zussman, J (ed): Acad. Press, New York, 720p.

Ohmoto, H. and Rye, R.O., 1979, Isotopes of sulphur and carbon, in Barned, H.L. (ed.), Geochemistry of hydrothermal ore deposits (2nd edition): Wiley, p.509-567.

Olympus website. Olympus Pacific Minerals Inc. website (olympuspacific.com)

O'Neil, J.R., Clayton, R.N. and Mayeda, T.K., 1969, Oxygen isotope fractionation in divalent metal carbonates. Journal of Chemical Physics, v.52, p.5547-5558.

Osanai, Y., Owada, M., Tsunogae, T., Toyoshima, T., Hokada, T., Trinh Van Long, Sajeev, L. and Nakano, N., 2001, Ultrahigh-temperature politic granulites from the Kontum Massif, central Vietnam: Evidence for East Asian Jaxtaposition at ca. 250 Ma. Gondwana Research, v.4, p.720-723.

Owada, M., Osanai, Y., Hokada, T. and Nakano, N., 2006, Timing of metamorphism and formation of garnet granite in the Kontum Massif, central Vietnam: Evidence from monazite EMP dating. Journal of Mineralogical and Petrological Sciences, v.101, p.324-328.

Owada, M., Osanai, Y., Nakano, N., Matsushita, T., Tran Ngoc Nam, Tsunogae T., Toyoshima, T., Bonh. P. and Kagami, H., 2007, Crustal anatexis and formation of two types of granitic magmas in the Kuntum Massif, central Vietnam; implications for magma processes in collision zones, Gondwana Research, v.12, n.4, p.428-437.

Oyarzun, R., Marquez, A., Lillo, J., Lopez, I. and Rivera, S., 2001, Giant versus small porphyry copper deposits of Cenozoic age in northern Chile: Adakitic versus normal calc-alkaline magmatism: Mineralium Deposita, v.36, p.794-798.

PanAust, 2012, PanAust Annual Report 2011.

PanAust website. PanAust website (www.panaust.com.au)

Pandalai, H.S., Jadhav, G.N., Mathew, B., Panchapakesan, V., Raju, K.K. and Patil, M.L., 2003, Dissolution channels in quartz and the role of pressure changes in gold and sulphide deposition in the Archean, greenstone-hosted, Hutti gold deposit, Karnataka, India. Mineralium Deposita, v.38, p.597-624.

Paton,C., Woodhead, J.D., Hellstrom, J.C. Hergt, J.M, Greig,A. and Maas, R., 2010, Improved laser ablation U-Pb zircon geochronology through robust down-hole fractionation correction. Geochemistry, Geophysics, Geosystems11, p.1525-2027.

Patterson, J., 2005, Khamthonglai (KTL) Cu-Au prospect Geological Model. Unpublished consultant report for Phu Bia Mining Ltd.

Pearce, J.A. and Gale, G.H., 1977, Identification of ore-deposition environment from trace element geochemistry of associated igneous host rocks. Geological Society Special Publication, v.7, p.14-24.

Pearce, J.A., Harris, N.B.W. and Tindle, A.G., 1984, Trace element discrimination diagrams for the tectonic interpretation of granitic rocks. Journal of Petrology, v.25, p.956-983.

Pearce, J. A. and Norry, M.J., 1979, Petrogenetic imlplications of Ti, Zr, Y and Nb variations in volcanic rocks. Cntribution Mineral Petrology, v.69, p.33-47.

Pham Khoan, Quach Van Gung and Bui Kim Thanh, 1995, The faults and intrusion of Vietnam's territory found according to the interpretation of geophysical data, Journal of Geology, Series B, v.5-6, 395p.

Phillips, G.N., Groves, D.I., Neall, F.B., Donnelly, T.H., Lambert, I.B., 1986, Anomalous sulphur isotope compositions in the Golden Mile, Kalgoolie. Economic Geology, v.81, p.2008-2015.

Purdy, J.W. and Jager, E., 1976, K-Ar ages on rock-forming minerals from the Central Alps: Memorie degli Instituti di Geologia e Mineralogia dell'U-niversita di Padova, v.30, p.1-31.

Quynh, N.N., Murfitt, R.H., Sirinawin, T. and Shywoluo, W., 2004, The Bong Mieu gold project, Phuoc Son-Tam Ky Suture, central Vietnam. Proceedings of PacRim Congress 2004, Adelaide, p.347-358.

Reich, M., Kesler, S.E., Utsunomiya, S., Palenik, C.S., Chryssoulis, S.L. and Ewing, R.C., 2005, Solubility of gold in arsenian pyrite. Geochimica et Cosmochimica Acta, v.69, n.11, p.2781-2796.

Richards, J.P., 2011, High Sr/Y arc magmas and porphyry Cu±Mo±Au deposits: Just add water. Economic Geology, v.106, p.1075-1081.

Richards, J.P. and Kerrich, R., 2007, Adakite-like rocks: Their diverse origins and questionable role in mettallogenesis. Economic Geology, v.102, p.537-576.

Ridd, M.F., 1971, Southeast Asia as part of Gondwanaland. Nature, London, v.234, p.531.

Robinson, B.W. and Kasakabe, M., 1975, Quantitative preparation of SO_2 for $^{34}S/^{32}S$ analyses from sulphides by combustion. Analytical Chemistry, v.47, n.7, p.1179-1181.

Roedder, E., 1984, Fluid inclusions. Reviews in Mineralogy, v.12, 644p.

Roedder, E and Bodnar, R.J., 1997, Fluid inclusion studies of hydrothermal ore deposits (Chapter 13). In: Barnes, H.L., (ed.), Geochemistry of hydrothermal ore deposits. John Wiley and Sons, INC., p.657-697.

Rollinson, H.R., 1993, Using Geochemical Data: Evaluation, Presentation, Interpretation: New York, Longman Group, 352p.

Rombach, C.S., Newberry, R.J., Goldfarb, R.J. and Smith, M., 2002, Geochronology and mineralization of the Liese zone, Pogo deposit, Alaska. Proceeding of Denver Annual Meeting of the Geological Society of America, 27-30 October 2002, Denver, Colorado, USA.

Russian Geological Survey, 1991, Cambodia Geological Map by Russian Geological Survey.

Rye, R.O., 1993, The evolution of magmatic fluids in the epithermal environment: the stable isotope perspective. Economic Geology, v.88, p.610-620.

Sajona, F.G. and Maury, R.C., 1998, Association of adakites with gold and copper mineralisation in the Philippines: Comptes rendus de l'Academic des sciences. Series II. Sciences de la terre et des planets, v.326, p.27-34.

Salam, A., 2013, Geology and genesis of the Chatree Au-Ag deposits, Phetchabun Province, central Thailand. Unpublished PhD thesis, CODES University of Tasmania, 250p.

Sanematsu, K., Murakami, H., Duangsurigna, S., Vilayhack, S., Duncan, R. and Watanabe, Y., 2011, Ar/Ar ages of granitoids from the Truong Son fold belt and Kontum massif in Laos. Journal of Mineralogical and Petrological Sciences, v.106, p.13-25.

Sanematsu, K., Murakami, H., Watanabe, Y., Duangsurigna, S. and Vilayhack, S., 2009, Perographic and geochronological studies of granitic rocks associated with Sn deposits in Laos. Proceedings of 59th Annual Meeting of the Society of Resource Geology (Japan), 24-26 June 2009, Tokyo, Japan, p.92 (poster).

Sang Quang Dinh, Crowford, A.J., Berry, R.F., 2010, Geochronology and geology of the northern margin of the Kontum Massif – central Vietnam. Annual report (Report No. 8) of the Ore Deposits of SE Projects, 15p.

Sangster, D.F., 1979, Sulphur and lead isotopes in stratabound deposits. In Wolf, K.H., (ed.) Handbook of strata-bound and stratiform ore deposits, Elservier, (Amsterdam), 261p.

Sasaki, A. and Ishihara, S., 1979, Sulfur isotopic compositions of the magnetite-series and ilmenite-series granitoids in Japan. Contributions to Mineralogy and Petrology, v.68, p.107-115.

Scott, S.D., 1973, Experimental calibration of the sphalerite geobarometer. Economic Geology, v.68, 466-474.

Scott, S.D., 1976, Application of the sphalerite geobarometer to regionally metamorphosed terranes. American Mineralogist, v.61, p.661-670.

Scott, S.D. and Barnes, H.L., 1971, Sphalerite geothermometry and geobarometry. Economic Geology, v.66, p.653-669.

Sengor, C. and Hsu, K.J., 1984, The Cimmerides of eastern Asia; history of the eastern end of Paleo-Tethys, in Memoires de la Societe Geologique de France, Nouvelle Serie, v.147, p.139-167.

Sengor, C., Altiner, D., Cin, A., Ustamomer, T. and Hsu, K.J., 1988, Origin and assembly of the Tethyside orogenic collage at the expense of Gondwana Land, in Aduley-Charles, M.G. and Hallam, A. (eds), Gondwana and Tethys Geological Society Special Publication n.37, p.81-119.

Seward, T.M. and Barnes, H.L., 1997, Metal transport by hydrothermal ore fluids (Chapter 9), in Barned, H.L. (ed.), Geochemistry of hydrothermal ore deposits (2nd edition): Wiley, p.435-486.

Shepherd, T.J., Rankin, A.H. and Alderton, D.H.M., 1985, A practical guide to fluid inclusion studies.

Sheppard, S.M.F., 1986, Characterization and isotopic variation in natural waters. Chapter 6, Review in Mineralogy, v.16.

Shikazono, N. and Shimizu, M., 1987, The Au/Ag ratio of native gold and electrum and the geochemical environment of gold vein deposits in Japan. Mineralium Deposita, v.22, p.309-314.

Sillitoe, R.H., 2000, Gold-rich porphyry deposits: Descriptive and genetic models and their role in exploration and discovery. Reviews in Economic Geology, v.13, p.347-375.

Sillitoe, R.H., 2010, Porphyry copper systems. Economic Geology, v.105, p.3-41.

Sitthithaworn, E., 1989, Gold mineralization at Phu Lon copper-iron skarn prospect in Northern Thailand. Unpublished MSc thesis at University of Western Ontario, London, Ontario, Canada, 131p.

Smith, S.G., Olberg, D. and Manini, A.J., 2005, The Sepon gold deposits, Laos; exploration, geology and comparison to Carlin-type gold deposits in the Great Basin: Geological Society of Nevada Symposium, Reno, Nevada, 2005.

Smoliar, M.I., Walker, R.J. and Morgan, J.W., 1996, Re-Os isotope constraints on the age of Group IIA, IIIA, IVA and IVB iron meteorites. Science, v.271, p.1099-1102.

Sone, M. and Metcalfe, I., 2008, Parallel Tethyan sutures in mainland Southeast Asia: New insights for Palaeo-Tethys closure and implications for the Indosinian orogeny. Comptes Rendus Geoscience, v.340, p.166-179.

Spear, S.F., 1993. Metamorphic phase equilibria and pressure-temperature-time paths. Mineralogical Society of America Monograph, Book Creafters Inc., 799p.

Spycher, N.F. and Reed, M.H., 1989, CHILLER: A program for computing water-rock reactions, boiling, mixing, and other reaction processes in aqueous-mineral-gas systems: Eugene, University of Oregon.

Srichan, W., Crawford, A.J. and Berry, R.F., 2009, Geochemistry and geochronology of Late Triassic volcanic rocks in the Chiang Khong region, northern Thailand. Island Arc, v.18, p.32-51.

Stacy, J.S. and Kramer, J.D., 1975, Approximation of terreatrial lead isotope evolution by a two-stage model. Earth and Planetary Science Letters, v.26, p.207-221.

Stein, H.J., Markey, R.J., Morgan, J.W., Du, A. and Sun, Y., 1997, Highly precise and accurate Re-Os ages for molybdenite from the East Qingling molybdenum belt, Shaaxi Province, China. Economic Geology, v.92, p.827-835.

Stevens, M.R. and Fulton, G.W., 2008, Technical report on feasibility studies for the Phuoc Son gold project in Quang Nam Province, Vietnam. Phuoc Son NI43-101 technical report, 324p.

Sullivan, J.R. and Kociumbas, M.W., 2004, A technical review of the Phuoc Son gold project in Quang Nam Province, Vietnam. Unpublished consultant report to Olympus Pacific Minerals Inc., 85p.

Sun, S.S. and McDonough, W.F., 1989, Chemical and isotopic systematics of oceanic basalts: implications for mantle composition and processes. In: Saunders, A.D., Norry, M.J., eds., Magmatism in the Ocean Basins: Geological Society Special Publication v.42, p.225-232.

Tate, N.M., 2003, Geology of the Long Chieng Track (LCT) Gold Deposit, Lao Peoples Democratic Republic; Unpublished consultant report for Pan Mekong Exploration Pty Ltd.

Tate, N.M., 2004, Mapping Notes for the Ban Houayxai Gold deposit, Lao Peoples Democratic Republic. Unpublished consultant report for Pan Mekong Exploration Pty Ltd.

Tate, N.M., 2005, Discovery, Geology and Mineralisation of the Phu Kham Copper-Gold Deposit Lao People's Democratic Republic; in JaB Mao, F. (ed.), Mineral deposit Research: Meeting of the Global Challenge, 8th Biennial SGA Meeting, 18-21 August 2005, Beijing, China, v.2, p.1077-1080.

Tate, N.M., 2006a, Review of copper prospects in the NEA Phu Bia Mining MEPA, Lao Peoples Democratic Republic. Unpublished consultant report for Pan Mekong Exploration Pty Ltd, 8p.

Tate, N.M., 2006b, Mineralisation model for the Phu He gold prospect, Lao Peoples Democratic Republic. Unpublished consultant report for Phu Bia Mining Ltd, 28p.

Taylor, B.E. and O'Neil, J.R., 1977, Stable isotope studies of metasomatic Ca-Fe-Ai-Si skarns and associated metamorphic and igneous rocks, Osgood Mountains, Nevada. Contributions to Mineralogy and Petrology, v.63, p.1-49.

Thai Goldfields, 2012, Thai Goldfields Annual Report 2011, 45p.

Thieblemont, D., Stein, G. and Lescuyer, J-L., 1997, Gisements epithermaux et porphyriques: la connexion adakite: C.R.Aead. Sci. Paris, Sciences de la terre et des planetes/Earth and Planetary Science, v.335, p.103-109.

Thomas, H.V., Large, R.R., Bull, S.W., Maslennikov, V., Berry, R.F., Fraser, R., Froud, S. and Moye, R., 2011, Pyrite and pyrrhotite textures and composition in sediments, laminated quartz veins, and reefs at Bendigo gold mine, Australia: Insights for ore genesis. Economic Geology, v.106, p.1-31.

Thompson, J.F.H. and Newberry, R.J., 2000, Gold deposits related to reduced granite intrusions, Reviews in Economic Geology, v.13, p.377-400.

Thuy, T.B.N., Satir, M., Siebel, W. and Chen, F., 2004, Granitoids in the Dalat zone, Southern Vietnam: age constraints on magmatism and regional geological implications. International Journal of Earth Sciences, v.93, p.329-340.

Townsend, A., Zongshou, Y., McGoldrick, P. and Hutton, J., 1998, Precise lead isotope ratios in Australian galena samples by high resolution inductively coupled plasma mass spectrometry: Journal of Analytical Atomic Spectrometry, v.13, p.809-813.

Tran Thanh Hai, 2003, Report on a visit to the Duc Bo Prospect, Quang Nam Province, central Vietnam. Unpublished Consultant Report to Anvil Mining, 25p.

Tran Thanh Hai, Khin Zaw, Halpin, J.A., Manaka, T., Hai, L.V., Hung, D.D. and Hung, N.B., 2009, Nature of the Phuoc Son-Tam Ky Suture in central Vietnam and implications for gold mineralization. Proceedings of the 10th biennial SGA meeting: 17-20 August 2009, Townsville, Australia, p. 963-965.

United Nations, 1990a, Atlas of mineral resources of the ESCAP region: Lao People's Democratic Republic, 19p.

United Nations, 1990b, Atlas of mineral resources of the ESCAP region: Viet Nam, 124p.

Vaughan, D.J. and Craig, J.R., 1997, Sulphide ore minerals stabilities, morphologies, and intergrowth textures (Chapter 8), in Barned, H.L. (ed.), Geochemistry of hydrothermal ore deposits (2nd edition): Wiley, p.367-434.

Vu Van Tich, Malyski, H. and Nguyen Van Vuong, 2007, Ar-Ar age of metamorphic and mylonitic rocks in northern part of the Kon Tum massif: evidence for the Indosinian movement along shear zones between Kon Tum massif and Truong Son Belt, VNU Journal of Science, Earth Sciences, 23, p.253-264.

Wallis, R. and Ward, M-C., 1997, A review of the mineral properties Olympus Pacific Minerals in Vietnam. Unpublished consultant report by Griffis and McOuat Limited, Toronto.

Webstbrook, S., 2006, Geology and mineralisation of Bohr Thong and Tharkek prospects. Unpublished consultant report for Phu Bia Mining Ltd, 22p.

Wiendenbeck, M., Alle, P., Corfu, F., Griffin W.L., Meier, M., Oberli, F., Vonquadt A., Roddick, J.C. and Speigel, W., 1995, 3 Natural Zircon Standards for U-Th-Pb, Lu-Hf, Trace-Element and REE Analyses. Geostandards Newsletter 19, p.1-23.

Wilkinson, J.J., 2001, Fluid inclusions in hydrothermal ore deposits. Lithos, v.55., p.229-272.

Williams-Jones, A.E., Bowell, R.J. and Migdisov, A.A., 2009. Gold in Solution. Elements, v.5, p.281-287.

Wilson, A.J., Cooke, D.R., Harper, B.J. and Deyell, C.L., 2007, Sulphur isotopic zonation in the cadia district, southeastern Australia: exploration significance and implications for the genesis of alkali porphyry gold-copper deposits. Mineralium Deposita, v.42, p.465-487.

Winchester, J.A. and Floyd, P.A., 1977, Geochemical discrimination of different magma series and their differentiation products using immobile elements. Chemical Geology, v.20, p.325-343.

Wood, B.L. and Large, R.R., 2007, Syngenetic gold in western Victoria; occurrence, age and dimensions. Australian Journal of Earth Sciences, v.54, n.5, p.711-732.

Woodhead, J., Hergt, J., Meffre, S., Large, R., Danyushevsky, L., and Gilbert, S., 2009, In situ Pb-isotope analysis of pyrite by laser ablation (multi-collector and quadrupole) ICPMS: Chemical Geology, v.262, p.344-354.

Woodhead, J., Hergt, J., Shelley, M., Eggins, S. and Kemp, R., 2004, Zircon Hf-isotope analysis with an excimer laser, depth profiling, ablation of complex geometries, and concomitant age estimation: Chemical Geology, v.209, p.121-135.

Woodhead, J. D., Swearer, S., Hergt, J. and Maas, R., 2005, In situ Sr-isotope analysis of carbonates by LA-MC-ICP-MS: interference corrections, high spatial resolution and an example from otolith studies: Journal of Analytical Atomic Spectrometry, v.20, p.22-27.

Yang, X-M. and Lentz, D.R., 2010, Sulphur isotopic systematics of granitoids from southwestern New Brunswick, Canada: implications for magmatic-hydrothermal processes, redox conditions, and gold mineralisation. Mineralium Deposita, v.45, p.795-816.

Yokart, B., 1977, Mineralogy and geochemistry of Lead-Zinc deposits in northwestern Thailand. Unpublished MSc thesis, Faculty of Science, Chiang Mai University, Chiang Mai, Thailand.

Yu, Z., Robinson, P., Townsend, A.T., Munker, C. and Crawford, A.J., 2000, Detection of geological materials for trace element determination of using ICP-MS. Geostandards Newsletter: The Journal of Geostandards and Geoanalysis, v.25, p.199-217.

Zartman, R.E. and Doe, B.R., 1981, Plumbotectonics-The model, Tectonophysics, v.75, p.135-162.

Zhang, X.C., Hofstra, A.H., Hu, R.Z., Emsbo, P., Su, W.C. and Ridley, W.I., 2005, Geochemisty and delta 34S of ores and ore stage iron sulphides in Carlin-type gold deposits, Dian-Qian-Gui area, China : Implications for ore genesis.,In Mao, J.W. and Bierlein, F.P. (eds.), 8th Biennial SGA meeting, Mineral deposit research: meeting the global challenge. Beijing, China, Springer, p.1107-1110.

Appendix I

Rock catalogue

		Rock Description				Specimen type submitted						
Utas#	Field Number	Class	Type	Composition	Rock Name	Hand specimen	Powder	Coarse Crush	Thin Section	Polished block	Fluid Inclus.	Other preps
177156	DSDH13@106.9m	ore			Ore	R						Laser Mount
177157	DSDH16@126.1m	ore			Ore	R						Laser Mount, S isotope
177158	DSDH111@78.8m	ore			Ore	R					FI	
177159	DSDH111@204.3m	metamorphic	clastic	Pelitic	Schist	R			1TS			S isotope
177160	DSDH112@29.9m	ore			Ore	R	PD					S isotope
177161	DSDH112@31.7m	igneous	plutonic	Mafic	Peridotite		PD		1TS			
177162	DSDH241@73.5m	igneous	intrusive	Felsic	Granite		PD					
177163	DSDH257@95.4m	igneous	intrusive	Intermediate	Dacite	R	PD					
177164	DSDH257@191.8m	metamorphic	intrusive	Mafic	Basalt	R	PD		1TS			
177165	DSDH257@336.4m	igneous	intrusive	Intermediate	Dacite		PD					
177166	DSDH257@351.7m	metamorphic	clastic	Pelitic	Schist							S isotope
177167	DSDH257@454.2m	ore			Ore	R			1TS			
177168	DSDH257@463.4m	ore			Ore				1TS		FI	Laser Mount
177169	DSDH257@463.5m	ore			Ore	R					FI	
177170	DSDH270@122.8m	ore			Ore	R					FI	S isotope
177171	DSDH270@187.6m	ore			Ore	R			1TS			
177172	DSDH270@232.0m	igneous	intrusive	Felsic	Granite		PD					
177173	DSDH270@290.3m	igneous	intrusive	Felsic	Granite		PD		1TS			
177174	DSDH270@375.9m	metamorphic	clastic	Pelitic	Schist	R			1TS			
177175	DSDH270@400.5m	metamorphic	clastic	Pelitic	Schist	R			1TS			
177176	DSDH270@430.2m	ore			Ore	R					FI	
177177	DSDH270@453.4m	ore			Ore	R					FI	
177178	KZVN0818	metamorphic	clastic	Pelitic	Schist	R						
177179	TMBD11-01	ore			Ore	R						
177180	TMBD11-02	ore			Ore	R						
177181	TMBD11-04	metamorphic	clastic	Pelitic	Schist	R						
177182	TMBD11-05	ore			Ore	R						
177183	TMBD11-06	metamorphic	clastic	Pelitic	Schist	R						
177184	TMBD11-07	ore			Ore	R					FI	S isotope
177185	TMBD11-08	ore			Ore	R						
177186	TMBD11-09	ore			Ore	R					FI	Laser Mount
177187	TMBD11-10	ore			Ore	R					FI	
177188	TMBD11-11	ore			Ore	R					FI	Laser Mount
177189	TMBD11-12	ore			Ore	R						
177190	TMBD11-13	ore			Ore	R						C-O isotope
177191	TMBD11-14	ore			Ore	R						
177192	TMBD11-15	ore			Ore	R					FI	Laser Mount, S isotope
177193	TMBD11-16	metamorphic	clastic	Pelitic	Schist	R						
177194	TMBD11-17	ore			Ore	R					FI	S isotope

177195	DSDH26@87.1m	ore			Ore	R					FI	Laser Mount
177196	DSDH40@94.3m	ore			Ore	R						
177197	DSDH40@145.4m	ore			Ore	R						
177198	DSDH40@147.3m	ore			Ore	R						
177199	DSDH40@148.8m	igneous	intrusive	Intermediate	Dacite	R						
177200	DSDH40@195.8m	ore			Ore	R					FI	
177201	DSDH74@132.7m	metamorphic	clastic	Pelitic	Schist	R			1TS			
177202	DSDH74@140.0m	ore			Ore	R					FI	Laser Mount
177203	DSDH74@164.3m	metamorphic	clastic	Pelitic	Schist	R						
177204	DSDH89@187.7m	igneous	intrusive	Intermediate	Dacite		PD					
177205	DSDH96@125.0m	igneous	intrusive	Intermediate	Dacite		PD		1TS			
177206	DSDH146@88.4m	ore			Ore	R					FI	C-O isotope
177207	DSDH146@88.8m	ore			Ore	R					FI	
177208	DSDH152@58.8m	metamorphic	intrusive	Mafic	Basalt	R	PD		1TS			
177209	DSDH155@101.2m	metamorphic	clastic	Pelitic	Schist	R						
177210	DSDH155@104.9m	ore			Ore	R					FI	S isotope
177211	DSDH199@230.2m	ore			Ore	R					FI	
177212	DSDH209@50.2m	metamorphic	clastic	Pelitic	Schist	R						
177213	DSDH209@128.2m	igneous	intrusive	Mafic	Gabbro	R			1TS			
177214	DSDH209@295.0m	ore			Ore	R					FI	Laser Mount
177215	DSDH209@303.6m	metamorphic	clastic	Pelitic	Schist	R						
177216	DSDH209@325.0m	ore			Ore	R						Laser Mount
177217	DSDH210@246.8m	ore			Ore	R					FI	
177218	DSDH212@180.0m	ore			Ore	R					FI	
177219	DSDH212@186.9m	ore			Ore				1TS			
177220	DSDH212@238.0m	ore			Ore				1TS			
177221	DSDH212@271.4m	igneous	intrusive	Intermediate	Andesite	R	PD		1TS			
177222	DSDH212@274.2m	ore			Ore	R			1TS			
177223	DSDH212@293.1m	ore			Ore	R						C-O isotope
177224	DSDH218@86.6m	igneous	intrusive	Intermediate	Andesite		PD					
177225	DSDH218@277.3m	metamorphic	intrusive		Calcsilicate	R			1TS			
177226	DSDH218@280.3m	metamorphic	intrusive		Calcsilicate	R			1TS			
177227	DSDH218@366.2m	ore			Ore						FI	
177228	DSDH218@436.3m	ore			Ore	R						
177229	DSDH224@24.3m	metamorphic	intrusive	Mafic	Basalt	R						
177230	DSDH224@272.5m	metamorphic	intrusive	Mafic	Basalt	R			1TS			
177231	DSDH224@298.9m	metamorphic	clastic	Pelitic	Schist	R						
177232	DSDH224@386.2m	metamorphic	intrusive	Mafic	Basalt	R						
177233	DSDH224@436.8m	ore			Ore	R						
177234	DSDH224@443.3m	ore			Ore	R					FI	
177235	DSDH224@445.5m	ore			Ore	R						
177236	DSDH224@445.7m	ore			Ore	R						
177237	DSDH226@160.3m	metamorphic	intrusive	Mafic	Basalt	R	PD					
177238	DSDH235@76.1m	metamorphic	intrusive	Mafic	Basalt	R	PD					
177239	DSDH235@124.5m	metamorphic	clastic	Pelitic	Schist	R						

177240	DSDH235@246.3m	metamorphic	clastic	Pelitic	Schist	R						
177241	DSDH235@264.9m	ore			Ore	R					FI	
177242	DSDH235@276.5m	metamorphic	clastic	Pelitic	Schist	R	PD		1TS			
177243	DSDH249@180.1m	ore			Ore	R			1TS			C-O isotope
177244	DSDH249@499.1m	ore			Ore	R					FI	
177245	DSDH249@515.2m	igneous	intrusive	Intermediate	Andesite	R	PD					
177246	DSDH250@227.9m	igneous	intrusive	Intermediate	Dacite	R	PD					
177247	DSDH250@323.0m	igneous	intrusive	Mafic	Basalt	R	PD		1TS			
177248	TMVN11-07	metamorphic	intrusive	Mafic	Amphibolite	R			1TS			
177249	TLDH01@58.9m	metamorphic	intrusive	Mafic	Basalt	R	PD		1TS			
177250	TLDH01@139.9m	metamorphic	biogenic	Carbonate	Marble	R			1TS			
177251	K7DH01@107.6m	ore			Ore	R					FI	S isotope, C-O isotope
177252	K7DH01@108.7m	igneous	intrusive	Felsic	Granite	R	PD		1TS			
177253	NVDH01@110.9m	ore			Ore	R			1TS			S isotope
177254	NVDH01@126.5m	ore			Ore							S isotope
177255	NVDH01@178.1m	metamorphic	clastic	Pelitic	Schist	R						S isotope
177256	NVDH01@178.4m	ore			Ore	R					FI	S isotope
177257	KRDH03@11.8m	ore			Ore	R						
177258	KRDH03@30.0m	ore			Ore	R						
177259	KRDH03@34.0m	ore			Ore	R						
177260	KRDH03@41.2m	ore			Ore	R						
177261	KRDH04@40.0m	ore			Ore	R					FI	Laser Mount
177262	KRDH08@18.3m	ore			Ore	R			1TS			S isotope
177263	KRDH08@82.9m	ore			Ore	R					FI	S isotope, C-O isotope
177264	KRDH11@45.7m	metamorphic	biogenic	Carbonate	Marble	R			1TS			
177265	KRDH13@67.1m	ore			Ore	R						S isotope, C-O isotope
177266	KRDH28@49.9m	ore			Ore	R			1TS			S isotope
177267	KRDH31@259.8m	igneous	intrusive	Felsic	Granite	R	PD		1TS			
177268	KRDH31@260.2m	igneous	intrusive	Felsic	Granite	R	PD					
177269	KRDH31@261.1m	igneous	intrusive	Felsic	Granite		PD					
177270	KRDH31@262.4m	igneous	intrusive	Felsic	Granite		PD					
177271	RHDH03@30.0m	ore			Ore	R						
177272	RHDH03@33.2m	ore			Ore	R						
177273	RHDH03@34.9m	metamorphic	intrusive	Mafic	Basalt	R			1TS			
177274	RHDH03@43.5m	metamorphic	intrusive	Felsic	Granite	R						
177275	RHDH03@61.9m	metamorphic	intrusive	Mafic	Basalt	R	PD		1TS			
177276	RHDH03@72.9m	ore			Ore	R					FI	S isotope
177277	RHDH03@74.5m	igneous	intrusive	Felsic	Granite	R	PD					
177278	RHDH03@86.2m	igneous	intrusive	Felsic	Granite	R	PD					
177279	RHDH03@89.1m	ore			Ore	R			1TS			S isotope
177280	RHDH04@79.8m	igneous	intrusive	Felsic	Granite		PD					
177281	RHDH04@80.6m	igneous	intrusive	Felsic	Granite	R	PD		1TS			
177282	RHDH04@81.5m	ore			Ore	R			1TS			S isotope
177283	KRDH23@50.6m	ore			Ore	R					FI	S isotope
177284	KRDH23@78.8m	ore			Ore	R			1TS			S isotope

177285	KRDH23@87.6m	ore			Ore	R					FI	S isotope
177286	KRDH25@53.1m	metamorphic	intrusive	Mafic	Basalt	R	PD					
177287	KRDH25@106.3m	metamorphic	biogenic	Carbonate	Marble	R			1TS			
177288	KRDH25@107.9m	ore			Ore	R					FI	S isotope
177289	BHDH02@82.2m	ore			Ore	R					FI	S isotope, C-O isotope
177290	BHDH02@98.5m	metamorphic	clastic	Pelitic	Schist	R			1TS			S isotope
177291	BHDH02@105.5m	igneous	intrusive	Felsic	Granite	R	PD					
177292	DSDH256@291.9m	metamorphic	clastic	Pelitic	Schist	R						S isotope, C-O isotope
177293	DSDH256@297.4m	ore			Ore	R					FI	S isotope, C-O isotope
177294	DSDH256@340.2m	ore			Ore						FI	S isotope
177295	DSDH267@45.9m	igneous	intrusive	Felsic	Granite		PD					
177296	DSDH267@387.1m	ore			Ore	R			1TS			
177297	DSDH267@424.1m	ore			Ore							S isotope
177298	DSDH267@425.9m	ore			Ore	R					FI	S isotope

Appendix II

Structural measurement data at Bai Dat underground

Appendix II. Measured structural data of foliation of the host rocks (mainly schists) at the Bai Dat Underground mine in the Phuoc Son deposit area, central Vietnam.

Measurement No.	Dipping direction (°)	Dipping angle (°)	Easting (mE)	Northing (mN)
1	284	45	792420	1708332
2	312	36	792400	1708300
3	276	10	792402	1708262
4	256	45	792419	1708245
5	330	40	792384	1708240
6	250	25	792382	1708228
7	283	44	792377	1708170
8	300	45	792405	1708142
9	271	44	792403	1708173
10	258	36	792399	1708213
11	270	44	792418	1708221
12	242	52	792422	1708230
13	241	65	792425	1708277
14	282	52	792426	1708288
15	282	62	792445	1708327
16	293	42	792442	1708322
17	308	36	792480	1708350
18	304	34	792470	1708300
19	262	54	792437	1708268
20	273	40	792447	1708266
21	345	33	792495	1708274
22	245	25	792515	1708290
23	325	33	792501	1708267
24	294	38	792486	1708257
25	332	38	792520	1708322
26	290	30	792488	1708228
27	346	32	792573	1708318
28	280	54	792500	1708155
29	283	18	792532	1708199
30	286	38	792535	1708210
31	335	50	792542	1708218
32	286	24	792575	1708260
33	294	37	792508	1708223
34	308	32	792522	1708235
35	315	32	792530	1708272
36	282	28	792497	1708210
37	298	42	792503	1708196
38	268	32	792482	1708225
39	255	45	792476	1708203
40	255	40	792455	1708138
41	312	40	792455	1708155
42	298	45	792462	1708163
43	330	35	792510	1708302
44	282	55	792540	1708310
45	345	46	792590	1708315
46	335	20	792595	1708330
47	295	24	792488	1708357
48	335	30	792494	1708370
49	325	30	792520	1708388
50	312	35	792540	1708393

Appendix II (cont.). Measured structural data of foliation of the host rocks (mainly schists) at the Bai Dat Underground mine in the Phuoc Son deposit area, central Vietnam.

Measurement No.	Dipping direction (°)	Dipping angle (°)	Easting (mE)	Northing (mN)
51	256	50	792410	1708270
52	290	42	792380	1708200
53	263	33	792390	1708242
54	315	28	792515	1708380
55	296	40	792458	1708345
56	267	36	792445	1708320
57	275	37	792430	1708305
58	274	45	792410	1708212
59	264	44	792400	1708190
60	293	60	792382	1708170
61	274	24	792392	1708286
62	255	48	792423	1708350
63	304	42	792465	1708348
64	228	66	792452	1708318
65	257	58	792430	1708288
66	276	44	792420	1708215
67	277	48	792407	1708173
68	265	28	792412	1708140
69	285	57	792450	1708268
70	290	54	792453	1708275
71	268	38	792473	1708215
72	272	60	792472	1708230
73	264	35	792472	1708252
74	280	30	792497	1708273
75	296	38	792499	1708278
76	324	25	792507	1708290

Appendix II. Measured structural data of post-metamorphism fault at the Bai Dat Underground mine site in the Phuoc Son deposit area, central Vietnam.

Measurement No.	Dipping direction (°)	Dipping angle (°)	Easting (mE)	Northing (mN)
1	275	40	792395	1708248
2	224	58	792402	1708218
3	110	76	792477	2708340
4	226	80	792475	1708320
5	84	72	792472	1708310
6	240	90	792470	1708310
7	270	80	792445	1708265
8	115	86	792452	1708272
9	270	79	792523	1708280
10	258	55	792524	1708280
11	110	76	792498	1708217
12	258	85	792520	1708158
13	325	42	792522	1708175
14	275	85	792525	1708215
15	85	85	792520	1708220
16	98	60	792518	1708222
17	272	70	792465	1708159
18	14	70	792596	1708332
19	284	76	792485	1708355
20	266	60	792490	1708360
21	278	80	792497	1708372
22	278	80	792530	1708390
23	276	75	792542	1708398
24	265	70	792522	1708394
25	280	83	792440	1708320
26	92	87	792438	1708245
27	258	90	792425	1708227
28	254	75	792395	1708178
29	258	38	792380	1708178
30	246	78	792405	1708315
31	235	84	792423	1708353
32	226	86	792400	1708283
33	286	74	792422	1708305
34	264	83	792426	1708232

Appendix III

LA-ICPMS zircon U-Pb age results

Appendix III. LA-ICPMS zircon U-Pb geochronological data of the selected intrusive units in the Phuco Son deposit area, central Vietnam.

Sample No. (& analysis No.)		Comments	Spot size (micron)	207 cor age	206Pb/238U +/-1 ster	U ppm	Th ppm	Pb ppm	Hf ppm	Ti ppm	Common Pb at age of zirc	206Pb/238U ratio	+/-1 RSE	208Pb/232Th ratio	+/-1 RSE	207Pb/206Pb ratio	+/-1 RSE
Dacitic porphyry at Bai Dat (1st analysis)																	
DSDH257-336.4m-1	my11a109	ok	34	**249**	3	1645	511	57	12236	5	0.852	0.0399	1.1%	0.0138	2.4%	0.0628	1.7%
DSDH257-336.4m-2	my11a114	older core (>261Ma at beginning)	34	**249**	5	361	533	16	7696	11	0.853	0.0408	1.8%	0.0138	3.4%	0.0783	4.3%
DSDH257-336.4m-3	my11a108	high U	34	**248**	3	5756	8403	259	9348	38	0.852	0.0394	1.0%	0.0119	1.5%	0.0532	0.7%
DSDH257-336.4m-4	my11a110	ok	34	**252**	3	608	403	23	11354	7	0.852	0.0402	1.1%	0.0123	1.6%	0.0564	1.8%
DSDH257-336.4m-5	my11a113	ok	34	270	3	1272	269	47	10383	10	0.854	0.0436	1.1%	0.0189	2.1%	0.0672	1.7%
DSDH257-336.4m-6	my11a106	through crystal at end	34	445	4	3716	905	213	14650	5	0.866	0.0717	1.0%	0.0257	1.5%	0.0598	1.0%
DSDH257-336.4m-7	my11a111	ok	34	445	4	6462	1648	385	14989	3	0.866	0.0716	0.8%	0.0220	1.2%	0.0566	0.6%
DSDH257-336.4m-8	my11a105	DO NOT USE poor isochron	34	1256	15	315	140	76	9727	13	0.943	0.2404	1.2%	0.0945	1.6%	0.1731	0.9%
DSDH257-336.4m-9	my11a112	DO NOT USE Not zircon prob sphene	34	1581	47						1.169	0.8114	1.7%	0.0819	2.9%	0.8023	0.9%
DSDH257-336.4m-10	my11a107	isochron 137±360 Ma & 2758±55 Ma	34	1979	23	189	189	83	9865	9	1.014	0.3889	1.2%	0.1152	1.3%	0.1894	0.7%
Dacitic porphyry at Bai Dat (2nd analysis)																	
DSDH257-336.4m-1	jn29c152	ok	32	**248**	3	1030	184	35	11680	2	0.852	0.0392	1.2%	0.0131	1.8%	0.0508	1.6%
DSDH257-336.4m-2	jn29c159	ok	32	**250**	3	530	425	23	7163	1474	0.853	0.0405	1.4%	0.0147	1.7%	0.0704	2.1%
DSDH257-336.4m-3	jn29c158	ok	32	348	5	1504	544	75	9685	17	0.859	0.0556	1.4%	0.0196	1.6%	0.0555	1.5%
DSDH257-336.4m-4	jn29c155	strong Pb loss at end	32	431	9	5802	5825	400	12901	19	0.865	0.0699	2.2%	0.0201	4.9%	0.0637	1.6%
DSDH257-336.4m-5	jn29c154	ok	32	432	9	2063	1523	142	12455	11	0.865	0.0706	2.2%	0.0242	1.7%	0.0712	2.0%
DSDH257-336.4m-6	jn29c153	ok	32	456	5	908	735	69	9609	6	0.867	0.0733	1.1%	0.0234	1.3%	0.0553	1.2%
DSDH257-336.4m-7	jn29c157	ok	32	460	5	3115	2921	250	8711	88	0.867	0.0743	1.2%	0.0242	1.3%	0.0595	0.8%
DSDH257-336.4m-8	jn29c156	old ore with younger rim (<1800Ma)	32	2914	49	184	106	112	9667	7	1.105	0.5816	1.3%	0.1584	1.6%	0.2265	1.0%
Foliated dacitic porphyry at Bai Dat (1st analysis)																	
DSDH257-94.5m-1	my11a119	ok	34	**437**	4	1451	640	90	8713	14	0.865	0.0703	0.9%	0.0213	1.4%	0.0570	0.9%
DSDH257-94.5m-2	my11a129	ok	34	**438**	4	1692	839	107	8495	17	0.865	0.0703	0.9%	0.0204	1.3%	0.0564	0.9%
DSDH257-94.5m-3	my11a127	slight Pb loss in middle	34	**440**	7	1533	854	91	9700	10	0.865	0.0708	1.6%	0.0210	1.9%	0.0573	2.0%
DSDH257-94.5m-4	my11a132	ok	34	**440**	4	1893	712	117	8825	16	0.866	0.0711	0.9%	0.0220	1.4%	0.0599	0.8%
DSDH257-94.5m-5	my11a125	slight Pb loss at end	34	**443**	6	1569	551	92	8263	251	0.866	0.0718	1.3%	0.0247	1.7%	0.0626	1.8%
DSDH257-94.5m-6	my11a134	ok	34	**444**	4	1444	458	88	8660	12	0.866	0.0714	0.9%	0.0218	1.4%	0.0572	1.0%
DSDH257-94.5m-7	my11a122	ok	34	**444**	4	1744	627	110	9832	14	0.866	0.0720	1.0%	0.0232	1.7%	0.0599	1.3%
DSDH257-94.5m-8	my11a126	ok	34	**448**	4	1698	762	109	9721	12	0.866	0.0721	0.9%	0.0213	1.3%	0.0585	1.0%
DSDH257-94.5m-9	my11a131	slight Pb loss at end	34	**450**	5	1658	776	101	8971	16	0.866	0.0724	1.2%	0.0208	1.5%	0.0569	1.5%
DSDH257-94.5m-10	my11a120	common Pb inclusion at both ends	34	**450**	6	1473	475	98	9648	39	0.867	0.0738	1.3%	0.0300	1.8%	0.0723	1.8%
DSDH257-94.5m-11	my11a130	ok	34	**450**	4	2358	1079	151	9539	19	0.866	0.0723	0.9%	0.0211	1.3%	0.0560	0.9%
DSDH257-94.5m-12	my11a128	slight Pb loss at end	34	**451**	4	4976	2610	341	10112	22	0.867	0.0740	1.0%	0.0268	1.8%	0.0722	1.5%
DSDH257-94.5m-13	my11a123	ok	34	**451**	4	1889	585	119	11031	46	0.866	0.0731	0.9%	0.0233	1.5%	0.0621	1.0%
DSDH257-94.5m-14	my11a124	slight Pb loss at end	34	**453**	6	1890	880	113	8856	19	0.866	0.0728	1.3%	0.0210	1.6%	0.0569	1.7%
DSDH257-94.5m-15	my11a133	Pb loss at beginning	34	**453**	6	2063	660	138	11546	33	0.866	0.0731	1.3%	0.0227	2.2%	0.0599	1.9%
DSDH257-94.5m-16	my11a121	ok	34	483	4	2177	764	143	10324	16	0.869	0.0780	0.9%	0.0218	1.3%	0.0579	0.9%
Foliated dacitic porphyry at Bai Dat (2nd analysis)																	
DSDH257-94.5m-1	jn29c144	ok	32	**437**	5	1916	1035	130	8667	19	0.865	0.0700	1.1%	0.0219	1.3%	0.0551	0.9%
DSDH257-94.5m-2	jn29c143	ok	32	**438**	4	1790	960	123	8302	19	0.865	0.0705	1.0%	0.0225	1.3%	0.0588	0.9%
DSDH257-94.5m-3	jn29c142	ok	32	**438**	4	1793	891	120	9264	18	0.865	0.0703	1.0%	0.0215	1.3%	0.0561	1.0%
DSDH257-94.5m-4	jn29c145	ok	32	**438**	5	2118	836	140	8903	6097	0.865	0.0705	1.1%	0.0237	1.6%	0.0580	1.1%
DSDH257-94.5m-5	jn29c148	ok	32	**438**	5	1634	782	109	9390	14	0.865	0.0703	1.1%	0.0215	1.3%	0.0563	1.0%
DSDH257-94.5m-6	jn29c147	ok	32	**439**	4	1577	676	105	8998	14	0.865	0.0706	1.0%	0.0226	1.3%	0.0569	1.0%
DSDH257-94.5m-7	jn29c140	ok	32	**441**	4	3166	2271	228	8849	1615	0.866	0.0709	1.0%	0.0222	1.2%	0.0573	0.8%
DSDH257-94.5m-8	jn29c137	ok	32	**444**	4	2114	957	142	9754	11	0.866	0.0713	1.0%	0.0225	1.3%	0.0552	0.8%
DSDH257-94.5m-9	jn29c139	ok	32	**446**	5	1259	552	88	8621	54	0.866	0.0726	1.1%	0.0263	1.9%	0.0657	1.6%
DSDH257-94.5m-10	jn29c150	ok	32	**447**	4	3389	780	216	12498	4	0.866	0.0718	1.0%	0.0227	1.3%	0.0563	0.7%
DSDH257-94.5m-11	jn29c138	ok	32	**452**	5	1800	591	119	10529	11	0.866	0.0727	1.2%	0.0226	1.5%	0.0566	1.1%
DSDH257-94.5m-12	jn29c141	ok	32	**453**	5	1572	718	107	9052	17	0.866	0.0728	1.1%	0.0218	1.5%	0.0558	1.3%
DSDH257-94.5m-13	jn29c146	ok	32	**469**	6	2180	1022	154	9204	17	0.867	0.0754	1.2%	0.0219	1.3%	0.0558	0.9%
DSDH257-94.5m-14	jn29c149	old core with younger rim <460 Ma	32	518	8	2722	756	217	11429	12	0.871	0.0837	1.5%	0.0264	1.8%	0.0583	1.4%
Dacitic porphyry at Bai Go (1st analysis)																	
DSDH89-187.7m-1	my11a092	Pb loss at end	34	**246**	3	3367	9243	206	7312	40	0.853	0.0420	1.3%	0.0128	1.4%	0.1098	2.8%
DSDH89-187.7m-2	my11a089	ok	34	**247**	2	2022	397	64	12938	5	0.852	0.0392	0.9%	0.0115	1.6%	0.0542	1.3%
DSDH89-187.7m-3	my11a095	ok	34	**251**	2	3966	6562	191	6820	29	0.852	0.0397	0.9%	0.0121	1.2%	0.0522	0.9%
DSDH89-187.7m-4	my11a093	common Pb inclusion at beginning	34	**253**	3	2018	711	82	13713	3	0.853	0.0416	1.3%	0.0180	3.5%	0.0794	2.6%
DSDH89-187.7m-5	my11a094	ok	34	**255**	3	1009	515	37	8798	5	0.852	0.0404	1.0%	0.0128	1.5%	0.0528	1.6%
DSDH89-187.7m-6	my11a091	DO NOT USE Pb loss	34	311	5	5337	9122	307	9868	86	0.856	0.0497	1.6%	0.0143	2.5%	0.0565	0.8%
DSDH89-187.7m-7	my11a088	ok	34	448	4	2333	2092	170	10767	4	0.866	0.0722	0.9%	0.0218	1.2%	0.0582	0.9%
DSDH89-187.7m-8	my11a097	ok	34	452	4	2104	1398	146	11613	2	0.866	0.0726	0.9%	0.0222	1.2%	0.0557	0.9%
DSDH89-187.7m-9	my11a096	ok	34	454	4	1257	680	84	11056	6	0.866	0.0729	0.9%	0.0221	1.3%	0.0561	1.1%
DSDH89-187.7m-10	my11a090	ok	34	455	4	3002	844	187	14605	4	0.866	0.0731	0.8%	0.0232	1.3%	0.0562	0.7%
DSDH89-187.7m-11	my11a087	ok	34	459	4	1429	766	97	11941	8	0.867	0.0739	0.9%	0.0233	1.3%	0.0572	0.9%
Dacitic porphyry at Bai Go (2nd analysis)																	
DSDH89-187.7m-1	jn29c176	ok	32	**248**	5	665	706	28	8230	16	0.852	0.0393	1.8%	0.0122	1.8%	0.0526	3.4%
DSDH89-187.7m-2	jn29c166	ok	32	**251**	3	1618	406	58	11174	5	0.852	0.0399	1.2%	0.0139	1.7%	0.0554	1.2%
DSDH89-187.7m-3	jn29c169	ok	32	**252**	3	893	381	42	10543	25	0.853	0.0427	1.2%	0.0257	2.4%	0.1045	2.1%
DSDH89-187.7m-4	jn29c171	ok	32	337	4	1372	1004	74	10606	8	0.858	0.0537	1.1%	0.0164	1.3%	0.0538	1.3%
DSDH89-187.7m-5	jn29c177	ok	32	356	4	1189	991	72	10026	8	0.860	0.0569	1.1%	0.0177	1.4%	0.0551	1.1%
DSDH89-187.7m-6	jn29c170	ok	32	357	4	2151	1108	117	12043	24	0.860	0.0571	1.0%	0.0174	1.4%	0.0547	1.1%
DSDH89-187.7m-7	jn29c175	ok	32	381	5	1562	669	95	11705	20	0.862	0.0619	1.3%	0.0261	2.9%	0.0677	2.2%
DSDH89-187.7m-8	jn29c174	ok	32	402	5	811	845	57	9562	18	0.863	0.0644	1.2%	0.0208	1.3%	0.0567	1.5%
DSDH89-187.7m-9	jn29c172	ok	32	432	5	2660	619	156	13444	8	0.865	0.0695	1.3%	0.0229	1.5%	0.0565	1.2%
DSDH89-187.7m-10	jn29c164	ok	32	436	5	1767	848	118	11313	5	0.865	0.0702	1.1%	0.0218	1.3%	0.0574	0.9%
DSDH89-187.7m-11	jn29c167	ok	32	467	5	1028	165	68	13506	2	0.867	0.0752	1.1%	0.0262	1.7%	0.0577	1.1%
DSDH89-187.7m-12	jn29c165	ok	32	711	12	86	55	12	10588	33	0.886	0.1185	1.7%	0.0636	1.7%	0.0758	2.9%
DSDH89-187.7m-13	jn29c168	ok	32	1013	11	241	173	42	10725	881	0.910	0.1711	1.1%	0.0509	1.5%	0.0773	1.3%
DSDH89-187.7m-14	jn29c173	ok	32	1112	13	255	144	49	9826	16	0.919	0.1900	1.2%	0.0604	1.4%	0.0841	1.2%
Granite at Khe Rin																	
KRD31-259m-1	my11a100	ok	34	**251**	2	4850	1012	160	12324	10	0.852	0.0399	0.9%	0.0123	1.5%	0.0546	0.8%
KRD31-259m-2	my11a101	short analysis	34	272	3	5689	2608	209	11348	11	0.854	0.0436	1.2%	0.0146	2.2%	0.0627	1.4%
KRD31-259m-3	my11a099	ok	34	475	4	1250	28	75	13751	8	0.868	0.0766	0.9%	0.0366	2.9%	0.0580	1.1%

Mean = 249.7±2.9 [1.2%] 95% conf.
Wtd by data-pt errs only, 0 of 4 rej.
MSWD = 0.39, probability = 0.76

Mean = 249±11 [4.3%] 95% conf.
Wtd by data-pt errs only, 0 of 2 rej.
MSWD = 0.032, probability = 0.86

Mean = 445.9±3.0 [0.68%] 95% conf.
Wtd by data-pt errs only, 0 of 15 rej.
MSWD = 1.5, probability = 0.11

Mean = 443±11 [2.5%] 95% conf.
Wtd by data-pt errs only, 0 of 13 rej.
MSWD = 0.15, probability = 1.000

Mean = 250.4±4.4 [1.8%] 95% conf.
Wtd by data-pt errs only, 0 of 5 rej.
MSWD = 1.9, probability = 0.10

Mean = 250.9±9.7 [3.9%] 95% conf.
Wtd by data-pt errs only, 0 of 3 rej.
MSWD = 0.047, probability = 0.95

Mean = 251.1±4.4 95% conf.
Wtd by data-pt errs only, 0 of 1 rej.
MSWD = 0.000, probability = 1.000

Appendix IV

XRF whole-rock geochemical results

Appendix IV. Whole-rock major, trace and rare earth elements of igneous units of Phuoc Son gold deposit area.

Sample #	DSDH257 @95.4m	DSDH257 @336.4m	DSDH96 @125m	DSDH250 @227.9m	DSDH40 @148.8m	DSDH89 @187.7m	DSDH212 @271.4m	DSDH218 @86.9m	DSDH249 @515.2m
Rock type	Foliated dacitic porphyry	Dacitic porphyry	Dacitic porphyry	Dacitic porphyry	Dacitic porphyry	Dacitic porphyry	Andesitic dyke	Andesitic dyke	Andesitic dyke
Location	Bai Dat	Bai Dat	Bai Go	Bai Go	Bai Go	Bai Go	Bai Go	Bai Go	Bai Go
SiO_2 (wt%)	72.40	64.00	65.73	65.63	64.72	65.00	54.39	54.86	49.05
TiO_2	0.27	0.53	0.54	0.53	0.53	0.52	0.50	0.78	1.05
Al_2O_3	15.15	15.95	16.41	15.76	16.34	16.20	20.95	16.99	14.04
Fe_2O_3	2.22	2.81	2.85	2.20	2.57	2.81	7.14	7.09	8.07
MnO	0.04	0.06	0.05	0.04	0.07	0.04	0.15	0.10	0.15
MgO	0.68	1.32	1.60	1.27	1.44	1.38	3.08	3.36	8.41
CaO	2.31	3.42	2.88	2.40	3.53	2.83	3.22	4.62	7.87
Na_2O	3.82	5.53	5.28	5.88	5.35	5.49	5.90	3.23	3.04
K_2O	1.88	2.28	2.35	2.35	2.51	2.28	1.94	2.73	1.31
P_2O_5	0.09	0.22	0.24	0.19	0.23	0.23	0.10	0.27	0.67
S	0.05	0.30	0.24	0.30	0.30	0.45	0.28	1.68	0.76
LOI	0.94	2.91	1.68	3.18	2.37	1.85	2.80	5.65	5.83
Total	100.00	100.00	99.63	99.43	99.64	99.99	100.18	99.68	99.50
Rb (ppm)	97.5	65	48	81	46	49.5	65.8	170	48.7
Sr	218	779	976	508	948	825	193	230	920
Cr	10	40			34	40	4.8	13.4	406
Cu	5	10	15	14	44	10	16.6	15.4	14.1
Ba	279	799	772	577	727	778	160	211	1000
Bi	0.04	0.13	<2	<2	<2	1.17	<2	<2	<2
Sn	1	1	<2	<2	<2	2	<1	1.6	<1
Zr	194	182	189	174	191	182	148	125	144
Mo	3	2				3	0.7	0.6	<0.5
Nb	6.3	4.8	6	5	4.1	5.2	5.1	8.3	12.1
V	20	57	55	43	55	65	86.8	233	181
Zn	31	54	30	30	37	41	245	82.4	110
Ni	7	13	8	6	8	16	2.9	3.1	172
Pb	20	12	16	10	14	15	46.6	7.8	11.3
Th	19.9	6.67	6	6	3	6.82	<2	6.8	5.3
Sc	3	4	4	4	6	4	29.1	21.7	20.2
U	8.76	1.68	2	<1.5	<2	1.67	<2	3.1	<2
Y	8.2	7	6	6	6	6.5	29.8	20.6	17.7
La	28.6	38.9	28	20	31	40.8	6.69	20.9	62.7
Ce	46	70.2	57	43	70	73.1	15.5	42.0	134.6
Pr	4.45	7.55				8.09	2.23		16.5
Nd	14.6	25	21	17	26	26.7	9.7	17.8	61.1
Sm	2.35	3.72				3.84	2.83		9.39
Eu	0.82	1.09				1.17	0.82		2.27
Gd	2.51	3.18				3.54	3.58		6.01
Tb	0.32	0.35				0.34	0.69		0.74
Dy	1.37	1.28				1.24	4.75		3.75
Ho	0.29	0.25				0.24	1.01		0.61
Er	0.8	0.74				0.7	3.25		1.67
Tm	0.15	0.13				0.11	0.48		0.22
Yb	0.79	0.67				0.55	3.12		1.32
Lu	0.12	0.1				0.09	0.47		0.19

Appendix IV (cont.). Whole-rock major, trace and rare earth elements of igneous units of Phuoc Son gold deposit area.

Sample #	DSDH241 @73.5m	DSDH270 @232m	DSDH270 @290.3m	DSDD267 @45.9m	K7DH10@ 108.7m	BODH2@ 105.5m	DSDH112 @29.9m	DSDH112 @31.6m	DSDH209 @128.2
Rock type	Granite dyke	Granite dyke	Granite dyke	Granite dyke	Granite dyke	Granite dyke	Gabbro	Gabbro	Gabbro
Location	Bai Dat	Bai Dat	Bai Dat	Bai Chuoi	K7	Bo	Bai Dat	Bai Dat	Bai Go
SiO_2 (wt%)	75.44	74.34	72.25	76.07	75.10	75.30	46.70	48.60	42.85
TiO_2	0.01	0.11	0.01	0.06	<0.01	0.01	0.16	0.19	0.10
Al_2O_3	14.06	14.84	15.39	13.62	15.00	14.70	2.06	2.07	1.11
Fe_2O_3	0.33	0.84	0.59	0.64	0.48	0.52	14.66	9.19	12.06
MnO	0.00	0.04	0.00	0.03	0.05	0.03	0.16	0.18	0.18
MgO	0.12	0.37	0.55	0.16	0.09	0.07	19.07	21.02	29.21
CaO	1.85	2.66	0.90	1.30	0.93	1.30	13.90	16.10	7.22
Na_2O	3.23	4.16	4.54	4.65	5.30	5.61	0.08	0.10	<0.03
K_2O	4.67	1.24	4.18	1.66	1.80	1.28	0.01	0.00	<0.01
P_2O_5	0.02	0.05	0.04	0.02	0.02	0.03	0.00	0.00	<0.02
S	0.32	0.10	0.50	0.20	0.10	0.12	6.11	0.20	0.04
LOI	0.42	1.01	1.27	1.47	0.99	0.84	2.94	2.70	7.10
Total	100.15	99.66	99.73	99.68	100.00	100.00	99.74	100.15	99.82
Rb (ppm)	77.7	45.6	163	75.1	103.5	93.9	<0.5	<0.5	<0.5
Sr	116	215	54.3	120	87.7	124	4.8	6.5	2
Cr	1.2	3	<1	1.7	10	10	1290	2479	1908
Cu	10.4	1.3	1.9	2.5	8	6	2898	56.8	48
Ba	386	269	1105	161	141.5	64	<4	<4	<4
Bi	<2	<2	<2	<2	0.67	2.64	<2	<2	<2
Sn	1	2.7	11	2.3	7	7	<1	<1	<2
Zr	33.6	92.1	34.7	37.4	29	30	1.5	2	1
Mo	0.6	<0.5	<0.5	<0.5	2	2	0.8	1.1	
Nb	8.6	5.7	24.0	10.8	17.5	22.8	2.5	2.5	<0.5
V	<3	5.5	<3	<3	7	8	187	225	121
Zn	3.6	14.8	7.8	16.2	16	22	81.2	37.4	55.0
Ni	4.1	2.9	2.4	2.7	6	6	1403	257	633
Pb	21	19.5	6.1	24.2	19	38	2.7	<1	<1.5
Th	6.6	15.2	7.3	7.5	7.42	12.45	<2	<2	<2
Sc	3.0	2.8	2.3	1.8	2	2	63.2	72.5	39
U	5.2	9.9	7.1	4.8	4.96	22.7	<2	<2	<2
Y	23.6	10.9	33.3	9.7	25.1	40.2	3.2	4.7	2.0
La	6.2	15.1	12.4	9	11	12.7	0.07	0.08	<4
Ce	12.6	28.0	25.4	16.5	22.9	23.3	0.22	0.32	<6
Pr					2.73	2.56	0.06	0.09	
Nd	<4	5	8.6	2.8	9.6	8.7	0.41	0.63	<4
Sm					3.45	3.33	0.24	0.35	
Eu					0.13	0.08	0.11	0.15	
Gd					4.19	4.73	0.43	0.60	
Tb					0.78	1.04	0.09	0.12	
Dy					3.96	5.88	0.60	0.80	
Ho					0.77	1.25	0.13	0.17	
Er					2.01	3.35	0.38	0.49	
Tm					0.33	0.54	0.06	0.07	
Yb					1.99	3.48	0.33	0.41	
Lu					0.28	0.47	0.05	0.06	

Appendix IV (cont.). Whole-rock major, trace and rare earth elements of igneous units of Phuoc Son gold deposit area.

Sample #	KRDH31 @259.8m	KRDH31 @260.2m	KRDH31 @261.1m	KRDH31 @262.4m	RHDH3@ 74.5m	RHDH3@ 86.2m	RHDH4@ 79.8m	RHDH4@ 80.6m	RHDH3@ 43.5m
Rock type	Granite	Granite	Granite	Granite	Granite	Granite	Granite	Granite	Granite
Location	Khe Rin	Khe Rin	Khe Rin	Khe Rin	Round Hill	Round Hill	Round Hill	Round Hill	Round Hill
SiO_2 (wt%)	74.10	74.30	79.69	75.06	74.70	73.80	74.30	74.30	73.76
TiO_2	0.26	0.31	0.16	0.19	0.28	0.28	0.29	0.29	0.31
Al_2O_3	12.90	12.85	9.38	10.34	12.15	11.95	11.85	12.00	12.10
Fe_2O_3	1.68	1.92	1.32	1.47	4.94	5.33	5.65	5.60	5.18
MnO	0.03	0.02	0.02	0.04	0.05	0.03	0.04	0.05	0.04
MgO	0.45	0.51	0.44	0.45	0.23	0.60	0.34	0.29	0.35
CaO	1.27	0.92	1.72	3.26	2.44	1.94	1.74	2.20	2.71
Na_2O	3.63	3.05	2.51	2.54	4.57	4.48	4.80	4.65	4.18
K_2O	3.47	3.67	2.17	2.46	0.17	0.52	0.19	0.14	0.24
P_2O_5	0.07	0.08	0.05	0.05	0.05	0.05	0.05	0.05	0.06
S	0.12	0.26	0.24	0.59	0.01	0.19	0.12	0.06	0.08
LOI	1.69	1.59	2.24	3.62	0.39	0.47	0.41	0.26	0.60
Total	99.97	99.99	99.70	99.48	100.00	99.97	99.98	100.00	99.52
Rb (ppm)	145.5	172.5	90.0	103.7	20.8	80.6	15.4	7.0	32.4
Sr	162.5	143.0	111.0	144.6	82.0	62.3	60.9	71.7	87.2
Cr	10.0	10.0	4.1	4.9	10.0	10.0	10.0	10.0	1.1
Cu	<5	15.0	1.3	6.3	<5	39.0	14.0	12.0	24.6
Ba	673.0	688.0	333.8	416.9	23.1	60.7	32.1	21.9	35.5
Bi	0.0	0.1	<2	<2	0.1	0.2	0.1	0.1	<2
Sn	2.0	2.0	<1	<1	13.0	4.0	1.0	1.0	<2
Zr	164.0	185.0	94.4	108.2	118.0	92.0	92.0	93.0	84.0
Mo	3	8	0.6	<0.5	2	3	3	3	
Nb	14.1	16.1	9.6	10.4	0.3	0.3	0.3	0.3	2.5
V	29.0	16.0	16.7	19.8	7.0	19.0	12.0	10.0	4.7
Zn	51.0	40.0	20.3	33.1	23.0	36.0	28.0	26.0	15.7
Ni	8.0	7.0	3.2	5.1	13.0	14.0	6.0	8.0	8.9
Pb	29.0	32.0	15.9	33.8	<5	<5	<5	<5	4.9
Th	25.5	33.8	15.2	16.8	0.4	0.3	0.3	0.3	<2
Sc	3.0	4.0	2.2	4.5	12.0	12.0	12.0	12.0	12.5
U	6.4	9.2	5.6	5.9	0.3	0.3	0.2	0.3	<2
Y	14.8	19.0	10.4	11.7	76.9	71.7	58.4	59.0	49.2
La	51.1	56.8	24.2	24.2	3.4	4.7	2.5	2.2	<4
Ce	88.3	99.0	46.8	44.2	11.7	16.4	8.3	7.5	<6
Pr	8.9	10.3			2.3	3.3	1.7	1.5	
Nd	28.6	32.6	15.9	14.2	14.3	19.2	10.2	9.1	4.5
Sm	4.5	5.3			5.9	7.9	4.3	4.0	
Eu	0.7	1.0			1.6	1.6	1.2	1.3	
Gd	4.5	5.6			9.0	11.6	6.7	6.5	
Tb	0.6	0.7			1.8	2.1	1.4	1.3	
Dy	2.6	3.4			11.5	11.7	8.8	8.5	
Ho	0.5	0.7			2.9	2.7	2.2	2.2	
Er	1.5	2.0			8.5	7.6	6.5	6.6	
Tm	0.2	0.3			1.4	1.2	1.0	1.1	
Yb	1.5	1.8			9.7	7.8	6.9	7.1	
Lu	0.2	0.3			1.5	1.2	1.0	1.1	

Appendix IV (cont.). Whole-rock major, trace and rare earth elements of igneous units of Phuoc Son gold deposit area.

Sample #	DSDH209@ 272.2m	DSDH224 @24.3m	DSDH224@ 272.5m	DSDH224@ 386.2m	DSDH235 @76.1m	DSDH152@ 58.8m	DSDH226@ 160.3m	DSDH257@ 191.8m
Rock type	Metabasite	Metabasite	Metabasite	Metabasite	Metabasite	Metabasite	Metabasite	Metabasite
Location	Bai Go	Bai Go	Bai Go	Bai Go	Bai Go	Bai Go	Bai Dat	Bai Dat
SiO_2 (wt%)	41.06	45.21	39.06	42.19	46.6	41.6	35.3	50.2
TiO_2	3.15	0.17	3.60	3.74	0.46	1.5	0.42	2.16
Al_2O_3	11.95	15.68	13.61	11.25	16	16.15	10.5	13.4
Fe_2O_3	17.51	13.12	25.27	21.58	9.37	15.7	9.93	13.25
MnO	0.29	0.15	0.24	0.38	0.14	0.17	0.19	0.21
MgO	5.53	8.84	7.13	5.50	9.86	8.1	14.8	6.54
CaO	8.40	13.02	6.85	10.01	9.65	12.4	16.55	8.45
Na_2O	1.71	1.05	1.17	1.18	2.9	1.21	0.31	3.84
K_2O	0.50	0.20	0.20	0.08	0.3	0.15	0.06	0.17
P_2O_5	0.43	0.02	0.03	0.73	0.01	0.01	0.01	0.23
S	0.89	<0.01	2.92	0.38	0.004	0.087	0.051	0.209
LOI	8.85	2.99	2.80	2.91	4.49	2.44	11.57	0.85
Total	99.39	100.44	99.96	99.54	99.96	99.94	99.99	100.00
Rb (ppm)	16	6	2.1	1.6	9.8	2	2.6	2.5
Sr	118	106	65	82	247	227	65.8	134.5
Cr	25	191	71	34	440	100	890	150
Cu	62	132	977	42	13	232	67	59
Ba	58	66	28	12	39.2	29.9	12.9	32.5
Bi	<2	<2	<2	<2	0.01	0.03	0.01	0.01
Sn	<2	<2	<2	<2	<1	<1	<1	2
Zr	194	5	15	39	8	8	7	170
Mo					2	2	2	3
Nb	13.4	<0.5	2.6	11.8	0.2	0.4	0.2	8.2
V	489	197	592	510	186	1050	227	382
Zn	178	99	139	154	87	97	68	123
Ni	16	82	83	25	147	67	165	56
Pb	2	<1.5	<1.5	<1.5	<5	5	<5	<5
Th	<2	<2	<2	<2	<0.05	0.05	<0.05	0.84
Sc	41	48	35	50	30	51	53	42
U	<2	<2	<2	<2	0.1	0.1	0.09	0.31
Y	52	4	3	55	8.9	6.6	8.4	42.4
La	11	<4	<4	5	0.8	0.6	<0.5	10.2
Ce	33	<6	<6	17	1.9	1.4	1.1	25.6
Pr					0.34	0.29	0.2	3.83
Nd	28	<4	<4	21	1.9	1.5	1.4	18
Sm					0.77	0.64	0.71	5.22
Eu					0.64	0.37	0.43	1.84
Gd					1.18	1.07	1.13	6.75
Tb					0.25	0.19	0.22	1.22
Dy					1.43	1.22	1.36	6.93
Ho					0.35	0.28	0.34	1.64
Er					0.96	0.78	0.96	4.42
Tm					0.16	0.14	0.17	0.69
Yb					0.97	0.72	0.93	4.39
Lu					0.14	0.11	0.15	0.63

Appendix IV (cont.). Whole-rock major, trace and rare earth elements of igneous units of Phuoc Son gold deposit area.

Sample #	RHDH3@ 34.9	KRDH25@ 53.1m	RHDH3@ 61.9m	TLDH1@58.9m	DSDH235 @276.5m	KRDH3@ 40.6m
Rock type	Metabasite	Metabasite	Metabasite	Metabasite	Schist	Schist
Location	Round Hill	Khe Do	Round Hill	Tra Long	Bai Go	Khe Rin
SiO_2 (wt%)	49.85	53.1	55.4	50.5	62.5	61.30
TiO_2	0.11	0.68	0.09	0.08	0.69	0.85
Al_2O_3	12.98	16.2	10.9	10.05	10.75	14.90
Fe_2O_3	12.12	13.2	10.5	8.4	8.78	7.44
MnO	0.27	0.15	0.28	0.14	0.08	0.24
MgO	11.63	3.06	10.4	15.05	5.65	5.25
CaO	9.51	8.95	9.12	11.45	2.29	1.64
Na_2O	1.94	0.86	1.98	0.75	0.27	0.23
K_2O	0.41	1.6	0.29	0.77	2.31	3.96
P_2O_5	<0.01	0.02	0.01	0.01	0.14	0.16
S	<0.01	0.126	0.004	<0.004	2.16	0.07
LOI	1.55	1.74	0.75	2.53	3.67	4.13
Total	100.35	100.00	99.99	100.05	102.65	100.11
Rb (ppm)	51	55.2	34.1	31.4	103	172
Sr	28	131	40.2	70.5	43.4	39
Cr	1067	30	1210	1350	80	114
Cu	<1	57	<5	<5	53	37
Ba	17	248	27	85.9	332	612
Bi	<2	0.12	0.17	0.09	0.45	<2
Sn	<2	1	3	1	3	3
Zr	2	21	4	11	144	185
Mo		2	2	2	10	
Nb	<0.5	0.2	0.2	0.2	12.4	14.2
V	309	321	201	162	146	215
Zn	80	86	78	81	103	117
Ni	194	18	186	286	69	50
Pb	<1	6	<5	<5	12	4
Th	<2	0.11	0.09	0.14	12.65	13
Sc	63	40	42	36	15	18
U	<2	0.09	0.11	0.22	3.19	4
Y	4	11.5	13.9	2.8	34.3	30
La	<4	0.6	<0.5	<0.5	35.6	27
Ce	<6	1.7	0.6	0.7	74.5	56
Pr		0.31	0.18	0.1	8.16	
Nd	<4	1.8	1.4	0.5	30.5	27
Sm		0.91	0.97	0.17	6.39	
Eu		0.41	0.4	0.09	1.24	
Gd		1.47	1.68	0.26	7.02	
Tb		0.32	0.33	0.06	1.09	
Dy		2.01	2.12	0.39	5.58	
Ho		0.51	0.51	0.11	1.28	
Er		1.47	1.46	0.33	3.44	
Tm		0.25	0.27	0.09	0.52	
Yb		1.56	1.63	0.45	3.41	
Lu		0.25	0.26	0.08	0.5	

Appendix V

Mugnetic susceptibility data

Appendix V. Magnetic susceptibility data of intrusive units in the Phuoc Son deposit area, central Vietnam.

Rock unit	Sample No.	Magnetic susceptibility (X 10^{-3} SI)				
		Mean value	1st measurement	2nd measurement	3rd measurement	4th measurement
Dacitic porphyry	DSDH250@227.9m	**0.253**	0.280	0.253	0.220	
	DSDH40@148.8m	**0.552**	0.557	0.547	0.562	0.407
Andesitic dyke	DSDH212@271.4m	**0.370**	0.348	0.414	0.344	0.392
	DSDH249@515.2m	**0.369**	0.369	0.378	0.303	
Granite dyke	DSDH270@290.3m	**0.088**	0.108	0.077	0.091	0.084
	K7DH01@108.7m	**0.181**	0.175	0.170	0.198	0.187
	BODH02@105.5m	**0.178**	0.233	0.152	0.145	0.204
Metagabbro	DSDH112@31.7m	**36.3**	38.9	35.3	33.2	37.2
	DSDH209@128.2m	**49.0**	50.0	48.1	47.5	49.8
Khe Rin granite	KRDH31@260.2m	**0.098**	0.081	0.096	0.120	0.100
Round Hill granite	RHDH03@43.5m	**29.4**	44.6	32.1	26.7	24.4
	RHDH03@74.5m	**32.2**	35.2	30.5	30.6	33.7
	RHDH03@86.2m	**35.2**	35.2	35.1	32.1	35.6
	RHDH04@79.8m	**14.4**	14.4	16.6	14.0	
	RHDH04@80.6m	**18.6**	19.2	17.0	19.2	17.9
Diorite	TMVN11-06	**0.235**	0.239	0.235	0.159	

Appendix VI

Re-Os molybdenite geochronological results

AIRIE
APPLIED ISOTOPE RESEARCH

Colorado State University
Knowledge to Go Places

Dr. Khin Zaw, and
Takayuki Manaka, PhD candidate
CODES ARC Centre of Excellence in Ore Deposits
University of Tasmania, Private Bag 126
Hobart, Tasmania 7001 Australia
Takayuki.Manaka@utas.eu.au
Khin.Zaw@utas.edu.au

Department of Geosciences
1482 Campus Delivery
Fort Collins, Colorado 80523-1482
(970) 491-5661
FAX: (970) 491-6307
www.cnr.colostate.edu/geo/

May 28, 2011

Dear Taka and Khin Zaw,

We have completed work on your sample RHDH03-89.1m from the Round Hill Au-Cu-W prospect in the Phuoc Son gold district, central Vietnam. The sample came to AIRIE as a small polished mount featuring abundant pyrite with lesser chalcopyrite, and traces of molybdenite, cassiterite, and sphalerite. Accompanying photomicrographs mapped sparse micron-size molybdenite blades in the matrix of this sample. SEM verified the blades were molybdenite. As I mentioned from the outset, this is not a straight-forward project for molybdenite Re-Os dating. Our approach was to drill out the four areas where you verified the presence of molybdenite and combine this powder, hoping for enough molybdenite, for a Re-Os analysis. It worked fairly well.

According to the information accompanying the sample, and based on e-mail queries and communications between us, I understand that the Au-Cu-W mineralization is hosted in veins within granite of *presumed* Ordovician age. (Thank you, Taka, for the nice write-up – this is very helpful for my working effectively with you.)

If the question is Ordovician *versus* Triassic age for the mineralization, I suggested that we may be able to discern this with the Re-Os dating, even if low levels of extractable molybdenite hampered precision on the age. The possibility to accomplish this, however, hinged on the absence of common Os. And, luckily, this was the case as we took great care to avoid other sulfides as we drilled the points indicated for molybdenite. Also, of necessity, we had to overspike the sample to be sure we had Re to measure – we used our most dilute spike (100 µl).

The Re-Os data were acquired using a Carius tube digestion in inverse *aqua regia* together with a mixed Re-double Os spike. Please keep the AIRIE Run number with the sample data, as that is our sole means of tracking all information on your samples in our database – from mineral separation, to spikes used, to mass spectrometry. Data are corrected for blanks and Os isotope fractionation. Blanks at this time were Re = 24.2 ±

0.2 pg and Os = 2.00 ± 0.02 pg with $^{187}Os/^{188}Os$ composition of 0.231 ± 0.001. Sample weight was 8 milligrams. The age calculation assumes an initial $^{187}Os/^{188}Os$ of 0.2.

Phuoc Son gold district, central Vietnam (Takayuki Manaka and Khin Zaw)
Round Hill Au-Cu-W prospect (RHDH03-89.1)
AIRIE Run MD-1232
Re = 0.0255 ± 0.0003 ppm
^{187}Os = 0.1406 ± 0.0002 ppb
Age = 525 ± 6 Ma

In my opinion, there is no possibility that the molybdenite in this sample from Round Hill is Triassic age. And, there remains a possibility that the age is Ordovician and not Cambrian as suggested by the calculated 525 Ma age. Keep in mind that we are working with very low levels of Re (25 ppb) and radiogenic ^{187}Os (141 ppt). Overspiking could introduce some error in the age. Also, our blanks were a little higher than usual during the time we analyzed the Round Hill sample. If we use lower blank values, as are more typical for our lab, the age changes less than 5 m.y. Therefore, in sum, I suggest a Cambrian age be considered; however, with a more reasonable sample of visible molybdenite to work with, it is possible that we would find the age to be Ordovician.

We may be able to improve on this result with additional work and using a larger drilled powder (but avoiding other sulfides so as not to risk common Os). Let me know if the company wants to support our pursuing this further to confirm a Cambrian (versus Ordovician) age. Regardless, the Re-Os information and suggested early Paleozoic age provided in this report should be useful for exploration programs aimed at discovery of Au-Cu-W mineralization in this region.

Let me know what you think of this result, and please include me as a distant co-author on publication of this Re-Os geochronology.

Please don't hesitate with any questions.

Regards,

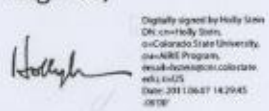

Dr. Holly Stein
Director, AIRIE Program

Dr. Holly J. Stein
Senior Research Scientist and Professor, Director, AIRIE Program
Department of Geosciences, Colorado State University, Fort Collins, CO 80523-1482 USA
Senior Research Scientist, Geological Survey of Norway, 7491 Trondheim, Norway
hstein@cnr.colostate.edu *www.airie.cnr.colostate.edu*

Appendix VII

Ar-Ar biotite geochronology

I: Analytical methods

II: Ar-Ar age results

ANALYTICAL METHODS

Sample Preparation and Irradiation

Biotite samples DSDH267@387.1m (Bai Chuoi) and DSDH270@187.6m (Bai Dat), together with aliquots of the Fish Canyon Tuff sanidine fluence monitor (28.02 Ma; Renne et al., 1998) were packaged in aluminium foil packets and co-irradiated in the CLICIT facility of the Oregon State University reactor for 100 MWH (irradiation number: UM#52).

Instrumentation

$^{40}Ar/^{39}Ar$ analyses were carried out in the Noble Gas laboratory of the School of Earth Sciences at the University of Melbourne, Australia. This facility includes a new generation, multi-collector Thermo Fisher Scientific ARGUSVI mass spectrometer linked to a stainless steel gas extraction/purification line and a Photon Machines Fusions 10.6 CO_2 laser system. The ARGUSVI mass spectrometer is a 13cm radius, 90˚ extended geometry, static vacuum, magnetic sector mass spectrometer housing a Nier-type source and a fixed array of five Faraday (with low noise 1 x 10^{12} Ω resistors) and one Compact Discrete Dynode (CDD) detectors. From high (H) to low (L) mass, the detectors are designated H2, H1, AX, L1, L2 and CDD (AX = axial). For the current study, argon isotopes were measured using the following configuration:

Detector	H2	H1	AX	L1	L2	CDD
Isotope		^{40}Ar	^{39}Ar	^{38}Ar	^{37}Ar	^{36}Ar

The ARGUSVI mass spectrometer has a volume of ~700 cm^3 and a nominal mass resolution of ~200. The sensitivity for argon is 3.55 x 10^{-17} moles/fA (~1 x 10^{-3} A/Torr) at 200μA trap current, as determined from measured aliquots of GA1550 biotite (McDougall and Roksandic, 1974).

The ARGUSVI gas extraction/purification line has a volume of ~240 cm^3 and comprises a central stainless steel manifold, laser sample chamber with ZnS window, Pfeiffer turbo-molecular/diaphragm pumping station, Varian 40 l/s ion pump, automated air pipette system, Sorb-AC SAES NP10 twin getter housing and automated VAT or manual Varian valves. The manifold, air pipette system, getter housing and MP10 VAT valves were supplied by Thermo Fisher Scientific.

Sample heating is achieved using the 55 W Fusions 10.6 CO_2 laser system, which is configurable to produce either focused laser beams of varying diameter from 150μm to 2mm (for laser fusion analyses) or a uniform 6 mm square beam that is used for step-heating.

Gas extraction and Analysis

After irradiation, the FCT and ACR sanidine grains were loaded into a copper holder with 6mm wide slots. The holder was placed into the stainless steel sample chamber with a ZnS cover slip and baked at ~180˚C overnight. Once extraction line ^{40}Ar rate-of-rise levels had decreased to <1fA/min, the sample chamber was exposed to the getters and the sanidine grains were outgassed using the CO_2 laser. Air aliquots from the automated pipette system were analysed prior to the standard and sample analyses to monitor mass discrimination and detector bias. Measurements of ^{40}Ar across the Faraday detector array show a systematic bias of up to 2% (H1/L2); however, this bias is highly reproducible and varies by <0.1% over prolonged periods (weeks to months). Consequently, bias corrections to sample/standard $^{40}Ar^*/^{39}Ar$ ratios are usually unnecessary. However, to reduce the possibility of detector bias, air aliquots and standard/samples were analysed sequentially on the same day or consecutive days. Linearity in Faraday detector response as a function of changing argon isotope signals has been demonstrated for the ARGUS mass spectrometer by Mark et al. (2009) and confirmed for our ARGUSVI using air shots of varying magnitude. Similarly, the CDD detector exhibits a linear response as a function of ^{36}Ar signal size over the range of ^{36}Ar values measured.

Gas introduced to the ARGUSVI mass spectrometer is equilibrated for 20s, before peak centering on mass 40 (H1) and subsequent multi-collector analysis of the five argon isotopes. Peak signals were collected for a period of 300 s and regressed to time zero. Line blanks were analysed between every 1 - 3 sample analyses and were typically <1.5 fA for ^{40}Ar, compared to >1000 fA for FCT sanidine analyses. Line blanks were subtracted from succeeding sample data.

The argon isotopic data from the sanidine samples is presented in Table 1 (1σ uncertainties). This data has been corrected for system blanks, radioactive decay, isotopic interferences and mass discrimination (including H1/CDD bias). Ca/K/Cl salts/glasses were not included in the irradiation package. Instead the average interference correction values reported by Aciego et al. (2010) for the OSU CLICIT facility were utilized: $(^{39}Ar/^{37}Ar)_{Ca}$ = (7.60 ± 0.09) x 10^{-4}; $(^{36}Ar/^{37}Ar)_{Ca}$ = (2.70 ± 0.02) x 10^{-4}; and $(^{40}Ar/^{39}Ar)_{K}$ = (7.30 ± 0.90) x 10^{-4}. Ages were calculated using the decay constants recommended by Steiger and Jager (1977) and an assumed age for FCT sanidine of 28.02 Ma (Renne et al., 1998). Plateau ages were calculated using ISOPLOT (Ludwig, 2012) and are defined as including >50% of the

total ^{39}Ar released, distributed over at least 3 contiguous steps, with $^{40}Ar^*/^{39}Ar$ ratios within agreement of the mean at the 95% confidence level (see McDougall and Harrison, 1999). Unless otherwise stated, calculated ages are reported at the 2σ level and include uncertainties in the J-values, but exclude errors associated with the age of the fluence monitor and the decay constants.

REFERENCES CITED

Aciego, S.M., Jourdan, F., DePaolo, D.J., Kennedy, B.M., Renne, P.R., and Sims, K.W.W., 2010, Combined U-Th/He and $^{40}Ar/^{39}Ar$ geochronology of post-shield lavas from the Mauna Kea and Kohala volcanoes, Hawaii: Geochimica et Cosmochimica Acta, v. 74, 1620 – 1635.

Ludwig, K.R., 2012, User's Manual for Isoplot 3.75. A Geochronological Toolkit for Microsoft Excel: Special Publication No. 5, Berkeley Geochronology Center, Berkeley, California, 75 pp.

Mark, D. F., Barfod, D., Stuart, Imlach, J., 2009, The ARGUS multicollector noble gas mass spectrometer: Performance for $^{40}Ar/^{39}Ar$ geochronology: Geochemistry, Geophysics, Geosystems, v. 10, p. 1-9.

Renne, P.R., Swisher, C.C., Deino, A.L., Karner, D.B., Owens, T.L., and DePaolo, D.J., 1998, Intercalibration of standards, absolute ages and uncertainties in $^{40}Ar/^{39}Ar$ dating: Chemical Geology, v. 145, p. 117–152.

Steiger, R.H., and Jäger, E., 1977, Subcommission on geochronology: convention on the use of decay constants in geo- and cosmochronology: Earth and Planetary Science Letters, v. 36, p. 359– 362.

Appendix VII-II. $^{40}Ar/^{39}Ar$ analytical results for biotite samples DSDH267-387.1m and DSDH270-187.6m.

Sample ID	Step No	Cum.% ^{39}Ar	^{40}Ar (x10^{-13} moles)	±	^{39}Ar (x10^{-14} moles)	±	^{38}Ar (x10^{-16} moles)	±	^{37}Ar (x10^{-16} moles)	±	^{36}Ar (x10^{-16} moles)	±	Ca/K	±	$\%^{40}Ar^*$	$^{40}Ar^*/^{39}Ar$	±	Age (Ma)	±
DSDH267-387.1m (Bai Chuoi)																			
J-Value = 0.024691 0.000004																			
	1	5.3	0.83731	0.00025	1.66350	0.00063	0.03148	0.00013	33.021	0.020	0.16758	0.00069	0.3474	0.0002	94.1	4.7357	0.0027	199.50	0.11
	2	10.6	0.83787	0.00029	1.67773	0.00065	0.01182	0.00010	6.128	0.022	0.06289	0.00053	0.0639	0.0002	97.8	4.8833	0.0027	205.37	0.11
	3	15.6	0.78984	0.00027	1.56947	0.00063	0.00758	0.00004	2.818	0.025	0.04036	0.00024	0.0314	0.0003	98.5	4.9566	0.0027	208.28	0.11
	4	20.5	0.77640	0.00025	1.53818	0.00054	0.00662	0.00004	1.383	0.027	0.03525	0.00022	0.0157	0.0003	98.6	4.9798	0.0024	209.21	0.10
	5	23.1	0.40216	0.00014	0.80353	0.00036	0.00242	0.00003	0.549	0.023	0.01286	0.00016	0.0120	0.0005	99.0	4.9576	0.0029	208.33	0.11
	6	26.0	0.45463	0.00015	0.91703	0.00033	0.00269	0.00004	0.384	0.038	0.01434	0.00022	0.0073	0.0007	99.1	4.9114	0.0025	206.49	0.10
	7	29.1	0.48789	0.00017	0.96415	0.00043	0.00298	0.00003	0.334	0.029	0.01584	0.00016	0.0061	0.0005	99.0	5.0118	0.0029	210.48	0.11
	8	33.5	0.71738	0.00022	1.40123	0.00048	0.00506	0.00002	0.367	0.027	0.02692	0.00013	0.0046	0.0003	98.9	5.0628	0.0024	212.50	0.09
	9	37.2	0.57555	0.00020	1.15269	0.00040	0.00284	0.00004	0.238	0.030	0.01512	0.00019	0.0036	0.0005	99.2	4.9543	0.0025	208.20	0.10
	10	43.5	1.00493	0.00033	1.99120	0.00076	0.00539	0.00003	0.287	0.033	0.02869	0.00017	0.0025	0.0003	99.1	5.0043	0.0025	210.18	0.10
	11	51.1	1.19051	0.00043	2.36569	0.00085	0.00630	0.00006	0.244	0.024	0.03352	0.00033	0.0018	0.0002	99.2	4.9905	0.0026	209.63	0.10
	12	57.3	0.96007	0.00035	1.94986	0.00086	0.00384	0.00004	0.237	0.022	0.02045	0.00019	0.0021	0.0002	99.4	4.8928	0.0028	205.75	0.11
	13	65.4	1.22387	0.00045	2.55100	0.00071	0.00461	0.00003	0.291	0.031	0.02455	0.00015	0.0020	0.0002	99.4	4.7692	0.0022	200.83	0.09
	14	76.2	1.63618	0.00067	3.38903	0.00142	0.00530	0.00002	0.244	0.031	0.02823	0.00011	0.0013	0.0002	99.5	4.8033	0.0028	202.19	0.11
	15	88.2	1.82219	0.00084	3.78644	0.00189	0.00551	0.00008	0.332	0.027	0.02933	0.00043	0.0015	0.0001	99.5	4.7895	0.0033	201.64	0.13
	16	94.7	0.93138	0.00039	2.04035	0.00098	0.00347	0.00007	0.234	0.034	0.01844	0.00036	0.0020	0.0003	99.4	4.5381	0.0030	191.60	0.12
	17	100.0	0.75436	0.00024	1.65711	0.00066	0.00581	0.00004	0.174	0.028	0.03091	0.00022	0.0018	0.0003	98.8	4.4972	0.0023	189.96	0.09
	Total																	**203.86**	**0.11**
DSDH270-187.6m (Bai Dat)																			
J-Value = 0.024687 0.000004																			
	1	37.1	1.90699	0.00063	3.67775	0.00121	0.01493	0.00011	0.588	0.027	0.07947	0.00058	0.0028	0.0001	98.8	5.1213	0.0025	214.79	0.10
	2	50.0	0.64033	0.00017	1.28167	0.00050	0.00296	0.00004	0.104	0.028	0.01577	0.00020	0.0014	0.0004	99.3	4.9597	0.0024	208.38	0.09
	3	58.7	0.42818	0.00012	0.86821	0.00027	0.00211	0.00004	0.051	0.007	0.01122	0.00020	0.0010	0.0001	99.2	4.8936	0.0021	205.76	0.08
	4	67.2	0.41549	0.00013	0.83940	0.00029	0.00211	0.00003	0.026	0.013	0.01122	0.00016	0.0005	0.0003	99.2	4.9104	0.0023	206.43	0.09
	5	73.8	0.32760	0.00011	0.65904	0.00014	0.00145	0.00004	0.077	0.011	0.00773	0.00020	0.0021	0.0003	99.3	4.9362	0.0021	207.45	0.08
	6	81.2	0.36931	0.00012	0.73285	0.00039	0.00177	0.00003	0.064	0.024	0.00940	0.00016	0.0015	0.0006	99.2	5.0015	0.0032	210.04	0.13
	7	90.4	0.45456	0.00015	0.91509	0.00030	0.00201	0.00004	0.076	0.028	0.01069	0.00022	0.0015	0.0005	99.3	4.9328	0.0024	207.32	0.10
	8	95.2	0.25149	0.00008	0.47311	0.00012	0.00080	0.00003	0.033	0.024	0.00424	0.00014	0.0012	0.0009	99.5	5.2892	0.0023	221.41	0.09
	9	97.1	0.10001	0.00005	0.18525	0.00014	0.00043	0.00001	0.006	0.022	0.00231	0.00008	0.0006	0.0021	99.3	5.3620	0.0048	224.27	0.19
	10	100.0	0.15545	0.00005	0.28924	0.00019	0.00169	0.00001	-0.005	-0.029	0.00901	0.00007	-0.0003	-0.0017	98.3	5.2823	0.0040	221.14	0.16
	Total																	**211.60**	**0.10**

Appendix VIII

Microprobe results of electrum fineness

Appendix VIII. Results of microprobe analysis (wt.%) of electrum from the Bai Dat and Bai Go deposits, Phuoc Son.

Sample No.	Ag	Au	Pb	As	Bi	S	Te	Total	Fineness	Remark
BAI DAT										
Vein										
TMBD11-15_1	42.05	57.66	0.00	0.01	0.00	0.10	0.01	99.8	**578**	
TMBD11-15_2	42.53	57.09	0.00	0.00	0.00	0.14	0.02	99.8	**573**	
TMBD11-15_3	37.24	61.48	0.00	0.00	0.00	0.06	0.05	98.8	**623**	
TMBD11-15_4	29.63	68.56	0.00	0.00	0.00	0.08	0.01	98.3	**698**	
TMBD11-15_5	45.21	54.19	0.00	0.01	0.00	0.20	0.04	99.6	**545**	
TMBD11-15_6	43.62	56.13	0.00	0.00	0.00	0.16	0.02	99.9	**563**	
TMBD11-15_7	46.98	52.30	0.00	0.00	0.00	0.37	0.02	99.7	**527**	
TMBD11-15_8	44.80	53.94	0.00	0.00	0.00	0.26	0.01	99.0	**546**	
TMBD11-09A_1	23.07	77.62	0.00	0.00	0.03	0.07	0.00	100.8	**771**	
TMBD11-09A_2	22.88	77.78	0.00	0.00	0.00	0.12	0.03	100.8	**773**	
TMBD11-09A_3	22.57	77.66	0.00	0.00	0.00	0.11	0.04	100.4	**775**	
TMBD11-09A_4	25.44	74.87	0.00	0.01	0.02	0.12	0.03	100.5	**746**	
TMBD11-09A_5	26.07	71.44	0.00	0.01	0.00	0.33	0.01	97.9	**733**	
TMBD11-09A_6	26.84	73.47	0.00	0.00	0.00	0.46	0.02	100.8	**732**	
TMBD11-09B_1	7.11	93.57	0.00	0.00	0.00	0.13	0.00	100.8	**929**	Inclusion of massive sphalerite
TMBD11-09B_2	6.91	93.67	0.00	0.01	0.00	0.08	0.00	100.7	**931**	Inclusion of massive sphalerite
TMBD11-09B_3	6.42	92.12	0.00	0.00	0.02	0.25	0.01	98.8	**935**	Inclusion of massive sphalerite
TMBD11-09B_4	8.11	87.85	0.00	0.00	0.00	0.41	0.01	96.4	**916**	Inclusion of massive sphalerite
DSDH257-454.2m_1	27.01	73.64	0.00	0.01	0.00	0.12	0.02	100.8	**732**	
DSDH257-454.2m_2	25.44	75.53	0.00	0.00	0.00	0.08	0.04	101.1	**748**	
DSDH257-454.2m_3	25.25	75.67	0.00	0.00	0.00	0.08	0.01	101.0	**750**	
DSDH257-454.2m_4	24.27	75.92	0.00	0.00	0.00	0.04	0.03	100.3	**758**	
DSDH257-454.2m_5	30.40	70.71	0.00	0.00	0.00	0.06	0.03	101.2	**699**	
DSDH257-454.2m_6	27.53	72.09	0.00	0.00	0.00	0.08	0.00	99.7	**724**	
DSDH257-454.2m_7	28.58	71.63	0.00	0.00	0.00	0.10	0.02	100.3	**715**	
DSDH257-454.2m_8	33.59	63.98	0.00	0.00	0.01	0.05	0.00	97.6	**656**	
Wall rock										
KZ0818b_1	0.00	96.09	0.00	0.00	0.07	0.12	0.02	96.3	**1000**	
KZ0818b_2	0.04	92.96	0.00	0.00	0.00	0.13	0.01	93.1	**1000**	
KZ0818b_3	0.00	81.95	0.00	0.00	0.00	0.12	0.01	82.1	**1000**	
KZ0818b_4	0.00	92.41	0.00	0.01	0.52	0.23	0.01	93.2	**1000**	
BAI GO										
DSDH26-87.1m_1	62.26	39.35	0.00	0.00	0.00	0.18	0.09	101.9	**387**	
DSDH26-87.1m_2	61.32	39.39	0.00	0.01	0.00	0.23	0.05	101.0	**391**	
DSDH26-87.1m_3	57.82	38.66	0.00	0.00	0.00	1.34	0.03	97.9	**401**	
DSDH26-87.1m_4	60.24	40.77	0.00	0.01	0.00	0.11	0.06	101.2	**404**	
DSDH209-295m_1	7.63	92.86	0.00	0.01	0.00	0.04	0.00	100.5	**924**	
DSDH209-295m_2	6.19	93.99	0.00	0.00	0.00	0.03	0.01	100.2	**938**	
DSDH209-295m_3	6.11	93.92	0.00	0.00	0.00	0.02	0.01	100.1	**939**	
DSDH209-295m_4	2.86	97.41	0.00	0.00	0.00	0.02	0.00	100.3	**971**	
DSDH209-295m_5	7.15	93.06	0.00	0.00	0.00	0.01	0.00	100.2	**929**	
DSDH209-295m_6	8.10	91.84	0.00	0.00	0.00	0.04	0.02	100.0	**919**	
DSDH209-295m_7	8.05	92.80	0.00	0.01	0.00	0.02	0.01	100.9	**920**	
DSDH209-295m_8	8.74	91.53	0.00	0.00	0.00	0.05	0.00	100.3	**913**	
DSDH210-246.8m_1	21.81	76.35	0.00	0.01	0.00	0.06	0.00	98.2	**778**	
DSDH210-246.8m_2	36.95	63.60	0.00	0.00	0.05	0.05	0.02	100.7	**633**	
DSDH210-246.8m_3	15.59	84.21	0.00	0.00	0.00	0.04	0.00	99.8	**844**	
DSDH210-246.8m_4	18.66	79.56	0.00	0.00	0.00	0.07	0.02	98.3	**810**	
DSDH210-246.8m_5	21.53	78.30	0.00	0.00	0.02	0.09	0.04	100.0	**784**	
DSDH210-246.8m_6	22.09	77.78	0.00	0.00	0.00	0.12	0.04	100.0	**779**	
DSDH210-246.8m_7	19.64	79.47	0.00	0.00	0.00	0.11	0.03	99.2	**802**	
DSDH210-246.8m_8	31.10	69.23	0.00	0.00	0.00	0.12	0.03	100.5	**690**	

Appendix IX

LA-ICPMS pyrite trace element geochemical results

I: Spot analyses

II: line analyses for mapping (CD-ROM)

Appendix IX-I. Trace element values in pyrite from the Bai Dat and Bai Go deposits determined by LA-ICPMS spot analysis.

Analysis ID	Pyrite type	Ti49	Cr53	Mn55	Fe57	Co59	Ni60	Cu65	Zn66	As75	Se77	Zr90	Mo95	Ag107	Cd111	Sn118	Sb121	Te125	Ba137	La139	W182	Au197	Tl205	Pb208	Bi209	Th232
Vein-located pyrite																										
DSDH209-325m-1	Homogeneous	15.02	0.644	0.86	465000	22151.0	311.64	9.675	7.223	69.746	2.94	0.000	0.265	15.778	0.536	1.432	613.972	1.97	0.06	0.00	0.17	0.1266	0.425	1854	0.909	0.000
DSDH209-325m-2	Homogeneous	2.67	-0.093	0.12	465000	3092.0	104.96	1.630	0.558	262.792	2.82	0.000	0.426	5.636	0.944	0.449	11.614	0.56	0.08	0.00	0.02	0.0215	0.632	2798	0.455	0.000
DSDH209-325m-3	Homogeneous	3.76	0.234	0.63	465000	2549.4	186.84	1.787	1.055	199.565	209.84	-0.007	1.860	1087.636	218.370	75.325	534.174	98.01	0.03	0.00	0.00	4.0952	154.102	661570	103.664	0.005
DSDH209-325m-4	Homogeneous	2.36	-0.417	4.83	465000	6894.5	45.21	0.083	1.157	352.841	0.52	0.000	0.242	0.840	0.114	3.134	1.857	0.37	0.01	0.00	0.00	0.0045	0.093	315	0.036	0.001
DSDH209-325m-5	Homogeneous	2.14	0.079	0.07	465000	2512.0	107.75	0.132	0.875	193.877	2.77	0.004	0.000	9.532	2.436	1.265	11.013	0.61	0.00	0.00	0.00	0.0017	3.438	14420	2.160	0.002
DSDH209-325m-6	Homogeneous	2.32	0.157	0.02	465000	2090.8	191.51	1.809	1.665	529.987	1.39	0.000	0.047	1.068	0.045	0.152	5.092	0.11	0.00	0.00	-0.01	0.0102	0.046	189	0.055	0.000
DSDH209-325m-7	Homogeneous	1.88	0.551	0.43	465000	2971.3	284.72	0.897	7.296	305.173	66.11	0.007	0.025	653.330	54.738	86.420	205.250	178.23	0.10	0.02	0.00	0.0054	72.461	314825	23.257	0.002
Host rock-located																										
DSDH13-106.9m-1	Fine-grained, aggregated inclusion	1.59	0.145	3.12	465000	93.2	62.65	0.218	2.283	0.040	4.48	0.000	0.512	0.075	0.081	0.087	0.099	0.08	1.25	0.00	93.39	0.0043	0.003	0.94	0.002	0.000
DSDH13-106.9m-2	Fine-grained, aggregated inclusion	2.84	-0.305	13.20	465000	93.2	62.07	-0.032	2.274	0.070	2.48	0.000	2.172	0.073	0.416	0.056	1.256	0.08	2.15	0.00	217.40	0.0009	0.012	49.93	0.001	0.000
DSDH13-106.9m-3	Fine-grained, aggregated inclusion	1.95	0.547	65.84	465000	89.2	65.49	-0.051	21.425	0.684	1.04	0.000	5.531	0.179	0.484	0.017	0.755	0.13	2.10	0.01	235.97	0.0046	0.006	14.80	0.000	0.000
DSDH13-106.9m-4	Fine-grained, aggregated inclusion	2.43	-0.048	1.63	465000	101.7	66.88	0.028	1.291	0.142	3.02	0.000	5.210	0.126	0.445	0.099	0.096	-0.26	1.98	0.00	173.51	0.0089	0.010	0.66	0.005	-0.001
DSDH13-106.9m-5	Fine-grained, aggregated inclusion	1.57	0.025	15.02	465000	95.0	58.74	0.027	10.227	0.223	2.99	0.000	1.430	0.324	0.340	-0.021	2.331	0.13	1.33	0.00	157.25	0.0009	0.024	49.49	0.003	0.002
DSDH13-106.9m-6	Fine-grained, aggregated inclusion	2.35	-0.093	84.24	465000	94.6	58.91	0.158	2.344	0.047	1.39	0.002	2.436	0.108	0.849	0.043	0.389	0.00	3.08	0.01	191.59	0.0025	0.033	85.13	0.007	0.000
DSDH13-106.9m-7	Homogeneous	2.32	0.338	0.21	465000	85.4	73.59	0.099	0.764	0.395	3.71	0.006	0.031	0.009	-0.030	0.046	0.321	0.00	0.17	0.00	17.52	0.0002	0.004	0.40	0.000	-0.002
DSDH13-106.9m-8	Homogeneous	1.61	0.187	0.15	465000	71.4	42.03	0.047	0.344	0.100	2.87	0.000	0.002	0.001	0.020	-0.060	0.224	0.00	-0.03	0.00	22.36	0.0005	-0.005	1.23	0.002	0.000
DSDH13-106.9m-9	Homogeneous	2.36	0.172	0.68	465000	194.2	133.35	-0.055	0.783	0.375	3.19	-0.003	-0.023	0.416	0.018	0.014	2.733	0.00	0.09	0.00	22.08	0.0038	0.006	9.12	0.002	-0.005
DSDH13-106.9m-10	Homogeneous	2.14	0.234	0.54	465000	81.2	48.22	0.128	0.396	0.253	-0.36	0.000	4.987	0.134	0.036	0.096	0.167	0.09	1.72	0.00	111.68	0.0021	0.006	0.23	-0.006	0.001
DSDH13-106.9m-11	Homogeneous	1.98	0.054	0.39	465000	50.5	37.95	0.077	0.406	0.332	0.64	0.000	0.000	0.009	0.000	0.111	0.051	-0.04	0.09	0.00	23.74	0.0018	0.001	0.32	0.002	0.000
DSDH13-106.9m-12	Homogeneous	1.73	0.103	0.11	465000	70.7	49.80	0.195	0.787	0.168	2.41	0.000	0.033	0.006	-0.032	0.089	0.015	0.09	0.06	0.00	33.33	0.0005	0.001	0.29	0.002	0.001
DSDH209-50.2m-1	Fine-grained, aggregated inclusion	1.91	0.418	165.16	465000	528.3	651.79	0.100	5.244	0.179	13.54	0.022	0.190	1.252	0.267	0.071	0.088	0.08	3.62	0.01	3.38	0.0008	0.042	8.57	0.019	0.071
DSDH209-50.2m-2	Fine-grained, aggregated inclusion	1.61	0.367	101.56	465000	548.8	947.66	0.126	3.500	0.073	5.49	0.014	0.043	1.385	0.388	0.092	0.048	0.22	2.68	0.03	1.55	0.0011	0.059	12.56	0.240	0.132
DSDH209-50.2m-3	Fine-grained, aggregated inclusion	2.97	0.000	590.45	465000	601.5	593.15	2.005	59.755	0.326	29.85	0.051	0.050	0.948	0.948	0.108	0.197	0.05	7.88	0.22	1.30	0.0083	0.055	27.77	0.525	0.034
DSDH209-50.2m-4	Fine-grained, aggregated inclusion	1.89	0.047	356.15	465000	551.2	753.20	31.685	22.834	0.179	7.07	0.026	0.118	0.612	0.767	0.068	0.121	0.00	5.71	0.17	1.23	0.0029	0.097	12.64	0.186	0.028
DSDH209-50.2m-5	Homogeneous	2.54	0.148	120.76	465000	435.9	565.94	1.304	50.500	0.149	6.72	0.016	0.132	0.737	0.000	0.111	0.226	0.05	0.82	0.06	2.74	0.0010	0.012	19.21	0.070	0.220
DSDH209-50.2m-6	Homogeneous	2.24	0.440	57.78	465000	800.7	1604.70	1.311	5.109	0.239	15.38	0.038	0.205	5.811	0.002	0.073	0.132	-0.13	0.65	0.10	4.93	0.0050	0.067	16.51	0.394	0.386
DSDH209-50.2m-7	Homogeneous	2.62	0.156	82.31	465000	410.5	1072.28	0.325	17.559	0.249	14.38	0.027	0.209	0.759	0.000	-0.002	0.112	0.51	43.90	0.08	3.84	0.0079	0.104	11.90	0.515	0.371
DSDH209-50.2m-8	Homogeneous	6.32	0.333	146.23	465000	474.9	694.52	1.052	24.567	0.189	4.82	0.033	0.149	3.427	0.077	0.080	0.209	0.20	7.91	0.04	3.04	0.3189	0.032	67.54	0.464	0.516
DSDH209-50.2m-9	Homogeneous	1.66	0.028	81.29	465000	419.1	900.63	0.321	25.230	0.472	13.58	0.023	0.211	2.183	0.036	0.048	0.062	0.09	1.82	0.07	4.15	0.0023	0.040	5.25	0.656	0.940
KZ0818b-1	Homogeneous	3.05	13.932	15.61	465000	14.2	316.01	6.780	3.220	487.972	25.39	0.002	0.003	0.584	0.038	0.045	17.916	5.18	0.00	0.00	0.01	0.0851	0.037	115.52	8.499	0.000
KZ0818b-2	Homogeneous	2.52	0.307	12.93	465000	2.3	269.09	8.371	1.319	775.568	35.60	0.008	0.021	0.381	0.000	0.146	27.024	8.44	0.02	0.02	0.01	0.1385	0.032	144.69	8.810	0.000
KZ0818b-3	Homogeneous	2.81	0.477	0.20	465000	0.2	7.57	1.489	0.569	154.310	31.14	0.000	0.000	0.040	0.027	0.188	2.690	3.47	0.03	0.00	-0.02	0.0090	0.000	12.72	0.827	0.004
KZ0818b-4	Homogeneous	534.16	26.782	21.06	465000	3.6	35.89	10.338	8.700	226.532	20.49	32.304	0.017	0.576	0.029	0.227	19.321	3.09	15.79	0.03	1.03	0.0626	0.108	93.69	7.050	0.252
KZ0818b-5	Homogeneous	1.36	-0.253	1.52	465000	0.7	332.44	8.157	0.537	931.009	31.68	0.069	0.042	0.379	0.115	0.185	34.200	10.00	0.01	0.01	0.00	0.1932	0.057	188.65	12.657	0.005
KZ0818b-6	Homogeneous	74.84	9.902	1202.21	465000	147.9	284.68	3.583	85.657	44.538	10.87	0.026	0.023	0.456	0.116	0.483	119.564	0.09	1.12	0.38	0.28	0.0432	30.191	57.04	0.091	0.029
KZ0818b-7	Homogeneous	23.87	1.723	4563.65	465000	5.8	12.56	2.248	39.043	0.462	2.35	0.000	0.124	0.003	0.278	2.667	21.483	0.00	1.95	2.17	1.29	0.0082	20.474	3.73	-0.004	0.067
KZ0818b-8	Homogeneous	102.70	10.287	1354.22	465000	8.4	15.21	1.318	96.166	1.633	2.64	3.022	0.081	0.000	0.317	0.785	47.038	0.00	24.38	0.38	0.63	0.0088	32.061	1.47	0.004	0.070

Appendix X

Microprobe results of sphalerite geochemistry

Appendix X. Results of microprobe analysis (wt.%) of sphalerite from the Bai Dat and Bai Go deposits, Phuoc Son.

	Sn	Cd	S	Zn	Cu	Fe	Mn	Pb	Ag	Sb	As	Total	FeS mol%	CdS mol%	MnS mol%	Pressure* (kbar)
Bai Dat																
TMBD11-15-1	0.04	1.32	34.07	57.87	0.00	7.30	0.04					100.64	12.27	1.51	0.081	7.46
TMBD11-15-2	0.05	1.26	33.91	56.59	0.00	7.65	0.04					99.50	13.04	1.48	0.072	6.62
TMBD11-15-3	0.10	1.32	34.24	57.72	0.00	7.40	0.04					100.83	12.45	1.52	0.073	7.26
TMBD11-15-4	0.00	1.27	34.16	57.35	0.00	7.48	0.04					100.30	12.63	1.47	0.081	7.06
TMBD11-15-5	0.00	1.31	34.14	57.72	0.00	7.90	0.04					101.11	13.17	1.50	0.083	6.47
TMBD11-15-6	0.00	1.29	33.96	57.18	0.00	7.88	0.04					100.36	13.25	1.50	0.087	6.39
TMBD11-15-6	0.00	1.26	34.33	57.11	0.00	7.84	0.03					100.57	13.21	1.46	0.064	6.43
TMBD11-15-7	0.04	1.28	33.98	57.36	0.00	7.89	0.03					100.57	13.23	1.48	0.059	6.41
TMBD11-09-1	0.10	1.22	33.98	62.97	0.01	3.14	0.00					101.43	5.24	1.29	0.003	N/A
TMBD11-09-2	0.04	1.20	32.92	57.98	0.00	2.91	0.02					95.07	5.26	1.38	0.031	N/A
TMBD11-09-3	0.02	1.18	33.50	59.91	0.00	2.99	0.01					97.60	5.24	1.31	0.013	N/A
TMBD11-09-4	0.03	1.18	32.52	54.48	0.01	2.75	0.02					90.98	5.30	1.43	0.038	N/A
TMBD11-09-5	0.10	1.22	33.10	57.87	0.00	2.89	0.01					95.18	5.24	1.40	0.014	N/A
TMBD11-09-6	0.05	1.11	30.76	47.13	0.00	2.44	0.00					81.50	5.43	1.57	0.007	N/A
TNBD11-12B-1	<0.03	0.99	32.97	63.30	<0.02	4.40	<0.01	<0.11	0.07	<0.03	<0.02	101.73	7.16	1.04	0.009	N/A
TNBD11-12B-2	<0.02	1.00	33.15	63.31	<0.02	4.34	0.02	<0.11	<0.06	<0.03	<0.02	101.82	7.06	1.05	0.035	N/A
TNBD11-12B-3	<0.03	1.00	33.03	63.40	<0.02	4.34	<0.01	<0.11	<0.06	<0.03	<0.02	101.76	7.05	1.05	0.009	N/A
TNBD11-12B-4	<0.02	0.94	33.18	63.32	0.02	4.37	<0.01	<0.13	<0.06	<0.03	<0.02	101.83	7.10	0.99	0.009	N/A
TNBD11-12B-5	<0.02	0.99	33.15	63.18	<0.02	4.38	<0.01	<0.10	<0.07	<0.03	<0.02	101.69	7.14	1.05	0.009	N/A
TNBD11-12B-6	<0.03	0.95	32.94	63.37	<0.02	4.40	<0.01	<0.11	<0.07	<0.03	<0.02	101.66	7.15	1.00	0.009	N/A
TNBD11-12B-7	<0.03	1.00	33.14	63.32	<0.02	4.39	<0.01	<0.09	<0.06	<0.03	<0.02	101.84	7.14	1.05	0.009	N/A
TNBD11-12B-8	<0.03	0.97	33.22	63.24	<0.02	4.40	<0.01	<0.10	<0.06	<0.03	<0.02	101.83	7.16	1.03	0.009	N/A
DSDH257-454.2m-1	<0.03	1.96	33.47	57.96	<0.02	8.57	0.13	<0.11	<0.06	<0.03	<0.02	102.10	14.08	2.23	0.254	N/A
DSDH257-454.2m-2	<0.03	1.97	33.41	57.85	<0.02	8.56	0.12	<0.12	<0.07	<0.03	<0.02	101.92	14.10	2.25	0.230	N/A
DSDH257-454.2m-3	<0.03	1.97	33.31	57.82	<0.02	8.51	0.11	<0.10	<0.06	<0.03	<0.02	101.72	14.03	2.25	0.218	N/A
DSDH257-454.2m-4	<0.03	1.98	32.97	57.66	<0.02	8.58	0.12	<0.09	<0.07	<0.03	<0.02	101.33	14.16	2.27	0.233	N/A
DSDH257-454.2m-5	<0.03	1.97	33.16	57.60	0.02	8.63	0.13	<0.12	0.11	<0.03	<0.02	101.63	14.24	2.26	0.258	N/A
DSDH257-454.2m-6	<0.03	1.97	33.07	57.76	<0.02	8.62	0.14	<0.10	<0.06	<0.03	<0.02	101.55	14.19	2.25	0.262	N/A
DSDH257-454.2m-7	<0.03	1.99	33.52	57.92	<0.02	8.43	0.11	<0.11	<0.06	0.04	<0.02	102.01	13.90	2.26	0.216	N/A
DSDH257-454.2m-8	<0.03	2.03	33.46	57.59	<0.02	8.53	0.13	<0.10	<0.07	<0.03	<0.02	101.75	14.10	2.33	0.254	N/A
Bai Go																
DSDH26-87.1m-1	0.15	3.78	32.97	53.93	0.24	7.97	0.02					99.06	14.08	4.51	0.034	5.55
DSDH26-87.1m-2	0.00	3.57	34.16	54.17	0.03	8.09	0.02					100.05	14.20	4.26	0.049	5.43
DSDH199-230.2m-1	<0.03	3.19	32.97	56.79	<0.02	8.57	0.05	<0.11	0.06	<0.03	<0.02	101.62	14.32	3.65	0.091	5.31
DSDH199-230.2m-2	<0.03	3.08	32.85	56.96	<0.02	8.56	0.04	<0.11	<0.06	<0.03	<0.02	101.49	14.28	3.51	0.083	5.35
DSDH199-230.2m-3	<0.03	3.12	33.12	56.77	<0.02	8.56	0.04	<0.11	<0.06	<0.03	<0.02	101.61	14.32	3.57	0.075	5.31
DSDH199-230.2m-4	<0.03	3.14	33.06	56.67	<0.02	8.49	0.04	<0.10	<0.06	<0.03	<0.02	101.40	14.24	3.61	0.072	5.39
DSDH199-230.2m-5	<0.03	3.10	32.90	56.09	<0.02	8.14	0.04	<0.11	<0.07	<0.03	0.02	100.29	13.85	3.60	0.071	5.77
DSDH199-230.2m-6	<0.03	3.10	32.77	56.32	<0.02	8.25	0.03	<0.10	0.11	<0.03	<0.02	100.57	13.97	3.58	0.050	5.65
DSDH199-230.2m-7	<0.03	3.10	33.03	56.79	<0.02	8.53	0.03	<0.10	<0.06	<0.03	<0.02	101.49	14.28	3.55	0.062	5.35
DSDH199-230.2m-8	<0.03	3.03	33.06	56.59	<0.02	8.38	0.05	<0.12	<0.07	<0.03	<0.02	101.11	14.11	3.49	0.090	5.52
DSDH249-499.1m-1	<0.03	3.88	33.12	55.89	<0.02	8.73	0.04	<0.12	<0.06	<0.03	<0.02	101.65	14.75	4.48	0.073	N/A
DSDH249-499.1m-2	<0.03	3.90	32.80	56.00	0.03	8.59	0.04	<0.10	<0.06	<0.03	<0.02	101.37	14.54	4.49	0.083	N/A
DSDH249-499.1m-3	<0.03	3.94	33.01	55.62	0.04	8.74	0.06	<0.11	<0.07	<0.03	<0.02	101.41	14.83	4.56	0.118	N/A
DSDH249-499.1m-4	<0.03	3.84	33.27	56.17	<0.02	8.80	0.05	<0.11	0.07	<0.03	<0.02	102.20	14.80	4.41	0.096	N/A
DSDH249-499.1m-5	<0.03	3.89	32.88	55.74	<0.02	8.83	0.04	<0.10	<0.06	<0.03	<0.02	101.37	14.93	4.49	0.078	N/A
DSDH249-499.1m-6	<0.03	3.88	32.72	55.70	<0.02	8.78	0.05	<0.11	<0.06	<0.03	0.02	101.16	14.88	4.48	0.099	N/A
DSDH249-499.1m-7	<0.03	3.88	32.82	56.11	<0.02	8.73	0.02	<0.12	<0.07	<0.03	<0.02	101.56	14.70	4.46	0.039	N/A
DSDH249-499.1m-8	<0.03	3.98	32.80	55.26	<0.02	8.96	0.04	0.10	<0.06	<0.03	<0.02	101.14	15.24	4.63	0.082	N/A
DSDH249-499.1m-9	<0.03	3.84	33.11	55.51	<0.02	8.99	0.05	<0.11	<0.06	<0.03	<0.02	101.50	15.21	4.45	0.105	N/A

* = calculated using equation of Hutchison and Scott (1981)

N/A = Not Applicable

Appendix XI

Sulphur isotope results

Appendix XI. Measured sulphur isotope data from the **Bai Dat** gold deposit in Phuoc Son.

	Sample No.	Sample type	Mineral	Method	Value (‰)	Au assay (g/t)	Remarks
1	KZ0818-a	Wall rock	Pyrite	Laser	**19.72**	N/A	Float collected at mine entrance
2	KZ0818-b	Wall rock	Pyrite	Laser	**18.43**	N/A	Float collected at mine entrance
3	KZ0818-c	Wall rock	Pyrite	Laser	**16.42**	N/A	Float collected at mine entrance
4	KZ0818-d	Wall rock	Pyrite	Laser	**19.32**	N/A	Float collected at mine entrance
5	KZ0818-e	Wall rock	Pyrite	Conventional	**15.36**	N/A	Float collected at mine entrance
6	KZ0818-f	Wall rock	Pyrite	Conventional	**16.56**	N/A	Float collected at mine entrance
7	KZ0818-g	Wall rock	Pyrite	Conventional	**17.97**	N/A	Float collected at mine entrance
8	TMBD11-01-a	Vein	Pyrrhotite	Conventional	**0.31**	Ore	Level-5 attack ramp
9	TMBD11-01-b	Vein	Pyrite	Conventional	**0.96**	Ore	Level-5 attack ramp
10	TMBD11-02	Vein	Pyrrhotite	Conventional	**1.10**	Ore	Level-5
11	TMBD11-04	Wall rock	Pyrite	Conventional	**-1.69**	N/A	Between Level-5 & Level-4 attack ramp
12	TMBD11-05-a	Vein	Sphalerite	Conventional	**-0.48**	Ore	Level-4 attack ramp
13	TMBD11-05-b	Vein	Pyrrhotite	Conventional	**-0.07**	Ore	Level-4 attack ramp
14	TMBD11-05-c	Vein	Galena	Conventional	**-3.75**	Ore	Level-4 attack ramp
15	TMBD11-06	Wall rock	Pyrrhotite	Conventional	**5.63**	N/A	Between Level-5 & Level-4 attack ramp
16	TMBD11-07	Vein	Galena	Conventional	**-0.82**	Ore	Level-4
17	TMBD11-08	Vein	Galena	Conventional	**-1.77**	Ore	Level-4
18	TMBD11-09-a	Vein	Galena	Conventional	**-1.78**	Ore	Level-4
19	TMBD11-09-b	Vein	Sphalerite	Conventional	**-0.33**	Ore	Level-4
20	TMBD11-10	Vein	Galena	Conventional	**-1.27**	Ore	Level-4
21	TMBD11-11-a	Vein	Pyrrhotite	Conventional	**-0.99**	Ore	Level-4
22	TMBD11-11-b	Vein	Sphalerite	Conventional	**-2.58**	Ore	Level-4
23	TMBD11-11-c	Vein	Galena	Conventional	**-0.57**	Ore	Level-4
24	TMBD11-12-a	Vein	Chalcopyrite-sphalerite	Conventional	**-0.58**	Ore	Level-2
25	TMBD11-12-b	Vein	Sphalerite	Conventional	**-0.16**	Ore	Level-2
26	TMBD11-13	Vein	Galena	Conventional	**-1.56**	Ore	Level-2
27	TMBD11-14	Vein	Sphalerite	Conventional	**-0.10**	Ore	Level-2
28	TMBD11-15	Vein	Sphalerite	Conventional	**0.17**	Ore	Level-1
29	TMBD11-16	Wall rock	Pyrite	Conventional	**10.00**	N/A	Level-1
30	TMBD11-17	Vein	Sphalerite	Conventional	**-0.51**	Ore	Level-1
31	DSDH13@106.0m-a	Vein	Pyrite	Laser	**0.32**	40.57	
32	DSDH13@106.0m-b	Vein	Pyrite	Laser	**-1.70**	40.57	
33	DSDH13@106.0m-c	Vein	Pyrite	Laser	**3.65**	40.57	
34	DSDH16@126.1m	Vein	Sphalerite	Conventional	**-0.32**	13.89	
35	DSDH111@78.8m-a	Vein	Sphalerite	Conventional	**-1.47**	21.6	
36	DSDH111@78.8m-b	Vein	Galena	Conventional	**-2.32**	21.6	
37	DSDH111@204.3m	Wall rock	Pyrite	Conventional	**-1.45**	N/A	
38	DSDH257@351.7m	Wall rock	Pyrrhotite	Conventional	**20.63**	N/A	
39	DSDH257@454.2m	Vein	Sphalerite	Conventional	**-0.62**	N/A	
40	DSDH257@463.4m	Vein	Pyrrhotite	Conventional	**7.42**	0.06	
41	DSDH257@463.5m	Vein	Pyrrhotite	Conventional	**7.76**	0.06	
42	DSDH270@122.8m	Vein	Pyrrhotite	Conventional	**4.74**	N/A	
43	DSDH270@365.1m	Wall rock	Sphalerite	Conventional	**-0.08**	N/A	
44	DSDH270@366.6m	Wall rock	Pyrrhotite	Conventional	**-8.55**	N/A	
45	DSDH270@375.9m	Wall rock	Pyrite	Conventional	**-2.51**	N/A	
46	DSDH270@400.5m	Wall rock	Pyrite	Conventional	**-2.34**	N/A	
47	DSDH270@430.2m	Vein	Pyrite	Conventional	**-0.37**	N/A	
48	DSDH270@444.0m	Wall rock	Pyrite	Conventional	**21.76**	N/A	
49	DSDH270@452.1m-a	Wall rock	Pyrite	Conventional	**-9.12**	N/A	
50	DSDH270@452.1m-b	Wall rock	Pyrrhotite	Conventional	**-11.45**	N/A	
51	DSDH270@453.4m-a	Vein	Pyrite	Conventional	**-15.32**	N/A	
52	DSDH270@453.4m-b	Vein	Pyrrhotite	Conventional	**-17.57**	N/A	
53	DSDH270@463.1m-a	Vein	Pyrite	Conventional	**13.88**	N/A	
54	DSDH270@463.1m-b	Vein	Pyrrhotite	Conventional	**13.11**	N/A	

N/A = Not Available.

Appendix XI (cont.). Measured sulphur isotope data from the **Bai Go** gold deposit in Phuoc Son.

	Sample No.	Sample type	Mineral	Method	Value (‰)	Au assay (g/t)
1	DSDH26-87.1m-a	Vein	Galena	Conventional	**-0.70**	9.2
2	DSDH26-87.1m-a	Vein	Pyrite	Conventional	**0.48**	9.2
3	DSDH40@94.3m	Vein	Pyrrhotite	Conventional	**1.88**	<0.01
4	DSDH40@145.4m	Vein	Galena	Conventional	**0.46**	0.36
5	DSDH40@147.3m-a	Vein	Chalcopyrite	Conventional	**1.41**	0.15
6	DSDH40@147.3m-b	Vein	Pyrrhotite	Conventional	**1.82**	0.15
7	DSDH40@195.8m-a	Vein	Pyrrhotite	Conventional	**1.07**	N/A
8	DSDH40@195.8m-b	Vein	Pyrite	Conventional	**1.98**	N/A
9	DSDH74-132.7m	Wall rock	Pyrite	Conventional	**-1.93**	0.09
10	DSDH74-140.0m	Vein	Pyrite	Conventional	**0.28**	0.87
11	DSDH74-164.3m	Wall rock	Pyrrhotite	Conventional	**0.41**	0.28
12	DSDH146@88.4m-a	Vein	Pyrrhotite-pyrite	Conventional	**1.51**	0.84
13	DSDH146@88.4m-b	Vein	Pyrite	Conventional	**1.13**	0.84
14	DSDH146@88.8m	Vein	Sphalerite	Conventional	**0.69**	5.83
15	DSDH155@101.2m	Wall rock	Pyrite	Conventional	**0.44**	4.42
16	DSDH155@104.9m	Vein	Pyrrhotite	Conventional	**0.70**	26.9
17	DSDH199@230.2m-a	Vein	Galena	Conventional	**1.50**	1.29
18	DSDH199@230.2m-b	Vein	Pyrite	Conventional	**3.89**	1.29
19	DSDH199@230.2m-c	Vein	Sphalerite	Conventional	**1.80**	1.29
20	DSDH199@232.3m-a	Vein	Pyrite	Conventional	**1.14**	24.6
21	DSDH199@232.3m-b	Vein	Galena	Conventional	**-0.47**	24.6
22	DSDH209@50.2m-c	Wall rock	Pyrite	Laser	**0.40**	0.18
23	DSDH209@50.2m-d	Wall rock	Pyrite	Laser	**0.01**	0.18
24	DSDH209@303.6m-a	Wall rock	Pyrite	Laser	**23.24**	0.06
25	DSDH209@303.6m-b	Wall rock	Pyrite	Laser	**25.97**	0.06
26	DSDH209@303.6m-a	Wall rock	Pyrite	Laser	**23.24**	0.06
27	DSDH209@303.6m-b	Wall rock	Pyrite	Laser	**25.97**	0.06
28	DSDH210@246.8m-a	Vein	Galena-pyrite	Conventional	**-0.44**	23
29	DSDH210@246.8m-b	Vein	Pyrite	Conventional	**0.42**	23
30	DSDH212@180.0m	Skarn	Pyrrhotite	Conventional	**-2.90**	0.04
31	DSDH212@186.9m	Skarn	Pyrrhotite-chalcopyrite	Conventional	**-2.18**	0.02
32	DSDH212@238.0m	Vein	Pyrite-pyrrhotite	Conventional	**1.29**	2.37
33	DSDH212@274.2m	Vein	Sphalerite	Conventional	**2.48**	0.91
34	DSDH212@293.1m	Vein	Pyrrhotite	Conventional	**2.42**	3.06
35	DSDH218@277.3m	Skarn	Magnetite-pyrrhotite	Conventional	**2.17**	<0.01
36	DSDH218@280.3m	Skarn	Pyrrhotite	Conventional	**0.32**	N/A
37	DSDH218@366.2m	Vein	Pyrrhotite	Conventional	**0.49**	0.47
38	DSDH218@436.3m-a	Skarn	Pyrrhotite-chalcopyrite	Conventional	**4.10**	<0.01
39	DSDH218@436.3m-b	Skarn	Chalcopyrite	Conventional	**3.86**	<0.01
40	DSDH224@436.8m-a	Vein	Galena	Conventional	**0.30**	0.07
41	DSDH224@436.8m-b	Vein	Pyrrhotite	Conventional	**1.42**	0.07
42	DSDH224@445.5m	Vein	Pyrite	Conventional	**2.25**	2.96
43	DSDH224@445.7m-a	Vein	Pyrite	Laser	**1.37**	2.96
44	DSDH224@445.7m-b	Vein	Pyrite	Laser	**1.12**	2.96
45	DSDH224@445.7m-c	Vein	Pyrite	Laser	**0.89**	2.96
46	DSDH224@445.7m-d	Vein	Pyrite	Laser	**1.09**	2.96
47	DSDH224@445.7m-e	Vein	Pyrite	Laser	**0.96**	2.96
48	DSDH224@445.7m-f	Vein	Pyrite	Laser	**2.32**	2.96
49	DSDH235-246.3m	Wall rock	Pyrite	Conventional	**-9.88**	0.02
50	DSDH235-264.9m	Vein	Pyrrhotite	Conventional	**1.05**	2.93
51	DSDH235-276.5m	Wall rock	Pyrrhotite	Conventional	**-5.47**	N/A
52	DSDH237@418.3m	Vein	Pyrite-pyrrhotite	Conventional	**1.36**	6.26
53	DSDH249@180.1m	Vein	Pyrrhotite	Conventional	**0.24**	0.01
54	DSDH249@495.6m	Wall rock	Pyrrhotite	Conventional	**-5.24**	0.03
55	DSDH249@499.1m-a	Vein	Pyrrhotite	Conventional	**1.47**	4.65
56	DSDH249@499.1m-b	Vein	Pyrite	Conventional	**1.92**	4.65
57	DSDH250-297m	Wall rock	Pyrite	Conventional	**-14.46**	<0.01

N/A = Not Available.

Appendix XI (cont.). Measured sulphur isotope data from other prospects in the Phuoc Son gold deposit area.

Sample No.	Sample type	Mineral	Value (‰)	Au assay (g/t)
Round Hill				
RHDH03@30.0m	Vein	Pyrite	**7.88**	N/A
RHDH03@33.2m	Vein	Pyrite	**7.93**	N/A
RHDH03@72.9m	Vein	Pyrite	**9.04**	N/A
RHDH03@89.1m	Vein	Pyrite	**8.65**	0.47
RHDH04@81.5m	Vein	Pyrite	**8.77**	N/A
Khe Rin				
KRDH03@11.8m	Skarn	Pyrite	**9.53**	<0.1
KRDH03@30.0m	Skarn	Pyrrhotite	**6.71**	<0.1
KRDH03@34.0m	Vein	Pyrite	**11.57**	0.24
KRDH03@41.2m	Vein	Pyrite	**18.66**	<0.1
KRDH04@40.0m	Vein	Pyrite	**7.66**	<0.1
KRDH08@18.3m	Skarn	Chalcopyrite	**9.77**	<0.1
KRDH08@82.9m	Skarn	Pyrrhotite	**8.32**	<0.1
KRDH13@67.1m	Vein	Pyrrhotite	**5.42**	0.12
KRDH28@49.9m	Skarn	Pyrite	**7.89**	6.88
Khe Do				
KRDH23@50.6m	Vein	Chalcopyrite	**3.77**	N/A
KRDH23@78.8m	Vein	Pyrrhotite	**6.96**	33.77
KRDH23@87.6m	Vein	Pyrite	**7.25**	6.82
KRDH25@107.9m	Vein	Pyrrhotite	**5.85**	6.67
K7				
K7DH01@107.6m-a	Vein	Pyrrhotite	**2.34**	1.14
K7DH01@107.6m-b	Vein	Pyrite-pyrrhotite	**2.47**	1.14
Bai Chuoi				
DSDH256@291.9m	Vein	Pyrrhotite-pyrite	**0.99**	<0.1
DSDH256@297.4m	Vein	Pyrite	**0.46**	0.34
DSDH256@340.2m	Vein	Galena-sphalerite	**0.16**	<0.1
DSDH267@424.1m	Vein	Pyrite	**0.78**	N/A
DSDH267@425.9m-a	Vein	Galena	**-2.13**	N/A
DSDH267@425.9m-b	Vein	Pyrrhotite	**0.38**	N/A
Nui Vang				
NVDH01@110.9m	Veinlet	Pyrrhotite	**2.48**	<0.1
NVDH01@126.5m	Veinlet	Pyrrhotite	**0.36**	<0.1
NVDH01@178.1m	Veinlet	Pyrrhotite	**0.46**	<0.1
NVDH01@178.4m	Veinlet	Pyrrhotite	**5.32**	<0.1
Bo				
BODH02@82.2m	Veinlet	Pyrite	**7.10**	1.54
BODH02@98.5m	Veinlet	Pyrrhotite	**15.47**	<0.1

N/A = Not Available.

Appendix XII

Carbon and oxygen isotope results

Appendix XII. Measured and calculated carbon and oxygen isotope data from the Bai Dat and Bai Go deposits in the Phuoc Son gold deposit area.

Sample no.	Sample type	Analysed mineral	**$\delta^{13}C_{PDB}$ ‰ (raw)**	$\delta^{13}C$ ‰ (300˚C)	$\delta^{13}C$ ‰ (400˚C)	**$\delta^{18}O_{SMOW}$ ‰ (raw)**	$\delta^{18}O$ ‰ (300˚C)	$\delta^{18}O$ ‰ (400˚C)
Bai Dat								
TMBD11-05	Vein	Carbonate	**-16.12**	-14.11	-13.45	**14.24**	8.66	10.99
TMBD11-07	Vein	Carbonate	**-21.34**	-19.33	-18.67	**8.86**	3.28	5.61
TMBD11-13B	Vein	Carbonate	**-24.12**	-22.11	-21.45	**6.00**	0.42	2.75
TMBD11-13	Vein	Carbonate	**-25.02**	-23.01	-22.35	**5.07**	-0.51	1.82
TMBD11-15	Vein	Carbonate	**-15.96**	-13.95	-13.29	**14.41**	8.83	11.16
TMBD11-17	Vein	Carbonate	**-7.48**	-5.47	-4.81	**23.15**	17.57	19.90
DSDH16@126.1m ****	Vein	Carbonate	**-7.62**	-5.61	-4.95	**23.00**	17.42	19.75
DSDH111@204.3m	Wall rock	Carbonate	**-4.29**	-2.28	-1.62	**26.44**	20.86	23.19
DSDH112@29.9m	Wall rock	Carbonate	**-8.90**	-6.89	-6.23	**21.69**	16.11	18.44
DSDH257@463.5m	Vein	Carbonate	**-6.43**	-4.42	-3.76	**24.23**	18.65	20.98
DSDH270@122.8m	Vein	Carbonate	**-3.97**	-1.96	-1.30	**26.77**	21.19	23.52
DSDH270@122.8m	Vein	Carbonate	**-2.98**	-0.97	-0.31	**27.79**	22.21	24.54
DSDH270@430.2m	Vein	Carbonate	**-2.82**	-0.81	-0.15	**27.95**	22.37	24.70
Bai Go								
DSDH74@132.7m	Wall rock	Carbonate	**-5.52**	-3.51	-2.85	**16.83**	11.25	13.58
DSDH146@88.8m	Vein	Carbonate	**-7.34**	-5.33	-4.67	**23.29**	17.71	20.04
DSDH146@88.4m	Vein	Carbonate	**-6.97**	-4.96	-4.30	**23.67**	18.09	20.42
DSDH155@104.9mB ****	Vein	Carbonate	**-10.35**	-8.34	-7.68	**20.19**	14.61	16.94
DSDH155@104.9m	Vein	Carbonate	**-7.88**	-5.87	-5.21	**22.74**	17.16	19.49
DSDH199@232.3m	Vein	Carbonate	**-6.29**	-4.28	-3.62	**24.38**	18.80	21.13
DSDH210@246.8m	Vein	Carbonate	**-5.80**	-3.79	-3.13	**24.88**	19.30	21.63
DSDH212@293.1m	Vein	Carbonate	**-7.10**	-5.09	-4.43	**23.54**	17.96	20.29
DSDH212@180.0m	Skarn	Carbonate	**-6.76**	-4.75	-4.09	**23.89**	18.31	20.64
DSDH212@186.9m	Skarn	Carbonate	**-6.70**	-4.69	-4.03	**23.95**	18.37	20.70
DSDH218@277.3m	Skarn	Carbonate	**-6.04**	-4.03	-3.37	**24.63**	19.05	21.38
DSDH235@124.5m	Wall rock	Carbonate	**-4.24**	-2.23	-1.57	**15.52**	9.94	12.27
DSDH249@499.1m	Vein	Carbonate	**-5.52**	-3.51	-2.85	**25.17**	19.59	21.92

***** H_2S separation to clean CO_2 gas.*

Appendix XII (cont.). Measured and calculated carbon and oxygen isotope data from the prospects in the Phuoc Son gold deposit area.

Sample no. (& sampled prospect)	**Sample type**	**Analysed mineral**	**$\delta^{13}C_{PDB}$ ‰ (raw)**	$\delta^{13}C$ ‰ (300˚C)	$\delta^{13}C$ ‰ (400˚C)	**$\delta^{18}O_{SMOW}$ ‰ (raw)**	$\delta^{18}O$ ‰ (300˚C)	$\delta^{18}O$ ‰ (400˚C)
Prospects								
BHDH02@82.2m (Bo)	Vein	Carbonate	**-5.62**	-3.61	-2.95	**25.07**	19.49	21.82
BODH02@82.2m (Bo)	Vein	Carbonate	**-5.81**	-3.80	-3.14	**24.87**	19.29	21.62
K7DH01@107.6mA (K7)	Vein	Carbonate	**-5.89**	-3.88	-3.22	**24.79**	19.21	21.54
K7DH01@107.6mB (K7) ****	Vein	Carbonate	**-5.96**	-3.95	-3.29	**24.72**	19.14	21.47
DSDH256@291.9m (Bai Chuoi)	Vein	Carbonate	**-7.12**	-5.11	-4.45	**23.52**	17.94	20.27
DSDH256@297.4m (Bai Chuoi)	Vein	Carbonate	**-6.99**	-4.98	-4.32	**23.65**	18.07	20.40
KRDH08@82.9m (Khe Rin)	Skarn	Carbonate	**-4.56**	-2.55	-1.89	**26.16**	20.58	22.91
KRDH13@67.1m (Khe Rin)	Skarn	Carbonate	**-9.11**	-7.10	-6.44	**21.47**	15.89	18.22
KRDH28@49.9m (Khe Rin)	Skarn	Carbonate	**-6.35**	-4.34	-3.68	**24.31**	18.73	21.06
KRDH11@45.7m (Khe Rin)	Marble	Carbonate	**-4.47**	-2.46	-1.80	**26.25**	20.67	23.00
KRDH23@87.6m (Khe Do)	Vein	Carbonate	**-1.31**	0.70	1.36	**29.51**	23.93	26.26
KRDH25@106.3m (Khe Do)	Marble	Carbonate	**0.37**	2.38	3.04	**31.24**	25.66	27.99
KRDH25@107.9m (Khe Do)	Vein	Carbonate	**-3.95**	-1.94	-1.28	**26.79**	21.21	23.54
NVDH01@110.9m (Nui Vang) ****	Vein	Carbonate	**-5.70**	-3.69	-3.03	**24.98**	19.40	21.73
NVDH01@178.1m (Nui Vang) ****	Vein	Carbonate	**-10.71**	-8.70	-8.04	**19.82**	14.24	16.57
RHDH03@72.9m (Round Hill)	Vein	Carbonate	**-13.94**	-11.93	-11.27	**16.49**	10.91	13.24
TLDH01@139.9m (Tra Long)	Marble	Carbonate	**0.98**	2.99	3.65	**31.87**	26.29	28.62

**** *H_2S separation to clean CO_2 gas.*

Appendix XIII

Fluid inclusion microthermometric results

Appendix XIII. Microtermometric data of fluid inclusions from the Bai Dat and Bai Go deposits, Phuoc Son

Sample No.	Inclusion No.	Inclusion type	Inclusion size (μm)	Host mineral	Visible CO_2 vol. % estimation	Last CO_2 melting temperature (°C)	Last ice melting temperature (°C)	Last clathrate melting temperature (ºC)	CO_2 liquid homogenisation temperature (ºC)	CO_2 vapour homogenisation temperature (ºC)	Halite dissolution temperature (ºC)	Salinity (wt.% NaCl eq.)	Calculated depth (bar)*
Bai Dat													
DSDH111-78.8m	1	IIIa	15	Quartz	10			3.9	27	370.0		10.67	5564
	2	IIIa	15	Quartz	20			4.7	26.3	365.4		9.50	4363
	3	IIIa	10	Quartz	10			4.2		336.0		10.24	
	4	IIIa	10	Quartz	30				23.9	350.0			
	5	IIa	5	Quartz						267.7			
	6	IIa	5	Quartz						368.2			
	7	IIb	5	Quartz						352.1			
	8	IIa	5	Quartz						354.2			
	9	IIIa	10	Quartz	10			3.7	17.8	322.0		10.96	4951
	10	IIIa	5	Quartz	10					326.0			
	11	IIb	10	Quartz						364.2			
	12	IIa	10	Quartz				2.7		278.5		12.32	
	13	IIa	10	Quartz				3.5		234.0		11.24	
	14	IIIa	10	Quartz				5.3		321.0		8.58	
	15	IIa	10	Quartz				2.5				12.59	
	16	IIa	10	Quartz						311.2			
	17	IIIa	10	Quartz						388.2			
	18	IIa	10	Quartz						379.2			
	19	IIa	15	Quartz		-57.5				379.1			
	20	IIa	15	Quartz						349.6			
	21	IIa	5	Quartz				4.5				9.80	
	22	I	5	Quartz		-57.1							
	23	IIa	20	Quartz			-10.0					13.94	
	24	IIa	10	Quartz						292.2			
	25	IIa	20	Quartz			-10.3			390.5		14.25	
	26	IIa	10	Quartz						307.3			
	27	IIIb	10	Quartz						439.0	375.0	44.80	
	28	IIa	10	Quartz			-16.0			369.7		19.45	
	29	IIa	15	Quartz				7.9		388.7		4.15	
	30	IIa	5	Quartz						314.5			
	31	IIa	20	Sphalerite						391.8			
	32	IIa	5	Quartz						333.8			
	33	IIa	5	Quartz						320.2			
	34	IIa	10	Quartz						360.4			
	35	IIa	10	Quartz						>500			

Sample No.	Inclusion No.	Inclusion type	Inclusion size (μm)	Host mineral	Visible CO_2 vol. % estimation	Last CO_2 melting temperature (°C)	Last ice melting temperature (°C)	Last clathrate melting temperature (°C)	CO_2 liquid homogenisation temperature (°C)	CO_2 vapour homogenisation temperature (°C)	Halite dissolution temperature (°C)	Salinity (wt.% NaCl eq.)	Calculated depth (bar)*
	36	IIa	10	Quartz			-10.1			255.2			
	37	IIa	10	Quartz						485.0			
	38	IIb	10	Quartz						462.3			
	39	IIa	25	Sphalerite			-5.8					8.95	
	40	IIa	10	Sphalerite						317.6			
	41	IIa	10	Sphalerite						301.5			
TMBD11-07(B)	1	IIIa	15	Quartz	0.2	-57.9		5.3	25.5	275.0		8.58	
	2	IIIa	20	Quartz						336.0			
	3	IIIa	15	Quartz		-57.5				246.0			
	4	IIIa	25	Quartz						340.5			
	5	IIIa	10	Quartz	0.3	-57.3		7.2	22.7	319.0		5.41	3651
	6	IIIa	15	Quartz	0.2	-57.7		7.1	24.0	316.5		5.59	4147
	7	IIIa	15	Quartz	0.3	-57.5	-18.6	5.5	26.6	295.9		8.26	3264
	8	IIIa	10	Quartz	0.3	-57.0		8.1	22.4	324.6		3.77	3692
	9	IIIa	5	Quartz	0.4	-57.3		7.5	22.8	309.5		4.88	3060
	10	IIIa	10	Quartz	0.4	-57.1		7.7	22.8	308.8		4.51	4048
	11	IIIa	25	Quartz	0.4	-57.4	-14.6	7.2	19.0	354.0		5.41	3706
	12	IIIa	20	Quartz	0.8	-57.4		7.8	12.5	283.0		4.33	
	13	IIIa	10	Quartz	0.2	-57.0		6.7	24.0	308.1		6.28	4035
	14	IIIa	10	Quartz	0.2	-57.0		6.0	27.0	278.5		7.45	4035
	15	IIIa	15	Quartz	0.4	-56.8		7.0	22.7	321.7		5.76	
	16	IIa	20	Quartz				4.9		313.0		9.19	
	17	IIIa	10	Quartz	0.3	-57.0		7.8	20.9	315.0		4.33	3642
	18	IIIa	15	Quartz	0.3	-57.2		6.0	22.8	321.0		7.45	3714
	19	IIa	20	Quartz		-56.9		6.6		351.4		6.45	
	20	IIIa	25	Quartz		-58.7			25.3	326.0			
	21	IIa	10	Quartz		-56.9		6.8		264.7		6.11	
	22	IIa	10	Quartz						285.3			
	23	IIIa	15	Quartz	0.3	-57.9		7.5	21.1	332.3		4.88	3859
	24	IIa	20	Quartz						328.7			
	25	IIIa	15	Quartz	0.3	-57.8		6.8	22.4	342.9		6.11	3966
	26	IIa	20	Quartz				8.1		252.3		3.77	
	27	IIa	20	Quartz						336.7			
	28	IIIa	20	Quartz	0.4	-57.4	-21.8	6.4	24.6	331.7		6.79	3245
	29	IIIa	10	Quartz	0.3	-57.5		7.1	24.0	320.2		5.59	3613
	30	IIIa	10	Quartz	0.2	-58.4		8.0	19.5	319.5		3.96	4298
	31	IIIa	10	Quartz	0.3	-58.5	-11.9	8.3	18.4	317.7		3.40	3749

Sample No.	Inclusion No.	Inclusion type	Inclusion size (µm)	Host mineral	Visible CO_2 vol. % estimation	Last CO_2 melting temperature (°C)	Last ice melting temperature (°C)	Last clathrate melting temperature (°C)	CO_2 liquid homogenisation temperature (°C)	CO_2 vapour homogenisation temperature (°C)	Halite dissolution temperature (°C)	Salinity (wt.% NaCl eq.)	Calculated depth (bar)*
DSDH257-463.4m	1	IIa	10	Quartz		-57.5		3.6	16.9			11.10	
	2	IIa	5	Quartz		-57.5			19.5				
	3	IIa	5	Quartz		-57.7			14.6				
	4	IIb	15	Quartz		-57.5							
	5	IIa	10	Quartz		-58.2			29.7				
	6	IIb	25	Quartz		-58.0							
	7	IIa	5	Quartz		-58.5							
	8	IIb	5	Quartz		-57.4							
	9	IIIa	10	Quartz						383.1			
	10	IIa	10	Quartz		-57.3		2.5				12.59	
	11	IIa	5	Quartz			-3.9			300.8		6.30	
	12	IIa	5	Quartz				8.3		347.7		3.40	
	13	IIa	5	Quartz						328.9			
	14	IIa	15	Quartz						340.6			
	15	IIa	5	Quartz						376.2			
	16	IIa	10	Quartz						379.0			
	17	IIa	5	Quartz						373.2			
	18	IIa	10	Quartz						362.5			
	19	IIa	10	Quartz						370.4			
	20	IIa	20	Quartz						381.4			
	21	IIa	5	Quartz		-57.7		2.4	18.7			12.72	
	22	IIa	5	Quartz		-57.3							
	23	IIa	5	Quartz			-0.3			346.0		0.53	
	24	IIa	5	Quartz				7.2				5.41	
	25	IIb	15	Quartz		-57.5			17.0				
	26	IIa	10	Quartz			-3.3			364.3		5.41	
	27	IIa	10	Quartz			-0.5			361.5		0.88	
	28	IIa	5	Quartz						339.0			
	29	IIb	5	Quartz			-3.5	7.6		387.4		4.70	
	30	IIa	5	Quartz						373.5			
	31	I	5	Quartz		-57.0							
	32	IIb	15	Quartz			-5.5		17.7			8.55	
	33	IIb	15	Quartz		-56.8							
	34	IIa	10	Quartz		-57.0							
	35	IIb	10	Quartz		-56.9							
	36	I	25	Quartz		-56.6							
	37	IIa	5	Quartz			-4.6					7.31	
	38	IIa	10	Quartz						349.8			

Sample No.	Inclusion No.	Inclusion type	Inclusion size (µm)	Host mineral	Visible CO_2 vol. % estimation	Last CO_2 melting temperature (°C)	Last ice melting temperature (°C)	Last clathrate melting temperature (°C)	CO_2 liquid homogenisation temperature (°C)	CO_2 vapour homogenisation temperature (°C)	Halite dissolution temperature (°C)	Salinity (wt.% NaCl eq.)	Calculated depth (bar)*
	39	IIa	5	Quartz						366.9			
	40	IIa	10	Quartz						413.8			
	41	IIa	10	Quartz						399.6			
	42	IIa	5	Quartz						394.6			
	43	IIa	10	Quartz				7.4		384.3		5.06	
	44	IIa	5	Quartz						386.4			
	45	IIa	5	Quartz				5.8		394.7		7.78	
	46	IIa	5	Quartz						376.2			
	47	IIa	10	Quartz			-4.4					7.02	
	48	IIa	5	Quartz				7.3		340.5		5.23	
	49	IIa	5	Quartz						336.7			
	50	IIa	5	Quartz						361.5			
	51	IIa	5	Quartz						374.2			
	52	IIa	10	Quartz						367.3			
	53	IIIa	15	Quartz		-58.1							
	54	IIa	10	Quartz		-58.7							
	55	IIa	5	Quartz			-10.5			310.3		14.46	
	56	IIa	15	Quartz			-3.5			343.5		5.71	
	57	IIIa	10	Quartz		-58.4	-1.2					2.07	
	58	IIb	5	Quartz		-58.4							
	59	IIa	5	Quartz			-3.4			295.8		5.56	
	60	IIa	5	Quartz			-3.5			299.8		5.71	
	61	IIa	5	Quartz				9.1				1.84	
	62	IIa	5	Quartz			-3.2			272.6		5.26	
	63	IIa	10	Quartz		-58.1							
	64	IIa	10	Quartz		-58.0							
	65	IIa	10	Quartz		-58.2							
	66	IIa	10	Quartz		-58.4							
	67	IIa	10	Quartz		-58.0							
	68	IIa	15	Quartz			-4.5			301.6		7.17	
	69	IIa	10	Quartz			-3.2			272.0		5.26	
	70	IIa	5	Quartz			-2.9			302.3		4.80	
	71	IIb	20	Quartz		-57.7		8		300.7		4.00	
	72	I	5	Quartz				7.5				4.88	
	73	IIIa	15	Quartz		-57.7		9.2				1.64	
	74	IIa	10	Quartz				9.7		349.8		0.63	
	75	IIa	10	Quartz				8.4				3.21	
	76	IIa	5	Quartz				8.1				3.77	

Sample No.	Inclusion No.	Inclusion type	Inclusion size (µm)	Host mineral	Visible CO_2 vol. % estimation	Last CO_2 melting temperature (°C)	Last ice melting temperature (°C)	Last clathrate melting temperature (ºC)	CO_2 liquid homogenisation temperature (ºC)	CO_2 vapour homogenisation temperature (ºC)	Halite dissolution temperature (ºC)	Salinity (wt.% NaCl eq.)	Calculated depth (bar)*
	77	IIa	5	Quartz				7.3				5.23	
	78	IIa	5	Quartz			-3.9			333.4		6.30	
Bai Go													
DSDH26-87.1m	1	IIb	30	Quartz				8.9				2.24	
	2	IIa	15	Quartz				5.0				9.04	
	3	IIa	10	Quartz						**283.5**			
	4	IIa	10	Quartz				8.0		326.5		3.96	
	5	IIa	10	Quartz						327.6			
	6	IIb	20	Quartz						**349.5**			
	7	IIb	5	Quartz			-1.5					2.57	
	8	IIb	5	Quartz			-2.5					4.18	
	9	IIb	15	Quartz						353.4			
	10	IIa	10	Quartz						**378.2**			
	11	IIa	10	Quartz						**393.5**			
	12	IIa	5	Quartz						313.2			
	13	IIa	10	Quartz			-4.2					6.74	
	14	IIa	10	Quartz						405.8			
	15	IIa	10	Quartz			-4.5			374.8		7.17	
	16	IIa	10	Quartz				5.9		368.5		7.62	
	17	IIa	10	Quartz		-57.8							
	18	IIa	10	Quartz						397.3			
	19	IIa	5	Quartz						356.0			
	20	IIa	10	Quartz						375.4			
	21	IIa	15	Quartz			-6.3			375.0		9.60	
	22	IIa	15	Quartz						354.0			
	23	IIa	10	Quartz						452.2			
	24	IIa	20	Quartz		-56.8				293.2			
	25	IIb	25	Quartz		-56.5		4.7		335.6		9.50	
	26	IIb	25	Quartz		-56.5				369.8			
	27	IIb	30	Quartz		-56.6							
	28	IIb	30	Quartz						365.4			
	29	IIa	25	Quartz		-70.3							
	30	IIb	25	Quartz		-56.8		7.7		287.5		4.51	
	31	I	35	Quartz		-56.8							
	32	IIa	15	Quartz						346.3			
	33	I	25	Quartz		-56.8							
	34	IIb	40	Quartz		-56.7							
	35	IIb	45	Quartz		-56.6							
	36	IIb	25	Quartz		-56.8							
	37	I	30	Quartz		-56.6							
	38	IIb	10	Quartz		-58.4							
	39	IIa	10	Quartz				8.0		385.0		3.96	

Sample No.	Inclusion No.	Inclusion type	Inclusion size (µm)	Host mineral	Visible CO_2 vol. % estimation	Last CO_2 melting temperature (°C)	Last ice melting temperature (°C)	Last clathrate melting temperature (°C)	CO_2 liquid homogenisation temperature (°C)	CO_2 vapour homogenisation temperature (°C)	Halite dissolution temperature (°C)	Salinity (wt.% NaCl eq.)	Calculated depth (bar)*
	40	IIa	5	Quartz						371.0			
	41	IIb	10	Quartz				5.7				7.94	
	42	IIa	5	Quartz			-5.4			309.7		8.41	
	43	IIa	15	Quartz			-4.8			349.2		7.59	
	44	I	5	Quartz		-57.7							
	45	IIa	5	Quartz		-57.8							
	46	IIa	5	Quartz		-57.9							
	47	IIa	5	Quartz			-2					3.39	
	48	IIa	5	Quartz			-1.8					3.06	
	49	IIa	5	Quartz			-2.3					3.87	
	50	IIa	10	Quartz			-4.1			334.5		6.59	
	51	IIa	10	Quartz			-3.8			335.1		6.16	
	52	IIa	5	Quartz				9.5				1.04	
	53	IIa	10	Quartz				8.0				3.96	
	54	IIa	5	Quartz				7.7				4.51	
	55	IIa	5	Quartz				7.6				4.70	
	56	IIIa	20	Quartz		-57.1	-2.2					3.71	
	57	I	5	Quartz		-57.6							
	58	IIa	5	Quartz			-7.5					11.10	
	59	IIa	5	Quartz				6.0				7.45	
	60	IIa	5	Quartz						363.8			
	61	IIa	5	Quartz			-4.5					7.17	
	62	IIa	15	Quartz			-3.5					5.71	
	63	IIa	5	Quartz			-3.3					5.41	
	64	IIa	5	Quartz			-3.5					5.71	
	65	IIa	5	Quartz			-3					4.96	
	66	IIa	5	Quartz			-4.2					6.74	
DSDH212-293.1m	1	IIa	5	Quartz						340.8			
	2	IIa	5	Quartz						327.4			
	3	IIb	10	Quartz						431.0			
	4	IIa	10	Quartz			-8.3			411.5		11.73	
	5	IIa	5	Quartz						388.3			
	6	IIa	5	Quartz						344.0			
	7	IIa	10	Quartz			-2.8			286.9		4.65	
	8	IIa	5	Quartz						407.7			
	9	IIa	5	Quartz			-3.4			280.5		5.54	
	10	IIa	5	Quartz			-3.0			291.4		4.94	
	11	IIa	5	Quartz			-2.5			290.6		4.17	
	12	IIa	5	Quartz			-1.8			382.3		3.06	
	13	IIIb	20	Quartz			-1.5			398.1		2.57	
	14	IIa	5	Quartz						326.0			
	15	I	10	Quartz		-59.0			-13.0				
	16	I	10	Quartz		-59.0			-12.7				

Sample No.	Inclusion No.	Inclusion type	Inclusion size (µm)	Host mineral	Visible CO_2 vol. % estimation	Last CO_2 melting temperature (°C)	Last ice melting temperature (°C)	Last clathrate melting temperature (°C)	CO_2 liquid homogenisation temperature (°C)	CO_2 vapour homogenisation temperature (°C)	Halite dissolution temperature (°C)	Salinity (wt.% NaCl eq.)	Calculated depth (bar)*
	17	IIa	15	Quartz			-3.0			313.7		4.94	
	18	IIa	5	Quartz			-2.5			270.1		4.17	
	19	IIa	5	Quartz						314.2			
	20	IIa	5	Quartz						409.8			
	21	IIa	10	Quartz						285.3			
	22	IIa	10	Quartz			-2.0			324.1		3.38	
	23	IIa	10	Quartz			-2.4			374.9		4.02	
	24	IIa	5	Quartz						392.3			
	25	IIa	10	Quartz			-9.7			>500		13.11	
	26	IIa	5	Quartz			-2.2			342.6		3.70	
	27	IIa	5	Quartz						310.9			
	28	IIa	5	Quartz						377.6			
	29	IIa	5	Quartz						364.5			
	30	IIa	10	Quartz			-2.2			332.6		3.70	
	31	IIa	5	Quartz						308.7			
	32	I	5	Quartz		-57.7							
	33	IIa	5	Quartz						376.7			
	34	IIa	5	Quartz						323.7			
	35	IIa	5	Quartz						321.7			
	36	IIa	5	Quartz						287.5			
	37	IIa	5	Quartz			-3.3			344.1		5.39	
	38	IIa	5	Quartz			-2.4			318.0		4.02	
	39	IIa	5	Quartz						263.0			
	40	IIa	5	Quartz						288.8			
	41	IIa	5	Quartz			-2.9					4.79	
	42	IIa	5	Quartz						391.4			
	43	IIa	5	Quartz						325.5			
	44	IIa	5	Quartz						361.9			
	45	IIa	5	Quartz						385.3			
DSDH249-499.1m	1	IIIa	15	Quartz		-60		7.3	12.0			5.23	
	2	IIa	10	Quartz		-60.8		5.0				9.04	
	3	IIa	10	Quartz	0.3	-58.4		7.1	20.0			5.59	
	4	IIb	10	Quartz						390.0			
	5	IIa	10	Quartz						324.4			
	6	IIa	5	Quartz						327.0			
	7	IIa	10	Quartz						390.8			
	8	IIIa	20	Quartz		-59.3				379.3			
	9	IIa	15	Quartz						391.0			
	10	IIa	10	Quartz				8.9		343.5		2.24	
	11	IIa	5	Quartz						333.6			
	12	IIa	10	Quartz		-57.7							
	13	IIa	10	Quartz		-57.3							
	14	IIa	5	Quartz		-57.4							

Sample No.	Inclusion No.	Inclusion type	Inclusion size (µm)	Host mineral	Visible CO_2 vol. % estimation	Last CO_2 melting temperature (°C)	Last ice melting temperature (°C)	Last clathrate melting temperature (°C)	CO_2 liquid homogenisation temperature (°C)	CO_2 vapour homogenisation temperature (°C)	Halite dissolution temperature (°C)	Salinity (wt.% NaCl eq.)	Calculated depth (bar)*
	15	IIa	10	Quartz			-0.3			412.8		0.53	
	16	IIa	10	Quartz			-1.1			357.0		1.91	
	17	IIb	10	Quartz						427.7			
	18	IIa	5	Quartz						371.2			
	19	IIa	5	Quartz						352.5			
	20	IIa	10	Quartz						401.2			
	21	IIa	5	Quartz						348.9			
	22	IIa	10	Quartz						265.3			
	23	IIa	5	Quartz			-0.4			368.6		0.70	
	24	IIa	5	Quartz						381.6			
	25	IIa	10	Quartz		-56.8							
	26	IIa	5	Quartz		-56.9							
	27	IIa	20	Quartz			-1.4			392.6		2.41	
	28	IIa	5	Quartz			-0.5					0.88	
	29	IIa	5	Quartz			-1					1.74	
	30	IIa	5	Quartz			-1					1.74	
	31	IIa	10	Quartz			-0.9					1.57	
	32	IIa	5	Quartz			-0.4			248.0		0.70	
	33	IIa	5	Quartz			-0.3					0.53	
	34	IIa	5	Quartz			-0.4					0.70	
	35	IIa	5	Quartz						346.8			
	36	IIa	10	Quartz			-0.7			358.5		1.22	
	37	IIb	10	Quartz						364.6			
	38	IIa	10	Quartz			-0.3					0.53	
	39	IIa	5	Quartz			-1.2					2.07	
	40	IIa	5	Quartz			-1.4					2.41	
	41	IIa	5	Quartz			-0.7			357.5		1.22	
	42	IIa	5	Quartz			-0.4					0.70	
	43	IIa	15	Quartz				2.2		337.6		12.98	
	44	IIa	5	Quartz				1.9		240.5		13.36	
	45	IIa	5	Quartz			-0.3			352.3		0.53	
	46	IIa	5	Quartz			-1.8			295.0		3.06	
	47	IIa	15	Quartz				1.3				14.10	
	48	IIa	25	Quartz				1.0		303.9		14.46	
	49	IIa	5	Quartz						426.0			
	50	IIa	5	Quartz						463.7			
	51	IIa	5	Quartz				0.1				15.50	
	52	IIa	5	Quartz			-9					12.85	
	53	IIa	10	Quartz						420.6			
	54	IIa	5	Quartz			-0.7			349.7		1.22	
	55	IIa	5	Quartz			-7.2					10.73	
	56	IIa	5	Quartz			-2.2			372.5		3.71	

*Calculated using FLINCOR software

Appendix XIV

Laser Raman Spectroscopic results

I: Gaseous composition

II: Daughter mineral identification

Appendix XIV-I

Laser Raman Spectroscopic results

(for gaseous compositions)

Appendix. XIV-I. Laser Raman Spectrometric data of fluid inclusions from Bai Dat deposit in the Phuoc Son deposit area, central Vietnam..

SAMPLE NUMBER	No. of analysis	CO_2 mol %	N_2 mol %	H_2S mol %	C_3H_8 mol %	CH_4 mol %	C_2H_6 mol %	NH_3 mol %	H_2 mol %	Remarks
DSDH111@78.8m	1	**96.6**	0.0	0.0	0.0	**3.4**	0.0	0.0	0.0	
	2	**98.1**	0.0	0.0	0.0	**1.9**	0.0	0.0	0.0	
	3	**97.8**	0.0	0.0	0.0	**2.2**	0.0	0.0	0.0	
	4	**96.7**	0.0	0.0	0.0	**3.3**	0.0	0.0	0.0	
	5	**94.0**	0.0	0.0	0.0	**6.0**	0.0	0.0	0.0	
TMBD11-13	1	**96.6**	**0.4**	0.0	0.0	**3.0**	0.0	0.0	0.0	
	2	**97.3**	0.0	0.0	0.0	**2.7**	0.0	0.0	0.0	
	3	**97.3**	0.0	0.0	0.0	**2.7**	0.0	0.0	0.0	
	4	**97.2**	**0.2**	0.0	0.0	**2.6**	0.0	0.0	0.0	
	5	**97.8**	**0.1**	0.0	0.0	**2.1**	0.0	0.0	0.0	
	6	**100.0**	0.0	0.0	0.0	0.0	0.0	0.0	0.0	
	7	**100.0**	0.0	0.0	0.0	0.0	0.0	0.0	0.0	multiphase
TMBD11-10	1	**95.1**	0.0	0.0	0.0	**4.9**	0.0	0.0	0.0	
	2	**94.9**	**2.8**	0.0	0.0	**2.3**	0.0	0.0	0.0	multiphase
	3	**93.1**	0.0	0.0	0.0	**6.9**	0.0	0.0	0.0	
	4	**90.5**	**6.6**	0.0	0.0	**3.0**	0.0	0.0	0.0	multiphase
	5	**93.8**	**2.4**	0.0	0.0	**3.8**	0.0	0.0	0.0	multiphase
	6	**93.2**	**0.4**	0.0	0.0	**6.4**	0.0	0.0	0.0	
TMBD11-09	1	**97.1**	**1.0**	0.0	0.0	**1.9**	0.0	0.0	0.0	
	2	**91.2**	**5.4**	**1.5**	0.0	**2.0**	0.0	0.0	0.0	
	3	**100.0**	0.0	0.0	0.0	0.0	0.0	0.0	0.0	
	4	**96.2**	0.0	0.0	0.0	**3.8**	0.0	0.0	0.0	multiphase
	5	**98.3**	0.0	0.0	0.0	**1.7**	0.0	0.0	0.0	multiphase
	6	**97.9**	0.0	0.0	0.0	**2.1**	0.0	0.0	0.0	multiphase
TMBD11-07	1	**94.7**	**2.0**	0.0	0.0	**3.3**	0.0	0.0	0.0	
	2	**62.9**	**35.4**	0.0	0.0	**1.8**	0.0	0.0	0.0	
	3	**91.2**	**0.9**	0.0	0.0	**7.9**	0.0	0.0	0.0	
	4	**97.5**	0.0	0.0	0.0	**2.5**	0.0	0.0	0.0	multiphase
	5	**98.0**	0.0	0.0	0.0	**2.0**	0.0	0.0	0.0	multiphase
	6	**97.6**	0.0	0.0	0.0	**2.4**	0.0	0.0	0.0	
DSDH270@453.4m	1	**80.6**	**14.0**	0.0	0.0	**5.4**	0.0	0.0	0.0	
	2	**74.1**	**21.0**	0.0	0.0	**4.9**	0.0	0.0	0.0	
	3	**54.6**	**43.6**	0.0	0.0	**1.8**	0.0	0.0	0.0	
DSDH257@463.4m	1	**94.8**	**4.8**	0.0	0.0	**0.4**	0.0	0.0	0.0	
	2	**97.0**	**2.5**	0.0	0.0	**0.4**	0.0	0.0	0.0	
	3	**95.7**	**3.9**	0.0	0.0	**0.4**	0.0	0.0	0.0	
	4	**97.5**	**2.2**	0.0	0.0	**0.3**	0.0	0.0	0.0	
	5	**96.8**	**2.8**	0.0	0.0	**0.4**	0.0	0.0	0.0	
	6	**100.0**	0.0	0.0	0.0	0.0	0.0	0.0	0.0	
	7	**100.0**	0.0	0.0	0.0	0.0	0.0	0.0	0.0	
	8	**97.2**	**2.3**	0.0	0.0	**0.5**	0.0	0.0	0.0	
	9	**97.9**	**1.7**	0.0	0.0	**0.4**	0.0	0.0	0.0	
	10	**97.9**	**1.8**	0.0	0.0	**0.2**	0.0	0.0	0.0	
DSDH257@463.5m	1	**0.7**	**15.5**	**0.9**	0.0	**82.9**	0.0	0.0	0.0	
	2	**0.9**	**15.5**	**0.7**	0.0	**82.9**	0.0	0.0	0.0	
	3	**93.6**	**4.0**	**0.2**	0.0	**2.2**	0.0	0.0	0.0	
	4	**93.2**	**3.9**	**0.5**	0.0	**2.4**	0.0	0.0	0.0	
	5	**98.5**	0.0	0.0	0.0	**1.5**	0.0	0.0	0.0	multiphase
	6	**67.7**	**22.5**	0.0	0.0	**9.8**	0.0	0.0	0.0	multiphase

Appendix. XIV-I (cont.). Laser Raman Spectrometric data of fluid inclusions from Bai Go deposit in the Phuoc Son deposit area, central Vietnam. .

SAMPLE NUMBER	No. of analysis	CO_2 mol %	N_2 mol %	H_2S mol %	C_3H_8 mol %	CH_4 mol %	C_2H_6 mol %	NH_3 mol %	H_2 mol %	Remarks
DSDH146@88.8m	1	**100.0**	0.0	0.0	0.0	0.0	0.0	0.0	0.0	
	2	**98.6**	0.0	0.0	0.0	**1.4**	0.0	0.0	0.0	
	3	**100.0**	0.0	0.0	0.0	0.0	0.0	0.0	0.0	
	4	**100.0**	0.0	0.0	0.0	0.0	0.0	0.0	0.0	
	5	**100.0**	0.0	0.0	0.0	0.0	0.0	0.0	0.0	
DSDH40@195.8m	1	**92.1**	0.0	0.0	0.0	**7.9**	0.0	0.0	0.0	
	2	**59.6**	0.0	0.0	0.0	**40.4**	0.0	0.0	0.0	
	3	**82.8**	0.0	0.0	0.0	**17.2**	0.0	0.0	0.0	
	4	**93.7**	0.0	0.0	0.0	**6.3**	0.0	0.0	0.0	
	5	**91.9**	0.0	0.0	0.0	**8.1**	0.0	0.0	0.0	
DSDH199@230.2m	1	**92.4**	0.0	0.0	0.0	**7.6**	0.0	0.0	0.0	
	2	**44.7**	0.0	0.0	0.0	**55.3**	0.0	0.0	0.0	
	3	**87.7**	0.0	0.0	0.0	**12.3**	0.0	0.0	0.0	
	4	**100.0**	0.0	0.0	0.0	0.0	0.0	0.0	0.0	
	5	**91.2**	0.0	0.0	0.0	**8.8**	0.0	0.0	0.0	
	6	**93.5**	0.0	0.0	0.0	**6.5**	0.0	0.0	0.0	
DSDH212@293.1m	1	**92.5**	**4.5**	0.0	0.0	**3.0**	0.0	0.0	0.0	
	2	**86.7**	**7.4**	0.0	0.0	**5.8**	0.0	0.0	0.0	multiphase
	3	**95.1**	0.0	0.0	0.0	**4.9**	0.0	0.0	0.0	multiphase
	4	**60.0**	0.0	0.0	0.0	**40.0**	0.0	0.0	0.0	multiphase
	5	**88.0**	0.0	0.0	0.0	**12.0**	0.0	0.0	0.0	multiphase
DSDH224@443.3m	1	**98.5**	0.0	0.0	0.0	**1.5**	0.0	0.0	0.0	
	2	**98.2**	0.0	0.0	0.0	**1.8**	0.0	0.0	0.0	
	3	**98.5**	0.0	0.0	0.0	**1.5**	0.0	0.0	0.0	
	4	**98.8**	0.0	0.0	0.0	**1.2**	0.0	0.0	0.0	
	5	**98.3**	0.0	0.0	0.0	**1.7**	0.0	0.0	0.0	
	6	**97.9**	0.0	0.0	0.0	**2.1**	0.0	0.0	0.0	
	7	**98.8**	0.0	0.0	0.0	**1.2**	0.0	0.0	0.0	
	8	**99.0**	0.0	0.0	0.0	**1.0**	0.0	0.0	0.0	
	9	**96.7**	0.0	0.0	0.0	**3.3**	0.0	0.0	0.0	
	10	**98.0**	0.0	0.0	0.0	**2.0**	0.0	0.0	0.0	
DSDH218@366.2m	1	**89.4**	0.0	0.0	0.0	**10.6**	0.0	0.0	0.0	
	2	**88.4**	0.0	0.0	0.0	**11.6**	0.0	0.0	0.0	
	3	**89.8**	0.0	0.0	0.0	**10.2**	0.0	0.0	0.0	
	4	**91.8**	0.0	0.0	0.0	**8.2**	0.0	0.0	0.0	
	5	**90.4**	**0.2**	0.0	0.0	**9.4**	0.0	0.0	0.0	
DSDH249@499.1m	1	**96.9**	0.0	0.0	0.0	**3.1**	0.0	0.0	0.0	
	2	**95.5**	0.0	0.0	0.0	**4.5**	0.0	0.0	0.0	
	3	**93.8**	0.0	0.0	0.0	**6.2**	0.0	0.0	0.0	
	4	**90.1**	0.0	0.0	0.0	**9.9**	0.0	0.0	0.0	multiphase

Appendix XIV-II

Laser Raman Spectroscopic results

(Mineral identification for solid-phase crystals)

TMBD11-07

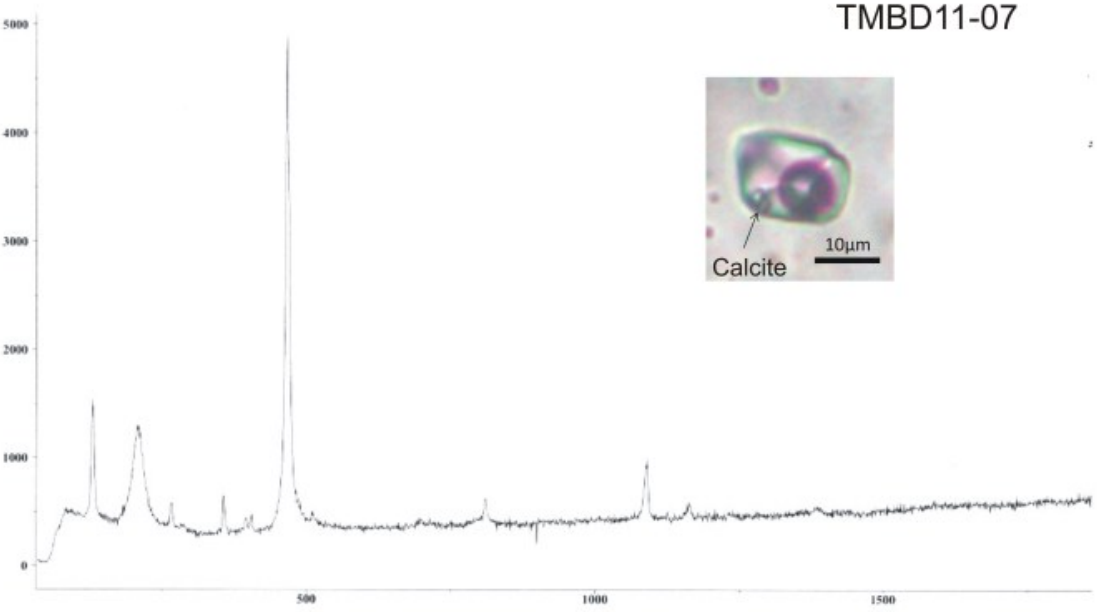

Sample	: TMBD11-07	Excit_line	: 514.532	Filtr	: ----
Operator	: Mernagh	Spectro	: 999.85	Accum	: 1
Date	: 17-02-112	Grating	: 1800	Objectiv	: x100
Power	: 50	Slit	: 100	File	: 11_07_4A
Time	: 30	Hole	: 400	Remark	: Calcite

Australian Government
Geoscience Australia

TMBD11-10

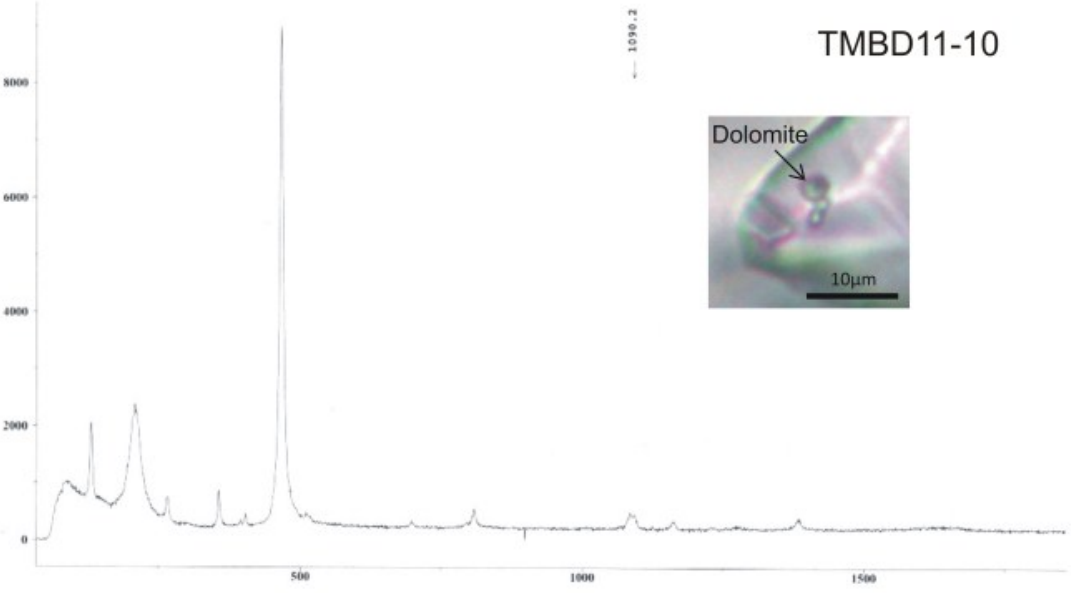

Sample	: TMBD11-10	Excit_line	: 514.532	Filtr	: ----
Operator	: Mernagh	Spectro	: 999.85	Accum	: 1
Date	: 16-02-112	Grating	: 1800	Objectiv	: x100
Power	: 50	Slit	: 100	File	: 11_10_2A
Time	: 30	Hole	: 400	Remark	: Dolomite?

Australian Government
Geoscience Australia

TMBD11-13

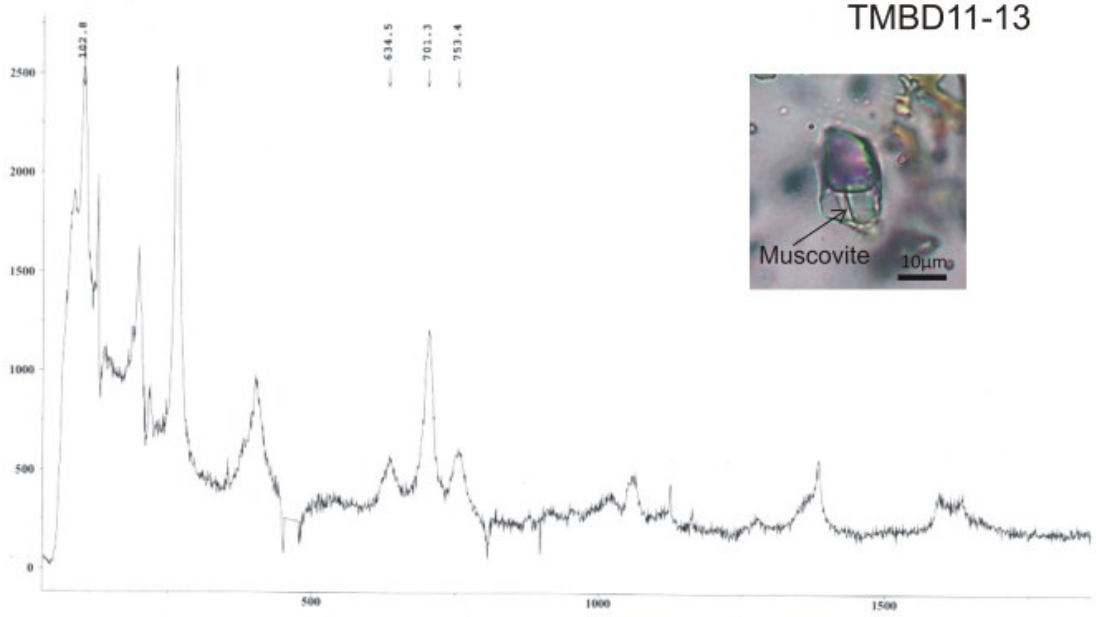

Sample	: TMBD11-13	Excit_line	: 514.532	Filtr	: ----
Operator	: Mernagh	Spectro	: 999.85	Accum	: 1
Date	: 15-02-112	Grating	: 1800	Objectiv	: x100
Power	: 50	Slit	: 100	File	: 11_13_7S
Time	: 30	Hole	: 400	Remark	: Muscovite

Australian Government
Geoscience Australia

DSDH257@463.5m

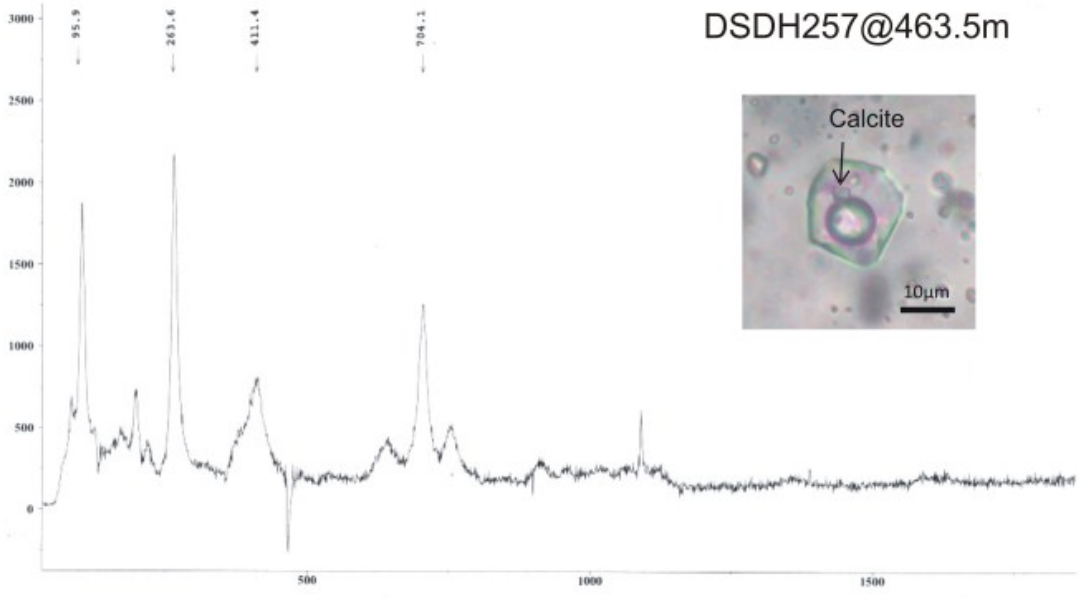

Sample	: DSD270-453.4m	Excit_line	: 514.532	Filtr	: ----
Operator	: Mernagh	Spectro	: 999.85	Accum	: 1
Date	: 17-02-112	Grating	: 1800	Objectiv	: x100
Power	: 50	Slit	: 100	File	: 453_4_3A
Time	: 20	Hole	: 400	Remark	: Muscovite

No gases detected

Australian Government
Geoscience Australia

DSDH270@453.4m

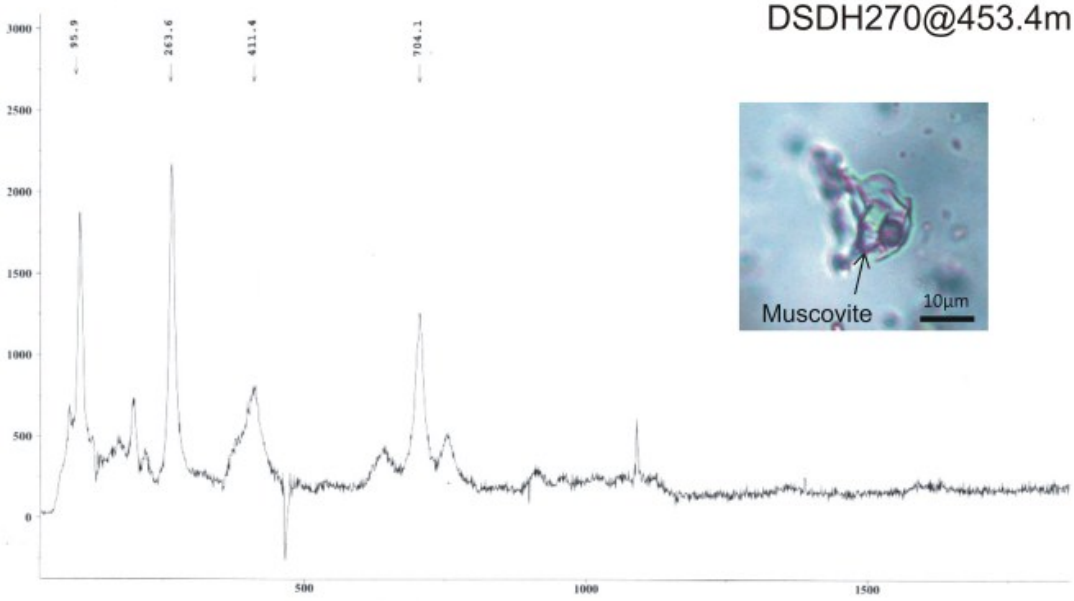

Sample	: DSD270-453.4m	Excit_line	: 514.532	Filtr	: ----
Operator	: Mernagh	Spectro	: 999.85	Accum	: 1
Date	: 17-02-112	Grating	: 1800	Objectiv	: x100
Power	: 50	Slit	: 100	File	: 453_4_3A
Time	: 20	Hole	: 400	Remark	: Muscovite No gases detected

Australian Government
Geoscience Australia

DSDH212@293.1m_a

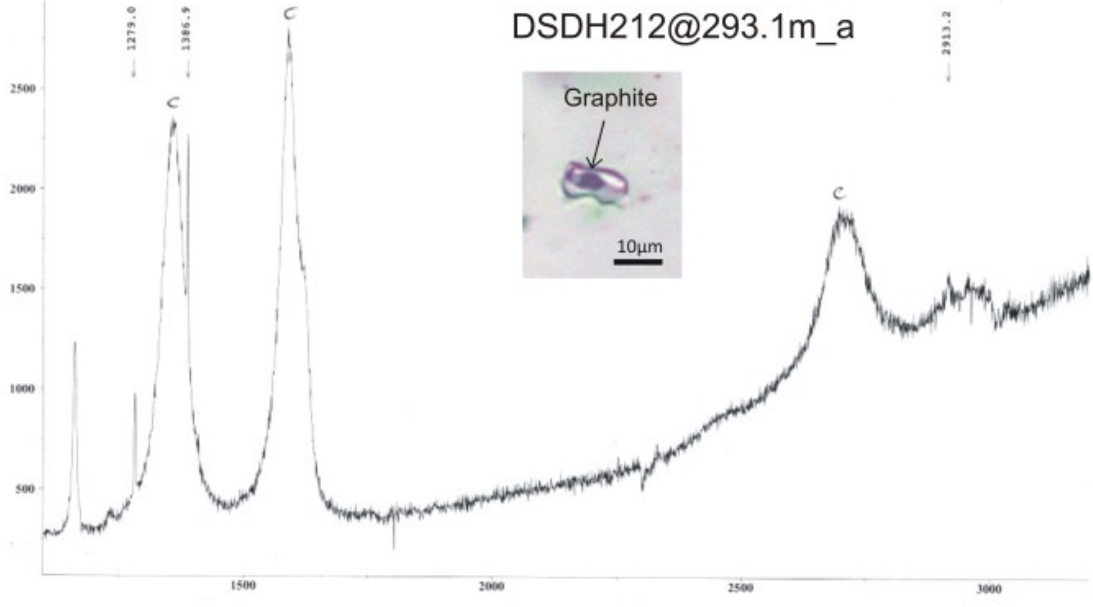

Sample	: DSDH212_293.1m	Excit_line	: 514.532	Filtr	: ----
Operator	: Mernagh	Spectro	: 1893.21	Accum	: 1
Date	: 22-02-112	Grating	: 1800	Objectiv	: x100
Power	: 50	Slit	: 100	File	: 293_1_2
Time	: 30	Hole	: 400	Remark	: Graphite

Australian Government
Geoscience Australia

DSDH212@293.1m_b

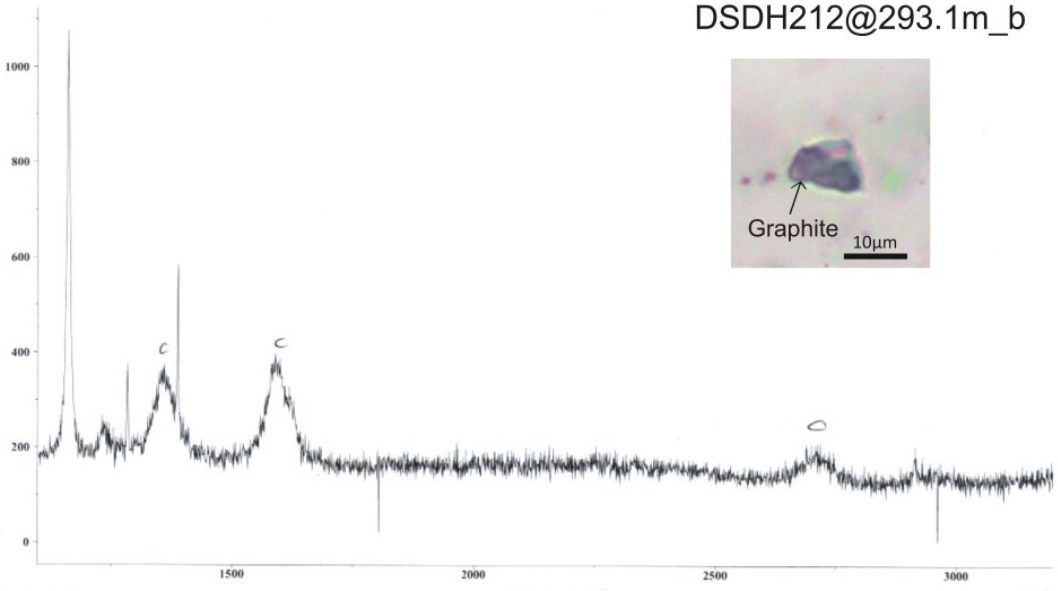

Sample	: DSDH212_293.1m	Excit_line	: 514.532	Filtr	: ----
Operator	: Mernagh	Spectro	: 1893.21	Accum	: 1
Date	: 22-02-112	Grating	: 1800	Objectiv	: x100
Power	: 50	Slit	: 100	File	: 293_1_3
Time	: 30	Hole	: 400	Remark	: + Graphite

Australian Government
Geoscience Australia